ISSN 0288-4534
CODEN: KPPJAD

KONA Powder and Particle Journal

No.39 (2022)

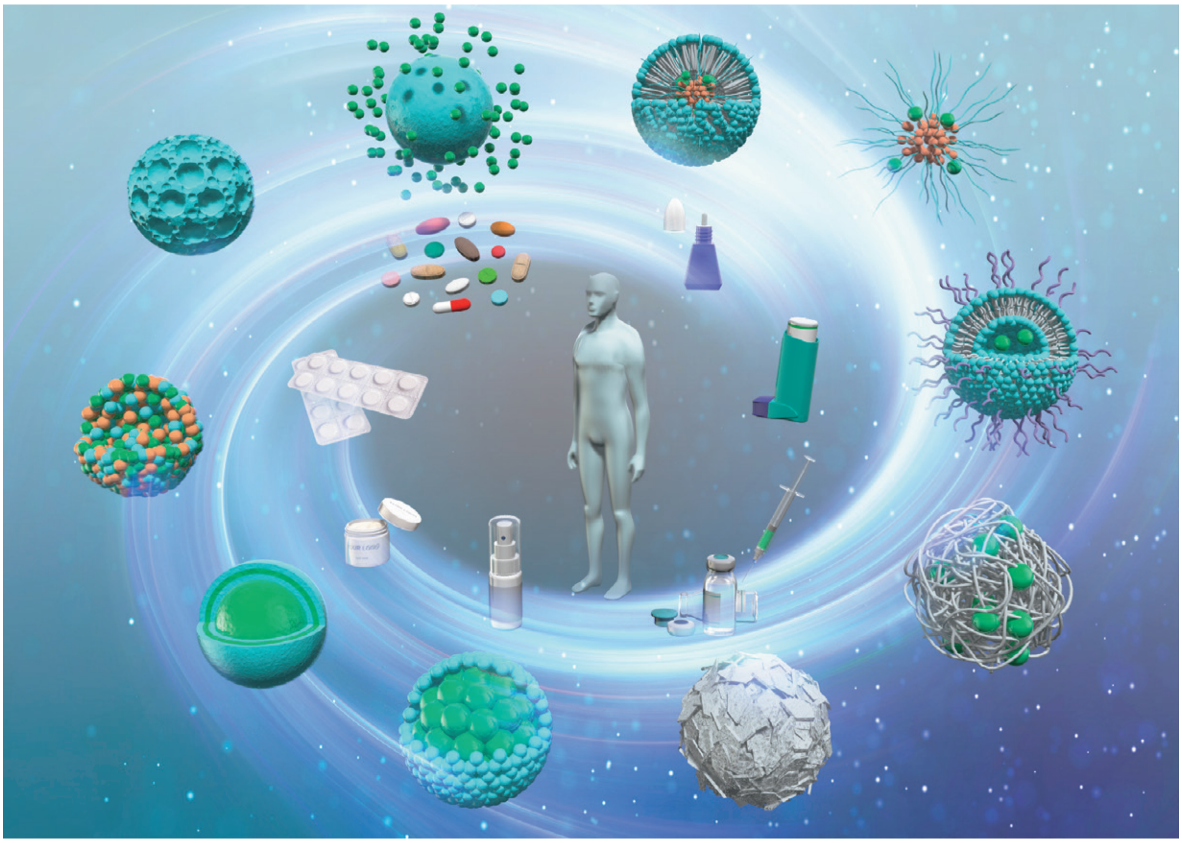

Hosokawa Powder Technology Foundation

available online-www.kona.or.jp

About this Journal

KONA Powder and Particle Journal is a refereed scientific journal that publishes articles in the field of powder and particle science and technology annually since 1983. This journal is distributed free of charge to the members of scientific communities and universities and research libraries throughout the world by the Hosokawa Powder Technology Foundation (www.kona.or.jp) established by Mr. Masuo Hosokawa in 1991.

The Chinese character “粉” in the cover is pronounced as “KONA” in Japanese, and means "Powder", which was hand-written by Mr. Eiichi Hosokawa, the founder of the Hosokawa Micron Corporation (www.hosokawamicron.co.jp/en/global.html).

About the Cover

Various types of particulate materials with controlled size, morphology, component and additive have been prepared via gas phase, liquid phase, and solid phase routes. These modified powder and particles have been applied as pharmaceutical drugs with different dosage forms ranging from tablets, capsules, eye drops, to injection. In order to achieve the effective and safe drug delivery, colloidal drug carriers such as liposomes, liquid emulsion, and polymeric nanoparticles have great potential to deliver drugs mainly by oral, pulmonary and ocular routes. Particle design research for a variety of pharmaceutical materials will contribute to the design of patient-friendly dosage forms to solve various issues related to the unmet medical needs of patients. Review on this topic is discussed on pp. 150–175.

Headquarters of Hosokawa Micron Corporation

Editorial Board

■ Publication Office
Hosokawa Powder Technology Foundation (www.kona.or.jp)
(in the headquarters building of Hosokawa Micron Corporation)
1-9, Shodaitajika, Hirakata-shi, Osaka 573-1132, Japan
E-mail: contact_zainq@hmc.hosokawa.com

■ Printing Office: Nakanishi Printing Co., Ltd., Japan
■ Publication Date: 10 January 2022

<Editorial>

<Review Papers>

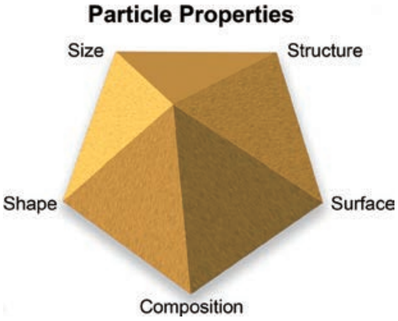
Particle Properties
Size
Structure
Shape
Surface
Composition

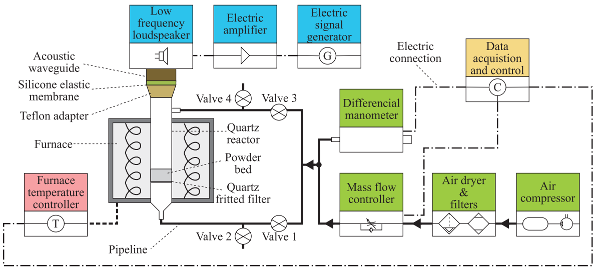
Low frequency loudspeaker
Electric amplifier
Electric signal generator
G
Electric connection
Data acquistion and control
C
Acoustic waveguide
Silicone elastic membrane
Teflon adapter
Furnace
Valve 4
Valve 3
Quartz reactor
Powder bed
Quartz fritted filter
Differencial manometer
Furnace temperature controller
T
Mass flow controller
Air dryer & filters
Air compressor
Valve 2
Valve 1
Pipeline

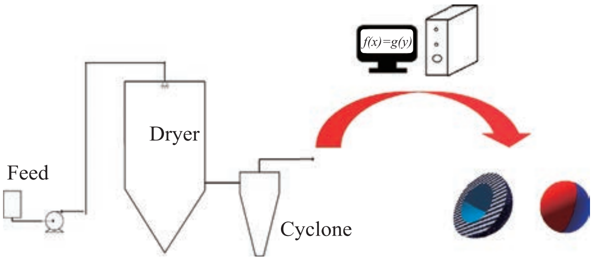
f(x)=g(y)
Dryer
Feed
Cyclone

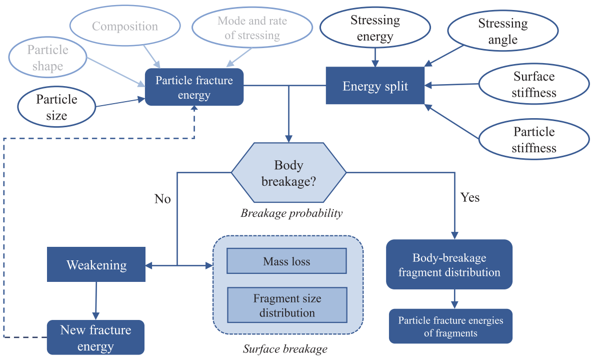
Composition
Mode and rate of stressing
Stressing energy
Stressing angle
Particle shape
Particle fracture energy
Energy split
Surface stiffness
Particle size
Particle stiffness
Body breakage?
No
Yes
Breakage probability
Weakening
Mass loss
Fragment size distribution
Body-breakage fragment distribution
New fracture energy
Particle fracture energies of fragments
Surface breakage

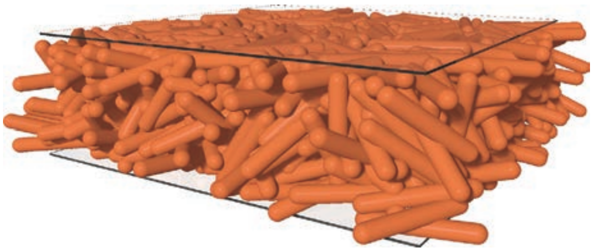

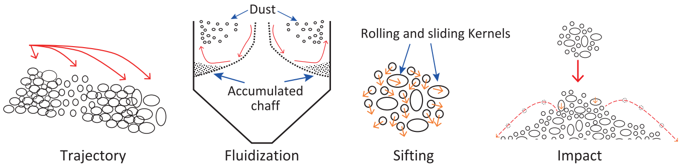
Dust
Accumulated chaff
Rolling and sliding Kernels
Trajectory
Fluidization
Sifting
Impact

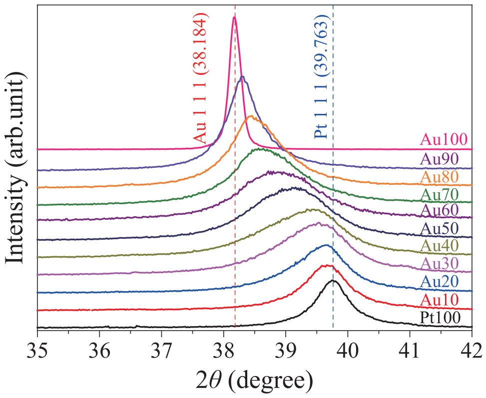
Au 1 1 1 (38.184)
Pt 1 1 1 (39.763)
Intensity (arb.unit)
Au100
Au90
Au80
Au70
Au60
Au50
Au40
Au30
Au20
Au10
Pt100
35
36
37
38
39
40
41
42
2θ (degree)

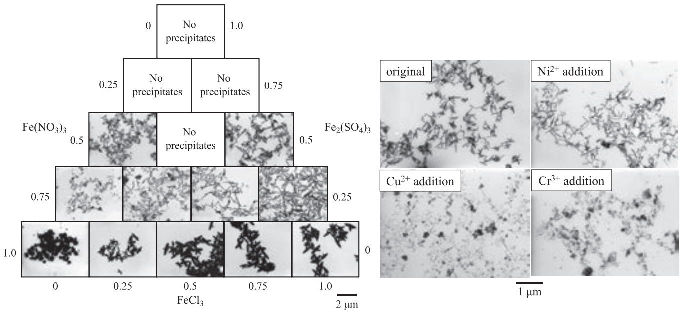
No precipitates
Fe(NO3)3
Fe2(SO4)3
FeCl3
0
0.25
0.5
0.75
1.0
2 µm
original
Ni2+ addition
Cu2+ addition
Cr3+ addition
1 µm

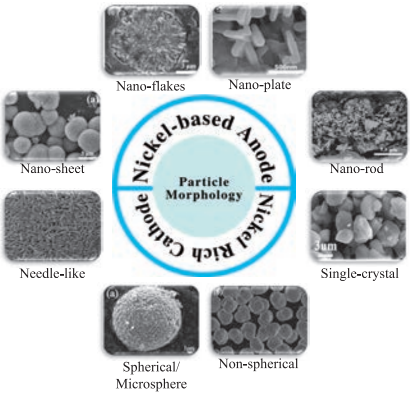
Nano-flakes
Nano-plate
Nano-sheet
Nano-rod
Nickel-based Anode
Particle Morphology
Cathode Nickel Rich
Needle-like
Single-crystal
Spherical/ Microsphere
Non-spherical

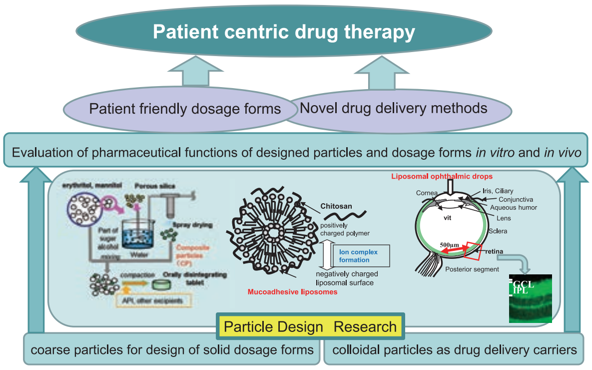
Patient centric drug therapy
Patient friendly dosage forms
Novel drug delivery methods
Evaluation of pharmaceutical functions of designed particles and dosage forms in vitro and in vivo
Liposomal ophthalmic drops
Cornea
Iris, Ciliary
Conjunctiva
Aqueous humor
Lens
Sclera
vit
500µm
retina
Posterior segment
GCL
IPL
Chitosan
positively charged polymer
Ion complex formation
negatively charged liposomal surface
Mucoadhesive liposomes
Particle Design Research
coarse particles for design of solid dosage forms
colloidal particles as drug delivery carriers

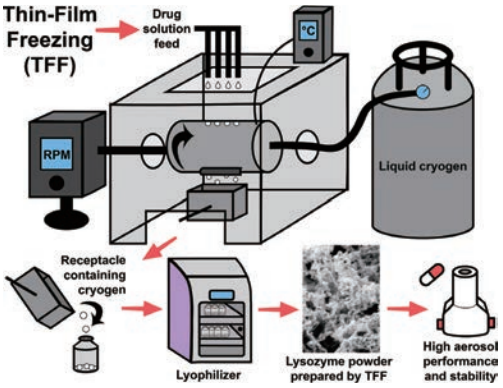
Thin-Film Freezing (TFF)
Drug solution feed
°C
RPM
Liquid cryogen
Receptacle containing cryogen
Lyophilizer
Lysozyme powder prepared by TFF
High aerosol performance and stability

<Original Research Papers>

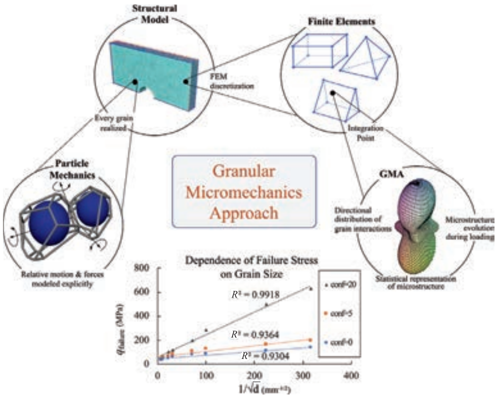
Structural Model
Finite Elements
FEM discretization
Every grain realized
Integration Point
Particle Mechanics
Granular Micromechanics Approach
GMA
Directional distribution of grain interactions
Microstructure evolution during loading
Relative motion & forces modeled explicitly
Statistical representation of microstructure
Dependence of Failure Stress on Grain Size
$R^2 = 0.9918$
$R^2 = 0.9364$
$R^2 = 0.9304$
conf=20
conf=5
conf=0
$q_{failure}$ (MPa)
800
600
400
200
0
100
200
300
400
$1/\sqrt{d}$ (mm$^{-1/2}$)

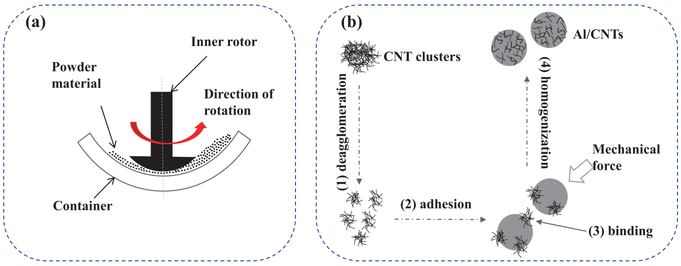
(a)
Inner rotor
Powder material
Direction of rotation
Container
(b)
CNT clusters
Al/CNTs
(1) deagglomeration
(4) homogenization
Mechanical force
(2) adhesion
(3) binding

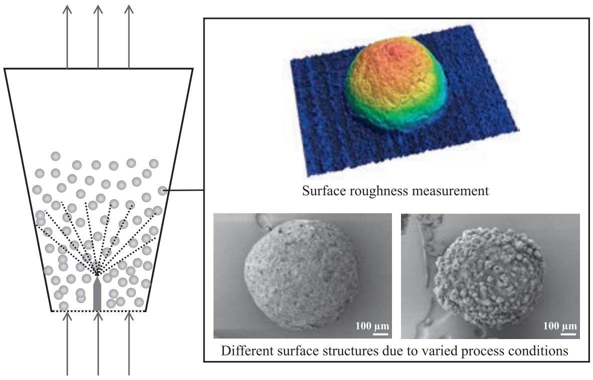
Surface roughness measurement
100 µm
100 µm
Different surface structures due to varied process conditions

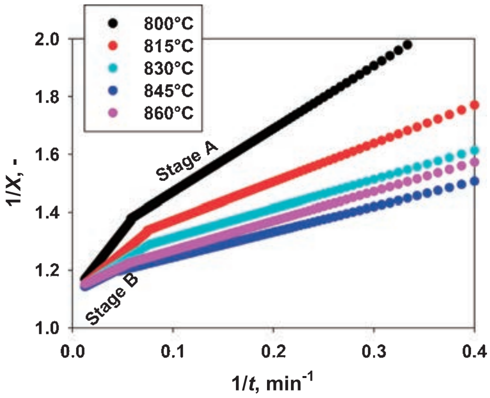
800°C
815°C
830°C
845°C
860°C
Stage A
Stage B
1/X, -
1/t, min⁻¹
2.0
1.8
1.6
1.4
1.2
1.0
0.0
0.1
0.2
0.3
0.4

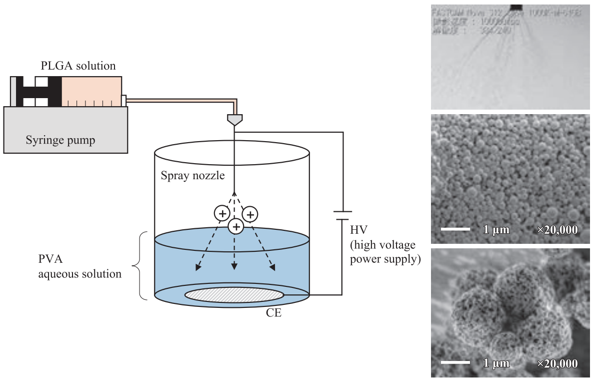

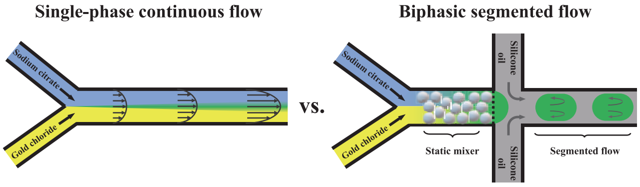

<Addition/Correction>

<Information Articles>

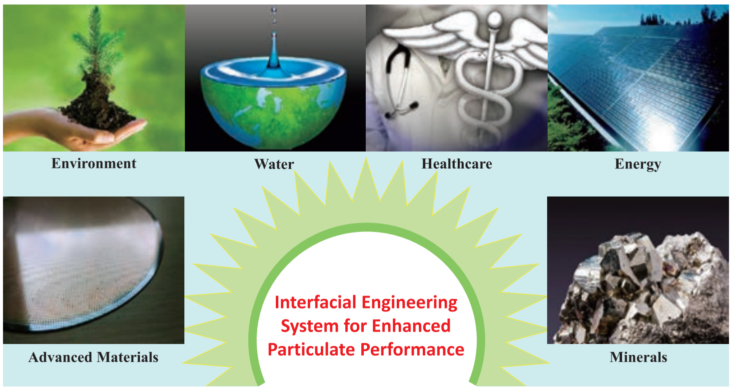

Selected research achievements for the KONA Award 2020: Interfacial engineering of particulate system for enhanced performance. (p. 276)

KONA Powder and Particle Journal No. 39 (2022) /https://doi.org/10.14356/kona.2022020 Editorial

Reviewer Appreciation

Kikuo Okuyama, Editor-in-Chief
Professor Emeritus, Hiroshima University, Japan

I would like to express my sincere gratitude to the reviewers for their hard work for the KONA Powder and Particle Journal. Thanks to the generous contributions of the volunteer reviewers as well as the interest of researchers in our journal, the number of submission to this journal is increasing after the registration on the major international journal platforms and its level is further improving. Thanks to their strong support and effort, I am pleased to inform that 2020 Impact Factor (JCR) of the KONA Powder and Particle Journal is increased to 2.897, with the CiteScore 2020 of 5.7. Because of the limited space of this annual journal, the number of papers published here is regrettably rather restricted. Therefore, only the papers of good quality will be selected for the journal and further improved and refined by the reviewing process. Moreover, we have created a channel on J-STAGE Data to enable authors to deposit, share and link to the data within their papers which will be or were published in this journal. J-STAGE Data which is the data repository provided by the Japan Science and Technology Agency (JST) enables KONA authors to contribute to the promotion of Open Science with the reviewers and editors.

The editorial team of the KONA Journal would like to take this opportunity to gratefully acknowledge the reviewers here and deeply appreciate their valuable time and professional contributions to the KONA Journal. We apologize to any reviewers who may have been inadvertently omitted from this list. We are sincerely grateful to all who have been of any assistance to the publication of this journal.

COPPENS, Marc-Olivier
HICKEY, Anthony
ICHIKAWA, Hideki
ISKANDAR, Ferry
KAWASAKI, Akira
KWADE, Arno
MEESTERS, Gabriel
MOUDGIL, Brij
OZEKI, Tetsuya
PURI, Virendra
RAJAMANI, Raj
RASTEIRO, Maria da Graça
SHIRAKAWA, Yoshiyuki
TAVARES, Luis Marcelo
YOKOYAMA, Toyokazu
ZHANG, Qiang

Kikuo Okuyama

October 2021

Editor's Preface

Wiwut Tanthapanichakoon
Asian / Oceanian Editorial Board
Fellow, Science Academy, the Royal Society of Thailand

It is my great honor and privilege to be invited by the Editor-in-Chief to write an Editor's Preface for the KONA Powder and Particle Journal No. 39. As mentioned by Prof. Brij M. Moudgil, the recent issues continue the tradition of presenting high quality review articles and original research papers. KONA is also reaching out to an ever-expanding cadre of researchers as illustrated by the diversity of discipline represented by the authors of the articles, thereby continuing to serve academic and industrial researchers from physical sciences to engineering and beyond.

As an international researcher who serendipitously entered this field and subsequently played a pivotal role as a sort of bridge between Thailand and Japan, I was greatly honored with an Imperial Decoration 'the Order of the Rising Sun, Gold Rays with Neck Ribbon' in Autumn 2016. Started over a half century ago, my relationship and involvement in powder/particle science and technology (or PST) encompass the establishment of the *Thai Powder Technology Center* with a strong support from Japan (Association of Powder Process Industry and Engineering; Society of Powder Technology) in 1992, followed by *Center of Excellence in Particle Technology*, both in Faculty of Engineering, Chulalongkorn University (CU) and the establishment of Thailand's *NANOTEC* (National Nanotechnology Center) in 2003 affiliated with National Science and Technology Development Agency. In retrospect, my serendipitous first brush with PST happened when I was an RA/PhD student in Prof. David M. Himmelblau's Lab, University of Texas at Austin from 1973–1978, and a Dr. Chikao Kanaoka, Kanazawa University (KZU), Japan, came to his Lab for 2 years as visiting scientist to carry out experimental research in atmospheric aerosol engineering. After graduation in late 1978, I immediately joined the Chemical Engineering Dept. of Chulalongkorn University in Bangkok and was persuaded by Dr. Kanaoka to apply for a short-term JSPS (Japan Society for the Promotion of Science) Fellowship to carry out research collaboration with him in Prof. Hitoshi Emi's Lab, KZU, in 1980. Starting essentially from scratch, in only 3 months I managed to develop, code, validate and simulate an innovative computer model for the stochastic convective diffusional deposition and dendritic growth of submicron aerosol particles on a single fiber using the Monte-Carlo method. It was deemed the first practical computer model of its kind as the random movement of submicron particles was governed by Brownian motion and the Langevin equation that was known to take a large amount of CPU time even on a supercomputer to simulate straight-forwardly without applying practical insight of Brownian diffusion to transform and simplify the equation.

As widely recognized globally, especially in the developed countries, powder/particle science and technology in Thailand has also played key roles in her industries and society, including environmental protection and human life well-being. For example, researchers of *NANOTEC* and their collaborators are active in developing and applying nanoparticle technology, including nanoencapsulation and nanosensors, to drug delivery and medical diagnosis (screening and monitoring) of diabetes, cervical cancer and breast cancer. Recently first-principle models and computer simulation of complex powder processing equipment have taken root in leading Thai industrial plants, including SCG Chemicals (*SCGCh*) where I am a full-time technology advisor, thanks to the availability of advanced software on CFD (Computational Fluid Dynamics) and DEM (Discrete Element Method) in tandem with high-performance computers as well as cloud computing.

Incidentally, I recently had an opportunity to fully participate over five weeks in an *Autonomous Systems AI Architect Training Workshop* offered by *SCGCh's* collaborator Microsoft. Based upon AI (more specifically, *deep reinforced learning* of AI machine learning coupled with availability of plant big data), a well-designed autonomous system should enable real-time optimization and control (*RTOC*) of large-scale chemical process plants, including powder/particle ones, in the foreseeable future. Currently, the insurmountable limitations of using reliable first-principle modeling of machinery and process equipment to simulate a large-scale petrochemical plant (which inevitably requires a huge amount of CPU time, thereby causing significant real time delay) in conjunction with huge collections of historical plant operational datasets (which generally suffer from lacking of diversity of wide-ranging operating conditions and reflect mostly steady-state non-dynamic conditions) have rendered the current implementation of plant-wide *RTOC* technically infeasible. However, a practical solution would be to develop and validate the necessary dynamic first-principle models of the whole process plant with the aid of decade-long historical plant data that include process disturbances and interruptions; then simulate the validated dynamic plant model to generate detailed dynamic responses to millions of different operational scenarios, including process disturbances and parametric uncertainty. Next an appropriately designed autonomous AI system is employed off-line to train itself using the generated big data and come up with reasonably reliable correlations between process inputs/parameters and the corresponding state variables/outputs. The derived correlations would next be used in place of the dynamic first-principle plant model to efficiently carry out timely plant-wide *RTOC*. The beauty of the AI methodology is that, even after the actual implementation of the *RTOC*, the autonomous system can continue to automatically learn and refine the existing correlations by making good use of the newly observed plant data. Though a dynamic powder processing system/plant is generally more complicated than a typical chemical plant, I believe that a similar, or perhaps some more innovative, AI methodology would be applicable to the implementation of *RTOC* of powder processing plants in the not too distant future. Last but not least, I look forward to the advent of articles related to AI and its applications to powder/particle science and technology in future issues of KONA Powder and Particle Journal.

Wiwut Tanthapanichakoon.

Wiwut Tanthapanichakoon
Asian / Oceanian Editorial Board
June 13, 2021

KONA Powder and Particle Journal No. 39 (2022) 3–28/https://doi.org/10.14356/kona.2022005 Review Paper

Progress in Multidimensional Particle Characterization†

Uwe Frank [1], Maximillian J. Uttinger [1], Simon E. Wawra [1], Christian Lübbert [1,2] and Wolfgang Peukert [1,2*]

[1] *Institute of Particle Technology (LFG), Friedrich Alexander Universität Erlangen-Nürnberg, Germany*
[2] *Interdisciplinary Center for Functional Particle Systems, Friedrich Alexander Universität Erlangen-Nürnberg, Germany*

Abstract

The properties of particle ensembles are defined by a complex multidimensional parameter space, namely particle size, shape, surface, structure, composition and their distributions. Macroscopic product properties are a direct result of these disperse particle properties. Therefore, the comprehensive multidimensional characterization of particle ensembles is a key task in any product design. However, the determination of complex property distributions is major challenge. We provide a broad overview of the current tools for multidimensional particle characterization. First, the mathematical handling of multidimensional (nD) property distribution is outlined as a necessary framework for the correct handling of nD particle size distributions (PSDs). Then, well-established techniques as well as recent developments with the potential to extract nD property distributions are reviewed. Ex-situ imaging techniques like electron tomography or Raman spectroscopy with AFM co-localization, for instance, provide a resolution on the level of single particles but are limited in terms of sample statistics. A particular focus lies therefore on methods in the gas and the liquid phase, which provide multidimensional particle properties either directly or by a combination of one-dimensional techniques.

Keywords: particle characterization, multidimensional measurement, nanoparticles, particle technology, particle properties, particle property distribution

1. Introduction

Modern micro- and nanoparticle systems are key to advancements in various applications including additive manufacturing (Ngo et al., 2018; Ligon et al., 2017), printable electronics (Kim D. and Moon, 2005), solar cells (Kim S.S. et al., 2008), fuel cells (Chan K.Y. et al., 2004), batteries (Wessells et al., 2012), medical applications (Murthy, 2007) and biomedical sensors (Polavarapu and Liz-Marzán, 2013). Functional particle systems are widely applied in many different fields because of their wide range of tunable physical properties. This rich behavior is the direct result of the five-dimensional parameter space that is defined by particle size, shape, surface, structure, and composition. The relationship between particle properties and the dispersity is known as property function and was first coined by (Rumpf, 1967)

$$\text{Property} = f\,(\text{dispersity}) \tag{1}$$

where the dispersity includes particle size, shape, surface, structure in terms of inner porosity, crystalline or amorphous phases and composition as well as their respective distributions. Examples for the manifold realizations of multidimensional (nD) particle systems are provided in **Table 1** and are highlighted in **Fig. 1**. The particle size ranges from about one nanometer for quantum dots up to several tens of centimeters for mineral particles. With the advent of nanoparticle technology, also particle shape came into focus. Prominent examples are plasmonic nanoparticles, where the shape influences the number and the position of the plasmonic resonance peaks (Yu R. et al., 2017). Below particle sizes of a few microns, particle surfaces become increasingly important. The ratio of van der Waals attraction between two spherical particles and particle weight scales with the inverse diameter squared, i.e. the dispersive particle interactions are orders of magnitude larger than the particle weight. Moreover, surface functionalization by molecules or small nanoparticles can be used to tailor particle-particle interactions and adhesion forces (Soto-Cantu et al., 2012; Giesbers et al., 2002). Core-shell structures are used for controlled release in life sciences or to enhance chemical stability.

The internal structure is most important for porous systems such as activated carbon, zeolites or metal-organic frameworks (MOF) (Holst and Cooper, 2010; Wang T.C.

---

† Received 15 July 2020; Accepted 19 August 2020
J-STAGE Advance published online 6 March 2021

* Corresponding author: Wolfgang Peukert;
Add: Cauerstraße 4, 91058 Erlangen, Germany
E-mail: wolfgang.peukert@fau.de
TEL: +49-9131-85-29400 FAX: +49-9131-85-29402

Table 1 Application examples of micro- and nanoparticle systems with multidimensional property distributions beyond size.

Disperse property	Application example
Shape	Plasmonic metal NPs [a], nanorods [b], platelets [a]
	2D materials, e.g. graphene [c], BN [d], MoS$_2$ [e]
	Semiconducting NPs, e.g. nanorods [f], tetrapods [g]
Surface	Control of surface energy [h], Hydrophilic-lipophilic balance [i]
	Roughness for controlled adhesion and powder flow [j]
	Surface chemistry for controlled reactivity [k]
	Charge for controlled colloidal stability [l]
	Toner size-charge (see E-SPART analyzer) [m]
	Core-shell microparticles, e.g. controlled release in life sciences [n]
	Core-shell semiconducting nanoparticles, e.g. CdSe@ZnS [o]
Structure	Amorphous vs crystalline particles [p]
	Polymorphic forms in pharmacy [q]
	Controlled pore size, e.g. in MOFs [r], zeolites [s] or pore size distributions, e.g. adsorbents such as activated carbon [t], CO$_2$-absorbers [u]
	Magnetic properties [v]
Complex compositions	Minerals [w]
	Semiconducting NPs, e.g. CIS [x], CZTS [y]
	Electrode materials, e.g. hybrid NPs [z], catalyst particles [aa]

[a] (Yu R. et al., 2017) [b] (Olson et al., 2015) [c] (Novoselov, 2011; Damm C. et al., 2015) [d] (Duan et al., 2016) [e] (Theerthagiri et al., 2017) [f] (Zhuang et al., 2020) [g] (Mokari et al., 2004) [h] Platz (Navrotsky, 2003; Finnegan et al., 2007) [i] (He et al., 2014; Maestro et al., 2012) [j] (Jallo et al., 2011; Tanaka et al., 2008; Esayanur et al., 2005) [k] (Yan et al., 2018) [l] (Kim K.M. et al., 2014; Zhong et al., 2012) [m] (Mazumder et al., 1991) [n] (Rey M. et al., 2020; Khan et al., 2015; Wang Y. et al., 2013) [o] (Zhang L. et al., 2011; Haubold et al., 2001; Gerdova and Haché, 2005) [p] (Dimitrov et al., 1999) [q] (Chistyakov and Sergeev, 2020) [r] (Hu J. et al., 2010; Brown J.W. et al., 2013) [s] (Roth et al., 2013) [t] (Yao and Lenhoff, 2004; Mangun et al., 2001) [u] (Del Rosso et al., 2016) [v] (Li Q. et al., 2017) [w] (Mogyorósi et al., 2003; Waychunas and Zhang H., 2008) [x] (So et al., 2016) [y] (Kannan et al., 2016) [z] (Lee J.S. et al., 2014) [aa] (Kleijn S.E.F. et al., 2012)

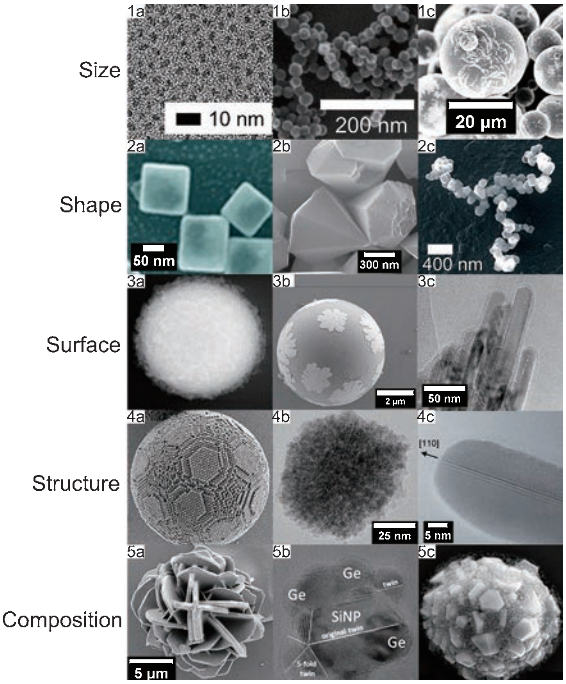

Fig. 1 Exemplary nano- and microparticle systems sorted by their underlying properties, which are defined by the five parameters namely size, shape, surface, structure and composition. Size: **(1a)** lead tin quantum dots, **(1b)** silicon nanoparticles, **(1c)** spherical polybutylene terephthalate polycarbonate blend particles. Shape: **(2a)** gold nanocubes after a HAuCl$_4$ solution was added, **(2b)** zinc oxide prisms, **(2c)** aggregated silicon nanoparticles in toluene. Surface: **(3a)** nanoparticle with complex surface, **(3b)** silver patches grown on borosilicate microsphere, **(3c)** functionalized ZnO nanorod. Structure: **(4a)** colloidal crystal, **(4b)** hematite mesocrystal, **(4c)** silver nanorod. Composition: **(5a)** Cu/Zn catalyst precursor, **(5b)** Silicon Germanium hybrid nanoparticle, **(5c)** kesterite crystal. Reproduced with permission from (Frank U. et al., 2019) Copyright 2019, Wiley.

et al., 2015; Hu Z. and Srinivasan, 2001). Also, particles, which are composed of several crystalline or amorphous phases, belong to that group. Minerals but also advanced semiconducting particles (e.g. CIS, CTZS, battery materials or active catalysts) often have a rich phase behavior (Hochella et al., 2008). Little is known if and how it depends on size. At the lower nanoscale, even the phase behavior of less intricate materials such as alumina (Sun J. and Simon, 2007) or CdS is size-dependent (Neeleshwar et al., 2005; Eom et al., 2013).

In order to study these complex phenomena, various nano- and microparticle systems have to be characterized with respect to structural (via the dispersity) and functional properties. Examples depending on the five-dimensional parameter space are highlighted in **Table 2**.

Characterization tools provide single mean or distributed parameters like the volume-equivalent, the hydrodynamic or the sedimentation-equivalent diameter (Modena et al., 2019). With increasing complexity in terms of nD particle parameters it becomes more and more difficult to interpret direct measurement results. Different combinations of dispersed particle properties can lead to the same value of a measured quantity, e.g. the volume of a particle. Combining results from different measurement techniques or using experimental setups, which are sensitive to nD properties directly, are therefore required in order to gain more information on complex particle systems.

The objective of this review is to provide an overview of past and current developments concerning the multidimensional characterization of particles. In a few recent cases,

Table 2 Multi-dimensional particle properties for technological and functional properties.

Technological properties	Transport properties: size, density, shape [a]
	Powder flow: surface, size, shape, structure [b]
	Packing characteristics: size, shape, structure [c]
	Colloidal stability: size, shape, composition [d]
Functional properties	Mechanical properties: size, structure, composition [e]
	Optical properties: size, shape, structure, composition [f]
	Electronic and magnetic properties: size, shape, structure, composition, surface [g]
	Chemical properties: surface, structure, composition [h]
	Sensory properties, e.g. taste: size, composition, structure [i]
	Thermodynamic properties, e.g. solubility, melting, sintering: size, surface, composition [j]

[a] (Hansen 2004; La Torre et al., 2007; Wawra et al., 2018) [b] (Schmidt J. et al., 2014) [c] (Parteli and Pöschel, 2016) [d] (Chemseddine and Weller H., 1993; Gudarzi, 2016) [e] (Herre P. et al., 2017) [f] (Yu R. et al., 2017; Link S. et al., 1999; Motl et al., 2010) [g] (Zhang W. et al., 2003; Sharma et al., 2010; Zhu M. et al., 2012) [h] (Domaschke et al., 2019) [i] (Fathi et al., 2013; Davidov-Pardo et al., 2015; Joye I.J. and McClements, 2014) [j] (Letellier et al., 2007; Guisbiers, 2019; Castro and Gouvêa, 2016; Li W. et al., 2016)

two-dimensional (2D) information was obtained from one single experiment as will be highlighted in this review. First, a thorough mathematical description of multidimensional particle ensembles will be provided. Comparability of measurement results from different techniques can be achieved by taking different weightings into account. The derivation of one-dimensional (1D) distributions from multidimensional distributions is always possible while the reverse case, i.e. the derivation of multidimensional distributions from 1D ones, is an ill-posed problem. Based on this theoretical background, the focus of the review lies on experimental procedures. Therefore, comprehensive techniques based on microscopic imaging and characterization methods for gas phase and liquid phase analysis are reviewed and critically discussed with respect to their potential for nD particle characterization.

2. Multidimensional particle size distributions

As the properties of nano- and micron-sized particles are typically distributed, mathematical tools for property distributions require a comprehensive description. Most often the size of particles is the key parameter, as many properties of particulate products are influenced by their size distribution. Only for spherical particles, the size can be described by using a single parameter, i.e. the diameter. In the general case, particle size of an irregular particle is understood in terms of an equivalent size, such as the diameter of a sphere of equal volume, equal surface or equal hydrodynamic transport behavior. To date, disperse particle systems are mostly characterized by one-dimensional (1D) particle size distributions (PSDs), which were comprehensively described by Rumpf and Leschonski (Leschonski K. et al., 1974a; 1974b). This concept has proven to be very useful for rather simple particle systems but must be expanded for the description of more complex particle systems. One general difficulty is that different particle parameter sets can lead to the same equivalent diameter, e.g. different diameter and length combinations of a rod-like particle result in the same volume-equivalent diameter. Therefore, a nD description of complex particle ensembles is required. In general, nD PSDs are defined as (Frank U. et al., 2019)

$$q_r(\vec{x}) = \frac{\text{Amount of kind } r \text{ in interval } d\vec{x}}{\text{interval size } d\vec{x} \text{ * total amount of kind } r} \tag{2}$$

with the nD PSD q_r of the random vector $\vec{\boldsymbol{x}} \in \mathbb{R}^n$. The distribution q_r fulfils several requirements, it is non-negative, integrable and normalized. The index r is related to the weighting of the PSD. Depending on the measurement technique, PSDs are differently weighted, based on the underlying physical measurement principles, e.g. counting ($r = 0$) or weighing, ($r = 3$). If not taken into account, the weighting introduces comparability issues between different measurement techniques (Modena et al., 2019). In the 1D scenario, it is very convenient to convert differently weighted PSDs into each other, e.g. from kind k to kind r (Leschonski K. et al., 1974a; 1974b)

$$q_r(x) = \frac{x^{r-k} q_k(x)}{M_{r-k,k}} \tag{3}$$

with the moment $M_{r-k,k} = \int_{x_{\min}}^{x_{\max}} x^{r-k} q_k(x)\, \mathrm{d}x$, which is calculated by integration from the minimum $x_{\min}$ to the maximum particle size $x_{\max}$. Of course, the situation is more complicated in the nD case. Here, weighting functions need to be considered and the notation is slightly adapted (Frank U. et al., 2019)

$$q_r(\vec{x}) = \frac{q_k(\vec{x})\,\kappa(\vec{x})}{M_{r,k}} \tag{4}$$

with the weighting function κ, which maps the random vector $\vec{x}$ to a positive scalar. An intuitive example is the volume of a regular, non-spherical particle (e.g. a rod or platelet), which is calculated from the particle geometry parameters of length and diameter. The denominator is defined as generalized moment $M_{r,k} = \int_{\vec{x}\in\mathbb{R}^n} q_k(\vec{x})\,\kappa(\vec{x})\,\mathrm{d}^n x$. A simple example for a 2D PSD alongside the extraction of 1D distributions of linked variables is presented in the following paragraphs.

2.1 Two-dimensional particle size distributions

The concept of 2D PSDs was recently illustrated for the example of normal-distributed gold nanorods, which are characterized by their length l and diameter d (Frank U. et al., 2019), and is recapped here for an intuitive way of understanding multidimensional distributions. Similar conclusions and relations hold true for the case of a 2D log-normal distribution with two log-scaled axis.

To demonstrate the influence of different weightings, the surface weighted q_2 and volume weighted q_3 distributions were calculated from the number-weighted PSD q_0 via Eq. 4. Here κ is replaced with functions for the surface and volume

$$S(d,l) = \frac{1}{2}\pi d^2 + \pi dl \tag{5}$$

$$V(l,d) = \frac{\pi}{4} d^2 l \tag{6}$$

A comparison of the obtained distributions can be found in **Fig. 2**. The function maximum is depicted with a star alongside an isoline, which illustrates the shape of the distribution. A significant shift within the distributions is clearly visible and stresses the importance of the different weightings. The stars indicate the modal values, which shift from finer to coarser values for the length and diameter.

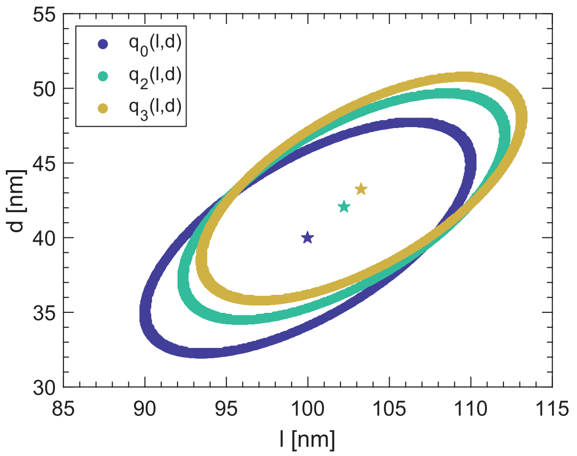

Fig. 2 Comparison of differently weighted PSDs. Depicted are the number-weighted q_0, surface-weighted q_2 and volume-weighted q_3 PSD of gold nanorods. The stars indicate the maximal values of the distribution. The line is an isoline at the value $\frac{1}{\sqrt{e}}\max(q_i)$. Reproduced with permission from (Frank U. et al., 2019). Copyright 2019, Wiley.

2.2 Calculation of one-dimensional data from two-dimensional particle size distributions

With the 2D PSDs at hand, it is possible to calculate respective 1D distributions. This can be performed either via marginalization or via the calculation of a linked variable. Marginalization is the simpler case. Here one can calculate the distributions for length and diameter simply by integration with respect to the complementary variable, e.g.

$$q_0(l) = \int_{d_{\min}}^{d_{\max}} q_0(l,d)\ \mathrm{d}d \tag{7}$$

The more general case is to obtain r weighted 1D distributions ρ of a linked variable y, like sedimentation coefficient, aspect ratio or volume. This can be achieved via conditional integration to obtain the cumulative distribution function (CDF) and subsequent derivation

$$\rho(y) = \frac{\mathrm{d}}{\mathrm{d}y} \int_{\{\vec{x}\in\mathbb{R}^n | f(\vec{x})\le y\}} q_r(\vec{x})\,\mathrm{d}^n x \tag{8}$$

with the mapping function $f(\vec{x})$. Applied to the 2D case of the aspect ratio v of a rod-like particle, which is defined as the ratio of length to diameter $v = l/d$, one obtains

$$\begin{aligned} \rho(v) &= \frac{\mathrm{d}}{\mathrm{d}v} \iint_{\{l,d\,|\frac{1}{d}\le v\}} q_0(l,d)\,\mathrm{d}l\ \mathrm{d}d \\ &= \frac{\mathrm{d}}{\mathrm{d}v} \int_{d_{\min}}^{d_{\max}} \int_{l_{\min}}^{d\cdot v} q_0(l,d)\,\mathrm{d}l\ \mathrm{d}d \end{aligned} \tag{9}$$

This can be interpreted as calculation of a cumulative distribution of the aspect ratio with subsequent derivation, which is illustrated in **Fig. 3**. The calculation of other distributions can be performed analogously. This procedure enables the calculation of various quantities from 2D nanoparticle property distributions.

Furthermore, 1D weight-dependent expected values (weight averages) E_r can be computed from the 1D distributions via evaluation of the integral

$$\begin{aligned} E_r(y) &= \int_{\mathbb{R}} y\rho(y)\,\mathrm{d}y \\ &= \int_{\mathbb{R}} y\left(\frac{\mathrm{d}}{\mathrm{d}y}\int_{\{\vec{x}\in\mathbb{R}^n | f(\vec{x})\le y\}} q_r(\vec{x})\,\mathrm{d}^n x\right)\mathrm{d}y \end{aligned} \tag{10}$$

Applied to the example above, one can obtain the number-weighted mean aspect ratio via

$$\begin{aligned} E_0(v) &= \int_{\mathbb{R}} v\rho(v)\,\mathrm{d}v \\ &= \int_{\mathbb{R}} v(\frac{\mathrm{d}}{\mathrm{d}v} \int_{d_{\min}}^{d_{\max}} \int_{l_{\min}}^{d\cdot v} q_0(l,d)\ \mathrm{d}l\ \mathrm{d}d)\ \mathrm{d}v \end{aligned} \tag{11}$$

Equivalent calculations for other physical quantities, e.g. mean sedimentation coefficient, mean mobility diameter etc. are possible.

In summary, this section provided a detailed overview of the current state-of-the-art for the mathematical handling of nD particle property distributions. However, their

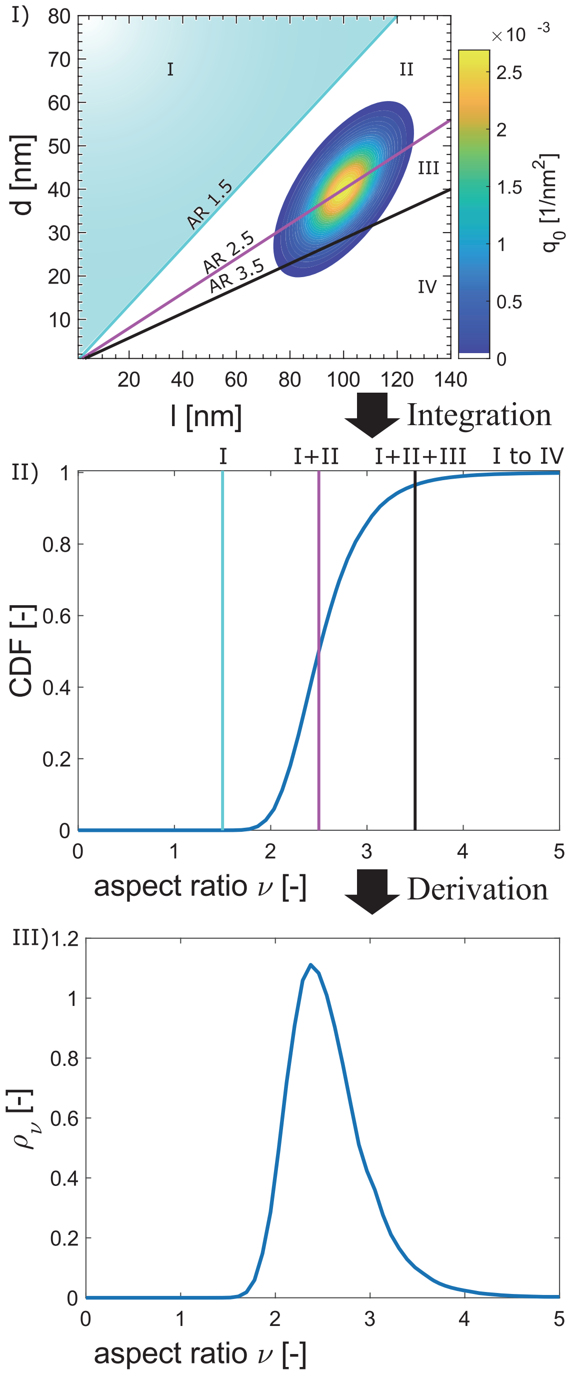

Fig. 3 Schematic way to obtain a distribution of a linked variable. In **(I)** a 2D Gaussian PSD is depicted alongside lines indicating different aspect ratios. In **(II)** the CDF is displayed, which is obtained by integration of the areas and which are defined by the lines of constant aspect ratios in **(I)**. Derivation of the CDF leads to the 1D distributions of the aspect ratio in **(III)**. Reproduced with permission from (Frank U. et al., 2019). Copyright 2019, Wiley.

experimental retrieval is a quite challenging task. Recent progress in novel experimental approaches allows the determination of higher dimensional property functions. In the following sections, we will present some of the most relevant characterization methods and briefly recap their underlying physical principle and the respective results.

3. Image analysis and microscopy

Manifold different analytical techniques exist to directly image particles. The underlying principles used for image characterization of samples vary across the length scales of the material systems under investigation. Apart from the multidimensional characterization in terms of geometry, other complementary techniques based on spectral or electronic characterization are used to retrieve correlations of certain physical properties like the size and chemical composition of particles. While it is possible to acquire detailed data on the single particle level, statistically reliable characterization of particle ensembles requires a significant number of measured particles. In the case of 1D properties, usually hundreds to thousands of particles are analyzed (Rice et al., 2013; Nacken T.J. et al., 2015; Verleysen et al., 2019). Estimations for sufficient particle numbers exist, see e.g. (Stieß, 1995). For instance, the determination of the median particle size within +/– 3 % accuracy and a confidence interval of 95 % requires counting of close to 5000 particles, counting only 400 particles leads an accuracy of only 10 %. For the determination of nD PSDs, the number of particles that need to be investigated must be even higher to avoid obtaining data of limited accuracy and reliability. Many publications using image based characterization are clearly below these numbers, even though software-based image analysis can help reducing the temporal effort of acquiring particle size and shape information (Verleysen et al., 2019; Frei and Kruis F.E., 2020).

Furthermore, microscopic techniques require careful sample preparation from the gas or liquid phase to separate individual particles on a substrate. Sampling can lead to various artefacts and systematic errors by size-selective deposition, drying or agglomeration.

3.1 Light microscopy

Imaging single particles (reasonably larger than the wavelength) with light enables determining their 2D projection on a substrate or directly in sufficiently dilute and thus optically transparent flowing systems. Particles on a substrate typically lie in their stable position while particles imaged in a flowing gas or liquid can be viewed from different projections. Analysis on-the-fly is excellent to image a very high numbers of particles to enhance the statistical reliability of such measurements. Image analysis of projected areas of particles in flow cells has been applied in order to retrieve nD information on particle properties (Bujak and Bottlinger, 2008). More details on the concepts of flow cells can be found in **Section 5.1**. Recently, a novel omics-like method has been proposed collecting images of > 2,000,000 particles (of several 10 µm in size) per sample in sediments, soils and dusts by a Sympatec GmbH QICPIC particle size and shape analyzer. The morphological descriptors of each particle including equivalent diameter, sphericity, aspect ratio and convexity were extracted as the "particle morphome", an outcome of the large data set (Sun Y. et al., 2019).

Furthermore, light microscopy is often used as a prior step to find a valid measurement position in spectroscopy applications like Raman or fluorescence spectroscopy. The combination of these techniques is rather common and therefore not subject of this review.

Raman spectroscopy itself can be a valuable tool for the analysis of the composition of a sample or the identification of polymorphs of e.g. organic crystals in pharmaceutical applications. A current trend in energy conversion and storage is towards particles consisting of three (e.g. chalcogenide such as $CuInS_2$), four (kesterites such as Cu_2InZnS_4) or even multinary components. The same holds true for complex catalyst or advanced battery materials. A particular challenge during synthesis is the formation and identification of binary, ternary or quaternary by-products (see e.g. (Ahmad et al., 2017)). Statistical composition mapping via Raman spectroscopy, supported by atomic force microscopy (AFM) co-localization, is very promising to study size-dependent composition in such particulate products (Nacken T. et al., 2015).

The limitations of using solely light microscopy in terms of particle projections can be overcome via the use of digital holography (DH), which allows determining the three-dimensional (3D) structure of micron-sized particles. DH is based on interferometric imaging. As shown in **Fig. 4**, interference patterns between diffracted light from the object and a reference wave are formed. Sophisticated image analysis allows to reconstruct intensity and phase images, which can be transformed to yield 3D information (Tahara et al., 2018).

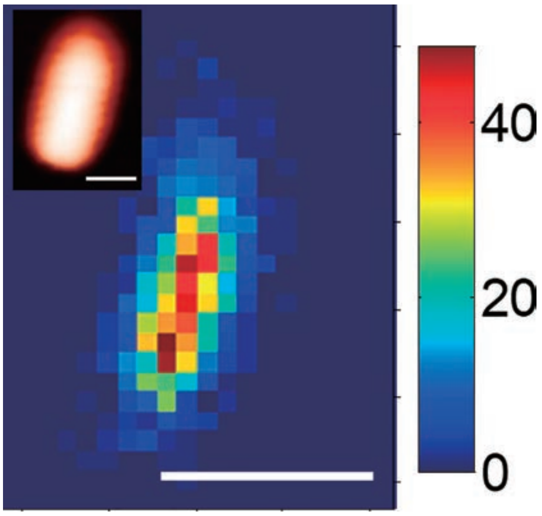

Fig. 4 Reconstructed spatial intensity image obtained from a gold nanorod covered with fluorophore, obtained via super-resolution microscopy. The oval shows the dimensions of the particle obtained via AFM (see inset). Scale bars are 50 nm, the colour coded heat map indicates the spatial fluorescence intensity distribution. Reproduced from (Willets et al., 2017) with permission from American Chemical Society, Copyright 2017.

The resolution of light-based microscopes is physically restricted by the Abbe diffraction limit, which hinders single particle investigations of nano-sized objects by conventional light microscopy (Siedentopf and Zsigmondy, 1902). The advent of super-resolution microscopy enhanced the measurement range for fluorescent labelled samples. The combination of other techniques with super-resolution microscopy is possible, although most applications are focusing on biological samples (Hauser M. et al., 2017). An example for the use of super-resolution microscopy for particle characterization is the determination of the particle geometry of anisotropic plasmonic particles. The single emission of the fluorophores that are attached to the particle can be utilized to determine the shape and size of the particle, as shown in **Fig. 4**. However, care needs to be taken to avoid localization errors due to the interaction of the fluorophore with the substrate or due to a changing dielectric environment (Willets et al., 2017).

3.2 Computed tomography

Using illumination sources with smaller wavelengths (electrons, X-rays, neutrons) considerably improves the resolution. The spatial resolution of X-ray computed tomography (X-ray CT) can reach below 100 nm (Maire and Withers, 2014) depending on the light source. Recently, Leißner et al. reviewed the application of X-ray CT in the field of particle technology (Leißner T. et al., 2020). The technique relies on the spatially resolved detection of the X-ray transmission of a sample. The 3D structure of an immobilized sample can be reconstructed from the detection of projections from different directions. Individual X-ray attenuations are assigned as grey values to volume elements. These depend on the material density and the average atomic number, which allows to distinguish between different materials but may also exclude certain materials or material combinations from thorough analysis due to similarities or - in contrast - large differences in grey values (Leißner et al., 2020; Ketcham and Carlson, 2001). This limitation can be overcome with higher experimental effort, by e.g. taking into account the energy- and material-specific attenuation of X-rays via hyperspectral X-ray tomography (Egan et al., 2015). Stochastic modelling of nD particle properties can further help to identify different material classes from a X-ray CT experiment (Furat et al., 2019). Correlations between particle composition and characteristic particle properties like volume, sphericity or the median grey value can be used to identify the 3D structure and material classes from an X-ray CT experiment. Therefore, the authors calibrated their stochastic model via scanning electron microscopy (SEM) – energy-dispersive

X-ray (EDX) measurements (see **Section 3.4**). Particle characterization of e.g. crystals via X-ray tomography can be improved by utilizing models of particle shape. The identification of the crystal's face normals offers thus interesting options for the robust evaluation of size- and shape distributions (Kovačević et al., 2014).

3.3 Atomic force microscopy

Atomic force microscopy (AFM) is a surface sensitive technique based on tracking the oscillation and the position of a cantilever equipped with a nano-sized tip close to the surface under investigation (Binnig et al., 1986). Various measurement modes exist, which not only allow the determination of the geometry of anisotropic particles via evaluation of the sample topography but also provide information on surface roughness or mechanical properties and adhesion forces (Voigtländer, 2019).

The combination of AFM with other techniques denoted as "Hybrid-AFM" provides access to additional information. Heating the sample at the measurement spot via an infrared light beam of a defined wavelength and measuring the heat-induced change in oscillation behavior of the cantilever enables measuring spectrally resolved infrared (IR) absorption. This way, correlating the chemical composition with topographic information is possible (Fu W. and Zhang W., 2017; Dazzi and Prater, 2017). Similar information can be obtained via a combination of Raman spectroscopy and AFM (Fu W. and Zhang W., 2017). For the example of the 2D material graphene, both techniques are complementary. While the lateral geometry of graphene sheets is easily accessible by AFM, the measured height of the sheets may be influenced by adsorbates at the surface. Using complementary Raman spectroscopy allows accurately determining the number of sheets (up to 5 layers) and their defect states (Eigler et al., 2014; Nacken T. et al., 2015). As the signals of both techniques are evaluated at the same sample position by co-localization, true multidimensional property distributions in terms of lateral sheet size and number of graphene sheets (thickness) can be acquired. This technique thus enables process optimization of the production of 2D materials (Halbig et al., 2016)

3.4 Electron microscopy

Scanning electron microscopy (SEM) and transmission electron microscopy (TEM) rely on the interaction of probing electrons with the sample. Typically, topographic or transmission images are used to determine the size and geometrical anisotropy of individual particles. Characterizing a significantly large number of particles allows obtaining the 2D length and diameter distributions of particles, see e.g. (Murphy et al., 2017; Elazzouzi-Hafraoui et al., 2008). However, the number of counted particles is often too small for a reliable statistical analysis. In other words, information on 2D distributions have to be taken with great care due to the underlying scatter of data.

The detection of secondary or backscattered electrons provides information on topography and composition. As for other microscopy-based techniques, the combination of imaging techniques with additional characterization methods can further enlarge the multidimensional dataset. SEM-based mineral liberation analysis can be used to determine the projected 2D area of a mineral via SEM, while complementary EDX measurements allow the characterization of the composition at the measurement position (Fandrich et al., 2007). From the overlay of 2D EDX and SEM images, equivalent circle diameters of particles can be calculated together with their densities from the individual specific mineral densities and EDX based area fractions. As a result 2D size and density distribution can be obtained, which allows analyzing e.g. separation processes in detail (Schach et al., 2019).

Furthermore, mechanical particle properties can be determined by mechanical testing directly in the SEM by nano-compression. The set-up described in (Romeis S. et al., 2012) allows to test several hundred particles for statistically reliable analysis (see **Fig. 5 I**). Elastic and inelastic deformation of carefully deposited individual particles allows to determine distributions of Young's modulus, yield stress, hardness, energy absorption or strain at the onset of the crack formation. All these quantities can be

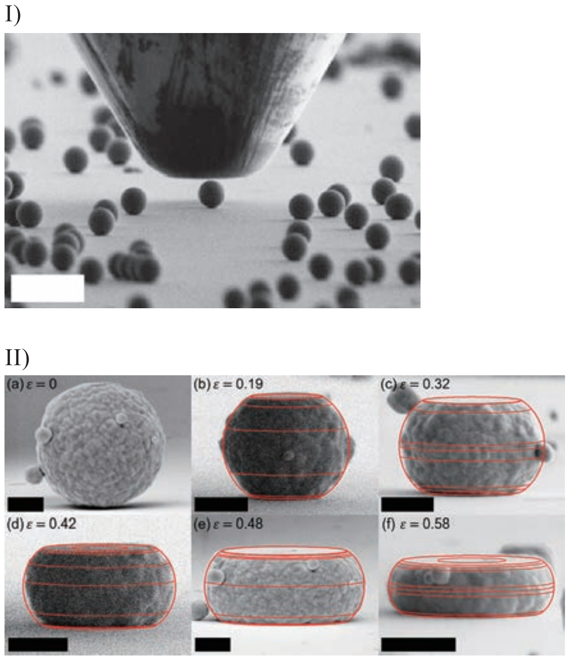

Fig. 5 **(I)** Nano-indentation of particles by a flat punch in an SEM, **(II)** Au particles (1 μm) after defined compression, the red lines indicate the particle shapes modelled by FEM. **(I)** adapted from (Paul J. et al., 2015b) with permission from Elsevier, Copyright 2015, **(II)** reprinted from (Paul J. et al., 2015a) with permission from Elsevier, Copyright 2015.

investigated depending on size. Additionally, the influence of further size-dependent properties such as the brittle-ductile transition of glass particles, different compositions or internal structures can be studied (Paul J. et al., 2015b). Furthermore, quantitative shape analysis is possible as highlighted in **Fig. 5 II**, which shows gold particles of 1 µm in diameter for various states of compression and particle shapes obtained from finite-element-method (FEM) simulation.

TEM uses higher energetic electrons than SEM enabling the spatial material transmission (Fultz and Howe, 2008) and provides thus access to the local particle structure. The 2D characterization of particles can be extended to three dimensions by applying 3D tomography (Miao et al., 2016; Song H. et al., 2019). This method relies on tilt series of TEM images obtained after careful sample preparation (Przybilla T. et al., 2018) as shown in **Fig. 6 I** or on TEM images from freely rotating particles in a graphene based liquid cell (Park J. et al., 2015). The obtained images are used to reconstruct the 3D morphology including the inner structure (Park J. et al., 2015), the inner porosity (Distaso M. et al., 2017) or the exact position of any primary particle in self-assembled supraparticles (Wang J. et al., 2018) as shown in **Fig. 6 II**. Therefore, this technique enables obtaining vast information on the single particle level. Various other measurement techniques such as energy-filtered TEM imaging, high resolution TEM imaging or diffraction based modes, which allow chemical or structural analysis, are available, but are beyond the scope of this review (Fultz and Howe, 2008).

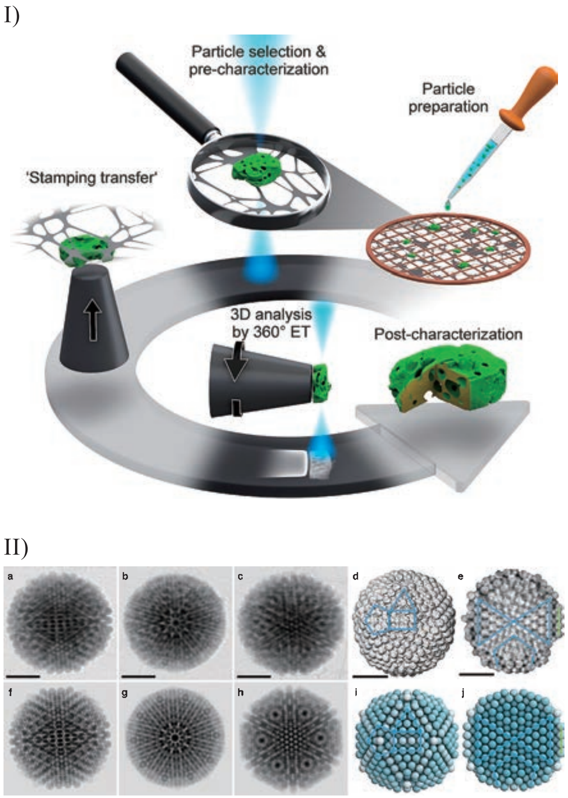

Fig. 6 **(I)** Flow chart of preparative work required for a 3D TEM tomography based reconstruction of the particle morphology. Reproduced with permission from (Przybilla T. et al., 2018) Copyright 2019, Wiley. **(II) (a–c)**: Bright field STEM images of a colloidal crystals. **(d–e:)** Reconstructed surface and inner structure. **(f–h)** TEM mimicking images of the colloidal cluster. **(i–j)** external and internal cross-sectional views. Reproduced from (Wang J. et al., 2018) under the terms of the CC-BY 4.0 license. Copyright: (2018) The Authors, published by Springer Nature.

4. Gas phase measurements

In the following section, basic principles of multidimensional particle characterization in aerosols are presented. Moreover, recent results for the determination of full 2D mass-mobility distributions and additional 1D distributions extracted from this data set are discussed.

An excellent possibility to analyze multidimensional particle properties in a gaseous environment is the coupling of different measurement devices like the differential mobility analyzer (DMA) with a subsequent measurement device. Examples are the combination of a DMA with a low pressure impactor to obtain radius and mass simultaneously (Schleicher et al., 1995), the simultaneous measurement of mass, surface and mobility diameter of silver agglomerates via coupling of DMA, inductively coupled plasma atomic emission spectrometry (ICP-AES), epiphaniometer (EPI) and condensation particle counter (CPC) (Weber A.P. et al., 1991).

4.1 DMA and low-pressure impactor

One of the earlier works on the retrieval of 2D property distributions from aerosol measurements was carried out by Schleicher et al. The simultaneous determination of size and density for submicron aerosol particles was demonstrated for metal nanoparticles (Pd, Ag, Co), carbon particles, oil droplets and oil burner exhaust (Schleicher et al., 1995).

The measurement itself is a two-step process. First a particle fraction with a certain electrical mobility is selected in a DMA, afterwards a low-pressure impactor classifies the particles according to inertia. The combination of those two devices allows to determine the particle density and mobility diameter of single particles. Prior to the DMA, the particle surface charge needs to be brought to charge equilibrium via a ^{63}Ni β^- radioactive source. The applied electrical field in the DMA leads to the separation of a mobility-selected particle fraction, which enters the low-pressure impactor. The particle properties in the gas stream can be estimated by a critical Stokes number. After calibration of the two devices, the density for a previously mobility-selected particle regime is detected. It is possible to gain even more information by using a further classifying step with a subsequent scanning measurement device for particle counting.

4.2 Tandem differential mobility analyzer

In tandem DMA systems, two DMAs are used in series, whereby the properties of the particles exiting the first DMA are manipulated before entering the second DMA. Tandem DMA setups are used at least since the 1980's for aerosol particle analysis. Depending on the type of manipulation performed on the particles that exit the first DMA, different properties of the particles can be derived from the second mobility analysis. One prominent type of manipulation is heating of the aerosol. Heating allows to determine the volume of metal particle aggregates by sintering the aggregates to a spherical shape or removal of organic material from particles which reveals properties on particle chemical composition (Shin W.G. et al., 2010; Tsai D.-H. et al., 2013).

The second prominent type of manipulation is the exposure of the particles to a different gas atmosphere that interacts with the particles either in form of condensation or chemical reactions (Wu et al., 2013; McMurry et al., 1983). Such gas phase manipulations reveal the fraction of hygroscopic particle material or the acidic material fraction, respectively.

4.3 Atmospheric-pressure ion mobility mass spectroscopy (IM-MS)

The outlined techniques in this section are related to ion mobility mass spectroscopy approaches, which consist generally of a two stage separation process. In the first step ions or particles are separated according to electrical mobility, while in the second step separation occurs according to the mass to charge ratio.

The development of atmospheric pressure mass analysis (APM) added a strong analytical tool for the analysis of aerosols (Ehara et al., 1996). The combination of a DMA and an APM is capable to attribute (effective) densities to particles as shown by McMurry for discrete particle sizes classified by the DMA (McMurry et al., 2002).

Pratsinis and co-workers analyzed nanoparticle agglomerates of silica in a diffusion flame. Upon leaving the flame, the agglomerates were classified with a DMA and their mass was measured with an APM resulting in their mass fractal dimension and dynamic shape factor while SEM/TEM images were used to determine primary particle diameters and agglomerate morphology. This combination was used to study the effects of flame process variables on particle characteristics in-depth (Scheckman et al., 2009).

Hogan et al. employed the DMA-APM combination to measure well resolved 2D size-density distributions. In their most recent publication (Li C. et al., 2020) it was demonstrated how a full 2D size-mass distribution can be obtained by ion mobility mass spectrometry and how 1D distributions can be derived from these datasets. The method was applied to several standard particles, i.e. polystyrene, latex and silica nanoparticles and porous mesostructured silica. In their setup, the aerosol is classified in a DMA according to the electrophoretic mobility. Subsequently, the particles are analyzed via an APM and condensation particle counter (CPC). This combination leads to a full 2D size-mass distribution function $\frac{\partial^2 n}{\partial d_p \partial m_p}$, with particle diameter d_p and mass m_p. Notably, this quantity cannot be measured directly but was obtained via the system transfer function and data inversion algorithms (Li C. et al., 2020). The schematic setup is shown in **Fig. 7** along with the 2D mass-diameter function, additional 1D data can be obtained from this 2D function.

For structural characterization of even smaller species, DMA classification can be combined with conventional mass spectrometry. Based on molecular dynamics (MD) simulations it is possible to attribute particle shapes to cluster ions (Ouyang et al., 2013). The observation of structural changes in molecular conformation is beautifully demonstrated on electrosprayed PEG, see e.g. **Fig. 8**, which is found in the gas phase in different - though very defined - levels of deconvolution (Larriba et al., 2014; Larriba and Fernandez de la Mora, 2012). These results show that the lower limit of the combined DMA-mass analysis is at the molecular level. Such analysis is though limited to narrow distributions of shape for each observed species. With broader shape distributions, different charge states, in which a species is observed, become indistinguishable

Beside the characterization of the mass of particles, access to the elemental composition of large particles is investigated since many years based on particle evaporation by either laser pulses or inductively coupled plasmas and mass analysis of the generated ions. A summary of such approaches that intend to reveal chemical compositions of particles is found in (Noble and Prather, 2000). While ICP ionization was quite rare in early setups for single particle mass spectrometry, this technology is on its way to a routine analysis today (Montaño et al., 2016). The access to particle morphology and composition has been shown using coherent X-ray radiation from a free electron laser for particle imaging and as ionization source (Loh et al., 2012).

4.4 Optical measurements

A cooperation between several universities and industrial partners in Germany demonstrated the benefits of multiparameter characterization approaches in the gas phase. Therefore, three new devices have been developed (Babick et al., 2018), which facilitate or support multidimensional

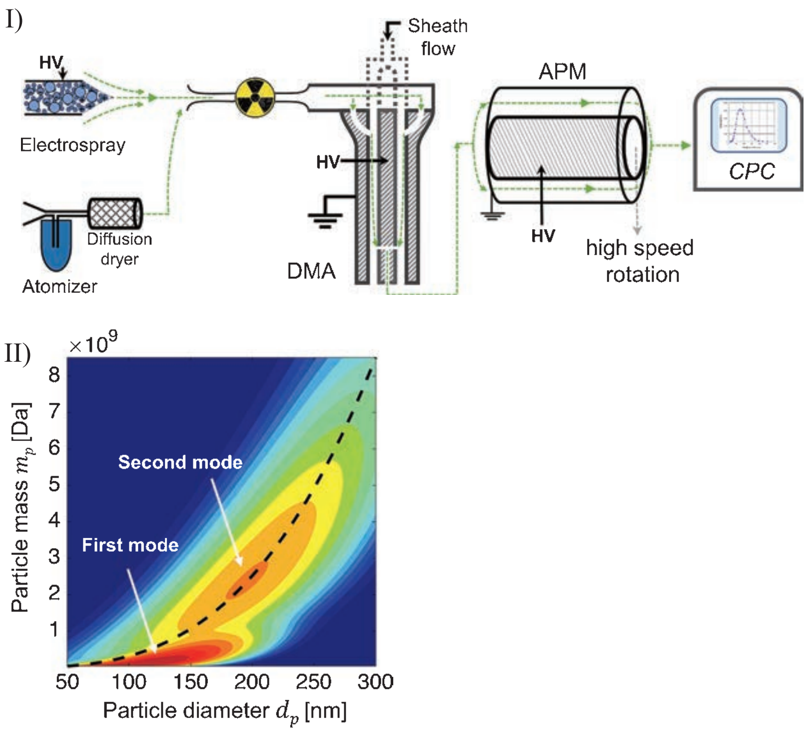

Fig. 7 **(I)** DMA-APM-CPC system for the IM-MS measurements, **(II)** simulated bimodal porous nanoparticles distribution of SiO_2 nanoparticles. Adapted with permission from (Li C. et al., 2020). Copyright 2020 American Chemical Society.

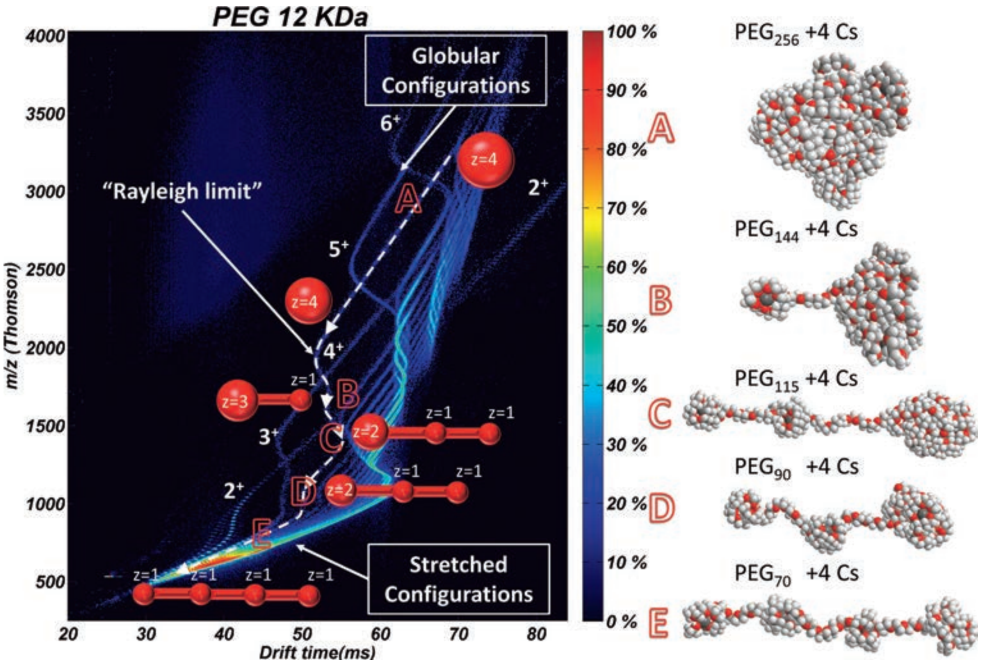

Fig. 8 Gas phase structures for PEG. Adapted with permission from (Larriba and La Mora, 2012). Copyright 2012 American Chemical Society.

characterization of aerosols and are principally suited for quasi-real-time measurements in technical processes. These systems probe the optical scattering pattern of single particles (laser light scattering in 3D, 3D-LSS) and aerosols (wide angle light scattering, WALS) or determine the aerodynamic diameter (or Stokes diameter) of finely resolved aerosol fractions (differential aerodynamic particle sizer, DAPS). The systems allow for a simultaneous determination of particle size and shape (WALS, 3D-LSS) or facilitate the rapid multiparameter characterization by combined analysis with other techniques, e.g., DAPS and differential electric mobility analysis (DEMA). For instance, the dynamic shape factor (obtained via e.g. DEMA and DAPS) and the fractal dimension (via WALS) reflect the morphology changes of SiO_2 aggregates in a sintering furnace by increasing temperature. The two parameters are not equivalent but provide complementary information on shrinking and loss of fractal structure, respectively. Highly resolved PSDs that refer to different particle properties, i.e. to different equivalent diameters, facilitate the quantification of particle shape.

Two of these devices will briefly be introduced here, namely, the 3D LSS and the WALS device. With the first one it is possible to measure the spatially distributed scattering signal of a single particle. In contrast to most common laser scattering instruments, scattering signals depending on the azimuth angle φ are detected too (see **Fig. 9**), which allows for the measurement of anisotropic nanoparticles (Babick et al., 2018). Possible particle sizes for detection range from 500 nm up to 5 µm.

The second instrument, WALS, depicted in **Fig. 10**, records scattered light signals over many angles (including forward- and backscattering, but no azimuthal angles) in a scattering plane with high resolution. This setup directly measures the intensity distribution for different angles, which is directly linked to particle size and the structure of agglomerates (Babick et al., 2018). With these developments, the comprehensive multidimensional characterization of aerosol particles can be further improved.

5. Characterization in the liquid phase

The comprehensive multidimensional characterization of nanoparticle ensembles directly in the liquid phase is of outmost importance for understanding the formation of particles and their formulation including colloidal stability of (nano) particles in numerous technical applications. Often, detailed knowledge of the particle property space is required for the determination and optimization of the macroscopic properties of the dispersions. The choice of analytic techniques depends upon the state of the (nano)

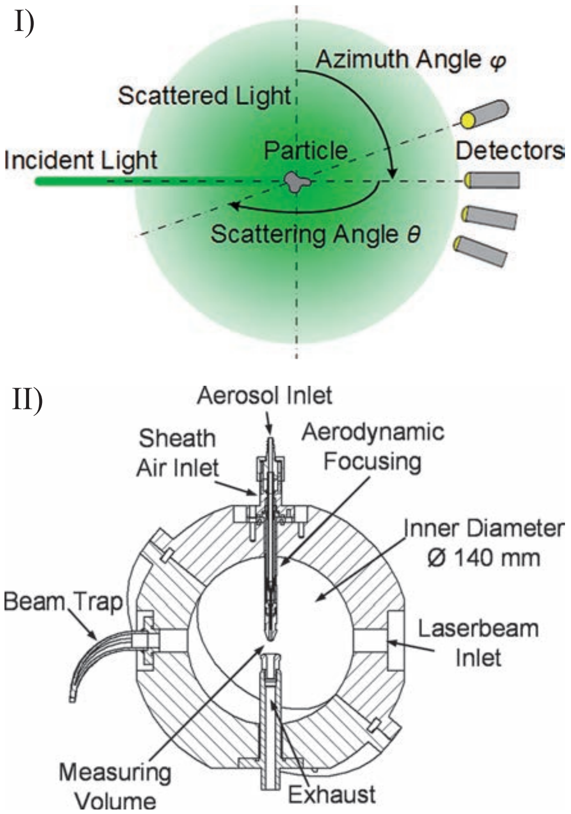

Fig. 9 **(I)** Detection scheme of the 3D LSS. **(II)** section of the spherical measurement chamber. Adapted with permission from (Babick et al., 2018). Copyright 2018, Wiley.

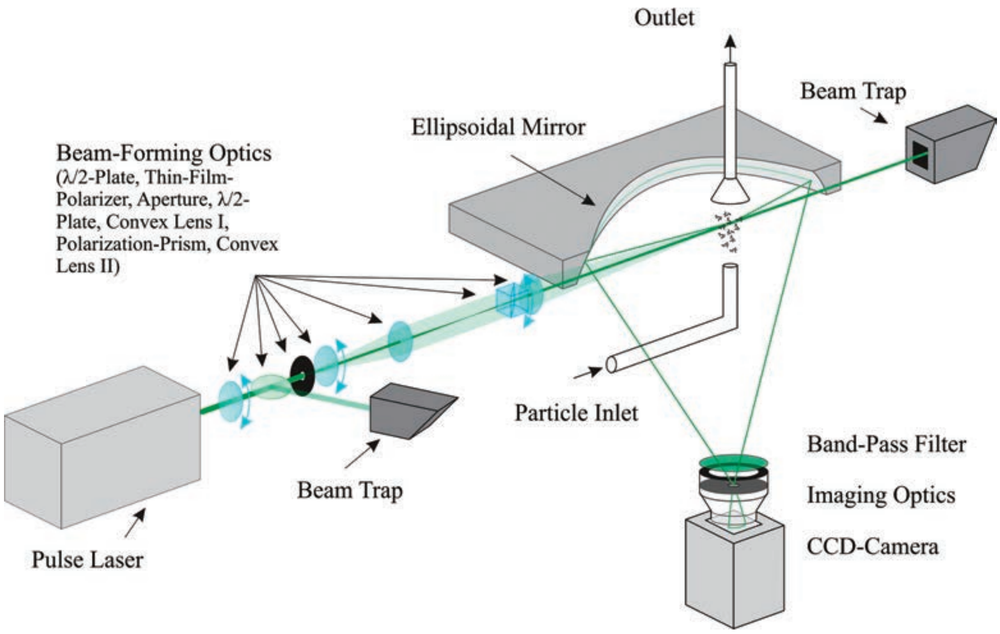

Fig. 10 WALS scheme with optical components. Reproduced with permission from (Babick et al., 2018). Copyright 2018, Wiley.

particles in the dispersion, the particles' hydrodynamic behavior as well as the functional particle property (e.g. light absorption or emission).

Single particle counting is only possible for particles larger than roughly half a micron. The application of super-resolution microscopy and its combination with other techniques has been outlined in the respective chapter on light microscopy. In the liquid phase, super-resolution microscopy has also been used in order to characterize dispersed particles. One example is the investigation of particle wetting behavior at the oil/water interface depending on the particle geometry: single particles are immersed in water containing a fluorescent dye; the distribution of the dye within the liquid and on the particle surface is determined via super-resolution microscopy (Aloi et al., 2019).

Ensemble techniques are based on ultrasound attenuation, light extinction or emission measurement. Electroacoustic spectroscopy provides access to the particle size distribution and the zeta potential even in opaque dispersions up to 40 vol-% (Dukhin A.S. and Goetz, 1998; Richter et al., 2005). Fractionating techniques like analytical (ultra-)centrifugation (AUC) or field flow fractionation (FFF) require rather dilute systems but yield superior information on the entire particle ensembles.

Most techniques are well-established in literature and have been extensively used in the past. However, their application with respect to multidimensional characterization is still at an early stage although considerable progress was achieved in recent years, examples are given in the following sections.

5.1 Image analysis in the flow

In the first part, we briefly address commercial applications for the characterization of µm-sized particles. There are existing commercial systems from Sympatec GmbH for dynamic imaging techniques targeting particle systems in the liquid phase, namely QICPIC and PICTOS. These can be efficiently used in order to analyze particle sizes up to several tens of millimeters through a flow setup and an automated image analysis algorithm (Sympatec, 2021). Malvern Panalytical Ltd combines image analysis techniques with Raman spectroscopy in order to analyze particle size, shape and chemical composition within one measurement (Malvern, 2021).

Mazotti and coworkers described a method that uses focused beam reflectance measurement in order to measure particle size and shape on a 2D grid (Kempkes et al., 2008). In particular, 2D growth rates are extracted from the measurements (Schorsch et al., 2014). In short, the suspension is illuminated using a xenon-flash lamp. Two images are recorded. The transmission image allows the analysis of the planar view on the particles directly in suspension. The reflection image contains information on the lateral view. For the determination of the nD PSD (i.e. axis length distribution), an automated image analysis algorithm is applied for the sorting of the particles into distinct particle classes. Each pair of projections is analyzed individually in order to extract volumetric information from two orthogonal projections. Examples for the shape classes are spheres (1D, the diameter as the characteristic length), needles (2D, cylinders with length and diameter) and cuboids (3D: length, width, and height). The key of these studies is the accurate extraction of particle dimensions from directly measured and simulated images. A multidimensional PSD can be reconstructed from the data and moments can be computed.

The group of Sundmacher developed a method to identify face-specific crystal growth rates based on an image analysis (Borchert et al., 2014). For this application, the flow cell analyzer QICPIC from Sympatec GmbH (Clausthal, Germany) was used in direct connection to a crystallizer. The authors reconstructed 3D crystal shapes from microscopic images with arbitrary orientations. A schematic representation of their setup and methodology is provided in the following figure. As nicely demonstrated in the lower panel of **Fig. 11**, it was possible to determine 2D PSDs of various particle shapes.

5.2 Laser diffraction

Laser diffraction (LD) also called laser diffraction spectroscopy or static light scattering or is a powerful and widely used technique to determine PSDs over a broad size range. Early developments were implemented by Leschonski and co-workers (Heuer and Leschonski K., 1985) by retrieving the one-dimensional PSDs of aerosols and particles in suspension. The technique is fast, precise, and cost efficient when compared to other characterization techniques. Eshel et al. critically evaluated the application of LD for the analysis of particle size distributions (Eshel et al., 2004).

The influence of particle shape on the measured PSD has been thoroughly investigated by the Scarlett group and others, see for instance (Ma et al., 2001; Eshel et al., 2004; Matsuyama and Yamamoto, 2005; Kang et al., 1994). Furthermore, 1D equivalent diameter distributions were measured for platelets and rods by calculating Fraunhofer diffraction patterns for arbitrary polyhedron particles (Heffels et al., 1996). Recently, a detailed analysis of LD of anisotropic particles was published providing information on particle orientation. Micropillars with elliptical cross-sections were used to determine the dependence between the spatial orientation of elongated particles and changes in the PSD (Font-Muñoz et al., 2020).

The angle-dependent intensity of scattered light can be correlated with the fractal dimension of aggregates comprised of a large number of primary nanoparticles. For the case of hematite aggregates, LD could be used to determine the

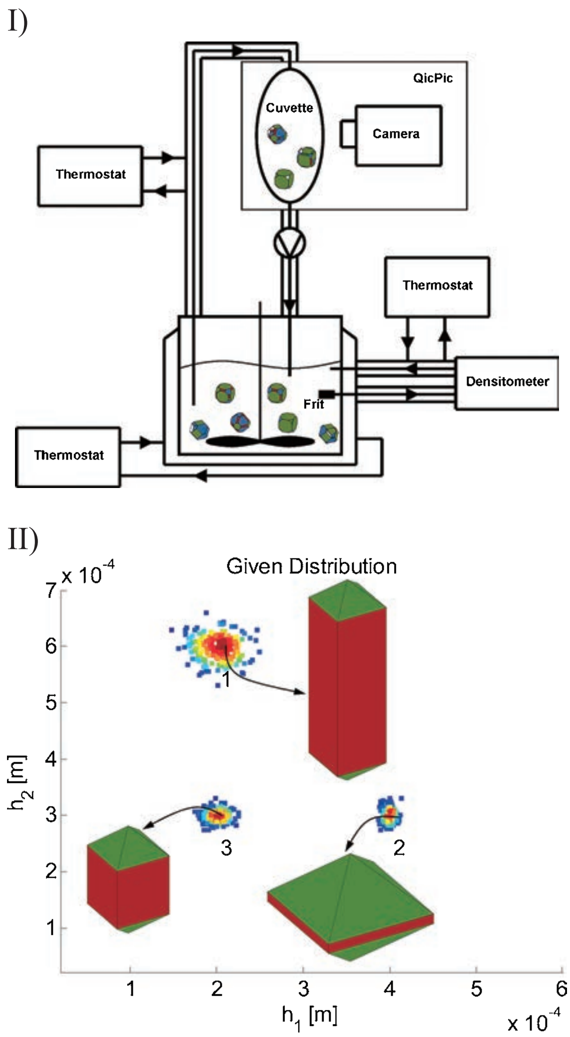

Fig. 11 **(I)** Shape distribution with sketches of representative shapes for each region. **(II)** Estimated distribution on the basis of synthetic images from which Fourier descriptors are extracted and used to match it with the closest entry in a precomputed database. Adapted with permission from (Borchert et al., 2014). Copyright 2014 American Chemical Society.

fractal dimension of differently aggregated structures. High fractal dimensions could be correlated with slow (“reaction-limited”) aggregation, while loose tenuous aggregates were found within the diffusion-limited aggregation regime (Raper and Amal, 1993). In an application example from the papermaking process, flocculation dynamics and the stability of floc against shear stress could be monitored for different polymer additives using LD. In particular, the influence of the floc structure on the stability could be assessed via the determination of the fractal dimension of the flocs (Rasteiro et al., 2008). Further information on LD of aerosols can be found in the reviews by Sorensen (Sorensen C.M., 2001; Sorensen C.M. et al., 2018).

5.3 Dynamic light scattering

Dynamic light scattering (DLS) is a well-established technique, which has been extensively used for the characterization of nanoparticle dispersions (Xu R., 2015). In short, DLS allows for a temporal analysis of the scattered signal decay due to Brownian movement of nanoparticles in a suspension (Berne and Pecora, 2000). This approach is frequently applied in order to measure the translational diffusion in colloidal systems, which can be exploited to calculate the hydrodynamic diameter and the respective hydrodynamic diameter distribution via the Stokes-Einstein relation close to infinite dilution. At higher concentration, concentration-dependent diffusion properties can be extracted as well.

Moreover, there are approaches for the extraction of more than a single parameter from DLS measurements. For non-spherical particles, e.g. in the case of nanorods, the additionally occurring rotational diffusion can be separated into two parts, namely tumbling and spinning motion around the symmetry axis of the nanorods. The orientation-averaged rotational diffusion coefficients can be extracted from DLS measurements together with the translational one by analyzing the differently polarized components of scattered light (Berne and Pecora, 2000; Glidden and Muschol, 2012). The translational diffusion coefficient D_T and the rotational diffusion coefficient D_R can be retrieved from the decay times of the scattering intensity (Berger Bioucas et al., 2019)

$$\tau_{\mathrm{C,T}} = \left(D_\mathrm{T} q^2\right)^{-1} \tag{12}$$

$$\tau_{\mathrm{C,mix}} = \left(D_\mathrm{T} q^2 + 6 D_\mathrm{R}\right)^{-1} \tag{13}$$

$\tau_{\mathrm{C,T}}$ is the mean decay time associated with translation diffusion and $\tau_{\mathrm{C,mix}}$ is the mean decay time associated with translation and rotational diffusion. The scattering vector is q. In particular, polarized DLS in a heterodyne detection scheme was shown to provide the orientation-averaged translational and rotational diffusion coefficients of gold nanorods in a single experiment (Berger Bioucas et al., 2019). The scattering geometry of the detection reduces multiple scattering effects and thus allows lower laser powers and hence reduced laser heating. This was demonstrated for non-transparent dispersions of gold nanorods dispersed in water and in water-glycerol mixtures (Berger Bioucas et al., 2019). Furthermore, from translational and rotational relaxation times, Glidden and Muschol derived an approach for directly obtaining particle dimensions of gold nanorods in the case of narrowly distributed samples (Glidden and Muschol, 2012), which was confirmed by confirmed by auxiliary TEM analysis.

5.4 Ultrasonic and electro-acoustic spectroscopy

The particle mass concentration and the PSD of suspended particles can be analysed by means of ultrasonic measurements. As the interaction of suspended particles and ultrasonic waves changes the sonic velocity as well as the extinction of sound waves, the changes of the frequency of the ultrasonic extinction can be evaluated in order to determine PSDs. The accessible particle sizes range from 10 nm up to 1 mm, which depends on the particle properties and the experimental setup (Riebel and Löffler, 1989).

Electroacoustic spectroscopy was pioneered by O'Brien (O'Brien, 1988) and Dukhin (Dukhin A.S. and Goetz, 2001). Electroacoustic spectroscopy deals with the interaction of electric and acoustic fields. In particular, it allows to measure the zeta potential of particles even in dense suspensions (O'Brien, 1988). The combination of both ultrasound sound absorption with electroacoustics provide the unique opportunity to characterize concentrated dispersions, emulsions and microemulsions in their natural state. Concentrated systems can reliably be measured with concentrations ranging up to 45 vol.-% (Dukhin A.S. and Goetz, 2001).

The combination of these techniques is extremely valuable for the characterization of colloidal stability without dilution and thus for the formulation of dispersions. Here we cite only one example from our own work. The simultaneous measurement of PSD and zeta potential paved the way to break the technical grinding limit around half a micron, which was postulated by Jimbo (Jimbo, 1992). Agglomeration during grinding in stirred media mills could be avoided by inline control of the particle stability in electrostatically stabilized dispersions. This way, the true grinding limit could be identified and clearly distinguished from an apparent grinding limit, which is the equilibrium of breakage and agglomeration. Nanomilling down to only 10 nm for refractory materials such as alumina and zirconia became thus possible (Stenger et al., 2005; Knieke et al., 2011), depending on the defect structures in the particles. So far, the defect structures in particles are largely unknown and remain a "universe inside" to be explored in future.

The strength of electroacoustic measurements can be extended to the determination of charge effects within pores. Electroacoustic measurements of the seismic electric current generated by ultrasound in wetted porous materials yield information on pore size distributions. This effect occurs when electric double layers inside the pore overlap or when the pore size is sufficiently large that for a given frequency the hydrodynamic flow cannot achieve a steady Poiseuille profile inside of the pores (Dukhin A. et al., 2013).

5.5 Small angle X-ray and neutron scattering

Li, Sensi and Lee published an extensive review on small angle X-ray scattering (SAXS) for nanoparticle research (Li T. et al., 2016). In short, the scattering behavior of a single particle depends on its geometry as well as on its surface properties (Hofman et al., 1993). Therefore, SAXS is a suitable method to characterize particle size and anisotropy. The measured intensity profile of a sample is the superposition of all particle scattering intensities and additionally influenced by the sample structure. Therefore, the analysis of disperse properties of nanoparticles via SAXS requires assumptions regarding size or shape. Typically, a suitable type of distribution must be chosen for the retrieval of particle size distributions. (Li T. et al., 2016).

As the intensity profile also depends on the particle shape, SAXS can also be used for the characterization of particle anisotropy. This was visualized for ellipsoids and cylinders in literature (Li T. et al., 2016) based on the Guinier-Porod model (Hammouda, 2010). However, it is not possible so far to determine full 2D PSDs solely from SAXS profiles due to the ill-posed inversion problem for the deconvolution of the scattering curve. A combination with other techniques can help to overcome this limitation. Hubert et al. were able to determine the growth dynamics of length and diameter of gold nanorods via SAXS based on prior information on the 2D PSD of the particles obtained by TEM (Hubert F. et al., 2012). Similar restrictions hold also true for Grazing Incidence Small Angle X-ray Scattering (GISAXS). This method allows the versatile characterization of nanostructures and thin films. To unravel its full potential for the investigation of the spatial organization, the depth profile or the morphology of the sample, the use of synchrotron radiation source is beneficial (Müller-Buschbaum, 2009; Renaud et al., 2009).

Another small angle scattering technique is small angle neutron scattering (SANS). In these experiments, neutron radiation is monitored in order to extract information about the particle size or shape. Further details on this technique have been provided by Blazek and Gilbert, focusing on the application of SAXS and SANS to the characterization of organic structures (Blazek and Gilbert, 2011). Strunz et al. characterized Ni_3Si-type nanoparticles by SANS. Combining TEM and SANS, it could be demonstrated that an amorphous shell forms on the particle core (Strunz et al., 2007).

In another example, SAXS and SANS have been combined. Core size and shell properties of ZnO quantum dots with a size below 6 nm were characterized by Unruh and co-workers by a combination of SANS and SAXS for the same sample. The X-rays provide information on the core of the nanoparticles due to the fact that X-rays are scattered at the electrons of the core atoms, while the neutrons are scattered at the cores of the organic shell atoms. These results were in excellent agreement with the nanoparticle analysis via analytical ultracentrifugation (AUC) and allowed to monitor changes of the shell during the ripening processes as a function of temperature (Schindler et al., 2015). Moreover, gold nanorods in aqueous solution were characterized by a combination of SAXS and SANS alongside TEM measurements. Based on these results, a direct measurement of the thickness of the surfactant layer CTAB on the surface of the gold nanorods was derived (Gómez-Graña et al., 2012).

5.6 Field flow fractionation

Throughout FFF an external field is applied to a suspension flowing through a narrow channel. The laminar parabolic flow velocity profile in the channel induces faster particle transport in the middle of the channel. The external field acts perpendicular to the flow, whereby the interplay of acting drag and field forces leads to a separation of particles in field direction. With the different particle velocities present, particles elute from the channel at different times and position in dependence of particle properties and the applied external field. FFF is subdivided into e.g. thermal, centrifugal, gravitational and asymmetric FFF (Baalousha et al., 2011). In particular, centrifugal FFF has recently been applied to separate silica nanoparticles and to determine number-based PSDs (Kato et al., 2019).

A step towards the determination of nD PSDs was conducted by Cölfen and coworkers. The authors studied asymmetric field flow fractionation (AF4) coupled to a multiple laser light scattering detector (Schmid et al., 2018). AF4 was used to measure diffusion coefficient distributions based on peak broadening corrected by a new algorithm, which uses diffusion coefficient distributions instead of a single mean diffusion coefficient. With this, it was possible to obtain a hydrodynamic diameter distribution with increased resolution. Further evaluation of the scattered light by deconvolution of the detector signals allowed calculating the corresponding molecular weights of formerly not properly separated signals. Their results are summarized in the **Fig. 12**. While FFF has shown to be a powerful method for the determination of pairs of two different parameters, the determination of full 2D PSDs is yet to be demonstrated.

AF4 was coupled with single particle inductively coupled plasma mass spectrometry (spICP-MS). spICP-MS is an emerging technique with respect to nanomaterial characterization as outlined in detail in (Mozhayeva and Engelhard, 2020). Degueldre et al. presented the underlying theoretical background of spICP-MS for characterizing nanoparticle dispersions (Degueldre et al., 2004), while Pace et al. presented a detailed study with a focus on sizing of nanoparticles (Pace et al., 2011). With this, the particle mass diameter distributions of silver nanoparticles were measured. Notably, the detector system of the MS analyzer requires a transfer into a carrier gas. So far, these methods yield a particle mass diameter distribution. The main advantage of spICP-MS is the discrimination of the nanoparticle based on elemental composition, whereas many current characterization techniques are unable to differentiate between different types of nanoparticles. Further classification prior to spICP-MS analysis is necessary to distinguish between particles with the same composition (Pace et al., 2011).

The complex issue of fractionation prior to spICP-MS was directly addressed in (Huynh et al., 2016). The authors

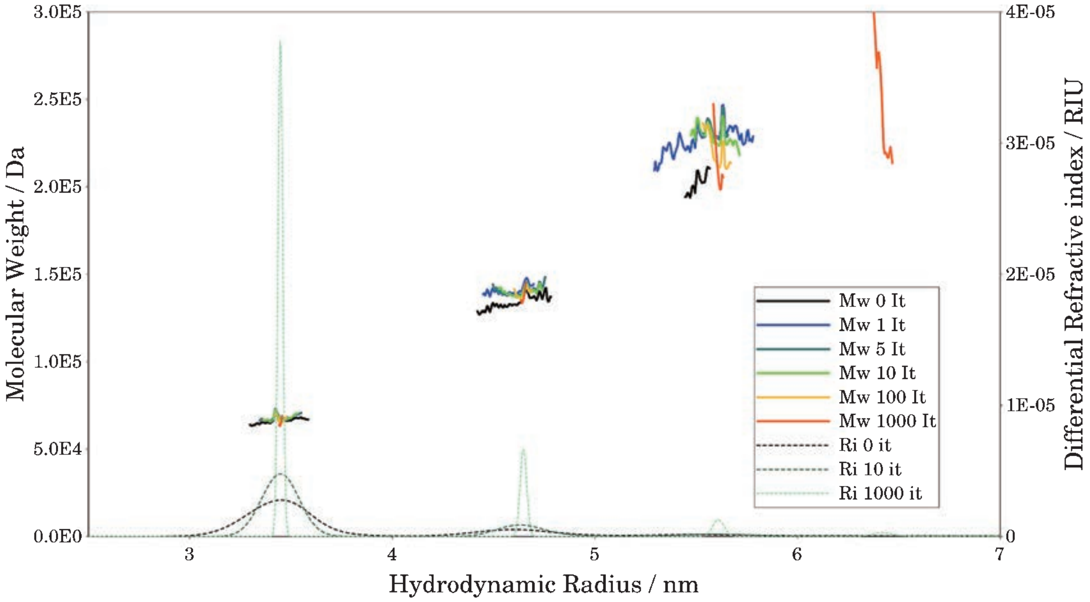

Fig. 12 Hydrodynamic radius distribution (Ri) and the respective molecular weight (M_W) of the analysed species as retrieved from a FFF measurement after deconvolution with varying number of algorithm iterations (It). Adapted with permission from (Schmid et al., 2018). Copyright 2018 American Chemical Society.

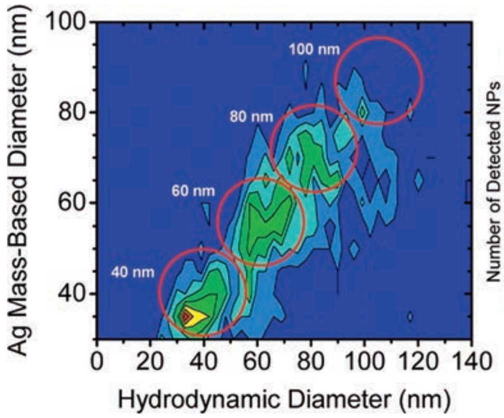

Fig. 13 Representative contour plot result of an AF4-spICP-MS analysis of a suspension containing 40 (571 ng/L), 60 (2.39 μg/L), 80 (5.25 μg/L), and 100 nm AgNPs (10.0 μg/L). Adapted with permission from (Huynh et al., 2016). Copyright 2016 American Chemical Society.

combined AF4 with spICP-MS to solve the current limitations of conventional ICP-MS or spICP-MS. This setup uses the advantages of two orthogonal characterization techniques based on different physical principles in order to simultaneously provide both mass and hydrodynamic diameters of the detected nanoparticles yielding a full 2D PSD. From this information relevant and otherwise hardly accessible properties such as layer thickness and aggregation states of nanoparticles can be obtained. AF4-spICP-MS was capable of measuring Ag NPs from suspensions, fractionating polydisperse AgNPs (see **Fig. 13**), and distinguishing AgNPs from Ag-SiO_2 NPs with similar Ag mass. One limitation of the method still is the quantification of defined nanoparticle sizes in heterogeneous samples.

5.7 2D analysis by analytical ultracentrifugation

Over decades, AUC was mostly used in the biomedical field with a few exceptions for the analysis of colloidal systems (Planken and Cölfen, 2010; Karabudak and Cölfen, 2016). Due to recent progress in the development of new detector systems, AUC can be considered as gold standard due to its unprecedented accuracy, reproducibility and resolution in a large range of applications (Walter J. et al., 2014; Karabudak et al., 2016; Pearson et al., 2018; Wawra et al., 2019).

In AUC experiments, the sedimentation of nanoparticles is tracked under the influence of a centrifugal field directly in the liquid phase with the use of an optical detection system. The temporal and radial evolution of the concentration profiles allow for the extraction of sedimentation (s) and diffusion coefficients (D) alongside their associated optical properties. Available detection systems allow combining extinction and fluorescence spectra with hydro- and thermodynamic properties (Uchiyama et al., 2016; Wawra et al., 2019). While sedimentation and diffusion depend both on size and shape of the particle, the particle density further influences the sedimentation process.

As AUC measurements provide combined information on sedimentation, diffusion properties and optical properties for small particles, multidimensional information can be obtained from a single experiment. Carney et al. used the combination of s and D to study the particle size and particle density distribution (Carney et al., 2011). For the case of spherical core-shell gold nanoparticles, the sedimentation and the diffusion coefficient depend on size and density. Therefore, it was possible to determine the core diameter distribution alongside the shell properties of the polydisperse core-shell gold nanoparticles. The results are illustrated in **Fig. 14** and were validated by auxiliary TEM analysis.

Furthermore, Nontapot et al. analyzed core-shell silica nanocrystals terminated with cyclohexane or allylamine via AUC (Nontapot et al., 2013). In their work, the effective particle density was determined by measuring the sedimentation properties of the nanoparticles in different solvents. Based on these results, the shell thickness could be calculated, which provided the effective 1D PSD in agreement with the data from other nanoparticle characterization techniques, namely DLS and TEM. Demeler et al. further addressed the issue of analyzing core-shell nanoparticles (Demeler et al., 2014). Their work demonstrated a powerful data evaluation tool, which is implemented in the UltraScan-III software. With this, it was possible to determine the effective density and molar mass for CdSe and PbS QDs from a single AUC experiment.

Thajudeen et al. (Thajudeen T. et al., 2017) combined the measured sedimentation coefficients from AUC in liquid phase and electrical mobility measurements from the combination of DMA and CPC in the gas phase via transfer of the nanorods from the liquid to the gas phase by an advanced electrospray technique (Lübbert and Peukert W., 2018). This work demonstrated that it is possible to determine mean values of length and diameter for Au and ZnO nanorods by combining the two techniques, as mobility diameter and sedimentation coefficients depend differently on the geometry of the rods. The results were validated by auxiliary TEM and SEM analysis. While this is a powerful technique for the description of this system, the measurement of a full 2D PSD was not yet possible.

Analytical centrifugation (AC) is an emerging technique for nanoparticle characterization (Detloff et al., 2007), which is more easily applicable than AUC, less expensive and delivers high sample throughput by parallelization of up 12 samples in one run. Interestingly, software tools for the comprehensive determination of PSD from AUC data have been transferred to AC (Walter J. et al., 2015). This step significantly enhanced the precision of the obtained distributions in particular for heterogeneous samples.

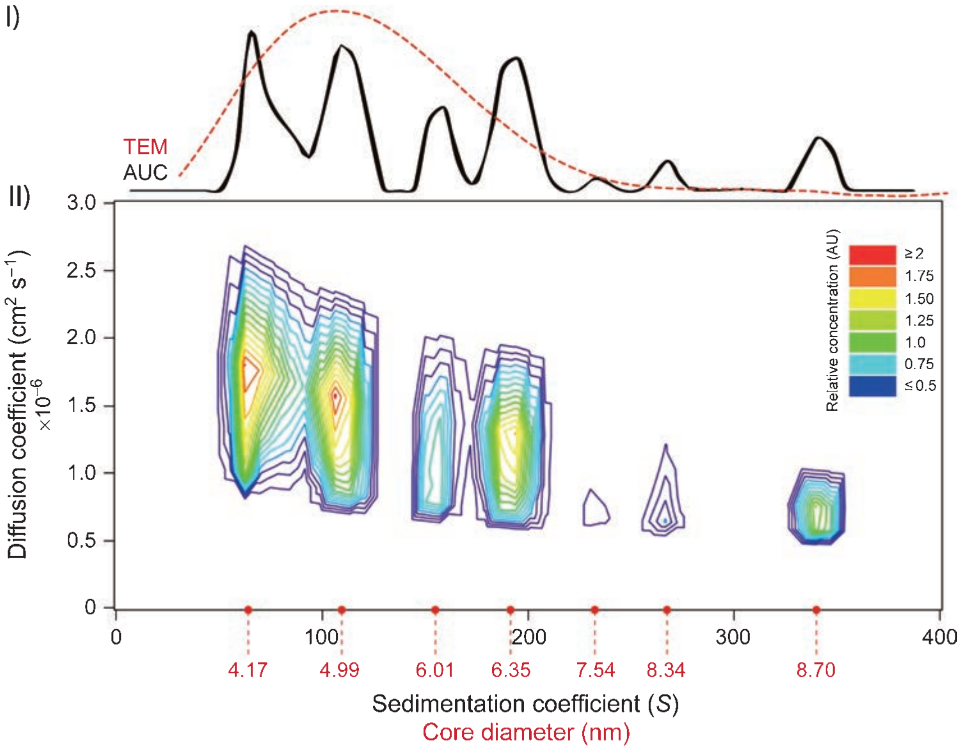

Fig. 14 **(I)** 1D sedimentation coefficient distribution (black) with TEM PSD (dashed red); **(II)** 2D sedimentation and diffusion coefficient distribution obtained with AUC of polydisperse gold nanoparticles. Reproduced with permission from (Carney et al., 2011) under the terms of the CC BY-NC-SA 3.0 license. Copyright: (2011) The Authors, published by Springer Nature.

Moreover, the recent development of sector-shaped centerpieces for AC experiments enabled the measurement of a full diffusion-corrected sedimentation coefficient distribution. With this, it is possible to determine the hydrodynamic diameter distribution and the core-diameter distribution of gold nanoparticles alongside the stabilizer shell thickness of 3 nm only (Uttinger et al., 2020).

5.8 Analytical ultracentrifugation: optical back coupling

A very promising technique for the characterization of plasmonic nanoparticles is the Optical Back Coupling (OBC) method (Wawra et al., 2018), which allows obtaining number-weighted 2D PSDs. Therefore, the sedimentation of particles within an AUC is tracked via a multiwavelength detector. This allows deducing sedimentation coefficient distributions for many different detection wavelengths. In return, extinction spectra can be extracted for defined intervals of the sedimentation coefficient distribution enabling to correlate the mean sedimentation coefficient of the respective interval with the spectra of the particles exhibiting these defined sedimentation properties, as shown in **Fig. 15** for gold nanorods.

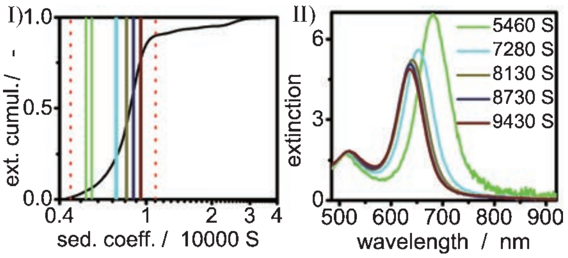

Fig. 15 **(I)** Cumulative sedimentation coefficient distribution at a wavelength of 480 nm with indicated separation in sedimentation coefficient intervals. **(II)** Spectra for selected intervals with associated mean sedimentation coefficient. Reproduced with permission from (Wawra et al., 2018) under the terms of the CC-BY 4.0 license. Copyright: (2018) The Authors, published by Springer Nature.

As the spectra of the gold nanorods as well as the sedimentation coefficients depend on the geometry of the particle, the combined optical and hydrodynamic information can be used to deduce length and diameter alongside the particle concentration. Therefore, the extracted spectra are analyzed using different optical models under the constrain of the interval's mean sedimentation coefficient. The length, diameter, aspect ratio, volume, surface and cross-sectional distributions can be readily obtained from these results. As the technique can be extended to other nonspherical plasmonic particles and can be used for determining relative amounts of particles of different shapes, it provides complete and quantitative insights into such particulate systems.

An exemplary 2D measurement is depicted in **Fig. 16 I**. The displayed TEM inset shows very good agreement

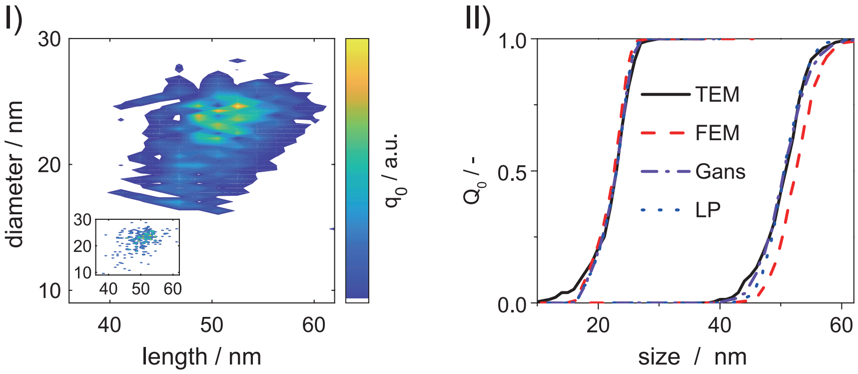

Fig. 16 **(I)** 2D PSD of a gold nanorod sample obtained using the Mie-Gans model. The axes correspond to length and diameter, while the heatmap indicates the distribution value. The inset shows results from TEM analysis. **(II)** Comparison of the 1D cumulative length and diameter distributions from TEM data and AUC for different optical models (Mie-Gans, FEM finite element methods, LP analytical longitudinal polarization model, which only considers polarizations along the length axis of the gold rod). Adapted with permission from (Wawra et al., 2018) under the terms of the CC-BY 4.0 license. Copyright: (2018) The Authors, published by Springer Nature.

of OBC and TEM. An even better comparison is possible via the 1D length and 1D diameter distributions. Eq. 4 can be used for the calculation of the reduced 1D distributions from the 2D PSD, integration leads to the cumulative distributions. All used optical models show excellent agreement with TEM statistics, see **Fig. 16 II**, which emphasizes the accuracy and potential of the OBC method for 2D characterization of plasmonic nanoparticle ensembles.

In addition to advances in the data analysis of plasmonic nanoparticle ensembles, a multi-wavelength emission detector has recently been developed for AUC (Wawra et al., 2019). These hardware developments significantly enlarge the measurement window of AUC for the detection of size-dependent emission properties of nanoparticles.

6. Conclusions

Modern particle systems are associated with a wide range of applications. The necessary functionality of micro- and nanoparticle systems is a direct result of the five dimensional parameter space that is defined by particle size, shape, surface, structure, and composition.

In the first part of this review, we provided the mathematical background for the comprehensive description of particle property distributions. These concepts extent the well-known 1D PSD to a multidimensional description of particle property distributions. In particular, it was shown how to calculate 1D distributions from 2D property distributions.

While the determination of 1D PSDs is well established, the direct retrieval of nD PSDs is a challenging task but necessary next step towards the control of the full particle property space. Recent progress in the description and characterization of multivariate particle property distributions is summarized.

Well-established techniques such as light microscopy, SEM and TEM or AFM allow for the retrieval of 2D projections of particles while more advanced 3D tomography provides full 3D information. Moreover, correlating the chemical composition with topographic or geometric information is possible by coupling spectroscopic measurements with AFM co-localization. However, most of these techniques, are very tedious, time-consuming and require complex sample handling. Moreover, the results are typically associated with the common problem of poor statistics. For nD PSDs, large sample numbers are required.

Early works for the determination of 2D property distributions were conducted for aerosols. The coupling of different measurement devices like the DMA with a subsequent device allows to determine nD property distributions. This has been demonstrated by coupling DMA and inductively coupled plasma atomic emission spectrometry, epiphaniometer, CPC and MS, for instance.

For µm-sized particles dispersed in the liquid phase, there are several techniques for nD characterization by image analysis in flowing systems. These are applied in order to investigate crystal growth kinetics in situ. Well-established scattering techniques such as DLS, SAXS or SANS allow for extracting information on the particle size and shape directly in liquid phase.

Fractionating techniques, such as FFF and A(U)C bear the advantage of particle separation prior to their detection. This enables the detailed analysis of individual fractions of an entire particle ensemble. In particular, AUC was successfully applied for a 2D analysis of core-shell nanoparticles by the analysis of sedimentation and diffusion properties. Recently, novel approaches were demonstrated for the coupling of optical and hydrodynamic properties of plasmonic nanoparticles in combination with a multi-wavelength detector to analyze number-weighted 2D dimensional distributions of diameter and length of gold nanorods.

In summary, our review discusses advances and experimental possibilities to characterize particle ensembles with respect to nD property distributions. Few techniques are available, which deliver multidimensional particle properties directly. As the complexity continues to increase, further method development is required. We foresee that clever combinations of several techniques will allow to shed light on the complex multiparameter space of fine particle systems. As often in science, progress strongly depends on our ability to "see" what is going on, i.e. advances in multidimensional particle characterization are mandatory for the further development and full exploitation of particulate products of high-added value.

Acknowledgements

The authors thank the Deutsche Forschungsgemeinschaft (DFG) for financial support through the priority program SPP 2045: "Highly specific and multidimensional fractionation of fine particle systems with technical relevance.", and projects PE427/37-1, PE 427/33-1. The authors gratefully acknowledge funding from the DFG through the collaborative research centers SFB 953 and SFB 1411.

References

Ahmad R., Nicholson K.S., Nawaz Q., Peukert W., Distaso M., Correlation between product purity and process parameters for the synthesis of Cu_2ZnSnS_4 nanoparticles using microwave irradiation, Journal of Nanoparticle Research, 19 (2017) 1–13. DOI: 10.1007/s11051-017-3932-5

Aloi A., Vilanova N., Isa L., Jong A.M. de, Voets I.K., Superresolution microscopy on single particles at fluid interfaces reveals their wetting properties and interfacial deformations, Nanoscale, 11 (2019) 6654–6661. DOI: 10.1039/C8NR08633H

Baalousha M., Stolpe B., Lead J.R., Flow field-flow fractionation for the analysis and characterization of natural colloids and manufactured nanoparticles in environmental systems: a critical review, Journal of Chromatography A, 1218 (2011) 4078–4103. DOI: 10.1016/j.chroma.2011.04.063

Babick F., Hillemann L., Stintz M., Dillenburger T., Pitz M., Hellmann A., Antonyuk S., Ripperger S., Huber F.J.T., Will S., Wernet R., Seipenbusch M., Gensch M., Weber A., Kiesler D., Kruis E., Friehmelt R., Sachweh B., Multiparameter characterization of aerosols, Chemie Ingenieur Technik, 90 (2018) 923–936. DOI: 10.1002/cite.201700094

Berger Bioucas F.E., Damm C., Peukert W., Rausch M.H., Koller T.M., Giraudet C., Fröba A.P., Translational and rotational diffusion coefficients of gold nanorods dispersed in mixtures of water and glycerol by polarized dynamic light scattering, The Journal of Physical Chemistry B, 123 (2019) 9491–9502. DOI: 10.1021/acs.jpcb.9b08274

Berne B.J., Pecora R., Dynamic Light Scattering: With Applications to Chemistry, Biology, and Physics, Dover Publications, Mineola, N.Y., 2000, ISBN: 0486442276.

Binnig, Quate, Gerber, Atomic force microscope, Physical Review Letters, 56 (1986) 930–933. DOI: 10.1103/PhysRevLett.56.930

Blazek J., Gilbert E.P., Application of small-angle X-ray and neutron scattering techniques to the characterisation of starch structure: a review, Carbohydrate Polymers, 85 (2011) 281–293. DOI: 10.1016/j.carbpol.2011.02.041

Borchert C., Temmel E., Eisenschmidt H., Lorenz H., Seidel-Morgenstern A., Sundmacher K., Image-based in situ identification of face specific crystal growth rates from crystal populations, Crystal Growth & Design, 14 (2014) 952–971. DOI: 10.1021/cg401098x

Brown J.W., Henderson B.L., Kiesz M.D., Whalley A.C., Morris W., Grunder S., Deng H., Furukawa H., Zink J.I., Stoddart J.F., Yaghi O.M., Photophysical pore control in an azobenzene-containing metal-organic framework, Chemical Science, 4 (2013) 2858. DOI: 10.1039/c3sc21659d

Bujak B., Bottlinger M., Three-dimensional measurement of particle shape, Particle & Particle Systems Characterization, 25 (2008) 293–297. DOI: 10.1002/ppsc.200800027

Carney R.P., Kim J.Y., Qian H., Jin R., Mehenni H., Stellacci F., Bakr O.M., Determination of nanoparticle size distribution together with density or molecular weight by 2D analytical ultracentrifugation, Nature Communications, 2 (2011) 335. DOI: 10.1038/ncomms1338

Castro R.H.R., Gouvêa D., Sintering and nanostability: the thermodynamic perspective, Journal of the American Ceramic Society, 99 (2016) 1105–1121. DOI: 10.1111/jace.14176

Chan K.-Y., Ding J., Ren J., Cheng S., Tsang K.Y., Supported mixed metal nanoparticles as electrocatalysts in low temperature fuel cells, Journal of Materials Chemistry, 14 (2004) 505. DOI: 10.1039/b314224h

Chemseddine A., Weller H., Highly monodisperse quantum sized CdS particles by size selective precipitation, Berichte der Bunsengesellschaft für physikalische Chemie, 97 (1993) 636–638. DOI: 10.1002/bbpc.19930970417

Chistyakov D., Sergeev G., The polymorphism of drugs: new approaches to the synthesis of nanostructured polymorphs, Pharmaceutics, 12 (2020) 34. DOI: 10.3390/pharmaceutics12010034

Damm C., Nacken T.J., Peukert W., Quantitative evaluation of delamination of graphite by wet media milling, Carbon, 81 (2015) 284–294. DOI: 10.1016/j.carbon.2014.09.059

Davidov-Pardo G., Joye I.J., McClements D.J., Food-grade protein-based nanoparticles and microparticles for bioactive delivery: fabrication, characterization, and utilization, Advances in Protein Chemistry and Structural Biology, 98 (2015) 293–325. DOI: 10.1016/bs.apcsb.2014.11.004

Dazzi A., Prater C.B., AFM-IR: Technology and applications in nanoscale infrared spectroscopy and chemical imaging, Chemical Reviews, 117 (2017) 5146–5173. DOI: 10.1021/acs.chemrev.6b00448

Degueldre C., Favarger P.-Y., Bitea C., Zirconia colloid analysis by single particle inductively coupled plasma–mass spectrometry, Analytica Chimica Acta, 518 (2004) 137–142. DOI: 10.1016/j.aca.2004.04.015

Del Rosso T., Rey N.A., Rosado T., Landi S., Larrude D.G., Romani E.C., Junior F.L.F., Quinteiro S.M., Cremona M., Aucelio R.Q., Margheri G., Pandoli O., Synthesis of oxocarbon-encapsulated gold nanoparticles with blue-shifted localized surface plasmon resonance by pulsed laser ablation in water with CO_2 absorbers, Nanotechnology, 27 (2016) 255602. DOI: 10.1088/0957-4484/27/25/255602

Detloff T., Sobisch T., Lerche D., Particle size distribution by space or time dependent extinction profiles obtained by analytical centrifugation (concentrated systems), Powder

Technology, 174 (2007) 50–55. DOI: 10.1016/j.powtec.2006.10.021

Dimitrov A.S., Miwa T., Nagayama K., A comparison between the optical properties of amorphous and crystalline monolayers of silica particles, Langmuir, 15 (1999) 5257–5264. DOI: 10.1021/la990225r

Distaso M., Apeleo Zubiri B., Mohtasebi A., Inayat A., Dudák M., Kočí P., Butz B., Klupp Taylor R., Schwieger W., Spiecker E., Peukert W., Three-dimensional and quantitative reconstruction of non-accessible internal porosity in hematite nanoreactors using 360° electron tomography, Microporous and Mesoporous Materials, 246 (2017) 207–214. DOI: 10.1016/j.micromeso.2017.03.028

Domaschke M., Zhou X., Wergen L., Romeis S., Miehlich M.E., Meyer K., Peukert W., Schmuki P., Magnéli-phases in anatase strongly promote cocatalyst-free photocatalytic hydrogen evolution, ACS Catalysis, 9 (2019) 3627–3632. DOI: 10.1021/acscatal.9b00578

Duan Z.-Q., Liu Y.-T., Xie X.-M., Ye X.-Y., Zhu X.-D., h-BN nanosheets as 2D substrates to load 0D Fe_3O_4 nanoparticles: a hybrid anode material for lithium-ion batteries, Chemistry–An Asian Journal, 11 (2016) 828–833. DOI: 10.1002/asia.201501439

Dukhin A., Swasey S., Thommes M., A method for pore size and porosity analysis of porous materials using electroacoustics and high frequency conductivity, Colloids and Surfaces A: Physicochemical and Engineering Aspects, 437 (2013) 127–132. DOI: 10.1016/j.colsurfa.2013.01.018

Dukhin A.S., Goetz P.J., Characterization of aggregation phenomena by means of acoustic and electroacoustic spectroscopy, Colloids and Surfaces A: Physicochemical and Engineering Aspects, 144 (1998) 49–58. DOI: 10.1016/S0927-7757(98)00565-2

Dukhin A.S., Goetz P.J., Acoustic and electroacoustic spectroscopy for characterizing concentrated dispersions and emulsions, Advances in Colloid and Interface Science, 92 (2001) 73–132. DOI: 10.1016/S0001-8686(00)00035-X

Egan C.K., Jacques S.D.M., Wilson M.D., Veale M.C., Seller P., Beale A.M., Pattrick R.A.D., Withers P.J., Cernik R.J., 3D chemical imaging in the laboratory by hyperspectral X-ray computed tomography, Scientific Reports, 5 (2015) 15979. DOI: 10.1038/srep15979

Ehara K., Hagwood C., Coakley K.J., Novel method to classify aerosol particles according to their mass-to-charge ratio—Aerosol particle mass analyser, Journal of Aerosol Science, 27 (1996) 217–234. DOI: 10.1016/0021-8502(95)00562-5

Eigler S., Hof F., Enzelberger-Heim M., Grimm S., Müller P., Hirsch A., Statistical raman microscopy and atomic force microscopy on heterogeneous graphene obtained after reduction of graphene oxide, The Journal of Physical Chemistry C, 118 (2014) 7698–7704. DOI: 10.1021/jp500580g

Elazzouzi-Hafraoui S., Nishiyama Y., Putaux J.-L., Heux L., Dubreuil F., Rochas C., The shape and size distribution of crystalline nanoparticles prepared by acid hydrolysis of native cellulose, Biomacromolecules, 9 (2008) 57–65. DOI: 10.1021/bm700769p

Eom N.S.A., Kim T.-S., Choa Y.-H., Kim W.-B., Kim B.S., Core-size-dependent properties of CdSe/CdS core/shell QDs, Materials Letters, 99 (2013) 14–17. DOI: 10.1016/j.matlet.2013.02.065

Esayanur M.S., Yeruva S.B., Rabinovich Y.I., Moudgil B.M., Interaction force measurements using atomic force microscopy for characterization and control of adhesion, dispersion and lubrication in particulate systems, Journal of Adhesion Science and Technology, 19 (2005) 611–626. DOI: 10.1163/1568561054890516

Eshel G., Levy G.J., Mingelgrin U., Singer M.J., Critical evaluation of the use of laser diffraction for particle-size distribution analysis, Soil Science Society of America Journal, 68 (2004) 736–743. DOI: 10.2136/sssaj2004.7360

Fandrich R., Gu Y., Burrows D., Moeller K., Modern SEM-based mineral liberation analysis, International Journal of Mineral Processing, 84 (2007) 310–320. DOI: 10.1016/j.minpro.2006.07.018

Fathi M., Varshosaz J., Mohebbi M., Shahidi F., Hesperetin-loaded solid lipid nanoparticles and nanostructure lipid carriers for food fortification: preparation, characterization, and modeling, Food and Bioprocess Technology, 6 (2013) 1464–1475. DOI: 10.1007/s11947-012-0845-2

Finnegan M.P., Zhang H., Banfield J.F., Phase stability and transformation in titania nanoparticles in aqueous solutions dominated by surface energy, The Journal of Physical Chemistry C, 111 (2007) 1962–1968. DOI: 10.1021/jp063822c

Font-Muñoz J.S., Jeanneret R., Tuval I., Basterretxea G., Method for the determination of preferential orientation of marine particles from laser diffraction measurements, Optics Express, 28 (2020) 14085–14099. DOI: 10.1364/OE.390388

Frank U., Wawra S.E., Pflug L., Peukert W., Multidimensional particle size distributions and their application to non-spherical particle systems in two dimensions, Particle & Particle Systems Characterization, 36 (2019) 1800554. DOI: 10.1002/ppsc.201800554

Frei M., Kruis F.E., Image-based size analysis of agglomerated and partially sintered particles via convolutional neural networks, Powder Technology, 360 (2020) 324–336. DOI: 10.1016/j.powtec.2019.10.020

Fu W., Zhang W., Hybrid AFM for nanoscale physicochemical characterization: recent development and emerging applications, Small, 13 (2017) 1603525. DOI: 10.1002/smll.201603525

Fultz B., Howe J., Transmission Electron Microscopy and Diffractometry of Materials, 3rd ed., Springer Berlin Heidelberg, Berlin, Heidelberg, 2008, ISBN: 3540738851.

Furat O., Leißner T., Bachmann K., Gutzmer J., Peuker U., Schmidt V., Stochastic modeling of multidimensional particle properties using parametric copulas, Microscopy and Microanalysis, 25 (2019) 720–734. DOI: 10.1017/S1431927619000321

Gerdova I., Haché A., Third-order non-linear spectroscopy of CdSe and CdSe/ZnS core shell quantum dots, Optics Communications, 246 (2005) 205–212. DOI: 10.1016/j.optcom.2004.10.068

Giesbers M., Kleijn J.M., Cohen Stuart M.A., Interactions between acid- and base-functionalized surfaces, Journal of Colloid and Interface Science, 252 (2002) 138–148. DOI: 10.1006/jcis.2002.8388

Glidden M., Muschol M., Characterizing gold nanorods in solution using depolarized dynamic light scattering, The Journal of Physical Chemistry C, 116 (2012) 8128–8137. DOI: 10.1021/jp211533d

Gómez-Graña S., Hubert F., Testard F., Guerrero-Martínez A., Grillo I., Liz-Marzán L.M., Spalla O., Surfactant (bi)layers on gold nanorods, Langmuir, 28 (2012) 1453–1459. DOI: 10.1021/la203451p

Gudarzi M.M., Colloidal stability of graphene oxide: aggregation in two dimensions, Langmuir, 32 (2016) 5058–5068. DOI: 10.1021/acs.langmuir.6b01012

Guisbiers G., Advances in thermodynamic modelling of nanoparticles, Advances in Physics: X, 4 (2019) 1668299. DOI: 10.1080/23746149.2019.1668299

Halbig C.E., Nacken T.J., Walter J., Damm C., Eigler S., Peukert W., Quantitative investigation of the fragmentation process and defect density evolution of oxo-functionalized graphene due to ultrasonication and milling, Carbon, 96 (2016) 897–903. DOI: 10.1016/j.carbon.2015.10.021

Hammouda B., A new Guinier-Porod model, Journal of Applied Crystallography, 43 (2010) 716–719. DOI: 10.1107/S0021889810015773

Hansen S., Translational friction coefficients for cylinders of arbitrary axial ratios estimated by Monte Carlo simulation, The Journal of Chemical Physics, 121 (2004) 9111–9115. DOI: 10.1063/1.1803533

Haubold S., Haase M., Kornowski A., Weller H., Strongly luminescent InP/ZnS core-shell nanoparticles, ChemPhysChem, 2 (2001) 331–334. DOI: 10.1002/1439-7641(20010518)2:5<331::AID-CPHC331>3.0.CO;2-0

Hauser M., Wojcik M., Kim D., Mahmoudi M., Li W., Xu K., Correlative super-resolution microscopy: new dimensions and new opportunities, Chemical Reviews, 117 (2017) 7428–7456. DOI: 10.1021/acs.chemrev.6b00604

He Z., Wang P., Liu D., Zhou Z., Hydrophilic-lipophilic balanced magnetic nanoparticles: preparation and application in magnetic solid-phase extraction of organochlorine pesticides and triazine herbicides in environmental water samples, Talanta, 127 (2014) 1–8. DOI: 10.1016/j.talanta.2014.03.074

Heffels C.M.G., Verheijen P.J.T., Heitzmann D., Scarlett B., Correction of the effect of particle shape on the size distribution measured with a laser diffraction instrument, Particle & Particle Systems Characterization, 13 (1996) 271–279. DOI: 10.1002/ppsc.19960130504

Herre P., Romeis S., Mačković M., Przybilla T., Paul J., Schwenger J., Torun B., Grundmeier G., Spiecker E., Peukert W., Deformation behavior of nanocrystalline titania particles accessed by complementary in situ electron microscopy techniques, Journal of the American Ceramic Society, 100 (2017) 5709–5722. DOI: 10.1111/jace.15072

Heuer M., Leschonski K., Results obtained with a new instrument for the measurement of particle size distributions from diffraction patterns, Particle & Particle Systems Characterization, 2 (1985) 7–13. DOI: 10.1002/ppsc.19850020102

Hochella M.F., Lower S.K., Maurice P.A., Penn R.L., Sahai N., Sparks D.L., Twining B.S., Nanominerals, mineral nanoparticles, and earth systems, Science, 319 (2008) 1631–1635. DOI: 10.1126/science.1141134

Hofman R., Westheim J.G.F., Fransen T., Gellings P.J., Improved SiO_2-coatings against high temperature sulphidation by internal stress reduction, Le Journal de Physique IV, 03 (1993) C9-865–C9-871. DOI: 10.1051/jp4:1993989

Holst J.R., Cooper A.I., Ultrahigh surface area in porous solids, Advanced Materials, 22 (2010) 5212–5216. DOI: 10.1002/adma.201002440

Hu J., Wang H., Gao Q., Guo H., Porous carbons prepared by using metal-organic framework as the precursor for supercapacitors, Carbon, 48 (2010) 3599–3606. DOI: 10.1016/j.carbon.2010.06.008

Hu Z., Srinivasan M.P., Mesoporous high-surface-area activated carbon, Microporous and Mesoporous Materials, 43 (2001) 267–275. DOI: 10.1016/S1387-1811(00)00355-3

Hubert F., Testard F., Thill A., Kong Q., Tache O., Spalla O., Growth and overgrowth of concentrated gold nanorods: time resolved SAXS and XANES, Crystal Growth & Design, 12 (2012) 1548–1555. DOI: 10.1021/cg2016116

Huynh K. an, Siska E., Heithmar E., Tadjiki S., Pergantis S.A., Detection and quantification of silver nanoparticles at environmentally relevant concentrations using asymmetric flow field-flow fractionation online with single particle inductively coupled plasma mass spectrometry, Analytical Chemistry, 88 (2016) 4909–4916. DOI: 10.1021/acs.analchem.6b00764

Jallo L.J., Chen Y., Bowen J., Etzler F., Dave R., Prediction of inter-particle adhesion force from surface energy and surface roughness, Journal of Adhesion Science and Technology, 25 (2011) 367–384. DOI: 10.1163/016942410X525623

Jimbo G., Chemical engineering analysis of fine grinding phenomenon and process, Journal of Chemical Engineering of Japan, 25 (1992) 117–127. DOI: 10.1252/jcej.25.117

Joye I.J., McClements D.J., Biopolymer-based nanoparticles and microparticles: fabrication, characterization, and application, Current Opinion in Colloid & Interface Science, 19 (2014) 417–427. DOI: 10.1016/j.cocis.2014.07.002

Kang S.H., Lyoo P.J., Kim D.W., Park J.H., Laser diffraction pattern analysis of various two-dimensional regular-shaped model particles, Advanced Powder Technology, 5 (1994) 33–42. DOI: 10.1016/S0921-8831(08)60623-8

Kannan A.G., Manjulavalli T.E., Chandrasekaran J., Influence of solvent on the properties of CZTS nanoparticles, Procedia Engineering, 141 (2016) 15–22. DOI: 10.1016/j.proeng.2015.08.1112

Karabudak E., Brookes E., Lesnyak V., Gaponik N., Eychmüller A., Walter J., Segets D., Peukert W., Wohlleben W., Demeler B., Cölfen H., Simultaneous identification of spectral properties and sizes of multiple particles in solution with subnanometer resolution, Angewandte Chemie International Edition, 55 (2016) 11770–11774. DOI: 10.1002/anie.201603844

Karabudak E., Cölfen H., The multiwavelength UV/Vis detector: new possibilities with an added spectral dimension, in: Uchiyama S., Arisaka F., Stafford W.F., Laue T. (Eds.), Analytical Ultracentrifugation—Instrumentation, Software, and Applications, Springer Japan, Tokyo, 2016, pp. 63–80. DOI: 10.1007/978-4-431-55985-6_5

Kato H., Nakamura A., Banno H., Determination of number-based size distribution of silica particles using centrifugal field-flow fractionation, Journal of Chromatography. A, 1602 (2019) 409–418. DOI: 10.1016/j.chroma.2019.05.055

Kempkes M., Eggers J., Mazzotti M., Measurement of particle size and shape by FBRM and in situ microscopy, Chemical Engineering Science, 63 (2008) 4656–4675. DOI: 10.1016/j.ces.2007.10.030

Khan I.U., Stolch L., Serra C.A., Anton N., Akasov R., Vandamme T.F., Microfluidic conceived pH sensitive core-shell particles for dual drug delivery, International Journal of Pharmaceutics, 478 (2015) 78–87. DOI: 10.1016/j.ijpharm.2014.10.010

Kim D., Moon J., Highly conductive ink jet printed films of nanosilver particles for printable electronics, Electrochemical and Solid-State Letters, 8 (2005) J30–J33. DOI: 10.1149/1.2073670

Kim K.-M., Kim H.M., Lee W.-J., Lee C.-W., Kim T.-I., Lee J.-K., Jeong J., Paek S.-M., Oh J.-M., Surface treatment of silica nanoparticles for stable and charge-controlled colloidal silica, International Journal of Nanomedicine, 9 Suppl 2 (2014) 29–40. DOI: 10.2147/IJN.S57922

Kim S.-S., Na S.-I., Jo J., Kim D.-Y., Nah Y.-C., Plasmon enhanced performance of organic solar cells using electrodeposited Ag nanoparticles, Applied Physics Letters, 93 (2008) 073307. DOI: 10.1063/1.2967471

Kleijn S.E.F., Lai S.C.S., Miller T.S., Yanson A.I., Koper M.T.M., Unwin P.R., Landing and catalytic characterization of individual nanoparticles on electrode surfaces, Journal of the American Chemical Society, 134 (2012) 18558–18561. DOI: 10.1021/ja309220m

Knieke C., Romeis S., Peukert W., Influence of process parameters on breakage kinetics and grinding limit at the nanoscale, AIChE Journal, 57 (2011) 1751–1758. DOI: 10.1002/aic.12408

Kovačević T., Reinhold A., Briesen H., Identifying faceted crystal shape from three-dimensional tomography data, Crystal Growth & Design, 14 (2014) 1666–1675. DOI: 10.1021/cg401780p

La Torre J.G. de, Echenique G.d.R., Ortega A., Improved calculation of rotational diffusion and intrinsic viscosity of bead models for macromolecules and nanoparticles, The Journal of Physical Chemistry B, 111 (2007) 955–961. DOI: 10.1021/jp0647941

Larriba C., Fernandez de la Mora J., Clemmer D.E., Electrospray ionization mechanisms for large polyethylene glycol chains studied through tandem ion mobility spectrometry, Journal of the American Society for Mass Spectrometry, 25 (2014) 1332–1345. DOI: 10.1007/s13361-014-0885-0

Larriba C., Fernandez de la Mora J., The gas phase structure of coulombically stretched polyethylene glycol ions, The Journal of Physical Chemistry B, 116 (2012) 593–598. DOI: 10.1021/jp2092972

Lee J.S., Shin D.H., Jun J., Lee C., Jang J., Fe_3O_4/carbon hybrid nanoparticle electrodes for high-capacity electrochemical capacitors, ChemSusChem, 7 (2014) 1676–1683. DOI: 10.1002/cssc.201301188

Leißner T., Diener A., Löwer E., Ditscherlein R., Krüger K., Kwade A., Peuker U.A., 3D ex-situ and in-situ X-ray CT process studies in particle technology—A perspective, Advanced Powder Technology, 31 (2020) 78–86. DOI: 10.1016/j.apt.2019.09.038

Leschonski K., Alex W., Koglin B., Teilchengrößenanalyse. 1. darstellung und auswertung von teilchengrößenverteilungen, Chemie Ingenieur Technik, 46 (1974a) 23–26. DOI: 10.1002/cite.330460105

Leschonski K., Alex W., Koglin B., Teilchengrößenanalyse. 1. darstellung und auswertung von teilchengrößenverteilungen (Fortsetzung), Chemie Ingenieur Technik, 46 (1974b) 101–106. DOI: 10.1002/cite.330460307

Letellier P., Mayaffre A., Turmine M., Solubility of nanoparticles: nonextensive thermodynamics approach, Journal of Physics: Condensed Matter, 19 (2007) 436229. DOI: 10.1088/0953-8984/19/43/436229

Li C., Lee A.L., Chen X., Pomerantz W.C.K., Haynes C.L., Hogan C.J., Multidimensional nanoparticle characterization through ion mobility-mass spectrometry, Analytical Chemistry, 92 (2020) 2503–2510. DOI: 10.1021/acs.analchem.9b04012

Li Q., Kartikowati C.W., Horie S., Ogi T., Iwaki T., Okuyama K., Correlation between particle size/domain structure and magnetic properties of highly crystalline Fe_3O_4 nanoparticles, Scientific Reports, 7 (2017) 9894. DOI: 10.1038/s41598-017-09897-5

Li T., Senesi A.J., Lee B., Small angle X-ray scattering for nanoparticle research, Chemical Reviews, 116 (2016) 11128–11180. DOI: 10.1021/acs.chemrev.5b00690

Li W., Xue Y., Cui Z., Size dependence of surface thermodynamic properties of nanoparticles and its determination method by reaction rate constant, Physica B: Condensed Matter, 495 (2016) 98–105. DOI: 10.1016/j.physb.2016.05.011

Ligon S.C., Liska R., Stampfl J., Gurr M., Mülhaupt R., Polymers for 3D printing and customized additive manufacturing, Chemical Reviews, 117 (2017) 10212–10290. DOI: 10.1021/acs.chemrev.7b00074

Link S., Wang Z.L., El-Sayed M.A., Alloy formation of gold–silver nanoparticles and the dependence of the plasmon absorption on their composition, The Journal of Physical Chemistry B, 103 (1999) 3529–3533. DOI: 10.1021/jp990387w

Loh N.D., Hampton C.Y., Martin A.V., Starodub D., Sierra R.G., Barty A., Aquila A., Schulz J., Lomb L., Steinbrener J., Shoeman R.L., Kassemeyer S., Bostedt C., Bozek J., Epp S.W., et al., Fractal morphology, imaging and mass spectrometry of single aerosol particles in flight, Nature, 486 (2012) 513–517. DOI: 10.1038/nature11222

Lübbert C., Peukert W., The mass transfer at Taylor cones, Journal of Aerosol Science, 123 (2018) 39–51. DOI: 10.1016/j.jaerosci.2018.05.014

Ma Z., Merkus H.G., van der Veen H.G., Wong M., Scarlett B., On-line measurement of particle size and shape using laser diffraction, Particle & Particle Systems Characterization, 18 (2001) 243–247. DOI: 10.1002/1521-4117(200112)18:5/6<243::AID-PPSC243>3.0.CO;2-4

Maestro A., Guzmán E., Santini E., Ravera F., Liggieri L., Ortega F., Rubio R.G., Wettability of silicananoparticle-surfactant nanocomposite interfacial layers, Soft Matter, 8 (2012) 837–843. DOI: 10.1039/C1SM06421E

Maire E., Withers P.J., Quantitative X-ray tomography, International Materials Reviews, 59 (2014) 1–43. DOI: 10.1179/1743280413Y.0000000023

Malvern Panalytical, Morphologi 4 range homepage, <www.malvernpanalytical.com/en/products/product-range/morphologi-range/> accessed 02.02.2021.

Mangun C.L., Benak K.R., Economy J., Foster K.L., Surface chemistry, pore sizes and adsorption properties of activated carbon fibers and precursors treated with ammonia, Carbon, 39 (2001) 1809–1820. DOI: 10.1016/S0008-6223(00)00319-5

Matsuyama T., Yamamoto H., Particle shape and laser diffraction: a discussion of the particle shape problem, Journal of Dispersion Science and Technology, 25 (2005) 409–416. DOI: 10.1081/DIS-200025692

Mazumder M.K., Ware R.E., Yokoyama T., Rubin B.J., Kamp D., Measurement of particle size and electrostatic charge distributions on toners using E-SPART analyzer, IEEE Transactions on Industry Applications, 27 (1991) 611–619. DOI: 10.1109/28.85472

McMurry P.H., Takano H., Anderson G.R., Study of the ammonia (gas)-sulfuric acid (aerosol) reaction rate, Environmental Science & Technology, 17 (1983) 347–352. DOI: 10.1021/es00112a008

McMurry P.H., Wang X., Park K., Ehara K., The relationship between mass and mobility for atmospheric particles: a new technique for measuring particle density, Aerosol Science and Technology, 36 (2002) 227–238. DOI: 10.1080/027868202753504083

Miao J., Ercius P., Billinge S.J.L., Atomic electron tomography: 3D structures without crystals, Science, 353 (2016) aaf2157. DOI: 10.1126/science.aaf2157

Modena M.M., Rühle B., Burg T.P., Wuttke S., Nanoparticle characterization: what to measure?, Advanced Materials, 31 (2019) 1901556. DOI: 10.1002/adma.201901556

Mogyorósi K., Dékány I., Fendler J.H., Preparation and characterization of clay mineral intercalated titanium dioxide nanoparticles, Langmuir, 19 (2003) 2938–2946. DOI: 10.1021/la025969a

Mokari T., Rothenberg E., Popov I., Costi R., Banin U., Selective growth of metal tips onto semiconductor quantum rods and tetrapods, Science, 304 (2004) 1787–1790. DOI: 10.1126/science.1097830

Montaño M.D., Olesik J.W., Barber A.G., Challis K., Ranville J.F., Single particle ICP-MS: advances toward routine analysis of nanomaterials, Analytical and Bioanalytical Chemistry, 408 (2016) 5053–5074. DOI: 10.1007/s00216-016-9676-8

Motl N.E., Ewusi-Annan E., Sines I.T., Jensen L., Schaak R.E., Au–Cu alloy nanoparticles with tunable compositions and plasmonic properties: experimental determination of composition and correlation with theory, The Journal of Physical Chemistry C, 114 (2010) 19263–19269. DOI: 10.1021/jp107637j

Mozhayeva D., Engelhard C., A critical review of single particle inductively coupled plasma mass spectrometry—a step towards an ideal method for nanomaterial characterization, Journal of Analytical Atomic Spectrometry, 35 (2020) 1740–1783. DOI: 10.1039/c9ja00206e

Müller-Buschbaum P., A basic introduction to grazing incidence small-angle X-ray scattering, in: Gomez M., Nogales A., Garcia-Gutierrez M.C., Ezquerra T.A. (Eds.), Applications of Synchrotron Light to Scattering and Diffraction in Materials and Life Sciences, Springer Berlin Heidelberg, 2009, pp.61–89, ISBN: 978-3-540-95968-7. DOI: 10.1007/978-3-540-95968-7_3

Murphy R.P., Hong K., Wagner N.J., Synthetic control of the size, shape, and polydispersity of anisotropic silica colloids, Journal of Colloid and Interface Science, 501 (2017) 45–53. DOI: 10.1016/j.jcis.2017.04.026

Murthy S.K., Nanoparticles in modern medicine: state of the art and future challenges, International Journal of Nanomedicine, 2 (2007) 129–141.

Nacken T., Damm C., Xing H., Rüger A., Peukert W., Determination of quantitative structure-property and structure-process relationships for graphene production in water, Nano Research, 8 (2015) 1865–1881. DOI: 10.1007/s12274-014-0694-6

Nacken T.J., Damm C., Walter J., Rüger A., Peukert W., Delamination of graphite in a high pressure homogenizer, RSC Advances, 5 (2015) 57328–57338. DOI: 10.1039/c5ra08643d

Navrotsky A., Energetics of nanoparticle oxides: interplay between surface energy and polymorphism, Geochemical Transactions, 4 (2003) 34–37. DOI: 10.1039/b308711e

Neeleshwar S., Chen C.L., Tsai C.B., Chen Y.Y., Chen C.C., Shyu S.G., Seehra M.S., Size-dependent properties of CdSe quantum dots, Physical Review B, 71 (2005) 201307. DOI: 10.1103/PhysRevB.71.201307

Ngo T.D., Kashani A., Imbalzano G., Nguyen K.T.Q., Hui D., Additive manufacturing (3D printing): A review of materials, methods, applications and challenges, Composites Part B: Engineering, 143 (2018) 172–196. DOI: 10.1016/j.compositesb.2018.02.012

Noble C.A., Prather K.A., Real-time single particle mass spectrometry: a historical review of a quarter century of the chemical analysis of aerosols, Mass Spectrometry Reviews, 19 (2000) 248–274. DOI: 10.1002/1098-2787(200007)19:4<248::AID-MAS3>3.0.CO;2-I

Nontapot K., Rastogi V., Fagan J.A., Reipa V., Size and density measurement of core-shell Si nanoparticles by analytical ultracentrifugation, Nanotechnology, 24 (2013) 155701. DOI: 10.1088/0957-4484/24/15/155701

Novoselov K.S., Nobel lecture: graphene: materials in the flatland, Reviews of Modern Physics, 83 (2011) 837–849. DOI: 10.1103/RevModPhys.83.837

O’Brien R.W., Electro-acoustic effects in a dilute suspension of spherical particles, Journal of Fluid Mechanics, 190 (1988) 71–86. DOI: 10.1017/S0022112088001211

Olson J., Dominguez-Medina S., Hoggard A., Wang L.-Y., Chang W.-S., Link S., Optical characterization of single plasmonic nanoparticles, Chemical Society Reviews, 44 (2015) 40–57. DOI: 10.1039/c4cs00131a

Pace H.E., Rogers N.J., Jarolimek C., Coleman V.A., Higgins C.P., Ranville J.F., Determining transport efficiency for the purpose of counting and sizing nanoparticles via single particle inductively coupled plasma mass spectrometry, Analytical Chemistry, 83 (2011) 9361–9369. DOI: 10.1021/ac201952t

Park J., Elmlund H., Ercius P., Yuk J.M., Limmer D.T., Chen Q., Kim K., Han S.H., Weitz D.A., Zettl A., Alivisatos A.P., Nanoparticle imaging. 3D structure of individual nanocrystals in solution by electron microscopy, Science, 349 (2015) 290–295. DOI: 10.1126/science.aab1343

Parteli E.J.R., Pöschel T., Particle-based simulation of powder application in additive manufacturing, Powder Technology, 288 (2016) 96–102. DOI: 10.1016/j.powtec.2015.10.035

Paul J., Romeis S., Herre P., Peukert W., Deformation behavior of micron-sized polycrystalline gold particles studied by in situ compression experiments and frictional finite element simulation, Powder Technology, 286 (2015a) 706–715. DOI: 10.1016/j.powtec.2015.09.020

Paul J., Romeis S., Mačković M., Marthala V.R.R., Herre P., Przybilla T., Hartmann M., Spiecker E., Schmidt J., Peukert W., In situ cracking of silica beads in the SEM and TEM—Effect of particle size on structure–property correlations, Powder Technology, 270 (2015b) 337–347. DOI: 10.1016/j.powtec.2014.10.026

Pearson J., Walter J., Peukert W., Cölfen H., Advanced multiwavelength detection in analytical ultracentrifugation, Analytical Chemistry, 90 (2018) 1280–1291. DOI: 10.1021/acs.analchem.7b04056

Planken K.L., Cölfen H., Analytical ultracentrifugation of colloids, Nanoscale, 2 (2010) 1849–1869. DOI: 10.1039/c0nr00215a

Polavarapu L., Liz-Marzán L.M., Towards low-cost flexible substrates for nanoplasmonic sensing, Physical Chemistry Chemical Physics: PCCP, 15 (2013) 5288–5300. DOI: 10.1039/c2cp43642f

Przybilla T., Zubiri B.A., Beltrán A.M., Butz B., Machoke A.G.F., Inayat A., Distaso M., Peukert W., Schwieger W., Spiecker E., Transfer of individual micro- and nanoparticles for high-precision 3D analysis using 360° electron tomography, Small Methods, 2 (2018) 1700276. DOI: 10.1002/smtd.201700276

Raper J.A., Amal R., Measurement of aggregate fractal dimensions using static light scattering, Particle & Particle Systems Characterization, 10 (1993) 239–245. DOI: 10.1002/ppsc.19930100505

Rasteiro M.G., Garcia F.A.P., Ferreira P., Blanco A., Negro C., Antunes E., The use of LDS as a tool to evaluate flocculation mechanisms, Chemical Engineering and Processing: Process Intensification, 47 (2008) 1323–1332. DOI: 10.1016/j.cep.2007.04.009

Renaud G., Lazzari R., Leroy F., Probing surface and interface morphology with grazing incidence small angle X-ray scattering, Surface Science Reports, 64 (2009) 255–380. DOI: 10.1016/j.surfrep.2009.07.002

Rey M., Uttinger M.J., Peukert W., Walter J., Vogel N., Probing particle heteroaggregation using analytical centrifugation, Soft Matter, 16 (2020) 3407–3415. DOI: 10.1039/d0sm00026d

Rice S.B., Chan C., Brown S.C., Eschbach P., Han L., Ensor D.S., Stefaniak A.B., Bonevich J., Vladár A.E., Hight Walker A.R., Zheng J., Starnes C., Stromberg A., Ye J., Grulke E.A., Particle size distributions by transmission electron microscopy: an interlaboratory comparison case study, Metrologia, 50 (2013) 663–678. DOI: 10.1088/0026-1394/50/6/663

Richter A., Babick F., Ripperger S., Polydisperse particle size characterization by ultrasonic attenuation spectroscopy for systems of diverse acoustic contrast in the large particle limit, The Journal of the Acoustical Society of America, 118 (2005) 1394–1405. DOI: 10.1121/1.2000773

Riebel U., Löffler F., The fundamentals of particle size analysis by means of ultrasonic spectrometry, Particle & Particle Systems Characterization, 6 (1989) 135–143. DOI: 10.1002/ppsc.19890060124

Romeis S., Paul J., Ziener M., Peukert W., A novel apparatus for in situ compression of submicron structures and particles in a high resolution SEM, The Review of Scientific Instruments, 83 (2012) 095105. DOI: 10.1063/1.4749256

Roth W.J., Nachtigall P., Morris R.E., Wheatley P.S., Seymour V.R., Ashbrook S.E., Chlubná P., Grajciar L., Položij M., Zukal A., Shvets O., Cejka J., A family of zeolites with controlled pore size prepared using a top-down method, Nature Chemistry, 5 (2013) 628–633. DOI: 10.1038/nchem.1662

Rumpf H., Über die Eigenschaften von Nutzstäuben, Staub-Reinhalt der Luft, 27 (1967) 3–13.

Schach E., Buchmann M., Tolosana-Delgado R., Leißner T., Kern M., van den Gerald Boogaart K., Rudolph M., Peuker U.A., Multidimensional characterization of separation processes—Part 1: Introducing kernel methods and entropy in the context of mineral processing using SEM-based image analysis, Minerals Engineering, 137 (2019) 78–86. DOI: 10.1016/j.mineng.2019.03.026

Scheckman J.H., McMurry P.H., Pratsinis S.E., Rapid characterization of agglomerate aerosols by in situ mass-mobility measurements, Langmuir, 25 (2009) 8248–8254. DOI: 10.1021/la900441e

Schindler T., Walter J., Peukert W., Segets D., Unruh T., In situ study on the evolution of multimodal particle size distributions of ZnO quantum dots: some general rules for the occurrence of multimodalities, The Journal of Physical Chemistry B, 119 (2015) 15370–15380. DOI: 10.1021/acs.jpcb.5b08005

Schleicher B., Künzel S., Burtscher H., Insitu measurement of size and density of submicron aerosol particles, Journal of Applied Physics, 78 (1995) 4416–4422. DOI: 10.1063/1.359849

Schmid M., Häusele B., Junk M., Brookes E., Frank J., Cölfen H., High-resolution asymmetrical flow field-flow fractionation data evaluation via Richardson-Lucy-based fractogram correction, Analytical Chemistry, 90 (2018) 13978–13986. DOI: 10.1021/acs.analchem.8b03483

Schmidt J., Sachs M., Blümel C., Winzer B., Toni F., Wirth K.-E., Peukert W., A novel process route for the production of spherical LBM polymer powders with small size and good flowability, Powder Technology, 261 (2014) 78–86. DOI: 10.1016/j.powtec.2014.04.003

Schorsch S., Ochsenbein D.R., Vetter T., Morari M., Mazzotti M., High accuracy online measurement of multidimensional particle size distributions during crystallization, Chemical Engineering Science, 105 (2014) 155–168. DOI: 10.1016/j.ces.2013.11.003

Sharma A., Singh A.P., Thakur P., Brookes N.B., Kumar S., Lee C.G., Choudhary R.J., Verma K.D., Kumar R., Structural, electronic, and magnetic properties of Co doped SnO_2 nanoparticles, Journal of Applied Physics, 107 (2010) 93918. DOI: 10.1063/1.3415541

Shin W.G., Mulholland G.W., Pui D.Y.H., Determination of volume, scaling exponents, and particle alignment of nanoparticle agglomerates using tandem differential mobility analyzers, Journal of Aerosol Science, 41 (2010) 665–681. DOI: 10.1016/j.jaerosci.2010.04.009

Siedentopf H., Zsigmondy R., Uber Sichtbarmachung und Größenbestimmung ultramikoskopischer Teilchen, mit besonderer Anwendung auf Goldrubingläser, Annalen der Physik, 315 (1902) 1–39. DOI: 10.1002/andp.19023150102

So D., Pradhan S., Konstantatos G., Solid-state colloidal $CuInS_2$ quantum dot solar cells enabled by bulk heterojunctions, Nanoscale, 8 (2016) 16776–16785. DOI: 10.1039/c6nr05563j

Song H., Yang Y., Geng J., Gu Z., Zou J., Yu C., Electron tomography: a unique tool solving intricate hollow nanostructures, Advanced Materials, 31 (2019) 1801564. DOI: 10.1002/adma.201801564

Sorensen C.M., Light scattering by fractal aggregates: a review, Aerosol Science and Technology, 35 (2001) 648–687. DOI: 10.1080/02786820117868

Sorensen C.M., Yon J., Liu F., Maughan J., Heinson W.R., Berg M.J., Light scattering and absorption by fractal aggregates including soot, Journal of Quantitative Spectroscopy and Radiative Transfer, 217 (2018) 459–473. DOI: 10.1016/j.jqsrt.2018.05.016

Soto-Cantu E., Cueto R., Koch J., Russo P.S., Synthesis and rapid characterization of amine-functionalized silica, Langmuir, 28 (2012) 5562–5569. DOI: 10.1021/la204981b

Stenger F., Mende S., Schwedes J., Peukert W., Nanomilling in stirred media mills, Chemical Engineering Science, 60 (2005) 4557–4565. DOI: 10.1016/j.ces.2005.02.057

Stieß M., Mechanische Verfahrenstechnik 1, Zweite, neubearbeitete Auflage, Springer Berlin Heidelberg, Berlin, Heidelberg, 1995.

Strunz P., Mukherji D., Pigozzi G., Gilles R., Geue T., Pranzas K., Characterization of core-shell nanoparticles by small angle neutron scattering, Applied Physics A, 88 (2007) 277–284. DOI: 10.1007/s00339-007-4008-7

Sun J., Simon S.L., The melting behavior of aluminum nanoparticles, Thermochimica Acta, 463 (2007) 32–40. DOI: 10.1016/j.tca.2007.07.007

Sun Y., Cai Z., Fu J., Particle morphomics by high-throughput dynamic image analysis, Scientific Reports, 9 (2019) 9591. DOI: 10.1038/s41598-019-46062-6

Sympatec, Dynamic Image Analysis <www.sympatec.com/en/particle-measurement/sensors/dynamic-image-analysis/> accessed 02.02.2021.

Tahara T., Quan X., Otani R., Takaki Y., Matoba O., Digital holography and its multidimensional imaging applications: a review, Microscopy, 67 (2018) 55–67. DOI: 10.1093/jmicro/dfy007

Tanaka M., Komagata M., Tsukada M., Kamiya H., Fractal analysis of the influence of surface roughness of toner particles on their flow properties and adhesion behavior, Powder Technology, 186 (2008) 1–8. DOI: 10.1016/j.powtec.2007.10.030

Thajudeen T., Walter J., Srikantharajah R., Lübbert C., Peukert W., Determination of the length and diameter of nanorods by a combination of analytical ultracentrifugation and scanning mobility particle sizer, Nanoscale Horizons, 2 (2017) 253–260. DOI: 10.1039/c7nh00050b

Theerthagiri J., Senthil R.A., Senthilkumar B., Reddy Polu A., Madhavan J., Ashokkumar M., Recent advances in MoS_2 nanostructured materials for energy and environmental applications—A review, Journal of Solid State Chemistry, 252 (2017) 43–71. DOI: 10.1016/j.jssc.2017.04.041

Tsai D.-H., DelRio F.W., Pettibone J.M., Lin P.-A., Tan J., Zachariah M.R., Hackley V.A., Temperature-programmed electrospray-differential mobility analysis for characterization of ligated nanoparticles in complex media, Langmuir, 29 (2013) 11267–11274. DOI: 10.1021/la402311c

Uchiyama S., Arisaka F., Stafford W.F., Laue T.M., (Eds.), Analytical Ultracentrifugation Instrumentation, Software, and Applications, Springer Japan, Tokyo, 2016, ISBN: 978-4-431-55983-2. DOI: 10.1007/978-4-431-55985-6

Uttinger M.J., Boldt S., Wawra S.E., Freiwald T.D., Damm C., Walter J., Lerche D., Peukert W., New prospects for particle characterization using analytical centrifugation with sector-shaped centerpieces, Particle & Particle Systems Characterization, 37 (2020) 2000108. DOI: 10.1002/ppsc.202000108

Verleysen E., Wagner T., Lipinski H.-G., Kägi R., Koeber R., Boix-Sanfeliu A., De Temmerman P.-J., Mast J., Evaluation of a TEM based Approach for Size Measurement of Particulate (Nano)materials, Materials, 12 (2019) 2274. DOI: 10.3390/ma12142274

Voigtländer B., Atomic Force Microscopy, 2nd ed. Springer, Cham, Switzerland, 2019. ISBN: 978-3-030-13653-6. DOI: 10.1007/978-3-030-13654-3

Walter J., Löhr K., Karabudak E., Reis W., Mikhael J., Peukert W., Wohlleben W., Cölfen H., Multidimensional analysis of nanoparticles with highly disperse properties using multiwavelength analytical ultracentrifugation, ACS Nano, 8 (2014) 8871–8886. DOI: 10.1021/nn503205k

Walter J., Thajudeen T., Süss S., Segets D., Peukert W., New possibilities of accurate particle characterisation by applying direct boundary models to analytical centrifugation, Nanoscale, 7 (2015) 6574–6587. DOI: 10.1039/c5nr00995b

Wang J., Mbah C.F., Przybilla T., Apeleo Zubiri B., Spiecker E., Engel M., Vogel N., Magic number colloidal clusters as minimum free energy structures, Nature Communications, 9 (2018) 5259. DOI: 10.1038/s41467-018-07600-4

Wang T.C., Bury W., Gómez-Gualdrón D.A., Vermeulen N.A., Mondloch J.E., Deria P., Zhang K., Moghadam P.Z., Sarjeant A.A., Snurr R.Q., Stoddart J.F., Hupp J.T., Farha O.K., Ultrahigh surface area zirconium MOFs and insights into the applicability of the BET theory, Journal of the American Chemical Society, 137 (2015) 3585–3591. DOI: 10.1021/ja512973b

Wang Y., Yang X., Liu W., Zhang F., Cai Q., Deng X., Controlled release behaviour of protein-loaded microparticles prepared via coaxial or emulsion electrospray, Journal of Microencapsulation, 30 (2013) 490–497. DOI: 10.3109/02652048.2012.752537

Wawra S.E., Onishchukov G., Maranska M., Eigler S., Walter J., Peukert W., A multiwavelength emission detector for analytical ultracentrifugation, Nanoscale Advances, 1 (2019) 4422–4432. DOI: 10.1039/C9NA00487D

Wawra S.E., Pflug L., Thajudeen T., Kryschi C., Stingl M., Peukert W., Determination of the two-dimensional distributions of gold nanorods by multiwavelength analytical ultracentrifugation, Nature Communications, 9 (2018) 4898. DOI: 10.1038/s41467-018-07366-9

Waychunas G.A., Zhang H., Structure, chemistry, and properties of mineral nanoparticles, Elements, 4 (2008) 381–387. DOI: 10.2113/gselements.4.6.381

Weber A.P., Baltensperger U., Gäggeler H.W., Tobler L., Keil R., Schmidt-Ott A., Simultaneous in-situ measurements of mass, surface and mobilitydiameter of silver agglomerates, Journal of Aerosol Science, 22 (1991) S257–S260. DOI: 10.1016/S0021-8502(05)80084-9

Wessells C.D., McDowell M.T., Peddada S.V., Pasta M., Huggins R.A., Cui Y., Tunable reaction potentials in open framework nanoparticle battery electrodes for grid-scale energy storage, ACS Nano, 6 (2012) 1688–1694. DOI: 10.1021/nn204666v

Willets K.A., Wilson A.J., Sundaresan V., Joshi P.B., Super-resolution imaging and plasmonics, Chemical Reviews, 117 (2017) 7538–7582. DOI: 10.1021/acs.chemrev.6b00547

Wu Z.J., Poulain L., Henning S., Dieckmann K., Birmili W., Merkel M., van Pinxteren D., Spindler G., Müller K., Stratmann F., Herrmann H., Wiedensohler A., Relating particle hygroscopicity and CCN activity to chemical composition during the HCCT-2010 field campaign, Atmospheric Chemistry and Physics, 13 (2013) 7983–7996. DOI: 10.5194/acp-13-7983-2013

Xu R., Light scattering: a review of particle characterization applications, Particuology, 18 (2015) 11–21. DOI: 10.1016/j.partic.2014.05.002

Yan J., Teo B.K., Zheng N., Surface chemistry of atomically precise coinage-metal nanoclusters: from structural control to surface reactivity and catalysis, Accounts of Chemical Research, 51 (2018) 3084–3093. DOI: 10.1021/acs.accounts.8b00371

Yao Y., Lenhoff A.M., Determination of pore size distributions of porous chromatographic adsorbents by inverse size-exclusion chromatography, Journal of Chromatography A, 1037 (2004) 273–282. DOI: 10.1016/j.chroma.2004.02.054

Yu R., Liz-Marzán L.M., García de Abajo F.J., Universal analytical modeling of plasmonic nanoparticles, Chemical Society Reviews, 46 (2017) 6710–6724. DOI: 10.1039/c6cs00919k

Zhang L., Blom D.A., Wang H., Au–Cu_2O core–shell nanoparticles: a hybrid metal-semiconductor heteronanostructure with geometrically tunable optical properties, Chemistry of Materials, 23 (2011) 4587–4598. DOI: 10.1021/cm202078t

Zhang W., Ge Q., Wang L., Structure effects on the energetic, electronic, and magnetic properties of palladium nanoparticles, The Journal of Chemical Physics, 118 (2003) 5793–5801. DOI: 10.1063/1.1557179

Zhong L., Fu S., Peng X., Zhan H., Sun R., Colloidal stability of negatively charged cellulose nanocrystalline in aqueous systems, Carbohydrate Polymers, 90 (2012) 644–649. DOI: 10.1016/j.carbpol.2012.05.091

Zhu M., Lin Y., Lo E.W.C., Wang Q., Zhao Z., Xie W., Electronic and magnetic properties of La_2NiMnO_6 and La_2CoMnO_6 with cationic ordering, Applied Physics Letters, 100 (2012) 062406. DOI: 10.1063/1.3683550

Zhuang T.-T., Li Y., Gao X., Wei M., García de Arquer F.P., Todorović P., Tian J., Li G., Zhang C., Li X., Dong L., Song Y., Lu Y., Yang X., Zhang L., Fan F., Kelley S.O., Yu S.-H., Tang Z., Sargent E.H., Regioselective magnetization in semiconducting nanorods, Nature Nanotechnology, 15 (2020) 192–197. DOI: 10.1038/s41565-019-0606-8

Authors' Short Biographies

Uwe Frank

Uwe Frank obtained his Bachelor and Master degrees in physics at the Friedrich Alexander University Erlangen-Nürnberg. Now he is a doctoral researcher at the Institute of Particle Technology in the group of Wolfgang Peukert. His main research fields contain the multidimensional characterization of anisotropic particle systems, the fundamentals of multidimensional particle technology and analytical ultracentrifugation.

Maximilian J. Uttinger

Maximilian J. Uttinger received his Bachelor degree in Chemical Engineering from Friedrich-Alexander University Erlangen-Nürnberg in 2014. Afterwards, Maximilian received his Master degree in Advanced Materials and Processes from Friedrich-Alexander University Erlangen-Nürnberg in 2017. Currently, he is a doctoral researcher at the Institute of Particle Technology in the group of Wolfgang Peukert. His research interest is on Analytical Ultracentrifugation and Analytical Centrifugation with a focus on non-ideal sedimentation behavior.

Simon E. Wawra

Simon Wawra received his Bachelor of Science degree in physics from the University of Bayreuth in 2013 and his Master of Science degree in physics from the Technical University of Dresden in 2015. Currently, Simon is a doctoral researcher at the Institute of Particle Technology in the group of Wolfgang Peukert. Simon's main research topic is the simultaneous hydrodynamic and optical characterization of nanoparticles using analytical ultracentrifugation.

Christian Lübbert

Dr.-Ing. Christian Lübbert received his Diploma in chemical engineering and environmental technology at the University of Cottbus (BTU Cottbus). He received his doctor's degree at the chair of Particle Technology (BTU Cottbus). Currently, he is working in Wolfgang Peukert's group at the Institute of Particle Technology (Friedrich-Alexander University Erlangen-Nürnberg). His work is focussed on electrosprays, mobility classified mass spectrometry and electrostatics effects in particle systems.

Wolfgang Peukert

Wolfgang Peukert studied Chemical Engineering at the University Karlsruhe, where he obtained his Dr-Ing. He was research engineer at Hosokawa Micron, Japan, R&D director of Hosokawa MikroPul, Cologne and board member of Hosokawa Int., New York. From 1998 until 2003 he held a full professorship at the Technical University of Munich. Since 2003 Wolfgang Peukert is the head of the institute of Particle Technology (LFG) at the Friedrich-Alexander University of Erlangen-Nuremberg. His research interests are widespread in Particle Technology with emphasis on nanoparticle technology, product design and formulation technology, interface science and engineering.

KONA Powder and Particle Journal No. 39 (2022) 29–44/https://doi.org/10.14356/kona.2022008 Review Paper

The Sevilla Powder Tester: A Tool for Measuring the Flow Properties of Cohesive Powders at High Temperatures[†]

Rahma Gannoun, José Manuel Pérez Ebrí, Alberto T. Pérez and José Manuel Valverde[*]

Facultad de Física, Universidad de Sevilla, Spain

Abstract

Understanding the flowability of cohesive powders at high temperature is of great importance for many industrial applications where these materials are handled at harsh thermal conditions. For instance, the Calcium-Looping (CaL) process, involving the transport, storage and fluidization of limestone powders at high temperature, is being considered nowadays as a promising technology for thermochemical energy storage (TCES) in concentrated solar power plants (CSP). In this context, the High Temperature Seville Powder Tester (HTSPT) is presented in this work as a useful tool to analyze how the flow behavior of cohesive powders changes with temperature. The manuscript reviews the main results obtained so far using this novel apparatus. The change of powder cohesiveness and therefore of powder flowability as depending on temperature, particle size, material properties and nanosilica surface coating is illustrated.

Keywords: calcium looping (CaL), HTSPT, flowability, thermochemical energy storage (TCES), fluidization

1. Introduction

The calcium looping (CaL) process has been widely investigated as a 2nd generation technology to capture CO_2 from fossil fuel power plants with already proven high efficiency in large scale pilot plants (1–2 MWh) (Barker, 1974; Blamey et al., 2010; Chacartegui et al., 2016; Kierzkowska et al., 2013; Prieto et al., 2016; Valverde, 2013). The CaL technology benefits from the abundance, low price and lack of toxicity of natural CaO precursors such as limestone and dolomite that can be used as raw material. Basically, the CaL process relies on the reversible calcination/carbonation reaction

$$CaCO_3\,(s) \rightleftarrows CaO\,(s) + CO_2\,(g) \qquad (1)$$
$$\Delta H_r^0 = 178\ \text{kJ/mol}$$

During the exothermic carbonation reaction, solid CaO particles react in a fluidized bed reactor at approximately 650 °C with the flue gas containing a small concentration of CO_2 (around 15 % vol). The carbonated particles are then taken to a fluidized bed calciner where the endothermic decomposition of $CaCO_3$ takes place to regenerate the CaO at temperatures above 900 °C in a high CO_2 concentration environment (Valverde, 2013; 2015). More recently, the CaL process has been the subject of several studies to store energy in concentrated solar power (CSP) plants (Chacartegui et al., 2016; Paksoy, 2007; Pardo et al., 2014). Currently, small scale pilot plants are under development showing promising results (Cordis, 2020).

Due to the growing need to employ green renewable energy, the massive deployment of CSP plants has come up as an affordable and highly efficient solution for electricity generation at large scale. However, the efficiency of CSP plants is hindered by the intermittence of solar direct radiation which leads to an unbalance between electricity production and demand. Thermal energy storage (TES) technologies allow releasing thermal energy to generate electricity when is required by means of heat storage materials, thus solving shortcomings and discontinuity issues. A major challenge to minimize the cost of CSP with storage and enhance its efficiency is to select adequate thermal energy storage system. Based on different factors, energy storage technologies are classified as sensible heat storage (SHS), latent heat storage (LHS), and thermochemical energy storage (TCES) (Hall and Hausz, 1979). Sensible heat storage stores and releases sensible heat by means of a change in the temperature of the material used. Synthetic oils, molten salts, liquid metals and concretes are the main sensible heat storage materials employable in CSP. Characterized by their high specific heat capacity, relatively low cost and acceptable safety, molten salts are being currently employed in commercial CSP plants (Fernández et al., 2014; Sang et al., 2015; Wu et al., 2017;

[†] Received 10 March 2021; Accepted 11 May 2021
J-STAGE Advance published online 26 June 2021

[*] Corresponding author: José Manuel Valverde;
Add: Avenida Reina Mercedes s/n, 41012 Sevilla, Spain
E-mail: jmillan@us.es
TEL: +34-954550960

Zhang et al., 2013). However, below temperatures around 200 °C, molten salts solidify, which requires keeping the whole circuit above this melting temperature even during prolonged periods of absence of solar direct solar radiation. In addition, above temperatures ~560 °C, molten salts degrade whereas the temperatures achievable at CSP plants with tower technology are around 1000 °C. Thus, the use of molten salts for power generation burdens the potential efficiency of CSP plants for power production. Moreover, molten salts are corrosive particularly at high temperature which requires the use of special equipment and therefore leads to high maintenance costs (Dunn et al., 2012; Ortega et al., 2008).

Latent heat storage or phase-change energy storage is based on the heat stored and released when the material experiences a phase change (evaporation, melting, crystallization etc.). The choice of phase change materials (PCMs) intended for TES applications needs to meet some suitable features: kinetic, physical, chemical, thermodynamic and, of course, economic affordability. Solid-liquid PCMs are the most used ones in research projects under development. Yet, these materials release low latent heat and only in the limited range of temperatures wherein phase transition occurs. In addition some significant drawbacks are their generally low thermal conductivity, phase separation, expensive maintenance costs, and also low operating temperature ranges (up to ~90 °C) (Herrmann and Kearney, 2002; Pintaldi et al., 2015; Sharma et al., 2009).

In this context, thermochemical energy storage (TCES) is considered as a promising technology for energy storage in CSP systems (Abedin, 2011; Cabeza et al., 2012; Paksoy, 2007; Tatsidjodoung et al., 2013), as demonstrated by the growing number of reviews published in the last years on this technology which is currently under development (André et al., 2016; Barker, 1974; Carrillo et al., 2019; Gil et al., 2010; Mahlia et al., 2014; Pardo et al., 2014). TCES relies on the storage/release of heat via reversible chemical reactions (Carrillo et al., 2019; Dinçer and Rosen, 2010). The most relevant advantages of TCES include the possibility of long term heat storage, high stored energy density, small energy loss and the suitability to operate at very high temperatures (up to 1000 °C or above (Abedin, 2011; Cabeza et al., 2012; Tatsidjodoung et al., 2013). Among the diverse options investigated for TCES a major candidate is the CaL process. Besides of the low cost, abundance and lack of toxicity of limestone used as raw material, a particularly relevant advantage of the integration of the CaL process in CSP plants is that the $CaCO_3$ calcination temperature fits in the range of temperatures attainable at the receiver of CSP plants with tower technology (Pinel et al., 2011).

A possible technique for operating the CaL process in CSP plants is to use fluidized bed reactors albeit other type of reactors such as falling particle, entrained flow and centrifugal particle reactors that might be better integrated in solar receivers are being investigated (Cordis, 2020; Esence et al., 2020; Karasavvas et al., 2020; Lisbona et al., 2020; Sarrion et al., 2016; Tesio et al., 2019; 2020), $CaCO_3$/CaO solids to be employed in the CaL-CSP integration would preferably be in the form of fine powders to mitigate reaction rate limiting mechanisms such as pore plugging (Benitez-Guerrero et al., 2017) that might hinder the process at the most favorable operating conditions for the CaL-CSP integration (Hanak et al., 2015). As it is well-known from experience, the lack of material flowability may be a serious issue in industrial applications where fine powders are employed due to their high cohesiveness, which can be enhanced even further at high temperatures (Chirone et al., 2020; Lettieri et al., 2000; Macrì et al., 2017; Tomasetta et al., 2011). The Sevilla Powder Tester (SPT) has proven itself as a reliable and accurate device for the characterization of cohesive powders (Barletta et al., 2019; Castellanos, 2005; Castellanos et al., 2004; Chen et al., 2009; Valverde et al., 2000; Zafar et al., 2015). Recently, it has been upgraded to be used at high temperatures. The present manuscript aims to present a detailed description of the so-called High Temperature Sevilla Powder Tester (HTSPT). We review the main results recently obtained by means of this novel setup, with a special focus on the effect of temperature on the tensile yield strength of fine powders as depending on particle size, surface coating and material properties.

2. A brief critical review on powder flowability testers

Exhaustive research has been conducted with the aim of exploring relevant techniques to assess the ability of powders to flow (Schwedes, 2003). Here we summarize the main methods envisaged from a critical comparative analysis.

One of these methods, as described in the book of the American Society for Testing and Materials Standards (ASTM, 1978), is based on measuring the time required by a certain amount of powder to discharge through a hopper. Hall and Cutress (1960) showed that this technique can be useful for metallic powders. An external energy source should be provided to enhance the flow for very cohesive powders, which introduces uncertainty to the results. A rheometer composed of shear heads, blades and pistons is another tool to evaluate powder flowability. To measure the rotational and axial forces, the components of the setup are rotated and stirred in the axial direction. A detailed description of the setup can be found in (Freeman, 2004). The reliability of these testers is somewhat compromised due to the lack of reproducibility. For instance, the history of the powder is dependent on the filling procedure, the applied load, the device used and the working conditions (Castellanos et al., 2004).

At the microscopic level, interparticle contact forces are ultimately the main drive for powder flowability (Quintanilla et al., 2001a). Thus, the direct measurement of these forces is the best method to understand the physical mechanism that governs powder flow behavior. Shimada et al. (2002) conceived an instrument to directly measure adhesive contact forces between particles or between a plane surface and a powder sample. This study concerned organic powders (potato starch, lactose and cornstarch). An advantage of the device is that it can handle fine and very cohesive particles (even below 10 μm in size). Thereafter, by means of a camera or microscope, it analyses the adhesion force for a selected individual particle. They compared the obtained results with those found by another direct method (the centrifugal method) based also on a post-process image analysis of powder avalanches in a rotating drum (Lüddecke et al., 2021; Quintanilla et al., 2001b). The authors confirmed that both methods agree qualitatively. Unfortunately, these techniques do not allow to control the stress state of the powder that greatly impacts the contact forces (Quintanilla et al., 2001a). In this context, Quintanilla et al. (2001a) employed an atomic force microscope (AFM) to determine the adhesion force between irregularly shaped particles of xerographic toners. The load force previously applied on the individual particles can be accurately controlled through this technique. Comparing their findings with the interparticle forces estimated from measurements of the bulk stresses in the Seville Powder Tester (SPT) (Castellanos et al., 2004), they reported an acceptable agreement. However, it should be highlighted that the results on the forces directly measured using the AFM technique showed a large degree of dispersion, which was attributed to the critical dependence of the adhesion contact forces to the highly variable local surface properties (Castellanos, 2005; Castellanos et al., 2004).

Recently, Marchetti and Hulme-Smith (2021) investigated the flowability of 11 metal powders with different properties and particle size distributions employing six different testers. The ability of the powders to flow was determined by means of diverse indicators such as the flow rate, Hausner ratio, basic flowability energy (BFE), compressibility (CPS), major principal stress (MPS), angle of internal friction (AIF), flow factor (FF), angle of repose, specific energy (SE), and the unconfined yield stress (UYS). The interested reader could find further details about the powder testers and the different parameters in (Marchetti and Hulme-Smith, 2021; Schwedes, 2003; Castellanos et al., 2004; Lettieri and Macrì, 2016).

Marchetti and Hulme-Smith (2021) demonstrated the existence of correlations between these different parameters to characterize powder flow. They reported that, for cohesive powders, the Hall and Carney funnels are blocked, while the flowability indicator for these devices is the flow rate. Consequently, they are not appropriate in this case. Indeed, thanks to their simplicity, the tests based on fundamental properties (all the mentioned tests except for the rheometer with shear cell device) are widely employed in industrial and academic fields. However, the insufficient reproducibility represents a serious drawback (Ghadiri et al., 2020; Santomaso et al., 2003).

The Jenike shear cell is one of the most commonly used testers. Firstly developed by Jenike in 1953 (Schwedes, 1976), the powder sample in this test is previously subjected to a controlled consolidation stress. The sample is contained in a cylindrical cell formed by two superposed steel rings. Once the normal load is withdrawn, the tester determines the minimum steady state shear stress that must be applied to initiate powder flow. However, the Jenike tester is not suitable to evaluate powder flowability at very small consolidations (typically below 1 kPa). Besides, this technique assumes that the powder shears in a horizontal slip plane homogeneously across the sample, which is uncertain (Svarovsky, 1987).

The Peschl shear cell (Barletta et al., 2005; 2007; Bruni et al., 2007a; 2007b) was presented as an alternative to circumvent some of the above mentioned problems. The tester is essentially based on the same technic as the previously cited cells albeit the shear stress is exerted by the rotation of the upper part of the annular shear cell containing the powder sample (Svarovsky, 1987). This tester allows to determine the powder flow for an unrestrained shear distance and for a constant shear surface. Nevertheless, non-negligible wall effects and non-uniformity of stress distribution may give rise to strong uncertainties (Castellanos et al., 2004).

The above reviewed shear testers are designed to be used only at ambient temperature. Early works to assess powder flowability at high temperature were carried out by Smith et al. (1997). These authors employed the Jenike shear cell to test $CaSO_4$ and $MgSO_4$ powder samples that were previously heated (up to 750 °C) although the sample temperature was not controlled during the tests. The authors demonstrated that the powder yield strength increased with temperature presumably due to the formation of agglomerates during heating. Kanaoka et al. (2001), Kamiya et al. (2002) and Tsukada et al. (2008) succeeded to control the temperature during the measurement by placing the shear cell inside a furnace. These authors mainly studied the adhesion behavior as represented by the variation of the shear yield stress of fly ash particles. Kanaoka et al. (2001) assumed that the samples behavior followed the Coulomb's law to estimate powder cohesion and the angle of internal friction. In general, they observed an increase in the shear yield stress with temperature, and therefore of cohesion, which was attributed to the formation of solid bridges during heating. Similar observations are reported by

Tsukada et al. (2008), who showed that this phenomenon can be attenuated by adding coarse silica particles.

More recently some works have modified the standard Schulze cell in order to study the effect of temperature (Chirone et al., 2015; 2020) (Macrì et al., 2017; Tomasetta et al., 2011). Further details about these studies will be discussed in section 5.

Although these tests have shown satisfactory results, assessing powder flowability at high temperature in fluidized beds would be desirable as this system stands as the most commonly used for an adequate temperature control, better efficiency of heat transfer and gas-solid contact (Ding et al., 2019). All in all, since interparticle forces are very sensitive to numerous parameters (humidity, temperature, particles' size and shape, solid mechanical properties, etc.) there is still a long way to go to fully understand powder flow behavior. Our HTSPT based on the fluidized bed technique is presented in detail in the next section as a further contribution to further exploring this critical issue.

3. Experimental setup

Fig. 1 shows a schematic view of the HTSPT used in the works reviewed in this manuscript. This setup is aimed to measure the tensile yield strength and porosity of fine powders as depending on temperature and consolidation stress. It is based on the original SPT originally conceived by Valverde et al. (2000). Essentially, the equipment is based on measuring the pressure drop of a controlled gas flow across the bed. The powder bed is held in a cylindrical quartz vessel of 4.5 cm diameter. A quartz porous plate is placed at the bottom of the vertical cylinder that serves as gas distributor. Before entering the bed reactor, the gas crosses a filter and dryer (model SMC IDFA3E) in order to get rid of pollutant particles or humidity that can modify particle surface properties and therefore powder cohesion (Schubert, 1984). Then a controlled gas flow is pumped through the bed by means of a digital mass flow controller (omega model FMA-2606A, 2000 sccm). The gas pressure drop across the powder is measured by a MKS differential pressure transducer that generates an analogue signal readable by the computer. The measured pressure drop has two contributions, the pressure drop across the powder bed and the pressure drop across the porous plate. Obtaining the pressure drop across the porous plate requires a calibration procedure which consists of measuring the pressure drop of the plate alone. This pressure is subtracted from the total pressure drop to obtain Δ*p*, the actual pressure drop across the powder bed. The registered pressure drop has an accuracy of ±5 Pa. A loudspeaker is placed at the top of the vessel that yields an acoustical excitation of 150 dB at a frequency of 130 Hz. This high intensity sound field is held for 5 s during the initialization procedure as explained below to disrupt any plugs or channels that may form and hinder fluidization, particularly in the case of highly cohesive powders (Valverde, 2013) yields an acoustical excitation of 150 dB at a frequency of 130 Hz. This high intensity sound field is held for 5 s during the initialization procedure as explained below to disrupt any plugs or channels that may form and hinder fluidization, particularly in the case of highly cohesive powders (Valverde, 2013). A set of valves is used to control the gas flow direction, when valves 1 and 3 are open while 2 and 4 are closed the gas flows upward across the powder bed. This is the operating mode for breaking and fluidize the bed. On the other hand, in the inverse situation (valves 1 and 3 closed while 2 and 4 open) the flow is directed downward, which is used for bed consolidation. The bed is placed inside a furnace which serves to put the bed at high temperature.

The fully automated setup starts by a standard initialization procedure during which a sufficiently high gas flow rate drives the bed into the bubbling fluidization regime for 30 s. Fluidization is assisted for the first 5 s by the sound

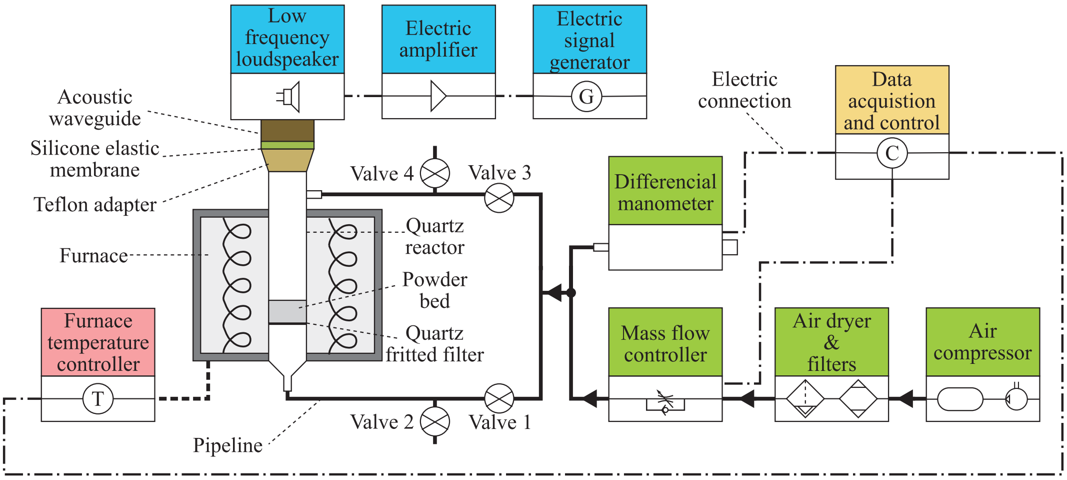

Fig. 1 HTSPT: schematic of the experimental set-up. Reprinted with permission from Ref. (Espin et al., 2020). Copyright: (2020) Elsevier.

excitation. Then the gas flow is turned off and the bed is left to settle for 30 s. This first step is important in order to ensure reproducibility of the initial state of the sample. In the second step the bed is heated by using a PID controller (Eurotherm 3216). When the target temperature is reached, a one-hour thermal stabilization period is set, aiming to guarantee a homogenous temperature distribution within the sample. Thereafter, the bed is subjected to a gradually increasing downward gas flow rate (by increments of 5 cm^3/min each 3 s) up to reach a target consolidation stress (ranging from the weight per unit area of the bed up to σ_c~2 kPa). When the target consolidation stress is met, the downward directed gas flow rate is maintained for 10 s. Then it is decreased progressively until it is stopped. In the last stage, a gradually increasing upward gas flow is imposed to put the bed under tension which allows to derive the tensile yield strength of the powder as a function of temperature and the previously imposed consolidation stress as explained below.

Importantly, in all the tests the height of the bed is kept below the bed diameter which allows us to dismiss wall retention effects to calculate the tensile yield stress. This critical issue is discussed in further detail in Castellanos et al. (2004).

4. Breaking and fluidization curves

The gas pressure drop across the powder bed Δp is made non-dimensional by the weight per unit area (W) in order to better assess when fluidization is reached ($\frac{\Delta P}{W} = 1$) which in turn helps to determine the tensile strength. By plotting the gas pressure drop through the bed as a function of the upward directed gas flow rate we obtain the so-called fluidization curve (**Fig. 2**). At small gas flow rates, the bed remains in a solid-like state and Δp increases linearly under the effect of frictional resistance through the bed. This linear behavior conforms to the Carman-Kozeny law at low Reynolds numbers (Carman, 1997)

$$\Delta p = \frac{E}{\psi_p^2 d_p^2} \frac{\eta}{\rho} \frac{h}{S} \frac{\varphi}{(1-\varphi)^2} q_m \tag{2}$$

where E is the empirical Ergun's constant (taking a typical value between 150 and 180 (Nedderman, 1992), d_p stands for the average particle diameter, ψ_p is the sphericity of the particle (ratio of the surface area of a sphere with same volume as the particle to the surface area of the particle), η is the dynamic viscosity of the gas, ρ alludes to the gas density, h and S are, respectively, the height and cross-sectional area of the powder bed, φ is the particle volume fraction and q_m is the gas flow rate.

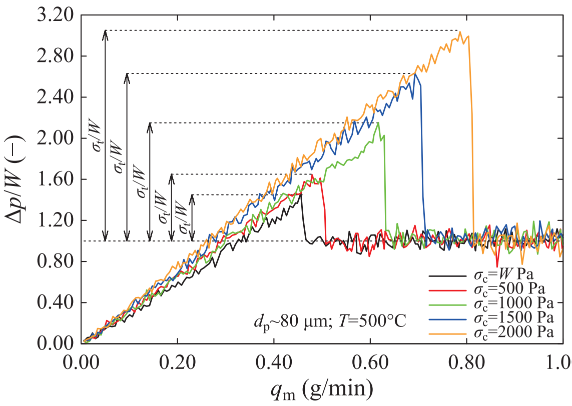

Fig. 2 Dimensionless pressure drop $\Delta p/W$ vs the gas flow rate q_m for $CaCO_3$ powder samples (average particle size $d_p = 88.02 \pm 0.7$ μm, $T = 500$ °C) previously subjected to different consolidation stresses σ_c as indicated. Reprinted with permission from Ref. (Espin et al., 2020). Copyright: (2020) Elsevier.

The pressure drop balances the powder weight per unit area at the so-called minimum fluidization gas flow rate q_{mf}. At this point, a non-cohesive powder would be fluidized. However, when interparticle adhesive forces are significant (compared to particle weight), the powder remains in a solid-like state as the gas flow is further increased over q_{mf}.

Then, the gas flow puts the bed under tension while the pressure drop continues to increase linearly. At a critical gas flow, interparticle adhesive forces are overcome and a sudden break of the powder occurs at the bottom of the bed while the pressure drop falls abruptly to a level around the powder weight per unit area. The tensile yield strength of the powder at the bottom of the bed is obtained from the overshoot of the gas pressure drop over the weight per unit area $\sigma_t = \Delta p_{max} - W$. As the gas flow rate is further increased over the breaking point, the pressure drop oscillates around the weight per unit area while the powder enters a heterogeneous fluidization state (see **Fig. 2**).

5. Effect of temperature

Studying the powder behavior at high temperatures is very important not only for the CaL process but also for many other industrial applications (hydrocarbons cracking, nuclear and metallurgical industries etc.) (Lettieri P. and Macrì D., 2016) where operating conditions involve the handling of powders at temperatures much higher than room temperature (Kunii D. et al., 1991). Several works have addressed the effect of temperature on the fluidization of powders. However, the reported observations on the minimum fluidization velocity are somewhat controversial. Different correlations have been proposed to predict the effect of temperature on the minimum fluidization velocity (Lettieri P. and Macrì D., 2016). However, these correlations are not reliable at high temperature. Furthermore, an extrapolation of the results to the tested conditions is required (Valverde et al., 2000; Yang et al., 1985). Some alternatives trying to solve this problem have been suggested (Wen and Yu, 1966), yet the evolution of the minimum fluidization velocity and bed voidage ε_{mf} with temperature is still considered as uncertain despite the several correlations reported in the literature (Botterill et al., 1982).

In order to check the efficiency and agreement between the different powder shear testers, Salehi et al. (2017) compared the results obtained with the Schulze ring shear tester, the Jenike shear tester and the Brookfield powder tester (PFT) using three different materials that belong to different Jenike powder classes (calcium lactate, calcium carbonate and dolomitic lime). Their results had shown that the degree of agreement between the different setups depends on the nature of powder tested. For instance, for dolomitic lime, the PFT and Schulze tester show a good agreement while the Jenike tester yielded higher cohesion values. For calcium lactate material, the Jenike and Schulze testers yield a considerable increase of the powder cohesion with consolidation stress, however the PFT measures do not uphold this observation. In all the cases, the Jenike tester give the higher cohesion values. In what concerns particularly $CaCO_3$ powders, the cohesion determined by the Schulze tester is typically higher than the estimated by the other testing devices. It is noteworthy that all the mentioned tests have been performed at ambient temperature due to technical limitations.

In regards to the assessment of powder flow properties as affected by temperature, Tomasetta et al. (2011) made some modifications to the standard annular Schulze shear cell. However, for small consolidations (typically below ~1 kPa), the results are not fully reliable. They attributed this issue to design problems. For this reason, only tests at higher consolidation stresses were realized. At high consolidations they confirmed that temperature (in the range up to 500 °C) does not have a significant impact on the powder flowability for all the materials tested (FCC powder, Corundum and fly ashes). Using the same setup, Chirone et al. (2015) investigated the flow characteristics at room temperature and at 500 °C of five different ceramic powders. Their findings show that the powder cohesiveness considerably increased with temperature and consolidation stress. However, for the samples with the smallest size, the powders were already very cohesive, and the effect of temperature was not significant. For powders of 20–38 µm particle size, there is an increase of cohesion of about 35 %. For samples of 63–88 µm particle size and over 88 µm particle size, a cohesion increase of 35 and 45 % at 500 °C was noticed.

The results demonstrated also that free flowing powders (63–88 µm and more than 88 µm) turned into easy flowing at 500 °C as a consequence of the increase in cohesion by 35 and 45 % respectively. In this context, for the same temperature range and using the same setup, Macrì et al. (2017) confirmed these observations but for two different types of TiO_2 powders (natural and synthetic).

Chirone et al. (2020) studied the flow behavior of powder samples sieved to obtain a range of particle sizes covering Group B, A and C of Geldart's classification at temperatures in the range between 25 °C and 500 °C in a heated fluidized bed. They found that the tensile strength of the powders was increased with temperature. They claimed that this behavior was not attributable only to the variation of interparticle forces with temperature but also to other factors such as the difference in particle size and bed expansion.

Durán-Olivencia et al. (2020) studied the effect of temperature on the tensile strength measured for limestone samples having an average particle size of about 50 µm (details on the powder used are illustrated in **Table A1**) by means of the HTSPT. Their results indicated a considerable increase of powder cohesiveness as the temperature was increased (**Figs. 3** and **4**). Moreover, the effect of temperature was further enhanced as the consolidation stress to which the sample was previously subjected was increased. The obtained results fitted well to the empirical correlation (**Fig. 5**).

$$\sigma_t = a + bT^{3/2} + c\sigma_c^{1/3} + bT^{3/2} \times \sigma_c^{1/3} \tag{3}$$

indicating the existence of a cross effect between temperature and consolidation. Thus, the consolidation stress can be considered as a promoter of the temperature effect on the tensile strength. The foregoing is of great importance. For instance, during their storage in CaL-CSP plants, the solids

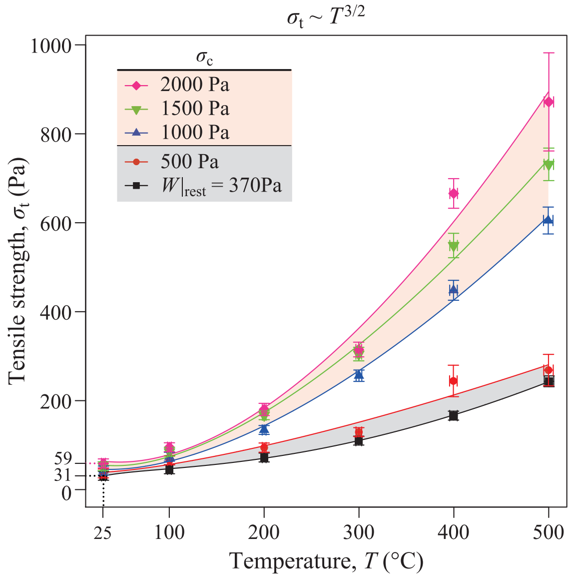

Fig. 3 Tensile strength measured for a limestone powder as a function of the temperature for different values of the previously applied consolidation stress σ_c: the gray highlighted area stands for $\sigma_c < 1000$ Pa, the red colored curve area represents the tensile strength values for $\sigma_c \geq 1000$ Pa. Reprinted with permission from Ref. (Durán-Olivencia et al., 2020). Copyright: (2020) Elsevier.

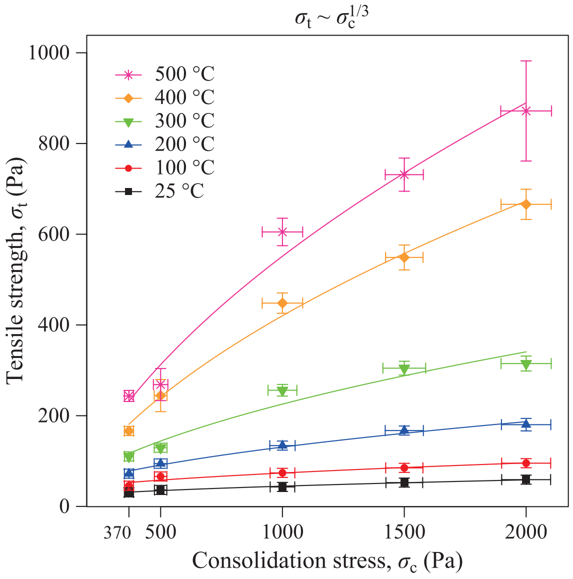

Fig. 4 Tensile strength of a limestone powder measured as a function of the previously applied consolidation stress for temperatures ranging between 25 °C and 500 °C. The solid lines represent the best fit to a power law $\sigma_t \sim \sigma_c^{1/3}$. Reprinted with permission from Ref. (Durán-Olivencia et al., 2020). Copyright: (2020) Elsevier.

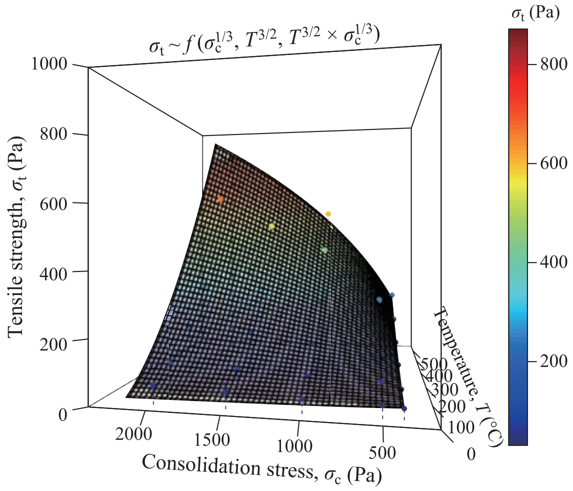

Fig. 5 3D representation of the tensile strength measured for a limestone powder as a function of consolidation stress and temperature. The plotted surface shows the cross effect existing between these parameters governed by the expression $\sigma_t = a + bT^{3/2} + c\sigma_c^{1/3} + bT^{3/2} \times \sigma_c^{1/3}$. The points are the experimental measures. Reprinted with permission from Ref. (Durán-Olivencia F.J. et al., 2020). Copyright: (2020) Elsevier.

could undergo various working conditions involving high consolidation stresses (above 1 kPa) and high temperatures (more than 300 °C).

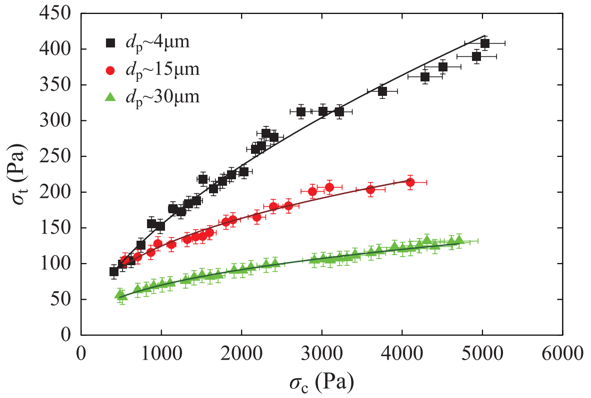

Fig. 6 Powder tensile strength σ_t as a function of the consolidation stress σ_c previously applied to the powder bed for $CaCO_3$ powder samples of particle size between 4 µm and 30 µm at room temperature. Reprinted with permission from Ref. (Espin et al., 2019). Copyright: (2019) Elsevier.

6. Effect of particle size on the powder tensile strength

Particle size is a major physical property that impacts the cohesive behavior of powders (Macrì et al., 2017; Chirone et al., 2020; Espin et al., 2019; 2020). As particle size is reduced, the gas-solid contact efficiency is enhanced, which promotes mass and heat transfer in solid-gas reactors. However, powder cohesiveness is also promoted, which hinders powder flowability and fluidizability (Castellanos, 2005). Using the SPT, Espin et al. (2019) showed that the tensile strength of limestone powders is notably enhanced as the average particle size is decreased. Importantly, the limestone powder samples used in these tests were obtained by aerodynamic classification yielding a narrow particle size distribution, which made possible to better analyze the relevant effect of temperature on powder cohesiveness as depending on particle size. The experiments revealed that there is a synergetic effect between the consolidation stress to which the powder was previously subjected and particle size on the increase of the tensile strength. The impact of the consolidation stress on the powder tensile strength becomes more marked for smaller particle sizes (**Fig. 6**). As seen in a previous work, the increase of temperature promotes further powder cohesiveness. This phenomenon may turn free flowing powders at ambient conditions into cohesive as temperature is increased whereas low cohesive powders may show a very cohesive behavior at high temperatures (Chirone et al., 2020). The effect of temperature and consolidation stress could be well fitted by a power law $\sigma_t = a\,\sigma_c^{b}$ where the value of b progressively increased from 0.3 to 0.9 as the temperature of the powder bed was increased in the range from ambient to 500 °C (**Fig. 7**). The results reported by Espin et al. (2020) revealed that powder flowability is critically influenced by particle size as depending on temperature. As it is clear from **Fig. 7** the impact of temperature on the powder tensile strength is strongly influenced by particle size. An appreciable increase of powder cohesiveness was observed when the temperature exceeded a certain threshold which depends on particle size at the relatively small consolidations tested. For relatively small particles (average particle size d_p = 30 μm) the increase of the tensile strength is appreciable already at temperatures below 100 °C. As particle size is increased, higher temperatures are required to promote notably the tensile strength. For instance, the temperature threshold that causes a significant effect on the tensile strength is about 300 °C for the powders with 60 μm and 80 μm particle size. This temperature is reduced to 200 °C when particle size is decreased to 45 μm. These results show the importance for practical applications of assessing the impairment of powder flowability with temperature as depending on particle size and the typical consolidation stresses to which the powders will be subjected during storage and transport. For thermal storage of $CaCO_3$ powders at industrial scale, consolidation stresses may be well above 1 kPa at temperatures clearly exceeding 300 °C (Valverde, 2013; 2015), which implies that powder flowability could be seriously hindered at the typical temperatures of the CaL process if fine particles (below ~60 um) are employed.

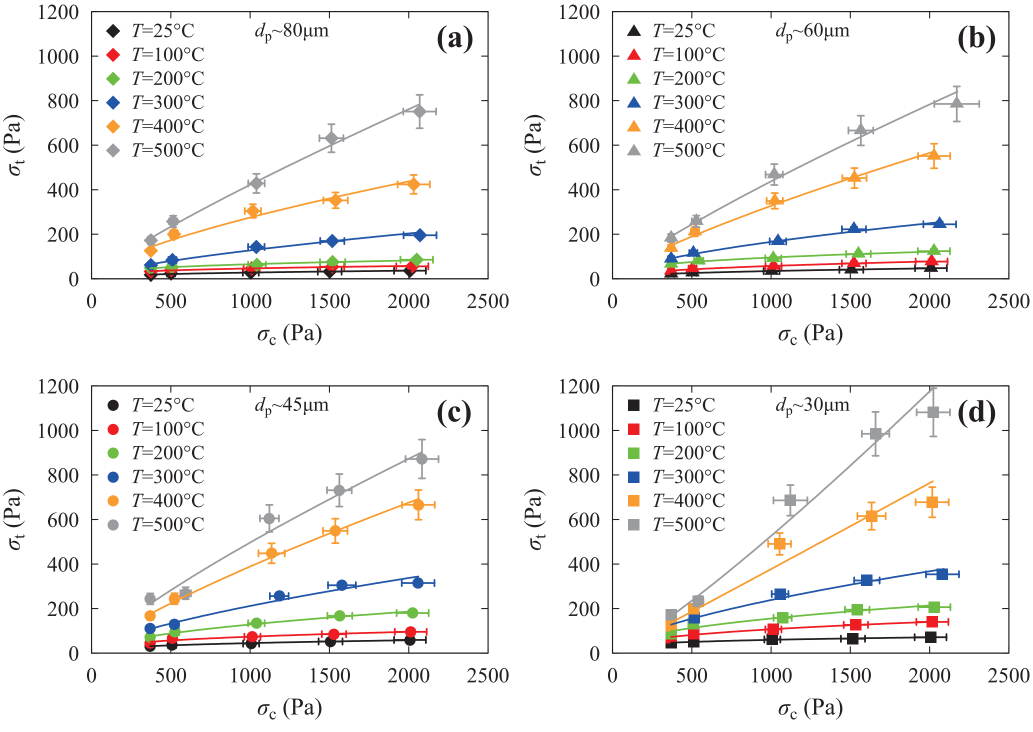

Fig. 7 Tensile strength σ_t versus the consolidation stress σ_c for $CaCO_3$ powders for different temperatures and particle size: **(a)** $d_p = 88.2 \pm 0.7$ μm; **(b)** $d_p = 59.3 \pm 0.8$ μm; **(c)** $d_p = 42.5 \pm 0.8$ μm; and **(d)** $d_p = 32 \pm 1$ μm. The solid lines are the best fits of the equation $\sigma_t = a\,\sigma_c^b$ to the experimental data. Reprinted with permission from Ref. (Espin et al., 2020). Copyright: (2020) Elsevier.

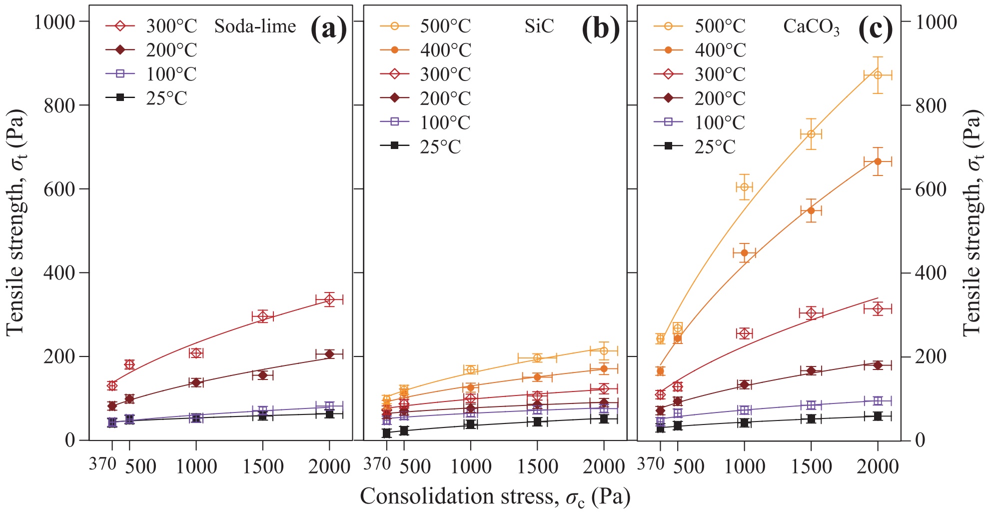

Fig. 8 Tensile yield strength σ_t of diverse powders measured as a function of the previously applied consolidation stress σ_c and temperature *T*. **(a)** $CaCO_3$, **(b)** soda-lime glass beads and **(c)** SiC powder samples. The solid lines represent the best fit of a power law to the data $\sigma_t = a\sigma_c^b$, with *b* close to unity. Reprinted with permission from Ref. (Durán-Olivencia et al., 2021).

7. Effect of material properties

Durán-Olivencia et al. (2021) tested the effect of the increase of temperature on the tensile yield strength for powders of similar particle size (between ~42 µm and ~72 µm) but of different materials (limestone, soda lime and SiC). The main results obtained are summarized in **Fig. 8**. These measurements revealed that, regardless of the powder nature, cohesiveness is augmented with temperature. This effect is especially appreciable when the temperature is $T \geq 200$ °C for limestone and soda-lime powders, with a negligible difference in the measured σ_t up to 300 °C for both materials as it can be clearly observed in **Fig. 9**. On the other hand, cohesiveness was promoted further for the soda-lime powder at higher temperatures. Powder beds could not be broken when the temperature was above 300 °C, even by the highest gas flow rates achievable in the test (q_{mmax} = 0.8 g/min), which indicates a great increase of the powder tensile strength near this temperature. Indeed, at temperatures above 300 °C, soda lime is close to its glass-transition temperature T_g (T_g ~520 °C) (Gerhard, 2017; Varshneya and Mauro, 2019). At this temperature, the powder transits from pure-solid to rubbery-like. This change is accompanied by an appreciable decrease of the material hardness and, therefore, a marked increase of the tensile strength according to contact mechanics predictions (Castellanos, 2005). In addition, high consolidation stresses promote further material softening as T approaches T_g. **Fig. 10** shows SEM picture of soda-lime powder samples after being heated up to 500 °C and subjected to a consolidation stress σ_c = 2 kPa. As may be seen, the particles have experienced a visible local deformation presumably due to material softening. Dimples are clearly seen at the surface of the glass beads which were arguably created at interparticle contact points during consolidation at high temperature. In contrast, powder samples of a much harder material (SiC) show values of the tensile strength up to four times smaller than those measured for the $CaCO_3$ powder of similar particle size for given values of the consolidation stress and temperature (**Fig. 8**). In the case of limestone, no deformations of the surface of the particles were appreciable after the samples (either silica coated or uncoated) were subjected to the high temperature fluidization cycles (Espin et al., 2020). These findings can be qualitatively explained by the change in the mechanical properties of the material as affected by temperature, particularly its hardness, which decreases significantly with temperature (Michel et al., 2004; Wheeler and Michler, 2013; Zhang et al., 2017) yielding an increase of the tensile strength as predicted by contact mechanics (Castellanos, 2005) when the particles deform plastically at contact points. Another important parameter to consider in the case of non-glass solids is the Tamman temperature T_{Tam} which is estimated as half of the melting point and indicates the temperature at which material deformation starts to be appreciable (Tammann, 1932).

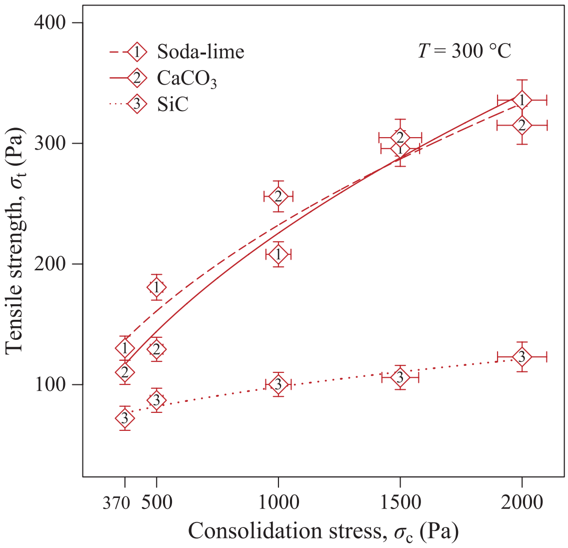

Fig. 9 Comparison of Tensile yield strength σ_t as a function of the previously applied consolidation stress σ_c for the different powders tested at T = 300 °C. Reprinted with permission from Ref. (Durán-Olivencia et al., 2021). Copyright: (2021) Elsevier.

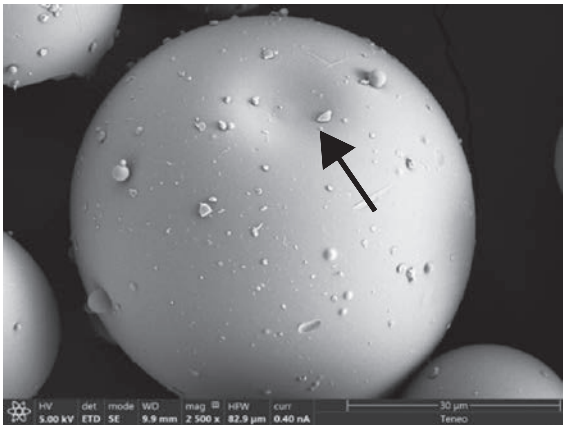

Fig. 10 SEM pictures of soda-lime glass beads after undergoing a consolidation stress of $\sigma_c \approx 2000$ Pa at a temperature of 500 °C (magnifications: 2500×). The arrow indicates permanent deformations on the beads surface suffered during consolidation at high T (not observed in the fresh sample). Reprinted with permission from Ref. (Durán-Olivencia et al., 2021).

For limestone, this temperature is approximately in the same order of the highest temperature tested in the works reviewed in this manuscript (T_{Tam} ($CaCO_3$) = 565 °C (Xu et al., 2016)), which would explain the appreciable increase in the tensile strength seen in this case as the material would soften considerably at temperatures close to T_{Tam} (**Fig. 8** (soda-lime particles)). However, in the case of SiC, the Tamman temperature is very high (T_{Tam} ~1238 °C (Xu et al., 2016)). Thus, the tensile strength measured for this powder in the range of tested temperatures (below 500 °C) is increased only slightly and powder flowability is not seriously compromised as is the case for the soda-lime and limestone powders.

8. Effect of nanosilica addition

The CaL process involves storing and handling $CaCO_3$/CaO powders at high temperatures and consolidations (Paksoy, 2007). As it has been shown in the works reviewed above (Durán-Olivencia et al., 2021; Espin et al., 2020), the increase of temperature rises the cohesiveness of the powders which could be a serious restraint to their flowability. The results shown in **Figs. 11** and **12** demonstrate that using nanosilica as additive at small concentrations can be a suitable solution to improve the flowability of diverse fine cohesive powders at ambient temperature (Chen et al., 2008; Quintanilla et al., 2006; Ramlakhan et al., 2000; Watson et al., 2001; Yang et al., 2005). Espin et al. (2019) demonstrated that for fine limestone powders the addition of nanosilica to cohesive limestone powders contributes to significantly reduce their tensile strength at ambient temperature (see **Fig. 11**). SEM pictures (**Fig. 13**) showed that $CaCO_3$ particles were uniformly coated with nanosilica when both powders were physically dry mixed by a simple procedure in a rotating drum. More recently Durán-Olivencia et al. (2021) extended this observation to a range of temperatures up to 500 °C. At 500 °C, nanosilica coating leaded to a reduction of the powder tensile strength up to half of the value measured for the pure limestone powder (**Fig. 12**). Moreover, it was shown that the effect of nanosilica persisted when the sample was subjected to repeated fluidization cycles (see **Fig. 13**).

Thus, a practical solution for CaL applications where fine limestone powders are to be employed would be the addition of nanosilica by small concentrations. Arguably, the physical mechanism behind this behavior is that the coating of limestone particles with nanosilica aggregates would effectively increase the hardness of interparticle contacts since silica is a much harder material than limestone thus mitigating contact plastic deformation and therefore reducing the increase of interparticle adhesion forces with consolidation and temperature, which would serve to mitigate the undesirable effect of high temperatures on powder flowability.

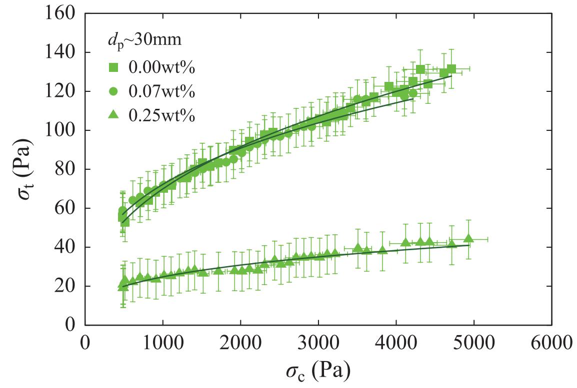

Fig. 11 Tensile yield strength as a function of the previously applied consolidation stress for limestone powder samples (d_p ~30 μm) mixed with nanosilica at different weight concentrations and ambient temperature. The experimental data are fitted to the equation $\sigma_t = a\sigma_c^b$ data. Reprinted with permission from Ref. (Espin et al., 2019). Copyright: (2019) Elsevier.

9. Conclusions

Nowadays, the deployment at large scale of power plants based on renewable energies is considered as a worldwide priority. Several technologies aiming to develop new alternatives based on non-polluting energy resources and using abundant, cheap and non-toxic materials that allow for a massive deployment of these technologies are conceived. In this regard CSP plants with energy storage are gaining an increasing interest.

However, a high efficiency and low-cost energy storage technology is still required for CSP plants to be competitive against fossil fuel-based plants. TCES is one of the most promising technologies for this goal, and the CaL process is a potential candidate to integrate TCES in CSP plants. Yet, the CaL process requires the handling and transport of

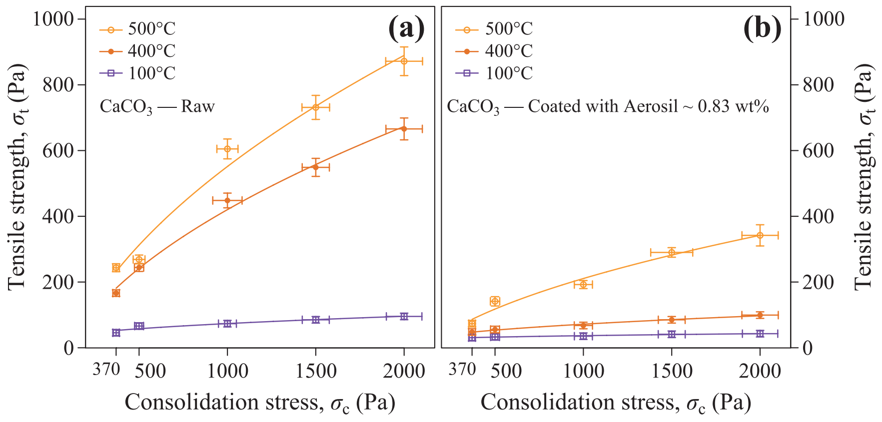

Fig. 12 Measured tensile yield strength σ_t as a function of the applied consolidation stress σ_c at different temperatures *T* for powder samples of **(a)** pure limestone and **(b)** limestone mixed with nanosilica (0.83 % by weight). Reprinted with permission from Ref. (Durán-Olivencia et al., 2021).

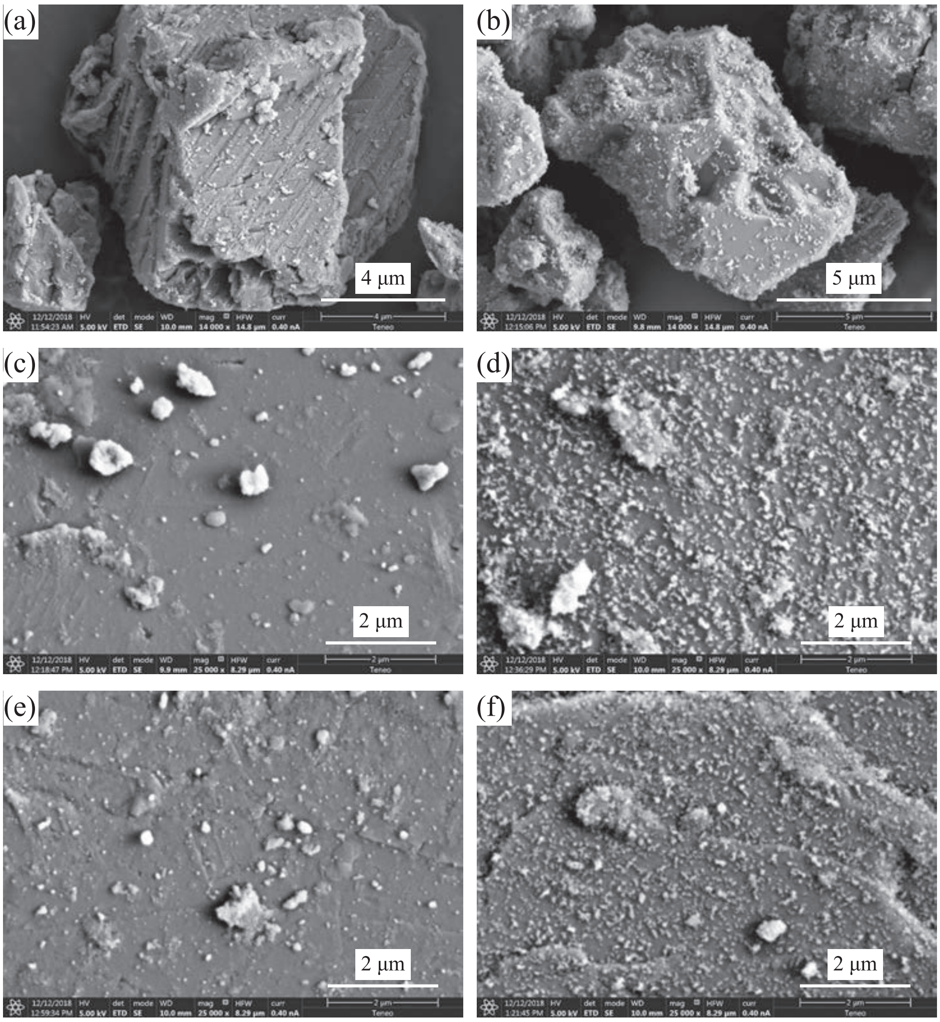

Fig. 13 SEM images of different size limestone particles coated with diffrent ratios of nanosilica : **(a)** $d_p \approx 4$ µm, 0.38 wt% SiO_2 ; **(b)** $d_p \approx 4$ µm, 1.88 wt% SiO_2 ; **(c)** $d_p \approx 15$ µm, 0.1 wt% SiO_2 ; **(d)** $d_p \approx 15$ µm, 0.5 wt% SiO_2 ; **(e)** $d_p \approx 30$ µm, 0.07 wt% SiO_2 ; **(f)** $d_p \approx 30$ µm, 0.25 wt% SiO_2. Reprinted with permission from Ref (Espin et al., 2019). Copyright : (2019) Elsevier.

$CaCO_3$ and CaO powders at high temperatures. This may be an issue as in many other powder processing industrial applications where high temperatures are involved. Thus, understanding the powder behavior at high temperatures is crucial to improve the efficiency of these processes. In this manuscript the HTSPT device designed for this purpose is presented and the main results so far obtained have been reviewed.

The HTSPT can measure the tensile yield strength of fine powders as a function of temperature and the previously applied consolidation stress as depending on temperature. Generally, the results obtained have shown that powder cohesiveness is adversely affected at high temperatures as the consolidation stress is increased. Moreover, particle size is a critical parameter that determines the effect of temperature. As particle size is decreased, limestone powders become significantly more cohesive for temperatures just above 100 °C. Furthermore, for limestone powders with an average particle size of ~50 µm and below, the tensile yield strength increases significantly because of a synergistic effect of temperature and consolidation stress. Consolidation of the powders greatly enhances the detrimental effect of temperature on the tensile strength since plastic deformation at interparticle contacts is promoted by a reduction of the material hardness. For example, the tensile yield stress raises by one order of magnitude at 500 °C when a limestone powder of particle size around 50 µm is subjected to a consolidation stress of σ_c ~2 kPa compared to the case when no consolidation stress is applied at ambient temperatures. Thus, relative free flowing powders at ambient temperature may become highly cohesive at high temperatures, which may pose a serious problem in industrial applications. Some material properties play a relevant role on the effect of temperature on powder cohesiveness. Thus, the negative effect of temperature is mitigated in materials with a high Tammann temperature and mechanical hardness as, for example, SiC powders whose flowability is not seriously compromised with temperature and would be therefore in this regard an excellent candidate for thermal energy storage. On the other hand, it has been shown that surface coating with nanosilica by means of dry physical mixing, is a practical and efficient solution to lessen the increase of powder cohesiveness with temperature for limestone powders.

Acknowledgements

This research was supported by the Spanish Government Agency “Ministerio de Economía y Competitividad” (grant number CTQ2017-83602-C2-2-R).

Appendix A

Table A1 Mechanical properties of the material tested, reprinted with permission from Ref. (Espin et al., 2020). Copyright: (2020) Elsevier.

Material	Particle Density ρ_p (kg/m^3)	Average Diameter d_p (µm)	Young’s Modulus *E* (GPa)	Mechanical Hardness *H* (GPa)	Poisson ratio ν (-)	Surface Energy γ (J/m^2)
$CaCO_3$	2700[a]	51[a]	25–88.19[b]	0.75–5.11[c]	0.21–0.34[d]	0.32–0.347[e]

References: a (data provided by the supplier),
b (Crystran, 2020; Daniel et al., 1982; Ghadami Jadval Ghadam, 2015; Gunda and Volinsky, 2011; Gupta, 2010; Lee et al., 2016; Shi et al., 2018; Surfacenet, 2020)
c (Gunda and Volinsky, 2011; Hubermaterials, 2020; Lee et al., 2016; Matweb, 2020; Shi et al., 2018)
d (Daniel et al., 1982; Gunda and Volinsky, 2011; Gupta, 2010; Lomboy et al., 2011; Materialsproject, 2020; Ramlakhan et al., 2000; Upadhyay, 2013)
e (Røyne et al., 2011; Santhanam. and Gupta, 1968)

References

Abedin A., A critical review of thermochemical energy storage systems, The Open Renewable Energy Journal, 4 (2011) 42–46. DOI: 10.2174/1876387101004010042

ASTM (American Society for Testing and Materials), Annual Book of ASTM Standards, 1978.

André L., Abanades S., Flamant G., Screening of thermochemical systems based on solid-gas reversible reactions for high temperature solar thermal energy storage, Renewable and Sustainable Energy Reviews, 64 (2016) 703–715. DOI: 10.1016/j.rser.2016.06.043

Barker R., The reactivity of calcium oxide towards carbon dioxide and its use for energy storage, Journal of Applied Chemistry and Biotechnology, 24 (1974) 221–227. DOI: 10.1002/jctb.2720240405

Barletta D., Donsì G., Ferrari G., Poletto M., Aerated flow of fine cohesive powders in a Peschl shear cell, Powders and Grains 2005—Proceedings of the 5th International Conference on Micromechanics of Granular Media, 2 (2005) 1033–1037.

Barletta D., Donsì G., Ferrari G., Poletto M., A rotational tester for the characterization of aerated shear flow of powders, Particle & Particle Systems Characterization, 24 (2007) 259–270. DOI: 10.1002/ppsc.200701115

Barletta D., Poletto M., Santomaso A.C., Chapter 4 bulk powder flow characterisation techniques, in: Hassanpour A., Hare C., Pasha M. (Eds.), Powder Flow: Theory, Characterisation and Application, The Royal Society of Chemistry, 2019, pp. 64–146, ISBN: 978-1-78801-224-9. DOI: 10.1039/9781788016100-00064

Benitez-Guerrero M., Sarrion B., Perejon A., Sanchez-Jimenez P.E., Perez-Maqueda L.A., Manuel Valverde J., Large-scale high-temperature solar energy storage using natural minerals, Solar Energy Materials and Solar Cells, 168 (2017) 14–21. DOI: 10.1016/j.solmat.2017.04.013

Blamey J., Anthony E.J., Wang J., Fennell P.S., The calcium looping cycle for large-scale CO_2 capture, Progress in Energy and Combustion Science, 36 (2010) 260–279. DOI: 10.1016/j.pecs.2009.10.001

Botterill J.S.M., Teoman Y., Yüregir K.R., The effect of operating temperature on the velocity of minimum fluidization, bed voidage and general behavior, Powder Technology, 31 (1982) 101–110. DOI: 10.1016/0032-5910(82)80009-0

Bruni G., Barletta D., Poletto M., Lettieri P., A rheological model for the flowability of aerated fine powders, Chemical Engineering Science, 62 (2007a) 397–407. DOI: 10.1016/j.ces.2006.08.060

Bruni G., Lettieri P., Newton D., Barletta D., An investigation of the effect of the interparticle forces on the fluidization behaviour of fine powders linked with rheological studies, Chemical Engineering Science, 62 (2007b) 387–396. DOI: 10.1016/j.ces.2006.08.059

Cabeza L.F., Sole C., Castell A., Oro E., Gil A., Review of solar thermal storage techniques and associated heat transfer technologies, Proceedings of the IEEE, 100 (2012) 525–538. DOI: 10.1109/jproc.2011.2157883

Carman P.C., Fluid flow through granular beds, Chemical Engineering Research and Design, 75 (1997) S32–S48. DOI: 10.1016/s0263-8762(97)80003-2

Carrillo A.J., González-Aguilar J., Romero M., Coronado J.M., Solar energy on demand: a review on high temperature thermochemical heat storage systems and materials, Chemical Reviews, 119 (2019) 4777–4816. DOI: 10.1021/acs.chemrev.8b00315

Castellanos A., The relationship between attractive interparticle forces and bulk behaviour in dry and uncharged fine powders, Advances in Physics, 54 (2005) 263–376. DOI: 10.1080/17461390500402657

Castellanos A., Valverde J.M., Quintanilla M.A.S., The Sevilla powder tester: a tool for characterizing the physical properties of fine cohesive powders at very small consolidations, KONA Powder and Particle Journal, 22 (2004) 66–81. DOI: 10.14356/kona.2004011

Cordis, 2020, <https://cordis.europa.eu/project/id/727348> accessed 24.05.2021.

Crystran, 2020, <https://www.crystran.co.uk/optical-materials/calcite-caco3> accessed 08 october.2020.

Chacartegui R., Alovisio A., Ortiz C., Valverde J.M., Verda V., Becerra J.A., Thermochemical energy storage of concentrated solar power by integration of the calcium looping process and a CO_2 power cycle, Applied Energy, 173 (2016) 589–605. DOI: 10.1016/j.apenergy.2016.04.053

Chen Y., Quintanilla M.A.S., Yang J., Valverde J.M., Dave R.N., Pull-off force of coated fine powders under small consolidation, Physical Review E, 79 (2009) 041305. DOI: 10.1103/PhysRevE.79.041305

Chen Y., Yang J., Dave R.N., Pfeffer R., Fluidization of coated group C powders, AIChE Journal, 54 (2008) 104–121. DOI: 10.1002/aic.11368

Chirone R., Barletta D., Lettieri P., Poletto M., Measurement of high temperature powder flow properties to estimate interparticle forces in high temperature fluidization, Proceedings of the 8th International Conference for Conveying and Handling of Particulate Solids (CHoPS 2015), 2015.

Chirone R., Poletto M., Barletta D., Lettieri P., The effect of temperature on the minimum fluidization conditions of industrial cohesive particles, Powder Technology, 362 (2020) 307–322. DOI: 10.1016/j.powtec.2019.11.102

Daniel I.M., Fibers A.C.D.-o.H.M., Their C., International A., Composite materials: testing and design (sixth conference): a conference, ASTM, Philadelphia, Pa. (1916 Race St., Philadelphia 19103), 1982, ISBN: 9780803148499 0803148496.

Dinçer İ., Rosen M.A., Energy Storage Systems, in: İ. Dinçer and M.A. Rosen (Eds) Thermal Energy Storage: Systems and Applications (Second Edition), 2010, pp. 51–82. DOI: 10.1002/9780470970751.ch2

Ding W., Chen G., Qin M., He Y., Qu X., Low-cost Ti powders for additive manufacturing treated by fluidized bed, Powder Technology, 350 (2019) 117–122. DOI: 10.1016/j.powtec.2019.03.042

Dunn R.I., Hearps P.J., Wright M.N., Molten-salt power towers: newly commercial concentrating solar storage, Proceedings of the IEEE, 100 (2012) 504–515. DOI: 10.1109/JPROC.2011.2163739

Durán-Olivencia F.J., Ebri J.M.P., Espín M.J., Valverde J.M., The cohesive behaviour of granular solids at high temperature in solar energy storage, Energy Conversion and Management, 240 (2021) 114217. DOI: 10.1016/j.enconman.2021.114217

Durán-Olivencia F.J., Espín M.J., Valverde J.M., Cross effect between temperature and consolidation on the flow behavior of granular materials in thermal energy storage systems, Powder Technology, 363 (2020) 135–145. DOI: 10.1016/j.powtec.2019.11.125

Esence T., Benoit H., Poncin D., Tessonneaud M., Flamant G., A shallow cross-flow fluidized-bed solar reactor for continuous calcination processes, Solar Energy, 196 (2020) 389–398. DOI: 10.1016/j.solener.2019.12.029

Espin M.J., Duran-Olivencia F.J., Valverde J.M., Role of particle size on the cohesive behavior of limestone powders at high temperature, Chemical Engineering Journal, 391 (2020) 123520. DOI: 10.1016/j.cej.2019.123520

Espin M.J., Ebri J.M.P., Valverde J.M., Tensile strength and compressibility of fine $CaCO_3$ powders. Effect of nanosilica addition, Chemical Engineering Journal, 378 (2019) 122166. DOI: 10.1016/j.cej.2019.122166

Fernández A.G., Ushak S., Galleguillos H., Pérez F.J., Development of new molten salts with $LiNO_3$ and $Ca(NO_3)_2$ for energy storage in CSP plants, Applied Energy, 119 (2014) 131–140. DOI: 10.1016/j.apenergy.2013.12.061

Freeman R., The importance of air content on the rheology of powders: an empirical study, American laboratory, 36 (2004) 8–10.

Gerhard C., Optics Manufacturing, CRC Press, Boca Raton, 2017, ISBN: 9781351228367. DOI: 10.1201/9781351228367

Ghadami Jadval Ghadam A., Investigation of mechanical properties prediction of synthesized nylon-66/nano-calcium carbonate composites, Journal of Particle Science & Technology, 1 (2015) 241–251. DOI: 10.22104/jpst.2015.307

Ghadiri M., Pasha M., Nan W., Hare C., Vivacqua V., Zafar U., Nezamabadi S., Lopez A., Pasha M., Nadimi S., Cohesive powder flow: trends and challenges in characterisation and analysis, KONA Powder and Particle Journal, 37 (2020) 3–18. DOI: 10.14356/kona.2020018

Gil A., Medrano M., Martorell I., Lázaro A., Dolado P., Zalba B., Cabeza L.F., State of the art on high temperature thermal energy storage for power generation. Part 1—Concepts, materials and modellization, Renewable and Sustainable Energy Reviews, 14 (2010) 31–55. DOI: 10.1016/j.rser.2009.07.035

Gunda R., Volinsky A.A., Tip-Induced calcite single crystal nanowear, MRS Proceedings, 1049 (2011) 1049-AA1005–1015. DOI: 10.1557/PROC-1049-AA05-15

Gupta N.S., Chitin: Formation and Diagenesis, Springer Netherlands, 2010, ISBN: 9789048196845. DOI: 10.1007/978-90-481-9684-5

Hall D., Cutress J., The effect of fines content, moisture and added oil on the handling of small coal, Institute of Fuels, 33 (1960) 63–72.

Hall E.W., Hausz W., Thermal energy storage for electric utility applications, Transactions of the American Nuclear Society: United States, 32 (1979) CONF-790602-(Summ.).

Hanak D., Anthony E., Manovic V., A review of developments in pilot plant testing and modelling of calcium looping process for CO_2 capture from power generation systems, Energy & Environmental Science, (2015) DOI: 10.1039/C5EE01228G

Herrmann U., Kearney D., Survey of Thermal energy storage for parabolic trough power plants, Journal of Solar Energy Engineering, 124 (2002) 145–152. DOI: 10.1115/1.1467601

Hubermaterials, 2020, <https://www.hubermaterials.com/> accessed 05-09.2020.

Kamiya H., Kimura A., Yokoyama T., Naito M., Jimbo G., Development of a split-type tensile-strength tester and analysis of mechanism of increase of adhesion behavior of inorganic fine powder bed at high-temperature conditions, Powder Technology, 127 (2002) 239–245. DOI: 10.1016/S0032-5910(02)00117-1

Kanaoka C., Hata M., Makino H., Measurement of adhesive force of coal flyash particles at high temperatures and different gas compositions, Powder Technology, 118 (2001) 107–112. DOI: 10.1016/S0032-5910(01)00300-X

Karasavvas E., Panopoulos K.D., Papadopoulou S., Voutetakis S., Energy and exergy analysis of the integration of concentrated solar power with calcium looping for power production and thermochemical energy storage, Renewable Energy, 154 (2020) 743–753. DOI: 10.1016/j.renene.2020.03.018

Kierzkowska A., Pacciani R., Müller C., CaO-based CO_2 sorbents: from fundamentals to the development of new, highly effective materials, ChemSusChem, 6 (2013). DOI: 10.1002/cssc.201300178

Kunii D., Levenspiel O., Brenner H., Fluidization Engineering, Elsevier Science, 1991, ISBN: 9780409902334.

Lee S.-W., Kim Y.-J., Lee Y.-H., Guim H., Han S.M., Behavior and characteristics of amorphous calcium carbonate and calcite using $CaCO_3$ film synthesis, Materials & Design, 112 (2016) 367–373. DOI: 10.1016/j.matdes.2016.09.099

Lettieri P., Macrì D., Effect of process conditions on fluidization, KONA Powder and Particle Journal, 33 (2016) 86–108. DOI: 10.14356/kona.2016017

Lettieri P., Yates J.G., Newton D., The influence of interparticle forces on the fluidization behaviour of some industrial materials at high temperature, Powder Technology, 110 (2000) 117–127. DOI: 10.1016/S0032-5910(99)00274-0

Lisbona P., Bailera M., Hills T., Sceats M., Díez L.I., Romeo L.M., Energy consumption minimization for a solar lime calciner operating in a concentrated solar power plant for thermal energy storage, Renewable Energy, 156 (2020) 1019–1027. DOI: 10.1016/j.renene.2020.04.129

Lomboy G., Sundararajan S., Kejin W., Subramaniam S., A test method for determining adhesion forces and Hamaker constants of cementitious materials using atomic force microscopy, Cement and Concrete Research, 41 (2011) 1157–1166. DOI: 10.1016/j.cemconres.2011.07.004

Lüddecke A., Pannitz O., Zetzener H., Sehrt J.T., Kwade A., Powder properties and flowability measurements of tailored nanocomposites for powder bed fusion applications, Materials & Design, 202 (2021) 109536. DOI: 10.1016/j.matdes.2021.109536

Macrì D., Poletto M., Barletta D., Sutcliffe S., Lettieri P., Analysis of industrial reactive powders flow properties at high temperature, Powder Technology, 316 (2017) 131–138. DOI: 10.1016/j.powtec.2016.10.064

Mahlia T.M.I., Saktisahdan T.J., Jannifar A., Hasan M.H., Matseelar H.S.C., A review of available methods and development on energy storage; technology update, Renewable and Sustainable Energy Reviews, 33 (2014) 532–545. DOI: 10.1016/j.rser.2014.01.068

Marchetti L., Hulme-Smith C., Flowability of steel and tool steel powders: a comparison between testing methods, Powder Technology, 384 (2021) 402–413. DOI: 10.1016/j.powtec.2021.01.074

Materialsproject, 2020, <https://materialsproject.org/materials/mp-3953/> accessed 15.04.2020.

Matweb, 2020, <http://matweb.com/> accessed 18.09.2020.

Michel M.D., Mikowski A., Lepienski C.M., Foerster C.E., Serbena F.C., High temperature microhardness of soda-lime glass, Journal of Non-Crystalline Solids, 348 (2004) 131–138. DOI: 10.1016/j.jnoncrysol.2004.08.138

Nedderman R.M., Statics and Kinematics of Granular Materials, Cambridge University Press, Cambridge, 1992, ISBN: 9780521404358.

Ortega J.I., Burgaleta J.I., Téllez F.M., Central receiver system solar power plant using molten salt as heat transfer fluid, Journal of Solar Energy Engineering, 130 (2008) 024501 (6 pages). DOI: 10.1115/1.2807210

Paksoy H.Ö., Thermal Energy Storage for Sustainable Energy Consumption: Fundamentals, Case Studies and Design, Springer Netherlands, Dordrecht, 2007, ISBN: 9781402052903. DOI: 10.1007/978-1-4020-5290-3

Pardo P., Deydier A., Anxionnaz-Minvielle Z., Rougé S., Cabassud M., Cognet P., A review on high temperature thermochemical heat energy storage, Renewable and Sustainable Energy Reviews, 32 (2014) 591–610. DOI: 10.1016/j.rser.2013.12.014

Pinel P., Cruickshank C.A., Beausoleil-Morrison I., Wills A., A review of available methods for seasonal storage of solar thermal energy in residential applications, Renewable and Sustainable Energy Reviews, 15 (2011) 3341–3359. DOI: 10.1016/j.rser.2011.04.013

Pintaldi S., Perfumo C., Sethuvenkatraman S., White S., Rosengarten G., A review of thermal energy storage technologies and control approaches for solar cooling, Renewable and Sustainable Energy Reviews, 41 (2015) 975–995. DOI: 10.1016/j.rser.2014.08.062

Prieto C., Cooper P., Fernández A., Cabeza L.F., Review of technology: thermochemical energy storage for concentrated solar power plants, Renewable and Sustainable Energy Reviews, 60 (2016) 909–929. DOI: 10.1016/j.rser.2015.12.364

Quintanilla M.A.S., Castellanos A., Valverde J.M., Correlation between bulk stresses and interparticle contact forces in fine powders, Physical Review E, 64 (2001a) 031301. DOI: 10.1103/PhysRevE.64.031301

Quintanilla M.A.S., Valverde J.M., Castellanos A., Adhesion force between fine particles with controlled surface properties, AIChE Journal, 52 (2006) 1715–1728. DOI: 10.1002/aic.10770

Quintanilla M.A.S., Valverde J.M., Castellanos A., Viturro R.E., Looking for self-organized critical behavior in avalanches of slightly cohesive powders, Physical Review Letters, 87 (2001b) 194301. DOI: 10.1103/PhysRevLett.87.194301

Ramlakhan M., Wu C.Y., Watano S., Dave R.N., Pfeffer R., Dry particle coating using magnetically assisted impaction coating: modification of surface properties and optimization of system and operating parameters, Powder Technology, 112 (2000) 137–148. DOI: 10.1016/S0032-5910(99)00314-9

Røyne A., Bisschop J., Dysthe D., Experimental investigation of surface energy and subcritical crack growth in calcite, Journal of Geophysical Research-Solid Earth, 116 (2011) B04204. DOI: 10.1029/2010jb008033

Salehi H., Barletta D., Poletto M., A comparison between powder flow property testers, Particuology, 32 (2017) 10–20. DOI: 10.1016/j.partic.2016.08.003

Sang L., Cai M., Zhao Y., Ren N., Wu Y., Burda C., Mixed metal carbonates/hydroxides for concentrating solar power analyzed with DSC and XRD, Solar Energy Materials and Solar Cells, 140 (2015) 167–173. DOI: 10.1016/j.solmat.2015.04.006

Santhanam A.T., Gupta Y.P., Cleavage surface energy of calcite, International Journal of Rock Mechanics and Mining Sciences & Geomechanics Abstracts, 5 (1968) 253–259. DOI: 10.1016/0148-9062(68)90013-2

Santomaso A., Lazzaro P., Canu P., Powder flowability and density ratios: the impact of granules packing, Chemical Engineering Science, 58 (2003) 2857–2874. DOI: 10.1016/s0009-2509(03)00137-4

Sarrion B., Valverde J.M., Perejon A., Perez-Maqueda L., Sanchez-Jimenez P.E., On the multicycle activity of natural limestone/dolomite for thermochemical energy storage of concentrated solar power, Energy Technology, 4 (2016) 1013–1019. DOI: 10.1002/ente.201600068

Schubert H., Capillary forces—modeling and application in particulate technology, Powder Technology, 37 (1984) 105–116. DOI: 10.1016/0032-5910(84)80010-8

Schwedes J., Fließverhalten von Schüttgütern in Bunkern, Chemie Ingenieur Technik, 1976, pp. 294–300, ISBN: 0009-286X.

Schwedes J.r., Review on testers for measuring flow properties of bulk solids, Granular Matter, 5 (2003) 1–43. DOI: 10.1007/s10035-002-0124-4

Sharma A., Tyagi V.V., Chen C.R., Buddhi D., Review on thermal energy storage with phase change materials and applications, Renewable and Sustainable Energy Reviews, 13 (2009) 318–345. DOI: 10.1016/j.rser.2007.10.005

Shi C., Palomo Sánchez A., Torgal F.P., Carbon dioxide sequestration in cementitious construction materials, Elsevier Science & Technology, Cambridge, United Kingdom, 2018, ISBN: 978-0-08-102444-7.

Shimada Y., Yonezawa Y., Sunada H., Nonaka R., Katou K., Morishita H., Development of an apparatus for measuring adhesive force between fine particles [Translated], KONA Powder and Particle Journal, 20 (2002) 223–230. DOI:

10.14356/kona.2002024

Smith D.H., Haddad G.J., Ferer M., Shear strengths of heated and unheated mixtures of $MgSO_4$ and $CaSO_4$ powders. Model pressurized fluidized bed combustion filter cakes, Energy & Fuels, 11 (1997) 1006–1011. DOI: 10.1021/ef970037d

Surfacenet, 2020, <https://www.surfacenet.de/calcite-217.html> accessed 08.11.2020.

Svarovsky L., Powder Testing Guide: Methods of measuring the physical properties of bulk powders, Published on behalf of the British Materials Handling Board by Elsevier Applied Science, 1987.

Tammann G., Lehrbuch der Metallkunde, Leipzig, 1932.

Tatsidjodoung P., Le Pierrès N., Luo L., A review of potential materials for thermal energy storage in building applications, Renewable and Sustainable Energy Reviews, 18 (2013) 327–349. DOI: 10.1016/j.rser.2012.10.025

Tesio U., Guelpa E., Ortiz C., Chacartegui R., Verda V., Optimized synthesis/design of the carbonator side for direct integration of thermochemical energy storage in small size concentrated solar power, Energy Conversion and Management: X, 4 (2019) 100025. DOI: 10.1016/j.ecmx.2019.100025

Tesio U., Guelpa E., Verda V., Integration of thermochemical energy storage in concentrated solar power. Part 2: Comprehensive optimization of supercritical CO_2 power block, Energy Conversion and Management: X, 6 (2020) 100038. DOI: 10.1016/j.ecmx.2020.100038

Tomasetta I., Barletta D., Poletto M., The effect of temperature on flow properties of fine powders, Chemical Engineering Transactions, 24 (2011) 655–660. DOI: 10.3303/cet1124110

Tsukada M., Kawashima K., Yamada H., Yao Y., Kamiya H., Analysis of adhesion behavior of waste combustion ash at high temperatures and its control by the addition of coarse particles, Powder Technology, 180 (2008) 259–264. DOI: 10.1016/j.powtec.2007.04.005

Upadhyay S.K., Seismic Reflection Processing: With Special Reference to Anisotropy, Springer Berlin Heidelberg, 2013, ISBN: 9783662098431. DOI: 10.1007/978-3-662-09843-1

Valverde J.M., Ca-based synthetic materials with enhanced CO_2 capture efficiency, Journal of Materials Chemistry A, 1 (2013) 447–468. DOI: 10.1039/c2ta00096B

Valverde J.M., On the negative activation energy for limestone calcination at high temperatures nearby equilibrium, Chemical Engineering Science, 132 (2015) 169–177. DOI: 10.1016/j.ces.2015.04.027

Valverde J.M., Castellanos A., Ramos A., Pérez A.T., Morgan M.A., Watson P.K., An automated apparatus for measuring the tensile strength and compressibility of fine cohesive powders, Review of Scientific Instruments, 71 (2000) 2791–2795. DOI: 10.1063/1.1150694

Varshneya A.K., Mauro J.C., Fundamentals of Inorganic Glasses, Third Edition, Elsevier, 2019, ISBN: 9780128162255. DOI: 10.1016/C2017-0-04281-7

Watson P.K., Valverde J.M., Castellanos A., The tensile strength and free volume of cohesive powders compressed by gas flow, Powder Technology, 115 (2001) 45–50. DOI: 10.1016/s0032-5910(00)00275-8

Wen C.Y., Yu Y.H., A generalized method for predicting the minimum fluidization velocity, AIChE Journal, 12 (1966) 610–612. DOI: 10.1002/aic.690120343

Wheeler J.M., Michler J., Indenter materials for high temperature nanoindentation, Review of Scientific Instruments, 84 (2013) 101301. DOI: 10.1063/1.4824710

Wu Y.-t., Li Y., Ren N., Ma C.-f., Improving the thermal properties of $NaNO_3$-KNO_3 for concentrating solar power by adding additives, Solar Energy Materials and Solar Cells, 160 (2017) 263–268. DOI: 10.1016/j.solmat.2016.10.013

Xu Y., Luo C., Zheng Y., Ding H., Wang Q., Shen Q., Li X., Zhang L., Characteristics and performance of CaO-based high temperature CO_2 sorbents derived from a sol–gel process with different supports, RSC Advances, 6 (2016) 79285–79296. DOI: 10.1039/c6ra15785h

Yang J., Sliva A., Banerjee A., Dave R.N., Pfeffer R., Dry particle coating for improving the flowability of cohesive powders, Powder Technology, 158 (2005) 21–33. DOI: 10.1016/j.powtec.2005.04.032

Yang W.-C., Chitester D.C., Kornosky R.M., Keairns D.L., A generalized methodology for estimating minimum fluidization velocity at elevated pressure and temperature, AIChE Journal, 31 (1985) 1086–1092. DOI: 10.1002/aic.690310706

Zafar U., Hare C., Calvert G., Ghadiri M., Girimonte R., Formisani B., Quintanilla M.A.S., Valverde J.M., Comparison of cohesive powder flowability measured by Schulze shear cell, raining bed method, Sevilla powder tester and new ball indentation method, Powder Technology, 286 (2015) 807–816. DOI: 10.1016/j.powtec.2015.09.010

Zhang H.L., Baeyens J., Degrève J., Cacères G., Concentrated solar power plants: review and design methodology, Renewable and Sustainable Energy Reviews, 22 (2013) 466–481. DOI: 10.1016/j.rser.2013.01.032

Zhang W., Sun Q., Zhu S., Wang B., Experimental study on mechanical and porous characteristics of limestone affected by high temperature, Applied Thermal Engineering, 110 (2017) 356–362. DOI: 10.1016/j.applthermaleng.2016.08.194

Authors’ Short Biographies

Rahma Gannoun

Holds a PhD (2019) in process-chemical engineering from the national school of engineers of Gabes in collaboration with laboratory of metrology and thermal measurement of the national school of engineers of Monastir. She was undergraduated as a chemical-process engineer in 2014 from the same school. Actually she has a post-doc fellowship with the faculty of physics (university of Seville). Her areas of interest include electrohydrodynamics, Computational fluid dynamics (CFD), heat transfer, renewable energy, fine powder flow.

José Manuel Pérez Ebrí

A member of the Electrohydrodynamics and Cohesive Granular Materials (EHD-CGM) research group at the Universidad de Sevilla (Seville, Spain). PhD in Science and Technology of New Materials (2016). He began his career as an industrial technical engineer in EHD-CGM group in 2005, where he took part in developing several experimental setups, one of his areas of interest. He worked four years in aeronautical industry as a materials engineer. He is developing his research activity in Ca-Looping process for CO_2 capture and mechanical properties of granular materials.

Alberto T. Pérez

Was born in El Puerto de Santa María (Spain) in 1962. He received his PhD degree from the Universidad de Sevilla in 1989, where he has developed his academic career. Since 2009 he is Full Professor of Electromagnetism in this university. His interests are primarily in electrohydrodynamics, powder flow, and electric behavior of colloids. He has authored more than 90 papers in indexed journals on these subjects. He is also a popular science writer. Professor Pérez is currently the head of the group of Electrohydrodynamics and Cohesive Granular Materials of the Universidad de Sevilla

José Manuel Valverde

Professor of electromagnetism and materials engineering. PhD in physics (1997). His research activity has been focused on the study of fluidization and the mechanical properties of granular materials. A main subject of current interest is development of novel techniques to enhance the CO_2 capture efficiency of CaO-based materials by means of the Ca-looping technology based on carbonation/calcination of natural limestone in fluidized beds. He has published over 100 papers mostly in Q1 journals with over 1000 citations.

KONA Powder and Particle Journal No. 39 (2022) 45–61/https://doi.org/10.14356/kona.2022019 Review Paper

Numerical Modelling of Formation of Highly Ordered Structured Micro- and Nanoparticles – A Review[†]

Jakub M. Gac

Faculty of Chemical and Process Engineering, Warsaw University of Technology, Poland

Abstract

The aerosol particles play a significant role in the environment and human health. They are also increasingly used in medicine (drug carriers), preparation (nanocatalysts) and many other fields. For these applications, the particles have to possess unique properties which arise directly from their structure and topology. Indeed, the functionality of the nanostructure particle is defined through its application, like chromatography, sensors, microelectronics, catalysis, and others. That is the reason why people are more and more interested in manufacturing structured particles. The structured particles are the particles with well-defined topological structure. Examples of such particles are porous particles, hollow particles (with the empty space inside), or multi-component particles with the segregation of components in the particle structure. Such particles usually have very interesting features, e.g. porous particles have a significantly larger surface area than the simple spherical particles with similar volume. The present paper contains a comprehensive review of the numerical simulation methods of the formation of highly ordered structured particles. The most important methods will be described in detail and their fields of application (with specific examples), advantages, limitations and information about their accuracy will be given.

Keywords: structured particles, particle synthesis, numerical modeling, self-organization

1. Introduction

The structured particles are the particles with well-defined, usually ordered, topological structure (Yang S.-M. et al., 2008). Examples of such particles are porous particles, hollow particles (with the empty space inside) or the multi-component particles with the segregation of components in the particle structure (e.g. core-shell particles).

Such particles usually have very interesting features, e.g. porous particles have a significantly bigger surface than the simple spherical particles with similar volume. This feature allows us to use these particles as a nanocatalytic objects. Even if the substance that builds the particle has not catalytic properties, the particles may be covered with the thin layer of catalyzing substance.

Hollow particles (HP), on the other side, may be considered as a carrier for encapsulation of molecules or nanoparticles (Liu B. and Hu X., 2020). Other possible applications of HP are coatings (polymeric HP are considered as a white pigment, competitive to conventionally applied TiO_2), cosmetics (carboxymethyl cellulose-based HP are applied for encapsulation of active ingredients of various cosmetics) and electronics (mesoporous polymeric HP are considered as a filler in the electrolyte membranes for solid-state batteries). For the possible application of HP see the comprehensive review of Wichaita et al. (2019) and references therein.

Core–shell particles (CSPs) are a class of particles which contain a core region and a shell layer covering a core. The core and the shell can be different materials or the same materials with different structures (e.g. solid core and highly porous shell). One of the possible applications of core-shell particles is chromatography, e.g. high-performance liquid chromatography, where silica core-shell microspheres are used as a packing material (Hayes et al., 2014).

CSPs are an example of composite particles. In general, by the concept of composite particles we understand particles made of at least two different substances. The atoms or molecules that make up a particle may be randomly distributed in its structure or create some geometrically ordered pattern. In the latter case, it can be said that the composite particle is a structural particle. Apart from CSPs, an example of these particles are the so-called Janus particles (JPs). They were named after the Roman god Janus, who had two faces, each facing a different direction. Similarly, Janus particles have two sides which exhibit different properties. E.g. one of these sides may be non-polar and the other polar. Such particles may exhibit properties and behavior similar to surfactant molecules (de Gennes, 1992). Another

---

[†] Received 11 May 2021; Accepted 3 August 2021
J-STAGE Advance published online 9 October 2021
Add: ul. Waryńskiego 1, 00-645 Warsaw, Poland
E-mail: jakub.gac@pw.edu.pl
TEL: +48-22-234-6508

example of Janus particles is when both sides are made from different materials (e.g. different metals), which may catalyze different chemical reactions. Such particles may catalyze a chemical reaction and, at the same time, move to regions where the concentration of reactants is higher.

One should also not forget about nano- and microcrystals. Such small crystals are often monocrystals i.e. the crystal lattice of the entire particle is continuous and has no defects nor grain boundaries (however, there are exceptions). Thus, the structure and morphology of nano- and microcrystals are defined by the geometry of crystal lattice. One of the most known examples are the snowflakes. Though they may differ in appearance and shape (“no two snowflakes are alike”—as the famous saying goes) but all of them have characteristic six-fold symmetry which arises from the hexagonal crystalline structure of ice.

The structure of matter, on a microscopic scale may dramatically influence its functionality. Engineering of particle structures on a microscopic scale would also lead to their unique optical, electrical, magnetic, or rheological properties maintaining at the same time the high surface area. The functionality of the nanostructure particle is defined through its application, like chromatography, sensors, microelectronics, catalysis, and others.

Well-controlled synthesis of nanomaterials and nanoscale characterization enables us to unambiguously correlate the structural properties with the physical, chemical and biological properties of nanomaterials, which form the core of nanoscience research. Excellent examples of the use of advanced particle engineering to design the structure and properties of catalysts are described in the review paper (Czelej et al., 2021). An essential requirement for nanomaterial synthesis is the uniformity of the final product in size, shape and chemical composition. Recently, many synthesis approaches have been developed to produce high-quality nanoparticles, nanorods, nanowires, or other nanostructures using metals, semiconductors and oxides (Mao et al., 2005; Mohanty, 2011).

Each of the types of structural particles mentioned can usually be obtained in several different ways. These methods depend on the particle structure itself and will be briefly presented in the next chapter. There is a suitable synthesis method to obtain a particle with a predetermined structure. A good guideline that helps to choose the appropriate method of particle synthesis may be to perform a numerical synthesis of such a particle. Numerical calculations, with the participation of a computer, allow for cheap and quick prediction of the effect of the assumed procedure. For this reason, in parallel with the methods of synthesizing particles of a given structure, methods of numerical modeling of the synthesis of such particles are being developed. Therefore, the chemical development of numerical methods related to the preparation of structural particles has taken place in the last 30 years. Currently, there are many methods that allow obtaining particles with a specific structure.

The purpose of this publication is to provide an overview of the numerical methods used to describe the formation of particles with a specific structure. Four of them we can call classic: these are groups of methods based on heat and mass balances, population balances, single atoms or molecules tracking (based on molecular dynamics) and Monte Carlo methods. They have been applied many times in numerous practical issues and constantly developed. Apart from them there will be described some less popular methods which may still be useful in specific issues.

2. Types of structured particles and method of their synthesis

Currently, many methods are known for the synthesis of structured particles. To choose the right one for a specific process, you must first determine what type of particles you want to get. Methods that will allow synthesizing, for example, HP, may not work at all in the case of JP and vice versa.

In general, all the methods of formation of particles, independently – structured or not – may be divided into two main groups: top-down and bottom-up (Verma et al., 2009; Fernandez et al., 2014). The first group of synthesis methods implies that the nano- or microparticles (NMPs) are synthesized by breaking larger structures (e.g. crushing, grinding or etching out crystals). A top-down method can thus be considered as an approach where the building blocks are removed from the substrate to form the particles (Aryal et al., 2019).

Oppositely, a bottom-up synthesis method means that the particles are synthesized by joining smaller structures together (e.g. atoms, molecules or smaller nanoparticles). A bottom-up approach can thus be viewed as a synthesis approach where the building blocks are added onto the substrate to form the particles (Betke and Kickelbick, 2014; Lesov et al., 2018).

From a practical point of view, the bottom-up synthesis is considered more advantageous than the top-down one, because the former usually leads to more homogeneous products with less defects and more homogenous chemical composition. Thus, in the next part of this paper, primarily the bottom-up methods will be considered.

Ones of the earliest known methods of synthesis of NMPs were the crystallization of particles from solutions (and similar precipitation) and spray drying (de Souza Lima et al., 2020). These methods have led usually to poorly structured particles. Indeed, by means of above-mentioned techniques particles with a wide range of sizes and shapes and a chemical composition that is difficult to control are obtained. Nevertheless, it is possible to obtain structured particles by means of these methods under strict conditions. Crystallization and precipitation may lead to the formation of nanocrystals and spray drying—to spherical particles, or even core-shell or hollow particles.

However, the more complex particle morphology, the more advanced methods should be used. Template methods may serve as an example of such a sophisticated and multistep approach, where first the template is synthesized, then modified to obtain the particle, and finally removed to create desired pores and voids in the structure. E.g. in the case of HP formation, the template is a simple spherical particle. This particle is then coated with a layer of the desired material and finally – removed, e.g. by means of etching (Liu B. and Hu X., 2020), leaving an empty shell. Following this description, we may conclude that the template method may be considered a combination of bottom-up (template formation, coating) and top-down (template removal) methods.

2.1 Hollow particles

Hollow particles (HPs), defined as particles (usually of spherical shape) with void space surrounded by a shell are ones of the most popular structured particles (Lou et al., 2008; Wang X. et al., 2016; Liu B. and Hu X., 2020). It has been observed that this type of particle morphology may appear during the spray drying technique when the solution or slurry is atomized into small droplets which are then evaporated (Mezhericher et al., 2010; 2011; Vehring, 2008). This technique, together with a similar gas blowing technique, was the most popular synthesis method of this kind of HPs (Kellerman, 2011; Tsotsas, 2012; Liu B. and Hu X., 2020).

Today, a lot of other methods for the formation of HPs are known. The most popular ones are collectively referred to as “colloidal templating” (Caruso et al., 1998). This group of methods boils down to producing a template on the basis of which the shell of HP is synthesized, and then removing this template (Tu and Gösele, 2005; Fan et al., 2007). In the group of templating methods we may distinguish hard-templating methods, soft templating methods and self-template methods (Liu B. and Hu X., 2020). During the hard templating methods hard templates with specific (usually spherical) shapes are synthesized first, and then their outer surface is coated with a layer of the desired material. During the soft-templating method, the role of “template” plays the droplet of emulsion or the bubble of gas (Hadiko et al., 2005). Finally, the core material is selectively removed to obtain the hollow structure (Lou et al., 2008). Finally, self-template methods denote direct synthesis without the need of additional templates (Zhang Q. et al., 2009). Methods from this group contain two stages: the synthesis of template nanomaterials and the transformation of templates into HP. The main difference between the conventional templating methods and self-templating methods, the templates used in self-templating methods are not only the templates used to formation of a void space inside the HP but also form the outer region – the crust of HP.

An exhaustive review of methods of synthesis HPs is presented in (Liu B. and Hu X., 2020).

2.2 Core-shell particles

Core–shell particles are the particles which contain an inner core and an outer shell (Ghosh Chaudhuri and Paria, 2012). The core and the shell differ in material type, in the structure (e.g. solid core and porous shell made from the same substance) or both of them (Hayes et al., 2014).

Core–shell particles are usually synthesized by a multiple-step process. The core is synthesized first and the shell is then formed on the core particle via different methods, depending on the type of core and shell materials and their morphologies (Ghosh Chaudhuri and Paria, 2012). Among these methods, layer-by-layer approach via electrostatic interaction, shell synthesis on pre-formed cores, droplet-based microfluidic method and many others can be mentioned. An exhaustive review of methods of synthesis of core-shell particles has been made in work (Hayes et al., 2014).

2.3 Janus particles and other composite particles

As it has been stated in Introduction, Janus particles (JP) are the particles which have two sides which exhibit different properties. They are probably the best-known and most widely used composite NMPs. The excellent overview of these particles’ properties, applications and synthesis methods is reviewed in the paper (Walther and Müller, 2013).

There are three principal methods of synthesizing JP (Walther and Müller, 2013). The first one is based on the self-assembly of block copolymers (Walther et al., 2007). As a result of this process, individual blocks of polymers form regions of a particle with different properties. This method allows obtaining JPs with various shapes, not only spherical ones (Liu Y. et al., 2003). The second method uses “masking” (blocking) of a part of the surface of an already formed particle and then surface modification of the unblocked part of the surface (Lin et al., 2010). After removing the masking agent, a particle is obtained having surface regions with different properties. Finally, the third method consists in creating droplets of emulsions composed of various substances, and then leading to phase separation in the droplets thus formed and their solidification. In addition to JPs, there are many particles that deserve to be called composite particles because of their complex, usually more or less ordered internal structure containing at least two substances with different properties. Some of them can be treated as certain modifications of the more popular structures described above. For example, if in a core-shell particle the outer shell is not a continuous, solid or porous spherical layer but a layer of smaller particles covering the core more or less closely, we are dealing with a raspberry-like particle (when the core is tightly covered with smaller particles) or core-satellite particle (when there are larger gaps between the particles covering the core and possibly the particles covering the core are of different sizes) (Mourdikoudis et al., 2015). Particles analogous to HPs but with multilayered crust are sometimes reported as "sandwich-like particles" (Liu Q. et al., 2020). Yolk-shell particles, like CSPs, have an inner spherical core and an outer spherical shell - but in their case, the shell is "too big" for the core: a small spherical nucleus can move freely in the space surrounded by the shell (Sun X. et al., 2020). There are many more such examples and it is to be expected that as nanotechnology develops, structured particles with an increasingly complex internal structure will be obtained.

These particles are usually synthetized by means of gas-phase or vapor-phase methods (Swihart, 2003) or by means of coating of simple particles with appropriate substance (Demirörs et al., 2009). Very promising method of synthesis of composite particles is flame spray pyrolysis (FSP) (Mädler et al., 2002; Chiarello et al., 2008). In FSP, the solution containing liquid precursor and fuel is atomized to form the droplets which are then evaporated and ignited by means of an additive small flame (so-called pilot flame) to form solid nano particles.

2.4 Other types of structured particles

In addition to the particles with the structure described above, other, less popular types can also be found in nanoengineering applications. Among them, porous particles, as well as superficially porous particles, are worth mentioning. The latter kind of particles has a structure somewhat similar to CSPs, where the core is a solid sphere, while the shell is characterized by the presence of pores of various sizes. Both of these particle segments can be made of the same substance and differ only in terms of internal structure—so it is not a composite particle. Porous and superficially porous particles are applied as catalyst supports (Ye et al., 2017) and filling in chromatographic columns (Wang X. et al., 2012).

Micro- and nanocrystals of various substances also may be considered structured particles. They have a well-defined shape which in turn results from the structure and symmetry of the crystal lattice of the substance under consideration. The formation of submicron-sized single crystals has long been studied both experimentally and theoretically.

Last but not least, viruses should be mentioned as an example of structured particles. These objects, which are intermediate between particles and living organisms, are characterized by a ordered structure, which consists of the nucleic acid (DNA or RNA), a shell (capsid) made of proteins and sometimes some other additional components. The structure of viruses is much more complicated than the structural particles discussed earlier, e.g. CSPs. Due to the great importance of viruses in medicine and biomedical engineering, there are recently more and more attempts to describe the formation of this type of "particles" numerically (Kraft et al., 2012). Most attention is paid to the modeling of capsid formation from protein subunits (Zlotnick, 1994).

The most popular and most often investigated types of structured particles are presented in **Fig. 1**.

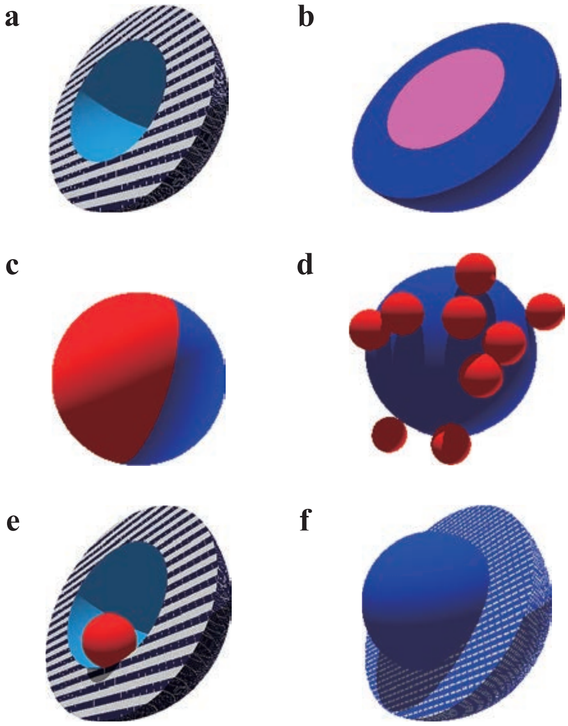

Fig. 1 Examples of structured particles: **(a)** hollow particle, **(b)** core-shell particle, **(c)** Janus particle, **(d)** raspberry-like (core-satellite) particle, **(e)** yolk-shell particle, **(f)** superficially porous particle.

3. Numerical models of formation of structured particles

3.1 Models based on heat and mass balance equations

One of the most popular groups of numerical models of the formation of NMPs are those based directly on equations of heat and mass balances (HMB). They are especially popular for considering droplet formation during the spray drying method; however, they are also applied to model some other processes of formation of NMPs, e.g. precipitation.

The aim of all those models is to formulate the mass balance equation which takes into account the mass flux from surrounding to the particle or vice versa. In parallel, the energy balance equation is formulated. Both of those equations, with proper initial and boundary conditions are solved using widely applied numerical schemes, e.g. finite difference method. Levi-Hevroni et al. (1995) and Mezhericher et al. (2007; 2008; 2011) have applied this scheme for the spray drying process. During the first stage of drying—evaporation of droplet—they considered the escape of solvent molecules from the droplet leading to a decrease in its radius (**Fig. 2a**). The mass balance equation—when assuming spherical symmetry of a droplet—takes a form of the ordinary differential equation describing the dependence of droplet radius on time (Levi-Hevroni et al., 1995):

$$\frac{\mathrm{d}R_\mathrm{d}}{\mathrm{d}t} = -\frac{1}{4\pi\rho_{\mathrm{d},w}R_\mathrm{d}^2}\dot{m}_\mathrm{v} \tag{1}$$

Where the mass flux $\dot{m}_\mathrm{v}$ is given as (Mezhericher M. et al., 2007):

$$\dot{m}_\mathrm{v} = h_\mathrm{D}\left(\rho_{\mathrm{v,s}} - \rho_{\mathrm{v},\infty}\right)A_\mathrm{d} \tag{2}$$

All the symbols are described in Nomenclature at the end of the paper.

The mass transfer coefficient h_D is obtained usually from the Ranz-Marshall correlation (Levi-Hevroni D. et al., 1995) and is a function of the diffusion coefficient of solvent vapor in air as well as viscosity and density of air. These parameters, together with solvent density ρ_d and saturated solvent vapor concentration $\rho_{\mathrm{v,s}}$, are dependent on the temperature of a droplet surface which may be obtained by solving a heat balance equation:

$$\rho_\mathrm{d}c_{p,\mathrm{d}}\frac{\partial T_\mathrm{d}}{\partial t} = \frac{1}{r^2}\frac{\partial}{\partial r}\left(k_\mathrm{d}r^2\frac{\partial T_\mathrm{d}}{\partial r}\right) \tag{3}$$

With the boundary condition at the droplet surface:

$$h_\mathrm{c}\left(T_\infty - T_\mathrm{d}\right) = \lambda\frac{\partial T_\mathrm{d}}{\partial r} + L_\mathrm{h}\frac{\dot{m}_\mathrm{v}}{A_\mathrm{d}} \tag{4}$$

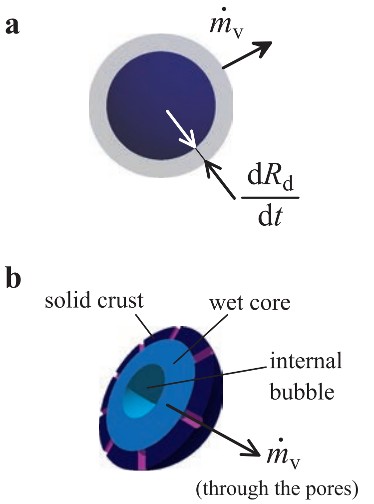

Fig. 2 Scheme of a model of hollow particle formation in spray drying process based on heat and mass balance equation: **(a)** first drying stage and **(b)** second drying stage.

The set of equation (1–4) is solved through the whole first drying period by means of well-known discretization methods (e.g. finite difference scheme). This period ends when the concentration of solutes or suspended particles in a droplet is big enough to start the formation of solid crust. The simulation of the second drying stage is much more complicated. In their early works, Mezhericher M. et al. (2007; 2008) considered the emerging crust as a porous solid medium through which further solvent evaporation took place. Because the further decrease of particle radius is impossible after the formation of the crust, the evaporation of a solvent results in formation of internal bubble inside the dried particle (**Fig. 2b**). That leads directly to the HP formation.

Later on, these authors have considered the more realistic crust structure as built from spherical nanoparticles suspended in droplet (Mezhericher et al., 2011; 2012). This approach allowed formulating the criterion of the final particle morphology: hollow particle or solid particle. Similar investigations – with the use of the same approach – have been done to investigate the morphology of particles obtained by means of spray pyrolysis (Lenggoro et al., 2000; Eslamian et al., 2006). The described model allowed the formulation of the conditions of solid or hollow particle formation for this process as well. Also, Shabde et al. (2005) have used the described method to simulate the formation of HP during spray drying. Likewise, Maurice et al. (2017) considered the dynamics of growth of internal bubble during the HP formation in spray drying process.

The main difficulty in the application of the numerical method described above is the existence of moving boundaries. Indeed, during the drying a droplet shrinks and thus the condition (4) is fulfilled for the different value of *r* at every time step. The Mezhericher group usually applies the method elaborated by Moyano and Scarpettini (2000) for one-dimensional moving boundary problem with implicit boundary conditions. They use the Landau's transformation in order to work with a fixed number of nodes at each time step despite the moving boundaries. Shabde et al. (2005), on the other hand, have used the gradient-weighted moving finite element method (Miller, 1997). Recently, a work (Larbi et al., 2021) appeared in which a spectral collocation method has been applied. This method is based on the expansion of the unknown function in terms of the Lagrange elementary polynomials. The solution of HMB equations comes down to finding the dependence of the coefficients of this expansion on time.

Another step towards the description of the structure of particle formed in the spray drying process is analyzing the distribution of concentration of solutes inside the droplet. The mass balance equation for the solute takes the form of convection and diffusion equation:

$$\frac{\partial c_{\mathrm{A}}}{\partial t} - v_r \frac{\partial c_{\mathrm{A}}}{\partial r} = \frac{1}{r^2}\frac{\partial}{\partial r}\left(D_{\mathrm{A}} r^2 \frac{\partial c_{\mathrm{A}}}{\partial r}\right) \tag{5}$$

The radial velocity of a solvent in a droplet v_{r} is dependent on the velocity of the droplet surface caused by its shrinking. Eqn. (5) may be transformed into:

$$\frac{\partial c_{\mathrm{A}}}{\partial t} = \frac{D_{\mathrm{A}}}{r_{\mathrm{d}}^2}\left(\frac{\partial^2 c_{\mathrm{A}}}{\partial R^2} + \frac{2}{R}\frac{\partial c_{\mathrm{A}}}{\partial R}\right) + \frac{R}{r_{\mathrm{d}}}\frac{\partial c_{\mathrm{A}}}{\partial R}\frac{\partial r_{\mathrm{d}}}{\partial t} \tag{6}$$

where r_{d} is a radius of a droplet and $R = r/r_{\mathrm{d}}$ denotes the normalized radial coordinate. Eqn. (6) is a base for the numerical model of particle formation elaborated by Vehring et al. (2007) and further developed by other authors under the name of VLF model (Chen X.D., 2011). Originally, the model assumed steady-state evaporation of a droplet what defined a proper boundary condition at the droplet surface. Later on, it has been extended to take into account the transient nature of the solute concentration profiles (Boraey and Vehring, 2014).

As a method of description of particle formation during spray drying, the VLF model has been applied mainly for the simulation of HPs formation. It allows finding out the time of drying of a droplet and the final thickness and density of a crust.

More advanced approaches use computational fluid dynamics (CFD) methods to solve HMB equations, e.g. finite element method (Vasiliauskas et al., 2015). Recently, Wu and Chung (2020) used the volume of fluid method to simulate the synthesis of HPs by means of spray drying process. At the expense of a significant complication of the mathematical apparatus, this approach makes it possible to follow the dynamics of particle synthesis without introducing additional assumptions, e.g. regarding the symmetry of the particle. The proposed model allowed directly distinguishing four sequential stages of the drying process: temperature adjustment, isothermal drying, crust formation, and crust thickening. While in the previously discussed papers, these stages were artificially separated, and for each of them, a slightly modified system of equations was used—in this case, one system of equations allows describing the entire drying process.

The methods based on mass and heat balance equations have also been applied for modeling of synthesis of NMPs other than HPs, e.g. core-shell particles. The works presenting the results of this type of simulation focus not on balance within a single emerging particle but rather on the entire system (apparatus) in which the particles are formed. In such an approach, the material balance, which describes rather chemical reactions taking place during the process than the convection and diffusion of compounds, is coupled with—usually simplified—population balance of particles, e.g. (Aul'chenko S. and Kartaev E., 2018). The authors use a single-liquid flow model to describe the synthesis of composite core-shell TiO_2-SiO_2 particles from the gas substrates (mixture of titanium tetrachloride and silica tetrachloride). The efficiency of solid particle formation is obtained from kinetic reactions—both homogeneous and heterogeneous—and phase transition between gas and solid phase. Such an approach, coupled with a simplified balance of particle number, allowed to calculate the average size of particles at an arbitrary time point. From this model any other properties of structured particles could be obtained, e.g. the mean thickness of silica shell—however, authors did not consider this properly.

Model based on heat and mass balances equations has been also applied for simulation of FSP method (Ren et al., 2021). Similarly as in work by Mezhericher group, authors of this works considered single droplet and assumed its spherical symmetry. The main difference between modeling of spray drying and FSP is considering the effects of chemical reactions in the last one.

A similar assumption has been applied in (Hamzehlou et al., 2016) to simulate the dynamic evolution of the morphology of polymer-polymer latex particles. This paper's main goal was to consider the formation of clusters of one of polymers (P1) at the surface of the particles built from the second polymer (P2). By considering the distribution of cluster size at different time points, the equilibrium morphology of particles (described as core-shell or hemispherical particles) and non-equilibrium one (a few of P1-clusters with various sizes deposited randomly on particle P2-surface) were recognized.

To sum up—a group of methods based on mass and energy balance equations has been found and still is widely used to describe the synthesis of particles with various morphologies. It also allows tracing the dynamics of the particle morphology over time and obtaining information about the quantitative distribution of parameters describing this morphology. With the help of this method, it is also possible to determine the structure of non-equilibrium particles (which are sometimes formed under not properly selected process conditions). The most important disadvantage of the described method is its relative complexity and high demand for computing power—and for this reason, other numerical methods are constructed, which sometimes constitute a better choice when it comes to particle synthesis description. These methods are described in the next section.

3.2 Multiple shells model

As mentioned above, the most challenging issue concerning the solution of differential balance equations (e.g.

modeling the droplet during spray drying process) are the moving boundaries of drying droplets. To get around this difficulty, a set of methods in which the droplet is divided into imaginary regions were proposed. These regions are characterized by the same value of the concentration of every solute and the same temperature. This is, of course, an idealization of real situation and these regions mimic the parts of dried droplet where these parameters are *nearly* the same. This group of numerical methods is usually called the distributed parameter methods (Wang S. and Langrish T.A.G., 2009). Because of the spherical symmetry of the drying droplet, the above-mentioned regions usually have a shape of concentric spherical shells (the central one is a full sphere); thus, the described method is also known under the name multiple shells model (Parienta D. et al., 2011).

The first method from this group simply utilized the mass balance equations discretized in respect to radial coordinate (Adhikari B. et al., 2007). Wang S. and Langrish T.A.G. (2009) have used an explicit form of the concentric shells to analyze the changes of solute concentration and temperature in every part of a droplet. Parienta D. et al. (2011) used the same model for investigations of diameter and composition change of exhaled respiratory droplets. Also, similar model has been applied to investigate the distribution of protein and sugar in an evaporating droplet (Grasmeijer N. et al., 2016a; 2016b). In the last work not only the droplet but also the layer of surrounding air was divided into concentric shells. This allowed the solvent evaporation rate from the droplet to be simulated directly rather than using mass transfer coefficients obtained from semi-empirical correlations.

All these works, however, did not describe the process of solid particle formation. In fact, as they analyzed the change of solute concentrations inside the droplets, their results may be accounted as numerical modeling of the first step of particle formation.

The second step, i.e. crust formation, has been modeled in (Gac and Gradoń, 2013a). The scheme of the method has been presented in **Fig. 3**. The authors assumed that the crystallization in this shell starts and the solid crust forms when in any of the shells (typically, it was the outermost shell) the supersaturation exceeds the critical value. In forthcoming time steps, this shell is not considered – the second shell becomes the outermost. During this period, the diameter of all the shells stops decreasing and remains constant till the end of the simulation. Instead, the concentration of all the compounds (including a solvent) in the central sphere decrease and finally reaches zero. When it is happened, in this sphere there is no solvent nor solutes —that means the gas bubble is formed. In next steps the concentration of solutes in the outermost shell increases (what may finally lead to the attachment of this shell to the solid crust) and the concentration of both solutes and solvent in the innermost shell decreases (what may result in the attachment of this shell to the central bubble). This scheme is repeated until all the shells do not belong to solid crust or gas bubble.

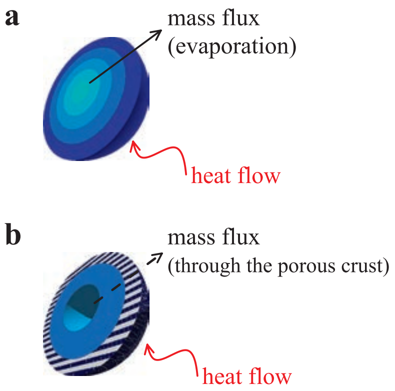

Fig. 3 Scheme of the multiple shell model of **(a)** a dried droplet and **(b)** a wet particle with solid crust (marked in black and white), wet core and a gas bubble inside.

The multiple shells model, as described above, has found its application not only for modeling the formation of NMPs. There are a few works which use a similar model to describe the thermal evolution of planetesimals (Weiss and Elkins-Tanton, 2013; Blackburn et al., 2017). These works describe the changes of temperature profile inside the spherical planetesimal and the change of aggregation state of its compounds – they, however, do not consider the change of the diameter of the body. In (Gac and Gradoń, 2013b) the multiple shells model has been adapted to simulate the evolution of deposits appearing during the drying of sessile droplets (e.g. the famous “coffee rings”).

It should be stated that the multiple shells model is characterized by a very simple mathematical apparatus. The transport of mass and energy is described here entirely using ordinary differential equations, which can be solved with not very advanced numerical techniques. However, for such a description to be applied, the simulation object (the resulting particle) must have an appropriate (usually spherical) symmetry. This condition, in principle, limits the scope of potential applications of the described model to hollow particles or core-shell particles. However, it is such a common morphology of particles produced in various processes that the described model can be considered, despite significant limitations in its applicability.

3.3 Models based on population balance equations

Population balance equations (PBEs) are widely used in several branches of modern science, mainly in chemical engineering, to describe the evolution of a population of particles. They define how populations of particles develop specific properties over time, taking into account such phenomena as nucleation, aggregation, coagulation, breakup of aggregates, evaporation, dissolution, etc. (Vetter et al., 2013; Hao et al., 2013).

Moving on to the modeling of synthesis of NMPs, the PBEs may be applied to describe the evolution of nanoparticles' agglomeration leading to the creation of the larger structured particle. This procedure is usually applied to model the formation of particles by means of spray drying. Handscomb et al. (2009a) applied the PBE method for modeling spray drying kinetics. As during spray drying HPs are often formed, the authors investigated the time it takes to form a solid crust for various conditions of the process. For a description of the drying of a droplet containing suspended solids, the dynamics of particle number density function inside the droplet $N(L,r,t)$ is analyzed, where L is particle size, r—its radial coordinate (spherical symmetry of dried droplet is assumed) and t—time. The equation fulfilled by function N has a form:

$$\frac{\partial}{\partial t}N+\frac{\partial}{\partial L}(GN)+\frac{1}{r^2}\frac{\partial}{\partial r}(r^2 v_r N)-\frac{1}{r^2}\frac{\partial}{\partial r}\left(r^2 D\frac{\partial N}{\partial r}\right)=0 \tag{7}$$

where G is the velocity of motion through the state space of internal coordinates, i.e. the linear growth rate. The authors have assumed that this growth rate is independent of particle size. For solving Eqn. (7) a moment method is employed to yield the evolution of the first four integer moments of the internal coordinate. In their subsequent work (Handscomb C.S. et al., 2009b), the same authors extended their model for droplets drying in the presence of a solid crust. The improved model incorporates crust thickening, along with wet and dry crust drying. That allows predicting not only the kinetics of a particle formation process but also its final structure: crust thickness and its porosity.

The PBEs method of modeling the formation of particles during the spray drying process has also been applied in (Bück et al., 2012). The authors considered the evolution of the distribution of nanoparticles suspended in dried droplets with particular emphasis on their aggregation. In contrast to the above-mentioned works, the effect of droplet shrinking on the PBE was not modeled as an artificial boundary source but as a flux term in the PBE. The authors of the discussed study also drew attention to the hierarchical structure of the solid crust formed during drying. They defined its porosity as $\varepsilon_{\mathrm{sh}}$, taking into account that the crust was formed from previously formed aggregates which also have internal porosity $\varepsilon_{\mathrm{agg}}$. The model proposed by the authors allowed finding out both the porosities. However, the potential of these results has not yet been fully exploited.

The modeling of synthesis of structured particles by means of PBEs seems to be one of the more general methods. A significant feature of this approach is a lack of detailed assumptions about the morphology of the formed particle. E.g. one need not assume that the final particle is of a spherical shape or spherical symmetry – these properties are to be obtained directly from the model.

The downside of the described method may be a relatively large complication of the mathematical apparatus. However, modern computers make it possible to overcome this difficulty.

3.4 Models based on single atoms, molecules or nanoparticles tracking

As it has been mentioned in Sec. 2, many structured NMPs are synthesized by means of bottom-up methods, i.e. as a result of joining of atoms, molecules or smaller particles (hereinafter referred to as the common term "individuals") into the desired structure. Therefore, an obvious method of numerical modeling of such a process is a direct tracking of the mentioned individuals making up the particle. This may be done by numerical solution of the equations of motion of individuals in form:

$$\ddot{\boldsymbol{x}}=\frac{1}{m}\boldsymbol{F}(\boldsymbol{x},\dot{\boldsymbol{x}},t) \tag{8}$$

In Eqn. (8) $\ddot{\boldsymbol{x}}$ denotes the second derivative of a position vector of individuals, i.e. the vector of acceleration and $\boldsymbol{F}$ is a vector of force, which may (or may not) depend on position vector, velocity vector and time. The most common method in this group is molecular dynamics (MD) which is widely used for the description of various phenomena occurring at the atomic or molecular level.

MD algorithms are common for the simulation of the behavior of structured particles at various conditions. For example, the alloying reaction in core-shell Al-Ni particle (Levchenko et al., 2010), changes in structure during the heating and cooling of such a particle (Song and Wen, 2010), melting behavior of core-shell Pt−Au nanoparticles (Yang Z. et al., 2008) and many others have been investigated by means of this method.

Of course, MD has also been applied for modeling of synthesis of structured NMPs. Förster et al. (2019) used a very simple MD model to investigate the dependence of a particle structure on the parameters of the interactions between the atoms. In their investigations, three kinds of atoms have been considered. The first kind represented an inert gas (the atoms of this species react neither with each other nor with atoms of other kinds). Two other species are reactive and interact with each other by means of classical Lennard-Jones (L-J) potential:

$$U_{ij}=4\varepsilon_{ij}\left[\left(\frac{\sigma_{ij}}{r_{ij}}\right)^{12}-\left(\frac{\sigma_{ij}}{r_{ij}}\right)^{6}\right] \tag{9}$$

In Eqn. (9) i and j denote the name of species of atoms (referred as A and B), ε_{ij} is a parameter describing the strength of interaction and σ_{ij}—a range of this interaction. By changes of these two parameters, three types of structures of NMPs have been observed. The most important parameter influencing the morphology of the obtained particles turned out to be ε_{ij}. It appeared that when $\varepsilon_{\mathrm{BB}} < \varepsilon_{\mathrm{AA}} < \varepsilon_{\mathrm{AB}}$ (i.e. the interaction between atom A and atom B is stronger than both between two atoms A and two atoms B) an alloy particle is obtained. When $\varepsilon_{\mathrm{BB}} < \varepsilon_{\mathrm{AB}} < \varepsilon_{\mathrm{AA}}$, most of the simulations ultimately result in a core-shell particle. When $\varepsilon_{\mathrm{AB}} < \varepsilon_{\mathrm{BB}} < \varepsilon_{\mathrm{AA}}$, the Janus particle is most frequently obtained, however also quite often (about a third of the cases), the formation of pure B particles and pure A particles is observed.

Another example of the application of MD for the formation of structured particles has been applied in (Singh et al., 2014). In this paper, an MD was used to model the gas-phase synthesis and growth of silicon–silver (Si–Ag) hybrid nanoparticles. For simulating such a real system more advanced model of interatomic interactions has been applied than L-J potential. While the latter takes into account the interactions of pairs of atoms, it may be applicable with good accuracy to describing rarefied gases, especially noble ones. However, this model may be too vague to describe, for example, metals in solid state. In this case, L-J potential allows insight into qualitative properties of an inner structure of formed particles. More specific problems require taking into account collective effects between atoms. One of the most popular models including these effects is the embedded atom method (Foiles et al., 1986; Daw et al., 1993) which is a semi-empirical, many-atom approximation describing potential for computing the total energy of a metallic system. This model has been applied by Singh et al. (2014) to describe the energy of interactions between Si and Ag atoms. The nanoparticles obtained in this process had a form of Janus or core-satellite particles. The simulations allowed concluding that the individual species first form independent clusters of Si and Ag without significant intermixing. The formation of stable hybrid structures took place in the subsequent stages of process. In addition to MD, other models are used in engineering applications, which also boil down to tracking the evolution of the system by solving equations describing the dynamics of individual particles included in it. An example of such model is dissipative particle dynamics (DPD)—a coarse-grained model, in which functional groups or polymer segments are considered as individual “particles” (coarse-grained beads) which interact with each other (Español and Warren, 1995). The forces acting between beds i and j are given by the formula:

$$F_{ij}\left(r_{ij}\right) = f\left(x\right) = \begin{cases} \varepsilon_{ij}\left(1 - r_{ij}/r_{\mathrm{c}}\right), \ r_{ij} < r_{\mathrm{c}} \\ 0, \ r_{ij} \geq r_{\mathrm{c}} \end{cases} \tag{10}$$

where r_{ij} is a distance between beds i and j, r_{c} is a range of interactions between beds and ε_{ij}—repulsion parameter, characterizing the magnitude of the force of interaction.

The DPD method has been applied in (Chen H. and Ruckenstein, 2012) to investigate the formation of complex colloidal particles formed by self-assembling a three-arm star-shaped polymer. By using this mathematical apparatus, pathways for a few kinds of structured particle formation have been identified, e.g. core-shell, multicore or stacked layered particle. The control parameters in the model were repulsion parameters between polymer segments and between polymer segments and solvent particles.

Similar methods can be used to track the movement of nanoparticles as they are used to create larger particles. Jabłczyńska et al. (2018) presented an experimental and modeling study of the formation of structured microparticles by spray drying of a droplet of slurry containing nanoparticles in one or two sizes. The change of droplet radius during the first stage of drying has been described by means of mass and heat balance equations as described in Sec. 3.1. The motion of nanoparticles inside the droplets has been tracked by direct solving of their equations of motion. To take into account the diffusion of nanoparticles inside the dried droplet, these equations have a form of overdamped Langevin equations:

$$\dot{\boldsymbol{x}} = \boldsymbol{F}\left(\boldsymbol{x}\right)/b + \Gamma\left(t\right) \tag{11}$$

Here b denotes a damping coefficient and $\Gamma(t)$ is a stochastic component of the motion. This component represents a white noise with zeroth mean value, i.e. it fulfills the conditions:

$$\left\langle \Gamma\left(t\right)\right\rangle = 0 \tag{12a}$$

$$\left\langle \Gamma\left(t_1\right)\Gamma\left(t_2\right)\right\rangle = 2D\delta\left(t_1 - t_2\right) \tag{12b}$$

It has been shown that as a result of spray drying of such droplets, solid (full) aggregates or hollow particles built from nanoparticles may appear. Implemented scenario depends on the process conditions: the temperature of the drying gas and the initial diameter of the slurry droplets. In the case of two sizes of primary nanoparticles and the formation of HP, self-organization of nanopraticles inside the crust may also appear. The larger nanoparticles form a hexagonal pattern while the smaller ones are trapped in void spaces between larger ones.

The molecular dynamics and related methods should be considered by far the most accurate models of the formation of structural particles. Indeed, in the case of these techniques, we directly follow the behavior of atoms, molecules or nanoparticles—i.e. the “building blocks” that form an organized particle. The main disadvantage of this group of methods is the long computation time. Especially in the case of the original MD method, a very large number of differential equations should be numerically solved, corresponding to the number of molecules or atoms involved in the particle synthesis. It should be emphasized that even a small particle consists of many hundreds of thousands or even millions of atoms or molecules (e.g. Förster et al., (2019) conducted simulations for 200,000 atoms). Another problem may be to formulate a realistic model of interactions between atoms and molecules that make up the particle. Especially when dealing with a composite particle composed of metal atoms, one should take into account the complicated effects resulting from the quantum mechanics of many bodies. However, it is worth paying attention to the fact that even a greatly simplified description using the L-J potential allows obtaining qualitatively (though not necessarily quantitatively) correct results.

The methods from the group discussed in this section should be used when interested in a detailed description of the particle structure. The models presented here allow describing any deviation of the final structure from symmetry. Also, the analysis of non-equilibrium structures ("failed" particles, formed under inappropriately selected process conditions) is possible using these methods (Jabłczyńska et al., 2018).

3.5 Monte Carlo methods

Monte Carlo (MC) algorithms are another group of numerical methods which found their application in numerical simulations of structured particles formation. The beginning of the development of these numerical methods had its place in the first half of 20th century. However, they became most popular after the dissemination of computers in applications for scientific computing. They found an application not only (and not even most of all) in the simulation of particle formation but also in many branches of physics, engineering, biology and even social sciences (e.g. for modeling of the dynamics of political views in society).

In a broader sense of the term, MC methods are understood as methods that use repeated random sampling to obtain numerical results (Metropolis et al., 1953; Metropolis, 1987). The concept that stands for this method boils down to the observation that the phenomena occurring in systems with many degrees of freedom can be described with a good accuracy as random phenomena. A trivial example is the modeling of diffusion by considering the random walking of test particles. By tracking these particles, one may find out, e.g. the dependence of their mean square distance on time and thus the diffusion coefficient of the particle. The extension of this simple method is Kinetic Monte Carlo (KMC) method which is intended to simulate the time evolution of physical process (Voter et al., 2007). This evolution is realized as a sequence of "jumps" between individual states of the system. The probability of all possible "jumps" is known and thus, the "jumps" are chosen randomly. Such a sequence of states may give a picture of exemplary realization of the evolution of a process. By repeating the simulation as described above, it is possible to describe the average dynamics of the studied phenomenon and estimate possible deviations from these average dynamics resulting from the random nature of its description.

The very first applications of MC method in particle formation modeling concerned particle agglomeration. Tandon and Rosner (1999) applied a very simple MC-based scheme to find the final size distribution of agglomerates. In the mentioned work, the probability of merging particles/agglomerates has been set as proportional to the coagulation kernel (obtained from collision theory). In every MC step, the pair of particles has been randomly chosen, then a random number from 0 to 1 has been generated and compared with the probability of merging. If the random number was lower than the probability, the aggregation took place. This simple method allowed obtaining the size distribution function, which was in good agreement with the one received by means of experiments or other numerical methods. Other papers presented the application of MC algorithms for modeling the synthesis of nanoparticles from microemulsions (Tojo et al., 1997a; 1997b; 1998) and the formation of the shell in core-shell nanocrystals in reverse micelle systems (Shukla and Mehra, 2006). All these early works focused on obtaining the size distribution function of the particles rather than on their internal structure.

Kinetic Monte Carlo method has also been applied for modeling the formation of structured particles. Gorshkov et al. (2014) have modeled shell formation of core-shell noble metal nanoparticles with a core made from gold and a shell—from silver or platinum. Based on their earlier work (Gorshkov et al., 2011), authors have considered the diffusion of point-like "atoms" (in general, standing for atoms, ions, or molecules) from the solution to the surface pre-formed core where they were adsorbed to form a shell. As a result of these simulations, the mean values of the parameters of particles (e.g. shell thickness) have been obtained. The numerical results appear to be in good agreement with experimental ones.

Another very popular group of MC models which have found their application for modeling of formation of NMPs are the Markov chain MC methods (Gilks et al., 1995; Andrieu et al., 2010). The clue of this conception is to obtain a chain of states of the system so these states have the desired probability distribution. For typical physical or engineering problems, this equilibrium distribution is the Boltzmann (or canonic) distribution which describes the probability of appearance of a specific state of the system as (Creutz et al., 1983):

$$p_{\mathrm{B}}(\boldsymbol{s}) \propto \exp\left(-\frac{E_{\mathrm{s}}}{k_B T}\right) \tag{13}$$

where $\boldsymbol{s}$ denotes the vector of parameters of state, E_{s}—energy of this state, k_B is the Boltzmann constant and T—temperature of the system. Generation of a Markov chain which has the canonic distribution may be done in many ways. The most popular is the Metropolis–Hastings algorithm. According to this algorithm, one starts from a randomly chosen state $\boldsymbol{s}$. To obtain the next state in Markov chain, the new state $\boldsymbol{s}_1$ is generated by random disturbing of state $\boldsymbol{s}$. The new state is accepted as an element of Markov chain with probability equal to $p_\mathrm{B}(\boldsymbol{s}_1)/p_\mathrm{B}(\boldsymbol{s})$. If a new state $\boldsymbol{s}_1$ would not be accepted, the previous state $\boldsymbol{s}$ appears once again in the Markov chain. Then the whole procedure is repeated. Thus, it can be easily concluded that the states with a relatively high probability p_B appear in Markov chain more often than those with low p_B.

The works in which Markov chain MC methods were used to model the formation of particles with internal structure has appeared since the beginning of the 21st century. The synthesis of composite latex particles of various morphology by means of two-step emulsion polymerization has been simulated using an MC algorithm (Duda and Vázquez, 2005). The authors considered a mixture of two kinds of polymers, A and B and water particles W. The interactions between these three types of individuals are described by the very simple scheme:

$$U_{ij}(r) = \begin{cases} \infty, & \text{if } r < \sigma_{ij} \\ 0, & \text{if } r > \sigma_{ij} \end{cases} \tag{14}$$

where U_{ij} denotes the potential energy between interacting particles, r—the distance between them, indexes i and j denote polymers A, B or water W. Finally, σ_{ij} is a diameter of particle i if $i = j$ or, for $i \neq j$ is defined as $\sigma_{ij} = 0.5(\sigma_{ii} + \sigma_{jj})(1 + \Delta_{ij})$. The parameter $\Delta_{ij} > 0$ for every pair i and j favors the grouping of particles of the same type and thus separation of the three compounds of the mixture. To complete the description of the system, the circular domain is introduced and the energy of every particle which leaves the domain is also assigned as infinity. The MC simulations are performed in the classical canonical ensemble. As a result, these simulations lead to (dependently on the concentrations of all the compounds) to various morphologies of structured particles: core-shell, sandwich-like, raspberry-like and some other.

When investigating the final structure of structured NMPs rather than the dynamics of the formation process, MC models have appeared to be more efficient than any others what has been shown in (Chandross, 2014). In this paper, the synthesis of core-shell Cu–Ag nanoparticles has been investigated. Two different methods have been applied. The first one was MD which has been used to track every individual Cu and Ag atom during the synthesis process. The second one was the MC model. The MC method performed random particle swaps (understood as the exchange of Cu and Ag atoms at each MC step) with a small random translation below 0.2 Å. The successive states have been used to construct the Markov chain in the manner described above. The simulations show that the final state of a particle was achieved in a shorter time with the MC method than with the molecular dynamics.

While most of the applications of MC algorithms concern core-shell particle formation—this group of methods is also suitable for modeling the formation of other composite particles. In the article by Sdobnyakov et al. (2020) various morphologies of composite CuNi particles obtained by the modified solution combustion synthesis in the air have been analyzed. The MC simulations showed the patterns of neck formation for various cases of the initial arrangement of copper and nickel nanoparticles. The final structures obtained numerically were again in good agreement with XRD measurements.

MC methods have also been used for modeling the formation of porous particles from self-assembly of amphiphilic block copolymers inside an oil-in-water emulsion droplet (Zheng L. et al., 2019). The authors of this work used the MC method to obtain the final structure of such particles what allowed to construct the morphological diagram of particles as a function of the surfactant concentration and the copolymer composition (represented by the volume fraction of the hydrophilic block). They observed, dependently on simulation parameters, various morphologies of particles: non-porous, particles with closed pores and opened ones.

Among the many modifications of MC, it is worth noting the dual population balance Monte Carlo method, which allows tracking the distributions of two kinds of particles present in the system. In Skenderović et al. (2018) this method has been applied to simulate the particle formation by means of flame spray pyrolysis, where the solid particles may form from the gas phase or by means of droplet drying.

As shown, the MC models are widely used to investigate structures of NMPs synthesized in many processes. The main field of application of this group of methods is the multi-component systems. MC models are then used for the investigation of the formation of, e.g., composite or core-shell particles. When we are interested in the structure of resulting particles, the group of MC methods seems to be the most suitable tool. However, using these methods makes it difficult to track the dynamics of the synthesis and determine the structure of transitional states. This issue may be approached to a certain extent by the use of kinetic Monte Carlo methods. When we are interested in synthesis dynamics rather than in final structures, other numerical methods are worth considering.

3.6 Other approaches

The previous sections discussed the most popular numerical models for the synthesis of structured NMPs. In addition to these popular models, each of which has been described and used in at least a few scientific papers—there exist also some other models of formation of structured particles. These models were usually less versatile and were constructed ad hoc to describe a specific process that resulted in forming particles with a well-defined structure. The possibilities of generalizing such models to other cases of organized particle synthesis are relatively little. In this section, one of these less common models will be presented because of their originality, clever construction or the importance of the process they describe.

Specific methods have to be applied for the simulation of the synthesis of HPs by means of colloidal templating methods. As already mentioned, the starting point for these methods is the synthesis of CSPs followed by the removal of the core using physical phenomena such as Ostwald ripening or the Kirkendall effect. The first of these phenomena is the mass transport from smaller particles (grouped within the core) to larger ones, which make up the outer layers of the primary particle (Zeng, 2007). This process is theoretically described by the following continuity equation:

$$\frac{\partial N}{\partial t} + \frac{\partial}{\partial L}\left(N\frac{\partial L}{\partial t}\right) = 0 \qquad (15)$$

Various methods of solution of Eqn. (15) are reviewed in (Baldan, 2002).

Kirkendall effect is the motion of the interface between two substances (usually metals) that occurs as a consequence of the difference in diffusion rates of the atoms of both kinds. This leads to the formation of vacancies between core and shell and shrinkage of the core and finally HPs (or yolk-shell particles). Therefore, since this phenomenon is based on diffusion processes, the Kirkendall effect models boil down to numerical solving of the diffusion equations of both components under geometrical conditions imposed by the shape and size of the originally formed CSP. From a numerical point of view, applied numerical schemes and methods are typical, e.g. finite difference methods (Gusak and Tu, 2009; Jana et al., 2013), the variational method of calculating the chemical potential of the atoms diffusing along with the core–shell boundary (Klinger et al., 2015) or the thermodynamic extremal principle which minimizes Gibbs free energy (Svoboda et al., 2009). Energy considerations have also been applied to the investigation of random shape fluctuations during the formation of HP from CSP by Kirkendall effect in room temperature (Erlebacher and Margetis, 2014). It has been (qualitatively only) shown that surface thickness fluctuations of the shell are highly probable at room temperature and may lead to exposure of the core as a result of arising of some pinholes. When core dissolves, pinholes quickly close and classic HP is formed.

For considerations of process dynamics and final structures of porous particles, the class of models which may be named “topological” has been formulated. This class is based on elementary laws of topology. Papers presenting this approach (Gradoń et al., 2004; Lee et al., 2010) investigate the formation of porous silica particles by means of spray drying of a mixture of silica and polystyrene latex (PSL) colloids above the decomposition temperature of PSL. PSL nanoparticles are much larger than silica ones and during the first stage of drying, they take such positions that the mutual distances between them are as large as possible. As long as their number in a single drop is properly selected, they are the vertices of regular polyhedron, e.g. when there are four PSL particles in a dried drop, their dots will form a regular tetrahedron. In the second stage of drying, pores (cavities) will be formed in these places due to the thermal decomposition of PSL.

Modeling of the formation of virus capsids has been developed since 1990s. First works in this subject (Zlotnick et al., 1994) applied the formalism similar to PBEs to describe the dynamics of merging of protein subunits to form icosahedral capsid. The described model assumes that the protein aggregates may join or dissociate. However, at each stage the appropriate value of the angle between the subunits is maintained—the same as the value of the double-wall angle in the icosahedra. Based on this approach, the kinetics of the concentration of all transition structures and complete capsids in time is determined. This approach to modeling the kinetics of capsid formation dominates the works in this field - sometimes KMC methods are used instead of PBEs (Kivenson and Hagan, 2010). In both cases, it is crucial to know the energy of interaction between protein subunits. For the formation of viruses with different shapes of capsid, e.g. tobacco mosaic virus, models more suited to their topology were elaborated. E.g. for the tobacco mosaic virus mentioned above, it is the so-called “zipper model” (Kraft et al., 2012). This model assumes the elongation of rod-like virus capsid by random binding of protein subunits along the helical line. In recent years works dealing with multiscale modeling of capsids formation (Wang B. et al., 2019) have appeared. Besides protein subunits merging modeling, these models also consider the protein conformation changes, what is done by means of MD-based methods.

Recently, multi-scale models and models combining several approaches described earlier have been gaining popularity. E.g. Buesser and Pratsinis (2011) proposed the simulation of gas-phase synthesis of CSPs (TiO_2-SiO_2) by coupling of CFD with tracking of single particle motion. An example of the application of multiscale model may be found in (Xiao and Chen, 2014). For simulation of synthesis of two components particles in the spray drying process, the molecular-level model has been coupled with a continuum diffusion approach. The latter description gave the information about the segregation of components in the particle, while the microscopic one allowed describing the composition of single molecules at the particle surface. Similar multi-scale model, basing on CFD has been also applied for modeling of TiO_2 structured nanoparticles by means of FSP (Torabmostaedi and Zhang T., 2018).

4. Conclusions and perspectives

Along with the progress of research on structured particles, their synthesis and application, the development of numerical methods and models is progressing, allowing predicting the kinetics of formation and properties of these particles. This subject is still new, which is due to the fact that numerical modeling of the synthesis of structural particles, firstly, required appropriate computing power of computers, and secondly—the development of proper methods of particle characterization, enabling the verification of the results of numerical simulations. In recent years, many numerical descriptions of the synthesis of particles with a given structure have been created and are still being prepared.

The most popular are (i) methods based on the numerical solution of the differential equations of mass and energy, (ii) closely related multi-layer methods, (iii) the molecular dynamics method and other methods allowing for tracking individual atoms, groups of atoms or molecules joining a particle, (iv) methods based on population balance equations; and (v) Monte Carlo methods. The choice of the method that will be used to describe and optimize a specific process for obtaining structured particles depends mainly on the properties of the particles to be described in this process. **Table 1** presents the possibilities of using the five most popular methods mentioned above to describe the synthesis of structural particles of various structures. As this table shows, molecular dynamics method and similar methods seem to be the most universal. Monte Carlo methods have an almost equally wide range of applications. It should be expected that in the near future, these methods will be most often used to simulate the NMPs synthesis processes and will be most intensively developed.

The greatest disadvantage of using these two most popular methods, i.e. the relatively long computation time and the high degree of complexity of the mathematical apparatus, has prompted and will probably continue to encourage scientists to develop other, less universal, but simpler models for the synthesis of particles with a specific structure. Models are used primarily by practitioners and experimenters to support their experiences. It is worth continuing to use these types of models where possible, being aware, however, that their use is limited to the assumptions made.

Table 1 Usefulness of most popular numerical models for modeling the synthesis of particles with a specific structure.

Model	HP	CSP	JPs and other composite
HMB equations	++	+	–
multiple shells	++	+	–
PBEs	++	–	–
MD and related	++	++	++
MC	+	++	++

++ Model has been successfully applied to simulation of synthesis of this kind of particles.
\+ Model might be potentially applied to simulation of synthesis of this kind of particles but there are no (or single) papers showing that.
– Model cannot be applied to simulation of synthesis of this kind of particles.

Acknowledgement

The author would like to thank Katarzyna Jabłczyńska of the Warsaw University of Technology for her valuable discussions on this topic.

Nomenclature

Abbreviations

CFD	computational fluid dynamics
CSP	core-shell particle
DPD	dissipative particle dynamics
FSP	flame spray pyrolysis
HMB	heat and mass balance
HP	hollow particle
JP	Janus particle
KMC	kinetic Monte Carlo method
L-J	Lennard-Jones potential
MC	Monte Carlo method
MD	molecular dynamics
NMPs	nano- and microparticles
PBE	population balance equation
PSL	polystyrene latex

Latin symbols

A_d	droplet surface (m^2)
b	damping coefficient in Langevin equation (kg/s)
c_A	concentration of solute A inside the droplet (kg/m^3, mol/m^3 or other concentration units)
D_A, D	diffusion coefficient (m^2/s)
E_s	energy of the microscopic state (J/mol)
F, $\mathbf{F}$	force (N)
G	linear growth rate of particles/cluster (m/s)
h_c	heat transfer coefficient ($W/m^2/K$)
h_D	mass transfer coefficient (m/s)
k_B	Boltzmann constant ($k_B = 1.38064852 \times 10^{-23}$ J/K)
L	particle internal coordinate (in PBE) – size (m)
L_h	heat of evaporation (J/kg)
m	mass (kg)
$\dot{m}_v$	mass flux (kg/s)
N	particle number density function (m^{-3})
P	pressure (Pa)
p_B	probability (-)
R	normalized radial coordinate (-)

r	radial coordinate (m)
r_c	range of interactions between beds (m)
r_d	radius of a droplet (m)
r_{ij}	distance between individuals (atoms, molecules, particles) i and j (m)
$\boldsymbol{s}$, $\boldsymbol{s}_1$	vector of parameters of state (various units)
t	time (s)
T	temperature (K)
T_d	temperature of a droplet (K)
T_∞	temperature of ambient (K)
U_{ij}	potential energy of interactions between individuals (atoms, molecules, particles) i and j (J)
$\boldsymbol{x}$	position (m)

Greek symbols

$\Gamma(t)$	stochastic component in Langevin equation (m/s)
δ	Dirac δ-function
ε_{ij}	parameter describing interactions between individuals (atoms, molecules, particles) i and j (various units)
λ	heat conductivity (W/m/K)
ρ_d	solvent density (kg/m^3)
$\rho_\mathrm{v,s}$	saturated solvent vapor concentration (kg/m^3)
$\rho_{\mathrm{v},\infty}$	solvent vapor concentration in the ambient (kg/m^3)
σ_{ij}	a range of interaction between individuals (atoms, molecules, particles) i and j (m)

References

Adhikari B., Howes T., Bhandari B.R., Use of solute fixed coordinate system and method of lines for prediction of drying kinetics and surface stickiness of single droplet during convective drying, Chemical Engineering and Processing: Process Intensification, 46 (2007) 405–419. DOI: 10.1016/j.cep.2006.06.018

Andrieu C., Doucet A., Holenstein R., Particle Markov chain Monte Carlo methods, Journal of the Royal Statistical Society: Series B (Statistical Methodology), 72 (2010) 269–342. DOI: 10.1111/j.1467-9868.2009.00736.x

Aryal S., Park H., Leary J.F., Key J., Top-down fabrication-based nano/microparticles for molecular imaging and drug delivery, International Journal of Nanomedicine, 14 (2019) 6631–6644. DOI: 10.2147/IJN.S212037

Aul'chenko S., Kartaev E., Numerical simulation of the synthesis of titania-silica composite nanoparticles in plasmachemical reactor, AIP Conference Proceedings, 2027 (2018) 040002. DOI: 10.1063/1.5065276

Baldan A., Review progress in Ostwald ripening theories and their applications to nickel-base superalloys Part I: Ostwald ripening theories, Journal of Materials Science, 37 (2002) 2171–2202. DOI: 10.1023/a:1015388912729

Betke A., Kickelbick G., Bottom-up, wet chemical technique for the continuous synthesis of inorganic nanoparticles, Inorganics, 2 (2014) 1–15. DOI: 10.3390/inorganics2010001

Blackburn T., Alexander C.M.O., Carlson R., Elkins-Tanton L.T., The accretion and impact history of the ordinary chondrite parent bodies, Geochimica et Cosmochimica Acta, 200 (2017) 201–217. DOI: 10.1016/j.gca.2016.11.038

Boraey M.A., Vehring R., Diffusion controlled formation of microparticles, Journal of Aerosol Science, 67 (2014) 131–143. DOI: 10.1016/j.jaerosci.2013.10.002

Bück A., Peglow M., Naumann M., Tsotsas E., Population balance model for drying of droplets containing aggregating nanoparticles, AIChE Journal, 58 (2012) 3318–3328. DOI: 10.1002/aic.13726

Buesser B., Pratsinis S.E., Design of gas-phase synthesis of core-shell particles by computational fluid–aerosol dynamics, AIChE Journal, 57 (2011) 3132–3142. DOI: 10.1002/aic.12512

Caruso F., Caruso R.A., Möhwald H., Nanoengineering of inorganic and hybrid hollow spheres by colloidal templating, Science, 282 (1998) 1111–1114. DOI: 10.1126/science.282.5391.1111

Chandross M., Energetics of the formation of Cu–Ag core–shell nanoparticles, Modelling and Simulation in Materials Science and Engineering, 22 (2014) 075012. DOI: 10.1088/0965-0393/22/7/075012

Chen H., Ruckenstein E., Formation of complex colloidal particles: morphologies and mechanisms, Soft Matter, 8 (2012) 8911–8916. DOI: 10.1039/C2SM26035B

Chen X.D., Sidhu H., Nelson M., Theoretical probing of the phenomenon of the formation of the outermost surface layer of a multi-component particle, and the surface chemical composition after the rapid removal of water in spray drying, Chemical Engineering Science, 66 (2011) 6375–6384. DOI: 10.1016/j.ces.2011.08.035

Chiarello G.L., Selli E., Forni L., Photocatalytic hydrogen production over flame spray pyrolysis-synthesised TiO_2 and Au/TiO_2, Applied Catalysis B: Environmental, 84 (2008) 332–339. DOI: 10.1016/j.apcatb.2008.04.012

Creutz M., Microcanonical Monte Carlo simulation, Physical Review Letters, 50 (1983) 1411–1414. DOI: 10.1103/PhysRevLett.50.1411

Czelej K., Colmenares J.C., Jabłczyńska K., Ćwieka K., Werner Ł., Gradoń L., Sustainable hydrogen production by plasmonic thermophotocatalysis, Catalysis Today, (2021). DOI: 10.1016/j.cattod.2021.02.004

Daw M.S., Foiles S.M., Baskes M.I., The embedded-atom method: a review of theory and applications, Materials Science Reports, 9 (1993) 251–310. DOI: 10.1016/0920-2307(93)90001-U

de Gennes P.G., Soft matter, Science, 256 (1992) 495–497. DOI: 10.1126/science.256.5056.495

Demirörs A.F., van Blaaderen A., Imhof A., Synthesis of eccentric titania−silica core−shell and composite particles, Chemistry of Materials, 21 (2009) 979–984. DOI: 10.1021/cm803250w

de Souza Lima R., Ré M.I., Arlabosse P., Drying droplet as a template for solid formation: a review, Powder Technology, 359 (2020) 161–171. DOI: 10.1016/j.powtec.2019.09.052

Duda Y., Vázquez F., Modeling of composite latex particle morphology by off-lattice Monte Carlo simulation, Langmuir, 21 (2005) 1096–1102. DOI: 10.1021/la048065t

Erlebacher J., Margetis D., Mechanism of hollow nanoparticle formation due to shape fluctuations, Physical Review Letters, 112 (2014) 155505. DOI: 10.1103/PhysRevLett.112.155505

Eslamian M., Ahmed M., Ashgriz N., Modelling of nanoparticle formation during spray pyrolysis, Nanotechnology, 17 (2006) 1674–1685. DOI: 10.1088/0957-4484/17/6/023

Español P., Warren P., Statistical mechanics of dissipative particle dynamics, Europhysics Letters (EPL), 30 (1995) 191–196. DOI: 10.1209/0295-5075/30/4/001

Fan H.J., Gösele U., Zacharias M., Formation of nanotubes and hollow nanoparticles based on Kirkendall and diffusion processes: a review, Small, 3 (2007) 1660–1671. DOI: 10.1002/smll.200700382

Fernandez Y.A.D., A. Gschneidtner T., Wadell C., H. Fornander

L., Avila S.L., Langhammer C., Westerlund F., Moth-Poulsen K., The conquest of middle-earth: combining top-down and bottom-up nanofabrication for constructing nanoparticle based devices, Nanoscale, 6 (2014) 14605–14616. DOI: 10.1039/C4NR03717K

Foiles S.M., Baskes M.I., Daw M.S., Embedded-atom-method functions for the fcc metals Cu, Ag, Au, Ni, Pd, Pt, and their alloys, Physical Review B, 33 (1986) 7983–7991. DOI: 10.1103/PhysRevB.33.7983

Förster G.D., Benoit M., Lam J., Alloy, Janus and core–shell nanoparticles: numerical modeling of their nucleation and growth in physical synthesis, Physical Chemistry Chemical Physics, 21 (2019) 22774–22781. DOI: 10.1039/C9CP04231H

Gac J.M., Gradoń L., A distributed parameter model for the spray drying of multicomponent droplets with a crust formation, Advanced Powder Technology, 24 (2013a) 324–330. DOI: 10.1016/j.apt.2012.08.004

Gac J.M., Gradoń L., A distributed parameter model for the drying of multicomponent aerosol and sessile droplets, Chemical Engineering Transactions, 32 (2013b) 1927–1932. DOI: 10.3303/CET1332322

Ghosh Chaudhuri R., Paria S., Core/shell nanoparticles: classes, properties, synthesis mechanisms, characterization, and applications, Chemical Reviews, 112 (2012) 2373–2433. DOI: 10.1021/cr100449n

Gilks W.R., Richardson S., Spiegelhalter D., Markov Chain Monte Carlo in Practice, CRC Press, 1995, ISBN: 9780412055515.

Gorshkov V., Kuzmenko V., Privman V., Modeling of growth morphology of core–shell nanoparticles, The Journal of Physical Chemistry C, 118 (2014) 24959–24966. DOI: 10.1021/jp506331u

Gorshkov V., Zavalov O., Atanassov P.B., Privman V., Morphology of nanoclusters and nanopillars formed in nonequilibrium surface growth for catalysis applications, Langmuir, 27 (2011) 8554–8561. DOI: 10.1021/la103113f

Gradoń L., Janeczko S., Abdullah M., Iskandar F., Okuyama K., Self-organization kinetics of mesoporous nanostructured particles, AIChE Journal, 50 (2004) 2583–2593. DOI: 10.1002/aic.10257

Grasmeijer N., Frijlink H.W., Hinrichs W.L.J., An adaptable model for growth and/or shrinkage of droplets in the respiratory tract during inhalation of aqueous particles, Journal of Aerosol Science, 93 (2016a) 21–34. DOI: 10.1016/j.jaerosci.2015.11.011

Grasmeijer N., Frijlink H.W., Hinrichs W.L.J., Model to predict inhomogeneous protein–sugar distribution in powders prepared by spray drying, Journal of Aerosol Science, 101 (2016b) 22–33. DOI: 10.1016/j.jaerosci.2016.07.012

Gusak A.M., Tu K.N., Interaction between the Kirkendall effect and the inverse Kirkendall effect in nanoscale particles, Acta Materialia, 57 (2009) 3367–3373. DOI: 10.1016/j.actamat.2009.03.043

Hadiko G., Han Y.S., Fuji M., Takahashi M., Synthesis of hollow calcium carbonate particles by the bubble templating method, Materials Letters, 59 (2005) 2519–2522. DOI: 10.1016/j.matlet.2005.03.036

Hamzehlou S., Leiza J.R., Asua J.M., A new approach for mathematical modeling of the dynamic development of particle morphology, Chemical Engineering Journal, 304 (2016) 655–666. DOI: 10.1016/j.cej.2016.06.127

Handscomb C.S., Kraft M., Bayly A.E., A new model for the drying of droplets containing suspended solids after shell formation, Chemical Engineering Science, 64 (2009a) 228–246. DOI: 10.1016/j.ces.2008.10.019

Handscomb C.S., Kraft M., Bayly A.E., A new model for the drying of droplets containing suspended solids, Chemical Engineering Science, 64 (2009b) 628–637. DOI: 10.1016/j.ces.2008.04.051

Hao X., Zhao H., Xu Z., Zheng C., Population balance-Monte Carlo simulation for gas-to-particle synthesis of nanoparticles, Aerosol Science and Technology, 47 (2013) 1125–1133. DOI: 10.1080/02786826.2013.823642

Hayes R., Ahmed A., Edge T., Zhang H., Core–shell particles: preparation, fundamentals and applications in high performance liquid chromatography, Journal of Chromatography A, 1357 (2014) 36–52. DOI: 10.1016/j.chroma.2014.05.010

Jabłczyńska K., Gac J.M., Sosnowski T.R., Self-organization of colloidal particles during drying of a droplet: modeling and experimental study, Advanced Powder Technology, 29 (2018) 3542–3551. DOI: 10.1016/j.apt.2018.09.036

Jana S., Chang J.W., Rioux R.M., Synthesis and modeling of hollow intermetallic Ni–Zn nanoparticles formed by the Kirkendall effect, Nano Letters, 13 (2013) 3618–3625. DOI: 10.1021/nl401467r

Kellerman D.W., Review of low dielectric constant thick film electronic ceramics using hollow microspheres, MRS Proceedings, 372 (2011) 239. DOI: 10.1557/PROC-372-239

Kivenson A., Hagan M.F., Mechanisms of capsid assembly around a polymer, Biophysical Journal, 99 (2010) 619–628. DOI: 10.1016/j.bpj.2010.04.035

Klinger L., Kraft O., Rabkin E., A model of Kirkendall hollowing of core–shell nanowires and nanoparticles controlled by short-circuit diffusion, Acta Materialia, 83 (2015) 180–186. DOI: 10.1016/j.actamat.2014.09.050

Kraft D.J., Kegel W.K., van der Schoot P., A kinetic zipper model and the assembly of tobacco mosaic virus, Biophysical Journal, 102 (2012) 2845–2855. DOI: 10.1016/j.bpj.2012.05.007

Larbi Z., Sadoun N., Si-Ahmed E., Legrand J., An efficient numerical prediction of the crust onset of a drying colloidal drop, International Journal of Heat and Mass Transfer, 165 (2021) 120613. DOI: 10.1016/j.ijheatmasstransfer.2020.120613

Lee S.Y., Gradon L., Janeczko S., Iskandar F., Okuyama K., Formation of highly ordered nanostructures by drying micrometer colloidal droplets, ACS Nano, 4 (2010) 4717–4724. DOI: 10.1021/nn101297c

Lenggoro I.W., Hata T., Iskandar F., Lunden M.M., Okuyama K., An experimental and modeling investigation of particle production by spray pyrolysis using a laminar flow aerosol reactor, Journal of Materials Research, 15 (2000) 733–743. DOI: 10.1557/jmr.2000.0106

Lesov I., Valkova Z., Vassileva E., Georgiev G.S., Ruseva K., Simeonov M., Tcholakova S., Denkov N.D., Smoukov S.K., Bottom-up synthesis of polymeric micro- and nanoparticles with regular anisotropic shapes, Macromolecules, 51 (2018) 7456–7462. DOI: 10.1021/acs.macromol.8b00529

Levchenko E.V., Evteev A.V., Riley D.P., Belova I.V., Murch G.E., Molecular dynamics simulation of the alloying reaction in Al-coated Ni nanoparticle, Computational Materials Science, 47 (2010) 712–720. DOI: 10.1016/j.commatsci.2009.10.014

Levi-Hevroni D., Levy A., Borde I., Mathematical modeling of drying of liquid/solid slurries in steady state one-dimensional flow, Drying Technology, 13 (1995) 1187–1201. DOI: 10.1080/07373939508917016

Lin C.-C., Liao C.-W., Chao Y.-C., Kuo C., Fabrication and characterization of asymmetric Janus and ternary particles, ACS Applied Materials & Interfaces, 2 (2010) 3185–3191. DOI: 10.1021/am1006589

Liu B., Hu X., Chapter 1—Hollow micro- and nanomaterials: synthesis and applications, in: Zhao Q. (Ed.), Advanced

Nanomaterials for Pollutant Sensing and Environmental Catalysis, Elsevier, 2020, pp. 1–38. DOI: 10.1016/B978-0-12-814796-2.00001-0

Liu Q., Wu Y., Xing F., Liu Q., Guo X., Huang C., B_2O_3@BPO_4 sandwich-like hollow spheres as metal-free supported liquid-phase catalysts, Journal of Catalysis, 381 (2020) 599–607. DOI: 10.1016/j.jcat.2019.11.028

Liu Y., Abetz V., Müller A.H.E., Janus cylinders, Macromolecules, 36 (2003) 7894–7898. DOI: 10.1021/ma0345551

Lou X.W. (David), Archer L.A., Yang Z., Hollow micro-/nanostructures: synthesis and applications, Advanced Materials, 20 (2008) 3987–4019. DOI: 10.1002/adma.200800854

Mädler L., Kammler H.K., Mueller R., Pratsinis S.E., Controlled synthesis of nanostructured particles by flame spray pyrolysis, Journal of Aerosol Science, 33 (2002) 369–389. DOI: 10.1016/S0021-8502(01)00159-8

Mao Y., Park T.-J., Wong S.S., Synthesis of classes of ternary metal oxide nanostructures, Chemical Communications, (2005) 5721–5735. DOI: 10.1039/B509960A

Maurice U., Mezhericher M., Levy A., Borde I., Particle formation from droplet containing nanoparticles: internal bubble growth, Drying Technology, 35 (2017) 969–984. DOI: 10.1080/07373937.2016.1263647

Metropolis N., The beginning of the Monte Carlo method, Los Alamos Science, 15 (1987) 125–130.

Metropolis N., Rosenbluth A.W., Rosenbluth M.N., Teller A.H., Teller E., Equation of state calculations by fast computing machines, The Journal of Chemical Physics, 21 (1953) 1087–1092. DOI: 10.1063/1.1699114

Mezhericher M., Levy A., Borde I., Theoretical drying model of single droplets containing insoluble or dissolved solids, Drying Technology, 25 (2007) 1025–1032. DOI: 10.1080/07373930701394902

Mezhericher M., Levy A., Borde I., Heat and mass transfer of single droplet/wet particle drying, Chemical Engineering Science, 63 (2008) 12–23. DOI: 10.1016/j.ces.2007.08.052

Mezhericher M., Levy A., Borde I., Theoretical models of single droplet drying kinetics: a review, Drying Technology, 28 (2010) 278–293. DOI: 10.1080/07373930903530337

Mezhericher M., Levy A., Borde I., Modelling the morphological evolution of nanosuspension droplet in constant-rate drying stage, Chemical Engineering Science, 66 (2011) 884–896. DOI: 10.1016/j.ces.2010.11.028

Mezhericher M., Naumann M., Peglow M., Levy A., Tsotsas E., Borde I., Continuous species transport and population balance models for first drying stage of nanosuspension droplets, Chemical Engineering Journal, 210 (2012) 120–135. DOI: 10.1016/j.cej.2012.08.038

Miller K., A geometrical-mechanical interpretation of gradient-weighted moving finite elements, SIAM Journal on Numerical Analysis, 34 (1997) 67–90. DOI: 10.1137/S0036142994260884

Mohanty U.S., Electrodeposition: a versatile and inexpensive tool for the synthesis of nanoparticles, nanorods, nanowires, and nanoclusters of metals, Journal of Applied Electrochemistry, 41 (2011) 257–270. DOI: 10.1007/s10800-010-0234-3

Mourdikoudis S., Chirea M., Zanaga D., Altantzis T., Mitrakas M., Bals S., Liz-Marzán L.M., Pérez-Juste J., Pastoriza-Santos I., Governing the morphology of Pt–Au heteronanocrystals with improved electrocatalytic performance, Nanoscale, 7 (2015) 8739–8747. DOI: 10.1039/C4NR07481E

Moyano E.A., Scarpettini A.F., Numerical stability study and error estimation for two implicit schemes in a moving boundary problem, Numerical Methods for Partial Differential Equations, 16 (2000) 42–61. DOI: 10.1002/(SICI)1098-2426(200001)16:1<42::AID-NUM4>3.0.CO;2-L

Parienta D., Morawska L., Johnson G.R., Ristovski Z.D., Hargreaves M., Mengersen K., Corbett S., Chao C.Y.H., Li Y., Katoshevski D., Theoretical analysis of the motion and evaporation of exhaled respiratory droplets of mixed composition, Journal of Aerosol Science, 42 (2011) 1–10. DOI: 10.1016/j.jaerosci.2010.10.005

Ren Y., Cai J., Pitsch H., Theoretical single-droplet model for particle formation in flame spray pyrolysis, Energy & Fuels, 35 (2021) 1750–1759. DOI: 10.1021/acs.energyfuels.0c03669

Sdobnyakov N., Khort A., Myasnichenko V., Podbolotov K., Romanovskaia E., Kolosov A., Sokolov D., Romanovski V., Solution combustion synthesis and Monte Carlo simulation of the formation of CuNi integrated nanoparticles, Computational Materials Science, 184 (2020) 109936. DOI: 10.1016/j.commatsci.2020.109936

Shabde V.S., Emets S.V., Mann U., Hoo K.A., Carlson N.N., Gladysz G.M., Modeling a hollow micro-particle production process, Computers & Chemical Engineering, 29 (2005) 2420–2428. DOI: 10.1016/j.compchemeng.2005.05.019

Shukla D., Mehra A., Modeling shell formation in core−shell nanocrystals in reverse micelle systems, Langmuir, 22 (2006) 9500–9506. DOI: 10.1021/la061499z

Singh V., Cassidy C., Grammatikopoulos P., Djurabekova F., Nordlund K., Sowwan M., Heterogeneous gas-phase synthesis and molecular dynamics modeling of Janus and core–satellite Si–Ag nanoparticles, The Journal of Physical Chemistry C, 118 (2014) 13869–13875. DOI: 10.1021/jp500684y

Skenderović I., Kotalczyk G., Kruis F.E., Dual population balance Monte Carlo simulation of particle synthesis by flame spray pyrolysis, Processes, 6 (2018) 253. DOI: 10.3390/pr6120253

Song P., Wen D., Molecular dynamics simulation of a core−shell structured metallic nanoparticle, The Journal of Physical Chemistry C, 114 (2010) 8688–8696. DOI: 10.1021/jp908788b

Sun X., Han J., Guo R., A mini review on yolk-shell structured nanocatalysts, Frontiers in Chemistry, 8 (2020). DOI: 10.3389/fchem.2020.606044

Svoboda J., Fischer F.D., Vollath D., Modeling of formation of binary-phase hollow nanospheres from metallic solid nanospheres, Acta Materialia, 57 (2009) 1912–1919. DOI: 10.1016/j.actamat.2008.12.038

Swihart M.T., Vapor-phase synthesis of nanoparticles, Current Opinion in Colloid & Interface Science, 8 (2003) 127–133. DOI: 10.1016/S1359-0294(03)00007-4

Tandon P., Rosner D.E., Monte Carlo simulation of particle aggregation and simultaneous restructuring, Journal of Colloid and Interface Science, 213 (1999) 273–286. DOI: 10.1006/jcis.1998.6036

Tojo C., Blanco M.C., López-Quintela M.A., Preparation of nanoparticles in microemulsions: a Monte Carlo study of the influence of the synthesis variables, Langmuir, 13 (1997a) 4527–4534. DOI: 10.1021/la9606207

Tojo C., Blanco M.C., López-Quintela M.A., Microemulsions as microreactors: a Monte Carlo simulation on the synthesis of particles, Journal of Non-Crystalline Solids, 235–237 (1998) 688–691. DOI: 10.1016/S0022-3093(98)00572-9

Tojo C., Blanco M.C., Rivadulla F., López-Quintela M.A., Kinetics of the formation of particles in microemulsions, Langmuir, 13 (1997b) 1970–1977. DOI: 10.1021/la9607870

Torabmostaedi H., Zhang T., Numerical simulation of TiO_2 nanoparticle synthesis by flame spray pyrolysis, Powder Technology, 329 (2018) 426–433. DOI: 10.1016/j.powtec.2018.01.051

Tsotsas E., Influence of drying kinetics on particle formation:

a personal perspective, Drying Technology, 30 (2012) 1167–1175. DOI: 10.1080/07373937.2012.685139

Tu K.N., Gösele U., Hollow nanostructures based on the Kirkendall effect: design and stability considerations, Applied Physics Letters, 86 (2005) 093111. DOI: 10.1063/1.1873044

Vasiliauskas R., Liu D., Cito S., Zhang H., Shahbazi M.-A., Sikanen T., Mazutis L., Santos H.A., Simple microfluidic approach to fabricate monodisperse hollow microparticles for multidrug delivery, ACS Applied Materials & Interfaces, 7 (2015) 14822–14832. DOI: 10.1021/acsami.5b04824

Vehring R., Pharmaceutical particle engineering via spray drying, Pharmaceutical Research, 25 (2008) 999–1022. DOI: 10.1007/s11095-007-9475-1

Vehring R., Foss W.R., Lechuga-Ballesteros D., Particle formation in spray drying, Journal of Aerosol Science, 38 (2007) 728–746. DOI: 10.1016/j.jaerosci.2007.04.005

Verma S., Gokhale R., Burgess D.J., A comparative study of top-down and bottom-up approaches for the preparation of micro/nanosuspensions, International Journal of Pharmaceutics, 380 (2009) 216–222. DOI: 10.1016/j.ijpharm.2009.07.005

Vetter T., Iggland M., Ochsenbein D.R., Hänseler F.S., Mazzotti M., Modeling nucleation, growth, and Ostwald ripening in crystallization processes: a comparison between population balance and kinetic rate equation, Crystal Growth & Design, 13 (2013) 4890–4905. DOI: 10.1021/cg4010714

Voter A.F., Introduction to Kinetic Monte Carlo Method, in: Sickafus K.E., Kotomin E.A., Uberuaga B.P. (Eds.), Radiation Effects in Solids, Springer Netherlands, Dordrecht, 2007, pp. 1–23. DOI: 10.1007/978-1-4020-5295-8_1

Walther A., André X., Drechsler M., Abetz V., Müller A.H.E., Janus discs, Journal of the American Chemical Society, 129 (2007) 6187–6198. DOI: 10.1021/ja068153v

Walther A., Müller A.H.E., Janus particles: synthesis, self-assembly, physical properties, and applications, chemical Reviews, 113 (2013) 5194–5261. DOI: 10.1021/cr300089t

Wang B., Zhang J., Wu Y., A multiscale model for the self-assembly of coat proteins in bacteriophage MS2, Journal of Chemical Information and Modeling, 59 (2019) 3899–3909. DOI: 10.1021/acs.jcim.9b00514

Wang S., Langrish T.A.G., A distributed parameter model for particles in the spray drying process, Advanced Powder Technology, 20 (2009) 220–226. DOI: 10.1016/j.apt.2009.03.004

Wang X., Barber W.E., Long W.J., Applications of superficially porous particles: High speed, high efficiency or both?, Journal of Chromatography A, 1228 (2012) 72–88. DOI: 10.1016/j.chroma.2011.07.083

Wang X., Feng J., Bai Y., Zhang Q., Yin Y., Synthesis, properties, and applications of hollow micro-/nanostructures, Chemical Reviews, 116 (2016) 10983–11060. DOI: 10.1021/acs.chemrev.5b00731

Weiss B.P., Elkins-Tanton L.T., Differentiated planetesimals and the parent bodies of chondrites, Annual Review of Earth and Planetary Sciences, 41 (2013) 529–560. DOI: 10.1146/annurev-earth-040610-133520

Wichaita W., Polpanich D., Tangboriboonrat P., Review on synthesis of colloidal hollow particles and their applications, Industrial & Engineering Chemistry Research, 58 (2019) 20880–20901. DOI: 10.1021/acs.iecr.9b02330

Wu B.-H., Chung C.A., Modeling and simulation of solid-containing droplet drying and different-structure particle formation, International Journal of Heat and Mass Transfer, 152 (2020) 119469. DOI: 10.1016/j.ijheatmasstransfer.2020.119469

Xiao J., Chen X.D., Multiscale modeling for surface composition of spray-dried two-component powders, AIChE Journal, 60 (2014) 2416–2427. DOI: 10.1002/aic.14452

Yang S.-M., Kim S.-H., Lim J.-M., Yi G.-R., Synthesis and assembly of structured colloidal particles, Journal of Materials Chemistry, 18 (2008) 2177–2190. DOI: 10.1039/B716393B

Yang Z., Yang X., Xu Z., Molecular dynamics simulation of the melting behavior of Pt−Au nanoparticles with core−shell structure, The Journal of Physical Chemistry C, 112 (2008) 4937–4947. DOI: 10.1021/jp711702y

Ye G., Sun Y., Zhou X., Zhu K., Zhou J., Coppens M.-O., Method for generating pore networks in porous particles of arbitrary shape, and its application to catalytic hydrogenation of benzene, Chemical Engineering Journal, 329 (2017) 56–65. DOI: 10.1016/j.cej.2017.02.036

Zeng H.C., Ostwald ripening: a synthetic approach for hollow nanomaterials, Current Nanoscience, 3 (2007) 177–181. DOI: 10.2174/157341307780619279

Zhang Q., Wang W., Goebl J., Yin Y., Self-templated synthesis of hollow nanostructures, Nano Today, 4 (2009) 494–507. DOI: 10.1016/j.nantod.2009.10.008

Zheng L., Wang Z., Yin Y., Jiang R., Li B., Formation mechanisms of porous particles from self-assembly of amphiphilic diblock copolymers inside an oil-in-water emulsion droplet upon solvent evaporation, Langmuir, 35 (2019) 5902–5910. DOI: 10.1021/acs.langmuir.9b00613

Zlotnick A., To build a virus capsid: an equilibrium model of the self assembly of polyhedral protein complexes, Journal of Molecular Biology, 241 (1994) 59–67. DOI: 10.1006/jmbi.1994.1473

Author’s Short Biography

Jakub M. Gac

PhD, DSc, Professor at the Faculty of Chemical and Process Engineering Warsaw University of Technology, Poland. 2005: MSc Physics; 2006: MSc Chemical Engineering; 2009: PhD Physics; 2017: DSc Chemical Engineering; 2018 - visiting professor, Federal Institute of Technology in Zürich (Switzerland). Scientific interests: aerosol physics and chemistry, functional particles and materials formation, gas and wastewater filtration, air quality monitoring and analysis, numerical modelling in chemical engineering. Author and co-author of over 60 peer-reviewed papers published in periodicals and conference proceedings and 2 books.

KONA Powder and Particle Journal No. 39 (2022) 62–83/https://doi.org/10.14356/kona.2022012 Review Paper

Review and Further Validation of a Practical Single-Particle Breakage Model †

Luís Marcelo Tavares

Department of Metallurgical and Materials Engineering, Universidade Federal do Rio de Janeiro, Brazil

---

Abstract

Particle breakage occurs in comminution machines and, inadvertently, in other process equipment during handling as well as in geotechnical applications. For nearly a century, researchers have developed mathematical expressions to describe single-particle breakage having different levels of complexity and abilities to represent it. The work presents and analyses critically a breakage model that has been found to be suitable to describe breakage of brittle materials in association to the discrete element method, either embedded in it as part of particle replacement schemes or coupled to it in microscale population balance models. The energy-based model accounts for variability and size-dependency of fracture energy of particles, weakening when particles are stressed below this value, as well as energy and size-dependent fragment size distributions when particles are stressed beyond it, discriminating between surface and body breakage. The work then further validates the model on the basis of extensive data from impact load cell and drop weight tests. Finally, a discussion of challenges associated to fitting its parameters and on applications is presented.

Keywords: particle breakage, fracture, modelling, impact, compression, discrete element method

---

1. Introduction

Single-particle breakage tests have long been used to analyze fracture phenomena (Arbiter et al., 1969; Schönert, 1972; Rumpf, 1973), study energy utilization in comminution processes (Rumpf, 1973; Schubert, 1987; Dan and Schubert, 1990; Tavares, 1999), analyze the effect of particle size, shape, material properties and modes of loading on particle breakage characteristics (Yashima et al., 1987; Tavares and King, 1998; Rozenblat et al., 2012; Saeidi et al., 2016; Saeidi et al., 2017; Lois-Morales et al., 2020), investigate energy-size reduction relationships (Piret, 1953; Bergstrom et al., 1961; Rumpf, 1973; Narayanan and Whiten, 1988; Morrell, 2004) and analyze material deformation response under applied stresses (Schönert, 1991; Sikong et al., 1990; Tavares and Almeida, 2020).

One application of single-particle breakage information that has grown significantly in recent decades has been to support mathematical models of comminution and mechanical degradation during handling. This information was initially used as part of phenomenological models of comminution devices, including ball mills, autogenous and semi-autogenous mills and cone crushers (Narayanan and Whiten, 1988; Napier-Munn et al., 1996), as well as of degradation during handling (Teo et al., 1990; Weedon and Wilson, 2000), although originally in a fairly simplistic way. Perhaps influenced by the conditions used in the standardized twin pendulum, and later also in the drop weight tester (JKDWT) by the Julius Kruttschnitt Mineral Research Centre (JKMRC) (Napier-Munn et al., 1996), attention was initially only given to the relationship between the energy applied and the resulting fragmentation at relatively high specific impact energies.

From the beginning of the 1990s, research on the discrete element method (DEM) applied to tumbling mills (Mishra and Rajamani, 1992; King and Bourgeois, 1993; Morrison and Cleary, 2006) has demonstrated that very few impacts occur at the high specific energies that are object of testing in the JKDWT, and that the majority of collisions occur at impact energies that are either able to only impose limited breakage to particles or break them only after repeated stressing. This led to recognition of the importance of deepening the investigation of conditions that result in primary breakage, including breakage probability, weakening by repeated impacts and progeny size distributions at very low specific impact energies (Tavares, 2007). This shed new light into the subject, which had been object of relatively scattered studies before then (Rumpf, 1973; Baumgardt et al., 1975; Krogh, 1980; Schönert, 1979; Yashima et al., 1987). Nevertheless, the importance of very

---

† Received 21 March 2021; Accepted 7 June 2021
J-STAGE Advance published online 7 August 2021
Add: COPPE/UFRJ, Cx. Postal 68505, CEP 21941-972, Rio de Janeiro, Brazil
E-mail: tavares@metalmat.ufrj.br
TEL: +55-21-2290-1544

low energy impacts was recognized over 70 years ago by Fred Bond, when developing the standard crushability test (Bond, 1947), in which particles are repeatedly stressed at increasing impact energies until primary breakage occurs (Tavares and Carvalho, 2007).

A definition that has a central role when dealing with particle breakage is that of particle fracture energy (Baumgardt et al., 1975; King and Bourgeois, 1993). It corresponds to the stressing energy below which the core of the particle is maintained unbroken, whereas potentially damaged, while the surface of the particle may lose mass due to abrasion-like breakage when it is subjected to a stressing event. This particle fracture energy varies from particle to particle as well as with particle size and defines the threshold between massive or body breakage at higher impact energies and surface breakage that occurs at lower stressing energies (Tavares and King, 1998).

As mathematical models of different mills, crushers and handling systems evolved, incorporating information from DEM, it became evident that more detailed information on particle breakage was necessary. It is worth mentioning that several approaches circumvented the need for this information by either using data from particle bed breakage tests (Datta and Rajamani, 2002) or from the process itself, by back-calculating the selection function from data (Capece et al., 2014; Wang et al., 2012). However, they are not as generally applicable given their more limited ability to decouple material from process (Tavares, 2017). As such, the most powerful approaches used in advanced mathematical models and simulations are particle-based, that is, require information on how individual particles respond to stresses, either when they are fully resolved in the DEM simulation or when they are not. It is important to recognize that in order to be useful in such models, particle response must be known under the variety of conditions to which it will be subjected to in a comminution device or a system that can cause mechanical degradation. These typically include widely varied particle sizes, stressing intensities, geometries and rates of stressing as well as modes of stress application.

A fairly large number of mathematical models describing particle breakage has been proposed in the literature, which may be potentially of use in association to advanced mathematical models and DEM simulations. In most of them the variable of interest is the stressing energy (Tavares and King, 1998; Vogel and Peukert, 2003; Morrison et al., 2007; Bonfils, 2017; Ballantyne et al., 2017), whereas in a few the variable of interest is impact velocity (Ghadiri and Zhang, 2002; Rozenblat et al., 2012) or force (Rodnianski et al., 2019). Also, several of these models have been proposed that relate the size distribution of fragments to the stressing energy applied, not discriminating between volume or surface breakage (Ballantyne et al., 2017; Ouchterlony and Sanchidrián, 2018). These models, however, are not meant to discriminate particles individually, being only suited to describe the response of the entire batch. Other models have been proposed to describe the so-called incremental breakage, lumping together surface breakage and weakening by repeated stressing (Morrison et al., 2007; Bonfils et al., 2016), being very limited when used in association to advanced mathematical models of comminution and degradation. Yet other models focused exclusively on surface breakage (Ghadiri and Zhang, 2002).

The present work analyzes critically and also presents further evidence of the validity of a comprehensive mathematical model proposed by the author and his co-workers over the last 25 years (Tavares, 1997; Tavares and King, 1998; Tavares and King, 2002; Tavares, 2009; Carvalho et al., 2015; Tavares and Chagas, 2021) and schematically shown in **Fig. 1** to describe several aspects of particle breakage.

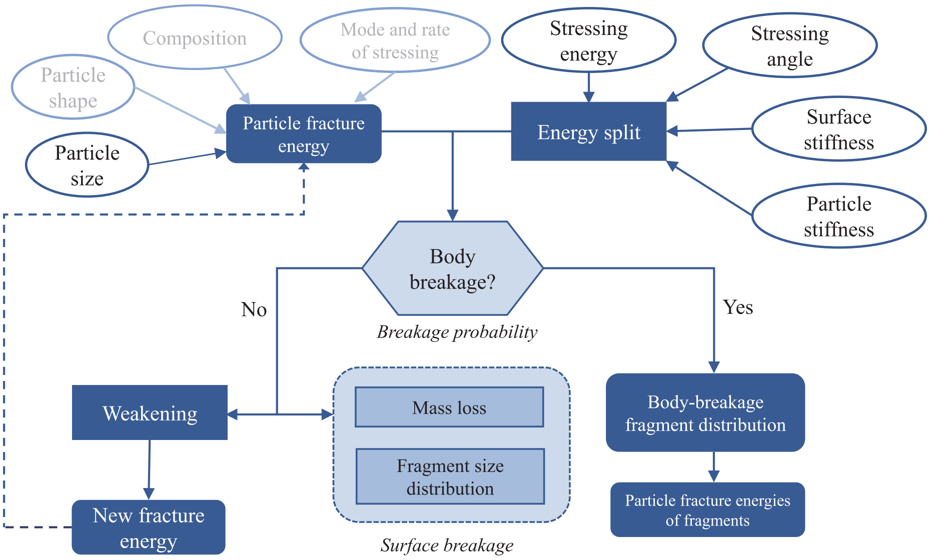

Fig. 1 General scheme of the breakage model.

2. Breakage probability

2.1 Body breakage probability distributions

Arguably, the central part of the model is the breakage probability (**Fig. 1**). It represents the relationship between the applied stressing energy and the resulting proportion of particles that have undergone body or massive breakage when particles contained in a batch are stressed under identical conditions. Breakage in this context is defined arbitrarily as loss of at least 10 % of the particle mass (Dan and Schubert, 1990; Tavares, 2007). Estimates of breakage probability may be obtained experimentally from tests in which lots of particles contained in narrow size ranges are subjected to impacts by propelling them, one-by-one, against a target at a controlled velocity or dropping them under gravity. In this case the mass-specific impact energy is given by

$$E_k = \frac{\overline{v}^2}{2} \tag{1}$$

where $\overline{v}$ is the average velocity at the instant of collision against the target, which can be obtained, for instance, from measurements using a high-speed camera (Cavalcanti et al., 2021).

Alternatively, an estimate of breakage probability may be obtained by impacting particles using a drop weight tester. Assuming no loss of momentum during drop of the impactor (free-fall), the specific impact energy may be given by

$$E_k = \frac{m\,g\,h}{\overline{m}_\mathrm{p}} \tag{2}$$

where m is the mass of the drop weight, $\overline{m}_\mathrm{p}$ is the average weight of particles in the lot tested, g the acceleration due to gravity and h the net drop height, that is, the distance between the bottom of the striker and the top of the particle.

In either case, the estimate of breakage probability for a given mass-specific impact energy E is given by the proportion broken, represented by the ratio

$$P(E_k) = \frac{N_\mathrm{b}}{N} \tag{3}$$

where N is the number of stressed particles and N_b is the number of particles that underwent body breakage as a result of application of the specific impact energy E_k. Although Eqn. (3) relates numbers of particles, it is assumed to be equivalent to the mass-based probability, given their narrow size range. In order to remove ambiguity in identifying which particles underwent breakage during execution of the test, each should be weighed individually prior to the test and also after each impact, to verify if loss of at least 10 % of their mass occurred. The measurement after the impact becomes obviously unnecessary if the particle suffered evident disintegration.

Either when particles are projected against a target or when a drop weight impacts individual particles, the specific impact energy E_k is actually a random variable, subjected to variability owing to the velocity of impact and, in the case of the later, also due to variability in particle weight. In addition to that, the proportion broken given by Eqn. (3) is only an estimate of the breakage probability, with the uncertainty reducing as the number of test-particles increase, provided no bias existed in selecting particles for the test. The magnitude of the sampling error has been estimated (Tavares, 2009) on the basis of the Binomial distribution, so that the confidence interval for the proportion broken is given by

$$\frac{N_\mathrm{b}}{N} \pm z\left(\frac{\alpha}{2}\right)\sqrt{\frac{\frac{N_\mathrm{b}}{N}\left(1-\frac{N_\mathrm{b}}{N}\right)}{N}} \tag{4}$$

where α is the significance and z is the reduced Gaussian distribution.

An example of data collected following this approach is presented in **Fig. 2**. Obtained from impact of iron ore pellets against a target, it exhibits the typical S shape and asymmetry, evident from the skewness of the distribution to the right.

A more direct and less time-consuming approach is to measure directly the energy required to break individual particles, using either slow compression devices (Sikong et al., 1990; Tavares, 2007; Rozenblat et al., 2011; Ribas et al., 2014; Campos et al., 2021) or instrumented drop weight test devices, such as the impact load cell (King and Bourgeois, 1993; Tavares and King, 1998; Bonfils, 2017; Lois-Morales et al., 2020), analyzing the distribution of data. While requiring more specialized equipment, this approach has the advantage of demanding significantly smaller sample volumes. In this approach, the force-

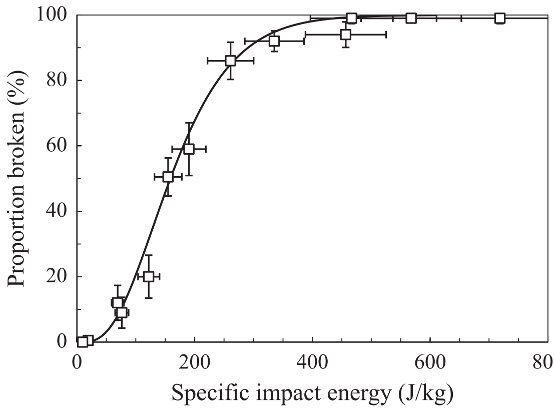

Fig. 2 Proportion broken as a function of specific impact energy from propelling fired iron ore pellets contained in the size range 12.5–9.0 mm against a steel target (data from Cavalcanti et al., 2021). Vertical error bars are given by Eqn. (4) and horizontal error bars were estimated from measurements of impact velocity using a high-speed camera.

deformation profile during loading of each particle is recorded and the mass-specific particle fracture energy E is given by numerical integration of the curve up to the deformation or force responsible for fracture

$$E = \frac{1}{m_\text{p}} \int_0^{\Delta_\text{c}} F \, \text{d}\Delta \tag{5}$$

where m_p is the weight of each individual particle, F the load, whereas Δ and Δ_c are the deformations and the deformation at primary fracture, respectively.

Typically, data in these tests present large variability (Tavares and King, 1998), so that they should be properly analyzed. A convenient method is order statistics, through which the test results are ranked in ascending order and the values $i = 1, 2, \ldots, N$ assigned to the ranked observations, where N is the total number of valid tests performed. The cumulative probability distribution estimates for the particle fracture energy are given by

$$P(E_i) = \frac{i - 0.5}{N} \tag{6}$$

An example of this type of data is shown in **Fig. 3** from impact-breakage of quartz particles. Different probability distributions have been proposed over the years to describe data such as in **Figs. 2** and **3**, including the lognormal and upper truncated lognormal (Baumgardt et al., 1975; King and Bourgeois, 1993; Tavares and King, 1998; Tavares and King, 2002), the logistic and log-logistic (Vervoorn and Austin, 1990; Rozenblat et al., 2011; 2012), the gamma (Cavalcanti and Tavares, 2019) and the Weibull distribution (Weichert, 1992; Salman et al., 2002; Vogel and Peukert, 2004), just to name a few that have been used to fit such data (Cavalcanti and Tavares, 2018). These distributions are typically skewed to the right, with either two or three parameters and with or without a clear upper limiting (truncation) value. **Fig. 3** compares some of the distributions to data. In particular when dealing with data from proportion broken, in which results only from relatively a limited number of stressing energies are available (**Fig. 2**), several distributions may provide fairly similar fit (Tavares, 1997), so that the selection of the most suitable distribution is not straightforward but is often not critical either. Differences in fit provided by the distribution functions are typically limited to the extremes (tails) of the data. In particular, the lower tail of the distribution, represented by the particles that are more amenable to breakage, is particularly important when describing degradation due to handling (Cavalcanti et al., 2021). On the other hand, the accurate description of the upper part of the distribution, in particular for the coarser particles, is particularly critical when using the model to predict breakage in tumbling mills, since it will determine the likelihood that particles will remain unbroken in spite of the collisions in the mill (Tavares and Carvalho, 2009).

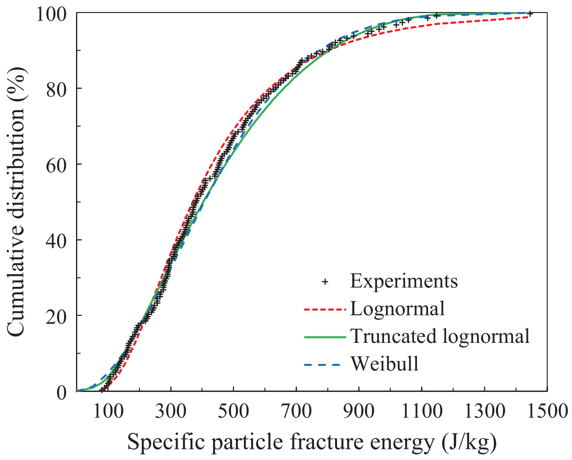

Fig. 3 Distribution of fracture energies from impact of 200 quartz particles contained in the size range 1.18–1.0 mm in the impact load cell device. Data from Tavares (1997).

A distribution that has demonstrated to be able to describe well the variability of the data is the upper truncated lognormal distribution, given by

$$P(E) = \frac{1}{2}\left[1 + \text{erf}\left(\frac{\ln E^* - \ln E_{50}}{\sqrt{2\sigma^2}}\right)\right] \tag{7}$$

and

$$E^* = \frac{E_\text{max}\, E}{E_\text{max} - E} \tag{8}$$

where $P(E)$ represents the breakage probability or the cumulative distribution, E is the mass-specific fracture energy of the particle, which corresponds to the maximum stressing energy that it can sustain in a collision and not break, E_max is the upper truncation value of the distribution, E_{50} and σ^2 are the median and the variance of the distribution, respectively. The upper truncation value is often represented by the ratio E_max/E_{50}. In the case when this ratio is equal to infinity, $E^* = E$ and Eqn. (7) becomes the lognormal distribution.

Besides stressing energy, several other variables also influence breakage probability (**Fig. 1**). The stiffness of the surface in contact is such a variable, which is analyzed in greater detail in 2.2, whereas the important effect of particle size is analyzed in section 2.3. The effect of impact angle on the breakage probability has been the object of some studies (Dan and Schubert, 1990; Salman et al., 2003; Tavares et al., 2018; Cavalcanti et al., 2021). In a comprehensive campaign of experiments in which iron pellets were propelled against a target (Tavares et al., 2018; Cavalcanti et al., 2021) it was found that breakage probability, and therefore body breakage, may be described considering only the normal component of the impact velocity, at least for impacts at angles that range from 90° (normal) to 30°. The effects of other variables, such as particle shape, stressing rate and mode of stressing (single or double) (**Fig. 1**) have been studied in the literature (Tavares, 2007; Bonfils, 2017; Saeidi et al., 2017; Lois-Morales et al., 2020) but the lack of a proper understanding on how they affect the several aspects of breakage for brittle materials in general made it impossible to properly account for them in the model. As such, it is advised that the user fits the model parameters using data that most closely match conditions that dominate in the device that is meant to be simulated.

Adapting Eqns. (7) and (8) to be used to describe discrete particles, such as those embedded in a DEM simulation (Tavares et al., 2020b; 2021) is quite straightforward, since it only requires randomly sampling the distribution every time a particle is created.

2.2 Effect of stiffness on body breakage probability

Analyzes in section 2.1 assumed that the stiffness of a particle is significantly smaller than that of the surface of the testing device or machine which is in contact with the particle. In several instances, however, that is not the case, so that a correction must be used. Given the local nature of the contacts involving application of stresses to particles and assuming validity of the Hertz contact theory (Tavares and King, 1998; Tavares et al., 2021), the proportion *e* of the stressing energy involved in any given event that is used to deform the particle is given by (Becker et al., 2001; Tavares and Carvalho, 2011; Tavares et al., 2021)

$$e = \frac{1}{1 + k_\mathrm{p} / k_\mathrm{s}} \tag{9}$$

where k_p is the particle stiffness (Tavares and King, 1998), k_s is the Hertzian stiffness of the surface in contact with the particle. For instance, Eqn. (9) may be used to estimate the proportion of the energy recorded using Eqn. (5) in the test that was actually dissipated in breakage of the particle. Since steel surfaces are typically used in the testing devices, with Young's modulus (Y) of 209 GPa and Poisson's ratio of 0.3, their stiffness [$k_\mathrm{s} = Y/(1 - \nu^2)$] is 230 GPa. The apparent particle stiffness may be estimated using a convenient procedure in an earlier work (Tavares and King, 1998), whereas a more accurate, but more laborious, measure may be obtained using a procedure that was recently proposed (Angulo et al., 2020). If the particle stiffness is significantly lower than that of the surface, then $e \cong 1$. However, in a collision involving two particles of the same material, then $e = 1/2$, with the energy being equally shared between the colliding particles.

In order to assess the validity of Eqn. (9), tests were conducted in an impact load cell device on limestone particles using different types of impactors. In this modified impact load cell device a rod rather than a drop ball is used as impactor (Tavares and King, 2004), so that tests were carried out comparing the specific fracture energies measured using steel or hard polymer (Polyether ether ketone or PEEK) impacting rods. The values of Hertzian stiffness of the impactors were estimated as 230 GPa for steel and 4.8 GPa for PEEK, this later calculated on the basis of data from manufacturer's catalogs (Young's modulus of 4.0 GPa with Poisson's ratio of 0.4). The median apparent stiffness for the limestone particles, estimated using the procedure proposed by Tavares and King (1998) was 6.4 GPa. **Fig. 4** shows that the energies required to break particles when the softer impactor (PEEK) is used are significantly higher than when steel surfaces are used. These higher values for the polymeric striker are consistent with the larger dissipation of the energy which results from using a striker with lower stiffness (Eqn. 9). Considering now the application of Eqn. (9) considering the stiffness values, **Fig. 4** shows the dashed line, which nearly superimposes to data for the steel striker, showing that the actual fracture energies of the limestone particles were independent of the striker used.

It is important to bear in mind that Eqn. (9) only accounts for the elastic part of the deformation (Tavares et al., 2021). Whenever stressing events occur with significant contribution from plastic deformation, Eqn. (9) provides only a conservative estimate. An example of this was the impact of iron ore pellets against an aluminum alloy plate, in which Eqn. (9) underestimated the energy dissipated on the impact surface, leading to incorrect predictions (Cavalcanti et al., 2021).

This effect of stiffness of the parts in contact can be dealt with readily using Eqn. (9) either in the case of applying the model to continuum distributions, such as in microscale population balance model formulations (Tavares, 2017), and in discrete forms imbedded in DEM (Tavares et al., 2020a; 2021).

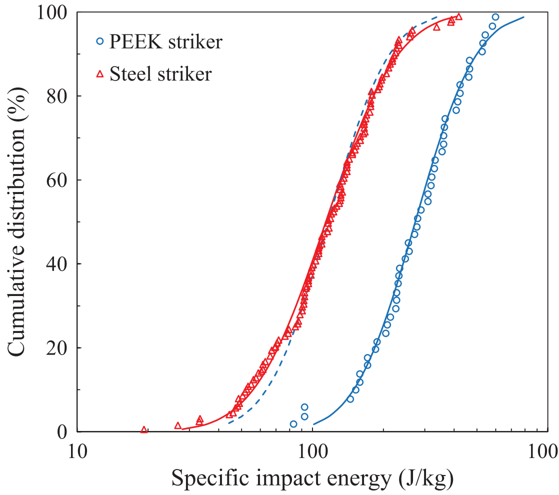

Fig. 4 Distribution of particle fracture energies of 4.75–4.0 mm limestone (Karslruhe) particles stressed with different strikers in an impact load cell device. Symbols are experimental data, solid lines the fit to the lognormal distribution, whereas the dashed line the fit to PEEK striker after applying Eqn. (9) (data from Tavares, 1997).

2.3 Size effect on body breakage probability

Besides stressing energy, the most critical variable influencing breakage probability is particle size. When dealing with brittle materials, it is expected that the stress or energy require for their fracture increases as particle sizes reduce (Schönert, 1979; Yashima et al., 1987; Tavares, 2007). However, such variation depends on material, with **Fig. 5** showing the distributions of particle fracture energies for a sample of gneiss.

Several expressions have been proposed in the literature to describe the size effect on the median value of the distribution (Vogel and Peukert, 2004; Rozenblat et al., 2012). In the present model the effect of particle size on E_{50} is described using an expression inspired in reliability theory (Tavares and King, 1998; Tavares and Neves, 2008), given by

$$E_{50,i} = \frac{E_\infty}{1+k_\mathrm{p}/k_\mathrm{s}}\left[1+\left(\frac{d_\mathrm{o}}{d_i}\right)^{\varphi}\right] \tag{10}$$

where E_∞, d_o and φ are model parameters that must be fitted to experimental data and d_i is the representative size of particles contained in size class i. k_p and k_s are the values of Hertzian stiffness of the particle and of the surface of the device used in measuring the breakage characteristics, respectively. As such, Eqn. (10) already incorporates the effect of stiffness of the tools, given by Eqn. (9).

Data from a variety of materials are presented in **Fig. 6**, which also shows the model fit. It is evident that the model is able to represent variations that range from power-law relationships of fracture energies with particle size up to cases in which a constant fracture energy is achieved at coarse sizes. Parameters of Eqn. (10) for these and other materials are presented in **Table 1**. Values of parameter φ vary from as low as about 0.7 to as high as 2. However, since it describes primarily the power-law increase of the median fracture energies with the reduction in particle size, this parameter is more prone to uncertainty, due to the challenge associated with estimations of fracture energies at fine sizes, as discussed in section 5.1. Values of parameter d_o, on the other hand, varied significantly, from values as low as 0.5 mm to values as high as 200 mm. When this value lies in the range of particle sizes tested (**Table 1**), it may be interpreted as a characteristic dimension of the material microstructure (Tavares and King, 1998; Tavares and Neves, 2008). On the other hand, values of d_o above these make it simply a fitting parameter with no particular physical meaning, implying that no clear plateau would have been reached in the measurements of fracture energies at coarse sizes.

Fitting all three parameters in Eqn. (10) typically requires data from at least five widely different particle size classes, ideally spanning at least two size decades. This is not typically a straight-forward task, since it would almost certainly require using multiple impact load cell or compression testing devices, given the different resolutions required.

Besides the effect of particle size on the median particle fracture energy, it is also worth examining its effect on the standard deviation of the distribution (Eqn. 7). For several materials, the variation of the standard deviation of the distribution may be considered small or negligible. An example of this is presented in **Fig. 7**, which shows data from **Fig. 5** plotted as a function of ratio between the specific particle fracture energy of individual particles and the median value E_{50} for each size. Since data approximately superimpose, forming a mastercurve, it may be assumed that the standard deviation of the distribution is invariable with particle size in the range studied. Values of the variance σ^2 have been found to vary, exceptionally, from as low as 0.15

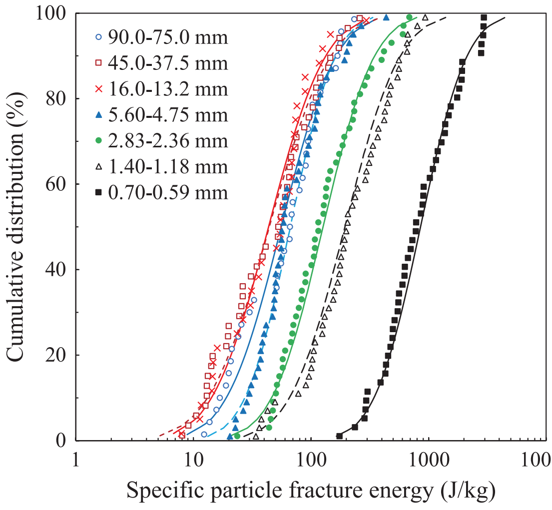

Fig. 5 Distribution of specific particle fracture energies for different particle sizes of gneiss (Santa Luzia quarry). Symbols represent experimental data and lines the fit to the lognormal distribution (Eqn. 7).

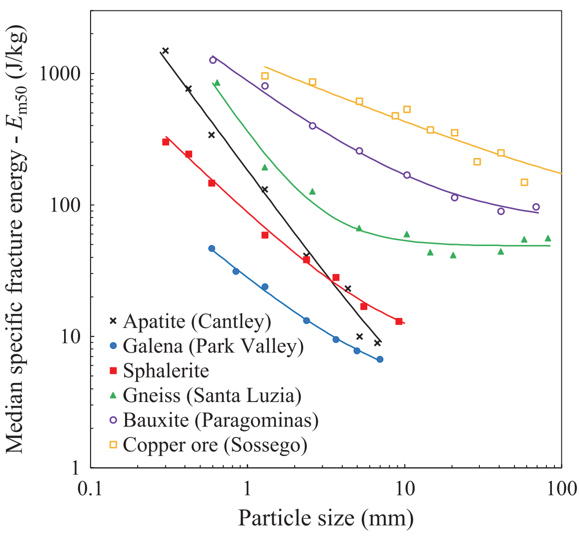

Fig. 6 Variation of median particle fracture energies of selected materials as a function of representative particle size.

Table 1 Values of parameters in the size model for selected materials (Eqn. 10).

Material	Source	Specific gravity (g/cm^3)	E_∞ (J/kg)	d_o (mm)	φ	Size range (mm)	Reference
Apatite	Cantley, Canada	3.21	1.50	19.3	1.62	0.25–8.00	Tavares (1997)
Galena	Park Valley, Idaho	7.40	3.19	7.31	1.03	0.70–7.60	Tavares (1997)
Gilsonite	Fort Duchesne, Utah	1.07	5.50	7.07	1.60	1.18–10.0	Tavares (1997)
Quartz	Karlsruhe, Germany	2.65	43.4	3.48	1.61	0.25–4.75	Tavares (1997)
Sphalerite	Na*	4.10	7.00	8.24	1.16	0.35–10.0	Tavares (1997)
Basalt	Utah	2.59	9.59	3.93	1.96	0.25–7.20	Tavares (1997)
Limestone	Karlsruhe, Germany	2.73	114	0.49	2.05	0.35–5.60	Tavares (1997)
Limestone	Cantagalo, Brazil	2.71	7.0	100.	0.80	0.50–37.5	Carvalho and Tavares (2013)
Limestone	Brazil	2.98	150	0.79	1.30	0.50–37.5	Carvalho and Tavares (2013)
Marble	Vermont	2.68	45.9	0.88	1.76	0.35–10.0	Tavares (2007)
Gneiss	Santa Luzia, Brazil	2.80	48.7	2.78	1.82	0.50–90.0	Tavares and Neves (2008)
Syenite	Vigné, Brazil	2.64	26.5	101.	0.67	0.50–90.0	Tavares and Neves (2008)
Granulite	Pedra Sul, Brazil	2.79	123	0.91	1.68	0.50–90.0	Tavares and Neves (2008)
Bauxite	Paragominas, Brazil	2.40	70.3	14.6	0.91	0.50–75.0	Tavares (2007)
Copper ore	Bingham Canyon, Utah	2.83	96.1	1.17	1.26	0.25–15.8	Tavares (2007)
Copper ore	Green Valley, Arizona	2.83	171	1.37	1.41	0.50–12.5	Tavares (2007)
Copper ore	Sossego mine, Brazil	2.93	60.0	400.	0.45	0.50–90.0	Carvalho and Tavares (2013)
Copper ore	NSW, Australia	2.75	22.5	41.1	0.71	0.35–37.5	Tavares et al. (2020b)
Iron ore	Newfoundland, Canada	3.80	47.3	1.08	2.30	0.25–15.0	Tavares (2007)
Iron ore	Eveleth mine, Minnesota	3.65	164	0.86	1.76	0.35–10.0	Tavares (1997)
Iron ore	Conceição mine, Brazil	2.80	16.8	20.1	0.84	2.36–80.0	Tavares and Carvalho (2011)
Iron ore	Australia	Na*	0.86	200.	1.21	2.36–90.0	Fandrich et al. (1998)
Cement clinker	CEMEX, Mexico	2.49	46.4	6.68	1.09	0.25–12.5	Tavares (1997)
Cement clinker	CEMEX, Mexico	2.49	100	5.04	0.92	0.25–12.5	Tavares (1997)

* Na: not available

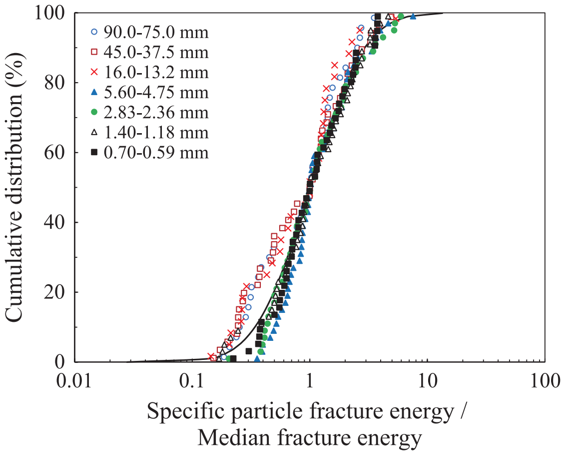

Fig. 7 Distributions of particle fracture energies of gneiss particles of different sizes (data from **Fig. 5**) plotted in normalized form.

to as high as 1.2, with typical values of about 0.7. For some materials, however, it has been found that the variability of the distribution increases for finer particle sizes (Barrios et al., 2011) and expressions that are analogous to Eqn. (10) have been successfully used to describe the data (Carvalho and Tavares, 2013). The ratio E_{max}/E_{50} also shows the same general trend as the variance with size. These variations are typically associated to rocks/ores, which behave as composites at coarser sizes, responding as individual minerals at finer sizes, with the corresponding wide range of fracture energies of the components.

2.4 Weakening by repeated stressing events

Breakage models in the literature have been proposed to describe the so-called incremental damage (Morrison et al., 2007; Bonfils et al., 2016), which is given by the proportion of fines generated as a function of repeated stressing. In these models, however, weakening by repeated stressing is confounded with the fines associated to surface breakage. Thus, a more rigorous approach is to describe the increase in breakage probability with the repeated impacts separately. Indeed, when the specific stressing energy involved in a collision is smaller than the fracture energy of the particle, the particle will not undergo breakage (**Fig. 1**), but will sustain internal crack-like damage, which will make it more amenable to break in a future stressing event. This weakening has been described on the basis of a model based on continuum damage mechanics (Kachanov, 1958), through which the specific fracture energy of the particle will be reduced to (Tavares and King, 2002; Tavares, 2009)

$$E' = E(1-D) \tag{11}$$

where E' is the fracture energy of the particle after the stressing event and D is the damage variable, which is given by (Tavares, 2009)

$$D = \left[\frac{2\gamma}{(2\gamma-5D+5)}\frac{eE_k}{E}\right]^{\frac{2\gamma}{5}} \tag{12}$$

where γ, the only fitting parameter in the model, is the damage accumulation coefficient, which characterizes the amenability of a material to sustain damage prior to catastrophically breaking, and eE_k is the specific energy in the collision available to the particle. Eqn. (12) is implicit but can be easily solved iteratively with the initial guess $D = 0$.

The constant γ is typically estimated through tests in which lots of particles are repeatedly impacted at a given specific energy and the proportion broken recorded (Eqn. 3). From the distribution of specific particle fracture energies, given by Eqns. (7) and (8) and the model Eqns. (11) and (12) the optimal value of the constant may be estimated. This is illustrated in **Fig. 8**, which compares the model fit to experiments. Tavares (2009) carried out a comprehensive study, which demonstrated that the constant γ is typically independent of particle size, with more limited data showing independence of particle shape. Also, it was observed that values of γ varied from about 1.5 for materials that are highly amenable to accumulate damage prior to breakage, up to 8.1 for materials with exceptionally little amenability to weaken by repeated stressing, with average values being in the range of 3 and 4. Finally, it has then been found that the value of γ is not directly influenced by the mechanical strength of the particle, but by its microstructure: it is often lower for materials with complex microstructures, which are more capable of sustaining damage prior to collapsing and higher for more brittle materials (Tavares, 2000).

Eqns. (11) and (12) are useful when the model is applied to individual particles, such as when it is embedded in a DEM simulation (Tavares et al., 2020a; 2021). An alternative formulation of the model, useful when it is applied in a continuum, such as associated to microscale population balance formulations (Tavares and Carvalho, 2009; Carvalho and Tavares, 2013; Oliveira et al., 2020), is given by

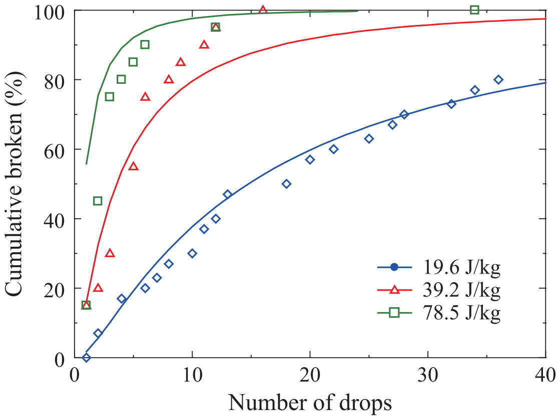

Fig. 8 Proportion broken from drops on a steel surface at different drop height (or specific impact energies) of 125–75 mm copper ore (Sossego) particles. Experimental results represent symbols and lines the model fit (Carvalho and Tavares, 2011).

$$P'(E) = \left[\frac{P(E/(1-D)) - P(eE_k)}{1-P(eE_k)}\right] \tag{13}$$

which should be solved in association to

$$D = \left[\frac{2\gamma(1-D)}{(2\gamma-5D+5)}\frac{eE_k}{E}\right]^{\frac{2\gamma}{5}} \tag{14}$$

where E in Eqns. (13) and (14) represent the fracture energy of the particle after the impact.

The model does not have a minimum threshold, that is, as E_k reduces, D vanishes in Eqns. (12) and (14). In practice, however, a minimum value of E_k is often selected, for computation efficiency, when using the model, so as to prevent computing damage in collisions with negligibly small magnitudes.

2.5 Surface breakage mass loss

In the breakage model the description of surface breakage is certainly in an earlier stage of development than the models described in sections 2.1 to 2.4. Surface breakage has been widely investigated as part of attrition studies and an elegant model has been proposed by Ghadiri and Zhang (2002). An adaptation of the model for the case when the controlled variable is the specific impact energy gives (Cavalcanti et al., 2019)

$$\xi_i = 100\kappa d_i eE_k \tag{15}$$

where κ is the attrition parameter, fitted from data, and d_i is the representative particle size. This model has been suc-

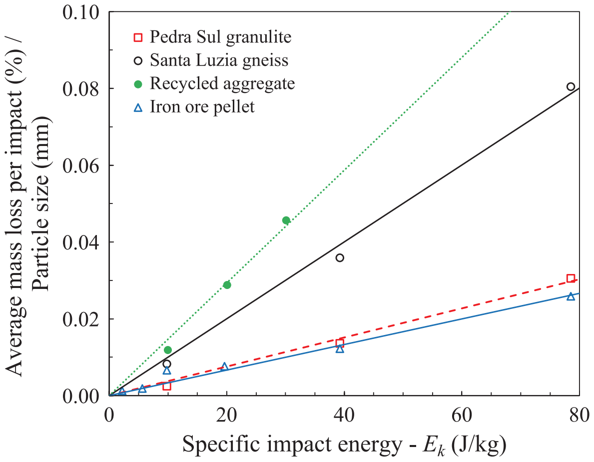

Fig. 9 Average percentage of mass loss per impact of selected materials dropped by gravity onto a thick steel plate. Gneiss and granulite: 22.4–19 mm; recycled aggregate: 14–10 mm; iron ore pellet: 12.5–9 mm.

cessfully applied to both natural and recycled aggregates (Cunha et al., 2014; Moreno-Juez et al., 2021) and iron ore pellets (Boechat et al., 2018; Cavalcanti et al., 2019). Unfortunately, it has only been validated for particles contained in a relatively limited (22–9 mm) range of sizes. Selected results are presented in **Fig. 9** for tests in which particles are dropped one-by-one by gravity and their mass loss recorded after each impact, showing the validity of the model.

Evidently, this model does not account for the fact that surface breakage tends to deviate from linearity as the number of impacts increases and neither for the dependency on particle shape, so it may only be used as a first approximation of a rather complex problem. In an attempt to account for the effect of impact angle on surface breakage, Cavalcanti et al. (2019) used the total energy dissipated in the collision, given by the sum of the normal and the shear energy loss estimated in DEM in place of E_k in Eqn. (15), obtaining good agreement to data from impact of iron ore pellets.

3. Breakage distribution

3.1 Breakage distribution function

As mentioned in the introductory section, several models have been proposed in the literature to describe the progeny size distribution from single-particle breakage. Several of them benefit from the fact that when cumulative progeny size distributions are plotted as a function of the relative fragment size, that is, the ratio between the sieve size and the representative size of the parent particles, they superimpose, independently of parent particle size. This representative parent particle size is given by the geometric mean sizes of the initial sieve sizes containing the tested lot.

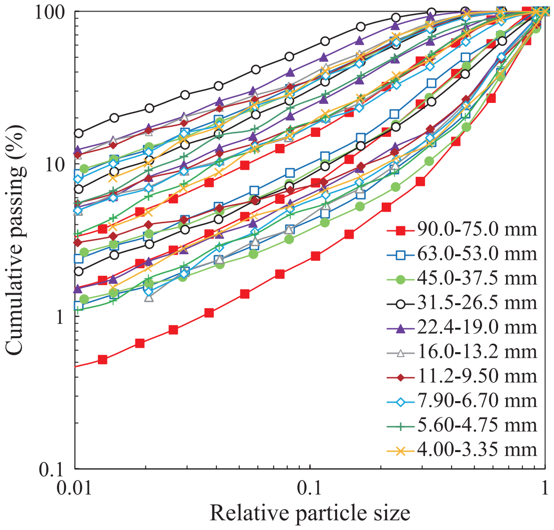

Fig. 10 Progeny size distributions from testing syenite particles from Vigné quarry contained in different size ranges in drop weight testers (modified from Tavares and Neves, 2008).

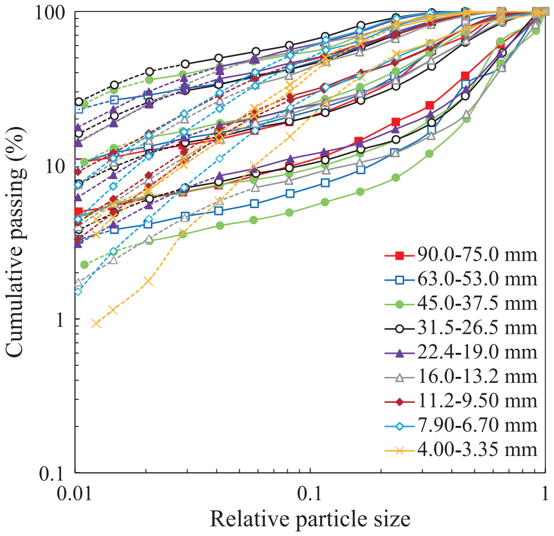

Fig. 11 Progeny size distributions from testing gneiss particles from Santa Luzia quarry contained in different size ranges in drop weight testers (modified from Tavares and Neves, 2008).

An illustration of this is presented in **Fig. 10**, which shows data for different initial sizes for syenite. In spite of the scatter, data for the different initial sizes superimpose reasonably well, demonstrating that such normalization of data in respect to the initial parent size is valid. This behavior has been explained on the basis of the fractal nature of breakage of brittle particulate materials (Tavares, 2007). However, for some materials such normalization is only valid above a minimum fragment size. This is illustrated in **Fig. 11** for a sample of gneiss. These so-called non-normalizable fragment size distributions have been identified to be associated to some brittle materials in which discontinuities concentrate in well-defined size scales, creating an inflection point in the cumulative fragment size distribution (Tavares and Neves, 2008; Powell et al., 2014). As such, data contained in sizes below this value should be treated separately, as addressed later in the section.

One convenient method to deal with data such as those in **Fig. 10** is to select particular markers on each curve. This is the so-called t_{10} procedure originally proposed by Narayanan and Whiten (1988). As part of this procedure the percentage of material passing different 1/*n*th fractions of the initial particle size, called t_ns, are estimated from the cumulative size distribution, typically interpolated using cubic splines. Commonly used values of *n* are 2, 4, 10, 25, 50 and 75. With the aim of representing the progeny size distribution in greater detail, additional markers may also be used, including 1.2 and 1.5 (Carvalho et al., 2015; Ballantyne et al., 2017). In order to illustrate this, breakage data in **Fig. 10** are presented in normalized form in **Fig. 12**, which shows that data for each *n* value follows well-defined trends as a function of t_{10}. The principle of the method is that, if the user has an estimate of the t_{10} value of the size distribution, likely from an expression that relates the initial particle size and the specific impact energy, the entire size distribution can be reconstructed (Napier-Munn et al., 1996; Tavares, 2017).

Several functional forms have been proposed over the years to describe cumulative progeny size distributions from drop weight tests, including the cubic splines (Narayanan and Whiten, 1988; Napier-Munn et al., 1996), the upper truncated Rosin-Rammler (King, 2001; Tavares, 2004) and combined exponential functions (Ballantyne et al., 2017). Given its ability to describe data with great flexibility, the incomplete beta function is used as part of the present model (Carvalho et al., 2015), given by

$$t_n(t_{10}) = \frac{100}{\int_0^1 x^{\alpha_n-1}(1-x)^{\beta_n-1}\,\mathrm{d}x} \int_0^{t_{10}/100} x^{\alpha_n-1}(1-x)^{\beta_n-1}\mathrm{d}x \quad (16)$$

where the cumulative mass of the particles passing a screen (t_n) with relative size *x* is calculated by the given t_{10} value of the distribution. In the model two parameters (α and β) must be fitted to each value of *n* selected. As such, with the seven *n* values (1.2, 1.5, 2, 4, 25, 50 and 75) a total of 14 parameters must be fitted from data, which is substantial.

Fig. 12 shows that data can be well described using Eqn. (16). The equation has also demonstrated to successfully fit the data for several other materials, as was also evident in previous publications (Barrios et al., 2011; Carvalho and Tavares, 2013; Carvalho et al., 2015). Unfortunately, given the lack of a proper physical description of fragmentation that would allow extrapolation of data, characterizing the response of a given material requires extensive testing over a range of stressing energies and sizes, which is a time-consuming task. Although it may be argued that each material has its well-defined breakage pattern, so that they will present different t_{10} versus t_n relationships such as the one presented in **Fig. 12** (Tavares and Neves, 2008), it is worthwhile to search for a mean distribution that would be able to describe data for a variety of materials with reasonable confidence.

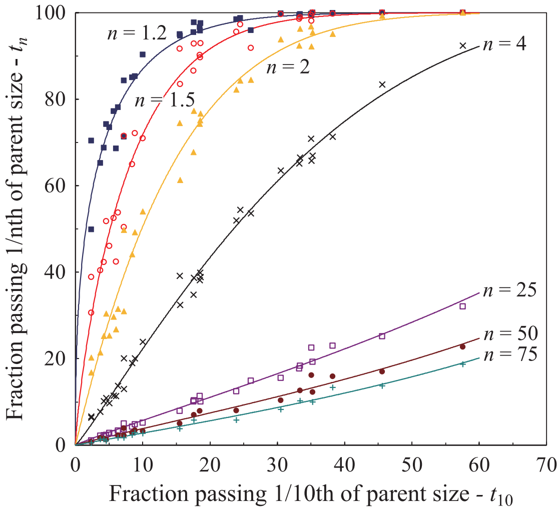

Fig. 12 Progeny size distributions presented in the normalized t_{10} versus t_n format for syenite from Vigné quarry (data from **Fig. 10**).

As such, data from drop weight tests of a total of 40 materials have been gathered (Tavares and Chagas, 2021) and plotted in normalized axes as those in **Fig. 12**, with results being presented in **Fig. 13** for selected values of *n*. A large scatter in the data appears, but it is also evident that data can be reasonably well represented using a single set of curves. The scatter in the graph in a logarithmic scale suggests the structure of the errors and the validity of the logarithmic objective function used in fitting the model parameters (Carvalho et al., 2015).

A more detailed examination of the data (Tavares and Chagas, 2021) allowed to conclude that the different types of materials (rocks, ores, cement clinkers and coals) did not appear particularly segregated in each of the plots in **Fig. 13**, which suggests the validity of the generalization proposed. The only exceptions were iron ores (Tavares and Chagas, 2021), which were not included in model fitting. Also, deviations were typically limited to the extremes of the size distributions, that is, either at the coarse ($t_{1.2}$ and $t_{1.5}$) or the fine (t_{50} or t_{75}) end.

The list of parameters that resulted from fitting the data in **Fig. 13** is presented in **Table 2**, covering the 40 materials (Tavares and Chagas, 2021). These parameters may be used as default in case of the absence of enough fragmentation data that would allow fitting of the various parameters in Eqn. (16) for a material of interest.

Fig. 14 is obtained by plotting the various t_n values as a function of normalized fragment size for selected t_{10} values using Eqn. (16) with parameters given in **Table 2**.

Although not included in the present work (Cavalcanti

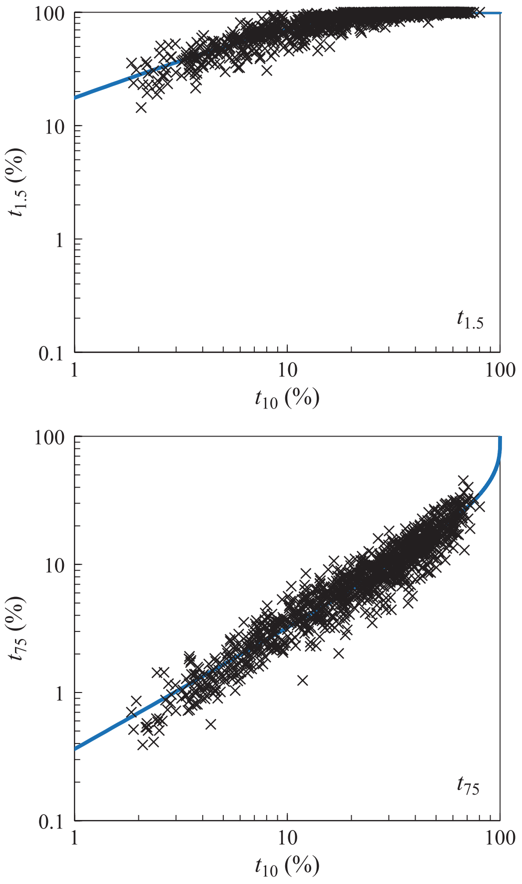

Fig. 13 Relationship between t_{10} and selected t_ns for a variety of materials, with the exception of iron ores. Solid lines represent the fit to the incomplete beta function (data from Tavares and Chagas, 2021).

Table 2 Optimal parameters of the incomplete beta function (Eqn. 16) for 40 materials (Tavares and Chagas, 2021), without including iron ores.

n	α_n	β_n
1.2	0.448	10.508
1.5	0.706	7.913
2	0.959	5.780
4	1.105	2.619
25	0.981	0.524
50	0.956	0.339
75	0.934	0.255

et al., 2021), data from projecting particles against a target could also be well described using the incomplete beta function and parameters from **Table 2**.

The normalizable breakage function can then be obtained from Eqn. (16) using the ratio between the fragment size D_i and the parent particle size d_j, so that

$$B_{ij}(t_{10}) = B(x, t_{10}) = \text{interp}(t_{10}, x) \tag{17}$$

where $x = d_i/D_j$.

As mentioned earlier in the section, there are instances in which the normalization approach proposed by the t_{10} procedure is not valid below a given fragment size D^*. This is the case of the so-called non-normalizable progeny size distributions, which appear typically when materials have a well-defined dimension in which discontinuities concentrate (Tavares, 2000). Indeed, non-normalizable breakage functions have occasionally been used with the population balance model equations for materials such as iron ores (Faria et al., 2019; Campos et al., 2019). **Table 3** shows examples of materials whose breakage description required the non-normalizable part of the breakage distribution.

This behavior can be described in the form of a power-law relationship below a minimum normalization size D^*,

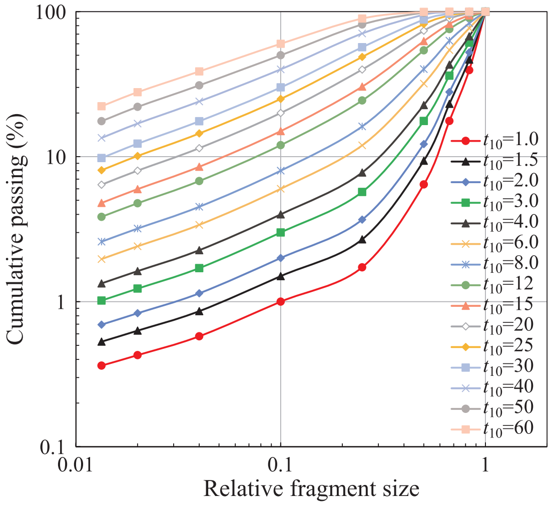

Fig. 14 Calculated normalized size distributions using the incomplete beta function and parameters from **Table 2** (Tavares and Chagas, 2021). Symbols represent the calculated t values for the different n markers, while lines are cubic spline fits (Eqn. 17) to these values.

Table 3 Fragment sizes below which progeny size distributions are not normalizable for selected materials (Eqn. 18).

Material	Particle size – D^* (mm)	η	Reference
Vermont marble	0.32	1.46	Tavares (1997)
Utah siltstone	0.15	0.59	Tavares (1997)
IOCC iron ore	0.35	1.83	Tavares (1997)
Pedra Sul granulite	0.17	0.64	Barrios et al. (2011)
Santa Luzia gneiss	0.80	0.80	Tavares and Neves (2008)

$$B_{ij} = B\left(D_i, d_j\right) = B_{i-j} \text{ for } D_i < D^* \\ B_{ij} = B\left(D_i, d_j\right)\left(\frac{D_i}{D^*}\right)^{\eta} \text{ for } D_i < D^* \tag{18}$$

which shows that the non-normalizable part of the distribution is attached to the fine end of the normalizable progeny size distribution obtained using the incomplete beta function (Eqn. 16). Values of the exponent η are shown in **Table 3** for selected materials. It is worth comparing these to the average slope at fine sizes from the model for the 40 materials (**Fig. 14**), which varies from 0.53 at low t_{10} values to 0.63 (Tavares and Chagas, 2021).

Adapting the present model to describe breakage of discrete particles in DEM has been carried out by different methods, depending on the shapes of particles. In the case of polyhedral particles (Tavares et al., 2020a) these have been used as part of the Voronoi tessellation scheme to create the appropriate fragment size distribution and are implemented in the commercial software Rocky DEM. On the other hand, in order to represent breakage of spherical particles in a DEM simulation, families of spherical progeny have been created for a variety of values of t_{10} using a procedure described elsewhere (Tavares and Chagas, 2021). This later has been implemented in the commercial software Altair EDEM (Tavares et al., 2021).

The described normalization procedure only accounts partially for the effect of particle size. The additional effect of particle size associated to the increase in resistance to breakage as particle sizes reduce, as well as the effect of stressing energy, are described using expressions presented in detail in section 3.2. In addition to those, studies have shown that other variables, such as impact geometry (Tavares, 2007; Saeidi et al., 2016), stressing rate (Saeidi et al., 2017) and mode of stressing, if single or double impact (Tavares, 2007), are known to have an influence on breakage distribution. However, the lack of a proper understanding of their effect made it unfeasible to take them into account explicitly in the model.

At stressing energies that are insufficient to cause body breakage, particles will undergo surface breakage. Carvalho and Tavares (2011) proposed to describe it using the Gaudin-Schuhmann equation

$$A_{ij} = 1 \text{ for } d_i \geq d_{\mathrm{A}} \\ A_{ij} = \left(\frac{d_i}{d_{\mathrm{A}}}\right)^{\lambda} \text{ for } d_i < d_{\mathrm{A}} \tag{19}$$

where d_{A} is the top size of surface breakage products, which together with λ, must be fit from data. The variation of these as a function of parent particle size and stressing energy has not been studied in as much detail in the literature. From tumbling tests d_{A} has been found to vary typically from about 0.20 to 0.45 mm (Tavares and Neves, 2008; Carvalho and Tavares, 2011). This parameter will likely be strongly influenced by parent particle size, but the data are not yet comprehensive enough to characterize such dependence (Cavalcanti et al., 2021).

3.2 Effect of particle size and stressing energy on body breakage distribution

In the original t_{10} method (Narayanan and Whiten, 1988; Napier-Munn et al., 1996), size-independent relationships between the stressing energy and the t_{10} value were proposed. In the present model the relationship accounts simultaneously for the effects of stressing energy and particle size, this later incorporated in the median fracture energy of particles (Tavares, 2009),

$$t_{10} = A\left[1 - \exp\left(-\frac{b'eE_k}{E_{50\mathrm{b}}}\right)\right] \tag{20}$$

where A and b' are model parameters fitted to experimental data, in which A corresponds to the maximum value of t_{10} that can be achieved when breaking a material in a single stressing event, whereas $E_{50\mathrm{b}}$ is the median specific fracture energy of particles that underwent breakage. The higher the specific impact energy E_k in comparison to the specific fracture energy of the particles, the higher the value of t_{10} and the finer the progeny size distribution. By using the median specific fracture energy of the particles that underwent breakage, Eqn. (20) is able to account for the particle size effect in breakage.

Data from a variety of materials have been fitted to Eqn. (20) and results are listed in **Table 4**. Values of parameter A, representing the maximum t_{10} value achieved in a single stressing event, were found to vary between about 40 to 75, with typical values around 50 %. This demonstrates that a limiting maximum fineness can be achieved in a single stressing event on individual particles, regardless of the intensity of the stressing energy. The product of the parameters ($A{*}b'$), which corresponds to the derivative of Eqn. (20) at the origin, represents the amenability of the material to fragmentation. Since the toughness of the material is already captured in the value of $E_{50\mathrm{b}}$, this product actually characterizes how effectively the stressing energy is used to create new fracture surfaces and fragments. Its values range from as low as 0.5 % to as high as 10 % (**Table 4**). As such, some grouping in respect to type of material has been observed (Tavares, 2000), in which materials with simple microstructures, such as individual minerals or crystals, present values below about 1 %, whereas most rocks and ores present values in the range from about 1 and 2 %. Values higher than 2 % have been observed for ores and rocks with poor intergranular bonding (Tavares, 2000), coals, as well as some porous materials, such as cement clinkers.

Typical results from fitting the model to data are presented in **Fig. 15**, which shows the good agreement

Table 4 Values of parameters *A* and *b'* (Eqn. 20) for selected materials.

Mineral/ore/rock	Source	*A*	*b'*	*A*b'*	Reference
Apatite	Cantley, Canada	45.4	0.012	0.52	Tavares (2007)
Quartz	Karlsruhe, Germany	38.8	0.018	0.68	Tavares (2007)
Hematite	Québec, Canada	45.6	0.016	0.75	Tavares (2007)
Galena	Park Valley, Idaho	44.5	0.018	0.78	Tavares (2007)
Copper-gold ore	Australia	66.2	0.013	0.85	Tavares et al. (2020b)
Granulite	Embu, Brazil	62.6	0.014	0.90	Tavares and Neves (2008)
Limestone	Utah	54.5	0.018	0.96	Tavares (2007)
Syenite	Vigné quarry, Brazil	58.0	0.017	0.97	Tavares and Neves (2008)
Limestone	Ribeirão Branco, Brazil	46.6	0.022	1.03	—
Copper ore (K)	Bingham Canyon, Utah	44.8	0.026	1.18	Tavares (2007)
Copper ore	Cyprus Sierrita, Arizona	58.9	0.020	1.20	Tavares (2007)
Granulite	Pedra Sul, Brazil	47.5	0.027	1.27	Tavares and Neves (2008)
Iron ore	Conceição Mine, Brazil	44.2	0.029	1.27	Tavares and Carvalho (2011)
Basalt	Utah	52.0	0.025	1.31	Tavares (2007)
Titanium ore	Titania, Norway	51.0	0.027	1.37	Tavares (2007)
Gneiss	Santa Luzia, Brazil	59.7	0.025	1.50	Tavares and Neves (2008)
Limestone #1	Brazil	53.3	0.033	1.76	Barrios et al. (2011)
Cement Clinker A	CEMEX, Mexico	69.2	0.028	1.91	Tavares (2007)
Copper ore (S)	Sossego, Brazil	67.7	0.029	1.96	Barrios et al. (2011)
Limestone #2	Brazil	63.4	0.033	2.09	Carvalho and Tavares (2013)
Cement Clinker B	CEMEX, Mexico	60.5	0.044	2.64	Tavares (2007)
Gold ore	South Africa	44.1	0.060	2.65	Pauw and Maré (1988)
Iron ore	Brazil	60.4	0.051	3.08	Carvalho and Tavares (2013)
Coal	Candiota, Brazil	44.1	0.091	4.01	—
Marble	Vermont	76.3	0.079	6.04	Tavares (2007)
Iron ore	Newfoundland, Canada	65.4	0.158	10.3	Tavares (2007)

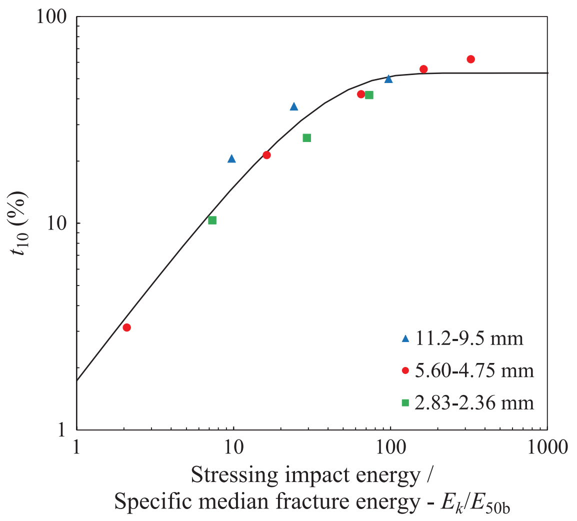

Fig. 15 t_{10} as a function of impact energy for different particle size ranges of limestone #1.

between the two. In some cases, however, the scatter is larger when particles of several sizes are included in the fit, potentially a consequence of effects that are not accounted for in the model, such as variation in standard deviation of the distribution with particle size, impact velocity and particle shape. The direct connection in the model between the breakage probability and the fragment distribution, offered by the normalizing value of E_{50b} in Eqn. (20), is considered an important feature, which renders internal consistency in the model.

Adapting the model given by Eqn. (20) to describe breakage of discrete particles results in the modified equation (Tavares et al., 2021)

$$t'_{10} = A\left[1-\exp\left(-\frac{b'keE_k}{E}\right)\right] \tag{21}$$

where *k* is a variable introduced because the mean and the median values of the distribution do not coincide (Tavares and Chagas, 2021). This expression has been used in association to discrete implementations of the model for the case of either spherical (Tavares and Chagas, 2020; Tavares et al., 2021) or polyhedral particles (Tavares et al., 2020a) in DEM.

4. Model implications

4.1 Primary body breakage function

In several mills and crushers, the breakage distribution function is widely used to describe the average size distribution from each stressing event inside the devices, playing a central role in traditional population balance models (Austin et al., 1984; King, 2001). In practice, rather than a true material property, it represents the result of model fitting, at best estimated on the basis of the size distribution from short grinding times (Austin et al., 1984).

For the case in which the particle is stressed with the minimum energy to produce body breakage, the resulting fragment distribution is called primary single-particle breakage function (Saeidi et al., 2016). In the few studies that attempted to measure directly this primary breakage distribution function of individual particles, Bourgeois (1993) estimated in about 2 % the value of t_{10} for quartz particles under double impact (Saeidi et al., 2016), whereas the corresponding value was about 1 % for iron ore pellets subjected to single impact (Cavalcanti et al., 2021). Tavares (2009) then demonstrated, for a sample of limestone, that it did not vary after each repeated impact. The importance of this primary single-particle breakage function has been demonstrated by Saeidi et al. (2016), who showed that it was possible to predict the response of a material in a drop weight tester to higher impact energies on the basis of this primary breakage function, besides Eqn. (10) and empirical functions representing probability of selection of fragments to secondary breakage. This has also been demonstrated to be valid in DEM environment, where the size distribution from higher impact energies could be predicted using the breakage model in the case of polyhedral particles in Rocky DEM (Tavares et al., 2020a) and Altair EDEM (Tavares et al., 2021).

The present model allows estimating this primary breakage function by considering the case in which $eE_k \cong E$ in Eqn. (21), giving

$$t'_{10} \cong A\left[1-\exp\left(-b'\right)\right] \tag{22}$$

Given the values of the constants A and b' (**Table 4**) and since at such low impact energies the constant k in Eqn. (22) may be considered equal to about 0.95 (Tavares and Chagas, 2021), then the resulting t_{10} values corresponding to primary breakage range from as low as 0.5 to, exceptionally, higher than 5 %. As such, from comparison with the experimental measurements by Bourgeois (1993) and Cavalcanti et al. (2021), values estimated using Eqn. (22) are likely an underestimation of the actual value. Nevertheless, they may be considered generally valid, given the challenge in estimating directly the primary body breakage function.

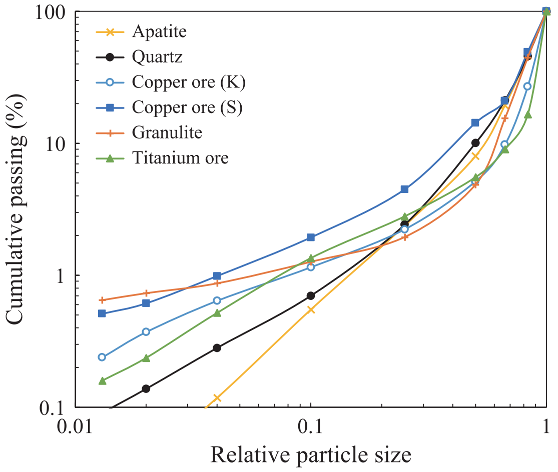

Fig. 16 Primary breakage functions for selected materials, obtained by fitting single-particle breakage data to the incomplete beta function for t_{10} given by Eqn. (22).

With the aim of illustrating the variations encountered for different materials, **Fig. 16** compares primary body breakage distribution functions for selected materials estimated using this approach. It shows the variations in shape and position of the primary fragment size distributions, representing differences in fragmentation pattern, with the single-phase materials (minerals) generating less fines than rocks/ores (Tavares, 2000).

4.2 Predicting the outcome of a single stressing event

Arguably, the simplest demonstration of the application of a breakage model is to predict the outcome of a single impact on individual particles, such as in drop weight tester (Napier-Munn et al., 1996; Tavares, 2007). The outcome of this single impact event, considering both body and surface breakage, may be described by the mass balance given by (Tavares and Carvalho, 2011)

$$\begin{aligned} w_i^* &= w_i\left[1-P_i\left(eE_k\right)\right]\left[1-\xi_i\left(eE_k\right)\right] \\ &+\sum_{j=1}^{i} w_j\left\{P_j\left(eE_k\right)b_{ij}\left(eE_k\right)+\xi_i\left(eE_k\right)\left[1-P_j\left(eE_k\right)\right]a_i\right\} \end{aligned} \tag{23}$$

where w_i^* and w_i are the weight fractions of the material contained in size class i after and before the impact event, respectively. ξ_i is the fractional generation of surface breakage products, a_{ij} is the surface breakage distribution function and b_{ij} is the energy-specific body breakage distribution function. The term $[1-P_i(eE_k)][1-\xi_i(eE_k)]$ on the right-hand side of Eqn. (23) represents the mass fraction of material that did not suffer body breakage during the stressing event and remained in the original size, whereas the term $\Sigma^{i}_{j=1} w_j \left[P_j\left(eE_k\right) b_{ij}\left(eE_k\right)\right]$ represents the proportion of material from size classes *i* and coarser that suffered body breakage and generated fragments reported to size class *i*. The term $\Sigma^{i}_{j=1} w_j \left\{\xi_i\left(eE_k\right)\left[1-P_j\left(eE_k\right)\right] a_i\right\}$ gives the cumulative proportion of surface breakage products that reports to size class *i*. $P_i(eE_k)$ is the probability that a particle contained in size class *i* will suffer body breakage when it captures energy eE_k from a collision event.

When varying the specific impact energy applied to a batch of particles, breakage can transition from no body breakage at very low impact energies, where all particles undergo only surface breakage, to body breakage of all particles at high impact energies. In between these are impact energies in which a fraction of the particles underwent body breakage, whereas the remainder only suffered surface breakage. This is illustrated in **Fig. 17** for particles of Pedra Sul granulite. In the figure, stressing energies above 360 J/kg were able to produce body breakage in the first impact on all particles, whereas those at 9 J/kg produced only surface breakage. For stressing energies between these, only a fraction of the particles underwent body breakage, resulting in size distributions that represent the transition between surface and body breakage. Unfortunately, validation data are available only for the higher impact energies, since at the lower impact energies the small amount of surface breakage products makes collection of accurate data a challenging task.

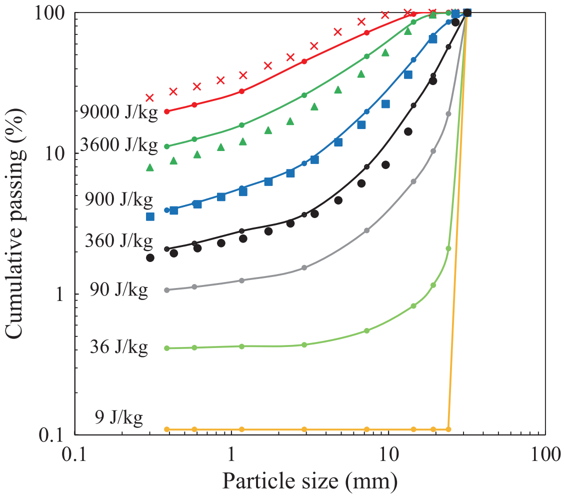

Fig. 17 Progeny size distributions from impact of 31.5–26.5 mm granulite (Pedra Sul) particles in a drop weight tester at variable specific impact energies. Large symbols represent experiments and lines and small circles model predictions. $\sigma = 0.90$, $\kappa = 4 \times 10^{-4}$ kg/mmJ. Other parameters given in **Tables 1** and **4**.

5. Discussion

5.1 Breakage testing and model fitting

The breakage model contains a variety of parameters that must be fitted on the basis of experiments. Although some parameters, in particular those related to the fragment size distribution, may be assumed as default, since their variation for different materials may be relatively limited (section 3.1), experiments are required to estimate the several remaining ones. The originally proposed and most direct approach to estimate parameters from the model was based on the use of the impact load cell device (Tavares, 2007). It is an instrumented drop weight tester in which the minimum energy required for primary fracture (Tavares and King, 1998) as well as the net energy absorbed (Tavares, 1999) may be estimated for each individual particle. Besides that, repeated impact tests have then been used to estimate the damage accumulation parameter (section 2.3), whereas the fragment size distributions from different impact energies served as the basis to fitting the parameters in the model described in 3.2. Slow compression tests can also be used to estimate the fracture energy distribution of particles. Data from non-instrumented devices can also be used to estimate the parameters in several of the model equations. For instance, the breakage probability distributions may be estimated from either standard drop weight tests (Baumgardt et al., 1975) or tests in which particles are projected against a target (Dan and Schubert, 1990; Cavalcanti et al., 2021). These later are particularly relevant when modeling with the aim of simulating material degradation during handling.

Although the detailed analysis of the experimental procedures and devices used to fit parameters in the breakage model is beyond the scope of the present work and is well covered in other publications (Tavares and King, 1998; Tavares, 2007; Rozenblat et al., 2012; Ribas et al., 2014; Bonfils, 2017), it is worthwhile to highlight some important issues related to the tests. Indeed, one key challenge when estimating the fracture energy of individual particles using Eqn. (5) is the identification of primary fracture. This primary fracture or primary body breakage point is given by the condition in which the force suddenly drops, given the inability of the particle to continue transmitting stresses. Such condition is relatively straightforward to identify in some cases, such as in **Fig. 18a**, which is often found from testing regularly-shaped brittle particles. In these cases separation of newly created fracture surfaces is rapid, resulting from propagation of a major crack through the entire particle, facilitating the identification of the fracture point, given the sudden drop in load. In other cases, however, identifying the instant of fracture can be far more challenging and amenable to subjective judgement. A few examples of such cases are also illustrated in **Fig. 18**.

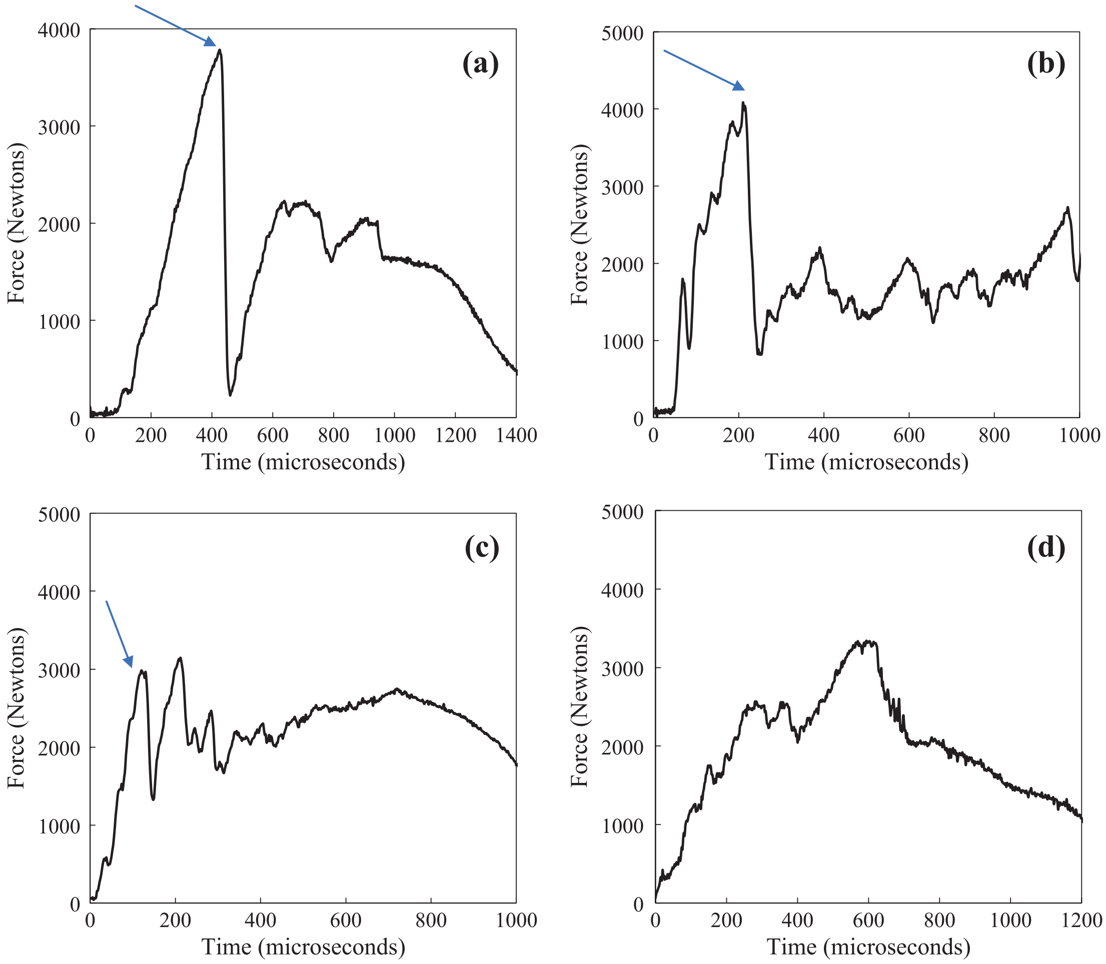

Fig. 18 Typical force-time profiles from breakage of single particles of 12.5–9.0 mm iron ore pellets and their fragments in an impact load cell device. Arrows depict presumed primary breakage point.

Fig. 18b shows the case in which the particle suffered chipping at approximately 100 ms, but that primary breakage is still relatively straightforward to identify. This response is often found while testing highly irregularly-shaped particles, in which a small fraction of their volume becomes subjected to concentration of tensile stresses early in the test, causing the appearance of such superficial cracks. Yet in other cases either multiple peaks appear (**Fig. 18c**) or no clear fracture point may be identified (**Fig. 18d**), requiring some subjectivity in identifying the fracture load. Challenges such as these appear in association to testing more deformable and/or less brittle materials. This can be associated to cases in which either a single crack or several cracks grow sub-critically, being responsible for not such a clear reduction in load at primary fracture. However, since no relative motion of the fragments occur, due to the limited brittleness of the particle, the fragments continue to be able to sustain load, preventing a drop in load-bearing ability of the particle and, therefore, identification of the instant of primary breakage. Techniques that can be used to assist in interpreting these results will be analyzed in greater detail in a future publication.

A few useful guidelines when conducting experiments with the aim of estimating the distribution of particle fracture energies are:

- Particles should be contained in very narrow size ranges, ideally resulting from sieving following a $\sqrt[4]{2}$ series;
- Particle selection for the test should be conducted randomly, so as to guarantee that each lot tested has approximately the same average weight;
- Sample preparation should be carried out carefully, so as to avoid the use of crushing processes that may be responsible for generating flaky material, such as roll crushing (Gupta, 2016). Ideally either no crushing or the adoption of the size reduction process that is meant to be used in the targeted industrial operation should be preferred. Also, size reduction processes which are known to induce cracks in particles, sub as high-pressure roll grinding (Tavares, 2005), should also be avoided, whenever possible, in this task;
- Differences in particle shapes introduce variability in the distribution (Tavares, 2007; Lois-Morales et al., 2020). One possibility to deal with this is to segregate particles contained within the $\sqrt[4]{2}$ series according to mass and

test separately. If that approach is not used, particles should be randomly selected and the size of the tested lot increased accordingly with the variability;

- The number of particles tested in each size range must be at least 30, but should increase as the variability of particle composition and shape in the sample also increases, so that 50 or 100 are typically optimal;
- In the case of tests in impact load cell devices, it is advisable to select an average specific impact energy for the test (Eqn. 2) that is just high enough to break the toughest particle in the lot. The use of specific impact energies that are much higher than those must be avoided, in particular in the case of testing less brittle materials, since they can lead to greater difficulty in identifying properly the load responsible for primary fracture (**Fig. 18d**).

While particles in the size range from 100 mm (Fandrich et al., 1998; Tavares, 2007) down to 0.25 mm (Tavares and Cerqueira, 2007) have been tested in impact load cell devices, the greatest challenge lies in measuring fracture energies of particles contained in the lower range and even finer sizes, given the tedious nature of testing single particles and the limitation in the resolution of the devices. Some researchers have demonstrated the potential of measuring the strength and fracture energies of fine particles in special devices (Steier and Schönert, 1972; Yashima et al., 1979; Sikong et al., 1990; Antonyuk et al., 2005; Nguyen et al., 2009; Yan et al., 2009). Ribas et al. (2014) showed the potential of using a commercially-available micro compression tester to measure the fracture energy distributions of single particles in the 45–37 μm size range, whereas Campos et al. (2021) recently applied it to test iron ore particles contained in the range of 45 to 150 μm, with good results. Nevertheless, due to the challenge in measuring breakage characteristics of single particles down to such fine sizes, some indirect estimation approaches have been proposed. Barrios et al. (2011) proposed testing particles as fine as 150 μm contained in monolayer particle beds, combining them to data from single-particle breakage tests at coarser sizes, and estimating the breakage parameters from back-calculation, with reasonable success. More recently, Tavares et al. (2020b) proposed combining measurements of particle fracture energies of particles at relatively coarse sizes to data from impact tests using a rotary breakage tester. This allowed estimating selected material breakage parameters of a copper-gold ore down to 350 μm (Tavares et al., 2020b).

Yet another alternative to estimate breakage parameters in Eqn. (10) is to back-calculate them from batch grinding tests, assuming that predictions using the UFRJ mechanistic mill model (Tavares and Carvalho, 2009; Carvalho and Tavares, 2013) are strictly accurate. This approach has been used to estimate breakage parameters of an iron ore from batch milling data (Carvalho et al., 2021) as well as of limestone to stirred milling data (Oliveira et al., 2020). In these cases, the parameters from Eqns. (7), (12), (16) and (20) were taken from similar ores.

Evidently, errors can appear in estimates from back-calculation, since they rely on the validity of the various assumptions. In the particular case when only batch grinding results are used, errors may be associated to the fact that any limitation in the mill model in describing the phenomenon would inevitably contaminate the estimates of material breakage parameters, partially contradicting the very approach of the advanced models in fully decoupling material from process. In addition to that, this approach also requires that some parameters be taken from similar materials, which also involves a potential source of bias, since each material is intrinsically unique in regard to breakage response.

As discussed in section 3.3, more effort should be dedicated to modeling the primary breakage function from single-particle breakage, given its central role in the application of the model in particular to discrete systems in DEM. One device that could be useful in this task is the rigidly-mounted roller mill, which crushes particles nearly individually between rigidly-mounted rollers with carefully controlled gaps (Böttcher et al., 2021). In spite of challenges in measuring the energy required to break particles contained in the finest sizes studied (45 μm), it provided good estimates of the size distribution of particles under stressing conditions that approach the minimum required for fracture (Campos et al., 2021).

5.2 Model applications

The breakage model described has been used either in complete form or in parts in simulating different systems of interest using a variety of approaches. In its discrete form it has been embedded in DEM as part of different particle replacement schemes. Initially, a cutdown version of the model, which did not incorporate description of weakening by repeated impacts (section 2.4), was implemented in EDEM (Jiménez-Herrera et al., 2018; Barrios et al., 2020), demonstrating some ability to describe breakage in both confined and unconfined particle beds. A more complete version of the model, incorporating a new stochastic description of particle replacement (Tavares and Chagas, 2021) was implemented in an updated version of EDEM (Tavares et al., 2021), demonstrating very good ability to predict unconfined breakage of particle beds. Both approaches were based on spherical particle replacement, which has the advantage of computational efficiency. This later implementation also incorporated description of the unresolved fines, which were added upon completion of the simulation to the size distribution given by the resolved spheres. The more complete version of the model has also been implemented in the commercial software package

Rocky DEM (Tavares et al., 2020a). Such implementation, based on breakage of polyhedral particles, provided very good predictions of breakage in unconfined particle beds (Tavares et al., 2020a) and cone crushing (André and Tavares, 2020).

The breakage model has also been widely used as part of advanced models of crushers and mills. For instance, Austin (2004a; 2004b) used the damage model from section 2.4 in a phenomenological model of high-speed hammer milling. The full version of the breakage model has been used to predict degradation during handling of materials (Tavares and Carvalho, 2011). It has also been used, coupled to DEM, to model crushing in a vertical shaft impact crusher (Cunha et al., 2014), as well as of degradation of recycled aggregate in a high-shear mixer (Moreno-Juez et al., 2021). The modeling approach has also been used to predict degradation of iron ore pellets during handling using slightly customized mathematical expressions (Cavalcanti et al., 2019; 2021; Tavares et al., 2018). The widest use of the model has been in association to a microscale population balance formulation, called UFRJ model, to describe grinding in media mills, including ball mills (Tavares and Carvalho, 2009; Carvalho and Tavares, 2013), semi-autogenous mills (Carvalho and Tavares, 2011) and stirred mills (Oliveira et al., 2020; 2021). A version of the ball mill model of continuous milling with some simplifications is available in the state-of-the-art mining and mineral processing plant simulator IES (Integrated Extraction Simulator).

6. Summary and conclusions

A practical model describing breakage of single particles has been proposed over the last 25 years. It discriminates body and surface breakage, accounting for the body breakage probability through the upper-truncated lognormal distribution. It is able to predict breakage by repeated impacts owing to a model describing weakening based on continuum damage mechanics. Body-breakage progeny size distribution is described using the incomplete beta function, which also considers the exceptional cases in which the material exhibits non-normalizable breakage response. With an empirical expression that describes the stressing energy and size-dependent breakage intensity, it can predict the size distribution of fragments from any stressing event.

This breakage model has been implemented and is now an integral part of particle replacement schemes embedded in commercial DEM software (Rocky DEM and Altair EDEM), through which it may be used to simulate a number of industrial processes of interest. It has also been incorporated in microscale population balance models describing several mill types, namely ball mills, stirred mills, autogenous and semi-autogenous, being even available (ball mill model) in the plant simulator IES.

While being able to account for several important variables that influence particle breakage, challenges are identified in application and fitting of the model parameters for particular applications. Being a single-particle-based model, challenges exist in estimating breakage parameters for fine particles. Establishing the validity of novel testing devices as well as of back-calculation approaches, is an important task. Further, modifications in the model in order to make it applicable to describe breakage of non-brittle materials (Tavares and Almeida, 2020) is another worthwhile task for advancing model applicability. Finally, models describing surface breakage, which are particularly relevant in predicting mechanical degradation during handling, require more attention, since they are still at a comparatively earlier stage of development and validation.

Acknowledgements

The author would like to thank the financial support from the Brazilian agencies CNPq (grant number 310293/2017-0) and FAPERJ (grant number E-26/202.574/2019), as well as the team of researchers in his group and outside collaborators for their contributions throughout the development of this work.

Nomenclature

A	parameter of the t_{10} versus specific impact energy relationship (%)
A_{ij}	proportion of particles finer than size i generated from surface breakage of particles in size class j (-)
a_{ij}	proportion of particles contained in size class i generated from surface breakage of particles in size class j (= $A_{i-1,j} - A_{ij}$) (-)
b'	parameter of the t_{10} versus specific impact energy relationship (-)
B_{ij}	proportion of particle finer than size class i resulting from body breakage of particles contained in size class j (-)
b_{ij}	proportion of particle contained in size class i resulting from body breakage of particles contained in size class j (= $B_{i-1,j} - B_{ij}$) (-)
D	damage variable (-)
D_i	sieve size (m)
D^*	minimum normalization size (m)
d_A	maximum size of surface breakage products (m)
d_i	representative size of particles contained in size class i (m)
d_o	parameter describing the variation of the particle fracture energy with particle size (m)

e	proportion of the impact energy dissipated in the particle (-)
E	mass-specific fracture energy of the particle (J/kg)
E_k	specific impact energy (J/kg)
E_max	upper truncation value of the distribution (J/kg)
E_{50}	median specific fracture energy (J/kg)
E_50b	median specific fracture energy of particle that broke in an event (J/kg)
E^*	variable used to incorporate the upper truncation in the lognormal distribution of particle fracture energies (J/kg)
E'	fracture energy of the particle after the stressing event (J/kg)
E_∞	parameter describing the variation of the particle fracture energy with particle size (J/kg)
F	force (N)
g	acceleration due to gravity (m/s^2)
h	net drop height (m)
k	variable introduced to correct the bias of using the median instead of the mean value of the distribution (-)
k_p	apparent particle stiffness (GPa)
k_s	apparent surface stiffness (GPa)
m	mass of the drop weight (kg)
m_p	weight of each individual particle (kg)
$\overline{m}_\mathrm{p}$	average weight of particles in the lot tested (kg)
N_b	number of particles that underwent body breakage (-)
N	number of stressed particles (-)
$P(E_k)$	proportion broken in impact of magnitude E_k (-)
t_n	proportion passing 1/n^th of the parent particle size in the fragments of a stressing event (-)
t_{10}	proportion passing 1/10$^\mathrm{th}$ of the parent particle size in the fragments of a stressing event (-)
$\overline{v}$	average velocity at the instant of collision against the target (m/s)
w_i	weight fraction of material contained in size class i (-)
x	relative fragment size (-)
Y	Young's modulus (GPa)
z	reduced Gaussian distribution (-)
α	significance level of the confidence interval
α_n	parameter of the incomplete beta function for t_n (-)
β_n	parameter of the incomplete beta function for t_n (-)
γ	damage accumulation coefficient (-)
Δ	deformation (m)
Δ_c	deformation at primary fracture (m)
η	parameter describing the shape of the non-normalizable part of the breakage distribution (-)
κ	attrition parameter (kg/mmJ)
λ	parameter in the non-normalizable body breakage function (-)
ν	Poisson's ratio (-)
ξ_i	proportion of attrition products (-)
σ	standard deviation of the lognormal distribution of fracture energies (-)
φ	parameter describing the variation of the particle fracture energy with particle size (-)

References

André F.P., Tavares L.M., Simulating a laboratory-scale cone crusher in DEM using polyhedral particles, Powder Technology, 372 (2020) 362–371. DOI: 10.1016/j.powtec.2020.06.016

Angulo S.C., Silva N.V., Lange D.A., Tavares L.M., Probability distributions of mechanical properties of natural aggregates using a simple method, Construction and Building Materials, 233 (2020) 117269. DOI: 10.1016/j.conbuildmat.2019.117269

Antonyuk S., Tomas J., Heinrich S., Mörl L., Breakage behaviour of spherical granulates by compression, Chemical Engineering Science, 60 (2005) 4031–4044. DOI: 10.1016/j.ces.2005.02.038

Arbiter N., Harris C.C., Stamboltzis G.A., Single fracture of brittle spheres, Transactions of the SME/AIME, 244 (1969) 118–133.

Austin L.G., A preliminary simulation model for fine grinding in high speed hammer mills, Powder Technology, 143–144 (2004a) 240–252. DOI: 10.1016/j.powtec.2004.04.017

Austin L.G., The effect of damage on breakage kinetics, Powder Technology, 143–144 (2004b) 151–159. DOI: 10.1016/j.powtec.2004.04.048

Austin L.G., Klimpel R.R., Luckie P.T., Process Engineering of Size Reduction: Ball Milling, Society of Mining Engineers of the AIME, 1984, ISBN: 9780895204219.

Ballantyne G.R., Bonfils B., Powell M.S., Evolution of impact breakage characterisation: re-defining t-family relationship, International Journal of Mineral Processing, 168 (2017) 126–135. DOI: 10.1016/j.minpro.2017.10.001

Barrios G.K.P., de Carvalho R.M., Tavares L.M., Extending breakage characterisation to fine sizes by impact on particle beds, Mineral Processing and Extractive Metallurgy, 120 (2011) 37–44. DOI: 10.1179/1743285510y.0000000002

Barrios G.K.P., Jiménez-Herrera N., Tavares L.M., Simulation of particle bed breakage by slow compression and impact using a DEM particle replacement model, Advanced Powder Technology, 31 (2020) 2749–2758. DOI: 10.1016/j.apt.2020.05.011

Baumgardt S., Buss B., May P., Schubert H., On the comparison of results in single grain crushing under different kinds of load, Proceedings of the 11th International Mineral Processing Congress, Cagliari, 1975, pp. 3–32.

Becker M., Kwade A., Schwedes J., Stress intensity in stirred media mills and its effect on specific energy requirement, International Journal of Mineral Processing, 61 (2001) 189–208. DOI: 10.1016/s0301-7516(00)00037-5

Bergstrom B.H., Sollenberger C.L., Mitchell Jr. W., Energy aspects of single particle crushing, Transactions of the AIME, 220 (1961) 367–372.

Boechat F.O., de Carvalho R.M., Tavares L.M., Simulation of mechanical degradation of iron ore pellets in a direct reduction furnace, KONA Powder and Particle Journal, 35 (2018) 216–225. DOI: 10.14356/kona.2018009

Bond F.C., Crushing tests by pressure and impact, Transactions of the AIME, 169 (1947) 58–66.

Bonfils B., Quantifying of impact breakage of cylindrical rock particles on an impact load cell, International Journal of Mineral Processing, 161 (2017) 1–6. DOI: 10.1016/j.minpro.2017.02.005

Bonfils B., Ballantyne G.R., Powell M.S., Developments in incremental rock breakage testing methodologies and modelling, International Journal of Mineral Processing, 152 (2016) 16–25. DOI: 10.1016/j.minpro.2016.04.010

Böttcher A.-C., Thon C., Fragnière G., Chagas A., Schilde C., Kwade A., Rigidly-mounted roll mill as breakage tester for characterizing fine particle breakage, Powder Technology, 383 (2021) 554–563. DOI: 10.1016/j.powtec.2021.01.055

Bourgeois F.S., Single-particle fracture as a basis for microscale modeling of comminution processes, Ph.D. thesis, The University of Utah, 1993. https://utah-primoprod.hosted.exlibrisgroup.com/permalink/f/dtufc4/UUU_ALMA21242038230002001

Capece M., Bilgili E., Davé R.N., Formulation of a physically motivated specific breakage rate parameter for ball milling via the discrete element method, AIChE Journal, 60 (2014) 2404–2415. DOI: 10.1002/aic.14451

Campos T.M., Bueno G., Barrios G.K.P., Tavares L.M., Pressing iron ore concentrate in a pilot-scale HPGR. Part 1: experimental results, Minerals Engineering, 140 (2019) 105875. DOI: 10.1016/j.mineng.2019.105875

Campos T.M., Bueno G., Rodriguez V.A., Böttcher A.-C., Kwade A., Mayerhofer F., Tavares L.M., Relationships between particle breakage characteristics and comminution response of fine iron ore concentrates, Minerals Engineering, 164 (2021) 106818. DOI: 10.1016/j.mineng.2021.106818

Carvalho R.M., Campos T.M., Faria P.M., Tavares L.M., Mechanistic modeling and simulation of grinding iron ore pellet feed in pilot and industrial-scale ball mills, Powder Technology, 392 (2021) 489–502. DOI: 10.1016/j.powtec.2021.07.030

Carvalho R.M., Secchi A.R., Tavares L.M., A new breakage function model and optimization procedure for mechanistic comminution models, Proceedings of the 14th European Symposium on Comminution and Classification, Gothenburg, 2015, pp. 42–45.

Carvalho R.M., Tavares L.M., Leaping forward in SAG and AG mill simulation using a mechanistic model framework, Proceedings of the International Autogenous Grinding, Semi-Autogenous Grinding and High-Pressure Roll Technology Conference, Vancouver, 2011, pp. 1–26.

Carvalho R.M., Tavares L.M., Predicting the effect of operating and design variables on breakage rates using the mechanistic ball mill model, Minerals Engineering, 43–44 (2013) 91–101. DOI: 10.1016/j.mineng.2012.09.008

Cavalcanti P.P., de Carvalho R.M., das Chagas A.S., da Silveira M.W., Tavares L.M., Surface breakage of fired iron ore pellets by impact, Powder Technology, 342 (2019) 735–743. DOI: 10.1016/j.powtec.2018.10.044

Cavalcanti P.P.S., Petit H.A., Thomazini A.D., de Carvalho R.M., Tavares L.M., Modeling of degradation by impact of individual iron ore pellets, Powder Technology, 378 (2021) 795–807. DOI: 10.1016/j.powtec.2020.10.037

Cavalcanti P.P., Tavares L.M., Statistical analysis of fracture characteristics of industrial iron ore pellets, Powder Technology, 325 (2018) 659–668. DOI: 10.1016/j.powtec.2017.11.062

Cavalcanti P.P., Tavares L.M., Static and dynamic compressive loading of fired iron ore pellets, Powder Technology, 354 (2019) 281–288. DOI: 10.1016/j.powtec.2019.06.006

Cunha E.R., Carvalho R.M., Tavares L.M., A predictive model of the Vertical Shaft Impact (VSI) crusher, Proceedings of the 9th International Comminution Symposium, Cape Town, 2014, 2014, v. 1. p. 1–13.

Dan C.C., Schubert H., Breakage probability, progeny size distribution and energy utilization of comminution by impact, Aufbereitungs-Technik, 31 (1990) 241–247.

Datta A., Rajamani R.K., A direct approach of modeling batch grinding in ball mills using population balance principles and impact energy distribution, International Journal of Mineral Processing, 64 (2002) 181–200. DOI: 10.1016/s0301-7516(01)00044-8

Fandrich R.G., Clout J.M.F., Bourgeois F.S., The CSIRO Hopkinson bar facility for large diameter particle breakage, Minerals Engineering, 11 (1998) 861–869. DOI: 10.1016/s0892-6875(98)00073-9

Faria P.M.C., Rajamani R.K., Tavares L.M., Optimization of solids concentration in iron ore ball milling through modeling and simulation, Minerals, 9 (2019) 366. DOI: 10.3390/min9060366

Ghadiri M., Zhang Z., Impact attrition of particulate solids. Part 1: a theoretical model of chipping, Chemical Engineering Science, 57 (2002) 3659–3669. DOI: 10.1016/s0009-2509(02)00240-3

Gupta V.K., Determination of the specific breakage rate parameters using the top-size-fraction method: preparation of the feed charge and design of experiments, Advanced Powder Technology, 27 (2016) 1710–1718. DOI: 10.1016/j.apt.2016.06.002.

Jiménez-Herrera N., Barrios G.K.P., Tavares L.M., Comparison of breakage models in DEM in simulating impact on particle beds, Advanced Powder Technology, 29 (2018) 692–706. DOI: 10.1016/j.apt.2017.12.006

Kachanov L.M., Time of the rupture process under creep conditions (in Russian), Izy Akad. Nank SSR Otd Tech Nauk, 8 (1958) 26–31.

King R.P., Modeling and Simulation of Mineral Processing Systems, 1st edition, Butterworth-Heinemann, London, 2001, ISBN: 978-0-08-051184-9.

King R.P., Bourgeois F.S., A new conceptual model for ball milling, Proceedings of the 18th International Mineral Processing Congress, Sydney, 1993, pp. 81–86.

Krogh S.R., Crushing characteristics, Powder Technology, 27 (1980) 171–181. DOI: 10.1016/0032-5910(80)85019-4

Lois-Morales P., Evans C., Bonfils B., Weatherley D., The impact load cell as a tool to link comminution properties to geomechanical properties of rocks, Minerals Engineering, 148 (2020) 106210. DOI: 10.1016/j.mineng.2020.106210

Mishra B.K., Rajamani R.K., The discrete element method for the simulation of ball mills, Applied Mathematical Modelling, 16 (1992) 598–604. DOI: 10.1016/0307-904x(92)90035-2

Moreno-Juez J., Tavares L.M., Artoni R., de Carvalho R.M., da Cunha E.R., Cazacliu B., Simulation of the Attrition of Recycled Concrete Aggregates during Concrete Mixing, Materials, 14 (2021) 3007. DOI: 10.3390/ma14113007

Morrell S., An alternative energy–size relationship to that proposed by Bond for the design and optimisation of grinding circuits, International Journal of Mineral Processing, 74 (2004) 133–141. DOI: 10.1016/j.minpro.2003.10.002

Morrison R.D., Cleary P.W., Using DEM to model ore breakage within a pilot scale SAG mill, Minerals Engineering, 17 (2004) 1117–1124. DOI: 10.1016/j.mineng.2004.06.016

Morrison R.D., Shi F., Whyte R., Modelling of incremental rock breakage by impact – for use in DEM models, Minerals Engineering, 20 (2007) 303–309. DOI: 10.1016/j.mineng.2006.10.015

Napier-Munn T.J., Mineral Comminution Circuits: Their Operation and Optimisation, Julius Kruttschnitt Mineral Research Centre, 1996, ISBN: 9780646288611.

Narayanan S.S., Determination of comminution characteristics from single particle breakage tests and its application to ball mill scale-up, Transactions of the Institution of Mining and Metallurgy C, 97 (1988) 115–124.

Nguyen V.B., Wang C.X., Thomas C.R., Zhang Z., Mechanical properties of single alginate microspheres determined by microcompression and finite element modelling, Chemical Engineering Science, 64 (2009) 821–829. DOI: 10.1016/j.ces.2008.10.050

Oliveira A.L.R., de Carvalho R.M., Tavares L.M., Predicting the effect of operating and design variables in grinding in a vertical stirred mill using a mechanistic mill model, Powder Technology, 387 (2021) 560–574. DOI: 10.1016/j.powtec.2021.04.057

Oliveira A.L.R., Rodriguez V.A., de Carvalho R.M., Powell M.S., Tavares L.M., Mechanistic modeling and simulation of a batch vertical stirred mill, Minerals Engineering, 156 (2020) 106487. DOI: 10.1016/j.mineng.2020.106487

Ouchterlony F., Sanchidrián J.A., The Fragmentation-energy fan concept and the Swebrec function in modeling drop weight testing, Rock Mechanics and Rock Engineering, 51 (2018) 3129–3156. DOI: 10.1007/s00603-018-1458-5

Pauw O.G., Maré M.S., The determination of optimum impact-breakage routes for an ore, Powder Technology, 54 (1988) 3–13. DOI: 10.1016/0032-5910(88)80043-3

Piret E.L., Fundamental aspects of grinding, Chemical Engineering Progress, 49 (1953) 56–63.

Powell M.S., Hilden M., Ballantyne G., Liu L.X., Tavares L.M., The appropriate, and inappropriate, application of the JKMRC t10 relationship, Proceedings of the 27th International Mineral Processing Congress, Santiago, Gecamin, 2014, v. 1, pp. 1–13.

Ribas L., Cordeiro G.C., Toledo Filho R.D., Tavares L.M., Measuring the strength of irregularly-shaped fine particles in a microcompression tester, Minerals Engineering, 65 (2014) 149–155. DOI: 10.1016/j.mineng.2014.05.021

Rodnianski V., Levy A., Kalman H., A new method for simulation of comminution process in jet mills, Powder Technology, 343 (2019) 867–879. DOI: 10.1016/j.powtec.2018.11.021

Rozenblat Y., Portnikov D., Levy A., Kalman H., Aman S., Tomas J., Strength distribution of particles under compression, Powder Technology, 208 (2011) 215–224. DOI: 10.1016/j.powtec.2010.12.023

Rozenblat Y., Grant E., Levy A., Kalman H., Tomas J., Selection and breakage functions of particles under impact loads, Chemical Engineering Science, 71 (2012) 56–66. DOI: 10.1016/j.ces.2011.12.012

Rumpf H., Physical aspects of comminution and new formulation of a law of comminution, Powder Technology, 7 (1973) 145–159. DOI: 10.1016/0032-5910(73)80021-x

Saeidi F., Tavares L.M., Yahyaei M., Powell M., A phenomenological model of single particle breakage as a multi-stage process, Minerals Engineering, 98 (2016) 90–100. DOI: 10.1016/j.mineng.2016.07.006

Saeidi F., Yahyaei M., Powell M., Tavares L.M., Investigating the effect of applied strain rate in a single breakage event, Minerals Engineering, 100 (2017) 211–222. DOI: 10.1016/j.mineng.2016.09.010

Salman A.D., Biggs C.A., Fu J., Angyal I., Szabó M., Hounslow M.J., An experimental investigation of particle fragmentation using single particle impact studies, Powder Technology, 128 (2002) 36–46. DOI: 10.1016/s0032-5910(02)00151-1

Salman A.D., Fu J., Gorham D.A., Hounslow M.J., Impact breakage of fertiliser granules, Powder Technology, 130 (2003) 359–366. DOI: 10.1016/s0032-5910(02)00237-1

Schönert K., Role of fracture physics in understanding comminution phenomena, Transactions of the SME/AIME, 252 (1972) 21–26.

Schönert K., Aspects of physics of breakage relevant to comminution, Proceedings of the 4th Tewksbury Symposium, Melbourne, 1979, pp. 3.1–3.9.

Schönert K., Advances in comminution fundamentals and impacts on technology, Aufbereitungs-Technik, 32 (1991) 487–494.

Schubert H., On the microprocesses of comminution. Aufbereitungs–Technik, 5 (1987) 237–246.

Sikong L., Hashimoto H., Yashima S., Breakage behavior of fine particles of brittle minerals and coals, Powder Technology, 61 (1990) 51–57. DOI: 10.1016/0032-5910(90)80065-7

Steier K., Schönert K., Verformung und Bruchphanomene unter druckbeanspruchung von sehr kleinen kornern aus Kalkstein, Quarz und Polystyprol, Dechema-Monographien, 69 (1972) 167–192.

Tavares L.M., Microscale investigation of particle breakage applied to the study of thermal and mechanical predamage, Ph.D. thesis, University of Utah, 1997. https://utah-primoprod.hosted.exlibrisgroup.com/permalink/f/1g0gstr/TN_cdi_proquest_journals_304394788

Tavares L.M., Energy absorbed in breakage of single particles in drop weight testing, Minerals Engineering, 12 (1999) 43–50. DOI: 10.1016/s0892-6875(98)00118-6

Tavares L.M., Role of particle microstructure in comminution, Proceedings of the 21st International Mineral Processing Congress, Rome, Elsevier, 2000, Vol. C, pp. C4-99–C4-106.

Tavares L.M., Optimum routes for particle breakage by impact, Powder Technology, 142 (2004) 81–91. DOI: 10.1016/j.powtec.2004.03.014

Tavares L.M., Particle weakening in high-pressure roll grinding, Minerals Engineering, 18 (2005) 651–657. DOI: 10.1016/j.mineng.2004.10.012

Tavares L.M., Breakage of single particles: quasi-static. In: A.D. Salman, M. Ghadiri, M.J. Hounslow (Eds.), Handbook of Particle Breakage, volume 12, 1st edition, Elsevier, 2007, pp. 3–68, ISBN: 9780444530806.

Tavares L.M., Analysis of particle fracture by repeated stressing as damage accumulation, Powder Technology, 190 (2009) 327–339. DOI: 10.1016/j.powtec.2008.08.011

Tavares L.M., A review of advanced ball mill modelling, KONA Powder and Particle Journal, 34 (2017) 106–124. DOI: 10.14356/kona.2017015

Tavares, L.M., André, F.P., Potapov, A., Maliska Jr., C., Adapting a breakage to discrete elements using polyhedral particles, Powder Technology, 362 (2020a), 208–220. DOI: 10.1016/j.powtec.2019.12.007

Tavares L.M., Carvalho R.M., Impact work index prediction from continuum damage model of particle fracture, Minerals Engineering, 20 (2007) 1368–1375. DOI: 10.1016/j.mineng.2007.08.021

Tavares L.M., Cavalcanti P.P., de Carvalho R.M., da Silveira M.W., Bianchi M., Otaviano M., Fracture probability and fragment size distribution of fired Iron ore pellets by impact, Powder Technology, 336 (2018) 546–554. DOI: 10.1016/j.powtec.2018.06.036

Tavares L.M., Cerqueira M.C., Statistical analysis of impact-fracture characteristics and microstructure of industrial Portland cement clinkers, Cement and Concrete Research, 36 (2006) 409–415. DOI: 10.1016/j.cemconres.2005.09.012

Tavares L.M., das Chagas A.S., A stochastic particle replacement strategy for simulating breakage in DEM, Powder

Technology, 377 (2021) 222–232. DOI: 10.1016/j.powtec.2020.08.091

Tavares L.M., das Neves P.B., Microstructure of quarry rocks and relationships to particle breakage and crushing, International Journal of Mineral Processing, 87 (2008) 28–41. DOI: 10.1016/j.minpro.2008.01.007

Tavares L.M., de Almeida R.F., Breakage of green iron ore pellets, Powder Technology, 366 (2020) 497–507. DOI: 10.1016/j.powtec.2020.02.074

Tavares L.M., de Carvalho R.M., Modeling breakage rates of coarse particles in ball mills, Minerals Engineering, 22 (2009) 650–659. DOI: 10.1016/j.mineng.2009.03.015

Tavares L.M., de Carvalho R.M., Modeling ore degradation during handling using continuum damage mechanics, International Journal of Mineral Processing, 101 (2011) 21–27. DOI: 10.1016/j.minpro.2010.07.008

Tavares L.M., de Carvalho R.M., Bonfils B., de Oliveira A.L.R., Back-calculation of particle fracture energies using data from rotary breakage testing devices, Minerals Engineering, 149 (2020b) 106263. DOI: 10.1016/j.mineng.2020.106263

Tavares L.M., King R.P., Single-particle fracture under impact loading, International Journal of Mineral Processing, 54 (1998) 1–28. DOI: 10.1016/S0301-7516(98)00005-2

Tavares L.M., King R.P., Modeling of particle fracture by repeated impacts using continuum damage mechanics, Powder Technology, 123 (2002) 138–146. DOI: 10.1016/S0032-5910(01)00438-7

Tavares L.M., King R.P., Measurement of the load–deformation response from impact-breakage of particles, International Journal of Mineral Processing, 74 (2004) S267–S277. DOI: 10.1016/j.minpro.2004.07.017

Tavares L.M., Rodriguez V.A., Sousani M., Padros C.B., Ooi J.Y., An effective sphere-based model for breakage simulation in DEM, Powder Technology, 392 (2021) 473–488. DOI: 10.1016/j.powtec.2021.07.031

Teo C.S., Waters A.G., Nicol S.K., Quantification of the breakage of lump materials during handling operations, International Journal of Mineral Processing, 30 (1990) 159–184. DOI: 10.1016/0301-7516(90)90013-o

Vervoorn P.M.M., Austin L.G., The analysis of repeated breakage events as an equivalent rate process, Powder Technology, 63 (1990) 141–147. DOI: 10.1016/0032-5910(90)80036-x

Vogel L., Peukert W., Breakage behaviour of different materials—construction of a mastercurve for the breakage probability, Powder Technology, 129 (2003) 101–110. DOI: 10.1016/S0032-5910(02)00217-6

Vogel L., Peukert W., Determination of material properties relevant to grinding by practicable labscale milling tests, International Journal of Mineral Processing, 74 (2004) S329–S338. DOI: 10.1016/j.minpro.2004.07.018

Wang M.H., Yang R.Y., Yu A.B., DEM investigation of energy distribution and particle breakage in tumbling ball mills, Powder Technology, 223 (2012) 83–91. DOI: 10.1016/j.powtec.2011.07.024

Weedon D.M., Wilson F., Modelling iron ore degradation using a twin pendulum breakage device, International Journal of Mineral Processing, 59 (2000) 195–213. DOI: 10.1016/S0301-7516(99)00066-6

Weichert R., Application of defect statistics and fracture mechanics for describing comminution processes, Zement-Kalk-Gips, 45 (1992) 51–57.

Yan Y., Zhang Z., Stokes J.R., Zhou Q.-Z., Ma G.-H., Adams M.J., Mechanical characterization of agarose micro-particles with a narrow size distribution, Powder Technology, 192 (2009) 122–130. DOI: 10.1016/j.powtec.2008.12.006

Yashima S., Kanda Y., Sano S., Relationships between particle size and fracture energy or impact velocity required to fracture as estimated from single particle crushing, Powder Technology, 51 (1987) 277–282. DOI: 10.1016/0032-5910(87)80030-x

Yashima S., Morohashi S., Saito F., Single particle crushing under slow rate of loading, Science Reports of the Research Institutes, Tohoku University Ser A, Physics, Chemistry And Metallurgy, 28 (1979) 116–133. http://hdl.handle.net/10097/28092

Author’s Short Biography

Luís Marcelo Tavares

Luís Marcelo Tavares is a Professor at Universidade Federal do Rio de Janeiro (UFRJ) in Brazil. He received his bachelor’s degree in Mining Engineering (honors) and his master’s degree from Universidade Federal do Rio Grande do Sul. He was awarded a Ph.D. degree in Extractive Metallurgy at the University of Utah. He has been a member of the faculty of UFRJ since 1998, where he is head of the Laboratório de Tecnologia Mineral and has been Department chairman. His research interests include particle breakage, advanced models of comminution and of degradation during handling, DEM, physical concentration, classification, iron ore processing and development of pozzolanic materials. He is a founding member and currently president of the Global Comminution Collaborative (GCC) and has received a number of awards from the Brazilian Association of Metallurgy, Materials and Mining (ABM).

KONA Powder and Particle Journal No. 39 (2022) 84–99/https://doi.org/10.14356/kona.2022009 Review Paper

Advances in the Rheological Characterization of Slurries of Elongated Particles[†]

Saif Shaikh, Scott Strednak and Jason E. Butler[*]

Department of Chemical Engineering, University of Florida, USA

Abstract

Inherent challenges regarding the rheological characterization of slurries of elongated particles have necessitated the development of alternatives to standardized rheometers. These methods of measurement, and the associated advances in the quantification of shear and normal stress measurements, are described. Also, recent advances in modeling and predictive capabilities are summarized. During shearing flows, confinement substantially influences the orientation distribution of the particles; this change in the microstructure impacts the rheology, even as the smallest confining dimension exceeds seven particle lengths. The slow development of the orientation distributions renders additional difficulties in evaluating the rheology. Achievements of the measurement methods include a universal shear viscosity as a function of concentration for a wide range of particle lengths to diameters (aspect ratios). The jamming limit (divergence of the viscosity with concentration) of the suspensions has been also shown to scale differently than for spheres. More general dynamics of the suspensions and the additional needs for measurement improvements are discussed.

Keywords: rheology, concentrated slurries, fibers, microstructure

1. Introduction

Suspensions, a class of complex fluids wherein an insoluble phase, either a solid or a liquid is dispersed in a liquid (Larson, 1999), are ubiquitous in nature. Suspended particles can be spherical or near-spherical, discs, or elongated in the form of fibers, and can be rigid or soft and flexible. Suspensions occur naturally, with macroscale examples such as lava and silt-laden rivers where the solid particles are anisotropic and polydisperse. At the microscale, blood is an example of another natural suspension where disc-like platelets are suspended in plasma. These suspensions can be further categorized on the basis of their particle sizes as Brownian and colloidal with sizes on the order of tens of nanometers to a few microns, to non-Brownian and non-colloidal for particle sizes larger than a few microns.

In industry, suspensions of non-colloidal particles are found in a wide variety of applications. Transport and processing of slurries containing wood fibers in the manufacture of paper products is an example where the particles are long and flexible (Lundell et al., 2011). Rod-like particles and flexible fibers are added to materials to create composite materials with enhanced strength and performance, as with fiber-reinforced concrete (Hassanpoura et al., 2012). Fibers, both rigid and flexible, are also added to modify the rheological properties of fluids used in the production of oil (Bivens et al., 2005; Elgaddafi et al., 2012; Hammond, 1995; Osiptsov, 2017). In contrast, the presence of fibrous minerals can have a detrimental impact on the operation of flotation processes (Patra et al., 2012; Somasundaran et al., 2019), which are often used at mining sites to separate high value minerals from a slurry.

Various trade-offs exist while designing and operating processes that contain particle suspensions. Decisions often center on the balance between high energy usage at high particle concentrations and high suspending fluid usage at low particle concentrations. Regarding the latter, concerns regarding overuse of water resources have been associated with many industries, including the example of mining and the operation of on-site flotation processes (Liu et al., 2011; Rao and Finch, 1989). At the other limit of high solids content, the viscosity of the suspension increases and even diverges as the solids content approaches maximum packing. As an immediate consequence, the power requirements for pumping and mixing suspensions can increase significantly, thereby significantly increasing processing costs.

Reliable, quantitative information on the rheology of suspensions can assist in managing these trade-offs. For suspensions of spheres that are non-Brownian and non-colloidal, there has been considerable development of

---

[†] Received 31 March 2021; Accepted 11 May 2021
J-STAGE Advance published online 26 June 2021

[*] Corresponding author: Jason E. Butler;
Add: Gainesville, Florida 32611, USA
E-mail: butler@che.ufl.edu
TEL: +1-352-392-2591

rheological models. For volume fractions $\phi < 0.02$ (i.e the the ratio of the total volume of the suspended particles to the total volume of the suspension), the viscosity η_s increases linearly according to Einstein's equation (Einstein, 1906),

$$\eta_s = \eta_f \left(1 + \frac{5}{2}\phi\right) \tag{1}$$

where η_f is the viscosity of the suspending fluid. Higher order corrections for suspension viscosity have been determined which extend the range of the volume fraction (Batchelor and Green, 1972). However, the complexity of the problem quickly surpasses analytical capabilities as the concentration is increased, and computational methods such as the Stokesian dynamics method (Brady and Bossis, 1988) must be employed in order to make progress on calculations of rheology based on first principles. Experimentally characterizing the rheology of concentrated suspensions of spheres can pose difficulties as well. Acrivos (1995) summarized discrepancies among published reports on the shear viscosity and attributed the differences to a number of effects including shear-induced migration (Leighton and Acrivos, 1987), which causes a non-uniform distribution of particles within the testing geometry. One generally accepted correlation for the shear viscosity of suspensions of non-Brownian spheres in Newtonian fluids over a wide range of volume fractions is given by the Krieger-Dougherty equation (Krieger and Dougherty, 1959),

$$\eta_s = \eta_f \left(1 - \frac{\phi}{\phi_m}\right)^{-[\eta]\phi_m} \tag{2}$$

where ϕ_m is the maximum volume fraction at which the particles pack randomly and $[\eta] \approx 2.5$. Still, some debate persists regarding rheological properties of concentrated suspensions of spheres, such as the sign of the first normal stress difference (Guazzelli and Pouliquen, 2018).

Making well-informed decisions regarding processes that utilize suspensions of particles that are non-spherical is hampered by a relative lack of data and incomplete information on how to interpret that data. In the specific case of suspensions of elongated particles, though the viscosity scales with an increasing particle volume fraction, the relationship is much more complex. As an example, **Fig. 1** shows rheological data obtained experimentally by Tapia et al. (2017) for rigid polyamide fibers of different aspect ratios and particle diameters. It is evident that the particle shape has a significant impact on the rheology, and hence equipment design as well as operating decisions must consider these factors. However, obtaining reliable and accurate rheological data can be challenging for these types of suspensions composed of large rigid fibers at high concentration owing to confinement effects and the tendency of the suspension microstructure to change drastically depending upon the pattern of shearing flow.

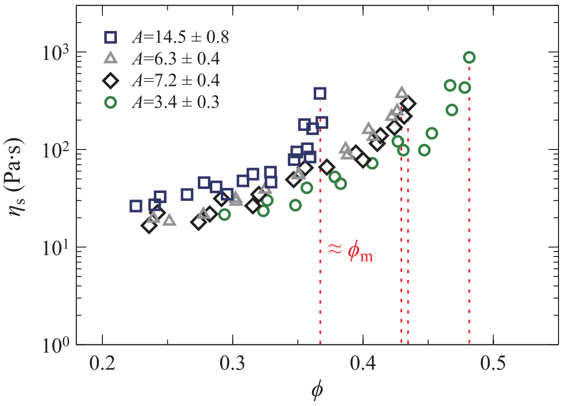

Fig. 1 Rheological data obtained from Tapia et al. (2017) showing the dependence of the shear viscosity η_s on the particle volume fraction ϕ for rigid fibers. The measured viscosities depend on the particle aspect ratio $A = L/d$, where L and d are the particle length and diameter, respectively. The results indicate that the viscosity diverges at a different volume fraction for each aspect ratio, which roughly corresponds to maximum random packing (ϕ_m).

This review focuses on the concentrated regime of slurries of elongated particles in effort to consolidate the sparse work done previously in this area and to summarize recent and ongoing studies. Section 2 outlines the properties of the particles and fluids, as well as the regimes of particle concentrations in the slurries under consideration in this review. Section 3 examines the rheological techniques and measurements in the semi-dilute (Section 1) and concentrated (Section 2) regimes of concentration, focusing on studies of the near-jamming limit. This section also explores the effects of time-varying flow fields, focusing on the relatively recent advances in oscillatory flows (Section 2). Normal stress differences, which are of importance in predicting shear-induced migration, are discussed in Section 4. Some comments on remaining challenges are offered in the conclusions.

2. Suspension properties

This review focuses on slurries of elongated particles in viscous Newtonian fluids. Many of the studies described use rod-shaped particles of aspect ratio, $A = L/d >> 1$, where L is the length of the rod and d is its diameter. Unless specified otherwise, these particles are sufficiently large to be non-Brownian. Consequently, the rotational Péclet number $Pe_r = \dot{\gamma}/d_r$ should be large, where $\dot{\gamma}$ is the rate of shear and d_r is the rotational diffusivity,

$$d_r = \frac{3kT\ln(2A)}{\pi\eta_f L^3} \tag{3}$$

for a rod of high aspect ratio. The fluid viscosity is η_f, k is the Boltzmann constant, and T is the temperature. An alternative definition for the rods to be non-Brownian requires a large Péclet number as defined by $Pe = L^2\dot{\gamma}/D_T$, where D_T is the mean center of mass diffusivity. Basing the definition of non-Brownian on $Pe >> 1$ is more stringent than using Pe_r since $Pe = 9Pe_r$.

The particles chosen for idealized experiments are monodisperse in length and diameter. The materials of these fibers are generally polymeric, for ease of production, use, and manipulation. Polyamides like Nylon-6 and polystyrene (PS) are used in conventional rheometry experiments owing to the ease of obtaining particles with a wide array of lengths, diameters, and aspect ratios, and mechanical strength. For imaging experiments, poly-methylmethacrylate (PMMA/acrylic) obtained from the core of fiber optic cables have been optimal owing to their uniform optical properties.

The suspending media are Newtonian in all of the work described in this review. The density of the fluids (or mixtures) were selected or altered to match the density of the particles; the particles neither sediment to the bottom or float to the top, negating any possible effects of gravity on the dynamics and rheology. The above-mentioned conditions are imposed upon the slurries to simplify the subsequent measurements and analyses, by assuming that in the absence of Brownian fluctuations and gravity, the motion of the particles in the slurries are primarily driven by the flow imposed upon them. For imaging experiments, the suspending media must also be chosen, or its composition altered, in order to match the refractive index of the particles. When the fluid is subsequently dyed with a fluorescing agent and properly illuminated, the contrast can be used to obtain spatial and orientation data.

The elongated particles on which this review focuses are rigid, neither stretching nor bending under the forces imposed by the flow. For materials that are relatively soft, shearing forces may be sufficient to bend a fiber and impact the dynamics and rheology. Consequently, criteria have been developed for estimating the stress at which fibers bend appreciably. Forgacs and Mason (1959) determined a critical stress, Σ_{crit}, at which a slender rod buckles under compressional flow as,

$$\Sigma_{\text{crit}} \approx \frac{E_{\text{b}}\left[\ln(2A)-1.75\right]}{2A^4} \tag{4}$$

where E_b is the bending modulus, estimated to be twice the Young's modulus of the particle. This model provided good agreement for the bending of polymer fibers in shearing flows with stresses of $\eta_f\dot{\gamma}$ (Forgacs and Mason, 1959). It is assumed that any deformation of the elongated fiber is negligible when the maximum stress exerted by the flow field is much smaller than Σ_{crit}. A number of authors have developed similar ideas, defining a ratio of the imposed fluid stresses of $\eta_f\dot{\gamma}$ and critical stresses as calculated using relations identical or similar to Eq. (4). Switzer and Klingenberg (1959) defined an effective stiffness, S^{eff}, as

$$S^{\text{eff}} = \frac{E_y \pi}{256\eta_{\text{f}}\dot{\gamma}A^4} \tag{5}$$

where E_y is the Young's modulus of the particle. Others (Lauga, 2007; Wandersman et al., 2010) inverted the ratio of shear stress and critical stress to create the "sperm number" S_P as,

$$S_{\text{P}} = \frac{8\eta_{\text{f}}\dot{\gamma}A^4}{E_y} \tag{6}$$

Young and Shelley (2007) corrected the value of critical stress used in the sperm number to give a slightly different dimensionless number of

$$S_{\text{P}}^{*} = \frac{128\eta_{\text{f}}\dot{\gamma}A^4}{E_y\left[\ln(2A)-0.5\right]} \tag{7}$$

Despite the differences in the various definitions, bending of a fiber can be ignored so long as the product of the imposed shear and viscosity ($\eta_f\dot{\gamma}$) are much smaller than the stress at which the fiber buckles.

The rheology and dynamics of suspensions of rigid fibers differ greatly depending on the extent to which rotation is impeded by the presence of other fibers. Consequently, (Doi and Edwards, 1978) suggested defining concentration regimes in terms of simple geometric constraints; examples are shown in **Fig. 2** of fibers randomly placed in a fixed volume at dilute, semi-dilute, and concentrated conditions.

a) $nL^3 = 0.75$, $\phi = 0.006$ **b)** $nL^2d = 0.5$, $\phi = 0.04$ **c)** $nL^2d = 3.0$, $\phi = 0.24$

Fig. 2 Images of rigid fibers of aspect ratio $A = L/d = 10$ placed randomly in a volume at concentrations within the **(a)** dilute ($nL^3 << 1$), **(b)** semi-dilute ($1/L^3 < n < 1/L^2d$), and **(c)** concentrated ($nL^2d > 1$) regime. The volume fraction ϕ corresponding to each dimensionless number density is given in the figure. At the highest concentration of $nL^2d = 3.0$, the suspension is isotropic for this aspect ratio.

For the case of dilute suspensions ($nL^3 << 1$), spherical volumes that enclose each particle do not generally overlap and each fiber can rotate freely. Here $n = N/V$ is the number density, the number of particles N per unit volume V of the suspension. Note the dimensionless number density nL^3 is equivalent to $4A^2\phi/\pi$, where ϕ is the particle volume fraction. In the semi-dilute region, fibers can no longer rotate freely. The upper limit of the semi-dilute regime ($nL^2d = 4A\phi/\pi \approx 1$) roughly corresponds to close packing of a collection of flattened discs having a diameter of L and thickness d. Further increases in concentration beyond $nL^2d = 1$ can occur while the spatial and orientation distribution remains isotropic, as demonstrated in **Fig. 2c** for $A = 10$ and $nL^2d = 3.0$. However at some point, maximum random packing is exceeded and adding more particles requires organizing the particle orientations into a nematic phase. Studies (Williams and Philipse, 2003) indicate that the maximum volume fraction at which sphero-cylinders can still pack randomly scales inversely with the aspect ratio. For the case of $A = 10$ shown in **Fig. 2**, maximum random packing occurs at $nL^2d \approx 4.7$, or $\phi \approx 0.37$; higher concentrations require aligning the fibers. At $A = 20$, the transition occurs at $\phi \approx 0.22$, or $nL^2d = 5.6$.

3. Shear rheology and structure

The rheology of suspensions of well-dispersed rigid fibers depends strongly upon the orientation distribution. As a quantitative example, the shear viscosity for dilute solutions of rigid fibers ($nL^3 < 1$) that are force-free (i.e. non-Brownian) is given by Batchelor (1970)

$$\eta_s = \eta_f\left(1 + cnL^3\left\langle p_x^2 p_y^2\right\rangle\right) \qquad (8)$$

where η_s is the viscosity of the suspension relative to that of the fluid (η_f), c is a constant that depends on the particle size and shape, and the expression ignores the small contributions to stress from the thickness of the particle, which is assumed to be of high aspect ratio. The brackets, $\langle\cdot\rangle$, indicate an average over all fibers in the suspension, where the fibers have an orientation of $\boldsymbol{p}$. Here, p_x and p_y represent the orientation components in the flow (x) and gradient (y) directions.

Generally, the orientation (and position) of each rod in a suspension is set by balancing the non-hydrodynamic torques (and forces) with hydrodynamic drag. In the particular case of a force-free fiber at dilute conditions, the fiber tumbles indefinitely in a well-defined orbit that depends on its initial orientation (Jeffery, 1922). Consequently the viscosity η_s oscillates in time as indicated in Eq. (8) owing to its dependence of the ever-changing orientation moment $\left\langle p_x^2 p_y^2\right\rangle$. Measurements performed by Ivanov et al. (1982) confirm that the viscosity oscillates during steady shear, though the amplitude of the oscillation decays over time. The decay to a steady value is likely due to small effects that influence the torque balance on the fibers, possibly including weak Brownian motion (Hinch and Leal, 1972) or inertia (Einarsson et al., 2015).

Thorough reviews of the rheology of dilute suspensions are available (Powell, 1991; Petrie, 1999) that discuss these issues in depth. The remainder of this section describes the measurement of more concentrated suspension where particle interactions begin to influence the orientation distributions and the measured rheology.

3.1 Semi-dilute concentrations

Fig. 3 shows viscosity measurements by Bibbó (1987) and Djalili-Moghaddam and Toll (2006) for glass and nylon fibers of aspect ratios $A \approx 32$ and 50. Measurements are shown for volume fractions of $\phi = 0.01$ to 0.1, which correspond to dimensionless number densities nL^3 spanning the semi-dilute concentration regime ($nL^3 > 1$ and $nL^2d < 1$).

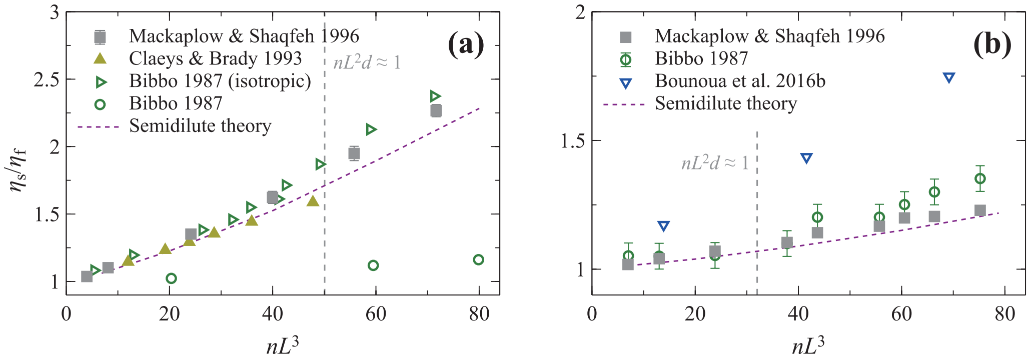

Fig. 3 Shear viscosity η_s relative to the fluid viscosity η_f as a function of fiber concentration nL^3 for aspect ratios of **(a)** $A \approx 50$ and **(b)** $A \approx 32$; the concentration range spans the semi-dilute regime of $nL^3 > 1$ and $nL^2d < 1$. Experimental measurements of Bibbó (1987) and Bounoua et al. (2016a) are compared to simulations (Mackaplow and Shaqfeh, 1996; Claeys and Brady, 1993) and the theory for semi-dilute suspensions of rigid rods by Shaqfeh and Fredrickson (1990). A value of $\left\langle p_x^2 p_y^2\right\rangle = 0.01$ was used when evaluating the theory numerically. Error bars are shown for the sets of data when available; for the data of Mackaplow and Shaqfeh (1996), the error is often smaller than the size of the data point.

Viscosities for higher aspect ratio fibers are expected to be larger at the same concentration and for the same orientation distribution, as indicated in the figure by the semi-dilute theory (Shaqfeh and Fredrickson, 1990) where the same value of 0.01 for $\langle p_x^2 p_y^2 \rangle$ was used in calculating the curves. Indeed, the experimentally measured viscosities in **Fig. 3** are larger for the higher aspect ratio fibers. However, the influence of the orientation distribution is strong: the viscosity of suspensions with fibers aligned with the flow was significantly lower than that of an isotropically distributed fibers as seen in **Fig. 3a** (isotropic versus non-isotropic data by Bibbó (1987)). For this reason, the influence of bounding walls in confined geometries must be considered when evaluating the measured rheology, especially as the concentration approaches and surpasses $nL^2d = 1$.

Beyond the dilute limit of $nL^3 = 1$, interactions between particles become increasingly important, and predicting the rheology depends on at least two complicated calculations. First, accurate determination of the spatial and orientation distribution is necessary. Second, calculations that relate the microstructure and stresses must be performed. In both cases as reviewed in detail by Butler and Snook (2018), hydrodynamic interactions between the particles must be considered. This differs from the dilute and concentrated regimes where the particles are either too far apart or the dynamics and rheology are dominated by direct particle-particle contacts. Calculations that consider hydrodynamic interactions between rigid rods, such as those shown in **Fig. 3**, are computationally expensive, hence predicting the microstructure and rheology for large numbers of fibers in the semi-dilute regime remains an outstanding challenge.

Some results shown in **Fig. 3** represent the high shear limit of the measured viscosity. In the semi-dilute regime, many slurries of rigid fibers exhibit shear-thinning rheology, where the measured viscosity decreases with increases in rate of shear (Ganani and Powell, 1985; Powell, 1991; Bricker et al., 2008; Bounoua et al., 2019). One example from Bricker et al. (2008) is shown in **Fig. 4** for a suspension of ellipsoids with a moderate aspect ratio of $A = 7$ at a concentration of $nL^3 = 4.4$ ($\phi = 0.07$). Although the particles were relatively small in these experiments, the value of the rotational Péclet number was large, ranging from approximately $Pe_r = 10^3$ at the lowest shear rate of $\dot{\gamma} = 0.1\ \mathrm{s}^{-1}$ to 10^6 at 100 s^{-1}. Note that **Fig. 4** also shows viscosity data over the same range of shear rates for spheres having properties (material of composition, volume of each particle, and method of manufacture) identical to that of the ellipsoids.

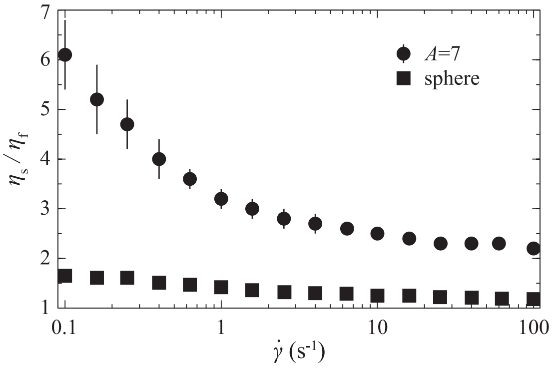

Fig. 4 Steady shear viscosity η_s as a function of shear rate for a suspension of ellipsoids of aspect ratio $A = 7$ and for spheres (Bricker et al., 2008). Both suspensions have a volume fraction of $\phi = 0.07$, and the particles differ only in their shape, as each particle was composed of an identical volume of polystyrene and was manufactured using the same process.

The substantial shear-thinning of the suspension of ellipsoids versus the spheres indicates a remarkable difference in the rheology originating from the shape of the particles. These results contradict numerical simulations (Dinh and Armstrong, 1984; Shaqfeh and Fredrickson, 1990; Schiek and Shaqfeh, 1995) which predict viscosities that are independent of shear-rate. Indeed, the rheology of suspensions of non-Brownian and non-colloidal particles is expected to be *pseudo*-Newtonian regardless of their shape: though attaining steady-state may require a large strain, or time, the steady viscosity of the fluids should be independent of shear rate. Many ideas regarding the origin of the shear thinning have been given, including the possibility that non-Newtonian suspending fluids are responsible (Bibbó et al., 1985; Maschmeyer and Hill, 1977) and that the fibers used in the experiments deform under the imposed stresses (Sepehr et al., 2004; Bennington et al., 1990). Attractive colloidal forces have also been incorporated into models to explain shear thinning (Chaouche and Koch, 2001; Bounoua et al., 2016b), and this line of investigation has been argued to be promising (Butler and Snook, 2018).

3.2 Concentrated suspensions

The rheology of suspensions of rod-shaped elongated particles in a Newtonian fluid beyond the semi-dilute regime remain largely unexplored. This is largely due to the difficulty in performing rheological experiments with large, rigid fibers at dimensionless number densities nL^2d above 1.0. Under these conditions, confinement is a significant issue. Standard rheological tooling employs shearing geometries having gaps between the bounding walls of $H \lesssim 1$ mm. This is particularly problematic for suspensions composed of non-colloidal fibers where the particles of interest can have lengths $L \gtrsim 0.1$ mm. Typically it has been assumed that the rheological measurements are not influenced by the bounding walls so long as $H/L > 2$ or 3 (Bibbó et al., 1985; Powell, 1991; Chaouche and Koch, 2001). This is true for dilute, or even semi-dilute, suspensions since the additional drag on any one rod rapidly decays as the distance from the bounding wall increases (Zurita-Gotor et al., 2007; Park and Butler, 2009). However, at higher concentrations the

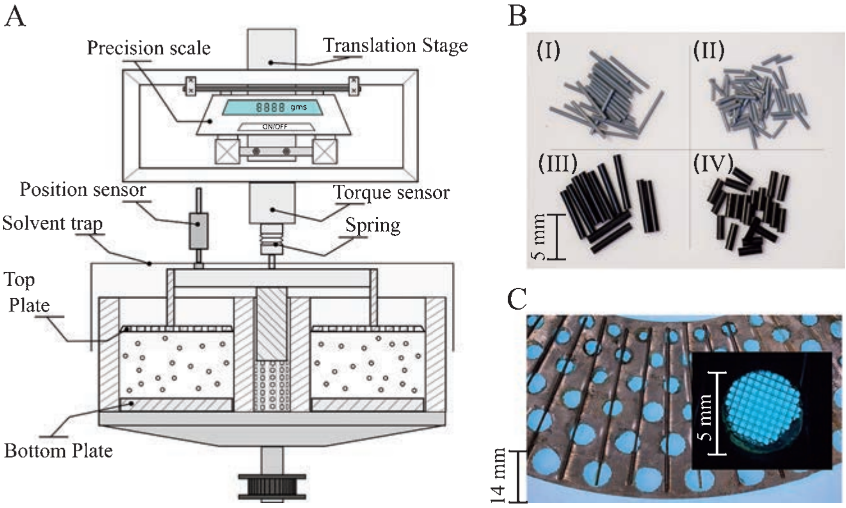

Fig. 5 Novel pressure-imposed rheometer used to measure bulk rheological properties at high concentrations near the jamming limit used by Tapia et al. (2017). **(A)** Schematic of the experimental setup. **(B)**: Microscope images of the plastic fibers. **(C)** Porous top plate with zoomed image of nylon mesh. From "Rheology of concentrated suspensions of non-colloidal rigid fibers" by Franco Tapia, Saif Shaikh, Jason Butler, Olivier Pouliquen, and Élisabeth Guazzelli, J. Fluid Mech (2017), vol. 827, R5. Reprinted with permission.

bounding walls have a strong effect on the rheology: the walls prevent particles from rotating and moving freely, altering the orientation distribution. This disturbance in the structure imposed by the wall propagates a significant distance into the fluid at high concentrations. The measured rheology will not match that of a bulk fluid unless the wall spacing is much larger than $3L$.

Consequently, Tapia et al. (2017) used a large, custom-built device to make the viscosity measurements shown in **Fig. 1**. The rheometer was originally constructed by Boyer et al. (2011a) and was used by them and Dagois-Bohy et al. (2015) to characterize a Newtonian fluid containing spheres. This "imposed load" rheometer consisted of a wide-gap annular shear cell with a movable top plate, as shown in **Fig. 5**. The movable top plate has a porous screen which allowed fluid to pass freely across the plate, but prevented fibers from passing. This enabled the dynamic adjustment of the particle volume fraction while maintaining the volume of the particles.

Experiments were conducted in two modes: conventional rheometry with a controlled volume and a novel "pressure-imposed" mode. For the former mode, the volume fraction of the suspension was maintained at a constant value by holding the top plate at a fixed height; the torque was measured as a function of rotation rate while also recording the normal force needed to prevent the top plate from moving. In the pressure-imposed mode, a constant normal force was applied to the top plate, allowing it to move while measuring the torque as a function of rotation rate. In this case, the volume fraction ϕ varied with the rate of rotation. The torque and rotation rate were used to calculate the shear viscosity η_s as a function of ϕ as shown in **Fig. 1**. The normal force on the plate was corrected for buoyancy and divided by the plate area to give a pressure P.

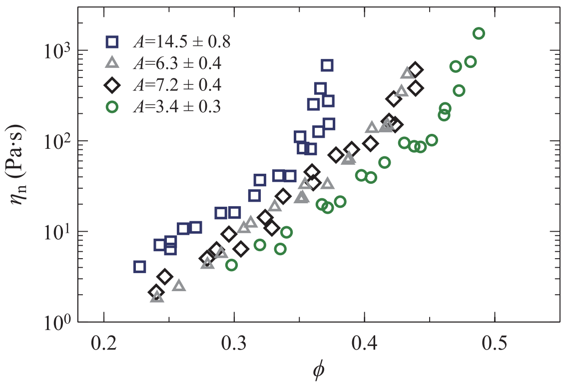

Fig. 6 Normal viscosity η_n for concentrated suspensions of rigid polyamide fibers suspended in a viscous Newtonian fluid (Tapia et al., 2017). The normal viscosity is a unique measurement, as it is a bulk rheological measure of particle pressure.

This quantity represents the particle pressure that the fluctuating particles exert on the porous plate and is reported as a normal viscosity,

$$\eta_n = \frac{P}{\eta_f \dot{\gamma}} \tag{9}$$

as was done by Morris and Boulay (1999). These results are shown in **Fig. 6**.

A unique result provided by these experiments is the measurement of the rheology at concentration ranges approaching maximum packing fraction, ϕ_m. These measurements were made possible by performing experiments in the "pressure-imposed" mode. **Fig. 1** and **Fig. 6** show that the shear and normal viscosities diverge at a value of ϕ that depends on the aspect ratio A of the fibers and corresponds closely to maximum random packing (ϕ_m) for each aspect ratio. As the concentration, ϕ approaches ϕ_m, the suspension approaches the "jamming transition". The maximum

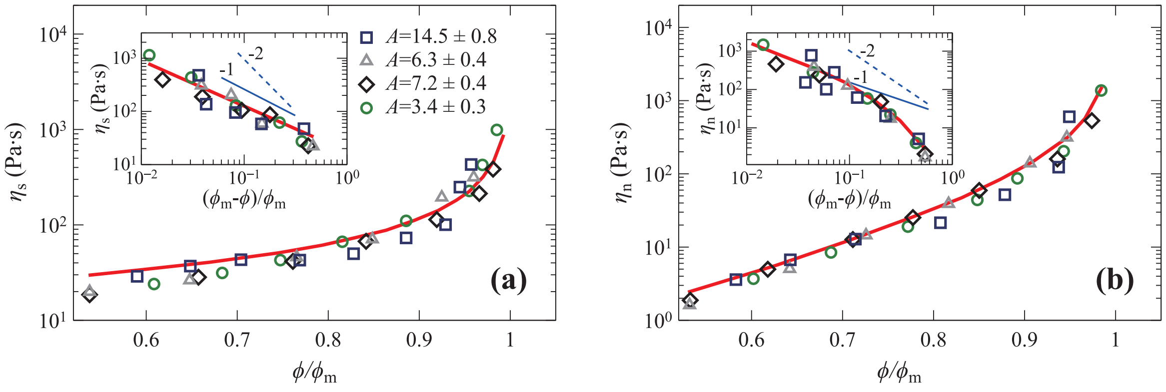

Fig. 7 **(a)** Shear viscosity and **(b)** normal viscosity of rod-shaped elongated particles as a function of increasing volume fraction ϕ collapse onto a single curve when scaled with the maximum packing fraction ϕ/ϕ_m (Tapia et al., 2017). The solid red curves corresponds to the model equations given in Eq. (10) and (11). The insets are log-log plots to determine the exponent value in Eq. (10) and is compared to that of spherical shaped particles (dashed).

packing fraction serves as an important scaling factor as well: as shown in **Fig. 7**, the rheological data collapses onto single-valued curves over the entirety of the range of particle sizes, aspect ratios, and concentrations measured in the experiments. Constitutive equations (Tapia et al., 2017) for the shear and normal viscosities, along with the coefficient of friction, developed using the maximum packing fraction as a scaling factor, are

$$\eta_s(\phi) = 14.51\left(\frac{\phi_m-\phi}{\phi_m}\right)^{-0.90} \tag{10}$$

$$\eta_n(\phi) = \eta_s(\phi)/\mu(\phi) \quad \text{and} \tag{11}$$

$$\mu(\phi) = \mu_s + c_1\left(\frac{\phi_m-\phi}{\phi}\right) + c_2\left(\frac{\phi_m-\phi}{\phi}\right)^2 \tag{12}$$

where μ_s is the coefficient of static friction, c_1 and c_2 are constants obtained from curve-fitting, and differ from the values obtained from experiments with spherical particles (Dagois-Bohy et al., 2015).

Shear-thinning rheology has also been reported for suspensions of elongated fibers in the concentrated regime and there is a wider range of measured values in this range of concentrations (Ganani and Powell, 1985; Powell, 1991). Theories similar to those mentioned at the end of Sec. 3.1 have been put forward to explain both observations, including the presence of attractive interparticle forces. Tapia et al. (2017) did not report shear-thinning behavior in their system, but did report finite yield stresses as have others. These yield stresses increased with increasing volume fraction and fiber aspect ratio. Many have attributed the yield stresses to attractive forces between the fibers, just as with shear thinning (Mongruel and Cloitre, 1999; Chaouche and Koch, 2001; Bounoua et al., 2016b).

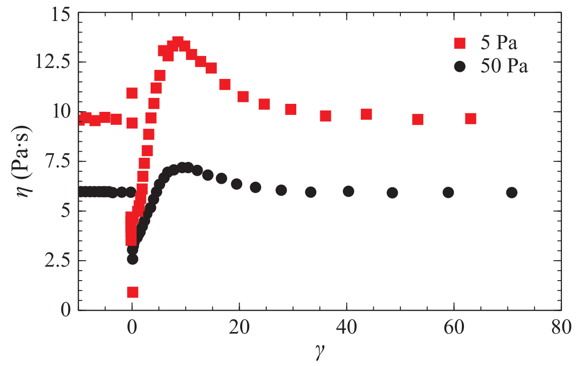

Fig. 8 The shear viscosity η_s before and after reversing the directions of flow at the strain value of $\gamma = 0$. The suspension was composed of rigid fibers with $A = 18$ and $nL^2d = 3.2$, and the measurements were made using a stress-controlled rheometer at two different values of the stress. Data is from Bounoua et al. (2019).

3.3 Unsteady shear rheology

As with other non-Newtonian fluids such as polymer and colloid solutions, rheological characterizations of fiber suspensions under time-varying shearing flows can probe the microstructure and forces that act within the system. However, the absence of Brownian motion and a well-defined equilibrium state for these fluids requires careful consideration regarding what is measured; for example, the Cox-Merz rule cannot be relied-upon for interpreting small amplitude oscillatory flows. Here, the shear reversal and oscillatory shear rheology for concentrated suspensions of fibers are described. As with steady shearing flows, a point of concern is the effect of confinement on the measurements.

3.3.1 Shear reversal

Bounoua et al. (2019) measured the time-dependent shear viscosities upon suddenly reversing the direction of a steady shearing flow. **Fig. 8** shows the measurements as a function of strain ($\gamma = \dot{\gamma}t$) for a concentrated suspension ($nL^2d = 3.2$, $\phi = 0.14$) of rigid fibers of aspect ratio $A = 18$;

the results share similarities with other studies of shear reversal of fiber suspensions (Sepehr et al., 2004). First, the samples were sheared until the viscosity reached steady state. Note that these suspensions of fibers were found to be shear thinning, consequently the steady shear viscosity differed depending upon the applied stress. The reversal was initiated at $\gamma = 0$ (i.e. $t = 0$), at which point the measured viscosity dropped significantly. The low point following the reversal was followed by a transient overshoot in the viscosity, before it returned to its steady value as confirmed by comparing viscosity values at large γ to the values at $\gamma < 0$, before reversing the flow direction.

Suspensions of non-colloidal spheres also exhibit reduction in the shear viscosity when the flow direction is suddenly changed following a period of steady shear (Gadala-Maria and Acrivos, 1980; Narumi et al., 2002; Blanc et al., 2011). Stresses resulting from the shearing flow of non-Brownian and non-colloidal particle suspensions have two sources: hydrodynamic and contact forces. The hydrodynamic contribution from each particle arises from the difference in velocity of the particle with the imposed shear flow and velocity disturbances caused by the other particles, which depends upon the relative arrangement of the particles. Direct contact forces between particles occur due to the breakdown of lubrication interactions, possibly because of surface roughness (Rampall et al., 1997; Ingber et al., 2006; Pham et al., 2015).

For shear-reversal of suspensions of spherical particles, detailed analysis (Peters et al., 2016) of Stokesian dynamics simulations indicate that the viscosity measured immediately after the reversal represents the purely hydrodynamic contributions to the shear viscosity, as the contact contribution disappears nearly entirely. During steady shearing flow, contact interactions build-up among the particles and contribute to the shear stresses. Suddenly reversing the direction of flow relieves the contact forces, which are purely repulsive, and the shear stress accordingly drops.

Similarly, the sudden drop in the viscosity shown in **Fig. 8** indicates the presence of contact interactions between the fibers. However, the overshoot in viscosity represents an important difference in the results as compared with spheres, where the viscosity returns to its steady value in a monotonic fashion. Bounoua et al. (2019) attributed the overshoot to weak attractive force between the particles, rather than the dynamics changes in the orientation distribution of the particles which surprisingly changes little during the course of the reversal process (Cieslinski et al., 2016). Measurements on suspensions of fibers that do not shear-thin (i.e. have no attractive forces) would presumably show no overshoot in the viscosity after shear reversal.

3.3.2 Oscillatory shearing

A suspension of rigid fibers undergoing oscillatory shear may yield vastly different measurements of the rheology, depending on the concentration, confinement, and strain amplitude of oscillation. **Fig. 9a** shows a strong qualitative difference for the latter case, where η'' (i.e. imaginary component of the complex viscosity) vanishes with increasing oscillation number (N) or remains finite, depending on the strain amplitude γ_0 of the oscillation (Franceschini et al., 2014). The rheological data reported is for aspect ratio $A = 11$ and a concentration of $\phi = 0.20$; importantly, the suspension was highly confined ($H/L = 1.5$).

Measurements (Franceschini et al., 2011; 2014; Strednak et al., 2021) and simulations (Snook et al., 2012; Strednak et al., 2021) of the orientation distribution under oscillatory flows also demonstrate a remarkable transition in the alignment as a function of strain amplitude. As shown in **Fig. 9b** for the same aspect ratio $A = 11$ and a concentration of $\phi = 0.20$, the order parameter S_θ is maximized when $\gamma_0 \approx 2.5$ ($\gamma_0\phi/\Phi_c \approx 1.25$ where $\Phi_c = 0.4$). Here,

$$S_\theta = 1 - 2 < \cos^2\theta > \tag{13}$$

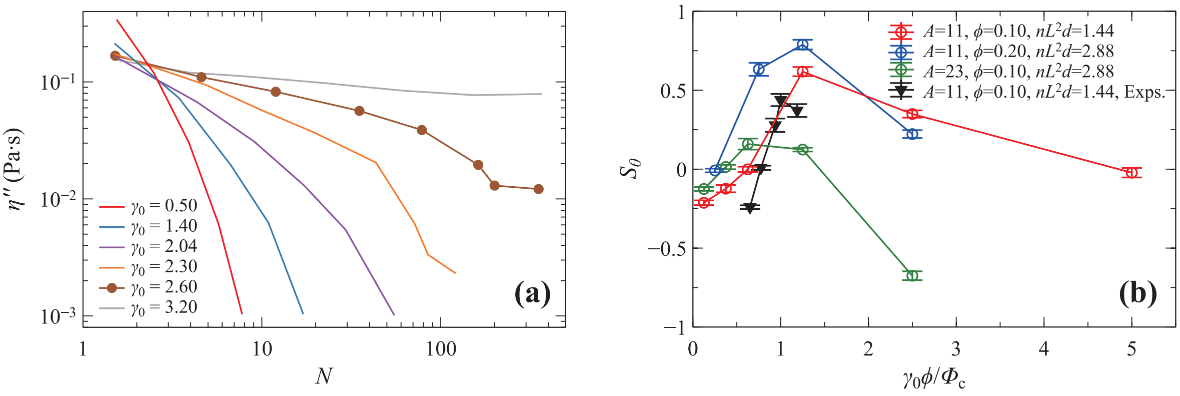

Fig. 9 Oscillatory rheology and orientation distribution for suspensions of rigid rods at a confinement of $H = 1.5L$. **(a)** The value of η'' as a function of oscillation number N at $A = 11$ and $\phi = 0.20$ for a range of strain amplitudes γ_0 (Franceschini et al., 2014). The result for $\gamma_0 < 2.60$ marks a transition between vanishing and persistent values for η''. **(b)** Simulated predictions (Strednak et al., 2021) and an experimental measurement (Franceschini et al., 2014) of the microstructure S_θ at steady state as a function of the rescaled strain amplitude, $\gamma_0\phi/\Phi_c$. A value of 0.4 was used for Φ_c.

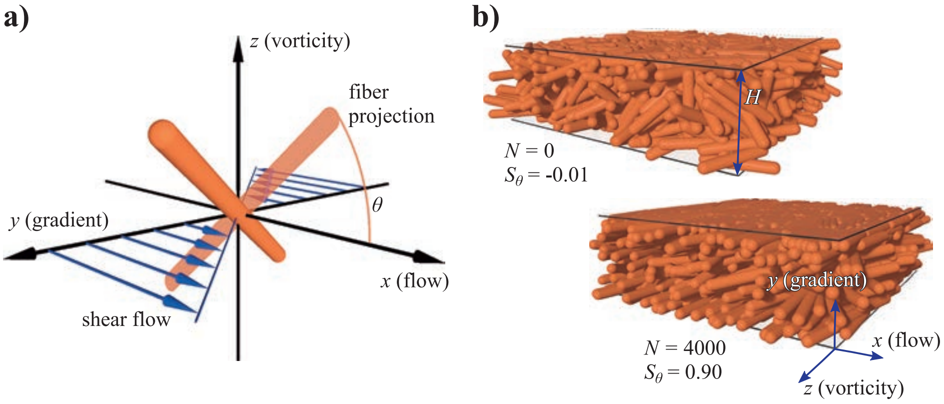

Fig. 10 **(a)** The angle between the fiber's projection in the flow-vorticity plane and the flow direction is θ. The x, y, and z directions are the flow, gradient, and vorticity directions, respectively. **(b)** Reproduced rendering of simulations from Strednak et al. (2021) showing an example initial ($N = 0$) and steady ($N = 4000$) distribution of the fibers for $H = 1.5L$, $A = 11$, $\phi = 0.20$, and $\gamma_0 = 2.5$. Larger values of S_θ reflect an increased alignment of fibers in the vorticity direction.

where θ is the angle between the fiber projection in the flow-vorticity plane and the flow direction as depicted in **Fig. 10a**; the brackets ($\langle\rangle$) indicate an average over all fibers. Note that fibers are perfectly aligned in the flow and vorticity directions when $S_\theta = -1$ and 1, respectively; the gradient direction is perpendicular to the flow-vorticity plane and is the same direction of the confinement in the experiments. Consequently, the large value of S_θ at $\gamma_0 \approx 2.5$ indicates strong alignment of the fibers in the vorticity direction, as can be directly seen in **Fig. 10b** which compares the initial and final distribution of the fibers predicted by simulations. Note that the simulated values of S_θ quantitatively matched the experimental results over a wide range of conditions (Strednak et al., 2021).

Franceschini et al. (2014) suggested that the transition in S_θ and η'' is controlled by a critical effective volume fraction (Φ_c) of the suspension. The effective volume fraction of a fiber suspension is the ratio of the volume swept out by all fibers during a cycle to the total volume of the suspension, and is therefore proportional to the strain amplitude γ_0. The critical effective volume fraction, Φ_c defines the combination of volume fraction ϕ and strain displacement γ_0 at which the particles are forced to contact. For oscillatory shear below Φ_c, Franceschini et al. (2014) speculated that η'' disappears as the suspension rearranges to avoid contact, though simulations indicate that at least some contacts persist (Snook et al., 2012; Strednak et al., 2021). Above Φ_c, contacts between particles must occur during the course of every oscillation and η'' remains finite. As seen in **Fig. 9a** for the case of $A = 11$ and $\phi = 0.20$, the transition in η'' occurs between $\gamma_0 = 2.0$ and 2.6. Consequently, Franceschini et al. (2014) defined $\Phi_c = \gamma_0\phi \approx 0.4$. This corresponds to the value of $\gamma_0\phi$ at which S_θ is maximized for the same conditions of $A = 11$ and $\phi = 0.20$ (blue circles in **Fig. 9b**).

Strednak et al. (2021) found that the maximum value of S_θ declined when the gap spacing H was increased while holding the fiber length L constant, both in experiments and simulations. This indicates that the vorticity alignment of the fibers is promoted by the bounding walls, as was speculated by Snook et al. (2012). This change in orientation distribution with H/L likely impacts the complex viscosity in a qualitative fashion as well. However, rheological data for oscillatory flow currently is lacking for large values of H/L.

4. Normal stresses

Suspensions can exhibit finite normal stress differences during shear. This non-Newtonian property of suspensions holds true even if the suspending fluid exhibits no normal stresses (i.e., the suspending fluid is Newtonian). Hence the normal stress differences originate with the particles, which must be present at a sufficiently high concentration for the normal stresses to be measurable. Non-zero normal stress differences can cause a number of effects, including shear-induced migration of particles within non-linear flows (Nott and Brady, 1994; Nott et al., 2011; Snook et al., 2016; Strednak et al., 2018).

4.1 Measuring normal stresses

Measuring normal stresses for suspensions of rigid fibers requires addressing at least two problems. As with other rheological characterizations, confinement of the particles at high concentrations creates difficulties when using standard shear cells. Additionally, the normal stresses are small and scale linearly with the rate of shear rather than quadratically, as with polymer solutions. As a result, normal stress differences cannot be measured at low rates of shear and concentration using most rotational rheometers, and inertial effects can alter the measurements if the shear rate is increased too much in an attempt to generate a larger force that can be resolved by the transducers.

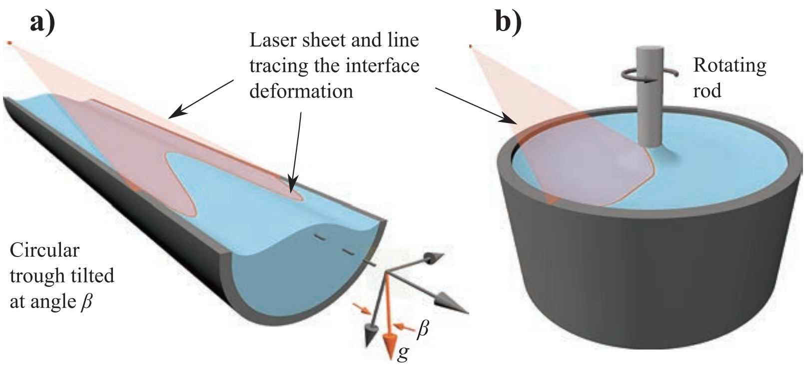

Fig. 11 Free surface flows used to evaluate normal stresses. **(a)** The interfacial deformation of a suspension flowing due to gravity through an open channel flow can be used to determine the second normal stress difference. **(b)** The value of $\alpha_2 + \alpha_1/2$ can be determined from the deformation of the interface in the Weissenberg geometry. In both cases, the deformation can be measured by imaging, from above, the intersection of the surface and a laser sheet projected at a low angle.

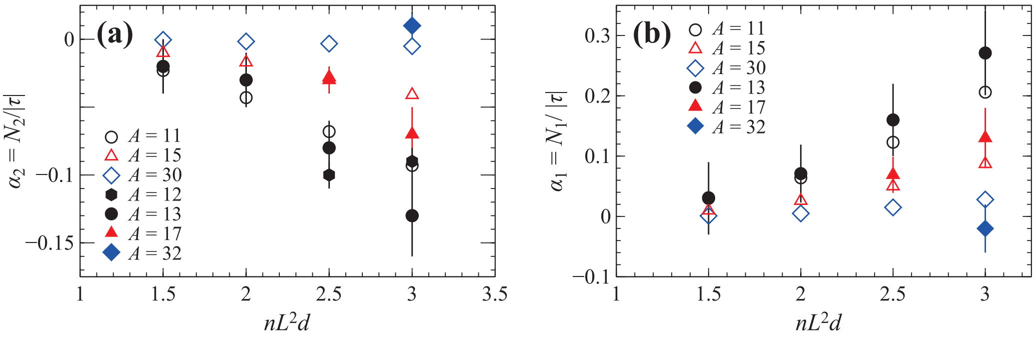

Fig. 12 **a)** The coefficient α_2 for the second normal stress difference as determined from the tilted trough experiments. **b)** The coefficient α_1 as calculated from combining the experimental results from the tilted trough and rotating rod geometries. The experimental results (filled symbols) are compared to simulation results (open symbols) for similar values of the fiber aspect ratios A. All results taken from Snook et al. (2014).

Two approaches for overcoming the challenges of experimentally measuring the normal stresses have been employed. The first makes use of the fact that normal stress differences deform the interface during slow free-surface flows as illustrated in **Fig. 11**. Because the geometries are large, confinement does not influence the measurement. Analysis and experimental approaches using free surface flows originally were developed for viscoelastic fluids (Beavers and Joseph, 1975; Wineman and Pipkin, 1966; Tanner, 1970). Also, the rotating rod geometry (Zarraga et al., 2000; Boyer et al., 2011b) and tilted trough (Couturier et al., 2011; Dai et al., 2013) previously were used to quantify normal stresses in suspensions of spheres. Whether or not the particles are spherical or rod-like, the analysis relating the interface deformations and normal stresses is similar, though also simpler than the analysis for elastic fluids. Each normal stress component is assumed to be proportional to the magnitude of the shear stress, $|\tau|$, and the results are reported as coefficients of the normal stress differences,

$$\alpha_1 = \frac{N_1}{|\tau|} \text{ and } \alpha_2 = \frac{N_2}{|\tau|} \tag{14}$$

where N_1 and N_2 are the first and second normal stress difference. Using either a domain perturbation method or a "cut-away" analysis, while accounting for the tendency of surface tension to flatten the surface, small interface deformation due to normal stress differences can be predicted accurately. The deformation of interface in the tilted trough is related to α_2, while analysis of the interface in the rotating rod geometry yields $\alpha_2 + \alpha_1/2$. Comparing the predicted deformations to those measured in experiments (see **Fig. 11**) enables determination of both coefficients.

The values of α_2 as determined from the tilted trough are shown in **Fig. 12a** (Snook et al., 2014). The values are strongly negative for small aspect ratios and high concentrations. In the case of the rotating rod geometry, Snook et al. (2014) reported that no deformation of the surface was observed across all tested conditions. Using the fact that $\alpha_2 + \alpha_1/2 \approx 0$ together with the results for α_2 gives $\alpha_1 > 0$ for small aspect ratios and high concentrations, as shown in **Fig. 12b**. The result contrasts with suspensions of spheres, where the interface dips near the rotating rod (Zarraga et al., 2000) and α_1 is zero or weakly negative.

The second approach for measuring the bulk normal stresses of rigid fibers used a custom-built torsional flow cell (Bounoua et al., 2016a). As originally described by Dbouk et al. (2013), the device uses an unusually large sep-

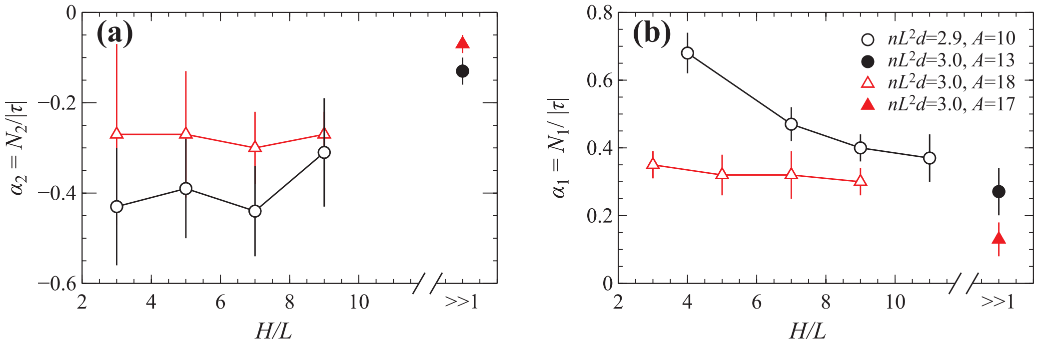

Fig. 13 The normal stress coefficients as a function of confinement, H/L, for **(a)** α_2, the second normal stress difference relative to the shear stress, and **(b)** α_1, the first normal stress difference coefficient. The results of Bounoua et al. (2016a) are compared to those from the free-surface measurements Snook et al. (2014) (marked as $H/L \gg 1$) at similar concentrations of $nL^2d \approx 3.0$ and aspect ratios A between 10 and 18.

aration of up to 2.5 mm between the two plates. An array of force transducers, flush mounted to the stationary plate, enabled measurement of both normal stress difference coefficients, α_1 and α_2 (Bounoua et al., 2016a). This device, by varying the plate spacing and using fibers with lengths of less than 0.5 mm, was used to characterize the normal stresses over a range of confinements from $H/L = 2$ to 11.

Fig. 13a compares measurements at $nL^2d \approx 3.0$ of Bounoua et al. (2016a) as a function of confinement with those from the free surfaces where H/L was very large. The results are qualitatively similar, with $\alpha_2 < 0$, $\alpha_1 > 0$, and the magnitude of the coefficients are smaller at higher aspect ratios. The results for α_1 and α_2 at the smaller aspect ratio of $A = 10$ indicate that the magnitudes decline as the confinement is relaxed, approaching the values attained using the much larger geometries. For the data with $A = 18$, the normal stress coefficients measured with the torsional flow cell are nearly independent of the confinement. However, the magnitude of the coefficients as measured at $H/L >> 1$ are quite different than those for which $H/L < 10$.

4.2 Origin and effects of normal stresses

Normal stress differences within non-colloidal suspensions can arise from hydrodynamic interactions as well as from contact stresses. For spheres at concentrations of $\phi > 0.20$, the balance of an implied shear flow, disturbance velocities created by the presence of the particles, and interparticle forces that maintain hydrodynamic interactions causes an asymmetry in the relative positions of particles pairs. This asymmetry generates a hydrodynamic contribution to the normal stress differences, and there are also contributions from the contact forces. Note that a dilute suspension of spheres ($\phi < 0.02$) has no normal stress differences, as the symmetry of the velocity disturbance does not allow for it. Unlike spheres, individual fibers in a sheared fluid can induce normal stress differences depending on the instantaneous angle with respect to the flow direction. However, normal stress differences do not exist in a dilute suspension since the orientation distribution remains symmetric relative to the flow direction.

Simulations by Snook et al. (2014) demonstrate that even under concentrated conditions, symmetry of the orientation distribution about the direction of flow is not broken. Consequently, the predicted normal stresses shown in **Fig. 12** originate solely from contact interactions. The predicted values of the normal stress coefficients correspond closely to the measured values. At fixed aspect ratio, the magnitudes of α_1 and α_2 are lower for low number densities since there are many fewer contacts. Likewise, fewer contacts occur at higher aspect ratios and fixed concentration, hence the normal stress coefficients (magnitudes) are lower. The relative signs of the coefficients can also be discerned from the simulations, which indicate the fibers align strongly with the direction of flow. As a result, the contact interactions, which are purely repulsive, are strongest in the gradient direction and weakest in the flow direction. This creates the positive values for α_1 and negative values for α_2.

Fig. 12 shows predictions from simulations with periodic boundaries rather than with solid bounding planes separated by a distance H in the gradient direction. However, Snook et al. (2014) also incorporated boundaries into the simulations and verified that the simulations predict that normal stress coefficients depend on confinement. This occurs because the bounding walls of the shearing geometry alter the orientation distribution, and hence the contact interactions between particles which control the normal stresses.

The existence of non-zero normal stresses in a sheared suspension of fibers implies that particles will migrate in inhomogeneous shearing flows according to theories for spherical particles (Nott and Brady, 1994; Nott et al., 2011). This migration creates a non-uniform concentration that further complicates predictions and rheological analysis of the flowing suspensions. The net migration of spheres from regions of high to low shear rates has been reported in multiple publications (Leighton and Acrivos, 1987; Altobelli et al., 1991; Hampton et al., 1997; Snook et al.,

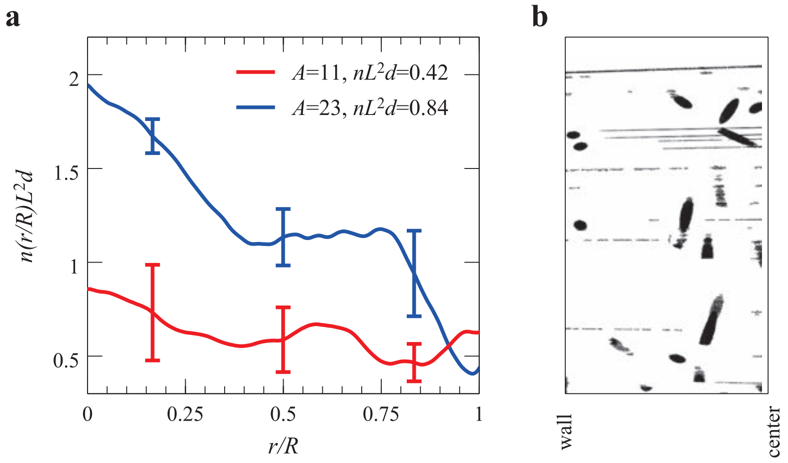

Fig. 14 Experimental data characterizing migration of fibers in tube flow with $L/R \approx 3$ (Strednak et al., 2018). **(a)** Concentration, $n(r/R)L^2d$, as a function of position r within a circular tube of radius R at the same volume fraction of $\phi = 0.03$ for two different aspect ratios of $A = 11$ and 23. In both cases, the ratio of R/L was identical. **(b)** Example image from experiments showing fibers ($A = 11$, $nL^2d = 0.42$) concentrated near the center of the tube.

2016). Currently, there are few studies of the shear-induced migration of rigid fibers, though these studies qualitatively agree with suspensions of spheres. For example, Mondy et al. (1994) measured the spatial distribution of ellipsoids of aspect ratios $A = 2$ to 18.4 within a wide-gap Couette flow and found results similar to that for spheres. More recent measurements (Strednak et al., 2018) indicate that fibers migrate within tube flow, away from the walls and toward the center as expected from observations of spheres. However, significant migration occurs at much smaller volume fractions in suspensions of fibers as compared to spheres. **Fig. 14** shows the position dependent concentration at steady-state for two different aspect ratios for suspensions at $\phi = 0.03$, whereas Snook et al. (2016) observed no particle migration for suspensions of spheres at $\phi < 0.1$. Generally, Strednak et al. (2018) found that the extent of migration for the rigid fibers was similar at the same value of $nL^2d = 4A\phi/\pi$, regardless of the aspect ratio.

5. Conclusions

Various studies related to the experimental and numerical determination of the rheology have been outlined in this review. However, the reviewed studies have been limited to relatively rigid fibers of uniform size suspended under neutrally buoyant conditions in a viscous fluid. Moving away from this limited set of conditions introduces a number of possible complexities, such as Brownian motion and viscoelasticity, to the fluid mechanics and rheology of the suspension system.

Even for the relatively large size of fiber suspensions described in this review, weak and attractive colloidal forces were discussed as a possible cause of shear-thinning. For strongly colloidal suspensions, the rheology can be more complex (Mewis and Wagner, 2011). Notably for some colloidal suspensions of fibers, shear thickening rheology is observed, wherein the viscosity of the suspension increases with an increase in shear rate. Reviews by Barnes (1989) and Brown and Jaeger (2014) provide an in-depth look at the shear thickening of colloidal suspensions of both spherical and elongated particles. At this length scale, various mechanisms are claimed to cause non-Newtonian rheological behavior; more recently, fiber orientation was also attributed to causing shear-thickening (Rathee et al., 2020). Furthermore, shear thickening in colloidal suspensions of elongated particles is often related to the jamming transition (Cates et al., 1998; Liu and Nagel, 1998). However, shear thickening for colloidal suspensions should not be confused with the jamming transition for non-colloidal slurries (i.e., divergence of viscosity with increased concentration), as discussed in Section 3.2.

The stipulated condition of monodispersity of particle size in the experimental and numerical studies described in this review is far removed from real-world applications. For colloidal suspensions near the jamming transition, it is observed that at the same volume fraction, the viscosity and normal stresses measured are lower than that of monodisperse suspensions (Pednekar et al., 2018). Marti et al. (2005) performed rheological measurements for concentrated non-colloidal suspensions, with polydispersity in both shape (mixture of spheres and fibers) and particle size. Accurate and rigorous experimental measurements of the rheology in polydisperse systems continues to be lacking, with particularly few results for suspensions of fibers.

Moving past neutrally buoyant, rigid elongated particles, flexibility adds additional restorative forces to the hydrodynamics and particle-particle interactions, leading to complex non-linear, and irreversible dynamics affecting bulk rheological measurements (du Roure et al., 2019). For non-neutrally buoyant particles in shearing flows, sedimentation (or creaming) is countered only partially by resuspension of spherical particles (Acrivos et al., 1993); the resulting inhomogeneity in the spatial distribution of particles will affect the bulk measurements of rheology. For further reading, Shaqfeh (2019) collates several studies of suspensions of various non-colloidal particles in viscoelastic fluids, including rigid fibers.

Finally, there is a lack of detailed numerical and experimental work describing the microstructure at concentrations beyond the dilute limit and up to the jamming transition. The dependence of bulk rheological measurements on the changes in the microstructure of slurries of elongated particles in flow have been discussed (Franceschini et al., 2011; Snook et al., 2012; Tapia et al., 2017; Strednak et al., 2018). The changes in the microstructure are irreversible in concentrated suspensions which contradict the reversible nature of the Stokes equations, which govern their hydrodynamics. As an illustrative example to motivate more detailed measurements, results obtained from experiments performed by Tapia et al. (2017) show that for higher particle aspect ratio, volume fractions measured exceeded the limit described by numerical simulations performed by Williams and Philipse (2003), who prescribed the maximum isotropic packing fraction of spherocylinders, suggesting local or bulk ordering of the particles. Additionally, the appearance of yield stresses, a phenomenon generally associated with fiber flexibility and studied extensively in the pulp industry, was observed in slurries of rigid particles near the jamming limit, warranting deeper examination.

Even within the limits placed upon the suspension properties, the studies discussed in this review demonstrate that the rheology of slurries of rigid elongated particles is complex and frequently non-intuitive. Recent publications make it clear that care must be taken in interpreting rheological quantities for rigid fibers, especially when measured using confined geometries at large concentration. Failure to consider this latter aspect on the measurements can result in inaccurate assessments of the bulk viscosity, normal stress differences, and oscillatory rheology and dynamics. The enhancements in the measurement and modeling for these systems have been aided significantly by numerical simulations that have been validated against experiments. Continuing advances likely will rely on simulations that incorporate the additional physical mechanisms described in the previous paragraphs.

Acknowledgements

This work was supported by the National Science Foundation (NSF Award No. 1511787 and 1602032) and the CPaSS industrial partners. Any opinions, findings, and conclusions or recommendations expressed in this material are those of the author(s) and do not necessarily reflect the views of the NSF or the CPaSS industry members.

References

Acrivos A., Bingham Award Lecture–1994 Shear-induced particle diffusion in concentrated suspensions of noncolloidal particles, Journal of Rheology, 39 (1995) 813–826. DOI:10.1122/1.550619

Acrivos A., Mauri R., Fan X., Shear-induced resuspension in a Couette device, International Journal of Multiphase Flow, 19 (1993) 797–802. DOI:10.1016/0301-9322(93)90043-T

Altobelli S., Givler R., Fukushima E., Velocity and concentration measurements of suspensions by nuclear magnetic resonance imaging, Journal of Rheology, 35 (1991) 721–734. DOI:10.1122/1.550156

Barnes H.A., Shear-thickening (dilatancy) in suspensions of nonaggregating solid particles dispersed in Newtonian liquids, Journal of Rheology, 33 (1989) 329–366. DOI:10.1122/1.550017

Batchelor G.K., Slender-body theory for particles of arbitrary cross-section in Stokes flow, Journal of Fluid Mechanics, 44 (1970) 419–440. DOI:10.1017/S002211207000191X

Batchelor G.K., Green J.T., The determination of the bulk stress in a suspension of spherical particles to order c^2, Journal of Fluid Mechanics, 56 (1972) 401–427. DOI:10.1017/S0022112072002435

Beavers G., Joseph D., The rotating rod viscometer, Journal of Fluid Mechanics, 69 (1975) 475–511. DOI:10.1017/S002211207500153X

Bennington C.P.J., Kerekes R.J., Grace J.R., The yield stress of fibre suspensions, The Canadian Journal of Chemical Engineering, 68 (1990) 748–757. DOI:10.1002/cjce.5450680503

Bibbó M.A., Rheology of semiconcentrated fiber suspensions, Ph.D. thesis, Massachusetts Institute of Technology (1987). http://hdl.handle.net/1721.1/14875

Bibbó M.A., Dinh S.M., Armstrong R.C., Shear flow properties of semiconcentrated fiber suspensions, Journal of Rheology, 29 (1985) 905–929. DOI:10.1122/1.549836

Bivens C.H., Boney C., Fredd C., Lassek J., Sullivan P., Engels J., Fielder E., Gorham T., Judd T., Mogollon A.E.S., Tabor L., Munoz A.V., Willberg D., New fibers for hydraulic fracturing, Oilfield Review (published by Schlumberger Ltd.), Summer Issue (2005) 34–43.

Blanc F., Peters F., Lemaire É., Local transient rheological behavior of concentrated suspensions, Journal of Rheology, 55 (2011) 835–854. DOI:10.1122/1.3582848

Bounoua S., Kuzhir P., Lemaire É., Normal stress differences in non-Brownian fiber suspensions, Journal of Rheology, 60 (2016a) 661–671.

Bounoua S., Lemaire É., Férec J., Ausias G., Kuzhir P., Shear-thinning in concentrated rigid fiber suspensions: aggregation induced by adhesive interactions, Journal of Rheology, 60 (2016b) 1279–1300. DOI:10.1122/1.4965431

Bounoua S.N., Kuzhir P., Lemaire E., Shear reversal experiments on concentrated rigid fiber suspensions, Journal of Rheology, 63 (2019) 785–798. DOI:10.1122/1.5097658

Boyer F., Guazzelli É., Pouliquen O., Unifying suspension and granular rheology, Physical Review Letters, 107 (2011a) 188301. DOI:10.1103/PhysRevLett.107.188301

Boyer F., Pouliquen O., Guazzelli É., Dense suspensions in rotating-rod flows: normal stresses and particle migration, Journal of Fluid Mechanics, 686 (2011b) 5. DOI:10.1017/jfm.2011.272

Brady J.F., Bossis G., Stokesian dynamics, Annual Review of Fluid Mechanics, 20 (1988) 111–157. DOI:10.1146/annurev.fl.20.010188.000551

Bricker J.M., Park H., Butler J.E., Rheology of semidilute suspensions of rigid polystyrene ellipsoids at high Peclet numbers, Journal of Rheology, 52 (2008) 941–955. DOI:10.1122/1.2930670

Brown E., Jaeger H.M., Shear thickening in concentrated suspensions: phenomenology, mechanisms and relations to jamming, Reports on Progress in Physics, 77 (2014) 046602. DOI:10.1088/0034-4885/77/4/046602

Butler J.E., Snook B., Microstructural dynamics and rheology of suspensions of rigid fibers, Annual Review of Fluid Mechanics, 50 (2018) 299–318. DOI:10.1146/annurev-fluid-122316-045144

Cates M.E., Wittmer J.P., Bouchaud J.P., Claudin P., Jamming, force chains, and fragile matter, Physical Review Letters, 81 (1998) 1841–1844. DOI:10.1103/PhysRevLett.81.1841

Chaouche M., Koch D.L., Rheology of non-Brownian rigid fiber suspensions with adhesive contacts, Journal of Rheology, 45 (2001) 369–382. DOI:10.1122/1.1343876

Cieslinski M.J., Baird D.G., Wapperom P., Obtaining repeatable initial fiber orientation for the transient rheology of fiber suspensions in simple shear flow, Journal of Rheology, 60 (2016) 161–174. DOI:10.1122/1.4938229

Claeys I.L., Brady J.F., Suspensions of prolate spheroids in Stokes flow. Part 2. Statistically homogeneous dispersions, Journal of Fluid Mechanics, 251 (1993) 443–477. DOI:10.1017/S0022112093003477

Couturier É., Boyer F., Pouliquen O., Guazzelli É., Suspensions in a tilted trough: second normal stress difference, Journal of Fluid Mechanics, 686 (2011) 26. DOI:10.1017/jfm.2011.315

Dagois-Bohy S., Hormozi S., Guazzelli É., Pouliquen O., Rheology of dense suspensions of non-colloidal spheres in yield-stress fluids, Journal of Fluid Mechanics, 776 (2015) R2. DOI:10.1017/jfm.2015.329

Dai S.C., Bertevas E., Qi F., Tanner R.I., Viscometric functions for noncolloidal sphere suspensions with Newtonian matrices, Journal of Rheology, 57 (2013) 493–510. DOI:10.1122/1.4774325

Dbouk T., Lobry L., Lemaire E., Normal stresses in concentrated non-Brownian suspensions, Journal of Fluid Mechanics, 715 (2013) 239. DOI:10.1017/jfm.2012.516

Dinh S.M., Armstrong R.C., A rheological equation of state for semiconcentrated fiber suspensions, Journal of Rheology, 28 (1984) 207–227. DOI:10.1122/1.549748

Djalili-Moghaddam M., Toll S., Fibre suspension rheology: effect of concentration, aspect ratio and fibre size, Rheologica Acta, 45 (2006) 315–320. DOI:10.1007/s00397-005-0021-y

Doi M., Edwards S.F., Dynamics of rod-like macromolecules in concentrated solution. Part 1, Journal Chemical Society, Faraday Transactions 2, 74 (1978) 560–570. DOI:10.1039/F29787400560

du Roure O., Lindner A., Nazockdast E.N., Shelley M.J., Dynamics of flexible fibers in viscous flows and fluids, Annual Review of Fluid Mechanics, 51 (2019) 539–572. DOI:10.1146/annurev-fluid-122316-045153

Einarsson J., Candelier F., Lundell F., Angilella J.R., Mehlig B., Effect of weak fluid inertia upon Jeffery orbits, Physical Review E, 91 (2015) 041002. DOI:10.1103/PhysRevE.91.041002.

Einstein A., A new determination of the molecular dimensions, Annalen der Physik, 19 (1906) 289–306.

Elgaddafi R., Ahmed R., George M., Growcock F., Settling behavior of spherical particles in fiber-containing drilling fluids, Journal of Petroleum Science Engineering, 84 (2012) 20–28. DOI:10.1016/j.petrol.2012.01.020

Forgacs O.L., Mason S.G., Particle motions in sheared suspensions: *IX*. Spin and deformation of threadlike particles, Journal of Colloid and Interface Science, 14 (1959) 457–472. DOI:10.1016/0095-8522(59)90012-1

Franceschini A., Filippidi E., Guazzelli É., Pine D.J., Transverse alignment of fibers in a periodically sheared suspension: an absorbing phase transition with a slowly varying control parameter, Physical Review Letters, 107 (2011) 250603. DOI:10.1103/PhysRevLett.107.250603

Franceschini A., Filippidi E., Guazzelli É., Pine D.J., Dynamics of non-Brownian fiber suspensions under periodic shear, Soft Matter, 10 (2014) 6722–6731. DOI:10.1039/C4SM00555D

Gadala-Maria F., Acrivos A., Shear-induced structure in a concentrated suspension of solid spheres, Journal of Rheology, 24 (1980) 799–814. DOI:10.1122/1.549584

Ganani E., Powell R.L., Suspensions of rodlike particles: literature review and data correlations, Journal of Composite Matter, 19 (1985) 194–215. DOI:10.1177/002199838501900301

Guazzelli É., Pouliquen O., Rheology of dense granular suspensions, Journal of Fluid Mechanics, 852 (2018). DOI:10.1017/jfm.2018.548

Hammond P., Settling and slumping in a Newtonian slurry, and implications for proppant placement during hydraulic fracturing of gas wells, Chemical Engineering Sciences, 50 (1995) 3247–3260. DOI:10.1016/0009-2509(95)00152-U

Hampton R.E, Mammoli A.A., Graham A.L., Tetlow N., Altobelli S.A., Migration of particles undergoing pressure-driven flow in a circular conduit, Journal of Rheology, 41 (1997) 621–640. DOI:10.1122/1.550863

Hassanpoura M., Shafighb P., Mahmudb H.B., Lightweight aggregate concrete fiber reinforcement – A review, Construction and Building Materials, 37 (2012) 452–461. DOI:10.1016/j.conbuildmat.2012.07.071

Hinch E.J., Leal L.G., The effect of Brownian motion on the rheological properties of a suspension of non-spherical particles, Journal of Fluid Mechanics, 52 (1972) 683–712. DOI:10.1017/S002211207200271X

Ingber M.S., Mammoli A.A., Vorobieff P., McCollam T., Graham A.L., Experimental and numerical analysis of irreversibilities among particles suspended in a Couette device, Journal of Rheology, 50 (2006) 99–114. DOI:10.1122/1.2169806

Ivanov Y., Van de Ven T.G.M., Mason S.G., Damped oscillations in the viscosity of suspensions of rigid rods. I. Monomodal suspensions, Journal of Rheology, 26 (1982) 213–230. DOI:10.1122/1.549664

Jeffery G.B., The motion of ellipsoidal particles immersed in a viscous fluid, Proceedings of the Royal Society London A, 102 (1922) 161–179. DOI:10.1098/rspa.1922.0078

Krieger I.M., Dougherty T.J., A mechanism for non-Newtonian flow in suspensions of rigid spheres, Transactions of the Society of Rheology, 3 (1959) 137–152. DOI:10.1122/1.548848

Larson R.G., The Structure and Rheology of Complex Fluids, Oxford university press, New York (1999), ISBN: 9780195121971.

Lauga E., Floppy swimming: viscous locomotion of actuated elastica, Physical Review E, 75 (2007) 041916. DOI:10.1103/PhysRevE.75.041916

Leighton D., Acrivos A., The shear-induced migration of particles in concentrated suspensions, Journal of Fluid Mechanics, 181 (1987) 415–439. DOI:10.1017/S0022112087002155

Liu A.J., Nagel S.R., Jamming is not just cool any more, Nature, 396 (1998) 21–22. DOI:10.1038/23819

Liu W., Moran C.J., Vink S., Quantitative risk-based approach for improving water quality management in mining, Environmental Science and Technology, 45 (2011) 7459–7464. DOI:10.1021/es201876c

Lundell F., Söderberg L.D., Alfredsson P.H., Fluid mechanics of papermaking, Annual Review of Fluid Mechanics, 43 (2011) 195–217. DOI:10.1146/annurev-fluid-122109-160700

Mackaplow M.B., Shaqfeh E.S.G., A numerical study of the rheological properties of suspensions of rigid, non-Brownian fibres, Journal of Fluid Mechanics, 329 (1996) 155–186. DOI:10.1017/S0022112096008889

Marti I., Höfler O., Fischer P., Windhab E.J., Rheology of concentrated suspensions containing mixtures of spheres and fibres, Rheologica Acta, 44 (2005) 502–512. DOI:10.1007/s00397-005-0432-9

Maschmeyer R.O., Hill C.T., Rheology of concentrated suspensions of fibers in tube flow. II. An exploratory study, Transactions of the Society of Rheology, 21 (1977) 183–195. DOI:10.1122/1.549453

Mewis J., Wagner N.J., Colloidal Suspension Rheology, Cambridge Series in Chemical Engineering, Cambridge University Press (2011). DOI:10.1017/CBO9780511977978

Mondy L.A., Brenner H., Altobelli S.A., Abbott J.R., Graham A.L., Shear-induced particle migration in suspensions of rods, Journal of Rheology, 38 (1994) 444–452. DOI:10.1122/1.550522.

Mongruel A., Cloitre M., Shear viscosity of suspensions of aligned non-Brownian fibres, Rheologica Acta, 38 (1999) 451–457. DOI:10.1007/s003970050196.

Morris J.F., Boulay F., Curvilinear flows of noncolloidal suspensions: the role of normal stresses, Journal of Rheology, 43 (1999) 1213–1237. DOI:10.1122/1.551021

Narumi T., See H., Honma Y., Hasegawa T., Takahashi T., Phan-Thien N., Transient response of concentrated suspensions after shear reversal, Journal of Rheology, 46 (2002) 295–305. DOI:10.1122/1.1428321

Nott P.R., Brady J.F., Pressure-driven flow of suspensions: simulation and theory, Journal of Fluid Mechanics, 275 (1994) 157–199. DOI:10.1017/S0022112094002326

Nott P.R., Guazzelli É., Pouliquen O., The suspension balance model revisited, Physics of Fluids, 23 (2011) 043304. DOI:10.1063/1.3570921

Osiptsov A.A., Fluid mechanics of hydraulic fracturing: a review, Journal of Petroleum Science and Engineering, 156 (2017) 513–535. DOI:10.1016/j.petrol.2017.05.019

Park J., Butler J.E., Inhomogeneous distribution of a rigid fibre undergoing rectilinear flow between parallel walls at high Peclet numbers, Journal of Fluid Mechanics, 630 (2009) 267–298. DOI:10.1017/S0022112009006545

Patra P., Bhambhani T., Vasudevan M., Nagaraj D., Somasundaran P., Transport of fibrous gangue mineral networks to froth by bubbles in flotation separation, International Journal of Mineral Processing, 104 (2012) 45–48. DOI:10.1016/j.minpro.2011.11.007

Pednekar S., Chun J., Morris J.F., Bidisperse and polydisperse suspension rheology at large solid fraction, Journal of Rheology, 62 (2018) 513–526. DOI:10.1122/1.5011353

Peters F., Ghigliotti G., Gallier S., Blanc F., Lemaire E., Lobry L., Rheology of non-Brownian suspensions of rough frictional particles under shear reversal: a numerical study, Journal of Rheology, 60 (2016) 715–732. DOI:10.1122/1.4954250

Petrie C.J.S., The rheology of fibre suspensions, Journal of Non-Newtonian Fluid Mechanics, 87 (1999) 369–402. DOI:10.1016/S0377-0257(99)00069-5

Pham P., Metzger B., Butler J.E., Particle dispersion in sheared suspensions: crucial role of solid-solid contacts, Physics of Fluids, 27 (2015) 051701. DOI:10.1063/1.4919728

Powell R.L., Rheology of suspensions of rodlike particles, Journal of Statistical Physics, 62 (1991). DOI:10.1007/BF01128178

Rampall I., Smart J.R., Leighton D.T., The influence of surface roughness on the particle-pair distribution function of dilute suspensions of non-colloidal spheres in simple shear flow, Journal of Fluid Mechanics, 339 (1997) 1–24. DOI:10.1017/S002211209600479X

Rao S.R., Finch J.A., A review of water re-use in flotation, Mineral Engineering, 2 (1989) 65–85. DOI:10.1016/0892-6875(89)90066-6

Rathee V., Arora S., Blair D.L., Urbach J.S., Sood A.K., Ganapathy R., Role of particle orientational order during shear thickening in suspensions of colloidal rods, Physical Review E, 101 (2020) 040601. DOI:10.1103/PhysRevE.101.040601

Schiek R.L., Shaqfeh E.S.G., A nonlocal theory for stress in bound, Brownian suspensions of slender, rigid fibers, Journal of Fluid Mechanics, 296 (1995) 271–324. DOI:10.1017/S0022112095002138

Sepehr M., Carreau P.J., Moan M., Ausias G., Rheological properties of short fiber model suspensions, Journal of Rheology, 48 (2004) 1023–1048. DOI:10.1122/1.1773783

Shaqfeh E.S.G., Fredrickson G.H., The hydrodynamic stress in a suspension of rods, Physics of Fluids A: Fluid Dynamics, 2 (1990) 7–24. DOI:10.1063/1.857683

Shaqfeh E.S.G., On the rheology of particle suspensions in viscoelastic fluids, AIChE Journal, 65 (2019) e16575. DOI:10.1002/aic.16575

Snook B., Butler J.E., Guazzelli É., Dynamics of shear-induced migration of spherical particles in oscillatory pipe flow, Journal of Fluid Mechanics, 786 (2016) 128–153. DOI:10.1017/jfm.2015.645

Snook B., Davidson L.M., Butler J.E., Pouliquen O., Guazzelli É., Normal stress differences in suspensions of rigid fibres, Journal of Fluid Mechanics, 758 (2014) 486–507. DOI:10.1017/jfm.2014.541

Snook B., Guazzelli É., Butler J.E., Vorticity alignment of rigid fibers in an oscillatory shear flow: Role of confinement, Physics of Fluids, 24 (2012) 121702. DOI:10.1063/1.4770141

Somasundaran P., Patra P., Bhambani T., Nagaraj D.R., Rheology of ore suspensions with fibrous minerals and its impact on flotation performance, Mining, Metallurgy & Exploration, 36 (2019) 111–116. DOI:10.1007/s42461-018-0040-8

Strednak S., Butler J.E., Bergougnoux L., Guazzelli É., Fiber alignment in oscillating confined shearing flows, Physical Review Fluids, 6 (2021) 014302. DOI:10.1103/PhysRevFluids.6.014302

Strednak S., Shaikh S., Butler J.E., Guazzelli É., Shear-induced migration and orientation of rigid fibers in an oscillatory pipe flow, Physical Review Fluids, 3 (2018) 091301. DOI:10.1103/PhysRevFluids.3.091301

Switzer L.H., Klingenberg D.J., Rheology of sheared flexible fiber suspensions via fiber-level simulations, Journal of Rheology, 47 (2003) 759–778. DOI:10.1122/1.1566034

Tanner R., Some methods for estimating the normal stress functions in viscometric flows, Transactions of the Society of Rheology, 14 (1970) 483–507. DOI:10.1122/1.549175

Tapia F., Shaikh S., Butler J.E., Pouliquen O., Guazzelli E., Rheology of concentrated suspensions of non-colloidal rigid fibres, Journal of Fluid Mechanics, 827 (2017) R5. DOI:10.1017/jfm.2017.552

Wandersman E., Quennouz N., Fermigier M., Lindner A., Du Roure O., Buckled in translation, Soft Matter, 6 (2010) 5715–5719. DOI:10.1039/C0SM00132E

Williams S.R., Philipse A.P., Random packings of spheres and spherocylinders simulated by mechanical contraction, Physical Review E, 67 (2003) 051301. DOI:10.1103/PhysRevE.67.051301

Wineman A.S., Pipkin A., Slow viscoelastic flow in tilted troughs, Acta Mechanica, 2 (1966) 104–115. DOI:10.1007/BF01176732

Young Y.N., Shelley M.J., Stretch-coil transition and transport of fibers in cellular flows, Physical Review Letters, 99 (2007) 058303. DOI:10.1103/PhysRevLett.99.058303

Zarraga I.E., Hill D.A., Leighton Jr D.T., The characterization of the total stress of concentrated suspensions of noncolloidal spheres in Newtonian fluids, Journal of Rheology, 44 (2000) 185–220. DOI:10.1122/1.551083

Zurita-Gotor M., Bławzdziewicz J., Wajnryb E., Motion of a rod-like particle between parallel walls with application to suspension rheology, Journal of Rheology, 51 (2007) 71–97. DOI:10.1122/1.2399084

Authors’ Short Biographies

Saif Shaikh

Saif Shaikh earned a Ph.D. in chemical engineering from the University of Florida, USA under the guidance of Dr. Jason E. Butler, as well as a Ph.D. in physics and mechanics of fluids from the University of Aix-Marseille, France. His doctoral work focused on characterizing the rheological behavior of concentrated suspensions of rigid, non-colloidal fibers. His contributions further extended the understanding of complex fluid dynamics near the fluid-solid transition, which remains largely unexplored. Saif is interested in applying his experimental skills and knowledge-base to help develop, optimize, and market products and technology to the scientific and industrial community.

Scott Strednak

Scott Strednak received B.S. degrees in Paper Science and Engineering and Chemical Engineering from North Carolina State University in 2014. He also received his Ph.D. in Chemical Engineering from the University of Florida in 2020, where he performed experimental and numerical work on spatial and orientation distributions of concentrated suspensions of rigid fibers in oscillatory flows.

Jason E. Butler

Jason E. Butler is a Professor of Chemical Engineering at the University of Florida (Gainesville, Florida). His educational and research expertise is the dynamics of complex fluids, and his work spans theoretical, computational, and experimental approaches to resolving questions that impact a wide range of applications. Among other achievements, Jason has contributed to the theory and modeling of sedimentation and rheology of non-spherical particles, the Brownian dynamics of rigid polymers and colloidal fibers, and the electrokinetics of polyelectrolytes.

KONA Powder and Particle Journal No. 39 (2022) 100–109/https://doi.org/10.14356/kona.2022014 Review Paper

A Review of Distribution and Segregation Mechanisms of Dockage and Foreign Materials in On-Farm Grain Silos for Central Spout Loading[†]

Fuji Jian

Department of Biosystems Engineering, University of Manitoba, Canada

Abstract

Dockage and foreign material (DFM) distribution in grain silos is an important factor in managing stored grain. The DFM distribution in grain silos is dictated by the segregation mechanisms of DFM during grain loading. Loading grain into silos from a central spout is a special case of heap flows of granular materials. However, our understanding of heap flows is still evolving, and no models are currently available to predict the dockage and foreign material distribution in grain silos. Based on an extensive literature review, this paper identified the dominant mechanisms of DFM segregations during central spout filling in grain silos and main factors influencing DFM distribution. The DFM distribution patterns were characterized. The experimental methods for analyzing DFM segregations and distribution were also reviewed. The gaps of our knowledge on segregation mechanisms and factors influencing segregation were summarized and future research directions and challenges were discussed.

Keywords: dockage and fine material distribution, segregation mechanism, farm silo, stored grain

1. Introduction

Flat and hopper bottom cylindrical silos (bins) are commonly used in North America for on-farm storage of crop grains (cereal grains, oil seeds, and pulses). In Canada and USA, almost all of the harvested crop grains are stored in this type of silos. Typically, grain is lifted to the roof height of silo with a grain auger (or a bucket elevator) and discharged into the silo through a central spout. Grain contains dockage and foreign materials (DFM), which are different from grain kernels in terms of physical properties, such as density, size, and shape. The differences between grain kennels and DFM result in segregation during silo loading, causing ununiform distribution of DFM in the grain bulk. Ununiform distribution of DFM leads to uneven airflow through the grain bulk, which adversely affects grain storage management operations, such as aeration, drying, and fumigation for insect control. For example, if airflow is uneven, grain at the low airflow locations might not be cooled or dried, which may lead to grain spoilage during storage. There are very limited studies on the DFM distribution in on-farm grain silos, although segregation in granular materials during handling has been extensively studied (Fan et al., 2017; Gray, 2018; Mosby et al., 1996). Applying the knowledge of particle segregation to analyzing the DFM distribution may help to better understand the distribution of DFM in grain silos, thus improving management of stored grain to reduce grain spoilage.

Loading grain into silos through a central spout from the roof top is a special case of surface flows of granular materials, that is, a thin layer of grain continuously flows on the top of a nearly quiescent granular bed. Even though granular surface flows are important in many industrial practices and natural systems, and have been extensively studied, our understanding of surface flows is still incomplete at present, and in particular no constitutive laws are currently able to predict and explain all the range of segregation behaviors of DFM in grain silos. The relevant segregation mechanisms involved in DFM distribution have yet to be identified, although there were several studies on DFM distribution inside grain silos (Bartosik and Maier, 2006; Chang et al., 1981; 1983; Jayas, 1987; Narendran et al., 2019; Salarikia, et al., 2021).

Fan et al. (2017) extensively reviewed physical mechanisms of heap segregation and developed predictive models. Similar reviews were conducted by Gray (2018), and Mosby et al. (1996). However, these reviews did not provide any specific information of heap segregation for farm grain silos filled by a central spout. The review in this article focused exclusively on the segregation of DFM inside on-farm grain silos. The main objectives of this review

---

[†] Received 21 June 2021; Accepted 2 August 2021
J-STAGE Advance published online 11 September 2021
Add: Winnipeg, MB R3T 5V6, Canada
E-mail: Fuji.jian@umanitoba.ca
TEL: +1-204-474-7965

were to identify the main mechanism(s) of DFM segregation and main factors influencing these mechanisms. Commonly used experimental methods and mathematical models to analyze segregations and DFM distribution were also reviewed.

2. Segregation mechanisms in grain silos filled by central spouting

Researchers have reported different mechanisms of particle segregation, including agglomeration, air current, avalanche, bouncing, displacement, embedding, fluidization, impact, percolation, push-away, rolling, sifting, sliding, and trajectory (Fan et al., 2017; Jian et al., 2019; Mosby et al., 1996; Tang and Puri, 2004). During grain loading and unloading, more than one of these mechanisms occur simultaneously, and some of these mechanisms overlap with each other or act as a special case of another mechanism. Jian et al. (2019) attributed the primary patterns of segregation to four main mechanisms in bulk grain handling: trajectory, fluidization, sifting, and impact segregation. Another phenomenon, avalanche, could result in sifting and fluidization segregation and induce variations of DFM distribution at the silo center and walls.

2.1 Trajectory segregation

When a mixture of particles with different sizes, shapes and densities leaves a loading equipment, such as a spout, auger, and conveyor, at an initial velocity, dense and larger particles have higher momentums than light and small particles. In addition, particle shape and size differences also result in different air drag forces while the particles are moving in the air. Due to this combined effect of momentum and drag force small and light particles do not travel as far as large and dense particles, and thus accumulate under the spout at the center of silos (**Fig. 1**). After the particles have landed on the heap, the momentum in the horizontal direction causes them to roll or slide along the heaped surface and small particles percolate through the pores among larger particles during rolling or sliding, resulting in sifting segregation. The momentum in the vertical direction pushes particles far away from the drop location, resulting in impact segregation.

If the initial velocity of particles leaving the loading equipment is zero in the horizontal direction, rolling and sliding occur on the surface of heap due to the difference in repose angle between different materials, resulting in sifting segregation.

The consequence of trajectory segregation during central spout loading is that fines, small stones, other particles larger and denser than grain kernels, such as internode and wild oat kernels, and other larger grain kernels with similar density are concentrated at the central of the silo (**Fig. 1**). This result was consistent with the observations reported in the literature. Salarikia et al. (2021) found that broken and shrunk kernels even distributed from the center to the walls in a grain silo. This could be explained by their similar shapes and densities as the small grain kernels, which were not segregated from the sound grain kernels. Other particles which are larger and less dense than grain kernels, such as chaff, straw, knuckle, rachis, and spikelet, could be more influenced by sifting segregation on the heap surface.

2.2 Impact segregation

When particles hit the heap surface, larger particle can push small particles further down the heap surface towards the silo periphery (**Fig. 1**) due to lower mass of the small particles (Carson et al., 1986). This impact segregation may result in a wider distribution of some small particles, while the larger particles mostly stay at the heap center. Narendran et al. (2019) found that small canola kernels were concentrated at the periphery of the bin filled with clean wheat mixed with soybean, red kidney bean, and canola. The authors suggested the impact segregation was responsible for the canola distribution, while some of red kidney bean and soybean kernels were embedded in the wheat mixture after pushing away the canola kernels. Furthermore, impact and trajectory segregation also result in the same distribution for large and heavy particles (like stones). For small particles, even though impact segregation can result in a different segregation pattern from trajectory and sifting segregation, its effect in farm silos might be minimum because of the low percentage of the large and

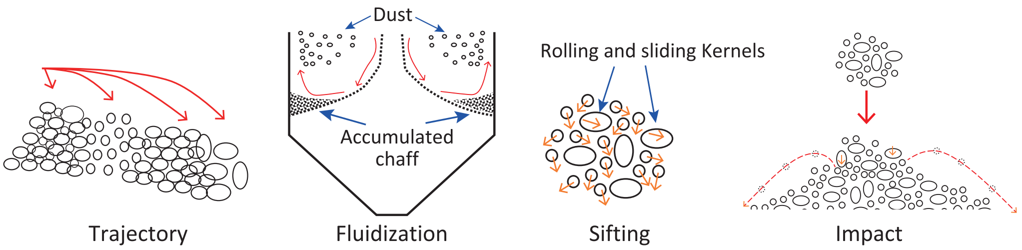

Fig. 1 Schematic of four primary segregation mechanisms in bulk materials.

heavy particles in grains (Jian et al., 2019). In other words, impact segregation might not a main mechanism for the DFM distribution pattern in farm silos.

2.3 Fluidization segregation

Fluidization segregation can occur when a grain bulk containing light materials such as dusts and small chaff is loaded into a silo and the drop height is high enough to induce air currents by the moving streams of grain (Carson et al., 1986; Mosby et al., 1996). The effect of the air currents increases with the increase of drop height and loading rate. This type of fluidization segregation results in settling of dust and chaff on the surface of the grain pile (**Fig. 1**), which might not influence the DFM distribution because dust and chaff on the heap surface would be further segregated on the heap surface due to the surface flows. Fluidization segregation can also occur when the grain mixture fluidizes on the surface of the heap and pushes lighter and larger particles away from the heap center (Zigan et al., 2008). This type of fluidization segregation might be more influenced by the avalanche segregation (**Fig. 2**). The dust content is usually much lower than other impurities in stored grain (Jian et al., 2019). Therefore, fluidization segregation in farm silos might not be a main mechanism influencing the DFM distribution.

2.4 Sifting (sieving) segregation

Sifting segregation occurs when particles are moving over each other (**Fig. 1**), e.g., particles in the grain bulk roll or slide down on the surface of a grain pile when the angle of the heap is larger than the repose angle of the grain bulk. The heap surface acts like a sieve and smaller particles are more likely to be embedded in the surface pores and gradually percolate down to the bottom of the moving layer, while larger particles have a higher probability of sliding or rolling down further from the top of the heap and stay on the surface (Ketterhagena et al., 2007; Nourmohamadi-Moghadami et al., 2020; Tang and Puri, 2004). Johanson et al. (2005) identified three requirements for sifting: 1) the fines must be small enough to fit through the pores in the coarse matrix; 2) inter-particle motion must exist to allow fine particle to be exposed to multiple voids, and 3) the fines need to be significantly free flowing to pass through the pores and result in percolation. Carson et al. (1986) concluded that sifting (sieving) was the most important mechanism in heap segregation when the content of fines was low because when there were enough large particles to form a moving layer, the fines could pass through this layer and percolate downwards. The effect of sifting segregation is that small particles end up at the locations close to the heap center, which is similar to the pattern of trajectory segregation. Grain bulks usually have low concentrations of fines and the size ratio of grain kernels to the fines is usually larger than 1.5 (Makse et al., 1998), which explains why stratification rarely occurs and the sifting segregation for fines in grain silos might be one of the main mechanisms.

2.5 Avalanche segregation

Avalanche segregation on heaped surfaces has been extensively studied (Dahmen et al., 2011; Fan et al., 2017; Gray, 2018; Lemieux and Durian, 2000; Pouliquen et al., 1997; Woodhouse et al., 2012), but not specific to loading of crop grain into storage silos. Narendran et al. (2019) were the first to report the occurrence of avalanche during grain loading. At low loading rates, the particles can build up at the apex of the pile and the dynamic angle of repose gradually increases. After the dynamic angle of repose becomes larger than the static repose angle of the heap, the dynamic angle collapses, which results in an intermittent and periodical avalanche. Sifting segregation occurs during avalanching because small particles percolate to the bottom of the flowing layer and large particles move upwards as the grain and DFM mixture moves along the heaped surface. This results in a stratification pattern which has interleaved layers of large and small particles. The stratification layers are then buried by subsequent avalanches, which ultimately may result in a Christmas tree distribution pattern. At high loading rates, the grain continuously moves down the heap, resulting in fines close to the drop point and the large particle close to the base of the heap or the silo walls (**Fig. 2**). Surface avalanches, during which the grain bulk can shear and dilate freely on the heap surface, provide the

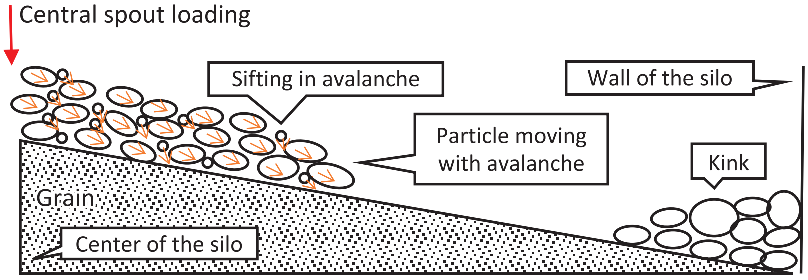

Fig. 2 Schematic of avalanche segregation and kink.

ideal conditions for segregation because: 1) shear force on the surface of the heap could slow down the moving of the particles and different velocities of different particles will enlarge spaces between them; 2) more large spaces make more particles sifting down possible; and 3) low velocities give particles more time to sift down. In certain situations (e.g., condensed chaff at the moving front of avalanches), the large particles are stopped before the flowing particles reach the base of the pile, which leads to the formation of a kink. This kink moves in the direction opposite to the flow of grain, conserving its profile until it reaches the top of the pile. When a grain bulk contains a small number of larger particles (than the grain kernels), a kink might not occur, but the silo walls might produce the same effect as the kink movement when grain kernels have a small repose angle (**Fig. 2**). A kink will not occur when grain particles in different avalanches move together. The phenomena of kink and Christmas tree have not been reported during grain loading.

A structure of “Christmas tree” had been observed in discrete avalanching flow (Gray, 2018; Khakhar et al., 2001; Lemieux and Durian, 2000). The “Christmas tree” distribution of DFM would not be observable during grain loading if frequency of avalanche is high so that grain mixtures in different avalanches move together at the same time. This high frequency can occur at high loading rate which was observed in most published studies (Bartosik and Maier, 2006; Chang et al., 1981; 1983; Jayas, 1987; Narendran et al., 2019; Salarikia et al., 2021) and during grain loading into farm silos (**Fig. 2**). If the total percentage of DFM is low, the “Christmas tree” distribution will not occur neither (Narendran et al., 2019).

Segregation patterns due to avalanches are dependent on several factors, including how the heap forms, the heap geometry, the loading rate, and the size ratios of the particles on the heap (Mosby et al., 1996). Even though avalanche is a simple phenomenon, its occurrence is difficult to predict, and it is not known how and when it occurs under what grain loading conditions. Therefore, DFM segregation due to avalanche is also not fully known. Avalanches might frequently and irregularly develop at the free surface of heaps. Therefore, segregation due to avalanche is complex because the heap geometry changes continuously during grain loading, and so do the static and dynamic angles of repose on the heap. The angle of repose is mostly influenced by irregularity of the particles (e.g., larger sphericity has a smaller repose angle) and the composition of the particle assembly at the apex, both might change continuously during grain loading. At the same time, high moving speed of avalanche can cause fines and larger particles to move far away from the central drop point, resulting in sifting segregation and wide distribution of fines. Grain mixtures can either segregate into layers or remain mixed, dependent on the balance between particle-size and particle-density segregation. Therefore, segregation due to avalanche could result in variations of DFM distribution even at the same grain loading conditions and might be the main reason causing the DFM variations at the center and walls. This speculation should be further verified.

3. Segregation mechanisms responsible for DFM distribution during grain loading

Grain loading consists of several consecutive steps: heap formation at the drop point, particles moving along the heap surface and stopping at the walls, and avalanches occurring at the apex of the heap. Therefore, multiple segregation processes (mechanisms) occur simultaneously when grain is loaded into the silo. Most experiments reported in the literature only presented the final conditions after the grain had been loaded into the silos. It is difficult to systematically assess each segregation mechanism at each step of grain loading.

In on-farm grain silos in Canada and USA, the DFM is usually lower than 1 % and occasionally could reach to the maximum 15 % (Jian et al., 2019). When the DFM concentration is low, the trajectory and sifting segregation might become more significant. Avalanching can intensify sifting segregation and fluidization segregation of chaff. Therefore, these main segregation processes (trajectory, sifting, and avalanche segregation) result in a concentrated distribution of smaller and denser particles (smaller than the sound grain kernels) at the center and larger and lighter (than the sound grain kernels) particles at the walls. The cleanest location (minimum amount of fines and chaff) is the annular area about the midway between the silo center and walls (Jayas, 1987; Salarikia et al., 2021). Even though different researchers had different conclusions on the dominant mechanisms of segregation and the factors influencing segregation, they usually reported this similar distribution pattern (Bartosik and Maier, 2006; Chang et al., 1981; 1983; Salarikia et al., 2021), and the only exception is the fine distribution in canola silos (Jayas, 1987) (**Table 1**). Chang et al. (1981) reported that more than 10 % fines were found at center of a corn silo, while less than 4 % fines were found at other locations. In a wheat silo, Chang et al. (1983) found more than 4 % of fines were at the silo center, while less than 4 % fines at other locations. In a 10-meter diameter silo, fine particles, dust, fragments, and foreign materials (corn and soybean kernels) mainly accumulated in the center, while chaff accumulated mostly near the walls (Salarikia et al., 2021). Jayas (1987) found chaff was concentrated near the walls of a canola silo.

Table 1 Measured distribution of dockage and foreign materials in different studies.

Test condition [a]	Definition of DFM	DFM distribution	Sources
Corn was dropped at 7 m height into a 6.4 m diameter flat bottom silo through a spout. Initial velocity was about 0.12 m/s	Particles passed through sieve (4.8 mm diameter round-hole) were fines	Fine at center ranged from 2 to 22 % and average of 4.5 % in the bin	(Chang et al., 1981)
Grain was dropped through an orifice at 7.4 m height into a silo with 6.4 m diameter. Choke flow with 0.6 to 0.7 m/s initial loading velocity. Initial fines were 2.00, 3.17, and 3.87 % for wheat, corn, and sorghum, respectively.	Particles passed through a sieve (1.6×9.5 mm^2 oblong-hole for wheat, 4.8 mm diameter round-hole for corn, 2.0 mm circle triangular-hole for sorghum) were fines	Fines were concentrated in the bin center within a radius of about 60 cm and as 4 to 5 times higher than the average	Chang et al. (1983)
Canola (6 to 10 % moisture content) was dropped at 7.2 m height into a 4.6 m diameter flat bottom silo	Chaff and canola were retained on a 1.7 mm and 1.18 mm opening meshes, respectively. Fines passed through the 1.18 mm mesh	Chaff was concentrated near walls. The center and walls had the similar fines	Jayas (1987)
Wheat (12.2 % moisture content) was dropped at 6 m height from a funnel with 0.2 m by 0.3 m outlet to a 10 m diameter flat bottom silo. Auger with 45 t/h was used to load the wheat to the funnel	Wheat kernels < 3.35 mm and > 2.0 mm. Other particles or other grains were ≥ wheat kernels (≥ 2.0 mm). Fines were pieces of broken wheat kernels, awn, broken chaff, and canola kernels (≥ 0.3 mm and < 2.0 mm. Dusts < 0.3 mm	Other particles were concentrated near the walls. Fines and dusts were concentrated at the bin center	Salarikia et al. (2021)
Yellow dent shelled corn was dropped at 7 m height into a 6.4 m diameter flat bottom bin through a spout. Initial fines were < 6 %	Particles passed a sieve (4.8 mm round hole opening) were fines, while retained on the sieve were corn	Fines in the center and walls ranged from 11.6 to 24.8 % and from 1.7 to 2.2 %, respectively	Stephens and Foster (1976)
Wheat mixture (including less than 6 % kidney bean, soybean, and canola) was dropped at 2.4 m height into a 2 m diameter circular steel ring	Three sieves with apertures of 7.09, 4.75 and 2.45 mm were used to separate the grain mixture. Grain mixture was cleaned before test	Canola was concentrated near walls, kidney and soybean were concentrated at the middle radius	Narendran et al. (2019)

[a] Drop height is the initial height and this height is gradually decreased as the increase of grain depth in the silo. Grain is dropped at the roof centers of the bins in all tests.

4. Factors influencing segregation

Many factors influence DFM distribution, including the bin size and shape; physical properties of particles (grain kernels and other materials), such as the size and size distribution and size ratio, percentage of dockage and foreign materials, density, moisture content, shape and shape factor, modulus of elasticity, friction coefficient, surface texture, cohesion, and adhesion; and process variables (loading method, loading direction and rate, drop height, size of the loading outlet, heap size, and mixing ratio). The factors that are mostly studied include the drop height, grain type, silo size, and composition of grain bulks. Less studied factors are the loading method, loading direction and speed (loading rate), and the size of loading outlet. There are several reports on DFM distribution by using spreaders. However, spreader is rarely used now due to the increased airflow resistance.

4.1 Drop height

Researchers have drawn different conclusions on the effect of drop height. Narendran et al. (2019) investigated the effect of three different drop heights of 0.8, 1.6 and 2.4 m on segregation of canola, kidney beans, and soybeans mixed with wheat in a 2 m diameter steel ring. All grains were cleaned before test and at ≤ 11 % moisture content (wet basis). They concluded that loading height significantly influenced the distribution for canola but not for soybeans and kidney beans and the DFM distribution in canola was mainly dictated by the impact segregation. Nourmohamadi-Moghadami et al. (2020) found that as the drop height decreased in a 1-m diameter bin filled with shelled corn, broken kernels and foreign materials found in the periphery of the bin decreased. They explained that the velocity of the particles in the flowing layer of the grain on the heap surface decreased as the drop height decreased, which gave more time to the small particles to be embedded among large particles. Wheat in a 10 m diameter silo was studied for five loading heights (1.6, 2.5, 3.4, 4.3 and 5.2 m) by Salarikia et al. (2021). They observed that the drop height significantly influenced the radial distribution of fine particles, dust, and fragments, but not the distribution of other grain kernels (corn, soybean, white bean) and other particles (straw, internode, knuckle, rachis, spikelet, large chaff, wild oat kernels and stem) mixed in the wheat. Even though the drop height influenced the fines and dusts, no particular distribution pattern was found. Chang et al. (1986) observed that the drop height up to 7.4 m had no significant effect on the distribution of fines in bulk corn. Jayas (1987) reported that the effect of drop height up to 7 m on the distribution of fines and chaff in canola was insignificant. These different observations could be explained by the low drop height in the reported studies (≤ 7 m) and different definitions of fines. A greater drop height mostly results in more impact segregation which embeds more larger particles and bounces more small particles away from the silo center. The amounts of larger particles and small particles are usually lower than the fines and chaff in grain silos, and therefore the drop height effect on DFM distribution might not be observable.

4.2 Silo diameter

Heap formation during grain loading is one of the main reasons that trigger particle segregation because sifting segregation occurs as the particles move down on the heap surface. Increase of the silo diameter leads to greater moving distances, hence large silos would intensify segregation (Mosby et al., 1996). However, Prasad (1974) reported that the distribution of dockage (smaller and larger than wheat kernels in bulk wheat) followed the same trend in 4.2 m and 5.4 m diameter bins. But it was not known whether this no-difference was caused specifically by the small silo diameters or not.

4.3 Size ratio

The difference in particle sizes (or the size ratio) is the most important reason for segregation in bulk materials. The degree of segregation increases with the increase of the size ratio. Unfortunately, size ratio was not reported in the literature related to the segregation of crop grain mixtures because it was difficult to quantify the size ratio in a crop grain mixture with different particle sizes. Therefore, size ratio can be estimated by using the average size of sound kernels and the average size of the segregated particles. Stephens and Foster (1978) pointed out that the segregation of fines (smaller than 1.2 mm) in wheat and sorghum (larger than 2.0 mm) was lower than the segregation in corn (larger than 4.8 mm). However, Chang et al. (1983) showed no difference in the trend of fine distribution between corn, wheat, and sorghum in 6.4 m diameter silos.

4.4 Percentage of DFM and moisture content

The percentage of DFM and moisture content of grain might also influence the particle segregation because: 1) grain kernel with a higher moisture content is usually larger than the same kernel with a lower moisture content; 2) grain kernels with different moisture contents might have different shapes and different friction forces between kernels; 3) different amounts of DFM could influence the occurrence (frequency and size) of avalanches and associated segregation; and 4) more DFM with a larger size ratio could result in more impact and kink segregations. In a silo, different parts might be subjected to different segregation mechanisms if the percentage of dockage and foreign materials, moisture content of the grain mixture change. However, Narendran et al. (2019) found that the percentage of other grains (kidney bean, soybean, and canola) in the wheat bulk did not have any significant effect on the distribution and segregation of the other grains.

4.5 Missing link

It is generally agreed that segregation can be influenced by many factors, but these factors are not all considered in most studies. Specifically, 1) most studies only separated the larger and smaller particles from the grain kernels (**Table 1**); 2) some factors were not controlled or difficult to control (**Table 1**), so the multifactor effects or interaction of multifactors might be missed if only examining the final DFM distribution; and 3) the segregation mechanisms might be induced from the DFM distribution, and these mechanisms are usually specified in a qualitative mode, which further contributes to the mystery of the effect of these factors on segregation.

5. Experimental studies

5.1 Focus of measurements

One of the main reasons why particle segregation is remained somewhat mysterious is that it is difficult to collect the evolving particle size distribution data to verify the segregation mechanisms. In grain storage management, the most concerned detrimental effects of DFM distribution are: airflow resistance during drying and aeration; insect multiplication and fungi infestation in concentrated DFM regions; uneven distribution of fumigants during fumigation; and uneven distribution of gases (CO_2, N_2, and O_2) during controlled atmosphere storage. Therefore, most methods used to measure the DFM segregation are designed to determine the airflow resistance and sample the loaded grain to determine the DFM distribution after the loading is completed. Compared to sampling grain for DFM determination, airflow resistance measurement is relatively easy because it only needs to run the fan and measure the airflow rate at the surface of the grain bulk. However, this method can only provide an indirect indication of the DFM distribution, not the actual DFM distribution.

5.2 Field studies

There are a few studies on the mechanisms of segregation of DFM in grain silos filled by center spouts (**Table 1**). Typical size on-farm grain silos with 4 to 10 m diameter and up to 7.5 m drop heights have been tested (**Table 1**). The tested crops included corn, wheat, sorghum, and canola. Most of these studies were aimed to compare the DFM distributions between spreader loading and spout loading. It was found that spreader loading increased the airflow resistance even though the DFM distribution was more even than spout loading. In these studies, grain at different locations was sampled after loading, and larger impurities (chaff), small impurities, and grain kernels were separated from the grain samples by using sieves. All these studies did not further separate the larger and smaller impurities except one study conducted by Salarikia et al. (2021). Salarikia et al. (2021) further separated the small impurities into shrunken and broken kernels, fine particles, and dusts and fragments. The larger impurities were further separated into stones, other grains, and other particles by using sieves. This further separation provided more details of the DFM distribution in silos.

5.3 Laboratory studies

Under lab conditions, the following factors influencing DFM distribution have been studied: drop height, components of the grain bulk (mixture), filling method, loading rate, and fill pipe diameter (Narendran et al., 2019). The lab studies have improved our understanding of DFM segregation mechanisms, but they are usually conducted by using smaller than 2 m diameter silos or rings, which limits the heap size (please refer 4.2).

5.4 Limitations of current studies

One of the common limitations in most studies is the focus on the DFM distribution without exploring the segregation mechanisms. Few studies have isolated the main segregation mechanisms from other mechanisms. If only measuring the final distribution, experiments are simple because just loading the grain mixture into a grain silo can achieve this goal. However, identifying particle movement and segregation mechanisms during their movement requires different approaches and complex techniques, such as high quality imaging and laser tracing (Lemieux and Durian, 2000; Pouliquen et al., 1997). Due to the lack of information associated with the segregation of moving grain kernels, segregation mechanisms and their impact on DFM distribution can only be inferred from the final observed DFM distribution, which might generate uncertainties. Currently, segregation mechanisms of grain kernels are also inferred from studies using non-grain kernels such as sand and lead particles. Some early studies on the segregation mechanisms of these non-grain particles used the mechanical approaches such as mass and momentum balances of the purely frictional fluid (Savage and Hutter, 1989), slow heap formation of cellular automata (Frette et al., 1996), conservation of particles being absorbed into the stationary heap or eroded from the heap into the flowing layer (Bouchaud et al., 1994), and quasi-two-dimensional heap formation of open and closed systems (Khakhar et al., 2001). These approaches and models are capable of describing the qualitative behavior of the system, but they cannot predict the quantitative distribution of DFM in grain silos because these predictions require the estimation of several phenomenological parameters associated with grain kernels and identification of the dominant segregation mechanisms, which have not been fully understood.

5.5 Inconsistencies

5.5.1 Confusion of definitions

Different studies use different definitions of DFM which might lead to different conclusions. For example, fines are usually defined in the literature as the particles smaller than grain kernels (**Table 1**). However, different grain kernels have different sizes, and the fines have different sizes in different reports. For example, Jayas (1987) defined the fines as the particles passing through a Tyler woven wire mesh with 1.18 mm opening and canola kernels were the underflow of a 1.70 mm opening and overflow of the 1.18 mm opening (**Table 1**). Chang et al. (1983) defined the particle passing 1.6×9.5 mm^2 oblong-hole for wheat, 4.8 mm diameter round-hole for corn, 2.0 mm circle triangular-hole for sorghum. Salarikia et al. (2021) defined the fines as the particles smaller than 2.0 mm. Therefore, fine distribution inside canola bulks should have different patterns from larger grain kernels if we define the fine as the particles less than the grain kernels. Salarikia et al. (2021) found dusts were concentrated in the bin center, while Jayas (1987) found fines were not concentrated at the center of the bin, and the concentration of fines near the bin center was almost equal to that near the sides of the bin. These results are not comparable due to the inconsistency in definitions.

5.5.2 Different sampling methods

Another reason generating different conclusions of DFM distribution might be the method of sampling. Different researchers used different sample sizes and units. Most researchers took less than 1 kg samples at few locations and only separated chaff and fines from the samples (Bartosik and Maier, 2006; Chang et al., 1981; 1983; Jayas, 1987). Considering the uneven distribution and low concentration of DFM, a few samples of 1 kg grain taken from a silo holding more than 100 tons of grain might not represent the DFM distribution (Jian et al., 2014). Salarikia et al. (2021) took about 22 kg at each sample location and different categories of DFM were further separated: stones, other grains, other particles, shrunken and broken kernels, fine particles, dusts, and fragments. Based on the larger samples, this study had different conclusions from other published studies on the distribution of shrinkage and broken grain kernels, other particles, dust and fragments, and small and larger grain kernels.

6. Mathematical and numerical modeling

6.1 Mathematical modeling

Even though there is no theoretical model developed to directly describe the DFM segregation in grain silos with spout filling, models related to heap segregation have been in existence. Some models are developed based on continuum of mass and advection diffusion combined with flux function. Some examples are the one-dimensional models developed by Bridgwater et al. (1985) and Savage and Lun (1988), and two-dimensional models developed by Dolgunin and Ukolov (1995). Many models are developed based on mixture theory (Gray and Ancey, 2015; Tunuguntla et al., 2014), and Gray et al. (2015) provided an extensive review on these models. Non-diffuse theory is also used by researchers to develop models describing particles sheared over large heap surface (Pouliquen et al., 1997; Pouliquen and Vallance, 1999; Woodhouse et al., 2012). Depth-averaged models have been developed to describe avalanches and finger instability (Woodhouse et al., 2012). Other approaches such as segregation induced by shear force (Fan and Hill, 2011), pure density (Tripathi and Khakhar, 2013), and size (Marks et al., 2012) have been tested. Gray et al. (2015) provided a review on the modeling of a single avalanche (without mass exchange). Even though these models mentioned above can help us to understand the segregation mechanisms, these models are not capable of predicting DFM segregation in silos because they only consider the binary mixture or three components. Gray (2018) reviewed these equations and solution techniques. Even though polydisperse mixture might be able to be modeled, some additive decomposition mechanisms must be introduced, hence the complexity. Marks et al. (2012) developed an alternative theory for polydisperse segregation with a continuous grain-size distribution that is closer to the reality of both industrial and geophysical materials. This model must be solved simultaneously in five dimensions: space, time, and the three dimensions of grain-size coordinates.

It should be noted that the models discussed above only considered the open flow. Segregation in grain silos is the closed flow except at the beginning of loading before grain reaches the walls. The complexity of these models, as well as the difficulties to solve the equations in the models, limits the practical applicability of these models to predicting particle distributions.

6.2 DEM modeling

The discrete element method (DEM) has been used to simulate the segregation of particle mixtures, but these simulations are mostly used as a tool to understand the segregation principles by using the idealized materials and are not yet at the stage of simulating segregation in real grain silos. For example, by using DEM simulation, Pereira et al. (2011) verified a continuum theory based on a species balance equation in the flowing layer by balancing the convective flow with diffusion and segregation fluxes. Khakhar et al. (1999) used transport equations from the kinetic theory of mixtures for a mixture of nearly elastic smooth particles to analyze density segregation. Marks et al. (2012) used the approach based on partial stresses in their DEM simulation. Tripathi and Khakhar (2013) simulated the segregation of granular mixtures of equal-size particles with different densities. Using three-dimensional DEM model, Fan and Hill (2011) proved that a gradient of shear rate alone could drive segregation in dense sheared systems. The effect of shear caused small particles to move to the regions of low shear rate and large particles in the opposite direction. Currently, DEM simulations are typically limited to spherical particles, and it is difficult to treat particles having irregular shapes and a wide size distribution directly because of mathematical complexity and computational demand. The compromise is to treat the particles as “spherical particles with an equivalent rolling behavior to the particle with arbitrary shape” (Shimoska et al., 2013). This assumption increases the prediction error, and the error is usually unacceptable for the grain industry because grain kernels and DFM are usually not spherical particles.

7. Challenges and directions for future research

A challenge of studying segregation in grain silos is the difficulty in collecting the reliable detailed data which can be used to identify the effect of individual segregation mechanisms. High speed camera and laser used to capture the motion of individual kernels during grain loading might be the examples of collecting the reliable detailed data for the understanding of segregation mechanisms. Another challenge is to develop predictive models capable of handling multiple segregation factors and mechanisms. Currently, researchers mostly focus on the final distribution which can be directly used for grain storage management. There are rarely fundamental studies on segregation mechanisms and factors influencing these segregation mechanisms. Without studying segregation mechanisms and factors influencing segregation, focusing only on the DFM distribution might impede the understanding of the segregation mechanisms.

8. Conclusions

Loading grain into silos from a central spout is a most common method used by the grain industry in the world and a special case of heap flows of granular materials. This loading method results in a concentrated distribution of smaller and denser particles (smaller than the sound grain kernels) at the center and larger and lighter (than the sound grain kernels) particles at the walls of silos. The main mechanisms responsible for this distribution pattern are trajectory, sifting, and avalanche segregations. The main factors influence these main segregation mechanisms are size ratio and percentage of DFM and moisture content, while the contribution of drop height and silo diameter to this distribution pattern is not known due to limited studies and contradictory reports on these factors. The following facts also contribute to our incomplete understanding of this distribution pattern: 1) both lab and field studies focus on final distribution of DFM; 2) inconsistencies of term definition, sampling method, and sample analysis; and 3) no theoretical model is developed to directly explain the DFM segregation in grain silos. One of challenges of studying segregation in grain silos is the difficulty in collecting the reliable detailed data which can be used to identify the effect of individual segregation mechanisms. Fundamental studies on segregation mechanisms and factors influencing these segregation mechanisms in the future might help our understanding of this distribution pattern and develop a theoretical model to predict this distribution pattern.

Acknowledgements

The author thanks the Natural Sciences and Engineering Research Council of Canada for partial funding of this study; and Canada Foundation for Innovation, Manitoba Research Innovation Fund, and several other partners for creating research infrastructure. The author thanks Dr. Qiang Zhang, University of Manitoba, Canada, for commenting on the earlier version of the manuscript.

References

Bartosik R.E., Maier D.E., Effect of airflow distribution on the performance of NA/LT in-bin drying of corn, Transactions of the ASABE, 49 (2006) 1095–1104. DOI: 10.13031/2013.21715

Bouchaud J.P., Cates M.E., Prakash J.R., Edwards S.F., A model for the dynamics of sandpile surface, Journal de Physique I, 4 (1994) 1383–1410. DOI: 10.1051/jp1:1994195

Bridgwater J., Foo W., Stephens D., Particle mixing and segregation in failure zones – theory and experiment, Powder Technology, 41 (1985) 147–158. DOI: 10.1016/0032-5910(85)87033-9

Carson J.W., Royal T.A., Goodwill D.J., Understanding and eliminating particle segregation problems, Bulk Solids Handling, 6 (1986) 141–146.

Chang C.S., Convers H.H., Lai F.S., Distribution of fines and bulk density of corn as affected by choke-flow, spout-flow, and drop-height, Transactions of the ASAE, 29 (1986) 618–620. DOI: 10.13031/2013.30201

Chang C.S., Converse H.H., Martin C.R., Bulk properties of grain as affected by self-propelled rotational type grain spreaders, Transactions of the ASAE, 26 (1983) 1544–1550. DOI: 10.13031/2013.34167

Chang C.S., Shackelford L.E., Lai F.S., Martin C.R., Miller B.S., Bulk properties of corn as affected by multiple-point grain spreaders, Transactions of the ASAE, 24 (1981) 1632–1636. DOI: 10.13031/2013.34504

Dahmen K.A., Ben-Zion Y., Uhl J.T., A simple analytic theory for the statistics of avalanches in sheared granular materials, Nature Physics, 7 (2011) 554–557. DOI: 10.1038/nphys1957

Dolgunin V.N., Ukolov A.A., Segregation modelling of particle rapid gravity flow, Powder Technology, 83 (1995) 95–103. DOI: 10.1016/0032-5910(94)02954-m

Fan Y., Hill K.M.T., Theory for shear-induced segregation of dense granular mixtures, New Journal of Physics, 13 (2011) 1–30. DOI: 10.1088/1367-2630/13/9/095009

Fan Y., Jacoba K.V., Reireich B., Lueptow R.M., Segregation of granular materials in bounded heap flow: a review, Powder Technology, 312 (2017) 67–88. DOI: 10.1016/j.powtec.2017.02.026

Frette V., Christensen K., Malthe-Sorensen A., Feder J., Jossang T., Meakin P., Avalanche dynamics in a pile of rice, Nature, 379 (1996) 49–52. DOI: 10.1038/379049a0

Gray J.M.N.T., Particle segregation in dense granular flows, Annual Review of Fluid Mechanics, 50 (2018) 407–433. DOI: 10.1146/annurev-fluid-122316-045201

Gray J.M.N.T., Ancey C., Particle-size and density segregation in granular free-surface flows, Journal of Fluid Mechanics, 779 (2015) 622–668. DOI: 10.1017/jfm.2015.438

Gray J.M.N.T., Gajjar P., Kokelaar P., Particle-size segregation in dense granular avalanches, Comptes Rendus Physique, 16 (2015) 73–85. DOI: 10.1016/j.crhy.2015.01.004

Jayas D.S., Resistance of bulk canola oilseed to airflow, PhD dissertation, University of Saskatchewan, 1987. http://hdl.handle.net/10388/7893

Jian F., Jayas D.S., White N.D.G., How many kilograms of grain per sample unit is big enough? Part II – Simulation of sampling from grain mass with different insect densities and distribution patterns, Journal of Stored Products Research, 56 (2014) 67–80. DOI: 10.1016/j.jspr.2013.05.006.

Jian F., Narendran R.B., Jayas D.S., Segregation in stored grain bulks: kinematics, dynamics, mechanisms, and minimization—a review, Journal of Stored Products Research, 81 (2019) 11–21. DOI: 10.1016/j.jspr.2018.12.004

Johanson K., Eckert C., Ghose D., Djomlija M., Hubert M., Quantitative measurement of particle segregation mechanisms, Powder Technology, 159 (2005) 1–12. DOI: 10.1016/j.powtec.2005.06.003

Ketterhagena W.R., Curtisb J.S., Wassgrenc C.R., Kongd A., Narayane P.J., Hancock B.C., Granular segregation in discharging cylindrical hoppers: a discrete element and experimental study, Chemical Engineering Science, 62 (2007) 6423 – 6439. DOI: 10.1016/j.ces.2007.07.052

Khakhar D.V., Mccarthy J.J., Ottino J.M., Mixing and segregation of granular materials in chute flows, Chaos, 9 (1999) 594–610. DOI: 10.1063/1.166433

Khakhar D.V., Orpe A.V., Andresen P., Ottino J.M., Surface flow of granular materials: model and experiments in heap formation, Journal of Fluid Mechanics, 441 (2001) 255–264. DOI: 10.1017/s0022112001005201

Lemieux P.A., Durian D.J., From avalanches to fluid flow: a continuous picture of grain dynamics down a heap, Physical Review Letters, 85 (2000) 4273–4276. DOI: 10.1103/physrevlett.85.4273

Makse H.A., Ball R.C., Stanley H.E., Warr S., Dynamics of granular stratification, Physical Review E, 58 (1998) 1–12. DOI: 10.1103/physreve.58.3357

Marks B., Rognon P., Einav I., Grain size dynamics of polydisperse granular segregation down inclined planes, Journal of Fluid Mechanics, 690 (2012) 499–511. DOI: 10.1017/jfm.2011.454

Mosby J., de Silva S.R., Enstad G.G., Segregation of particulate materials – mechanisms and testers, KONA Powder and Particle Journal, 14 (1996) 31–43. DOI: 10.14356/kona.1996008

Narendran R.B., Jian F., Jayas D.S., Fields P.G., White N.D.G., Segregation of canola, kidney bean, and soybean in wheat bulks during bin loading, Powder Technology, 344 (2019) 307–313. DOI: 10.1016/j.powtec.2018.12.042

Nourmohamadi-Moghadami A., Zare D., Singh C.B., Stroshine R.L., Filling of a grain silo. Part 1: Investigation of fine material distribution in a small scale center-filled silo, Biosystems Engineering, 191 (2020) 145–156. DOI: 10.1016/j.biosystemseng.2020.01.001

Pereira G., Sinnott M., Cleary P., Liffman K., Metcalfe G., Stalo I., Insights from simulations into mechanisms for density segregation of granular mixtures in rotating cylinders, Granular Matter, 13 (2011) 53–74. DOI: 10.1007/s10035-010-0223-6

Pouliquen O., Delour J., Savage S.B., Fingering in granular flows, Nature, 386 (1997) 816–817. DOI: 10.1038/386816a0

Pouliquen O., Vallance J.W., Segregation induced instabilities of granular fronts, Chaos, 9 (1999) 621–630. DOI: 10.1063/1.166435

Prasad D.C., Abiotic and biotic characteristics of freshly-harvested grain, MSc dissertation, University of Manitoba, 1974. http://hdl.handle.net/1993/13475

Salarikia A., Jian F., Jayas D.S., Zhang Q., Segregation of dockage and foreign materials in wheat during loading into a 10-meter diameter corrugated steel bin, Journal of Stored Products Research, 93 (2021) 101837. DOI: 10.1016/j.jspr.2021.101837

Savage S.B., Hutter K., The motion of a finite mass of granular material down a rough incline, Journal of Fluid Mechanics, 199 (1989) 177–215. DOI: 10.1017/s0022112089000340

Savage S.B., Lun C.K.K., Particle size segregation in inclined chute flow of dry cohesionless granular solids, Journal of Fluid Mechanics, 189 (1988) 311–335. DOI: 10.1017/s002211208800103x

Shimoska A., Nousou I., Shirakawa Y., Hidaka J., Effect of particle shape on size segregation of particles, Chemical Engineering Transactions, 32 (2013) 2143–2148. DOI: 10.3303/CET1332358

Stephens L.E., Foster G.H., Bulk properties of wheat and grain sorghum as affected by a mechanical grain spreader, Transactions of the ASAE, 19 (1978) 1217–1221. DOI: 10.13031/2013.35471

Tang P., Puri V., Methods for minimizing segregation: a review, Particulate Science and Technology, 22 (2004) 321–337. DOI: 10.1080/02726350490501420

Tripathi A., Khakhar D.V., Density difference-driven segregation in a dense granular flow, Journal of Fluid Mechanics, 717 (2013) 643–669. DOI: 10.1017/jfm.2012.603

Tunuguntla D.R., Bokhove O., Thornton A.R., A mixture theory for size and density segregation in shallow granular free-surface flows, Journal of Fluid Mechanics, 749 (2014) 99–112. DOI: 10.1017/jfm.2014.223

Woodhouse M.J., Thornton A.R., Johnson C.G., Kokelaar B.P., Gray J.M.N.T., Segregation-induced fingering instabilities in granular free-surface flows, Journal of Fluid Mechanics, 709 (2012) 543–580. DOI: 10.1017/jfm.2012.348

Zigan S., Thorpe R.B., Tuzun U., Enstad G.G., Battistin F., Theoretical and experimental testing of a scaling rule for air current segregation of alumina powder in cylindrical silos, Powder Technology, 183 (2008) 133–145. DOI: 10.1016/j.powtec.2007.11.030

Author's Short Biography

Fuji Jian

Dr. Fuji Jian is a professional engineer and Assistant Professor in the Department of Biosystems Engineering at the University of Manitoba, Canada. Fuji's research interests are in post-harvest grain quality, stored-product protection, drying and aeration of grains, insect control, particle segregation, and sensor development with the sole purpose to enhance food safety and security. He is the lead author in 85 of more than 100 technical articles in scientific journals, conference proceedings and books.

KONA Powder and Particle Journal No. 39 (2022) 110–118/https://doi.org/10.14356/kona.2022002 Review Paper

Synthesis of Noble Metals and Their Alloy Nanoparticles by Laser-Induced Nucleation in a Highly Intense Laser Field†

Takahiro Nakamura*, **Yuki Yamazaki and Shunichi Sato**

Institute of Multidisciplinary Research for Advanced Materials, Tohoku University, Japan

Abstract

The synthesis of noble metals and their alloy nanoparticles by laser-induced nucleation is described. Femtosecond laser pulses with an energy on the order of mJ were tightly focused to create an intensity of 10^{14} W/cm^2 or more in an aqueous solution of noble metal ions. The intense laser field generated solvated electrons and hydrogen radicals that have a highly reducing ability, resulting in nucleation through the reduction of the noble metal ions and particle growth through ripening. This laser-induced nucleation method can be performed without any reducing agents. Excess irradiation of chloroauric acid solution led to the formation of a stable colloidal solution of gold nanoparticles without any surfactants. Additionally, the irradiation of a mixed solution of different noble metal ions formed solid–solution alloy nanoparticles, even though these metals were immiscible in the bulk. Moreover, the laser-induced nucleation made it possible to form quinary solid-solution alloy nanoparticles of noble metals. The mechanism of superior catalytic activity found for alloy nanoparticles by using Rh–Pd–Pt solid–solution nanoparticles is discussed in terms of elemental distributions inside the particles.

Keywords: high-intensity laser field, femtosecond laser, nanoparticles, solutions, noble metals

1. Introduction

Lasers have a variety of excellent features in terms of wavelength, output, pulse width, spectral width, and so on. As a result, many applications have been developed in a wide range of fields, such as communication, information technology, and medicine in both academic and industrial societies. In particular, in laser processing, lasers are rapidly expanding the application range, for example, heating, welding, cutting, drilling, marking, surface modification, particle synthesis and thin film deposition by laser ablation, and additive manufacturing. From the viewpoint of the morphological transformation of a material, these process techniques include top-down or bottom-up approaches between large- and small-scale materials. One of the merits of laser processing is the ability to sustain the crystalline structure, composition, and property of the materials during the process.

Currently, with the progress of laser technology, especially, ultrafast pulse generation and regenerative amplification, the laser output has become strong enough to generate an unprecedented ultra-intense optical field. Supposing that a laser pulse with a pulse energy of 1 mJ and a pulse width of 100 fs is focused to an area of 10 μm^2 by aberration-free optics, the peak intensity at the focal point will be 10^{17} W/cm^2, according to calculations. This value is comparable to the Coulomb field inside the hydrogen atom, which is 5.0×10^{11} V/m, corresponding to the light intensity of 7.0×10^{16} W/cm^2. Such an ultrahigh electric field is not achievable by conventional electric techniques and is expected to result in a novel reaction field in materials science. The reaction in this unprecedented field would be different from those in a thermal equilibrium state at high temperature achieved by commonly used processing techniques and could offer an ultimate reaction field that has never existed on Earth. Highly intense laser science, however, has mainly focused on gas-phase reactions (Cornaggia et al., 1995; Cornaggia, 1995; Castillejo et al., 1999; Talebpour et al., 2000), where the density of atoms, ions, fragments, and molecules are dilute enough to ignore their interactions. As a result, the production of species and molecules different from the starting materials in a condensed state, such as a liquid or solid, has been outside of the scope of highly intense laser science for a long time.

As a next step, small particle synthesis by laser irradiation of a solid target immersed in liquid has been reported, which utilized the high energy density state created by the confinement effect of plasma in liquid (Wang et al., 2002; Pearce et al., 2004). In this pulsed laser ablation in liquid (PLAL), a uniformly dense reaction field was formed to

---

† Received 30 June 2020; Accepted 16 August 2020

* Corresponding author: Takahiro Nakamura;
Add: 2-1-1 Katahira, Aoba-ku, Sendai 980-8577, Japan
E-mail: nakamu@tohoku.ac.jp
TEL: +81-22-217-5672 FAX: +81-22-217-5671

avoid the generation of large debris by suppressing the laser energy. In contrast, as mentioned earlier, if ultrashort laser pulses with an energy on the order of mJ are strongly focused to a diffraction-limited small spot, an ultrahigh intense laser field can be created in condensed matter, like liquid or solid, by using a commercially available regenerative amplifier laser system. In this intense laser field, photoionization and photodissociation of materials will instantly lead to the formation of high-temperature and high-density plasma. The expansion of the plasma will be strongly suppressed, and the temperature will be rapidly cooled down by the surrounding high-density and low-temperature materials, resulting in a non-equilibrium process that is much faster than conventional processes.

We focused on the non-linear and non-equilibrium reaction field created near the focal point of ultrafast laser pulses with a high peak power and addressed the nanoparticle (NP) synthesis of noble metals and their alloys in the highly intense laser field. In this review, we describe the distinguishing properties found for NPs fabricated by highly intense laser irradiation of aqueous solutions of metallic ions, especially, the synthesis of stable colloidal solutions of gold (Au) NPs without any dispersants, the catalytic activity of alloy NPs, and the synthesis of solid–solution quinary alloy NPs.

2. Experimental procedures

A schematic drawing of the experimental setup is shown in **Fig. 1**. Focused femtosecond laser pulses were irradiated on aqueous solutions of metal ions held in a fused-silica cuvette for a predetermined time. The laser pulses were generated from a regenerative amplifier of a mode-locked Ti:sapphire oscillator. The center wavelength was 800 nm, the pulse width was 100 fs, the maximum pulse energy was 6 mJ, and the maximum repetition rate was 1 kHz. The laser pulses were delivered from the side of the cuvette and were focused near the center of the cuvette by an aspherical lens with a focal length of 8 mm and a numerical aperture of 0.5. The lens diameter of 10 mm was the same as the beam diameter of the laser pulses. In **Fig. 1**, the drawing corresponds to a stationary system, where the liquid sample was held in the cuvette, whereas a flow system was available by circulating the liquid sample with a feed pump to substantially increase the production rate of NPs (Muttaqin et al., 2015). This was because the liquid flow was able to remove the bubbles that were generated by the laser irradiation of the liquid sample, as shown in **Fig. 1**, and interrupted normal focusing of the laser pulses.

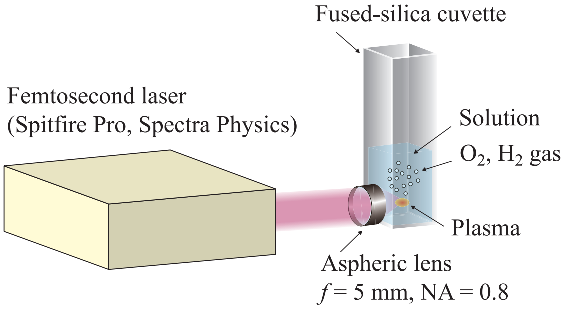

Fig. 1 Schematic of the experimental setup.

The intensity of light at the focus can be calculated to be 3×10^{18} W/cm^2 if we ignore the aberration of the focusing optics. However, the lens used in the experiment was not optimized for this experimental condition. The diameter of the focus was estimated to be 175 μm mainly due to the spherical aberration at the interfaces between air/glass and glass/liquid, resulting in an intensity at the focus of 2.5×10^{14} W/cm^2, which was sufficiently strong enough to induce photodissociation and photoionization of the liquid sample.

3. Formation mechanism of noble metal and alloy nanoparticles in the highly intense laser field

The nanoparticle synthesis of noble metals and their alloys that we developed was not based on a conventional morphological change of materials but a physicochemical reaction induced by the highly intense laser field. The process is accomplished by the reduction of metal ions with solvated electrons and hydrogen radials, which are generated by photodissociation and photoionization of water molecules. Below, the synthesis of gold (Au) NPs by highly intense laser irradiation of an aqueous chloroauric acid solution is presented as a typical example. When an aqueous chloroauric acid solution was irradiated, a bright flash of plasma emission near the focal point and the generation of hydrogen and oxygen gas were observed. With increasing irradiation time, the transparent aqueous solution changed to red purple, which corresponded to localized surface plasmon resonance (LSPR) of Au NPs at approximately 520 nm. In fact, many spherical Au NPs with an average size of 10 nm were observed by transmission electron microscopy (TEM). From these observations, the following mechanism for the nanoparticle synthesis was inferred.

$$\begin{aligned} 2\mathrm{H_2O}\ (h\nu) &\rightarrow 2\mathrm{H_2O}^{*} \rightarrow 2\mathrm{H_2O}^{+} + 2\mathrm{e}^{-} \\ &\rightarrow 2\mathrm{e}^{-}_{\mathrm{aq}} + \mathrm{OH}^{\bullet} + \mathrm{H_3O}^{+} \end{aligned} \tag{1}$$

$$\begin{aligned} &\mathrm{e}^{-}_{\mathrm{aq}} + \mathrm{H_3O}^{+} \rightarrow \mathrm{H}^{\bullet} + \mathrm{H_2O} \\ &\qquad k_1 = 2.3 \times 10^{10}\ \mathrm{dm^3 mol^{-1} s^{-1}} \end{aligned} \tag{2}$$

$$\begin{aligned} &\mathrm{e}^{-}_{\mathrm{aq}} + \mathrm{OH}^{\bullet} \rightarrow \mathrm{OH}^{-} \\ &\qquad k_2 = 3.0 \times 10^{10}\ \mathrm{dm^3 mol^{-1} s^{-1}} \end{aligned} \tag{3}$$

$$M^{+} + e^{-}_{aq} \rightarrow M^{0} \tag{4}$$

$$M^{+} + H^{\bullet} \rightarrow H^{+} + M^{0} \tag{5}$$

$$M^{0} + M^{0}_{2} \rightarrow \cdots \rightarrow M^{0}_{n} \tag{6}$$

When an intense laser is used to irradiate an aqueous solution, solvated electrons (e^{-}_{aq}), hydrogen radicals ($H^{\bullet}$), and hydroxy radicals ($OH^{\bullet}$) are generated by multi-photon absorption and avalanche photoionization (Eqs. 1 and 2). According to a pump–probe experiment, this process would be completed in several hundred femtoseconds. Monte Carlo simulations predicted that the solvated electrons recombine on the picosecond order (Eqs. 2 and 3), and the formation of hydroxy ions is more dominant (Thomsen et al., 1999). The redox potentials of a solvated electron and hydrogen radical are –2.77 V_{SHE} and –2.10 V_{SHE}, respectively, which are high enough to reduce metal ions in aqueous solution, resulting in the formation of neutral metal atoms (Eqs. 4 and 5) and NPs (Eq. 6) owing to the nucleation and succeeding ripening process. Because the reduction process completes on the picosecond order as mentioned above, the particle growth is limited in a short period just after every laser pulse. Additionally, the short reaction time results in the reaction being localized to a small area near the laser focus. In summary, metal nanoparticle formation by "laser-induced nucleation" is characterized as reducing agent-free with a short reaction time and localized reaction. Of note, the reaction free from any reducing agents results in significant benefits, such as simplification of the formation process and clean particle surfaces.

4. Gold nanoparticles with high dispersion stability without a dispersant

The progress of particle formation can be monitored through the absorption peak of specific ions or the LSPR of the Au NPs. Once the absorbance of a species of interest becomes saturated, the reduction of metal ions is mostly completed; thus, we can cease laser irradiation. For the irradiation of the chloroauric acid solution, the Au NPs aggregated and precipitated sooner or later. However, when the irradiation was continued after absorbance saturation, the Au NPs showed morphological stability, and the colloidal solution remained in the dispersed state for at least several months (Nakamura et al., 2013). Next, we discuss the phenomenological change that occurred to the Au NPs with increasing irradiation time.

Fig. 2 shows the UV–visible absorption spectra of the chloroauric acid solution with a concentration of 2.5×10^{-4} mol/L recorded every 30 s during the laser irradiation. The repetition rate of the laser pulses was 30 Hz. All the spectra were obtained by subtracting the data for the sample before the laser irradiation. At the beginning, remarkable changes were not observed. After 3 min, the absorbance at approximately 520 nm corresponding to the LSPR of Au NPs appeared and increased with increasing irradiation time, as indicated by the arrow in the figure. This visible change of the LSPR rapidly decreased and stopped at 14 min. The peak absorbance corresponding to the LSPR is plotted as a function of the irradiation time in **Fig. 3**. A rapid rise of the LSPR absorbance from 3 min to 14 min is clearly visible. After 14 min of irradiation, the LSPR absorbance gradually decreased.

The termination of the rapid increase of absorbance at 14 min suggested that the auric ions in the solution were mostly exhausted by laser irradiation. Although reduction of auric ions was not further expected, a morphological change in Au NPs can be expected upon extending the laser irradiation. When laser irradiation was continued after the

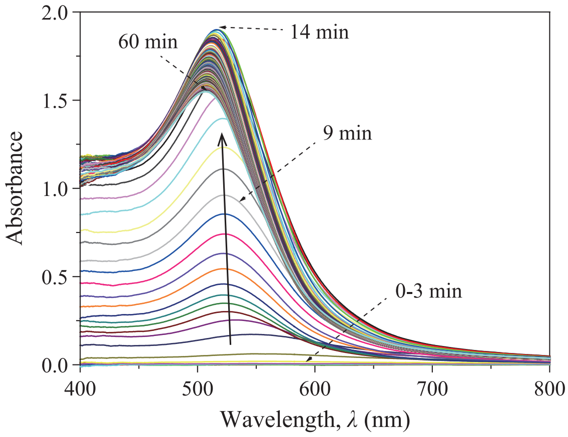

Fig. 2 UV–visible absorption spectra of the chloroauric acid solution at a concentration of 2.5×10^{-4} mol/L measured every 30 s in situ during laser irradiation.

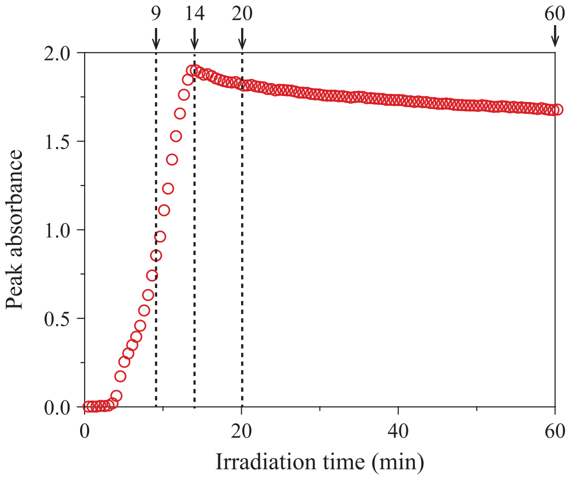

Fig. 3 Time variation of the LSPR peak absorbance in the UV–visible absorption spectra of the chloroauric acid solution measured in situ during laser irradiation.

termination, the shape and size of the Au NPs were investigated by TEM observations. **Fig. 4** shows the TEM images of the Au NPs fabricated by laser-induced nucleation with different irradiation times. The Au NPs coalesced with others until 14 min. Upon further irradiation, the particles were partly dispersed, and the particle size became smaller. At 60 min, the nanoparticles were well dispersed, and the particle size became much smaller. The particle size variation with irradiation time is shown in **Fig. 5**. The particle size variation is clearly observable in the TEM images. Specifically, the dispersion and the mean size of the particles became smaller with irradiation time. The UV–visible absorption spectra showed no significant difference after 14 min of irradiation, whereas the morphology of the Au NPs drastically changed, as shown in the TEM images. These findings suggested that the electronic property of the Au NPs was affected by the excess laser irradiation.

We analyzed the long-time dispersion stability because the Au NPs were well dispersed after 60 min, as shown in **Fig. 4(d)**. In **Fig. 6**, we show the absorption spectra of the colloidal solution of Au NPs 1 day and 2 weeks after preparation with different irradiation times. Each inset shows

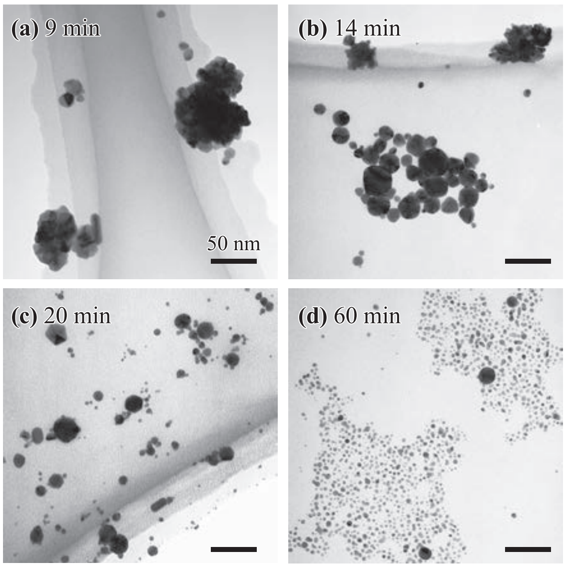

Fig. 4 TEM images of the Au NPs fabricated by laser-induced nucleation with irradiation times of **(a)** 9, **(b)** 14, **(c)** 20 and **(d)** 60 min.

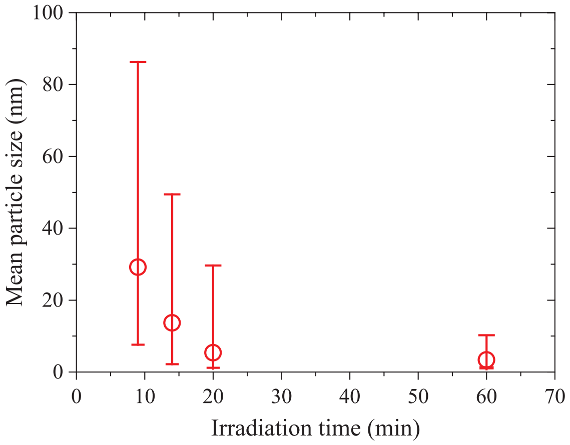

Fig. 5 Mean particle size of the fabricated nanoparticles as a function of irradiation time.

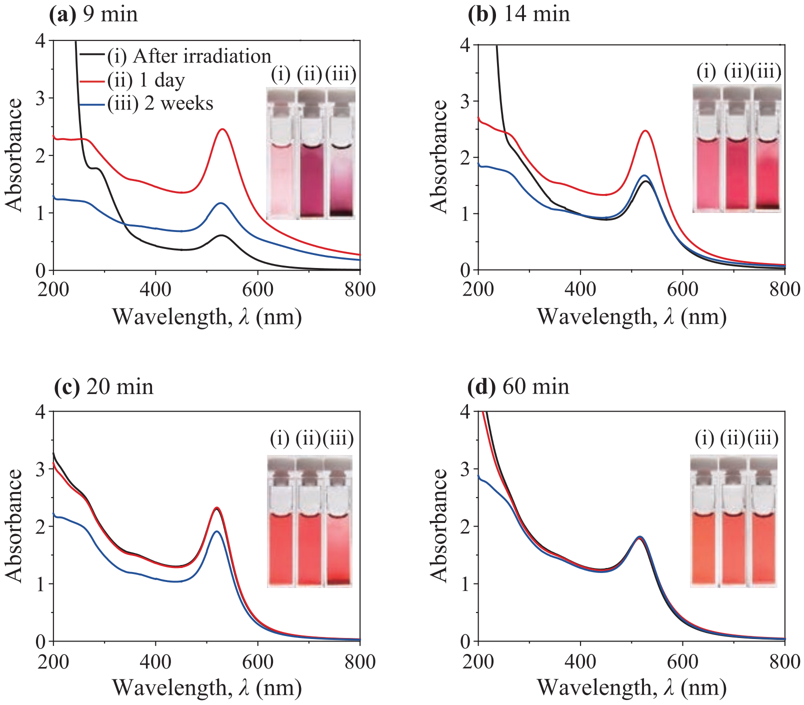

Fig. 6 Long-time variation of the UV–vis. absorption spectra of the colloidal solutions of Au NPs prepared by laser-induced nucleation for different irradiation times of **(a)** 9, **(b)** 14, **(c)** 20, and **(d)** 60 min. Insets: photographs of the colloid solution (i) just after irradiation, (ii) 1 day later, and (iii) 2 weeks later.

photographs of the solutions. For the irradiation times of 9 and 14 min, the LSPR peak became predominant 1 day after irradiation. At this irradiation time, the reduction of auric ions was not completed, and the Au NPs grew via a self-catalytic effect. The particles were aggregated 2 weeks later, as shown in **Figs. 6(a)** and **(b)**. For the irradiation time of 20 min, the increase in the LSPR peak 1 day after preparation became small likely because the reduction of auric ions was almost competed, and further growth of the particles was inhibited.

In contrast, the UV–visible absorption spectra of the colloidal solution prepared with 60 min of irradiation time showed no significant change even after 2 weeks, as shown in **Fig. 6(d)**. This stable dispersion state was maintained for at least several months. The zeta potential of the Au NPs in suspension was approximately –30 mV, meaning that the particle surface was negatively charged. A similar result was been reported for Au NPs fabricated by PLAL (Sylvestre et al., 2004), where the colloidal dispersion stability of the Au NPs was attributed to the partial surface oxidation and the transfer of negative charge from the chloride ions during the intense laser ablation of the bulk Au in water. Additionally, fragmentation by the prolonged irradiation, which effectively reduced the particle size, should have contributed to the dispersion stability through the increase of the specific surface area of the NPs.

5. Structure of multi-elemental alloy nanoparticles and their catalytic activity

Laser-induced nucleation can produce not only noble metal nanoparticles (Nakamura et al., 2008; 2011) but also alloy nanoparticles of noble metals from mixed aqueous solutions with different noble metal ions, e.g., gold (Au) and silver (Ag) (Herbani et al., 2011). The compositional distribution in the synthesized nanoparticles was uniform, meaning that the nanoparticles were a solid solution (Herbani et al., 2012; Sarker et al., 2013). Most noble metals (rhodium (Rh), palladium (Pd), Ag, iridium (Ir), platinum (Pt), and Au) crystallize in a face-centered cubic (fcc) structure, except for ruthenium (Ru) and osmium (Os), which have a hexagonal closely packed (hcp) structure. Accordingly, their alloys can be solid solutions, but some alloys are phase-separated. For example, the Au–Pt alloy exhibits phase separation in a wide composition range in bulk, as shown by its binary phase diagram. Despite this physical inclination in the bulk, laser-induced nucleation can synthesize all-proportional solid–solution Au–Pt alloy NPs from a mixed ion solution of chloroauric acid and chloroplatinic acid (Nakamura et al., 2012). The solid–solution of the Au–Pt alloy is considered to be a metastable state. Accordingly, it is presumed that the synthesis of solid–solution Au–Pt NPs is possible not by the conventional thermal equilibrium process but by laser-induced nucleation, which accompanies rapid cooling of the reaction field. The synthesis of all-proportional solid–solution alloy NPs has been achieved for other combinations of noble metals (Sarker et al., 2015; Nakamura and Sato, 2015). Not only binary but also ternary alloy NPs were synthesized (Sarker et al., 2014).

Because the properties of solid–solution alloy NPs of noble metals are not well known, it is attractive to determine the unknown properties of those NPs. Below, we focus on Rh–Pd–Pt NPs, which have been utilized as a three-way catalyst for emission gas purification of automobiles, and show the catalytic activity of solid–solution Rh–Pd–Pt alloy NPs produced by laser-induced nucleation (Sarker et al., 2019).

A mixed aqueous solution of rhodium (III) chloride trihydrate, palladium (II) chloride, and hydrogen hexachloroplatinate (IV) hexahydrate at a concentration of 2.5×10^{-4} mol/L was prepared. In this case, citric acid at 10 wt% was added to improve the particle size dispersion for improved evaluation of the catalytic activity. The prepared solution was irradiated by laser pulses at a repetition rate of 100 Hz for 30 min, which was much longer than the time required for the reduction of noble metal ions in the solution. The structure and composition of the NPs obtained were analyzed by a scanning TEM with energy dispersive X-ray spectroscopy (STEM–EDS).

The STEM images and elemental mappings of the fabricated NPs are shown in **Fig. 7(a)**. Three elements distributed uniformly in the entire particle. The EDS analysis revealed that the elemental composition was $Rh_{29}Pd_{35}Pt_{36}$, which was close to the initial mixing ratio of metallic ions of Rh:Pd:Pt = 1:1:1 in the mixed aqueous solution. These observations suggested that solid–solution alloy NPs were formed and their composition reflected the initial mixing ratios of noble metal ions in the aqueous solution.

The catalytic activity of the Rh–Pd–Pt alloy NPs was evaluated through oxidation of carbon monoxide (CO). The conversion ratio from CO to carbon dioxide (CO_2) was measured in a reaction chamber with 1 % CO and 0.5 % O_2 in helium gas for pure metal and their alloy NPs supported on γ–alumina particles. **Fig. 8** shows the CO conversion ratios as a function of reaction temperature for the pure metal and their binary and ternary alloy NPs prepared by laser-induced nucleation. Among the pure metal NPs, Rh was most active at low temperature. In contrast, the catalytic activity of the Pt NPs was low owing to the well-known surface poising and the adsorption of CO on the particle surface.

The catalytic activities of binary and ternary alloy NPs were improved compared with the Pt NPs but almost the same as those of Rh and the Pd NPs. It has been reported that Rh–Pt (Alayoglu and Eichhorn., 2008) and Pd–Ru (Kusada et al., 2014) alloy NPs show higher activity than

(a) As-prepared

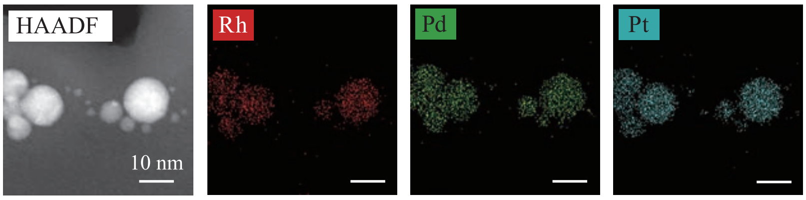

(b) Heat-treated

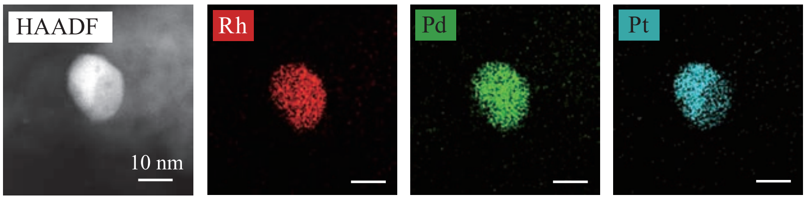

Fig. 7 STEM–EDS mappings for **(a)** the Rh–Pd–Pt alloy NPs prepared by laser-induced nucleation from a mixed ion solution and **(b)** the Rh–Pd–Pt alloy NPs after heat treatment.

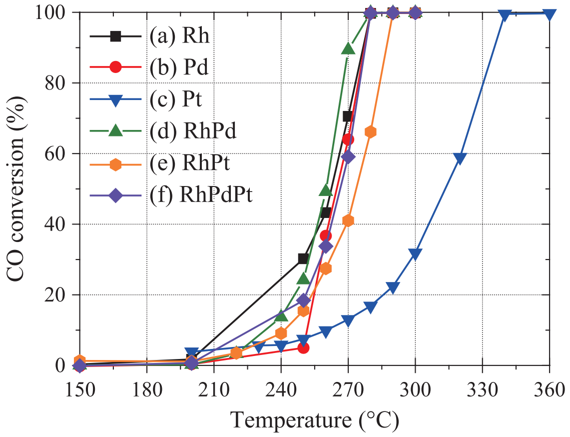

Fig. 8 Catalytic CO conversion of the Rh, Pd, Pt, Rh–Pd, Rh–Pt, Rh–Pt, and Rh–Pd–Pt NPs as a function of temperature. Reprinted from Ref. (Sarker et al., 2019) under the terms of the CC-BY-NC 3.0 license. Copyright: (2019) The Authors, published by The Royal Society of Chemistry.

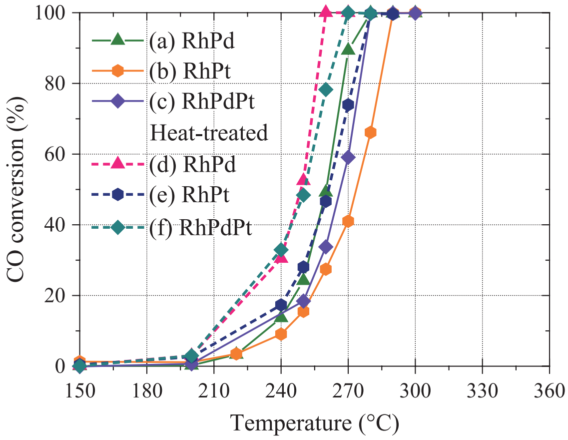

Fig. 9 Catalytic CO conversion of the alloy NPs before and after heat treatment. Reprinted from Ref. (Sarker et al., 2019) under the terms of the CC-BY-NC 3.0 license. Copyright: (2019) The Authors, published by The Royal Society of Chemistry.

their pure metal NPs. This catalytic enhancement of the alloy NPs was attributed to the electron displacement owing to the core–shell structure in the Rh–Pt NPs and the defects due to the mismatch of crystal structures of bulk Rh (fcc) and Ru (hcp) for Rh–Ru NPs. In contrast, the homogeneous structure of the alloy NPs prepared by laser-induced nucleation could not contribute to the activity. This encouraged us to compare homogeneous NPs with inhomogeneous solid–solution alloy NPs, which can be formed by heat treatment of solid–solution alloy NPs.

The STEM images of the heat-treated NPs and the elemental mappings are shown in **Fig. 7(b)**. The elemental components, especially Pt, were inhomogeneously distributed in the NPs after heat treatment compared to the as-prepared NPs, as shown in **Fig. 7(a)**. **Fig. 9** shows the catalytic activities of the NPs with heat treatment. Clearly, the catalytic activity of the heat-treated NPs increased at low temperature as expected. This result explicitly verified that the enhanced catalytic activities of the alloy NPs in the preceding studies were intimately related to the inhomogeneity of the elemental distribution inside the NPs.

This method was able to form solid–solution alloy NPs simply by mixing ion solutions of different noble metals. In addition to binary and ternary alloy NPs, the formation of quaternary and quinary alloy NPs was achieved by laser-induced nucleation. **Fig. 10(a)** shows a STEM–HAADF image of the NPs fabricated in the mixed metal ion solutions of Rh, Pd, Ir, Au, and Pt. Corresponding elemental maps by EDS are depicted in **Figs. 10(b)–(f)**. Every element was uniformly distributed inside the particles, suggesting that quinary solid–solution alloy NPs were formed. Observations using high-resolution transmittance electron microscopy revealed that the NPs were polycrystalline. According to the definition (Miracle, 2019), the nanoparticles synthesized here were of a high-entropy alloy because they contained five elements. Because the crystalline structures of Rh, Pd, Ir, Au, and Pt are unexceptionally fcc, as mentioned before, it is easy to assume that their solid–solution

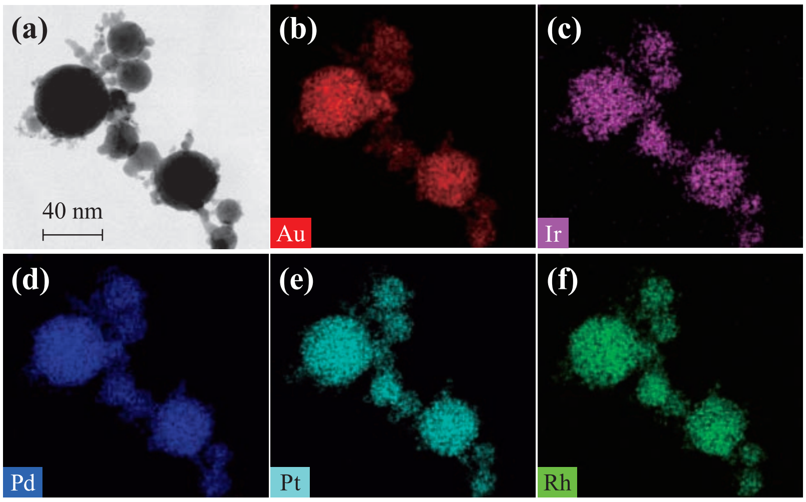

Fig. 10 **(a)** STEM–HAADF image of nanoparticles formed by laser-induced nucleation using the mixed metal ion solutions of Rh, Pd, Ir, Au and Pt. **(b)–(f)** corresponding elemental EDS maps.

alloy NPs can be formed. However, their binary phase diagrams suggest that six out of ten combinations are immiscible. Miscible combinations are limited to the Au–Pd, Ir–Rh, Pd–Pt, and Pt–Rh systems, indicating the difficulties involved in the formation of their solid–solution alloy NPs. Thus, the non-thermal equilibrium process achieved by the laser-induced nucleation may be a promising tool for the formation of high-entropy alloy NPs.

6. Conclusion

We demonstrated the nanoparticle formation of noble metals and their alloys in the highly intense laser field generated by tightly focusing ultrashort optical pulses in aqueous solution. This “laser-induced nucleation” is free from a reducing agent because the highly intense laser irradiation of the aqueous solution was able to produce solvated electrons and hydrogen radials directly from water molecules, which act as strong reducing agents for metal ions. Prolonged irradiation of chloroauric acid solution resulted in the formation of an Au colloidal solution with a stable dispersive state over several months. Owing to the ultrafast and non-thermal nature of the intense laser process, solid–solution alloy NPs were formed even though the elements were immiscible in the bulk. The solid–solution alloy NPs with a homogeneous elemental distribution contributed to the superior catalytic activity of the alloy NPs, which were formed by a conventional chemical process and had an inhomogeneous elemental distribution.

With the progress of laser technology, the intense laser field will offer an extremely non-linear, non-equilibrium, high-temperature and high-pressure field that has never existed on Earth. We are expecting that this unprecedented state opens the door to ultimate technologies in both science and industry.

Nomenclature

EDS	Energy dispersive X-ray spectroscopy
fcc	face-centered cubic
HAADF	High angle annular dark field
hcp	hexagonal close-packed
LSPR	Localized surface plasmon resonance
NP	Nanoparticle
PLAL	Pulsed laser ablation in liquid
STEM	Scanning transmission electron microscopy
TEM	Transmission electron microscopy
k	rate constant of reaction (dm^3 mol^{-1} s^{-1})
λ	wavelength of light (m)
V_{SHE}	redox potential for standard hydrogen electrode (V)

References

Alayoglu S., Eichhorn B., Rh–Pt bimetallic catalysts: synthesis, characterization, and catalysis of core–shell, alloy, and monometallic nanoparticles, Journal of the American Chemical Society, 130 (2008) 17479–17486. DOI: 10.1021/ja8061425

Castillejo M., Couris S., Koudoumas E., Martín M., Ionization and fragmentation of aromatic and single-bonded hydrocarbons with 50 fs laser pulses at 800 nm, Chemical Physics Letters, 308 (1999) 373. DOI: 10.1016/S0009-2614(99)00636-3

Cornaggia C., Carbon geometry of $C_3H_3^+$ and $C_3H_4^+$ molecular ions probed by laser-induced Coulomb explosion, Physical Review A, 52 (1995) R4328. DOI: 10.1103/physreva.52.r4328

Cornaggia C., Schmidt M., Normand D., Laser-induced nuclear motions in the Coulomb explosion of $C_2H_2^+$ ions, Physical Review A, 51 (1995) 1431. DOI: 10.1103/physreva.51.1431

Herbani Y., Nakamura T., Sato S., Synthesis of near-monodispersed Au-Ag nanoalloys by high intensity laser irradiation of metal ions in hexane, The Journal of Physical Chemistry C, 115 (2011) 21592. DOI: 10.1021/jp205547t

Herbani Y., Nakamura T., Sato S., Synthesis of platinum-based binary and ternary alloy nanoparticles in an intense laser field, Journal of Colloid and Interface Science, 375 (2012) 78. DOI: 10.1016/j.jcis.2012.02.030

Kusada K., Kobayashi H., Ikeda R., Kubota Y., Takata M., Toh S., Yamamoto T., Matsumura S., Sumi N., Sato K., Nagaoka K., Kitagawa H., Solid solution alloy nanoparticles of immiscible Pd and Ru elements neighboring on Rh: changeover of the thermodynamic behavior for hydrogen storage and enhanced CO-oxidizing ability, Journal of the American Chemical Society, 136 (2014) 1864. DOI: 10.1021/ja409464g

Miracle D.B., High entropy alloys as a bold step forward in alloy development, Nature Communications, 10 (2019) 1805. DOI: 10.1038/s41467-019-09700-1

Muttaqin, Nakamura T., Sato S., Synthesis of gold nanoparticle colloids by highly intense laser irradiation of aqueous solution by flow system, Applied Physics A, 120 (2015) 881. DOI: 10.1007/s00339-015-9314-x

Nakamura T., Herbani Y., Sato S., Fabrication of solid-solution gold–platinum nanoparticles with controllable compositions by high-intensity laser irradiation of solution, Journal of Nanoparticle Research, 14 (2012) 785. DOI: 10.1007/s11051-012-0785-9

Nakamura T., Herbani Y., Ursescu D., Banici R., Dabu R.V., Sato S., Spectroscopic study of gold nanoparticle formation through high intensity laser irradiation of solution, AIP Advances, 3 (2013) 082101. DOI: 10.1063/1.4817827

Nakamura T., Magara H., Herbani Y., Sato S., Fabrication of silver nanoparticles by highly intense laser irradiation of aqueous solution, Applied Physics A, 104 (2011) 1021. DOI: 10.1007/s00339-011-6499-5

Nakamura T., Mochidzuki Y., Sato S., Fabrication of gold nanoparticles in intense optical field by femtosecond laser irradiation of aqueous solution, Journal of Materials Research, 23 (2008) 968. DOI: 10.1557/jmr.2008.0115

Nakamura T., Sato S., Green and facile synthesis of Pd–Pt alloy nanoparticles by laser irradiation of aqueous solution, Journal of Nanoscience and Nanotechnology, 15 1 (2015) 426. DOI: 10.1166/jnn.2015.8846

Pearce S.R.J., Henleya S.J., Claeyssensa F., Maya P.W., Hallamb K.R., Smitha J.A., Rossera, K.N., Production of nanocrystalline diamond by laser ablation at the solid liquid interface, Diamond Related Materials, 13 (2004) 661. DOI: 10.1016/j.diamond.2003.08.027

Sarker M.S.I., Nakamura T., Herbani Y., Sato S., Fabrication of Rh based solid-solution bimetallic alloy nanoparticles with fully-tunable composition through femtosecond laser irradiation in aqueous solution, Applied Physics A, 110 (2013) 145. DOI: 10.1007/s00339-012-7467-4

Sarker M.S.I., Nakamura T., Kameoka S., Hayasaka Y., Yin S., Sato S., Enhanced catalytic activity of inhomogeneous Rh-based solid-solution alloy nanoparticles, RSC Advances, 9 (2019) 38882. DOI: 10.1039/c9ra06167c

Sarker M.S.I., Nakamura T., Sato S., Composition-controlled ternary Rh–Pd–Pt solid-solution alloy nanoparticles by laser irradiation of mixed solution of metallic ion, Journal of Material Research, 29 7 (2014) 856. DOI: 10.1557/jmr.2014.62

Sarker M.S.I., Nakamura T., Sato S., All-proportional solid-solution Rh–Pd–Pt alloy nanoparticles by femtosecond laser irradiation of aqueous solution with surfactant, Journal of Nanoparticle Research, 17 (2015) 259. DOI: 10.1007/s11051-015-3056-8

Sylvestre J-.P., Poulin S., Kabashin A.V., Sacher E., Meunier M., Luong J.H.T., Surface chemistry of gold nanoparticles produced by laser ablation in aqueous media, The Journal of Physical Chemistry B, 108 (2004) 16864. DOI: 10.1021/jp047134+

Talebpour A., Bandrauk A.D., Vijayalakshmi K., Chin S.L., Dissociative ionization of benzene in intense ultra-fast laser pulses, Journal of Physics B: Atomic, Molecular and Optical Physics, 33 (2000) 4615. DOI: 10.1088/0953-4075/33/21/307

Thomsen C.L., Madsen D., Keiding S.R., Thøgersen J., Christiansen O., Two-photon dissociation and ionization of liquid water studied by femtosecond transient absorption spectroscopy, The Journal of Chemical Physics, 110 (1999) 3453. DOI: 10.1063/1.478212

Wang J.B., Zhang C.Y., Zhong X.L., Yang G.W., Cubic and hexagonal structures of diamond nanocrystals formed upon pulsed laser induced liquid–solid interfacial reaction, Chemical Physics Letters, 361 (2002) 86. DOI: 10.1016/S0009-2614(02)00871-0

Authors’ Short Biographies

Takahiro Nakamura

Associate Professor T. Nakamura received his Bachelor’s degree in Engineering in 1999, Master’s degree in Engineering in 2001, and Doctorate in Engineering in 2004 from the Tohoku University. He started his academic career with laser materials processing. He worked as an Assistant Professor (from 2005 to 2015) and as an Associate Professor (from 2015 to now) in Institute of Multidisciplinary Research for Advanced Materials, Tohoku University. His research topics cover broad area in laser materials processing.

Yuki Yamazaki

Yuki Yamazaki received his Bachelor’s and Master’s degrees in Engineering from the Tohoku University in 2016 and 2018, respectively. He is now working in IBM Japan Ltd.

Shunichi Sato

Professor S. Sato received his Bachelor’s degree in Science in 1981, Master’s degree in Engineering in 1983, and Doctorate in Engineering in 1992 from the Tohoku University. He started his academic career with laser application to bioscience and medicine, and expanded his interest to materials science. He became Professor of Institute of Multidisciplinary Research for Advanced Materials, Tohoku University in 2003. He has believed in the extreme potential of light and is trying to explore its hidden peculiarities.

KONA Powder and Particle Journal No. 39 (2022) 119–129/https://doi.org/10.14356/kona.2022003 Review Paper

Influence of Anions and Cations on the Formation of Iron Oxide Nanoparticles in Aqueous Media †

Hidekazu Tanaka

Department of Chemistry, Graduate School of Natural Science and Technology, Shimane University, Japan

Abstract

Recently, various types of functionalized metal oxide nanoparticles have been used for many applications because of their unique chemical and physical properties. To synthesize metal oxide nanoparticles, liquid-phase synthesis techniques have been developed. The production process of metal oxide nanoparticles in aqueous media is extremely complex because the formation, crystal structure, crystallinity, chemical composition, and morphology of the particles are considerably dependent on the preparation conditions (e.g., anion and cation concentrations and species, additives, solution pH, reaction temperature, and reaction time). Accordingly, clarifying these effects is fundamental to accurately understand the formation mechanism of metal oxide nanoparticles to further develop new functionalized nanoparticles. In this review, the influence of anions (Cl^-, SO_4^{2-}, and NO_3^-) and cations (Ni^{2+}, Cu^{2+}, and Cr^{3+}) on the formation and structure of iron oxide nanoparticles in aqueous media is described.

Keywords: metal oxide nanoparticle, liquid-synthesis, particle formation, iron oxide particle, anion, cation

1. Introduction

In industries, various types of functionalized metal oxide nanoparticles, such as iron oxide, silica gel, alumina, zinc oxide, and titania, have been developed and used for many applications (e.g., catalysis, adsorbent, biomedicine, magnetic data storage, agriculture, fuel cell, pigment, and sensor material) because of their unique chemical and physical properties (Iler R.K., 1979; Cornell R.M. and Schwertmann U., 1996; 2000; Fujishima A. et al., 1999; Rodríguez J.A. and Fernández-García M., 2006; Chavali M.S. and Nikolova M.P., 2019; Korotcenkov G. et al., 2019). To further improve the particle properties, controlling the particle shape and size, monodispersity, and crystallinity is necessary. However, in general, the synthesis of high-quality nanoparticles, such as monodisperse single-crystal nanoparticles, is considerably difficult (Matijević E., 1985; Sugimoto T., 1987; 2001; Pelizzetti E., 2011). Metal oxide nanoparticles can be produced using solid, liquid, and gas-phase synthesis techniques. Among these, the liquid-phase synthesis affords several advantages (Gutch A. et al., 2004; Feng J. et al., 2015; Karatutlu A. et al., 2018): (1) low-cost particle production can be performed; (2) surface active nanoparticles can be obtained; (3) particles from a homogeneous solution can be prepared; (4) preparation conditions (e.g., reaction temperature and time, anion and cation concentrations, additives, solution pH, and raw materials) can be easily controlled; (5) particle shape and size can be regulated by the abovementioned preparation conditions and method. Based on these benefits, various liquid-phase synthesis techniques for the production of metal oxide nanoparticles have been developed, and approximately 45 % of functionalized nanoparticles are synthesized through these methods in the industry (Charitidis C.A. et al., 2014). The liquid-phase synthesis can be classified into two approaches: "*Top-down approach*" and "*Bottom-up approach*." In the "*Top-down approach*," nanoparticles are synthesized by etching the macro-sized or micro-sized bulk materials in aqueous media (e.g., wet milling, lithography, laser ablation, and chemical etching). In the "*Bottom-up approach*," nanoparticles are prepared by assembling small blocks, such as atoms and molecules, in aqueous media (e.g., sol-gel, precipitation, pyrolysis, and chemical reduction methods).

The formation and growth processes of metal oxide nanoparticles in aqueous media have been investigated (Ostwald W.Z., 1900; LaMer V.K. and Dinegar R.H., 1950; Reiss H., 1951; LaMer V.K., 1952; Feitknecht W., 1959; Lifshitz I.M. and Slyozov V.V., 1961; Hsu P.M., 1972; Hsu P.M. and Ragone S.E., 1972; Misawa T. et al., 1974; Dousma J. et al., 1976; 1978; 1979; Murphy P.J. et al., 1976; Blesa M.A. and Matijević E., 1989; Cornell R.M. and Schwertmann U., 1996; 2000; Ishikawa T., 1997; Schultz M. et al., 1999; Jolivet J-P., 2000; Kandori K., 2002; Tamura

---

† Received 28 July 2020; Accepted 1 October 2020
J-STAGE Advance published online 28 November 2020
Add: 1060 Nishikawatsu, Matsue, Shimane 690-8504, Japan
E-mail: hidekazu@riko.shimane-u.ac.jp
TEL/FAX: +81-852-32-6823

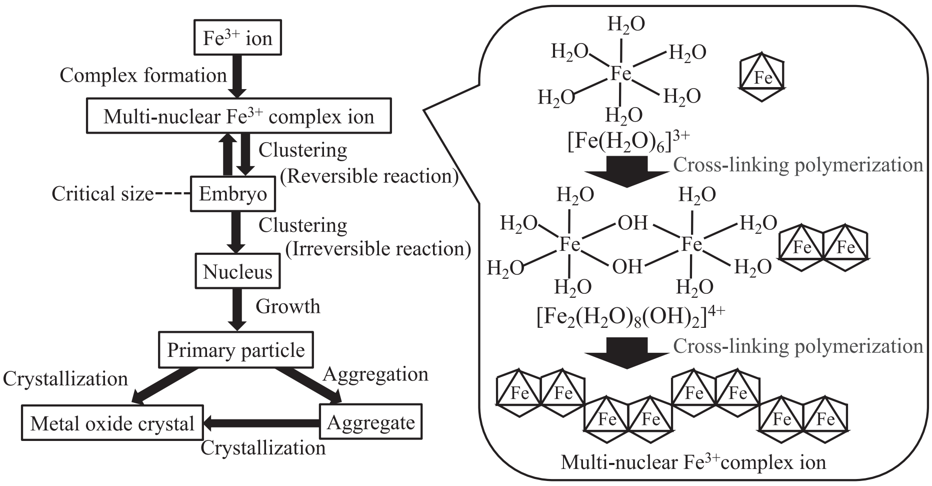

Fig. 1 Formation and growth processes of iron oxide particles from aqueous Fe^{3+} solution.

H., 2008; Thanh N.T.K. et al., 2014; Plote J., 2015). **Fig. 1** shows the formation and growth processes of iron oxide nanoparticles from aqueous Fe^{3+} solution.

$$Fe^{3+} + 6H_2O \rightarrow Fe(H_2O)_6^{3+} \tag{1}$$

The $Fe(H_2O)_6^{3+}$ ions are hydrolyzed to generate $Fe(OH)_n(H_2O)_{6-n}^{3+}$ ions (n = 1–6) via protolysis reaction (2).

$$Fe(H_2O)_6^{3+} + nH_2O \rightarrow Fe(OH)_n(H_2O)_{6-n}^{3+} + nH_3O^+ \tag{2}$$

Further, the $Fe(OH)_n(H_2O)_{6-n}^{3+}$ ions are condensed via oxolation reaction (3).

$$>Fe–OH + HO–Fe< \rightarrow >Fe–O–Fe< + H_2O \tag{3}$$

Then, the >Fe–O–Fe< groups are hydrolyzed via olation reaction (4).

$$>Fe–O–Fe< + H_3O+ \rightarrow >Fe–OH–Fe< + H_2O \tag{4}$$

Reactions (1)–(4) continuously proceed to yield multi-nuclear Fe^{3+} complex ions. These ions further grow to produce an embryo through ion collisions in which the reaction continuously breaks down and reforms during the reversible reaction stage. When the embryo exceeds a certain critical size, it becomes a nucleus, which is considerably more stable. The generated nucleus is further grown to form fine primary particles, which transform into crystals via two possible routes: "*aggregation mechanism*" and "*ion diffusion growth mechanism*". In the former route, aggregates are generated by the agglomeration of primary particles. During aging, the primary particles in the aggregates solidify into crystalline particles. In the latter mechanism, solute ions are diffused and deposited on the primary particles to form crystalline particles. The growth process of α-FeOOH particles is depicted in **Fig. 2**. In this case, the primary particles composed of fine crystals are regularly combined by –O– and –OH– bonds to crystallize as α-FeOOH. Accordingly, the formation process of metal oxide nanoparticles is considerably complex and is not fully understood. The formation, crystal structure, crystallinity, chemical composition, and particle morphology are extremely dependent on the preparation conditions, such as anion and cation concentrations and species, additive, solution pH, and reaction temperature and time. Among these, anion and cation were observed to markedly affect the formation and structure of iron oxides. The phase stability of γ-FeOOH was lowered by Cl^- and SO_4^{2-} (Sudakar S. et al., 2003). Moreover, the increase of $[SO_4^{2-}]/[Cl^-]$ ratio in the aqueous $Fe_2(SO_4)_3$–$FeCl_3$ solution accelerated the α-FeOOH formation (Oh S.J. et al., 2002). Further, the addition of SO_4^{2-} and SO_3^{2-} significantly impeded the formation and crystallization of β-FeOOH (Ishikawa T. et al., 2005; Kamimura T. et al., 2005; Tanaka H. et al., 2016a; b). The crystallization and growth of α-FeOOH and β-FeOOH particles were inhibited by adding Cu^{2+}, Ni^{2+}, Cr^{3+}, and Ti^{4+} (Inouye K. et al., 1968; 1972; Ishikawa T. et al., 2000; 2001; 2002; 2003; 2009; Nakayama T. et al., 2005; Tanaka H. et al., 2013a; b). Accordingly, elucidating these effects

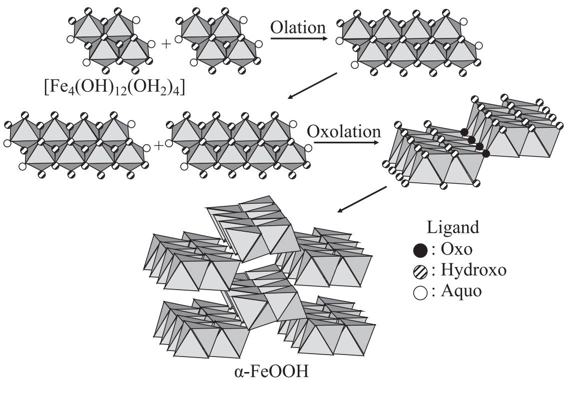

Fig. 2 Growth process of α-FeOOH crystal.

is fundamental to accurately understand the formation mechanism of metal oxide nanoparticles.

In this review, the influence of anions and cations on the formation and structure of iron oxide nanoparticles is described based on our research. The iron oxide nanoparticles were synthesized in the presence of anions (Cl^-, SO_4^{2-}, and NO_3^-) and cations (Ni^{2+}, Cu^{2+}, and Cr^{3+}) (Tanaka H. et al., 2013a; b; 2015; 2016a; 2018). The results can aid in developing new functionalized nanomaterials using the liquid-phase synthesis technique.

2. Influence of anions on formation of iron oxide particles

The influence of anions on the formation of iron oxide nanoparticles was examined by synthesizing the particles from Fe^{3+} solutions containing Cl^-, NO_3^-, and SO_4^{2-}. A mixture of aqueous $FeCl_3$, $Fe_2(SO_4)_3$, and $Fe(NO_3)_3$ solutions were aged at 50 °C for 48 h. Prior to aging, the solution pH was approximately 2. The generated precipitates were filtered out, thoroughly washed with deionized-distilled water, and air-dried at 50 °C.

The amount of products formed is shown in **Fig. 3**. This amount is increased by incrementing the quantity of $FeCl_3$ added to the $FeCl_3$–$Fe(NO_3)_3$ system. In the $Fe(NO_3)_3$–$Fe_2(SO_4)_3$, $Fe_2(SO_4)_3$–$FeCl_3$, and $FeCl_3$–$Fe(NO_3)_3$–$Fe_2(SO_4)_3$ systems, increasing the quantity of $Fe_2(SO_4)_3$ addition reduces the amount of formed products. The amount of these products eventually become zero when higher amounts of SO_4^{2-} are added. These results indicate that the formation of iron oxides is inhibited by the addition of SO_4^{2-}.

The major formation species of iron oxides is shown in **Fig. 4**. Iron-oxyhydroxysulfate ($Fe_8O_8(OH)_6(SO_4)\cdot nH_2O$: Schwertmannite) is formed by adding SO_4^{2-}, however, the addition of a large amount of SO_4^{2-} prevents the generation of iron oxides. In contrast, β-FeOOH is mainly yielded in the $FeCl_3$–$Fe(NO_3)_3$ system, and α-FeOOH is only generated in the $Fe(NO_3)_3$ system, indicating that the $FeCl_3$–$Fe(NO_3)_3$ system favors the formation of β-FeOOH rather than α-FeOOH.

Transmission electron microscopy (TEM) images of the formed particles are shown in **Fig. 5**. The spherical α-FeOOH particles with an average diameter of 358 nm are generated in the $Fe(NO_3)_3$ system. In the $FeCl_3$–$Fe(NO_3)_3$ system, the spherical α-FeOOH particles virtually diminish, and rod-shaped β-FeOOH particles are observed. Further, as the amount of added Cl^- increases, the mean length and width of β-FeOOH particles increase from 677 nm to 1.48 μm and from 130 to 238 nm, respectively. Hence, the incorporation of NO_3^- slightly suppresses the growth of β-FeOOH particles. In the $Fe(NO_3)_3$–$Fe_2(SO_4)_3$ system, needle-like Schwertmannite particles with a mean length and width of approximately 260 and 15 nm, respectively, are mainly formed. By adding NO_3^-, the Schwertmannite particles disappear, and irregular-shaped α-FeOOH particles with an average size of 68 nm are generated. In the $Fe_2(SO_4)_3$–$FeCl_3$ system, increasing the amount of added SO_4^{2-} decreases the particle size of β-FeOOH and forms Schwertmannite particles (mean length = 136 nm, mean width = 49 nm). In the $FeCl_3$–$Fe(NO_3)_3$–$Fe_2(SO_4)_3$ system, due to the Schwertmannite, only needle-like particles with a length and width of approximately 310 and 40 nm are recognizable. These facts reveal that the presence of SO_4^{2-} in the aforementioned system remarkably precludes the formation of α-FeOOH and β-FeOOH particles and produces needle-like Schwertmannite particles. Note that a higher SO_4^{2-} content in the solution inhibits the formation of particles. Thus, the effect of SO_4^{2-} on the formation of iron oxide particles is greater than that of Cl^- and NO_3^-.

These results indicate that anions, such as SO_4^{2-}, Cl^-, and NO_3^-, affect the formation, crystallization, and particle growth of iron oxides, and the effect is in the order $SO_4^{2-} >> Cl^- > NO_3^-$. The affinity of anions to Fe^{3+} can be evaluated through the stability constant (log K) of Fe^{3+} complexes with anions. The stability constant of Fe^{3+} complexes with SO_4^{2-} is 4.1 and is considerably larger than that with NO_3^- (1.0) and Cl^- (0.6), indicating the strong

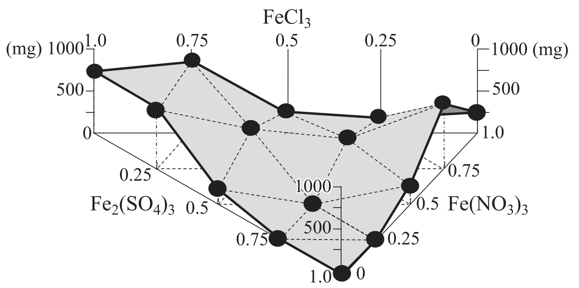

Fig. 3 Plots of amount of products formed in $FeCl_3$–$Fe(NO_3)_3$–$Fe_2(SO_4)_3$ system. Adapted with permission from Ref. (Tanaka H. et al., 2013a). Copyright: (2013) Elsevier B.V.

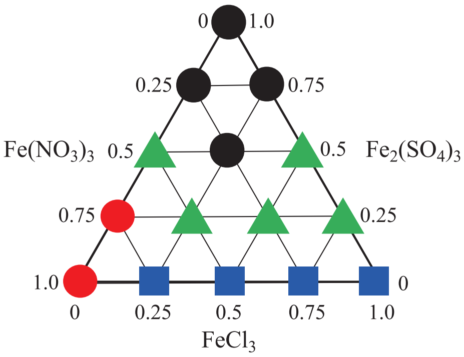

Fig. 4 Major iron oxides formed in $FeCl_3$–$Fe(NO_3)_3$–$Fe_2(SO_4)_3$ system. (🔴) α-FeOOH, (🟦) β-FeOOH, (▲) Schwertmannite, (⚫) no precipitates. Adapted with permission from Ref. (Tanaka H. et al., 2013a). Copyright: (2013) Elsevier B.V.

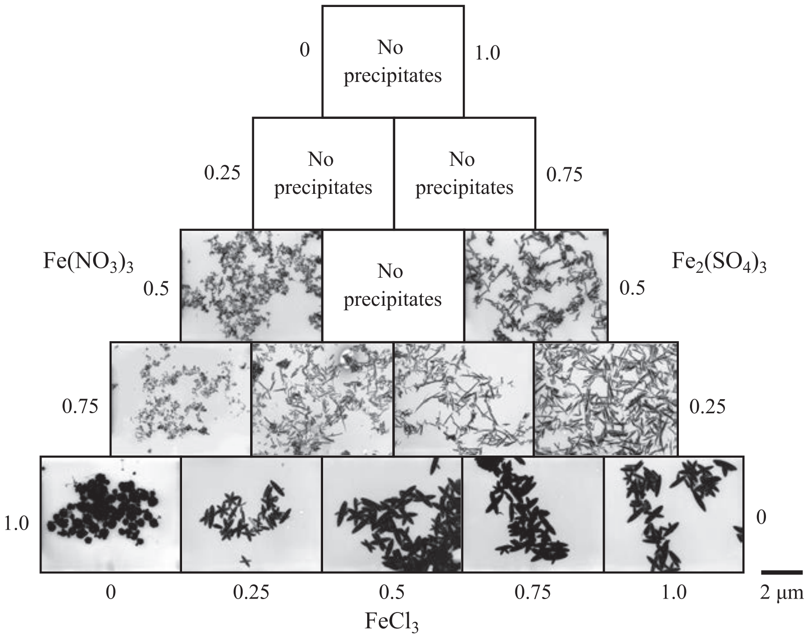

Fig. 5 TEM images of the particles formed in $FeCl_3$–$Fe(NO_3)_3$–$Fe_2(SO_4)_3$ system. Adapted with permission from Ref. (Tanaka H. et al., 2013a). Copyright: (2013) Elsevier B.V.

coordination of SO_4^{2-} with Fe^{3+} compared with NO_3^- and Cl^- (Sillen L.G. and Martell A.E., 1964). Hence, the SO_4^{2-}-containing aqua Fe^{3+} complex $[Fe(SO_4)_m(H_2O)_{6-m}]^{3+}$ is formed in the $Fe(NO_3)_3$–$Fe_2(SO_4)_3$, $Fe_2(SO_4)_3$–$FeCl_3$ and $FeCl_3$–$Fe(NO_3)_3$–$Fe_2(SO_4)_3$ systems via hydrolysis reaction (5).

$$Fe^{3+} + mSO_4^{2-} + (6-m)H_2O \rightarrow [Fe(SO_4)_m(H_2O)_{6-m}]^{3+} \quad (5)$$

Moreover, $[Fe(SO_4)_m(H_2O)_{6-m}]^{3+}$ is hydrolyzed via protolysis reaction (6).

$$[Fe(SO_4)_m(H_2O)_{6-m}]^{3+} + nH_2O \rightarrow [Fe(OH)_n(SO_4)_m(H_2O)_{6-n-m}]^{3+} \quad (6)$$

Consequently, when a small amount of SO_4^{2-} is added, the major product becomes Schwertmannite containing SO_4^{2-}. Upon increasing the amount of added SO_4^{2-}, the SO_4^{2-} content in the $[Fe(SO_4)_m(H_2O)_{6-m}]^{3+}$ ions increases and the number of active >Fe–OH groups is reduced, resulting in the suppression of olation reaction (3). Accordingly, no precipitates are generated at higher SO_4^{2-} contents in the solution. In contrast, β-FeOOH is mainly produced in the $FeCl_3$–$Fe(NO_3)_3$ system. The stability constants of Fe^{3+} complexes with Cl^- and NO_3^- are considerably lower than that with SO_4^{2-}. Hence, the addition of Cl^- and NO_3^- prevents the progress of reactions (1)–(4), leading to the formation of the amorphous precursor of α-FeOOH and β-FeOOH particles during aging. It has been established that the isoelectric point (*iep*) of iron oxides and oxyhydroxides, such as α-FeOOH, β-FeOOH, γ-FeOOH, Fe_3O_4, and α-Fe_2O_3, is a neutral pH, and aforementioned materials have a positive surface charge in the acidic solution (Cornell R.M. and Schwertmann U., 1996; 2000). Moreover, the ionization energy of NO_3^- is larger than that of Cl^- (Lang P.F. and Smith B.C., 2003). Therefore, the added Cl^- preferentially adsorbs on the surface of the amorphous precursor to form Cl^--containing β-FeOOH particles. However, the decrease in the amount of added Cl^- reduces the size of β-FeOOH particles, indicating the inhibition of their growth as a result of the adsorption of NO_3^- on the precursors.

To clarify the influence of anion and solution pH on the formation of iron oxide nanoparticles, the particles were synthesized from the $FeCl_3$–$Fe_2(SO_4)_3$–$Fe(NO_3)_3$ system at different $OH^-/3Fe^{3+}$ molar ratios. The $OH^-/3Fe^{3+}$ ratio ranges 0–1.5 through the addition of NaOH solutions. The pH titration curves of aqueous $FeCl_3$, $Fe_2(SO_4)_3$, and $Fe(NO_3)_3$ solutions are shown in **Fig. 6**. All the curves are practically identical, indicating that the solution pH is independent of the anions. At $OH^-/3Fe^{3+} = 0$–1.0, the solution pH becomes practically constant (i.e., 2–3) because of the reaction of Fe^{3+} with the added OH^- to precipitate $Fe(OH)_3$. At $OH^-/3Fe^{3+} > 1.0$, the pH level of the solution suddenly increases because all the Fe^{3+} transforms into $Fe(OH)_3$. The major products synthesized at $OH^-/3Fe^{3+} = 0$–1.5 are shown in **Fig. 7**. At $OH^-/3Fe^{3+} = 0.5$, the hydrated iron oxide $Fe_2O_3{\bullet}nH_2O$ particles are mainly produced in the $FeCl_3$–$Fe(NO_3)_3$ system. In contrast, the $Fe_2(SO_4)_3$–$FeCl_3$, $Fe(NO_3)_3$–$Fe_2(SO_4)_3$, and $FeCl_3$–$Fe_2(SO_4)_3$–$Fe(NO_3)_3$ systems enhance the α-FeOOH formation. This is caused by the transformation of Schwertmannite during aging because this material is among the precursors of α-FeOOH (Cornell R.M. and Schwertmann U., 1996; 2000; Tanaka

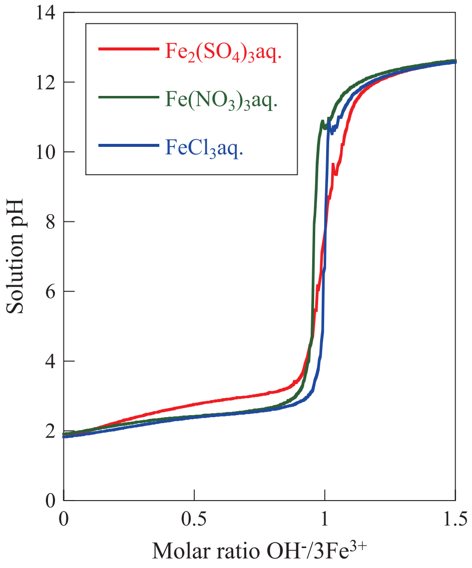

Fig. 6 pH titration curves of aqueous $FeCl_3$, $Fe(NO_3)_3$ and $Fe_2(SO_4)_3$ solutions. Adapted with permission from Ref. (Tanaka H., 2015). Copyright: (2015) The Society of Powder Technology, Japan.

H. et al., 2013a; 2015; 2016a; Muguruma et al., 2015). The major products at $OH^-/3Fe^{3+} = 1.0$ and 1.5 (pH levels are approximately 7 and 14, respectively) are ferrihydrites ($Fe_5HO_8 \cdot 4H_2O$) and α-FeOOH, respectively. The foregoing means that raising the solution pH before aging lowers the influence of anions on the structure and composition of iron oxide nanoparticles.

3. Influence of cations on formation of iron oxide nanoparticles

The influence of cations on the formation of iron oxide nanoparticles was examined by synthesizing the α-FeOOH particles with Ni^{2+}, Cu^{2+}, and Cr^{3+}. Metal salts, such as $NiSO_4$, $CuSO_4$, or $Cr(NO_3)_3$, and $FeSO_4$ were dissolved in O_2-free deionized-distilled water, of which the metal/Fe atomic ratio of the solution was 0–0.1. The aqueous NaOH solution was added to the solution until the $OH^-/2Fe^{2+}$ ratio reached 0.05. The generated suspension was aged in bubbling air at 50 °C for 24 h. The resulting precipitate was filtered out, washed with deionized distilled water, and air-dried at 50 °C.

X-ray diffraction (XRD) patterns of the products synthesized with Ni^{2+}, Cu^{2+}, and Cr^{3+} are shown in **Fig. 8**. As shown in **Fig. 8(A)**, with the addition of Ni^{2+}, the intensity and position of α-FeOOH peaks remain virtually unchanged. As shown in **Fig. 8(B)**, with Cu^{2+} addition, the α-FeOOH peaks are weakened and broadened by increasing the Cu/Fe ratio. A similar tendency is observed with the addition of Cr^{3+} as shown in **Fig. 8(C)**. Besides, the α-FeOOH peaks vanish at Cr/Fe ≥ 0.04 and broad peaks ascribed to Schwertmannite are developed. Furthermore,

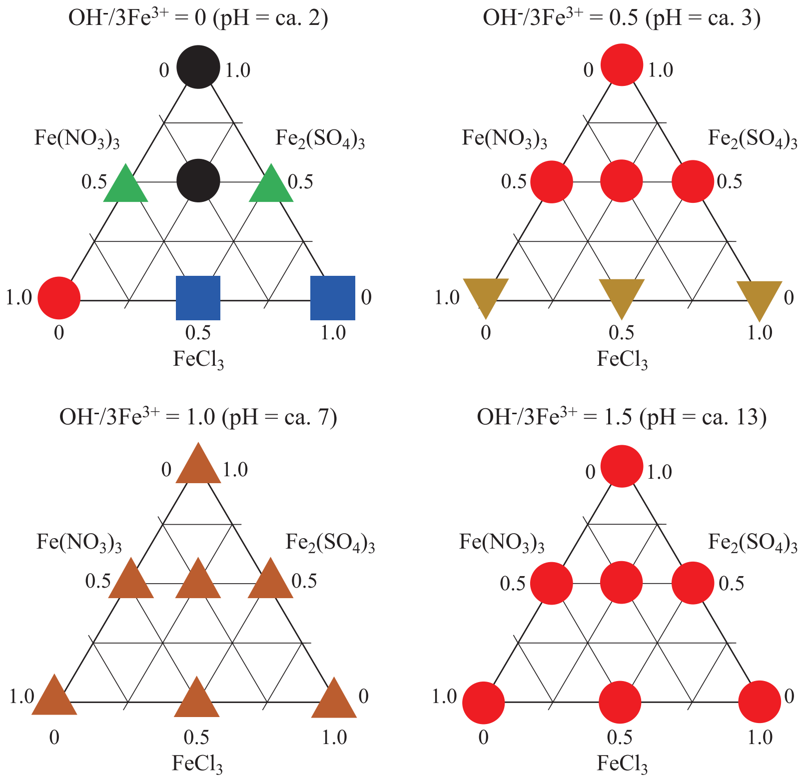
$OH^-/3Fe^{3+} = 0$ (pH = ca. 2)

$OH^-/3Fe^{3+} = 0.5$ (pH = ca. 3)

$OH^-/3Fe^{3+} = 1.0$ (pH = ca. 7)

$OH^-/3Fe^{3+} = 1.5$ (pH = ca. 13)

Fig. 7 Major product of the iron oxides formed at $OH^-/3Fe^{3+} = 0$–1.5. (●) α-FeOOH, (■) β-FeOOH, (▲) Schwertmannite, (●) no precipitates, (▼) $Fe_2O_3 \cdot nH_2O$, (▲) Ferrihydrite. Adapted with permission from Ref. (Tanaka H., 2015). Copyright: (2015) The Society of Powder Technology, Japan.

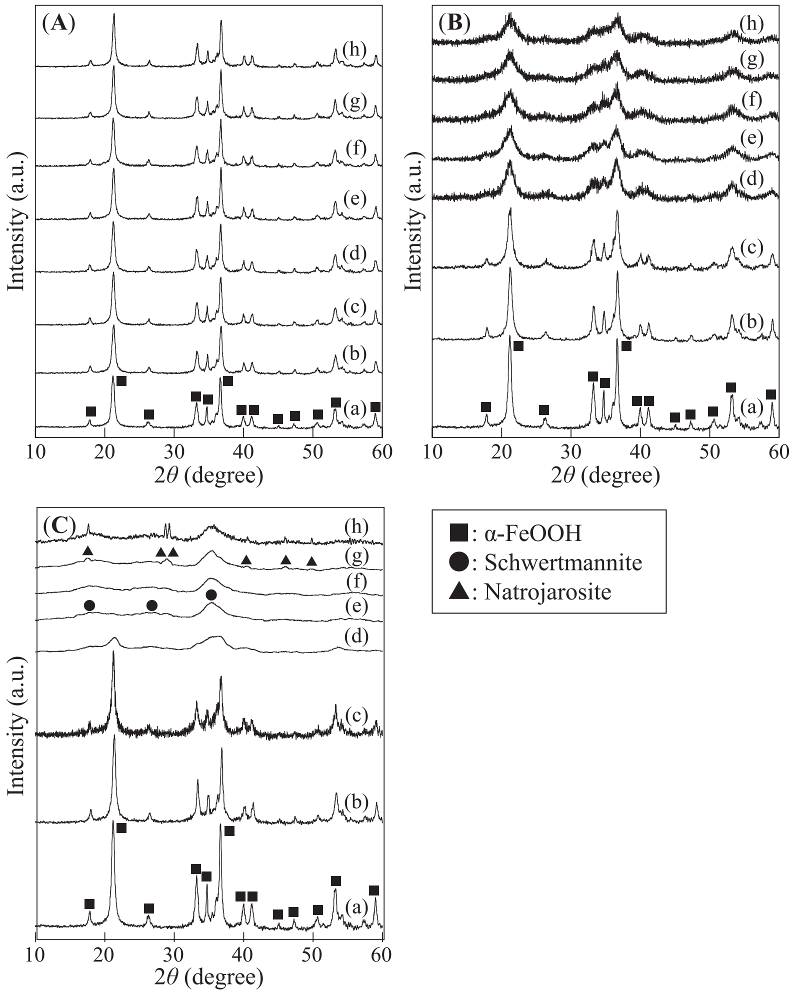

Fig. 8 XRD patterns of the products synthesized in the presence of **(A)** Ni^{2+}, **(B)** Cu^{2+} and **(C)** Cr^{3+}. metal/Fe: **(a)** 0, **(b)** 0.005, **(c)** 0.01, **(d)** 0.02, **(e)** 0.04, **(f)** 0.06, **(g)** 0.08, **(h)** 0.1. Adapted with permission from Ref. (Tanaka H. et al., 2018). Copyright: (2018) Elsevier B.V.

sharp peaks due to Natrojarosite $NaFe_3(SO_4)_2(OH)_6$ appear at $Cr/Fe \geq 0.08$. Hence, the addition of Cu^{2+} and Cr^{3+} inhibits the crystallization of α-FeOOH and a considerable amount of added Cr^{3+} impedes the transformation of Schwertmannite into α-FeOOH. The crystallite size of α-FeOOH, which is calculated using the Scherrer equation, is plotted against the metal/Fe ratio in **Fig. 9**. The crystallite size is 24.1 nm when metal/Fe = 0 and it decreases as the Cu/Fe ratio increases up to 0.02, indicating that the crystallization of α-FeOOH is inhibited. The Cr^{3+} addition also reduces the crystallite size and its effect is slightly higher than that of Cu^{2+} addition. Nonetheless, no considerable influence is observed by Ni^{2+} addition. These results indicate that the addition of Cu^{2+} and Cr^{3+} inhibits the crystallization of α-FeOOH and the effect is in the order $Cr^{3+} > Cu^{2+} >> Ni^{2+}$.

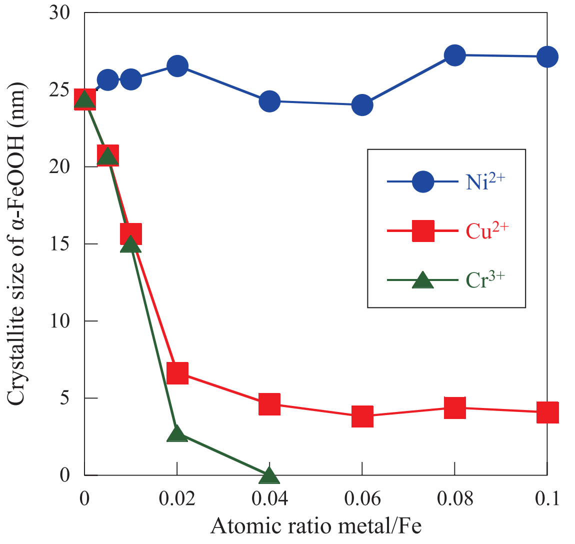

Fig. 9 Crystallite size of α-FeOOH vs. atomic ratio metal/Fe. Adapted with permission from Ref. (Tanaka H. et al., 2018). Copyright: (2018) Elsevier B.V.

In **Fig. 10** is plotted the metal/Fe atomic ratio of the particles estimated from the Ni, Cu, Cr, and Fe contents against the metal/Fe ratio of the solution. It is clearly observed that the Cr/Fe ratio of the particles is considerably larger than that of the solution. However, the Cu/Fe and Ni/

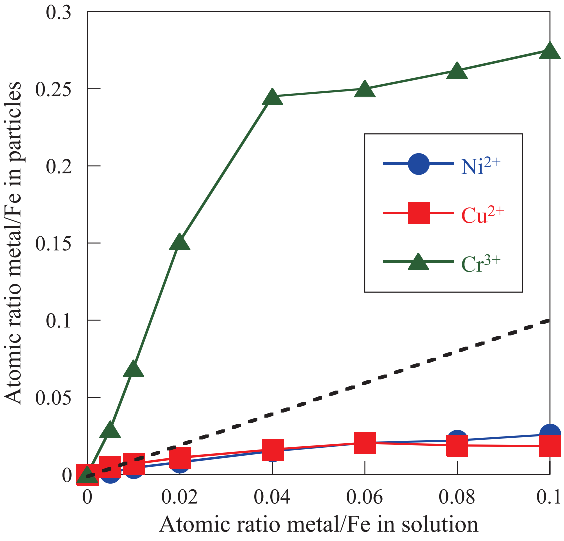

Fig. 10 Plots of atomic ratio metal/Fe in particles against atomic ratio metal/Fe in solution. Adapted with permission from Ref. (Tanaka H. et al., 2018). Copyright: (2018) Elsevier B.V.

Fe ratios of the particles are lower than those of the starting solutions. These indicate that the added Cr^{3+} is more easily incorporated in the particles than Fe^{3+}, in contrast, the uptake of Ni^{2+} and Cu^{2+} is difficult.

TEM images of the particles generated in the presence of Ni^{2+}, Cu^{2+}, and Cr^{3+} are shown in **Fig. 11**. When metal/Fe = 0, rod-shaped α-FeOOH particles with a length and width of approximately 270 and 40 nm, respectively, are recognized. The morphology of α-FeOOH particles is unchanged by Ni^{2+} addition, indicating that the added Ni^{2+} has no considerable influence on the growth of α-FeOOH particles. At Cu/Fe = 0–0.01, no significant change in the morphology of α-FeOOH particles is observed. At Cu/Fe ≥ 0.02, the rod-shaped α-FeOOH particles transform into irregular α-FeOOH particles with a size of approximately 65 nm. Similar to Cu^{2+} addition, with Cr^{3+} addition, increasing the Cr/Fe ratio up to 0.01 substantially reduces the size of α-FeOOH particles to approximately 50 nm and alters the rod-shaped particles into irregular ones. These results indicate that the growth of α-FeOOH particles is considerably suppressed by Cu^{2+} and Cr^{3+} addition. At Cr/Fe ≥ 0.04, irregular-shaped Schwertmannite particles with a size of approximately 25 nm are observed. Furthermore, hexagonal Natrojarosite particles with a size of approximately 0.8 μm appear when Cr/Fe ≥ 0.06.

The formation and crystallization of iron oxide particles considerably depend on the solution pH (Misawa T. et al., 1974; Blesa M.A. and Matijević E., 1989; Cornell R.M. and Schwertmann U., 1996; 2000; Tamura H., 2008). The solution pH before aging is plotted as a function of metal/Fe atomic ratio in **Fig. 12**. The solution pH before aging is 7.0 at metal/Fe = 0 and is essentially not altered by Ni^{2+} addition. Further, the solution pH before aging is reduced by adding Cu^{2+} and Cr^{3+} up to metal/Fe = 0.02 and remains practically constant at approximately 4.5 and 4.0, respectively. This is due to the formation of $Cu(OH)_2$

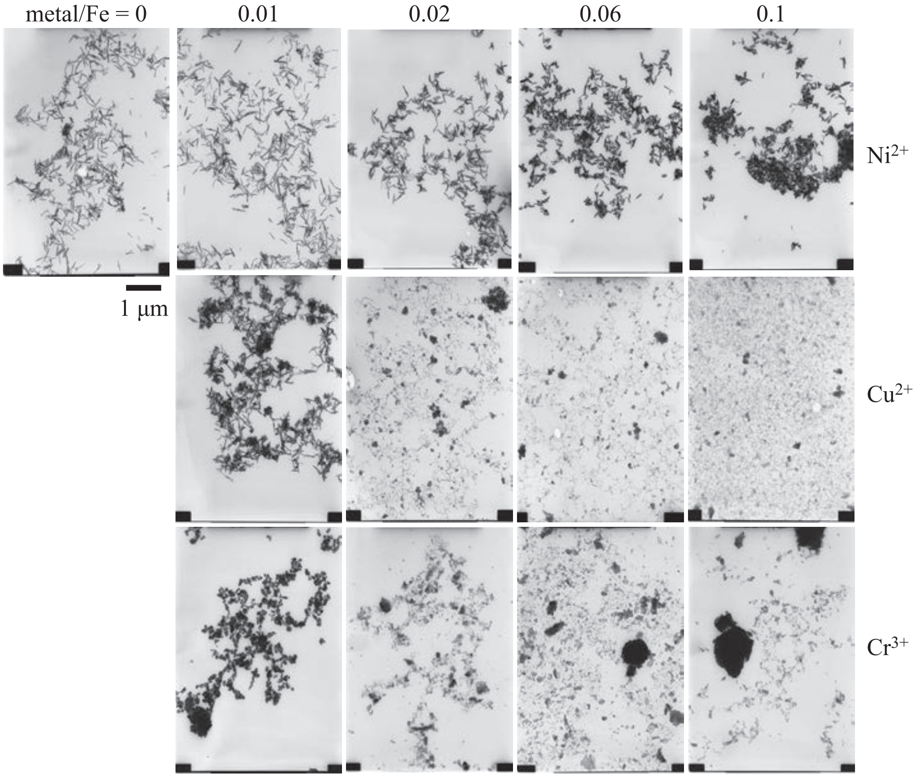

Fig. 11 TEM images of the particles generated with Ni^{2+}, Cu^{2+} and Cr^{3+}. Adapted with permission from Ref. (Tanaka H. et al., 2018). Copyright: (2018) Elsevier B.V.

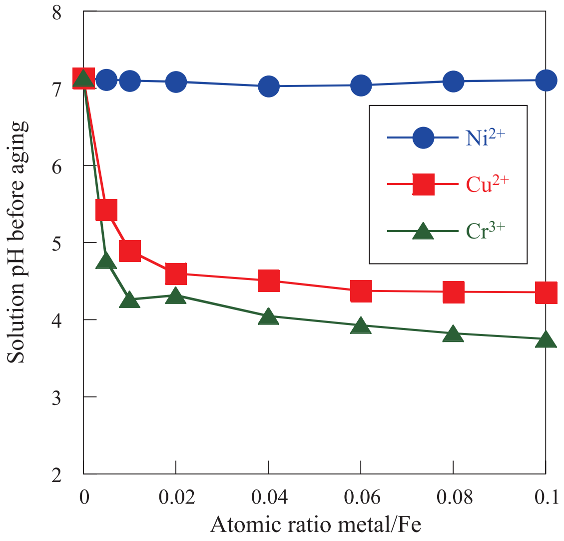

Fig. 12 Plots of the solution pH before aging as a function of atomic ratio metal/Fe. Adapted with permission from Ref. (Tanaka H. et al., 2018). Copyright: (2018) Elsevier B.V.

and $Cr(OH)_3$ through the addition of NaOH solution because the reactions of Cu^{2+} and Cr^{3+} with OH^- progress at $pH \geq 4.2$ and ≥ 4.0, respectively (Baes Jr C.F. and Mesmer R.E., 1986). Hence, lowering the solution pH before aging by adding Cu^{2+} and Cr^{3+} suppresses the crystallization and particle growth of α-FeOOH. To verify this, α-FeOOH particles were prepared at pH = 4.0 and 7.0 without metal ion addition. The XRD patterns and TEM images of the obtained particles are depicted in **Fig. 13**. It is evident that the reduction in solution pH before aging significantly weakens and broadens the α-FeOOH peaks. Moreover, the crystallite size of α-FeOOH obtained at pH = 4.0 is 7 nm less than that at pH = 7.0 (24 nm). Further, the rod-shaped particles become irregular with a size of ca. 30 nm. These results indicate that reducing the solution pH before aging by adding Cu^{2+} and Cr^{3+} considerably prevents the crystallization and particle growth of α-FeOOH. The crystal structure of α-FeOOH consists of double chains of edge-shared Fe^{3+} octahedron, as shown in **Fig. 2** (Cornell R.M. and Schwertmann U., 1996; 2000). The ionic radii of octahedral Ni^{2+} (0.069 nm) and Cu^{2+} (0.072 nm) are larger than that of octahedral Fe^{3+} (0.064 nm), hence, the substitution of Ni^{2+} and Cu^{2+} with Fe^{3+} in the α-FeOOH crystal is difficult (Shannon R.D., 1976). The solution pH before aging is markedly decreased by addition of Cu^{2+} and Cr^{3+}, consequently impeding the growth of α-FeOOH crystals and particles, nonetheless, Ni^{2+} addition exhibits no distinct influence. In contrast, the added Cr^{3+} is easily incorporated into the α-FeOOH crystal by substitution with Fe^{3+} to form α-$Cr_xFe_{1-x}OOH$ solid solution because the ionic radius of Cr^{3+} in the octahedron (0.063 nm) is the same as that of Fe^{3+} (0.064 nm) (Shannon R.D., 1976). Further, increasing the amount of added Cr^{3+} induces the formation of Cr^{3+}-doped Schwertmannite particles. As mentioned above, Schwertmannite is one of the precursors of α-FeOOH. Therefore, the incorporation of Cr^{3+} into Schwertmannite stabilizes its crystal structure, thus inhibiting its transformation into α-FeOOH. Consequently, the formation, crystallization, and particle growth of α-FeOOH are markedly impeded by Cr^{3+}, and the effect is in the order $Cr^{3+} > Cu^{2+} >> Ni^{2+}$.

4. Conclusions

Recently, various functionalized metal oxide nanoparticles with unique chemical and physical properties have been developed and applied in the fields of chemical

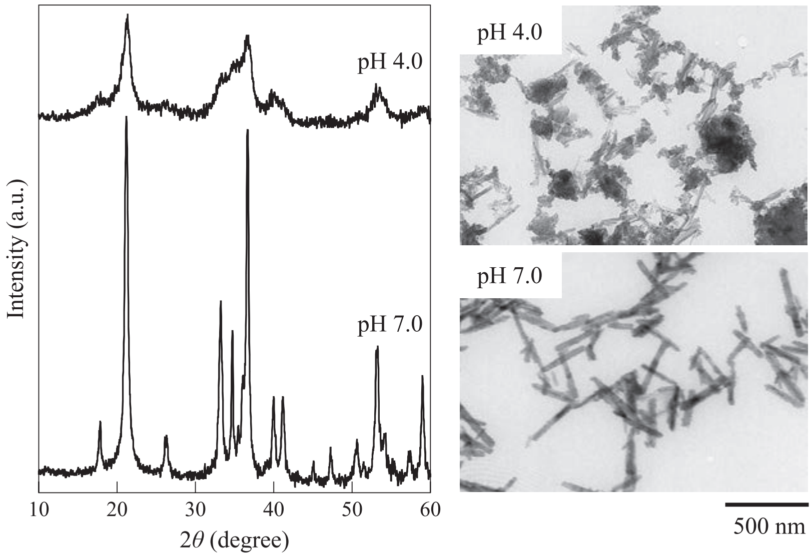

Fig. 13 XRD patterns and TEM images of α-FeOOH particles prepared at pH = 4.0 and 7.0. Adapted with permission from Ref. (Tanaka H. et al., 2018). Copyright: (2018) Elsevier B.V.

engineering, medicine, food, cosmetics, environment, etc. The particle properties are extremely dependent on the crystal structure, crystallinity, chemical composition, and particle morphology. Therefore, nanoparticles with high crystallinity, homogeneous chemical composition, uniform shape and size, and narrow particle size distribution possess excellent chemical and physical properties. However, the synthesis of such particles is extremely difficult. Hence, many researchers have investigated the synthesis of high-quality nanoparticles using the liquid-phase synthesis technique. The formation of nanoparticles is considerably affected by a number of factors, such as the anion and cation concentrations and species, additive, solution pH, and reaction temperature and time. To derive high-quality nanoparticles, gaining insight on the fundamental principles of the formation mechanism and process of nanoparticles is necessary. Accordingly, a systematic study of the particle formation is absolutely essential for the development of new functionalized nanoparticles.

Acknowledgements

The author profoundly expresses gratitude to Professor Emeritus Tatsuo Ishikawa of Osaka University of Education and Dr. Takenori Nakayama of Kobe Steel Co., Ltd., for supporting this research. This study was partly supported by Grants-in-Aid for Scientific Research (C) (20K05156 and 17K06862) the Next Generation Tatara Co-Creation Centre (NEXTA), Shimane University. Here, NEXTA is established with Grant-in-aid for the Promotion of Regional Industries and Universities from Cabinet Office, Japan.

References

Baes Jr C.F., Mesmer R.E., The Hydrolysis of Cations, Krieger Publishing Company, Florida, 1986, ISBN: 978-0471039853. DOI: 10.1002/bbpc.19770810252

Blesa M.A., Matijević E., Phase transformation of iron oxides, oxyhydroxides, and hydrous oxides in aqueous media, Advances in Colloid Interface Science, 29 (1989) 173–221. DOI: 10.1002/chin.198935372

Charitidis C.A., Georgiou P., Koklioti M.A., Trompeta A.-F., Markakis V., Manufacturing nanomaterials: from research to industry, Manufacturing Review, 1 (2014) 11. DOI: 10.1051/mfreview/2014009

Chavali M.S., Nikolova M.P., Metal oxide nanoparticles and their applications in nanotechnology, SN Applied Sciences, 1 (2019) 607. DOI: 10.1007/s42452-019-0592-3

Cornell R.M., Schwertmann U., The Iron Oxides, Wiely, 1996, ISBN: 978-3527302741. DOI: 10.1002/3527602097

Dousma J., de Bruyu P.L., Hydrolysis-precipitation studies of iron solutions. I. Model for hydrolysis and precipitation from Fe(III) nitrate solutions, Journal of Colloid and Interface Science, 56 (1976) 527–539. DOI: 10.1016/0021-9797(76)90119-3

Dousma J., de Bruyu P.L., Hydrolysis-precipitation studies of iron solutions. II. Aging studies and the model for precipitation from Fe(III) nitrate solutions, Journal of Colloid and Interface Science, 64 (1978) 154–170. DOI: 10.1016/0021-9797(78)90345-4

Dousma J., de Bruyu P.L., Hydrolysis-precipitation studies of iron solution. III. Adsorption of growth model to the formation of colloidal α-FeOOH from acidic solutions, Journal of Colloid and Interface Science, 72 (1979) 314–320. DOI: 10.1016/0021-9797(79)90113-9

Dousma J., Ottelander D., de Bruyu P.L., The influence of sulfate ions on the formation of iron(III) oxide, Journal of Inorganic and Nuclear Chemistry, 41 (1979) 1565–1568. DOI: 10.1016/0022-1902(79)80176-1

Dousma J., Van Den Hoven J.T.J., de Bruyu P.L., The influence of chloride ions on the formation of iron(III) oxyhydroxide, Journal of Inorganic and Nuclear Chemistry, 40 (1978) 1089–1093. DOI: 10.1016/0022-1902(78)80515-6

Feitknecht W., Studies of the influence of chemical factors on the corrosion of metals, Chemistry and Industry, 36 (1959) 1102–1109.

Feng J., Biskos G., Schmidt-Ott A., Toward industrial scale synthesis of ultrapure singlet nanoparticles with controllable sizes in a continuous gas-phase process, Scientific Reports, 5 (2015) 15788. DOI: 10.1038/srep15788 (2015)

Fujishima A., Hashimoto K., Watanabe T., TiO_2 Photocatalysis: Fundamentals and Applications, Tokyo Bkc, 1999, ISBN: 9784939051036.

Gutch A., Mühlrngweg H., Krämer M., Tailor-made nanoparticles via gas phase synthesis, Small, 1 (2004) 30–46. DOI: 10.1002/smll.200400021

Hsu P.M., Nucleation, polymerization, and precipitation of FeOOH, Journal of Soil Science, 23 (1972) 407–419. DOI: 10.1111/j.1365-2389.1972.tb01671.x

Hsu P.M., Ragone S.E., Ageing of hydrolyzed iron(III) solutions, Journal of Soil Science, 23 (1972) 17–31. DOI: 10.1111/j.1365-2389.1972.tb01637.x

Iler R.K., The Chemistry of Silica: Solubility, Polymerization, Colloid and Surface Properties and Biochemistry of Silica, Wiley, 1979, ISBN: 9780471024040.

Inouye K., The role of copper (II) in the oxidation of ferrous hydroxide colloid with special reference to the corrosion of iron in an SO_2-containing environment, Journal of Colloid and Interface Science, 27 (1968) 171–179. DOI: 10.1016/0021-9797(68)90024-6

Inouye K., Ishii S., Kaneko K., Ishikawa T., The effect of copper(II) on the crystallization of α-FeOOH, Zeitschrift für Anorganische und Allgemeine Chemie, 391 (1972) 86–96. DOI: 10.1002/zaac.19723910111

Ishikawa T., Formation and structures of iron oxides, Zairyo-to-Kankyo, 46 (1997) 411–417. DOI: 10.3323/jcorr1991.46.411

Ishikawa T., Synthesis, structure and modification of iron oxide nanoparticles, Bulletin of The Iron and Steel Institute of Japan, 14 (2009) 215–221.

Ishikawa T., Miyamoto S., Kandori K., Nakayama T., Influence of anions on the formation of β-FeOOH rusts, Corrosion Science, 47 (2005) 2510–2520. DOI: 10.1016/j.corsci.2004.10.016

Ishikawa T., Motoki T., Kato R., Yasukawa A., Kandori K., Nakayama T., Yuse F., Structures of β-FeOOH particles formed in the presence of Ti(IV), Cr(III), and Cu(II) ions, Journal of Colloid and Interface Science, 250 (2002) 74–81. DOI: 10.1006/jcis.2002.8257

Ishikawa T., Motoyoshi N., Yasukawa A., Kandori K., Nakayama T., Yuse F., Influence of metal ions on formation of α-FeOOH rust -single and multiple additions of Cu(II), Ni(II) and

Ti(IV)-, Zairyo-to-Kankyo, 50 (2001) 155–161. DOI: 10.3323/jcorr1991.50.155

Ishikawa T., Nakayama T., Approach to enhancement mechanism of resistance to corrosion of weathering steels by artificially synthesized rusts, Zairyo-to-Kankyo, 52 (2003) 140–154. DOI: 10.3323/jcorr1991.52.140

Ishikawa T., Yamashita H., Yasukawa A., Kandori K., Nakayama T., Yuse F., Structures of Ti(IV)-doped α-FeOOH particles, Journal of Materials Chemistry, 10 (2000) 543–547. DOI: 10.1039/A905433B

Jolivet J-P., Metal Oxide Chemistry and Synthesis: From Solution to Solid State, Wiley, New York, 2000, ISBN: 978-0471970569.

Kamimura T., Nasu S., Segi T., Tazaki T., Miyuki H., Morimoto S., Kubo T., Influence of cations and anions on the formation of β-FeOOH, Corrosion Science, 24 (2005) 2531–2542. DOI: 10.1016/j.corsci.2004.10.014

Kandori K., Iron oxide particles, in: Hubbard A.T. (Eds.), Encyclopedia of Surface and Colloid Science, Marcel Dekker, New York, 2002, pp. 3126–3469, ISBN: 978-0824707965.

Karatutlu A., Barhoum A., Sapelkin A., Chapter 1 - Liquid-phase synthesis of nanoparticles and nanostructured materials, in: Barhoum A., Makhlouf A.S.H. (Eds.), Emerging Applications of Nanoparticles and Architecture Nanostructures, Elsevier, 2018, pp.1–28, ISBN: 978-0-323-51254-1. DOI: 10.1016/B978-0-323-51254-1.00001-4

Korotcenkov G., Thomas S., Sunny A.T., Velayudhan P. (Eds.), Colloidal Metal Oxide Nanoparticles: Synthesis, Characterization and Applications, Elsevier, 2019, ISBN: 9780128133576. DOI: 10.1016/C2016-0-03725-7

LaMer V.K., Nucleation in phase transitions, Industrial & Engineering Chemistry, 44 (1952) 1270–1277. DOI: 10.1021/ie50510a027

LaMer V.K., Dinegar R.H., Theory, production and mechanism of formation of monodispersed hydrosols, Journal of the American Chemical Society, 72 (1950) 4847–4854. DOI: 10.1021/ja01167a001

Lang P.F., Smith B.C., Ionization energies of atoms and atomic ions, Journal of Chemical Education, 80 (2003) 938–946. DOI: 10.1021/ed080p938

Lifshitz I.M., Slyozov V.V., The kinetics of precipitation from supersaturated solid solutions, Journal of Physics and Chemistry of Solids, 19 (1961) 35–50. DOI: 10.1016/0022-3697(61)90054-3

Matijević E., Production of monodispersed colloidal particles, Annual Review of Materials Research, 15 (1985) 483–516. DOI: 10.1146/annurev.ms.15.080185.002411

Misawa T., Hashimoto K., Shimodaira S., On the mechanism of atmospheric rusting of iron and protective rust layer on low alloy steels, Boshoku-Gijutsu, 23 (1974) 17–27. DOI: 10.3323/jcorr1974.23.1_17

Muguruma M., Tanaka H., Ishikawa T., Nakayama T., Influence of metal ions on the transformation of artificial Schwertmannite rust particles into α-FeOOH, Zairyo-to-Kankyo, 64 (2015) 235–239. DOI: 10.3323/jcorr.64.235

Murphy P.J., Posner A.M., Quirk J.P., Characterization of hydrolyzed ferric ion solutions. A comparison of the effects of various anions on the solutions, Journal of Colloid and Interface Science, 56 (1976) 312–319. DOI: 10.1016/0021-9797(76)90256-3

Nakayama T., Ishikawa T., Konno T.J., Structure of titanium-doped goethite rust, Corrosion Science, 47 (2005) 2521–2530. DOI: 10.1016/j.corsci.2004.11.030

Oh S.J., Kwon S.-J., Lee J.-Y., Yoo J.-Y., Choo W.-Y., Oxidation of Fe^{2+} ions in sulfate- and chloride-containing aqueous medium, Corrosion, 58 (2002) 498–504. DOI: 10.5006/1.3277640

Ostwald W.Z., Über die vermeintliche Isomerie des roten und gelben Quecksilberoxyds und die Oberflächenspannung fester Körper, Zeitschrift für Physikalische Chemie, 34 (1900) 495–503. DOI: 10.1515/zpch-1900-3431

Pelizzetti E., Fine Particles Science and Technology: From Micro to Nanoparticles, Springer, 2011, ISBN: 9789401066006.

Plote J., Fundamental growth principles of colloidal metal nanoparticles -a new perspective, CrystEngComm, 17 (2015) 6809–6830. DOI: 10.1039/C5CE01014D

Reiss H., The growth of uniform colloidal dispersions, Journal of Chemical Physics, 19 (1951) 482–487. DOI: 10.1063/1.1748251

Rodríguez J.A., Fernández-García M. (Eds.), Synthesis, Properties, and Applications of Oxide Nanomaterials, Wiley, 2006, ISBN: 9780471724056. DOI: 10.1002/0470108975

Schultz M., Burckhardt W., Barth St., Investigations on thermally forced hydrolysis and phase formation in aqueous iron(III) nitrate solutions, Journal of Materials Science, 34 (1999) 2217–2227. DOI: 10.1023/A:1004553019739

Schwertmann U. and Cornell R.M., Iron Oxides in the Laboratory: Preparation and Characterization, Wiely, 2000, ISBN: 978-3527296699. DOI: 10.1002/9783527613229

Shannon R.D., Revised effective ionic radii and systematic studies of interatomic distances in halides and chalcogenides, Acta Crystallographica, A32 (1976) 751–767. DOI: 10.1107/S0567739476001551

Sillen L.G., Martell A.E., Stability Constants of Metal-Ion Complexes, The Chemical Society, London, 1964, ISBN: 978-0851860190.

Sudakar S., Subbanna G.N., Kutty T.R.N., Effect of anions on the phase stability of γ-FeOOH nanoparticles and the magnetic properties of gamma-ferric oxide derived from lepidocrocite, Journal of Physics and Chemistry of Solids, 64 (2003) 2337–2349. DOI: 10.1016/S0022-3697(03)00270-1

Sugimoto T., Preparation of monodispersed colloidal particles, Advances in Colloid and Interface Science, 28 (1987) 65–108. DOI: 10.1016/0001-8686(87)80009-X

Sugimoto T., Monodispersed Particles, Elsevier, 2001, ISBN: 9780444895691.

Tamura H., The role of rusts in corrosion and corrosion protection of iron and steel, Corrosion Science, 50 (2008) 1872–1883. DOI: 10.1016/j.corsci.2008.03.008

Tanaka H., Elucidation of atmospheric corrosion mechanism of steels by artificially synthesized iron rust particles, Journal of the Society of Powder Technology, Japan, 52 (2015) 398–404. DOI: 10.4164/sptj.52.398

Tanaka H., Hatanaka N., Muguruma M., Ishikawa T., Nakayama T., Influence of anions on the formation of artificial steel rust particles prepared from acidic aqueous Fe(III) solution, Corrosion Science, 66 (2013a) 136–141. DOI: 10.1016/j.corsci.2012.09.011

Tanaka H., Hatanaka N., Muguruma M., Nishitani A., Ishikawa T., Nakayama T., Influence of anions on the structure and morphology of steel rust particles prepared by aerial oxidation of acidic Fe(II) solutions, Advanced Powder Technology, 27 (2016a) 2291–2297. DOI: 10.1016/j.apt.2016.09.004

Tanaka H., Inoue M., Ishikawa T., Nakayama T., Simulating study of atmospheric corrosion of steels in a coastal industrial zone: effect of SO_3^{2-} on the formation of β-FeOOH rust particles synthesized from $FeCl_3$ solutions, Corrosion Science, 66 (2016b) 241–245. DOI: 10.1016/j.corsci.2016.07.019

Tanaka H., Miyafuji A., Ishikawa T., Nakayama T., Influence of Ni(II), Cu(II) and Cr(III) on the formation, morphology and molecular adsorption properties of α-FeOOH rust particles prepared by aerial oxidation of neutral Fe(II) solutions, Advanced Powder Technology, 29 (2018) 9–17. DOI: 10.1016/j.apt.2017.09.015

Tanaka H., Miyafuji M., Kandori K., Ishikawa T., Nakayama T., Effect of Cu(II) on the formation, morphology and molecular adsorption properties of α-FeOOH rust particles prepared from acidic Fe(III) solutions, Corrosion Science, 66 (2013b) 337–342. DOI: 10.1016/j.corsci.2012.09.039

Thanh N.T.K., Maclean N., Mahiddine S., Mechanisms of nucleation and growth of nanoparticles in solution, Chemical Reviews, 114 (2014) 7610–7630. DOI: 10.1021/cr400544s

Author's Short Biography

Hidekazu Tanaka

Hidekazu Tanaka received his Ph.D. from the Tokyo Metropolitan University in 1999. He worked as a JSPS Research Fellow PD at the Osaka University of Education from 1999 to 2000. He joined at the Shimane University as an Assistant Professor in 2000 and an Associate Professor in 2006. In 2014, he became a Professor of Graduate school of Natural Science and Technology at Shimane University. His research interest is wet-synthesis of highly functionalized inorganic particles by control of the particle morphology and modification of the surface structure focusing on the surface functional groups.

KONA Powder and Particle Journal No. 39 (2022) 130–149/https://doi.org/10.14356/kona.2022015 Review Paper

High Performance Nickel Based Electrodes in State-of-the-Art Lithium-Ion Batteries: Morphological Perspectives[†]

Agus Purwanto[1,2*], Shofirul Sholikhatun Nisa[1,2], Ike Puji Lestari[1,2], Muhammad Nur Ikhsanudin[1,2], Cornelius Satria Yudha[1,2] and Hendri Widiyandari[2,3]

[1] *Chemical Engineering Department, Faculty of Engineering, Universitas Sebelas Maret, Indonesia*
[2] *Centre of Excellence for Electrical Energy Storage Technology, Universitas Sebelas Maret, Indonesia*
[3] *Physics Department, Faculty of Mathematics and Natural Science, Universitas Sebelas Maret, Indonesia*

Abstract

Li-ion batteries with “nickel” as the main material or the highest ratio material on the cathode or anode electrode have attracted considerable attention. Nickel has high strength and corrosion resistance. Nickel has also been utilized successfully as the cathode and anode materials. The specific capacity and energy and power density of the material increased with increasing nickel content. However, several problems have limited the use of nickel-based Li-ion batteries. Problems such as cation mixing, the properties of nickel, and highly Ni-rich compounds leading to side reactions, influence the electrochemical performance of Li-ion batteries. The morphology is another factor affecting the electrochemical performance. Further studies will be needed to synthesize materials with the desired morphology and determine how the morphology affects the electrochemical performance. In a morphological perspective, extensive morphological adjustments are a pathway to a long and stable life cycle. In this light, nickel-based electrodes are manufactured continuously and will always be considered for next-generation secondary energy storage. The morphology of nickel-based active materials is one of the main factors determining the high-performance of Li-ion batteries.

Keywords: morphology, Li-ion batteries, nickel-rich electrode, anode and cathode

1. Introduction

Nickel is the main highlight among researchers and industry. It is considered a versatile element because it is applied in various materials and technologies. The metal has high strength and corrosion resistance. Thus, it is often essential in construction materials, such as well-known stainless steels (Dewangan et al., 2015). Recently, nickel has found new applications in electrochemical energy storage that will permit increased mobility and flexibility. Interestingly, with current environmental issues, such as global warming and air pollution, nickel-based energy storage will be required in developing and developed countries (Ye et al., 2021).

Secondary batteries with nickel-derived active materials have been developed since the 19th century. Nickel-cadmium is the first nickel-based rechargeable battery that was successfully commercialized back in the early 20th century. Since its discovery, poor electrochemical performance and treating highly toxic spent Ni-Cd batteries have become major challenges. Its successor, Nickel-metal hydride (NiMH), also faces problems limiting its application, such as high self-discharge and low cycle life. The drawbacks of nickel-based energy storage have become alarming. Therefore, during the shift to new technology, Li-ion batteries, nickel-based electrodes were “temporally” left behind (Elbert et al., 2010; Lee et al., 2009).

Since their successful commercialization, it was predicted that Li-ion batteries would dominate the energy storage market. However, the dependence on cobalt-based materials, such as $LiCoO_2$, cannot endure (Nitta et al., 2015; Toprakci et al., 2010). Cobalt is toxic and its exploitation has caused more harm than good. Even with relatively good stability, it has low real capacity because full Li-ion storage capacity was limited to 50 % to avoid explosions caused by thermal and design failure. In addition, cobalt is very expensive compared to other common transitional metals. These problems have shifted the concerns of researchers and industries back to nickel as an electrode material (Kalyani and Kalaiselvi, 2005).

Nickel has been used successfully utilized as both cathode and anode materials. Layered structured lithium

---

[†] Received 31 May 2021; Accepted 16 June 2021

[*] Corresponding author: Agus Purwanto;
Add: Jl. Ir. Sutami 36A, Surakarta, Central Java 57126, Indonesia
E-mail: aguspurwanto@staff.uns.ac.id
TEL/FAX: +62-271-662118

transitional metal oxides (LTMO) were recently considered high-performance and high energy density cathode materials. Based on **Fig. 1**, the proportion of nickel in LTMOs has increased gradually over the past two decades, e.g., the development of NMCs (lithium nickel manganese cobalt oxide) and NCA (lithium nickel cobalt aluminum oxide) (Yan et al., 2020). While there is no classification of NCA, NMC cathode materials are classified based on the composition of the transitional metals and the types can be seen in **Fig. 1**. Extensive efforts to increase the nickel content in NMCs cathode materials have been reported. The specific capacity, energy density, and power density of the material increase with increasing nickel content. However, several problems are still being faced during its implementation. Nickel-rich cathode materials, such as $LiNiO_2$, $LiNi_{1-x-y}Co_xMn_yO_2$ ($x + y < 4$), and $LiNi_{0.8}Co_{0.15}Al_{0.05}O_2$, are often produced with poor electrochemical properties because of cationic exchange between Li^+ and Ni^{2+} from their lattices, where the cell suffers high irreversible capacity loss during its use (Lei et al., 2019a). Nickel-rich materials are also hygroscopic, which means they attract water molecules when not stored and handled properly. Highly reactive nickel-rich compounds at elevated working voltages also result in undesirable side reactions between the nickel-rich cathodes and the aprotic carbonate-rich electrolyte, producing unwanted side products that cause a rapid decrease in capacity or lifetime. Studies have confirmed that the cation mixing level can be reduced by the synthesis conditions and doping process in a nickel-rich cathode. Hygroscopicity can be overcome by proper storage conditions or coating of materials (Huang et al., 2014). The unwanted side reactions that occur during cell use can also be suppressed by coating the materials. However, adding a coating to a nickel-rich cathode is considered uneconomical because the coating process requires additional processing and production (Lu X. et al., 2019). Tailoring the particle morphology can also reduce the reactivity of Ni-rich cathodes. In addition, different morphologies result in different electrochemical behavior in Li-ion cells (Hwang et al., 2012).

Nickel-based anodes have undergone continuous development to replace existing carbonaceous anodes (Zuniga et al., 2019). Carbonaceous anodes have low gravimetric and volumetric capacity. To obtain commercialized artificial graphite, an extremely high heating process is necessary. Even with excellent performance, Li dendrite formation is an alarming phenomenon in graphite anodes because it can potentially cause battery failures. These concerns prove that state-of-the-art anode materials are urgently needed. Metal-based anodes, specifically nickel-based anodes, such as nickel oxides, nickel hydroxides, and nickel sulfides, are being developed continuously. The high capacity, high conductivity, easy recycling and reuse, and high availability make the metal-based anodes economically attractive. However, large capacity loss during the initial cycle often occurred because the Li storage mechanism involves a conversion and alloying-dealloying process (Wang L. et al., 2018). This problem can be overcome by morphological tailoring.

As Ni-rich Li-ion batteries are the market giant for current and future energy storage, an understanding of the factors that affect the electrochemical performance of the cells is required. Accordingly, because the morphology of the particle affects the electrochemical performance, this paper presents a review of nickel-based electrode synthesis toward its electrochemical behavior based on a morphological perspective.

2. Particle morphology for nickel-based anode material

Currently, various nickel-based materials have been applied as the anode material in Li-ion batteries. Oxides, hydroxides, sulfides, carbonates, and oxalates of nickel as anode material are representative examples. The electrochemical performance of these materials is mostly improved because of their unique morphologies. This section discusses the morphology of the nickel-based materials and their electrochemical performance.

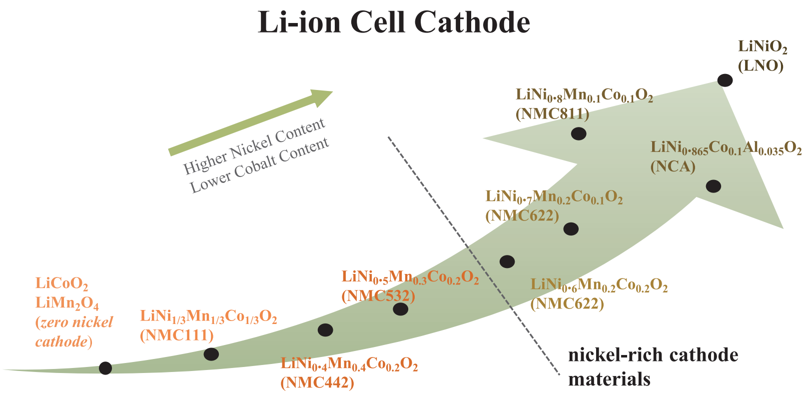

Fig. 1 The developments of LTMO-based cathodes.

2.1 Nanosheets nickel-based anode materials

Nanosheets $Ni(OH)_2$ has been developed and successfully applied as an active material of Li-ion batteries. Various precursors of $Ni(NO_3)_2 \cdot 6H_2O$ and $NiCl_2 \cdot 6H_2O$ provide uniform and ultra-thin nanosheet particle with particle dimension range between 20–30 µm. Particle morphology from $NiSO_4 \cdot 6H_2O$ showing larger particle with dimension range between 30–50 µm. The electrochemical performance of $Ni(OH)_2$ are 1790/1157, 1945/1282, and 2019/1358 mAh g^{-1} with columbic efficiencies 65, 66, and 67 % (Li Yanwei et al., 2017). Modification of $Ni(OH)_2$ by Al doping has been reported. The study showed the addition of Al slightly alter the particle dimension with specific capacity of 681 mAh g^{-1} at 20 % Al content and capacity retention of 50 % after 30 cycles (Li Y. et al., 2016).

Cycle ability of $Ni(OH)_2$ can be improved by Ti_3C_2 lamination via hydrometallurgy method. In the study, $Ni(OH)_2/Ti_3C_2$ electrode material has Li capacity of 121.3 mAh g^{-1}, higher than pure $Ni(OH)_2$ (117.6 mAh g^{-1}) with stable cycle performance after 1000 cycles (Li C. et al., 2020). Double hydroxide metal transition, Nickel-cobalt, with ultrathin graphene surface layer is an alternative to a stable electrochemical cycle performance of nanosheets $Ni(OH)_2$ (Shi et al., 2017). $Ni(OH)_2$ blending with PANI and graphene oxide exhibited improved cycle ability with only 15.6 % capacity drop after 2000 cycles (Ma et al., 2016). This technique also successfully implemented in Ni-Co phosphates which had excellent cycling ability and stability after 9000 cycles (Li B. et al., 2017).

2.2 Nanoflakes nickel-based anode materials

Nanoflakes $Ni(OH)_2$ was obtained via precipitation and hydrazine assisted reduction process. Blended with rGO, the material delivered high initial capacity of 1500 mAh g^{-1} and 1003 mAh g^{-1} after 40 cycles (Zhu et al., 2014). Nanoflake NiO as anode material was successfully obtained by chemical liquid deposition in Ni-foam followed by atmospheric heat treatment at 350 °C. The material delivered discharge capacity of 1.94 mAh cm^{-2} and capacity retention 71.1 % after 140 cycles (Ni et al., 2013). Another approach to obtain nanoflake NiO is via chemical bath deposition before being inserted into Ni foam. It exhibited initial capacity of 700 mAh g^{-1} and 490 mAh g^{-1} after 50 cycles (Huang et al., 2009). Nanoflake NiS from hydrothermally treated $NiCl_2$ and metal alloying was also reported. The electrochemical performance test showed initial discharge capacity of 584.6 mAh g^{-1} and capacity retention of 34.2 % after 30 cycles (Zhu et al., 2011). Flake-shaped carbon-NiS was obtained also via hydrothermal process with addition of glucose as carbon source. The material initial and 20th discharge capacity was 575.4 mAh g^{-1} and 200 mAh, respectively (Wang et al., 2013).

2.3 Nanoplate nickel-based anode materials

Nanoplate $Ni(OH)_2$/Graphene anode material was produced by hydrothermal reaction of $NiNO_3$, ammonia and graphene at 150 °C for 12 h. It exhibited Initial specific capacity of 1318 mA/g and average capacity loss of about 0.11 % after 100 cycles (Du et al., 2018).

2.4 Nanorod nickel-based anode materials

SEM analysis of a NiS-graphene composite revealed nanorod morphological particles. NiS-graphene with a nanorod morphology was produced using the Hummers method followed by thermal reduction. The NiS to graphene mass ratio that indicates a nanorod morphology was 2:1.

The electrochemical performance test revealed an initial discharge capacity of 458 mAh g^{-1}. This was smaller than NiS:graphene = 1:1, which had been discussed elsewhere in the sub-chapter nanosheet reported (Geng et al., 2014). The NiS nanorod morphology also could be produced using a solvothermal reaction. The raw material for the Ni-source and S-source was nitrate-based and C_2H_5NS, respectively. SEM showed that the concentration of the reactant solution affected the morphology of the particle. All concentrations produced a nanorod morphology, but higher concentrations resulted in a decrease in NiS particle size. The electrochemical test revealed good performance. The initial discharge capacity was 670 mAh g^{-1}, and good cycling stability was observed after 100 cycles (Long et al., 2016). Nickel oxalate ($NiC_2O_4 \cdot 2H_2O$) nanorod particles were synthesized using a hydrothermal method. The temperature of the hydrothermal process influenced the particle morphology. An urchin-like nanorod morphology was observed when the reaction took place at 130 °C. On the other hand, the ratio and size of the nanorod particles increased when the reaction occurred at 170 °C. The initial discharge capacity was 1109 mAh g^{-1} with cycling stability of 85 % (Oh et al., 2016). Nickel oxalate was also used as a precursor material for NiO (Du et al., 2020).

2.5 Nanospike nickel-based anode materials

NiS with nano-spike morphology was obtained using a hydrothermal method in an autoclave reactor performed at a temperature of 160 °C for 24 hours. **Fig. 2a** shows a nano-spike particle. The electrochemical performance test was conducted on a coin cell-type cell with NiS as the cathode and Li-foil as the anode. The best initial discharge specific capacity was 550 mAh g^{-1}. Cycling stability after 100 cycles revealed 60 % capacity retention from its initial capacity (Sonia et al., 2014). The NiS powder was modified by adding a camphoric carbon solution to the raw material to form "camphoric carbon wrapped NiS". SEM and TEM

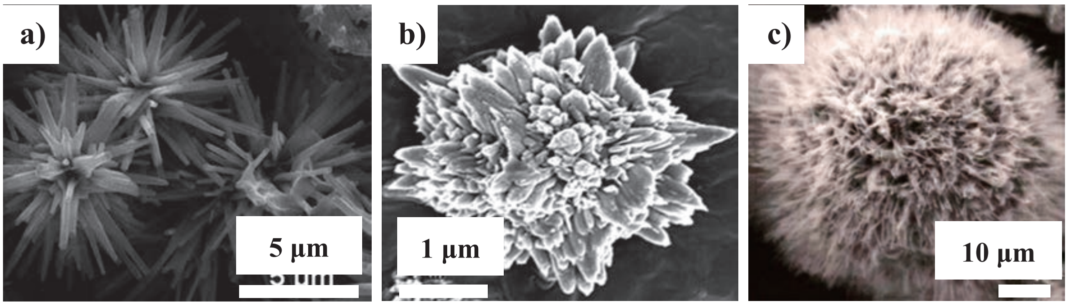

Fig. 2 **(a)** Nano-spike morphology of NiS material, reprinted with permission from Ref. (Sonia et al., 2014) Copyright (2014) Elsevier B.V. **(b)** NiS flower-like particle, reprinted with permission from Ref. (Ma et al., 2015) Copyright (2015) Springer Nature Limited, **(c)** NiS Urchin-like particle, reprinted with permission from Ref (Mi et al., 2013) Copyright (2013) RSC Publishing.

revealed nano-spike particles. The modified-NiS was produced using a hydrothermal method in an autoclave reactor at 160 °C for 24 hours. The electrochemical performance test showed an initial discharge capacity of 500 mAh g^{-1}. The test revealed 75 % capacity retention after 100 cycles, showing good cycling stability performance. The use of camphoric carbon increased the cyclic performance (Sebastian et al., 2014).

2.6 Urchin and flower like material

NiS material with an urchin-like morphology could be obtained by adding cetyltrimethylammonium bromide (CTAB) as an assistant. The flower-like NiS particles were synthesized using a hydrothermal method. **Fig. 2b** presents an SEM image of a flower-like NiS particle. The raw material for the Ni-source was a nitrate salt and NaSCN for the S-source. The highest initial discharge capacity was 6733 mAh g^{-1}. The cycling stability was tested until 10 cycles, showing 85 % capacity retention (Ma et al., 2015). NiS with an urchin-like particle morphology was synthesized from a nickel complex as a precursor using a solvothermal method. **Fig. 2c** shows the NiS urchin-like particle morphology. The electrochemical performance was assessed using a coin-cell type cell. The initial discharge capacity of the battery was 597.3 mAh g^{-1} with a voltage window of 1.0–3.0 V (Mi et al., 2013).

Table 1 summarizes the summary of nickel-based anode morphology and their electrochemical behavior. A nickel-based anode with a unique morphology showed excellent performance in Li-metal batteries. With small or nanoscale size, each material can store Li, even with good cycling ability. In contrast to the graphitic or carbon-based anode, the insertion of Li-ions uses a conversion mechanism rather than an intercalation mechanism.

Fig. 3 shows the role of morphology towards the electrochemical properties of nickel-based anode material in Li-ion batteries. Studies showed that the nanostructure property of anode material has significant roles in improving the electrochemical performance. It offers a large contact of electrolyte to the surface of the material which is beneficial for high current applications. Some of the structure such as nanorods, nanowalls, nanoflakes has a rigid structure that is able to accommodate volume change strain during prolonged cycle of charge and discharge at relatively high current. However, the capacity value is not only affected by the morphology, but also the type of material and its lithiation-delithiation mechanism which will not be discussed deeply. The cycle stability of the anode is also greatly improved by addition of 2D nano-material such as graphene, reduced graphene oxide (rGO), and Ti_3C_2.

The main disadvantage of the conversion anode is the poor initial coulombic efficiency caused by a permanent Li reaction with some of the anode. In Li-metal batteries, the high Li-loss during the first cycle can be compensated for by the abundant Li source of the Li anode. In full cells, limited Li from the cathode materials can deteriorate the electrochemical performance of the cells. Even with a unique morphology, the initial lithiation capacity of Li in conversion anodes is still much larger than the de-lithiation capacity. However, efforts to increase the usability of conversion-type materials for Li-ion full cells, such as a Li-rich cathode material, material incorporation with carbon, and pre–lithiation of conversion anodes, are still being made (Qiu et al., 2018; Wei et al., 2020).

3. Nickel rich cathodes and their precursors

The synthesis of nickel-rich cathodes generally involves two processes: the formation of nickel-rich cathode precursors and high-temperature lithiation. The formation of precursors often determines the morphology of the final products, even after undergoing a long heat-treatment process. In this section, the formation of secondary particles is not discussed because the secondary particles are often related to the final morphology of the particle. The mechanism for the formation of secondary particles will be discussed in the next segment.

Table 1 Preparation of Ni-based particle for anode material of Li-ion batteries.

Ni-based Materials	Methods	Modification	Morphological feature	Electrochemical Performance (Capacity/ Cycle/Rate)	Reference
$Ni(OH)_2$	Precipitation	—	Ultra-thin nanosheet	2019/1358 mAh g^{-1}/0.1 C	(Li Yanwei et al., 2017)
$Ni(OH)_2$	Precipitation	Al-doping 20 % w/w	Nanosheet	681 mAh g^{-1}/30 cycles/0.1 C	(Li Y. et al., 2016)
$Ni(OH)_2$	Hydrothermal	$Ni(OH)_2$/ delaminated-Ti_3C_2	Nanosheet	121 mAh g^{-1}/1000 cycles/0.1 C	(Li C. et al., 2020)
Ni-Co-hydroxide	Hydrothermal	Combine Co-Ni hydroxide	Nanosheet	373 mAh g^{-1}/500 cycles/0.1 C	(Shi et al., 2017)
$Ni(OH)_2$	One-step in-situ polymerization	GO/PANI blending	Nanosheet	Capacity fading 15.6 % after 2000 cycles	(Ma et al., 2016)
$Ni(OH)_2$	precipitation	rGO blending	Nano-flakes	1500/40 cycles/0.1 C	(Zhu et al., 2014)
NiO	CLD and graft growth under air condition	—	Nano-flakes	1.94 mAh cm^{-2}/140 cycles/0.1 C	(Ni et al., 2013)
NiO	CBD	—	Nano-flakes	700 mAh g^{-1}/50 cycles/0.1 C	(Huang et al., 2009)
NiO	Hydrothermal	Graphene blending	Nanoplate	1318 mAh g^{-1}/100 cycles/0.1 C	(Du et al., 2018)
NiO	Thermal decomposition	Ni-foam as starting material	Nanowalls	1020/704 mAh g^{-1}/60 cycles at various rates (0.2-10C)	(Wang et al., 2011)
NiS	Hydrothermal	Cladding carbon (C-NiS)	Flake-shape	575.4 mAh g^{-1}/30 cycles	(Wang et al., 2013)
NiS/G (1:1)	Hummers method continued with thermal reduction	Mass ratio NiS to graphene	Nanosheet	887 mAh g^{-1}/60 cycles/0.1 C	(Geng et al., 2014)
NiS/G (2:1)	Hummers method continued with thermal reduction	Mass ratio NiS to graphene	Nanorod	458 mAh g^{-1}/60 cycles/0.1 C	(Geng et al., 2014)
NiS	Solvothermal	Reactant concentration	Nanorod	670 mAh g^{-1}/100 cycles	(Long et al., 2016)
NiS	Hydrothermal	Reaction time (24 h)	Nano-spike	550 mAh g^{-1}/100 cycles/0.1 C	(Sonia et al., 2014)
Camphoric carbon wrapped -NiS	Hydrothermal	Addition of camphoric carbon	Nano-spike	550 mAh g^{-1}/100 cycles/0.1 C	(Sebastian et al., 2014)
NiS	Hydrothermal	CTAB assistant	Flower-like	6733 mAh g^{-1}/10 cycles	(Ma et al., 2015)
NiS	Solvothermal	Nickel complex precursor	Urchin-like	597.3 mAh g^{-1}	(Mi et al., 2013)
$NiC_2O_4 \cdot 2H_2O$	Hydrothermal	Reaction temperature	Nanorod	1109 mAh g^{-1}	(Oh et al., 2016)

3.1 Nanosheets precursor to nickel-based cathode materials

Nickel manganese cobalt (NMC)-based spherical precursors were assembled using a solvothermal method. $Ni(NO_3)_2 \cdot 6H_2O$, $Co(NO_3)_2 \cdot 6H_2O$, and $Mn(NO_3)_2$ with a mol ratio of 14:3:3 were dissolved in 50 mL of ethanol. The operational conditions were RTP (Room temperature and pressure). A clear solution was placed in an autoclave and heated to 160 °C for 12 hours. The precipitate was then washed with absolute ethanol and dried at 80 °C for 8 hours in air. The morphology analysis shows microsphere flower-like particles with diameters of approximately 2–6 µm. All the microsphere flower-like particles were comprised of nanosheets (Fu et al., 2014). **Fig. 4a** gives an example of a nanosheet primary particle.

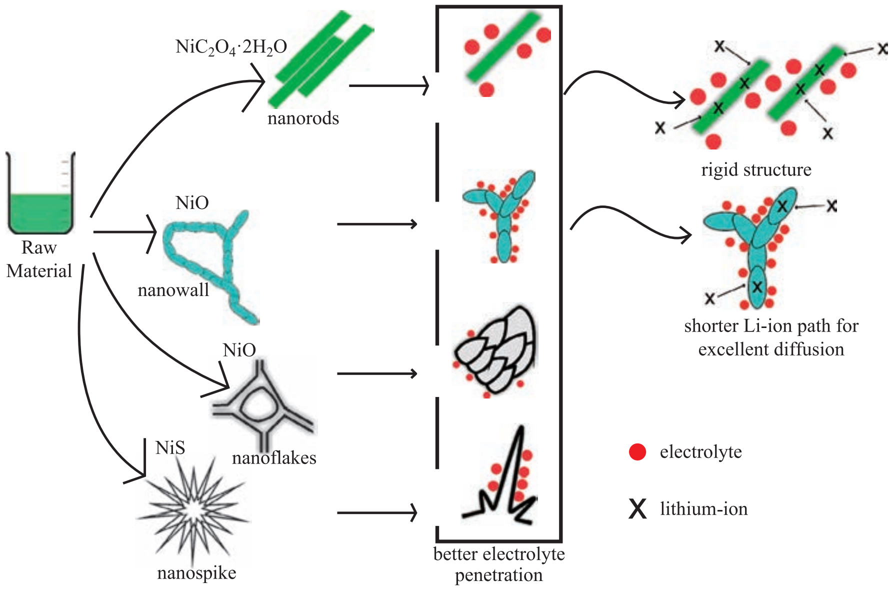

Fig. 3 Schematic illustration of the morphology effect on the Li-ion transport mechanism.

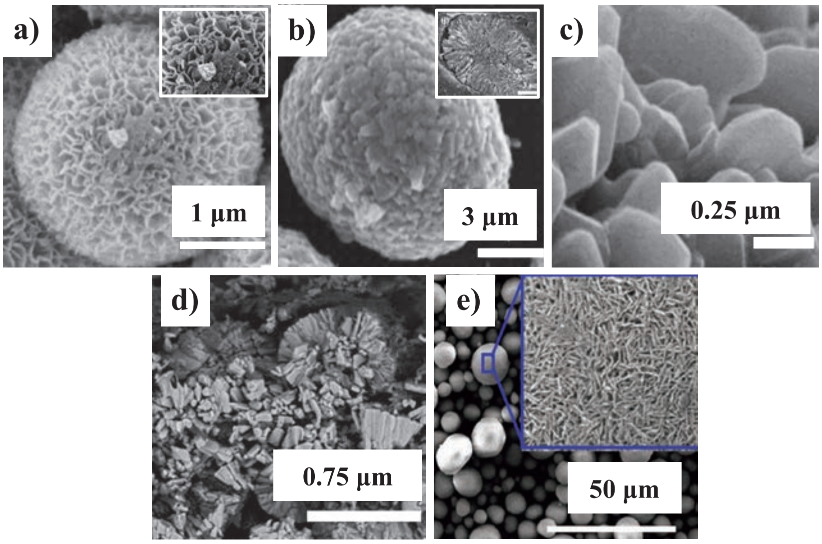

Fig. 4 **(a)** Nanosheet primary particle of NMC-based material, reprinted with permission from Ref. (Fu et al., 2014) Copyright (2014) ACS Publications, **(b)** Nanoflake primary particle of NMC-811 cathode material, reprinted with permission from Ref. (Mo et al., 2020) Copyright (2020) Elsevier B.V., **(c)** Nanoplate primary particle of NCA cathode material, reprinted with permission from Ref. (Wang Q. et al., 2018) Copyright (2018) Electrochemical Science Group, **(d)** Nanorod primary particle of NMC cathode material, reprinted with permission from Ref. (Sun et al., 2019) Copyright (2019) ACS Publications, **(e)** Needle-like particle of NCA-material, reprinted with permission from Ref. (Duan et al., 2018) Copyright (2018) Elsevier B.V.

3.2 Nanoflakes precursor to nickel-based cathode materials

Ni-rich nano-flake particles, NMC-811 ($LiNi_{0.8}Mn_{0.1}Co_{0.1}O_2$) hydroxide precursor, can be prepared using a coprecipitation method. The raw materials for Ni, Mn, and Co sources were diluted in a mixture of NaOH and NH_4OH. A calcination process was then performed under O_2 atmospheric conditions at 750 °C for 12 hours. The secondary particle morphology was spherical and assembled from cross-flake particles. The precursor was mixed with LiOH and TiO_2 to make a cathode material before sintering (Mo et al., 2020). **Fig. 4b** presents SEM images of a nanoflake particle. NMC-811 precursor synthesis is another way to improve the performance of Li-ion batteries.

3.3 Nanoplate precursor to nickel-based cathode materials

NCA ($LiNi_{0.80}Co_{0.15}Al_{0.05}O_2$) with a nanoplate morphology was obtained using sol-gel methods. The first research used raw materials: $Ni(CH_3COO)_2·6H_2O$, $Co(CH_3COO)_2·4H_2O$, $Al(NO_3)_3·8H_2O$, and $LiCH_3COO$ with a molar ratio of 10.5:8:1.5:0.5. All the ingredients were dissolved in ethylene glycol with a concentration of 0.5 M and stirred for 8 hours at 85 °C. After the powder was formed and dried, it was ground to reduce the particle size, calcined, and sintered to prepare the cathode material (Wang Q. et al., 2018). **Fig. 4c** shows the nanoplate primary particles of the NCA cathode material. The second study used a nitrate-based raw material for Li, Ni, Co, and Al. $C_{16}H_{36}O_4Ti$ was used as the Ti doping source. All the materials were dissolved in ethylene glycol and stirred for 8 hours at 85 °C (Li J. et al., 2020).

NMC-622 ($LiNi_{0.6}Mn_{0.2}Co_{0.2}O_{22}$) is another cathode material with a nanoplate morphology that was obtained from ammonia-induced coprecipitation. The first step involved mixing 12 M $NH_3{\bullet}H_2O/(Ni^{2+}$, Co^{2+}, and $Mn^{2+})$ at a molar ratio of 6:1 for 30 minutes under inert conditions (using N_2). Subsequently, the metal salts were added to the first solution and stirred for four hours. Stirring was continued at 95 °C for six hours to evaporate NH_3 and allow precipitation. The slurry was filtered, washed, and dried in an oven. Li_2CO_3, as the Li source, was added to a 7 % excess, calcined, and sintered to produce the Li-NCA cathode material (Liu et al., 2016). The NMC cathode material ($LiNi_{0.70}Mn_{0.15}Co_{0.15}O_2$) with increasing Li^+ ion diffusion showed good cycling ability. The manufacturing of this material was through a coprecipitation method followed by a hydrothermal method. The Ni, Mn, and Co metal sources were acetate salts combined at a Ni:Mn:Co molar ratio of 0.7:0.15:0.15. All the materials dissolved, and NaOH was added as a precipitating agent under inert conditions (Ar). The pH of the solution was maintained at 11. The solution was then moved to another reactor and filled to 80 % of the maximum volume. PVP (polyvinylpyrrolidone) was then added for the hydrothermal process, which was performed at 150 °C for four hours. Subsequently, the temperature was decreased naturally to ambient temperature. The slurry was then filtered, washed, and dried $[Ni_{0.70}Mn_{0.15}Co_{0.15}O_2(OH)_2]$. The last steps were the calcination and sintering processes (Tian et al., 2016).

3.4 Nanorods precursor to nickel-based cathode materials

The NMC-622 hydroxide precursor ($Ni_{0.6}Mn_{0.2}Co_{0.2}(OH)_2$) as cathode material of Li-ion batteries was comprised of nanorod particles (**Fig. 4d**). This precursor was synthesized using a controlled coprecipitation method in a continuous stirred tank reactor on a large scale with a volume of 200 L. The Ni, Co, and Mn sources were sulfate salts dissolved in deionized water. NaOH and $NH_3{\cdot}H_2O$ were added separately into the continuous stirred tank reactor. The ammonium concentration was controlled to 4–5 g/L, and the pH was 11.5–12. The solid/precipitant formed was separated and dried in an oven and producing $Ni_{0.6}Mn_{0.2}Co_{0.2}(OH)_2$. The precursor had a micro-spherical morphology with a surface covered with nanorod-like particles (Yang et al., 2019). A full concentration gradient (FCG) of the nanorod primary particle as a cathode material ($LiNi_{0.54}Mn_{0.30}Co_{0.16}O_2$) was made from the $[(Ni_{0.54}Mn_{0.30}Co_{0.16})(OH)_2]$ precursor material. The raw materials for Ni, Co, and Mn were $NiSO_4{\cdot}6H_2O$, $CoSO_4{\cdot}7H_2O$, and $MnSO_4{\cdot}H_2O$, respectively. A coprecipitation method was used to manufacture the precursor. The base material with a molar ratio of Ni:Mn:Co = 0.5:0.3:0.2 was added slowly to a Ni-rich solution containing Ni:Mn = 0.7:0.3. The homogenous solution was moved into the tanks with a stirrer, and N_2 was introduced to achieve inert conditions. NaOH solution and NH_4OH solution were added slowly to the tank as a chelating agent. The precursor was filtered and dried at 100 °C until all moisture had been removed. (Noh et al., 2014).

3.5 Needle-like precursor to nickel-based cathode materials

Needle-like particles were identified on the morphological test results of the NCA and NMC precursor for Li-ion batteries. $Ni_{0.815}Co_{0.15}Al_{0.035}(OH)_2$ was mixed with an $NH_4H_2PO_4$ solution to form a homogenous slurry and dried naturally. After the mixture had dried completely, Li_2CO_3 was added to the mixture. The mixture was sintered at 750 °C for 16 hours (O_2 condition) to form $LiNi_{0.815}Co_{0.15}Al_{0.035}O_2$. The resulting product was comprised of needle-like particles covered with $NH_4H_2PO_4$ (Tang et al., 2017). The Al-gradient composition to Ni and Co metal sources was also promising as material doping for the $Ni_{0.815}Co_{0.15}Al_{0.035}(OH)_2$ precursor. First, a $Ni_{0.815}Co_{0.15}Al_{0.035}(OH)_2$ precursor was synthesized by a coprecipitation method with $NH_3{\cdot}H_2O$ as a chelating agent. $Al(NO_3)_3{\cdot}9H_2O$ was dissolved in distilled water to form a homogenous solution, followed by the addition of a 32 % NaOH solution until a clear solution had formed. Distilled water was then added to the mixture to control the concentration of $[Al(OH)_x]^{3-x}$. The pH of the solution was 12–13 (Duan et al., 2016).

An Al-doped Ni-Co-hydroxide precursor $[Ni_{0.90}Co_{0.07}Al_{0.03}(OH)_2]$ exhibited uniform needle-like NCA particles (**Fig. 4e**). The Ni and Co sulfate salts sources were used to synthesize the $Ni_{0.928}Co_{0.072}(OH)_2$ precursor. The Al-source was obtained from the Al-based material dissolved in a 32 % NaOH solution to form $Al(NO_3)_3$. The $Ni_{0.928}Co_{0.072}(OH)_2$ precursor was then added to $Al(NO_3)_3$. The mixture was stirred at 500 rpm and 60 °C with CO_2. The mixture was washed with deionized water and dried in a vacuum oven. Dried $Ni_{0.90}Co_{0.07}Al_{0.03}(OH)_2$ was mixed with $LiOH{\cdot}H_2O$ and sintered in oxygen to form $LiNi_{0.90}Co_{0.07}Al_{0.03}O_2$ (Duan et al., 2018). The NCA material was modified by replacing Al with W to increase the cycling stability. The first step involved synthesizing $[Ni_{0.9}Co_{0.1}]$

Table 2 Nickel-rich cathode precursors and their morphology.

Precursors	Metal Sources/Modification	Methods	Temperature (°C)/ Time/Condition	Morphological feature	Reference
NMC-OH	Nitrates	Solvothermal	160	Nanosheet	(Fu et al., 2014)
NMC-811-OH	Sulfates	Precipitation		Nano-flake	(Mo et al., 2020)
NCA	Ni-Co-Li-acetate Al-nitrate	Sol-gel	85/8 h stirring	Nanoplate	(Li J. et al., 2020)
NMC-622	Ni-Co-nitrate Mn-$Mn(Ac)_2$	Ammonia-induced and coprecipitation	96/6 h ammonia evaporation	Nanoplate	(Liu et al., 2016)
NMC-7 1.5 1.5	Acetate	Hydrothermal	150/4 h process	Nanoplate	(Tian et al., 2016)
NMC-622	Sulfate	Coprecipitation	—	Nanorod	(Yang et al., 2019)
NMC-FCG	Sulfate/NMC-532 solution added into NM-73 solution	Coprecipitation		Nanorod	(Noh et al., 2014)
NCA-OH	Commercial precursor-$NH_4H_2PO_4$ combined	—		Needle-like	(Tang et al., 2017)
Al-doped-NCA	Sulfate/Al doping	Coprecipitation		Needle-like	(Duan et al., 2016)
NCA	Ni-Co-OH with addition of Al-nitrate		60/500 rpm/CO_2 condition	Needle-like	(Duan et al., 2018)
NCW	Ni-Co-sulfate/replacement of Al with W	Precipitation	Inert (N_2) condition	Needle-like	(Ryu et al., 2019)
NMC-811	Commercial precursor + PVP	Pre-oxidized process	40	Needle-like	(Zhang et al., 2018)
NMC-811	Sulfate	Solid state with controlled crystallization	50	Needle-like	(Yang G. et al., 2020)
Al-doped-NMC-811	Commercial precursor/Al doping from nitrate source		80/sol phase	Needle-like	(Du et al., 2021)

$(OH)_2$ using a precipitation method from the sulfate salts. WO_3 was then dissolved in distilled water and added slowly to the Ni-Co precursor. Subsequently, the mixture was washed, filtered, and dried. The process took place under inert conditions (N_2). LiOH was then added, and the mixture was sintered to form $LiNi_{0.90}Co_{0.09}W_{0.01}O_2$. An analysis of the surface morphology revealed needle-like particles (Ryu et al., 2019). NMC-811 needle-like primary particles could be realized using a pre-oxidized process (Zhang et al., 2018), solid-state method with controlled crystallization and high-temperature operation (Yang G. et al., 2020), and Al-doping to cover the surface of the NMC-811-hydroxide precursor ($Ni_{0.8}Mn_{0.1}Co_{0.1}(OH)_2$) (Du et al., 2021). The pre-oxidized method was performed by mixing 0.005 g of polyvinylpyrrolidone (PVP) with the NMC-81-hydroxide precursor and dissolved in distilled water. This was followed by the addition of 3 wt.% $Mn(NO_3)_2$ to the mixture. The resulting mixture was heated to 40 °C until the water had vaporized. $LiOH·H_2O$ was then added to the dried powder and sintered to produce $LiNi_{0.54}Mn_{0.30}Co_{0.16}O_2$ doped with 3 % $Mn(NO_3)_2$ (Zhang et al., 2018). The second method was controlled crystallization followed by a solid-state method. Ni, Mn, and Co sulfate salts were dissolved in distilled water and stirred in a N_2 atmosphere. Subsequently, a 2M NaOH solution was added as a precipitation agent. The temperature was maintained at 50 °C and a pH of 11.2 (Yang G. et al., 2020). Al doping was then performed. A dilute $Al(NO_3)_3 \cdot 9H_2O$ in citric acid solution with a molar ratio 1:1 was produced. The mixture was stirred and heated until 80 °C to form a sol phase. The NMC-811-hydroxide precursor was then added and stirred. The resulting solution was heated until all the solvent had evaporated. The dried precursor was mixed with $LiOH·H_2O$ and sintered to form $LiNi_{0.80}Mn_{0.10}Co_{0.10}O_2$ (Du et al., 2021). **Table 2** summarizes reported morphologies of nickel-rich cathode precursors which obtained through various synthesis techniques.

4. Nickel-rich cathode materials

4.1 Primary particles morphology of nickel-based cathode material

A nanosheet morphology is found widely in electrode materials, particularly Ni-rich material for Li-ion batteries.

NMC-811 ($LiNi_{0.8}Mn_{0.1}Co_{0.1}O_2$), as a Ni-rich cathode material, showed spherical morphology and provided a high rate and excellent cycling characteristics. In some cases, however, the primary morphology represents another type of morphology. Xu et al. generated NMC-811 with a nanosheet primary morphology and a spherical secondary morphology. The modified coprecipitation method was combined with a solid-state method to make radially aligned single-crystal primary particles (RASC-NMC). This material used NMC-OH as a precursor. The crystal was approximately 50 nm in diameter with an average length of 300–1000 nm. The specific capacity based on charge-discharge analysis was 195.3 mAh g^{-1} at the 1st cycle. The cycling stability revealed up to 95.5 % (172.7 mAh g^{-1}) of the initial capacity (195.3 mAh g^{-1}) after 300 cycles (Xu et al., 2019). The nanosheet morphology of NMC-811 can also be controlled by setting the ammonia concentration during the coprecipitation method. Controlling the ammonia concentration helped improve the area of exposed {010} planes of NMC-811 ($LiNi_{0.8}Mn_{0.1}Co_{0.1}O_2$) material. The electrochemical test showed an excellent capacity of 201.6 mAh g^{-1} at the first cycle at a current rate of 0.2 C with capacity retention of up to 90 % after the 100th cycle (Su et al., 2018). Other NMC cathode materials were also manufactured using different precursor materials and methods. $LiNi_{0.7}Mn_{0.15}Co_{0.15}O_2$ was synthesized from a Ni-Mn-Co spherical precursor using a solvothermal method. This Ni-rich NMC cathode material exhibited a secondary flower-like morphology assembled from nanosheets. The electrochemical performance showed a specific capacity of 184.7 mAh g^{-1}. The cycling data were taken between 1–100 cycles (Fu et al., 2014). The hydrothermal method can modify the morphology of the NMC material. The primary morphology was nanosheet particles, which were arranged into single spherical particles as second particles. The specific capacity was 189.5 mAh g^{-1}. After the 100th cycle, the specific capacity decreased until 135.5 mAh g^{-1}. The capacity retention decreased to 73.0 % (Liu et al., 2019).

Ni-rich, NMC-811 cathode nano-flake particles can be prepared by modifying the NMC-OH precursors with the addition of TiO_2 and LiOH before sintering. TiO_2 doping helps improve the electrochemical performance and reduce the internal strain and the durability of the NMC-811 structure as a cathode material. The initial specific capacity was 258 mAh g^{-1}. The capacity decreased to 79 % when charged under a 1 C current rate for 150 cycles (Mo et al., 2020). Nanoplate NCA ($LiNi_{0.80}Co_{0.15}Al_{0.05}O_2$) showed excellent capacity. The best sintering conditions of the NCA-precursor were 750 °C for 12 hours. The highest initial discharge capacity was 210.4 mAh/g at a current rate of 0.1 C. The columbic efficiency was 88.1 %. The cell was tested only until 40 cycles, but 90 % capacity retention was achieved (Wang Q. et al., 2018). Ti doping of the $LiNi_{0.80}Co_{0.15}Al_{0.05}O_2$ cathode material improved the cycling stability considerably. The modified NCA with Sn doping was arranged chemically as $LiNi_{0.80}Co_{0.09}Ti_{0.06}Al_{0.05}O_2$. Good performance was achieved with a capacity retention of 90.6 % after 500 cycles (Li J. et al., 2020).

NMC-622 ($LiNi_{0.6}Mn_{0.2}Co_{0.2}O_2$) with a nanoplate morphology showed excellent high-rate capability. The initial discharge capacity with a current rate of 0.2 C was 173 mAh/g. In further current rate tests at 20 °C, the capacity retention was 67 % with a value of 77 mAh/g. The cycling stability was tested until 100 cycles and reached 91 % (Liu et al., 2016). NMC-622 nano-rod morphology showing good electrochemical performance with ~81 % capacity retention after 300 cycles (Yang et al., 2019). Combination of two kinds of NMC cathode material that have different molar composition of Ni, Mn, and Co showing good cycle with 70.3 % of capacity retention after 1000 cycles. This material is made by combining $LiNi_{0.70}Mn_{0.25}Co_{0.05}O_2$ and $LiNi_{0.58}Mn_{0.25}Co_{0.17}O_2$. The final composition is $LiNi_{0.60}Mn_{0.25}Co_{0.15}O_2$. Morphology analysis shows spherical particle and the primary particle is rod-shape particle (Noh et al., 2013).

$NH_4H_2PO_4$-doped NCA ($LiNi_{0.815}Co_{0.15}Al_{0.035}O_2$) with a needle-like morphology electrochemical performance was tested. The initial discharge capacity of NCA with a 1 % mass was 195.3 mAh/g. This capacity was greater than that of the pure NCA material with an initial discharge capacity of 172.3 mAh/g. The capacity retention was 70.2 % from the initial discharge specific capacity after 100 cycles (Tang et al., 2017). Another study of $LiNi_{0.815}Co_{0.15}Al_{0.035}O_2$ doped with an Al-gradient doped solution showing excellent electrochemical performance. The initial discharge capacity was 187.5 mAh/g, and 93.4 % capacity retention was achieved after 200 cycles (Duan et al., 2016). Al doping was also performed to manufacture $LiNi_{0.90}Co_{0.07}Al_{0.03}O_2$. The initial discharge capacity was 224.6 mAh/g and after 100 cycles, 93.4 % capacity retention was observed (Duan et al., 2018). Tungsten (W) was the alternative metal source to replace Al. The presence of W greatly increased the cycling stability. $LiNi_{0.90}Co_{0.09}W_{0.01}O_2$ (NCW) exhibited needle-like primary particles. The initial discharge capacity was 231.2 mAh/g^{-1}, which is greater than the NCA cathode material (223.5 mAh/g). The cycling stability test showed that the capacity of the NCW material was 92 % of the initial capacity. This result is more significant than the NCA material, with only 63 % of capacity retention (Ryu et al. (2019).). The effect of primary particles shapes towards their electrochemical performance are summarized in **Table 3**.

4.2 Secondary particles morphology of nickel-based cathode materials

The secondary particles of a Ni-rich cathode material

Table 3 The effect of nickel-rich cathode primary particles toward its electrochemical properties.

Material	Precursor/Modification	Morphological feature	Electrochemical Properties (Capacity/Cycle/Rate)	Reference
NMC-811	NMC-811-OH/Modified coprecipitation and solid-state	Nanosheet	195 mAh g^{-1}/300 cycles/0.1 C	(Xu et al., 2019)
NMC-811	NMC-OH/Modification of ammonia concentration controlled	Nanosheet	201 mAh g^{-1}/100 cycles/0.2 C	(Su et al., 2018)
NMC-7 1.5 1.5	NMC precursor with solvothermal method	Nanosheet	184.7 mAh g^{-1}/100 cycles/0.1 C	(Fu et al., 2014)
NMC-8.5 0.75 0.75	NMC precursor with hydrothermal method	Nanosheet	189.5 mAh g^{-1}/300 cycles/0.2 C	(Liu et al., 2019)
NMC-811	NMC-OH/TiO_2 doping	Nano-flake	258 mAh g^{-1}/150 cycles/1 C	(Mo et al., 2020)
NCA	NCA-OH	Nano-flake	210.4 mAh g^{-1}/40 cycles/0.1 C	(Wang Q. et al., 2018)
NMC-622	NMC-OH	Nanoplate	173 mAh g^{-1}/100 cycles/0.2 C	(Liu et al., 2016)
NMC-622	NMC-OH	Nanorod	193.6 mAh g^{-1}/300 cycles	(Yang et al., 2019)
NMC-6 2.5 1.5	Combination of NMC-7 2.5 0.5-OH and NMC-5.8 2.5 1.7-OH	Rod-shape	206 mAh g^{-1}/1000 cycles	(Noh et al., 2013)
NMC-5.4 3 1.6	Modification of Ni/Mn/Co concentration gradient (FCG)	Nanorod	183.7 mAh g^{-1}/100 cycles	(Noh et al., 2014)
NCA-8.15 1.5 0.35	NCA-OH/$NH_4H_2PO_4$ doping	Needle-like	195.3 mAh g^{-1}/200 cycles/0.1 C	(Tang et al., 2017)
NCA-8.15 1.5 0.35	NCA-OH/Al-gradient-doped	Needle-like	187.5 mAh g^{-1}/200 cycles	(Duan et al., 2016)
NCA-9 0.7 0.3	NCA-OH/Al-doped	Needle-like	224.6 mAh g^{-1}/100 cycles	(Duan et al., 2018)
NCW-9 0.9 0.1	NCW-OH/Replacing Al with W	Needle-like	231.2 mAh g^{-1}/200 cycles/0.1 C	(Ryu et al., 2019)
NCA	Pre-oxidized method	Needle-like	175 mAh g^{-1}/100 cycles	(Zhang et al., 2018)
NCA	Solid state with controlled crystallization	Needle-like	187.7 mAh g^{-1}/100 cycles	(Yang G. et al., 2020)
NCA	Al-doping	Needle-like	171.4 mAh g^{-1}/1000 cycles/1 C	(Du et al., 2021)

consist of agglomerated primary particles that form a larger and denser particle. Secondary particle formation reduces the high surface area of primary particles if they are present in singular particles (Barai et al., 2019). The reduction was proven efficient in hindering unwanted reactions between the active materials with the electrolyte (Qiu et al., 2017b; Yudha et al., 2019). The morphology of the nickel-rich cathode materials strongly depends on the synthesis process and the presence of additives that help control the secondary particle shape.

4.2.1 Microsphere / spherical Particles

Coprecipitation of transitional metal with high-nickel content is the most used technique to obtain micron-sized spherical particles of the nickel-rich cathode. The spherical morphology of a particle was formed from the agglomeration of crystal nuclei into larger particles. The formation of large or secondary spherical particles is in accordance with the Ostwald ripening mechanism, where the rate of crystal formation is in balance with the rate of crystal dissolution (Seo and Lee, 2017). Extensive studies focused on the effects of the synthesis parameters on the morphology, such as pH, concentration, mixing speed, stirrer type, reaction time, and precipitating agents (Zhu Q. et al., 2019). Hydroxide coprecipitation uses dissolved hydroxide compounds, such as sodium hydroxide, lithium hydroxide, or potassium hydroxides, as the precipitating agent. An ammonia solution is often introduced during the process to reduce the reaction rate avoid uneven particle growth. For hydroxide coprecipitation, the optimal pH to form high-density spherical secondary particles is 10–11 (Chen et al., 2018; Purwanto et al., 2018). The temperature during the coprecipitation process also is a factor determining the final morphology. In most cases, hydroxide and carbonate coprecipitation of nickel-rich cathode materials produced dense micron-sized secondary particles, while oxalate precipitation showed rock-like particles. Various chelating agents were reported to replace ammonia during hydroxide and carbonate coprecipitation. Acid or base chelating agents, such as EDTA, citric acid, sulfosalicylic acid, lactic acid, or their conjugates, such as EDTA-2Na, and sodium lactate, have been used as greener alternatives to ammonia. The excessive use of ammonia can cause environmental issues and health risks for humans and animals (Nam et al., 2015).

Quanzhong Zhu et al. (Zhu Q. et al., 2019) proposed a formation mechanism for spherical or microspheres secondary particle of Ni-rich cathode material in coprecipitation techniques. This began with crystal nuclei formation during the initial precipitation of single-crystal primary particles. With time, these single-crystal particles agglomerate into polycrystalline grains. These polycrystalline grains form initial secondary particles with rough surfaces from the aggregated particles. Because the formation of single-crystal nuclei occurs continuously, these primary particles are adsorbed onto the surface of the initial secondary particles. The process of single-crystal adsorption to the initial secondary particle continues with time. The primary particles become smooth, and the secondary particles grow with dense properties due to a decrease in particle porosity. In the nickel-rich cathode, the residence time to obtain smooth micro-spherical particles increases with increasing nickel content. The resulting microsphere particles also need to be treated delicately during the lithiation process because microsphere particles can be broken easily due to mechanical forces, such as the milling process.

In addition to coprecipitation, it was reported that the sol-gel, spray drying technique, and spray pyrolysis techniques can be adapted to produce micro-spherical particles. For spray methods, spherical particles were formed by the formation of spherical droplets using a droplet maker, such as nebulizer and spray nozzles (Kadota and Shirakawa, 2021). The resulting droplets can be tuned easily. Thus, a more homogenous and consistent particle morphology can be obtained. With the addition of additives to the spray solution, the produced particles can have a smooth morphology. **Table 4** lists the effects of chelating agents for nickel-rich cathode materials on their morphology and electrochemical performance.

Based on **Table 4** spherical shaped nickel-rich cathode materials have good electrochemical performances. However, the perfectly shaped spherical particle with high density and relatively large particle size has higher specific capacity, higher cycle retention and improved rateability. A High density and large secondary particle size of nickel-rich cathode material has better stability toward undesired chemical reaction between electrolyte, which sometimes has HF content, with the surface of the cathode particle that is related to its surface area. High density spherical particles with narrow particle size distribution also improve the overall density of the particle due to better packing factor. Thus, this type of particle has multiple benefits compared to the other shape particles.

According to multiple researches, spherical particle with narrow distribution can be obtained via coprecipitation method which tightly controlled its process parameters. Spherical particle with high tap density often achieved by a strict control of pH level, which depends on the composition of the metals, temperature of coprecipitation, flow rates, retention time and more importantly ageing process. Extensively large secondary particles can cause poor Li-ion transfer during the charge and discharge process. Thus, product optimization via control of particle size distribution is highly required knowledge for the development of nickel-rich cathode materials.

4.2.2 Non-spherical/agglomerated particles

Several studies have reported the formation of spherical Ni-rich cathode materials, as listed in **Table 4**. In microsphere particles, however, micro-cracks in secondary particles are often occurring. These micro-cracks increase exposure to the internal areas of the particles, which promote unwanted reactions causing rapid capacity fading (Kleiner et al., 2015; Yoon et al., 2017). Furthermore, they also increase the bulk density of the overall particles. Some studies stated that non-spherical particles are preferred to avoid the formation of particle grain cracks. However, non-spherical particles with a low density are not preferred because they will also suffer from particle breakage during the electrochemical charge-discharge process.

The formation of non-spherical/agglomerated nickel-rich cathode material particles is often found in the literature (Purwanto et al., 2020). Qiu et al. reported that polyhedral-shaped particles could be produced by oxalic acid crystallization of NCA cathode material produce (Qiu et al., 2017a; 2017b). Using the same crystallization/precipitating agent, Wu (Wu et al., 2015) claimed that micro-rod particles of NCA have better compaction factors than spherical particles, which can avoid micro-cracks even when it was cycled at high temperature. Zheng et al. precipitated Ni, Co, and Mn using ammonium oxalate, producing a rod-shaped precursor. After high sintering lithiation, however, the morphology of the precursor changed from rod to rock-like particles (Zeng and Zhang, 2020) A urea-assisted hydrothermal technique was developed to produce silkworm-like NMC811 particles, but slight particle cracking was observed (**Fig. 5a,b,c**) after the material was cycled 100 times (Lei et al., 2019b; Zhang et al., 2017). Therefore, micro-cracking and particle breakage would likely occur when repeatedly used especially at high rate and high operating temperature.

4.3 Single crystal

Micron-sized single crystals of Ni-rich cathode have been successfully developed. Single crystal has a large energy density owing to its pore-free and high strength (Duan et al., 2017; Li et al., 2018). This particle was pioneered because polycrystalline materials are prone to intergranular fracture during battery cell operation (Qian et al., 2020).

Although the polycrystalline particles are randomly oriented, this intergranular fracture is caused by primary

Table 4 Summary of Ni-rich cathode synthesis techniques toward its properties.

Cathode materials	Methods	Chelating agents/ Additives	Morphological feature	Electrochemical Performance (Capacity/Cycle/ Rate)	Reference
NCA	Coprecipitation	Ammonia	Dense spherical particles, 5–12 μm	196 mAh/g/95 % after 50 cycles/150 mAh/g at 2 C	(Hu et al., 2012)
	Coprecipitation	Ammonia	Dense spherical particle, 4–6 μm	206 mAh/g/80 % after 50 cycles at 55 °C/~130 mAh/g at 5 C 55 °C	(Kim et al., 2014)
	Coprecipitation	5-Sulfosalicylic acid	Dense spherical particles, ~4–8 μm	203 mAh/g/90 % after 200 cycles at 1 C/174 mAh/g at 1 C	(Xie et al., 2015)
	Coprecipitation	EDTA	Dense spherical particles, ~10 μm	193 mAh/g/90 % after 100 cycles at 1 C/-	(Xie et al., 2016)
	Coprecipitation	Ammonia	Dense spherical particles, ~10 μm	183 mAh/g/91 % after 100 cycles at 1 C/140 mAh/g at 5 C	(Seo and Lee, 2017)
	Spray pyrolysis	Citric acid-Ethylene glycol-DCCA	Spherical particles, ~1 μm	218 mAh/g/100 % after 20 cycles at 0.1 C/-	(Ju et al., 2010)
	Spray pyrolysis		Spherical/yolk shell particles, 1.1–1.6 μm	225 mAh/g/89 % after 49 cycles at 0.2 C/129 mAh/g at 1 C	(Yang et al., 2014)
	Flame spray pyrolysis	Urea	Quasi-spherical	124 mAh/g/81 % after 200 cycle at 0.5 C/-	(Nurcahyani et al., 2020)
	Spray drying	Glycerol	Spherical, 10–20 μm	200 mAh/g/91 % after 200 cycles at 1 C/130 mAh/g at 5 C	(Zhang J. et al., 2020)
	Spray drying	Citric acid	Spherical and hollow particles, 10–50 μm	188 mAh/g/94 % after 100 cycles at 0.5 C/-	(Park and Chan Kang, 2014)
NMC-622	Coprecipitation	Ammonia	Dense spherical particles, 10–20 μm	172 mAh/g/94 % after 100 cycles at 1 C/143 mAh/g at 10 C	(Liang et al., 2014)
	Coprecipitation	Sodium lactate	Quasi-spherical particles, ~4 μm	201 mAh/g/78 % after 100 cycles at 0.1 C/~120 mAh/g at 5 C	(Xu et al., 2018)
	Coprecipitation	Ammonia	Quasi-spherical particles, < 8 μm	155 mAh/g/96 % after 30 cycles at 0.5 C/-	(Fu et al., 2011)
	Coprecipitation	Ammonia	Quasi-spherical particles, < 1.2 μm	186 mAh/g/95 % after 10 cycles at 0.5 C/~50 mAh/g at 5 C	(Ronduda et al., 2020)
	Sol-gel	Citric acid	Spherical particles, 800 nm	174 mAh/g/87 % after 100 cycles at 1 C/~70 mAh/g at 10 C	(Lee et al., 2016)
	Spray pyrolysis		Spherical particles, 5–13 μm	—	(Tian et al., 2018)
NMC-7 1.5 1.5 ($LiNi_{0.7}Mn_{0.15}Co_{0.15}O_2$)	Coprecipitation	Ammonia	Dense spherical particles, 6–21 μm	185 mAh/g/95 % after 50 cycles at 0.2 C/-	(Lu et al., 2014)
	Coprecipitation	Ammonia	near-spherical particles, 200–500 nm	164 mAh/g/-/-	(Zhang et al., 2012)
NMC-712 ($LiNi_{0.7}Mn_{0.1}Co_{0.2}O_2$)	Sol-gel	Citric acid	Quasi-spherical with 300–800 nm primary particle	205 mAh/g/86.24 % after 100 cycles/137 mAh/g at 5 C	(Dong et al., 2019)
NMC-811	Coprecipitation	Ammonia	Dense spherical particles, 14–16 μm	202 mAh/g/96 % after 200 cycles at 1 C/~54 mAh/g at 10 C	(Duan et al., 2020)
	Coprecipitation	Ammonia + NH_4F	Dense spherical particles, ~10 μm	202 mAh/g/94 % after 100 cycles at 2 C/~141 mAh/g at 10 C	(Yue et al., 2013)
	Coprecipitation-Spray Dry	Ammonia	Dense spherical particles, ~12 μm	~175 mAh/g/86 % after 100 cycles at 1 C/~130 mAh/g at 10 C	(Huang et al., 2019)
	Flame spray pyrolysis		Spherical particles, 1 μm	178 mAh/g/85 % after 25 cycles at 1 C/-	(Abram et al., 2019)
	Hydro/Solvothermal	Ethylene glycol	Spherical particles, 6–8 μm	201 mAh/g/81 % after 100 cycles at 0.1 C/142 mAh/g at 10 C	(Gu et al., 2021)
	Spray pyrolysis		Submicron particles from spherical particle breakage	197 mAh/g/93 % after 80 cycles at 1 C/173 mAh/g at 5 C	(Li Yan et al., 2018)
NFA ($LiNi_{0.8}Fe_{0.15}Al_{0.05}O_2$)	Coprecipitation	Ammonia	Spherical particle, ~8–10 μm	190 mAh/g/88 % after 100 cycles at 0.33 C/110 mAh/g at 1 C	(Muralidharan et al., 2020)
LNMO ($LiNi_{0.9}Mn_{0.1}O_2$)	Coprecipitation	Ammonia	Spherical particle, ~10 μm	~220 mAh/g/86 % after 100 cycles at 0.5 C/~145 mAh/g at 10 C	(Sun et al., 2013)
	Coprecipitation	Ammonia	Spherical particle, ~3 μm	197 mAh/g/94 % after 100 cycles at 0.2 C/-	(Ma et al., 2020)
LNO ($LiNiO_2$)	Coprecipitation	Ammonia	Spherical particle	216 mAh/g/80 % after 200 cycles at 1 C/121 mAh/g at 5 C	(Mu et al., 2020)

particles pushing against each other, causing significant pressure (Langdon and Manthiram, 2021). The methods were used for the synthesis of precursors and cathode materials including co-precipitation, molten salt and spray pyrolysis (**Table 5**). Xing Xu et al. succeeded in producing radially aligned single-crystal hydroxide precursors of NMC 811. The two aspects examined were optimizing the ammonia concentration as a precipitating agent and the stirring speed. A high ammonia concentration (8 mol/L in this study) can adjust and promote the direction of growth of the primary particles. A high stirring speed can result in strong and homogeneous mechanical agitation, which prevents the nucleation and re-agglomeration of small secondary particles (Xu et al., 2019). Xinming Fan et al. examined the morphology of the precursor and NMC 831106 material after sintering, as shown in **Fig. 6**.

The NMC precursors showed a good secondary flower morphology. After sintering, the particles became micron-sized particles with a smooth surface (Fan et al., 2020). Another study, the synthesis of single-crystal Ni-rich with NaCl flux was carried out. NaCl functions as a growth flux for primary particles, reducing the temperature and sintering time (Bi et al., 2020; Lee et al., 2020). Jie Zhu et al. used spray pyrolysis method to produce a single crystal NMC 811. The precursor was synthesized from a chloride salt solution that was then aerosolized using an ultrasonic nebulizer and passed through a furnace tube at 800 °C. The microsphere, fine size, and mesoporous precursors were obtained from this method (Zhu et al., 2020).

Fig. 7 shows the effect of morphology of nickel-rich cathode towards its likability to pulverized during prolonged charge-discharge process. In contrast to nickel-based

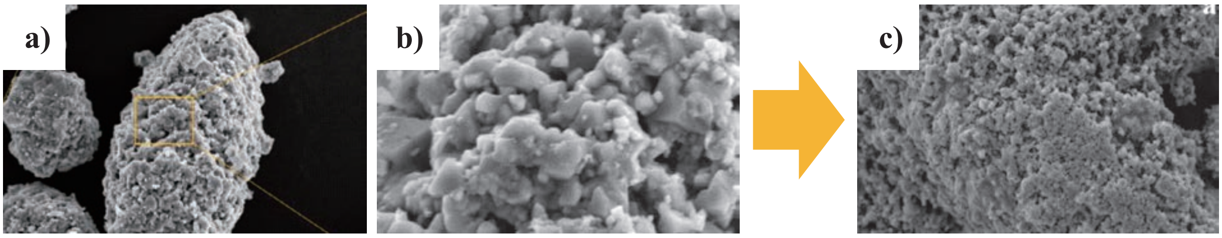

Fig. 5 **(a,b)** Silkworm like NMC811 particles before cycles and **(c)** after 100 cycles, reprinted with permission from Ref. (Lei et al., 2019b) Copyright (2019) Elsevier B.V.

Table 5 Single crystal nickel-rich cathode materials.

Sample	Synthesis method	Precursor	*T* (°C)	Particle size (μm)	Specific capacity	Ref.
NMC-761410	Coprecipitation and molten salt	Hydroxide precursor	900	3	182.3 mAh/g at 0.1 C	(Bi et al., 2020)
NMC-811	Coprecipitation	Hydroxide precursor	740	—	197.9 mAh/g at 0.1 C	(Xu et al., 2019)
NMC-811	Spray pyrolysis	Oxide precursor	900	1–5	211 mAh/g at 0.1 C	(Zhu et al., 2020)
NMC-811	Coprecipitation or molten salt		850	1	—	(Zhu and Chen, 2019)
NMC-811	Coprecipitation	Hydroxide precursor	830	1–4	—	(Yang C. et al., 2020)
NMC-811	Commercial	Hydroxide precursor	800–960	1–1.5	194 mAh/g at 0.1 C	(Zhao et al., 2019)
NMC-910603	Coprecipitation	Hydroxide precursor	820	1–2.5	203.8 mAh/g at 0.1 C	(Lee et al., 2020)
NCA-880903	Coprecipitation	Hydroxide precursor	840	4–5	240 mAh/g at 0.1 C	(Zhang H. et al., 2020)
LNO	Commercial	Hydroxide precursor	800	—	—	(Weber et al., 2020)

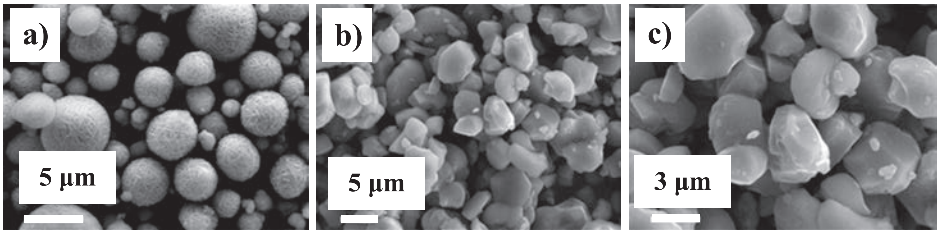

Fig. 6 Morphology and elemental distribution in single crystal NMC. SEM images of **(a)** precursor and **(b,c)** sintered single crystal NMC, reprinted with permission from Ref. (Fan et al., 2020) Copyright (2020) Elsevier B.V.

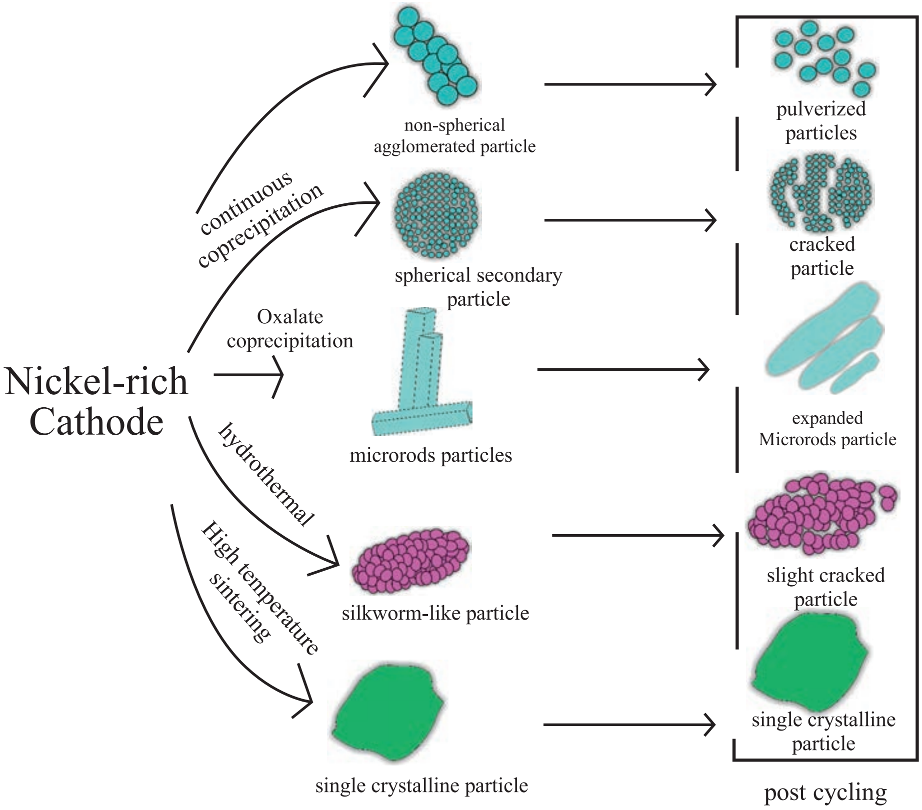

Fig. 7 Schematic illustration of secondary particle cracking phenomena in various nickel-rich cathode material.

anode, over exposure of electrolyte with the surface of nickel-rich cathode materials can promote the formation of inactive phases due to the reaction of nickel with electrolyte. On the exposed surface created due to particle pulverization, a new SEI layer also occur which increase the impedance and Li-ion mobility resistance, thus lower the electrochemical properties. In **Fig. 7**, microcracks often occurs in a particle with visible agglomeration of primary particles.

5. Current advances and future projection

Applications of lithium-ion batteries that require high specific energy coupled with lower prices have encouraged the development of nickel-based electrodes. The successful of NCA and NMC materials, especially for electric vehicles, has made researchers constantly develop these materials. But, cobalt, which was originally doped for the material, is reconsidered because of its relatively high price. Thus, cobalt-free and nickel-rich materials were raised to be popular in the future. Various attempts were made to obtain superior material, especially for the morphology of the material. Currently, several efforts were determined to directly control the morphology of nickel containing particles using scalable, continuous and rapid method such as via fast drying, flash spray pyrolysis, vapor phase deposition, laser techniques, plasma assisted techniques, and fast crystallization. Thus, it opens a new opportunity to directly tune the morphology of nickel-based material that concern towards the overall feasibility and economical aspect (Purwanto et al., 2018; L. Wang et al., 2018).

It has been mentioned in the previous section that the morphology of the cathode material directly affects the electrochemical performance. Thus, efforts to get the most favorable morphology need to be done by modifying the synthesis parameters. First, doping modifications are carried out in order to make the morphology more regular (Ryu et al., 2019). Some dopant can affect the primary particle thereby increasing the stability of the cycle, previously assigned to cobalt. Second, the morphology for both cobalt-free and Ni-rich materials is single crystal. Materials with high nickel content have a limited life cycle due to their greater surface-electrolyte reactivity and lower structural integrity. Single-crystal proved to be able to limit the surface reactivity and cracking of these particles (Langdon and Manthiram, 2021). However, single crystal materials still face challenges in terms of irreversible structural degradation and longer ionic transport pathways. Small cracks in single crystal can also block Li^+ transport (Wang et al., 2021). These challenges may be interesting to research for the future.

6. Conclusion

Thorough morphological analysis of nickel-based electrodes for Li-ion batteries was performed. Materials, such as nickel oxide, nickel hydroxide, nickel oxalates, and nickel sulfide, can be applied to Li-ion batteries. However, unique morphological features, such as shapes and nanoscale sizes of such materials, are strongly required. The nano-scaled unique morphology of the nickel-based anode can suppress the large lithium irreversibility and increase its electrical and electrochemical features.

Numerous studies on the morphological tuning of nickel-rich cathode materials have been reported. Among other morphologies, micron-sized spherical particles are largely applied and used, even commercialized in Li-ion batteries. However, spherical particles suffer from micro-cracking, which can cause rapid capacity decay and cell chemistry failures. Non-spherical secondary polycrystalline particles have also been studied; however, the particles still have micro-cracking problems. A crack-free single-crystalline morphology is currently the focus of research, and techniques to obtain such particles in a nickel-rich cathode are still under development due to several problems:

(1) High-temperature sintering, which favors the formation of the rock salt phase and large Li-loss;
(2) Flux induced synthesis, which reduces the contact between the oxidative atmosphere and is crucial for stable nickel-rich cathodes formation;
(3) Post-production handling, such as milling and storage, is necessary in low humidity areas for a high-nickel content cathode.

In a morphological perspective, extensive morphological tuning for the race toward stable, long life cycle, nickel-based electrodes are being performed continuously and will always be considered for the next generation of secondary energy storage. The morphology of nickel-based active materials is one of the major determining factors for high-performance Li-ion batteries.

Acknowledgment

This paper is supported by Indonesia Endowment Fund for Education (LPDP / Lembaga Pengelola Dana Pendidikan) through Pendanaan Riset Inovatif Produk (Rispro) Invitasi grant no.PRJ-6/LPDP/2020.

References

Abram C., Shan J., Yang X., Yan C., Steingart D., Ju Y., Flame aerosol synthesis and electrochemical characterization of Ni-rich layered cathode materials for Li-ion batteries, ACS Applied Energy Materials, 2 (2019) 1319–1329. DOI: 10.1021/acsaem.8b01892

Barai P., Feng Z., Kondo H., Srinivasan V., Multiscale computational model for particle size evolution during coprecipitation of Li-ion battery cathode precursors, Journal of Physical Chemistry B, 123 (2019) 3291–3303. DOI: 10.1021/acs.jpcb.8b12004

Bi Y., Tao J., Wu Y., Li L., Xu Y., Hu E., Wu B., Hu J., Wang C., Zhang J.G., Qi Y., Xiao J., Reversible planar gliding and microcracking in a single-crystalline Ni-rich cathode, Science, 370 (2020) 1313–1318. DOI: 10.1126/science.abc3167

Chen T., Li X., Wang H., Yan X., Wang L., Deng B., Ge W., Qu M., The effect of gradient boracic polyanion-doping on structure, morphology, and cycling performance of Ni-rich $LiNi_{0.8}Co_{0.15}Al_{0.05}O_2$ cathode material, Journal of Power Sources, 374 (2018) 1–11. DOI: 10.1016/j.jpowsour.2017.11.020

Dewangan A., Patel A., Bhadania A., Stainless steel for dairy and food industry: a review, Journal of Material Science & Engineering, 4 (2015) 1–4. DOI: 10.4172/2169-0022.1000191

Dong S., Zhou Y., Hai C., Zeng J., Sun Y., Shen Y., Li X., Ren X., Qi G., Zhang X., Ma L., Ultrathin CeO_2 coating for improved cycling and rate performance of Ni-rich layered $LiNi_{0.7}Co_{0.2}Mn_{0.1}O_2$ cathode materials, Ceramics International, 45 (2019) 144–152. DOI: 10.1016/j.ceramint.2018.09.145

Du F., Li X., Wu L., Hu D., Zhou Q., Sun P., Xu T., Mei C., Hao Q., Fan Z., Zheng J., Tailoring the Al distribution in secondary particles for optimizing the electrochemical performance of $LiNi_{0.8}Co_{0.1}Mn_{0.1}O_2$, Ceramics International, (2021). DOI: 10.1016/j.ceramint.2021.01.161

Du M., Li Q., Pang H., Oxalate-derived porous prismatic nickel/nickel oxide nanocomposites toward lithium-ion battery, Journal of Colloid and Interface Science, 580 (2020) 614–622. DOI: 10.1016/j.jcis.2020.07.009

Du Y., Ma H., Guo M., Gao T., Li H., Random oriented hexagonal nickel hydroxide nanoplates grown on graphene as binder free anode for lithium ion battery with high capacity, Chemical Physics Letters, 699 (2018) 167–170. DOI: 10.1016/j.cplett.2018.03.056

Duan J., Dong P., Wang D., Li X., Xiao Z., Zhang Y., Hu G., A facile structure design of $LiNi_{0.90}Co_{0.07}Al_{0.03}O_2$ as advanced cathode materials for lithium ion batteries via carbonation decomposition of $NaAl(OH)_4$ solution, Journal of Alloys and Compounds, 739 (2018) 335–344. DOI: 10.1016/j.jallcom.2017.12.236

Duan J., Hu G., Cao Y., Tan C., Wu C., Du K., Peng Z., Enhanced electrochemical performance and storage property of $LiNi_{0.815}Co_{0.15}Al_{0.035}O_2$ via Al gradient doping, Journal of Power Sources, 326 (2016) 322–330. DOI: 10.1016/j.jpowsour.2016.07.008

Duan J., Wu C., Cao Y., Huang D., Du K., Peng Z., Hu G., Enhanced compacting density and cycling performance of Ni-riched electrode via building mono dispersed micron scaled morphology, Journal of Alloys and Compounds, 695 (2017) 91–99. DOI: 10.1016/j.jallcom.2016.10.158

Duan J., Zhang R., Zhu Q., Xiao H., Huang Q., The effect of controlling strategies of pH and ammonia concentration on preparing full concentration gradient $Ni_{0.8}Co_{0.1}Mn_{0.1}(OH)_2$ via coprecipitation in a pilot-scale reactor, Energy Technology, 8 (2020) 1–12. DOI: 10.1002/ente.201901437

Elbert P., Onder C., Gisler H.J., Capacitors vs. batteries in a serial hybrid electric bus, IFAC Proceedings Volumes (IFAC-PapersOnline), 43 (2010) 252–257. DOI: 10.3182/20100712-3-DE-2013.00020

Fan X., Hu G., Zhang B., Ou X., Zhang J., Zhao W., Jia H., Zou L., Li P., Yang Y., Crack-free single-crystalline Ni-rich layered NCM cathode enable superior cycling performance of lithium-ion batteries, Nano Energy, 70 (2020) 104450. DOI: 10.1016/j.nanoen.2020.104450

Fu C., Li G., Luo D., Li Q., Fan J., Li L., Nickel-rich layered microspheres cathodes: lithium/nickel disordering and electrochemical performance, ACS Applied Materials and Interfaces, 6 (2014) 15822–15831. DOI: 10.1021/am5030726

Fu C., Zhou Z., Liu Y., Zhang Q., Zheng Y., Li G., Synthesis and electrochemical properties of Mg-doped $LiNi_{0.6}Co_{0.2}Mn_{0.2}O_2$ cathode materials for li-ion battery, Journal Wuhan University of Technology, Materials Science Edition, 26 (2011) 211–215. DOI: 10.1007/s11595-011-0199-z

Geng H., Kong S.F., Wang Y., NiS nanorod-assembled nanoflowers grown on graphene: morphology evolution and Li-ion storage applications, Journal of Materials Chemistry A, 2 (2014) 15152–15158. DOI: 10.1039/c4ta03440f

Gu H., Wang J., Wang Z., Tong J., Qi N., Han G., Zhang M., Self-assembled porous $LiNi_{0.8}Co_{0.1}Mn_{0.1}O_2$ cathode materials with micro/nano-layered hollow morphologies for high-power lithium-ion batteries, Applied Surface Science, 539 (2021) 148034. DOI: 10.1016/j.apsusc.2020.148034

Hu G., Liu W.M., Peng Z., Dua K., Cao Y.B., Du K., Cao Y.B., Synthesis and electrochemical properties of $LiNi_{0.8}Co_{0.15}Al_{0.05}O_2$ prepared from the precursor $Ni_{0.8}Co_{0.15}Al_{0.05}OOH$, Journal of Power Sources, 198 (2012) 258–263. DOI: 10.1016/j.jpowsour.2011.09.101

Huang B., Li X., Wang Z., Guo H., Xiong X., Synthesis of Mg-doped $LiNi_{0.8}Co_{0.15}Al_{0.05}O_2$ oxide and its electrochemical behavior in high-voltage lithium-ion batteries, Ceramics International, 40 (2014) 13223–13230. DOI: 10.1016/j.ceramint.2014.05.029

Huang B., Liu D., Zhang L., Qian K., Zhou K., Cai X., Kang F., Li B., An efficient synthetic method to prepare high-performance Ni-rich $LiNi_{0.8}Co_{0.1}Mn_{0.1}O_2$ for lithium-ion batteries, ACS Applied Energy Materials, 2 (2019) 7403–7411. DOI: 10.1021/acsaem.9b01414

Huang X.H., Tu J.P., Xia X.H., Wang X.L., Xiang J.Y., Zhang L., Zhou Y., Morphology effect on the electrochemical performance of NiO films as anodes for lithium ion batteries, Journal of Power Sources, 188 (2009) 588–591. DOI: 10.1016/j.jpowsour.2008.11.111

Hwang I., Lee C.W., Kim J.C., Yoon S., Particle size effect of Ni-rich cathode materials on lithium ion battery performance, Materials Research Bulletin, 47 (2012) 73–78. DOI: 10.1016/j.materresbull.2011.10.002

Ju S.H., Kim J.H., Kang Y.C., Electrochemical properties of $LiNi_{0.8}Co_{0.2-x}Al_xO_2$ $(0 \le x \le 0.1)$ cathode particles prepared by spray pyrolysis from the spray solutions with and without organic, Metals and Materials International, 16 (2010) 299–303. DOI: 10.1007/s12540-010-0421-0

Kadota K., Shirakawa Y., Particle preparation and morphology control with mutual diffusion across liquid-liquid interfaces, KONA Powder and Particle Journal, 38 (2021) 122–135. DOI: 10.14356/kona.2021006

Kalyani P., Kalaiselvi N., Various aspects of $LiNiO_2$ chemistry: a review, Science and Technology of Advanced Materials, 6 (2005) 689–703. DOI: 10.1016/j.stam.2005.06.001

Kim C., Park T.-J., Min S.-G., Yang S.-B., Son J.-T., Effects of iron doping at 55 °C on $LiNi_{0.85}Co_{0.10}Al_{0.05}O_2$, Journal of the Korean Physical Society, 65 (2014) 243–247. DOI: 10.3938/jkps.65.243

Kleiner K., Dixon D., Jakes P., Melke J., Yavuz M., Roth C., Nikolowski K., Liebau V., Ehrenberg H., Fatigue of $LiNi_{0.8}Co_{0.15}Al_{0.05}O_2$ in commercial Li ion batteries, Journal of Power Sources, 273 (2015) 70–82. DOI: 10.1016/j.jpowsour.2014.08.133

Langdon J., Manthiram A., A perspective on single-crystal layered oxide cathodes for lithium-ion batteries, Energy Storage Materials, 37 (2021) 143–160. DOI: 10.1016/j.ensm.2021.02.003

Lee J.H., Kim H.H., Wee S.B., Paik U., Effect of additives on the dispersion properties of aqueous based $C/LiFePO_4$ paste and its impact on lithium ion battery high power properties, KONA Powder and Particle Journal, 27 (2009) 239–245. DOI: 10.14356/kona.2009022

Lee S.H., Sim S.J., Jin B.S., Kim H.S., High performance well-developed single crystal $LiNi_{0.91}Co_{0.06}Mn_{0.03}O_2$ cathode via LiCl-NaCl flux method, Materials Letters, 270 (2020) 127615. DOI: 10.1016/j.matlet.2020.127615

Lee S.W., Kim H., Kim M.S., Youn H.C., Kang K., Cho B.W., Roh K.C., Kim K.B., Improved electrochemical performance of $LiNi_{0.6}Co_{0.2}Mn_{0.2}O_2$ cathode material synthesized by citric acid assisted sol-gel method for lithium ion batteries, Journal of Power Sources, 315 (2016) 261–268. DOI: 10.1016/j.jpowsour.2016.03.020

Lei Y., Ai J., Yang S., Jiang H., Lai C., Xu Q., Effect of flower-like $Ni(OH)_2$ precursors on Li^+/Ni^{2+} cation mixing and electrochemical performance of nickel-rich layered cathode, Journal of Alloys and Compounds, 797 (2019a) 421–431. DOI: 10.1016/j.jallcom.2019.05.065

Lei Y., Ai J., Yang S., Lai C., Xu Q., Nb-doping in $LiNi_{0.8}Co_{0.1}Mn_{0.1}O_2$ cathode material: Effect on the cycling stability and voltage decay at high rates, Journal of the Taiwan Institute of Chemical Engineers, 97 (2019b) 255–263. DOI: 10.1016/j.jtice.2019.02.006

Li B., Gu P., Feng Y., Zhang G., Huang K., Xue H., Pang H., Ultrathin nickel–cobalt phosphate 2D nanosheets for electrochemical energy storage under aqueous/solid-state electrolyte, Advanced Functional Materials, 27 (2017) 1605784. DOI: 10.1002/adfm.201605784

Li C., Xue Z., Qin J., Sawangphruk M., Yu P., Zhang X., Liu R., Synthesis of nickel hydroxide/delaminated-Ti_3C_2 MXene nanosheets as promising anode material for high performance lithium ion battery, Journal of Alloys and Compounds, 842 (2020) 155812. DOI: 10.1016/j.jallcom.2020.155812

Li F., Kong L., Sun Y., Jin Y., Hou P., Micron-sized monocrystalline $LiNi_{1/3}Co_{1/3}Mn_{1/3}O_2$ as high-volumetric-energy-density cathode for lithium-ion batteries, Journal of Materials Chemistry A, 6 (2018) 12344–12352. DOI: 10.1039/c8ta03363c

Li J., Liu M., An J., Tian P., Tang C., Jia T., Butt F.K., Yu D., Bai W., Cao C., Feng X., The synergism of nanoplates with habit-tuned crystal and substitution of cobalt with titanium in Ni-rich $LiNi_{0.80}Co_{0.15}Al_{0.05}O_2$ cathode for lithium-ion batteries, Journal of Alloys and Compounds, 829 (2020) 154555. DOI: 10.1016/j.jallcom.2020.154555

Li Yan, Li X., Wang Z., Guo H., Wang J., Spray pyrolysis synthesis of nickel-rich layered cathodes $LiNi_{1-2x}Co_xMn_xO_2$ $(x = 0.075,\ 0.05,\ 0.025)$ for lithium-ion batteries, Journal of Energy Chemistry, 27 (2018) 447-450. DOI: 10.1016/j.jechem.2017.11.025

Li Y., Pan G., Xu W., Yao J., Zhang L., Effect of Al substitution on the microstructure and lithium storage performance of nickel hydroxide, Journal of Power Sources, 307 (2016) 114–121. DOI: 10.1016/j.jpowsour.2015.12.129

Li Yanwei, Xu W., Xie Z., Zhang L., Yao J., Structure and lithium storage performances of nickel hydroxides synthesized with different nickel salts, Ionics, 23 (2017) 1625–1636. DOI: 10.1007/s11581-017-1983-3

Liang L., Du K., Peng Z., Cao Y., Duan J., Jiang J., Hu G., Co-precipitation synthesis of $Ni_{0.6}Co_{0.2}Mn_{0.2}(OH)_2$ precursor and characterization of $LiNi_{0.6}Co_{0.2}Mn_{0.2}O_2$ cathode material for secondary lithium batteries, Electrochimica Acta, 130 (2014) 82–89. DOI: 10.1016/j.electacta.2014.02.100

Liu W., Hua W., Zheng Z., Zhong B., Zhang Z., Facile synthesis of hierarchical porous Ni-rich $LiNi_{0.6}Co_{0.2}Mn_{0.2}O_2$ cathode material with superior high-rate capability, Ionics, 22 (2016) 1781–1790. DOI: 10.1007/s11581-016-1710-5

Liu Y., Yao W., Lei C., Zhang Q., Zhong S., Yan Z., Ni-rich oxide $LiNi_{0.85}Co_{0.05}Mn_{0.1}O_2$ for lithium ion battery: effect of microwave radiation on its morphology and electrochemical property, Journal of The Electrochemical Society, 166 (2019) A1300–A1309. DOI: 10.1149/2.0151908jes

Long P., Xu Q., Peng G., Yao X., Xu X., NiS nanorods as cathode materials for all-solid-state lithium batteries with excellent rate capability and cycling stability, ChemElectroChem, 3 (2016) 764–769. DOI: 10.1002/celc.201500570

Lu X., Zhang N., Jahn M., Pfleging W., Improved capacity retention of SiO_2 -coated $LiNi_{0.6}Mn_{0.2}Co_{0.2}O_2$ cathode material for lithium-ion batteries, Applied Sciences, 9 (2019) 3671. DOI: 10.3390/app9183671

Lu Z.G., Tan X.X., Tang Y.G., Zhou K.C., $LiNi_{0.7}Co_{0.15}Mn_{0.15}O_2$ microspheres as high-performance cathode materials for lithium-ion batteries, Rare Metals, 33 (2014) 608–614. DOI: 10.1007/s12598-013-0097-y

Ma L., Su L., Zhang J., Zhao D., Qin C., Jin Z., Zhao K., A controllable morphology GO/PANI/metal hydroxide composite for supercapacitor, Journal of Electroanalytical Chemistry, 777 (2016) 75–84. DOI: 10.1016/j.jelechem.2016.07.033

Ma R., Zhao Z., Fu J., Lv H., Li C., Wu B., Mu D., Wu F., Tuning cobalt-free nickel-rich layered $LiNi_{0.9}Mn_{0.1}O_2$ cathode material for lithium-ion batteries, ChemElectroChem, 7 (2020) 2637–2642. DOI: 10.1002/celc.202000443

Ma Z., Yuan X., Zhang Z., Mei D., Li L., Ma Z.F., Zhang L., Yang J., Zhang J., Novel flower-like nickel sulfide as an efficient electrocatalyst for non-aqueous lithium-air batteries, Scientific Reports, 5 (2015) 1–9. DOI: 10.1038/srep18199

Mi L., Chen Y., Wei W., Chen W., Hou H., Zheng Z., Large-scale urchin-like micro/nano-structured NiS: controlled synthesis, cation exchange and lithium-ion battery applications, RSC Advances, 3 (2013) 17431–17439. DOI: 10.1039/c3ra42859a

Mo Y., Guo L., Jin H., Du B., Cao B., Chen Yigao, Li D., Chen Yong, Building nickel-rich cathodes with large concentration gradient for high performance lithium-ion batteries, Journal of Power Sources, 468 (2020) 228405. DOI: 10.1016/j.jpowsour.2020.228405

Mu L., Kan W.H., Kuai C., Yang Z., Li L., Sun C.J., Sainio S., Avdeev M., Nordlund D., Lin F., Structural and electrochemical impacts of mg/mn dual dopants on the $LiNiO_2$ cathode in Li-metal batteries, ACS Applied Materials and Interfaces, 12 (2020) 12874–12882. DOI: 10.1021/acsami.0c00111

Muralidharan N., Essehli R., Hermann R.P., Parejiya A., Amin R., Bai Y., Du Z., Belharouak I., $LiNi_xFe_yAl_zO_2$, a new cobalt-free layered cathode material for advanced Li-ion batteries, Journal of Power Sources, 471 (2020) 228389. DOI: 10.1016/j.jpowsour.2020.228389

Nam K.M., Kim H.J., Kang D.H., Kim Y.S., Song S.W., Ammonia-free coprecipitation synthesis of a Ni-Co-Mn hydroxide precursor for high-performance battery cathode materials, Green Chemistry, 17 (2015) 1127–1135. DOI: 10.1039/c4gc01898b

Ni S., Li T., Lv X., Yang X., Zhang L., Designed constitution of NiO/Ni nanostructured electrode for high performance lithium-ion battery, Electrochimica Acta, 91 (2013) 267–274. DOI: 10.1016/j.electacta.2012.12.113

Nitta N., Wu F., Lee J.T., Yushin G., Li-ion battery materials: present and future, Materials Today, 18 (2015) 252–264. DOI: 10.1016/j.mattod.2014.10.040

Noh H.J., Chen Z., Yoon C.S., Lu J., Amine K., Sun Y.K., Cathode material with nanorod structure—an application for advanced high-energy and safe lithium batteries, Chemistry of Materials, 25 (2013) 2109–2115. DOI: 10.1021/cm4006772

Noh H.J., Ju J.W., Sun Y.K., Comparison of nanorod-structured $Li[Ni_{0.54}Co_{0.16}Mn_{0.30}]O_2$ with conventional cathode materials for li-ion batteries, ChemSusChem, 7 (2014) 245–252. DOI: 10.1002/cssc.201300379

Nurcahyani C., Anjani A.E., Purwanto A., Yudha C.S., Hasanah L.M., Dyartanti E.R., Nur A., Flame-assisted spray pyrolysis of lithium nickel cobalt aluminum oxide leaching stream, AIP Conference Proceedings, 2219 (2020) 030003. DOI: 10.1063/5.0003156

Oh H.J., Jo C.H., Yoon C.S., Yashiro H., Kim S.J., Passerini S., Sun Y.K., Myung S.T., Nickel oxalate dihydrate nanorods attached to reduced graphene oxide sheets as a high-capacity anode for rechargeable lithium batteries, NPG Asia Materials, 8 (2016) e270. DOI: 10.1038/am.2016.59

Park G.D., Chan Kang Y., Characteristics of precursor powders of a nickel-rich cathode material prepared by a spray drying process using water-soluble metal salts, RSC Advances, 4 (2014) 44203–44207. DOI: 10.1039/c4ra08524h

Purwanto A., Yudha C.S., Ikhwan Muhammad K., Algifari B.G., Widiyandari H., Sutopo W., Synthesis of $LiNi_{0.8}Co_{0.15}Al_{0.05}O_2$ cathode material via flame-assisted spray pyrolysis method, Advanced Powder Technology, 31 (2020) 1674–1681. DOI: 10.1016/j.apt.2020.01.035

Purwanto A., Yudha C.S., Ubaidillah U., Widiyandari H., Ogi T., NCA cathode material: synthesis methods and performance enhancement efforts NCA cathode material: synthesis methods and performance enhancement efforts, Materials Research Express, 5 (2018) 122001. DOI: 10.1088/2053-1591/aae167

Qian G., Zhang Y., Li L., Zhang R., Xu J., Cheng Z., Xie S., Wang H., Rao Q., He Y., Shen Y., Chen L., Tang M., Ma Z., Single-crystal nickel-rich layered-oxide battery cathode materials: synthesis, electrochemistry, and intra-granular fracture, Energy Storage Materials, 27 (2020) 140–149. DOI: 10.1016/j.ensm.2020.01.027

Qiu H., Du T., Wu J., Wang Y., Liu J., Ye S., Liu S., Towards deriving Ni-rich cathode and oxide-based anode materials from hydroxides by sharing a facile co-precipitation method, Dalton Transactions, 47 (2018) 6934–6941. DOI: 10.1039/c8dt00893k

Qiu Z., Zhang Y., Wang D., Xia S., A ternary oxide precursor with trigonal structure for synthesis, Solid State Electrochem, 21 (2017a) 3037–3046. DOI: 10.1007/s10008-017-3643-y

Qiu Z., Zhang Y., Xia S., Yao Y., A facile method for synthesis of $LiNi_{0.8}Co_{0.15}Al_{0.05}O_2$ cathode material, Solid State Ionics, 307 (2017b) 73–78. DOI: 10.1016/j.ssi.2017.04.011

Ronduda H., Zybert M., Szczęsna-Chrzan A., Trzeciak T., Ostrowski A., Szymański D., Wieczorek W., Raróg-Pilecka W., Marcinek M., On the sensitivity of the Ni-rich layered cathode materials for li-ion batteries to the different calcination conditions, Nanomaterials, 10 (2020) 1–21. DOI: 10.3390/nano10102018

Ryu H.H., Park K.J., Yoon D.R., Aishova A., Yoon C.S., Sun Y.K., $Li[Ni_{0.9}Co_{0.09}W_{0.01}]O_2$: a new type of layered oxide cathode with high cycling stability, Advanced Energy Materials, 9 (2019) 1–7. DOI: 10.1002/aenm.201902698

Sebastian S.T., Jagan R.S., Rajagoplan R., Paravannoor A., Menon L.V., Subramanian K.R.V., Nair S.V., Balakrishnan A., Lithium-ion storage performance of camphoric carbon wrapped NiS nano/micro-hybrids, RSC Advances, 4 (2014)

11673–11679. DOI: 10.1039/c4ra00176a

Seo J., Lee J., Fast growth of the precursor particles of $Li(Ni_{0.8}Co_{0.16}Al_{0.04})O_2$ via a carbonate co-precipitation route and its electrochemical performance, Journal of Alloys and Compounds, 694 (2017) 703–709. DOI: 10.1016/j.jallcom.2016.10.062

Shi J., Du N., Zheng W., Li X., Dai Y., He G., Ultrathin Ni-Co double hydroxide nanosheets with conformal graphene coating for highly active oxygen evolution reaction and lithium ion battery anode materials, Chemical Engineering Journal, 327 (2017) 9–17. DOI: 10.1016/j.cej.2017.06.080

Sonia T.S., Anjali P., Roshny S., Lakshmi V., Ranjusha R., Subramanian K.R.V., Nair S.V., Balakrishnan A., Nano/micro-hybrid NiS cathodes for lithium ion batteries, Ceramics International, 40 (2014) 8351–8356. DOI: 10.1016/j.ceramint.2014.01.041

Su Y., Chen G., Chen L., Li W., Zhang Q., Yang Z., Lu Y., Bao L., Tan J., Chen R., Chen S., Wu F., Exposing the {010} planes by oriented self-assembly with nanosheets to improve the electrochemical performances of Ni-Rich $Li[Ni_{0.8}Co_{0.1}Mn_{0.1}]O_2$ microspheres, ACS Applied Materials and Interfaces, 10 (2018) 6407–6414. DOI: 10.1021/acsami.7b18933

Sun H.H., Weeks J.A., Heller A., Mullins C.B., Nanorod gradient cathode: preventing electrolyte penetration into cathode particles, ACS Applied Energy Materials, 2 (2019) 6002–6011. DOI: 10.1021/acsaem.9b01116

Sun Y.K., Lee D.J., Lee Y.J., Chen Z., Myung S.T., Cobalt-free nickel rich layered oxide cathodes for lithium-ion batteries, ACS Applied Materials and Interfaces, 5 (2013) 11434–11440. DOI: 10.1021/am403684z

Tang Z.F., Wu R., Huang P.F., Wang Q.S., Chen C.H., Improving the electrochemical performance of Ni-rich cathode material $LiNi_{0.815}Co_{0.15}Al_{0.035}O_2$ by removing the lithium residues and forming Li_3PO_4 coating layer, Journal of Alloys and Compounds, 693 (2017) 1157–1163. DOI: 10.1016/j.jallcom.2016.10.099

Tian C., Nordlund D., Xin H.L., Xu Y., Liu Y., Sokaras D., Lin F., Doeff M.M., Depth-dependent redox behavior of $LiNi_{0.6}Mn_{0.2}Co_{0.2}O_2$, Journal of The Electrochemical Society, 165 (2018) A696–A704. DOI: 10.1149/2.1021803jes

Tian J., Su Y., Wu F., Xu S., Chen F., Chen R., Li Q., Li J., Sun F., Chen S., High-rate and cycling-stable nickel-rich cathode materials with enhanced Li^+ diffusion pathway, ACS Applied Materials and Interfaces, 8 (2016) 582–587. DOI: 10.1021/acsami.5b09641

Toprakci O., Toprakci H.A.K., Ji L., Zhang X., Fabrication and electrochemical characteristics of $LiFePO_4$ powders for lithium-ion batteries, KONA Powder and Particle Journal, 28 (2010) 50–73. DOI: 10.14356/kona.2010008

Wang L., Sun Juncai, Sun Jing, Hydrothermal synthesis of nanostructured NiS and its optimisation as cathode material for rechargeable lithium battery, International Journal of Nanomanufacturing, 9 (2013) 303–310. DOI: 10.1504/IJNM.2013.056056

Wang L., Zhang G., Liu Q., Duan H., Recent progress in Zn-based anodes for advanced lithium-ion batteries, Materials Chemistry Frontiers, 2 (2018) 1414–1435. DOI: 10.1039/c8qm00125a

Wang Q., Zhang L., Zhao P., Du Z., Facile synthesis of a high-capacity $LiNi_{0.8}Co_{0.15}Al_{0.05}O_2$ nanoplate cathode with a 010 orientation for lithium-ion batteries, International Journal of Electrochemical Science, 13 (2018) 10382–10389. DOI: 10.20964/2018.11.15

Wang X., Li X., Sun X., Li F., Liu Q., Wang Q., He D., Nanostructured NiO electrode for high-rate Li-ion batteries, Journal of Materials Chemistry, 21 (2011) 3571–3573. DOI: 10.1039/c0jm04356g

Wang Y., Wang E., Zhang X., Yu H., High-voltage "single-crystal" cathode materials for lithium-ion batteries, Energy and Fuels, 35 (2021) 1918–1932. DOI: 10.1021/acs.energyfuels.0c03608

Weber R., Li H., Chen W., Kim C.-Y., Plucknett K., Dahn J.R., In situ XRD studies during synthesis of single-crystal $LiNiO_2$, $LiNi_{0.975}Mg_{0.025}O_2$, and $LiNi_{0.95}Al_{0.05}O_2$ cathode materials, Journal of The Electrochemical Society, 167 (2020) 100501. DOI: 10.1149/1945-7111/ab94ef

Wei S., Di Lecce D., Brescia R., Pugliese G., Shearing P.R., Hassoun J., Electrochemical behavior of nanostructured NiO@C anode in a lithium-ion battery using $LiNi_{1/3}Co_{1/3}Mn_{1/3}O_2$ cathode, Journal of Alloys and Compounds, 844 (2020) 155365. DOI: 10.1016/j.jallcom.2020.155365

Wu N., Wu H., Yuan W., Liu S., Liao J., Zhang Y., Facile synthesis of one-dimensional $LiNi_{0.8}Co_{0.15}Al_{0.05}O_2$ microrods as advanced cathode materials for lithium ion batteries, Journal of Materials Chemistry A, 3 (2015) 13648–13652. DOI: 10.1039/C5TA02767E

Xie H., Du K., Hu G., Duan J., Peng Z., Zhang Z., Cao Y., Synthesis of $LiNi_{0.8}Co_{0.15}Al_{0.05}O_2$ with 5-sulfosalicylic acid as a chelating agent and its electrochemical properties, Journal of Materials Chemistry A, 3 (2015) 1–21. DOI: 10.1039/C5TA05266A

Xie H., Hu G., Du K., Peng Z., Cao Y., An improved continuous co-precipitation method to synthesize $LiNi_{0.80}Co_{0.15}Al_{0.05}O_2$ cathode material, Journal of Alloys and Compounds, 666 (2016) 84–87. DOI: 10.1016/j.jallcom.2016.01.064

Xu L., Zhou F., Kong J., Chen Z., Chen K., Synthesis of $Li(Ni_{0.6}Co_{0.2}Mn_{0.2})O_2$ with sodium DL-lactate as an eco-friendly chelating agent and its electrochemical performances for lithium-ion batteries, Ionics, 24 (2018) 2261–2273. DOI: 10.1007/s11581-017-2363-8

Xu X., Huo H., Jian J., Wang L., Zhu H., Xu S., He X., Yin G., Du C., Sun X., Radially oriented single-crystal primary nanosheets enable ultrahigh rate and cycling properties of $LiNi_{0.8}Co_{0.1}Mn_{0.1}O_2$ cathode material for lithium-ion batteries, Advanced Energy Materials, 9 (2019) 1–9. DOI: 10.1002/aenm.201803963

Yan W., Yang S., Huang Y., Yang Y., Guohui Yuan, A review on doping/coating of nickel-rich cathode materials for lithium-ion batteries, Journal of Alloys and Compounds, 819 (2020) 153048. DOI: 10.1016/j.jallcom.2019.153048

Yang C., Zhu Z., Wei W., Zhou L., Superior cycle stability of single crystal nickel-rich layered oxides with micron-scale grain size as cathode material for lithium-ion batteries, International Journal of Electrochemical Science, 15 (2020) 5031–5041. DOI: 10.20964/2020.06.03

Yang G., Qin X., Wang B., Cai F., Gao J., Well-ordered spherical $LiNi_{0.8}Co_{0.1}Mn_{0.1}O_2$ cathode material for lithium-ion batteries, Journal of Materials Research, 35 (2020) 51–57. DOI: 10.1557/jmr.2019.307

Yang H., Liu P., Chen Q., Liu X., Lu Y., Xie S., Ni L., Wu X., Peng M., Chen Yanbin, Tang Y., Chen Yanfeng, Fabrication and characteristics of high-capacity $LiNi_{0.8}Co_{0.15}Al_{0.05}O_2$with monodisperse yolk–shell spherical precursors by a facile method, RSC Advances, 4 (2014) 35522. DOI: 10.1039/c4ra04122d

Yang X., Tang Y., Zheng J., Shang G., Wu J., Lai Y., Li J., Zhang Z., Tailoring structure of Ni-rich layered cathode enable robust calendar life and ultrahigh rate capability for lithium-ion batteries, Electrochimica Acta, 320 (2019) 134587. DOI: 10.1016/j.electacta.2019.134587

Ye Z., Qiu L., Yang W., Wu Z., Liu Y., Wang G., Song Y., Zhong B., Guo X., Nickel-rich layered cathode materials for lithium-ion batteries, Chemistry – A European Journal, 27 (2021) 4249–4269. DOI: 10.1002/chem.202003987

Yoon C.S., Jun D.W., Myung S.T., Sun Y.K., Structural stability of $LiNiO_2$ cycled above 4.2 v, ACS Energy Letters, 2 (2017) 1150–1155. DOI: 10.1021/acsenergylett.7b00304

Yudha C.S., Muzayanha S.U., Hendri W., Iskandar F., Sutopo W., Purwanto A., Widiyandari H., Synthesis of $LiNi_{0.85}Co_{0.14}Al_{0.01}O_2$ cathode material and its performance in an NCA / graphite full-battery, Energies, 12 (2019) 1886. DOI: 10.3390/en12101886

Yue P., Wang Z., Wang J., Guo H., Xiong X., Li X., Effect of fluorine on the electrochemical performance of spherical $LiNi_{0.8}Co_{0.1}Mn_{0.1}O_2$ cathode materials via a low temperature method, Powder Technology, 237 (2013) 623–626. DOI: 10.1016/j.powtec.2012.12.061

Zeng T., Zhang C., An effective way of co-precipitating Ni^{2+}, Mn^{2+} and Co^{2+} by using ammonium oxalate as precipitant for Ni-rich Li-ion batteries cathode, Journal of Materials Science, 55 (2020) 11535–11544. DOI: 10.1007/s10853-020-04753-w

Zhang C., Qi J., Zhao H., Hou H., Deng B., Tao S., Su X., Wang Z., Qian B., Chu W., Facile synthesis silkworm-like Ni-rich layered $LiNi_{0.8}Co_{0.1}Mn_{0.1}O_2$ cathode material for lithium-ion batteries, Materials Letters, 201 (2017) 1–4. DOI: 10.1016/j.matlet.2017.04.121

Zhang H., Yang S., Huang Y., Xianhua H., Synthesis of non-spherical $LiNi_{0.88}Co_{0.09}Al_{0.03}O_2$ cathode material for lithium-ion batteries, Energy & Fuels, 34 (2020) 9002–9010. DOI: 10.1021/acs.energyfuels.0c01692

Zhang J., Xu S., Hamad K.I., Jasim A.M., Xing Y., High retention rate NCA cathode powders from spray drying and flame assisted spray pyrolysis using glycerol as the solvent, Powder Technology, 363 (2020) 1–6. DOI: 10.1016/j.powtec.2019.12.057

Zhang L., Dong T., Yu X., Dong Y., Zhao Z., Li H., Synthesis and electrochemical performance of $LiNi_{0.7}Co_{0.15}Mn_{0.15}O_2$ as gradient cathode material for lithium batteries, Materials Research Bulletin, 47 (2012) 3269–3272. DOI: 10.1016/j.materresbull.2012.08.002

Zhang Q., Su Y., Chen L., Lu Y., Bao L., He T., Wang J., Chen R., Tan J., Wu F., Pre-oxidizing the precursors of Nickel-rich cathode materials to regulate their Li^+/Ni^{2+} cation ordering towards cyclability improvements, Journal of Power Sources, 396 (2018) 734–741. DOI: 10.1016/j.jpowsour.2018.06.091

Zhao Z., Huang B., Wang M., Yang X., Gu Y., Facile synthesis of fluorine doped single crystal Ni-rich cathode material for lithium-ion batteries, Solid State Ionics, 342 (2019) 115065. DOI: 10.1016/j.ssi.2019.115065

Zhu J., Chen G., Single-crystal based studies for correlating the properties and high-voltage performance of $Li[Ni_xMn_yCo_{1-x-y}]O_2$ cathodes, Journal of Materials Chemistry A, 7 (2019) 5463–5474. DOI: 10.1039/c8ta10329a

Zhu J., Zheng J., Cao G., Li Y., Zhou Y., Deng S., Hai C., Flux-free synthesis of single-crystal $LiNi_{0.8}Co_{0.1}Mn_{0.1}O_2$ boosts its electrochemical performance in lithium batteries, Journal of Power Sources, 464 (2020) 228207. DOI: 10.1016/j.jpowsour.2020.228207

Zhu L.Z., Han E.S., Cao J.L., Synthesis and characteristics of NiS for cathode of lithium ion batteries, Advanced Materials Research, 236–238 (2011) 694–697. DOI: 10.4028/www.scientific.net/AMR.236-238.694

Zhu Q., Xiao H., Zhang R., Geng S., Huang Q., Effect of impeller type on preparing spherical and dense $Ni_{1-x-y}Co_xMn_y(OH)_2$ precursor via continuous co-precipitation in pilot scale: a case of $Ni_{0\cdot6}Co_{0\cdot2}Mn_{0\cdot2}(OH)_2$, Electrochimica Acta, 318 (2019) 1–13. DOI: 10.1016/j.electacta.2019.06.008

Zhu X., Zhong Y., Zhai H., Yan Z., Li D., Nanoflake nickel hydroxide and reduced graphene oxide composite as anode materials for high-capacity lithium ion batteries, Electrochimica Acta, 132 (2014) 364–369. DOI: 10.1016/j.electacta.2014.03.132

Zuniga L., Gonzalez G., Chavez R.O., Myers J.C., Lodge T.P., Alcoutlabi M., Centrifugally spun α-Fe_2O_3/TiO_2/carbon composite fibers as anode materials for lithium-ion batteries, Applied Sciences, 9 (2019) 4032. DOI: 10.3390/app9194032

Authors' Short Biographies

Agus Purwanto

Agus Purwanto is a Professor at Chemical Department Sebelas Maret University, Indonesia. He received his Ph.D. degree in Chemical Engineering from Hiroshima University, Japan. His research interest is in the synthesis and characterization of functional materials for energy storage and conversion. One of the research interests is the development li-ion battery materials, optimization and its application.

Authors' Short Biographies

Shofirul Sholikhatun Nisa

Shofirul Sholikhatun Nisa received her bachelor's degree in 2019 from the Chemical Engineering Department, Universitas Sebelas Maret. She continued her master's studies at the same department and university and is now in final year. She is very interested in the field of energy storage especially Li-ion batteries. Currently, her research focus is on the synthesis of NMC materials, especially Ni-rich materials.

Ike Puji Lestari

Ike Puji Lestari is a master student at the Department of Chemical Engineering, Universitas Sebelas Maret. Previously she received her bachelor's degree in the same department in 2019. Currently she is working on a novel silicon based anode material for Li-ion batteries.

Muhammad Nur Ikhsanudin

Muhammad Nur Ikhsanudin received his bachelor's degree in 2020 from the Chemical Engineering Department, Universitas Sebelas Maret. He continued his master's studies at the same department and university and is now in first year. He is very interested in the field of energy storage especially Li-ion batteries. Currently, His research focus is on the anode-free Li-ion batteries.

Cornelius Satria Yudha

Cornelius Satria Yudha received his bachelor degree (2015) and master degree (2019) in chemical engineering, Universitas Sebelas Maret. Currently, He is a young researcher at University Centre of Excellence for Electrical Storage Technology (CE-FEEST), Universitas Sebelas Maret. His research interest is hydrometallurgical processing of novel material for state-of-the-art secondary energy storage development.

Hendri Widiyandari

Hendri Widiyandari is a lecturer at Physics Department Sebelas Maret University, Indonesia, since 2018. Before that, she was a lecturer at the Department of Physics, Diponegoro University, Indonesia, from 1999 until 2017. She received her Ph.D. degree in Chemical Engineering from Hiroshima University, Japan. Her research interest is in the synthesis and characterization of functional materials for energy storage and conversion. One of the research interests is the development of active materials for Li-ion batteries.

KONA Powder and Particle Journal No. 39 (2022) 150–175/https://doi.org/10.14356/kona.2022017 Review Paper

Contribution of Particle Design Research to the Development of Patient-Centric Dosage Forms[†]

Hirofumi Takeuchi

Laboratory of Advanced Pharmaceutical Process Engineering, Gifu Pharmaceutical University, Japan

Abstract

A variety of dosage forms have been developed in order to achieve effective and safe drug delivery in topical or systemic drug administrations. In this review, formulation research and process issues related to a popular oral dosage form, the tablet, are introduced. Research on oral dosage forms, including orally disintegrating tablets (ODTs) and films (ODFs), which have recently been developed with an aim toward more patient-centric drug therapy, is also introduced. Another trend in recent drug therapy is an increase in the number of large bioactive molecules among the newly developed active pharmaceutical ingredients (APIs). To design dosage forms for these APIs, novel dosage form design and administration routes are required. For this purpose, we have tried to effectively use the polymer-coated liposomes in oral, pulmonary and ophthalmic administration. For example, suitable polymers were introduced for the design of specific administration routes, such as mucoadhesive liposomes for oral administration. The key point in these researches is the particle design for the component particles of final dosage forms, both in the case of coarse powder particle design for formulating solid dosage forms and in the case of colloidal particle design, such as the design of liposomes for peptide drug delivery.

Keywords: particle design, patient centric therapy, orally disintegrating tablets, drug delivery systems, mucoadhesive liposomes

1. Introduction

One of the most important roles of dosage forms is to deliver the drug into the body. The most common delivery route is that of oral administration, in which the drug is taken by mouth like food and then absorbed in the digestive tract. The active pharmaceutical ingredient (API) is transported to the whole body via the systemic blood stream. Since taking drugs by this route is similar to eating food, the administration can be performed by the patients themselves, and thus oral administration is said to be the method with the best compliance and adherence of the patients. Of course, many other dosage forms are also known, such as injections that are delivered directly into the body, inhalants that allow local administration to the pharynx, and ointments or patches that are expected to act mainly on the skin. These various dosage forms and their names are defined in the pharmacopoeia in each country. In the current (17th edition) Japanese Pharmacopoeia, various dosage form names are listed in each administration routes.

One of the reasons why many dosage forms are required is that the optimal and most efficiently administered dosage form must be designed according to the characteristics and therapeutic purpose of the API. Furthermore, in recent years, the concept of dosage form design for drug administration has evolved, with increasing consideration for the patients who are actually administered the drug—that is, the design of patient-centric dosage forms. Even in oral administration, which is the most preferable administration method for patients, there is an increasing demand for formulation development so that administration can be carried out more easily. For example, orally disintegrating tablets (ODTs) that disintegrate in the oral cavity before swallowing without or with a small amount of water are more convenient for patients. Jelly-like formulations and oral films have also been developed to promote ease of swallowing and administration.

One of the motivations underlying the development of ODTs and other easy-to-take dosage forms is the growing need for medical treatment of the elderly in aging societies, but a growing interest in child-friendly administration modalities has also been a factor. Regarding the former, age-related aspiration is a life-threatening problem, and aspiration pneumonia is ranked as the leading cause of death among the elderly. Although aspiration applies to all situations, including diet, the risk of aspiration should be reduced as much as possible in the administration of

---

[†] Received 23 June 2021; Accepted 29 July 2021
J-STAGE Advance published online 2 October 2021
Add: 5-6-1 Mitahora-Higashi, Gifu 502-8585, Japan
E-mail: takeuchi@gifu-pu.ac.jp
TEL: +81-58-237-8572

therapeutic drugs. In recent years, there has also been a great deal of interest in drug administration to children. When there is no suitable tablet for pediatric dosing, tablets are crushed in the pharmacy to match the prescription. In addition to the labor this requires on the part of the pharmacist, certain functions inherent to the formulation design, such as sustained release, may be impaired by such pulverization. In addition, the division may reduce the accuracy of the drug dose. Even if the pulverization proceeds without such problems, there is a concern that the receiving child may not be able to take the powder well or may refuse to take it entirely due to its unpleasant taste. Against this background, the development of pediatric content formulations as well as the development of dosage forms that facilitate administration to children are underway. Examples of such dosage forms include syrups that have been known for a long time, jelly preparations that are newly listed in the Japanese Pharmacopoeia, and oral film preparations. Also, regarding the size of tablets, a mini tablet with a diameter of about 1 to 4 mm is available as one of the new dosage forms.

The administration of drugs is classified into two types: systemic administration, in which a drug is delivered systemically through the bloodstream after administration, and topical administration, in which a drug is administered directly to the site where its effects are needed. In either case, it is often necessary to deliver the drug into the body more efficiently by using suitable dosage forms and formulations. Sustained-release preparations, in which the drug is gradually released, are one of the delivery modes considered in the preparation design. Orally administered sustained-release preparations control the amount of drug released on the preparation side to control the amount of drug delivered systemically. As a result, specific effects are possible, such as preventing the blood concentration of the drug from reaching a region where side effects may occur, and being able to increase the dose and thus reduce the number of doses. Coating is a typical preparation technique for achieving release control from the dosage forms. A matrix-type tablet, which is prepared with a material suitable for sustained release as the excipient, is also a commonly used dosage form design that achieves release control (McGinity, 1997).

In the case of designing oral preparations of the most common small molecule drugs, it is necessary to pay close attention to the solubility of the drug. In oral administration, the first barrier for delivery into the body is the gastrointestinal tract, and thus the drug must dissolve quickly before absorption there. A drug to be absorbed must pass through epithelial cells in the gastrointestinal tract, and some hydrophobicity of the drug molecules contributes to this permeability. On the other hand, high hydrophobicity of the drug molecules will lead to weak solubility of the crystal. It is well known that this balance between solubility and permeability needs to be taken into consideration (Amidon et al., 1995), and for some time attempts have been made to improve the solubility of poorly soluble drugs in formulation. Such efforts have included miniaturization of drug crystals and solid dispersion technology, and these preparation technologies have been applied to many actual preparations. In the former case, it can be easily imagined that the effective surface area at the time of dissolution is increased and the dissolution characteristics are improved by miniaturization. However, considering the individual processes in the actual manufacture of the final product, mixing the finely pulverized powder into the formulation may lead to problems, including problems with mixing uniformity or a decrease in fluidity during transportation. The latter method, i.e., solid dispersion, has the advantage of potentially achieving greater saturation solubility compared with miniaturization and thus has been anticipated as a useful technology for more than two decades. The biggest issue is the storage stability of the drug in its amorphized state, and the choice of carrier used for the solid dispersion and the mechanism of the amorphization are related.

In formulation design, along with paying attention to the characteristics of the drug crystals, the technology for forming the final dosage form is an important research subject. For example, even in the case of tablet preparation, it is essential to study particle design and formulation design based on the characteristics of the materials (excipients, disintegrants, binders, etc.) that make up the tablet shape having the pharmaceutically required functions. In addition, when special functions such as a significant reduction in disintegration time are required, such as for orally disintegrating tablets, which have been actively developed in recent years, more multifaceted research is required than for the prescription design of ordinary tablets. We have also conducted research on particle design related to tablet excipients, particle design of excipients and binders useful for the formulation design of orally disintegrating tablets, and analysis of compression molding processes using such particles. In developing new dosage forms such as oral film preparations (orodispersible films) and jelly preparations that are expected to have similar functions, we have been working on the basic formulations and the processes of formulation design and preparation methods. For convenience of handling and portability, we have also reported the concept of easily re-dispersible powdered emulsion of oily drugs (dry emulsions) (Takeuchi et al., 1991) or powdered jellies (dry jellies), which can be easily prepared by adding water before use (Kakino et al., 2017).

On the other hand, in order to guarantee the quality of final products, it is necessary to examine the validity of the production process. In addition, it is important to confirm the production process using the actual formulation on a production process scale, because the occurrence of unexpected locking obstacles such as sticking during compaction of pharmaceutical powder formulation poses a major obstacle to production. To address these issues, we have tried to analyze the compression process using a tableting analyzer to detect tablet failures, and to understand the relationship between particle characteristics and sticking phenomena. In addition, these studies have led to the recent study of continuous production. Research on these formulation processes is essential for pharmaceutical companies and has been extensively conducted, but so far, there have been only a small number of papers concerned with conventional formulation research.

Targeting, in which the drug is selectively delivered the desired site in the body, is a field of pharmaceutics research. The development of a drug delivery system that uses submicron-sized carrier particles to deliver drugs to the target site started at late 1970's (Couvreur et al., 1979). Liposomes were also anticipated to be candidates for particulate drug carriers (Knight, 1981). These fine particles for drug delivery are sometimes called colloidal drug delivery systems (Kreuter, 1994). Active targeting, which utilizes the affinity of substances localized on the cell surface to achieve particle accumulation at the delivery site, has been of interest to many researchers. On the other hand, after administering such submicron particles into the blood by injection, it is necessary to prevent their distribution to other unintended organs or sites for as long as possible. This has been especially important in the development and commercialization of liposome injections containing anticancer agents such as doxorubicin. The same principle applies to the case of topical administration, and the effect of the encapsulated drug depends on how the movement of the microparticulate preparation is controlled after administration. Looking at the development status of drugs in recent years, the size of drug molecules has clearly been increasing. In particular, drugs modeled on hormones, peptides, antibodies, etc., produced in the body have a molecular weight of several thousand to several hundred thousand daltons. Similar to targeting, research on such drugs using a fine particle carrier to deliver them into the body is also in progress.

Insulin is a typical drug with a high molecular weight. Insulin is a substance that is originally produced in the body and has the function of lowering the glucose concentration in the blood when its level is high. Insulin developed as a commercial product has saved the lives of many diabetic patients. For type I diabetic patients who are deficient in insulin, administration before each meal, i.e., just before the glucose concentration in the blood rises, is the most effective treatment method. Injection is the most popular method of delivering insulin into the body, and self-injection is also permitted. In addition, a prefilled syringe-type of insulin in which the injection solution is pre-set in a syringe has also been made available. The pain of injection is alleviated by making the diameter of the needle sufficiently small. A unit called a gauge (G) is used for the thickness of the injection needle: the larger the G value, the thinner the needle. The needle for insulin injection is usually 30 G (outer diameter, 0.31 ± 0.02 mm) or more, which is considerably thinner than the needle used for normal blood sampling (21–23 G: outer diameter, 0.81–0.64 mm). This is another example of pharmaceutical development research progressing in consideration of the needs of actual patients.

Injections are the most common dosage form for high molecular weight drugs, and the development of more patient-friendly optimal dosage forms is still being considered as an important research topic. In the case of insulin, attempts to develop administration methods other than injection have included the commercial development of a powder inhalant to deliver insulin into the body via absorption from the lungs. We have also conducted research focusing on liposome particle design with the aim of developing novel delivery methods other than injection of macromolecular drugs. Among them, polymer-coated liposomes with a mucosal adhesion function have potential for use in the development or oral administration preparations of high molecular drugs. In addition to oral administration, the usefulness of drug transpulmonary absorption using liposomes has also been investigated. We have also suggested the possibility of using eye drops to deliver the drug to the posterior segment of the eye.

As mentioned above, there are various aspects to pharmaceutical formulation research. All the research we have conducted in this field has a common theme: particle design. Such design can range from powder particles to nanoparticles such as liposomes. That is, regardless of the final dosage form, the goal has been to control the characteristics of the basic powder particles and nanoparticles in order to develop the pharmaceutical function and contribute to drug delivery. Moreover, keeping the goal of administration to humans in mind, we have aimed to design dosage forms that will realize the gentlest possible drug administration in actual patients. The author would like to introduce some of the representative researches and their background.

2. Formulation design for improving drug dissolution and absorption

2.1 Micronizing drug crystals and dosage form design

It is well known that the size of drug crystals affects the dissolution rate of drugs (Takeuchi, 2019). As the drug dissolution rate is an important factor in preparing pharmaceutical tablets, it is not rare to pulverize or control the drug crystal to an appropriate size in the manufacture of tablets. In the case of pharmaceutical preparation of poorly water-soluble drugs, a jet mill is often used in pulverizing pharmaceutical crystals. Many active ingredients are organic powders and generally do not have a very high melting point. Therefore, when pulverization to a few microns is required, there is often a concern that the crystal shape may change due to heat generated during pulverization, and thus a jet mill that is relatively unlikely to generate heat is used.

Drug crystals that have been refined to submicron size (usually 100–200 nm in average particle size) are called nanocrystals, and the state in which submicron-sized drug crystals are dispersed in a liquid is called nanocrystal suspension. In addition to improving the dissolution properties, submicron-sized particles exhibit gastrointestinal retention due to tissue adhesion (Ponchel et al., 1997). It has also been reported that the nanocrystal suspension of drug improved its absorption extensibly in comparing AUC (area under curve) values compared with the usual preparation (Liversidge and Cundy, 1995). Regarding the preparation methods, there are roughly two types of methods for refining drug crystals to submicron size: the breakdown method and the build-up method. Well-known breakdown technologies are 1) the pearl milling (bead/ball milling) method (Liversidge et al., 2003), which prepares particles by crushing them using a large number of beads in a medium, and 2) the high-pressure homogenization method (Müller and Peters, 1998; Keck and Müller, 2006), which prepares micronized particles by passing them through narrow gaps at high pressure. These breakdown-type processes also have problems such as relatively long operation time, concern about contaminants generated from the medium, and high energy requirement. Elan's NanoCrystal® technology based on a breakdown method is known a commercially widely used one.

Drug crystals that require improved dissolution properties often have problems with wettability, and even if they are micronized by pulverizing, the effective specific surface area at the time of dissolution does not increase as expected. Conversely, the micronization may cause aggregation and lead to a decrease in the effective surface area for dissolution. To solve this problem, we designed composite particles containing disintegrants by use of a spray drying technique (Takeuchi et al., 1987a). When a poorly water-soluble model drug tolbutamide and PCS® (partially pregelatinized starch), the latter of which has high sphericity, were formulated as disintegrants, the resulting spray-dried particles were spherical and showed excellent fluidity. Because the powder X-ray diffraction analysis of spray-dried particles showed the existence of drug crystals on the particles and the particle sizes of spray-dried particles were comparable to those of PCS particles, the structure of the spray-dried particles was estimated to consist of the drug microcrystals embedded on the surface of PCS, as shown in **Fig. 1(A)**. The dissolution test revealed that the obtained composite particles had significantly improved solubilizing property compared to the original drug crystalline powder and the spray-dried drug alone (**Fig. 2**). The drug release rate depended on the drug formulating ratio to core particle, PCS. When observed under a microscope, the drug embedded particles were found to swell rapidly upon contact with water, indicating that the prescribed disintegrant worked effectively. A preparation of ordered mixture-like composite particles of poorly-water soluble

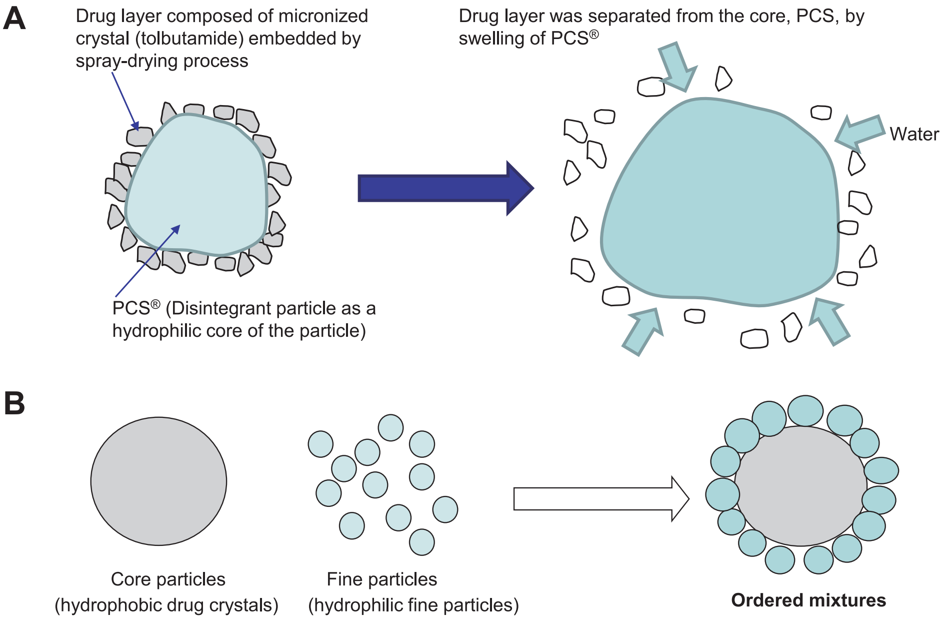

Fig. 1 Particle design of poorly water soluble drugs for improving their dissolution properties **(A)** Drug embedding system with a disintegrant prepared by spray-drying technique for improvement of dissolution of poorly water soluble drugs and **(B)** Ordered mixtures of hydrophobic drug particles with hydrophilic fine particles.

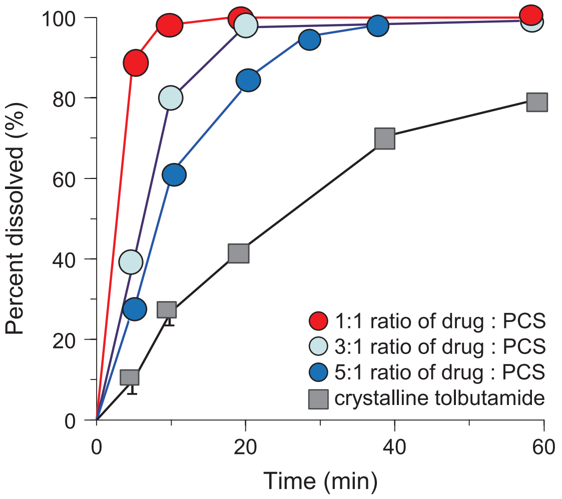

Fig. 2 Dissolution profiles of a poorly water soluble drug, tolbutamide, spray-dried with a disintegrant, PCS® (Drug embedding system).

drug and hydrophilic excipient particles such as Neusilin® (**Fig. 1(B)**) was also demonstrated with a dry mixing process by using a vibrating ball mill and a mechanical fusion system (Mechanofusion®). The resultant dissolution profiles of the poorly water-soluble drug indomethacin (IMC) from the composite particles were 3-fold to 4-fold faster. It is presumed that the particles having excellent hydrophilicity increased the hydrophilicity of the drug crystals by coating their surface and increased the effective surface area in drug dissolution.

As an attempt at nanocrystal preparation by the build-up method, we tried to control the crystallization of a poorly water-soluble drug using a Pure Nano high-pressure crystallizer (manufactured by Microfluidics) in which the poor solvent addition precipitation method was applied to the precision mixing technique using a high-pressure homogenizer (Takeuchi and Onodera, 2015). By increasing the pressure of the reaction field, a high-strength shear field is formed inside the reaction vessel, and the reactants are mixed in a turbulent state in which the strong energy dissipation mechanism is activated. In the case of crystallization, it was expected that a smaller size of crystals could be obtained by this method compared with the usual mixing operation with a normal stirrer. After preparing a fine crystal suspension of phenytoin as a model of a poorly water-soluble drug and polyvinyl alcohol (PVA) as a dispersion stabilizer, the crystal form, solubility, absorbability after oral administration, etc., of the crystals were evaluated (Tahara et al., 2016). In the case of high-pressure crystallization, the particle size was about half of that in the case of normal crystallization. Moreover, there was no change in the crystal form. The solubilizing property of the prepared particles was remarkably improved. When each phenytoin sample was orally administered to rats and the bioavailability was compared by the drug concentration in blood, the AUC value in the high-pressure crystallization product administration group was 2-fold higher than that of the usual crystallization product.

2.2 Solid dispersion particle prepared by spray drying

The term solid dispersion of a pharmaceutical preparation refers to a preparation in which the drug is dispersed in a solid carrier in an amorphous state. More precisely, the drug is dispersed as a molecule or a cluster in the carrier solids. It is well known that drugs in the amorphous state have excellent dissolution properties (Takeuchi, 2019). However, the amorphous state is generally unstable, and crystallization during storage is one of the strictly required points for pharmaceutical preparations. From this point of view, the selection of the carrier to be blended is important, and many studies have been conducted to determine the best carriers. Furthermore, it has been pointed out that the preparation process in which the drug is first dissolved and the solvent is distilled off, has an energy problem. However, in recent years, the proportion of poorly soluble drugs among the drugs developed has been extremely large, and improvement of solubility has become an extremely important issue. Thus, solid dispersions are one of the important methods for improving the dissolution property of poorly water-soluble drugs.

Research on solid solutions is often said to be the first research on solid dispersion systems (Sekiguchi and Obi, 1961; Chiou and Riegelman, 1969; Simonelli et al., 1969), but research on pharmaceutical preparations has been actively conducted since the 1980s. In order to amorphize drug crystals, it is important to use an appropriate carrier, and water-soluble polymers such as polyvinylpyrrolidone (PVP) have been studied as useful carriers (Corrigan et al., 1983; 1984; Ford et al., 1986). We selected a spray-drying technique to prepare solid dispersion particles, because the resultant particles are spherical and tend to be freely flowing. As a new carrier for preparing the solid dispersion particles prepared by spray-drying, we used fumed silica (Aerosil®), which is insoluble in water but extremely hydrophilic, and is prepared by the spray method (Takeuchi et al., 1987b).

Enteric coating polymer (Eudragit L and hydroxypropyl methylcellulose phthalate (HPMCP)) was also examined as a candidate for carriers. An attempt was made to prepare solid dispersion particles by dissolving dilute ammonia water in which the model drug tolbutamide was dissolved and dispersing or dissolving each carrier. As a result of evaluating the spray-dried particles prepared with a 1:1 ratio of drug: silica by powder X-ray diffraction, it was clarified that the drug exists in an amorphous state in the particles. Crystallization of the drug was observed when the prescribed amount of silica for the drug was reduced, indicating that the interaction between the drug and silica

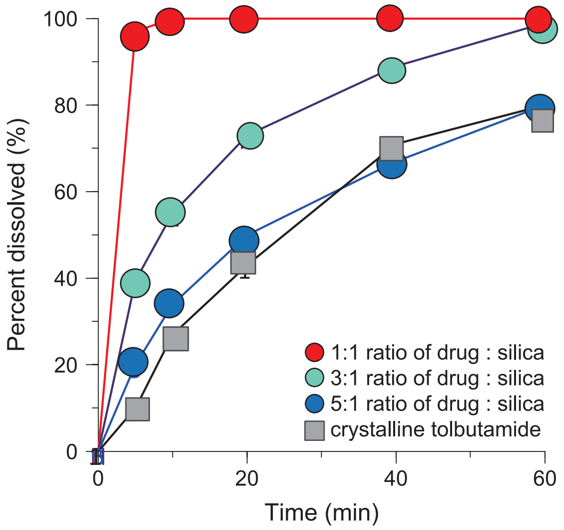

Fig. 3 Dissolution profiles of tolbutamide from spray-dried solid dispersion particles with silica or crystalline tolbutamide.

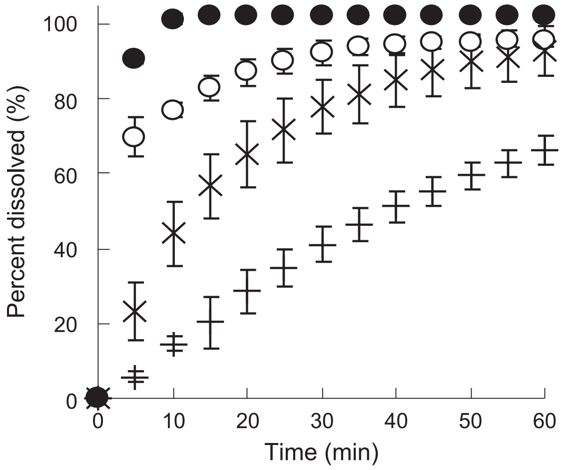

Fig. 4 Dissolution profiles of IMC from solid dispersion particles with Aerosil 200 or Sylysia 350.
+: Original IMC, ×: Spray-dried IMC, ○: Solid dispersion particles with Aerosil 200, ●: Solid dispersion particles with Sylysia 350.

particle surface contributed to the amorphization. All of the particles obtained from the characteristics of the spray drying process were spherical and had excellent fluidity. As shown in **Fig. 3**, the fastest drug dissolution was confirmed for the solid dispersion particles prepared with a 1:1 ratio of drug: silica, in which complete amorphization of the drug was confirmed. When the ratio of silica was reduced, the elution rate was delayed according to the ratio, and at a ratio of 5:1 it became almost the same as the raw crystalline of tolbutamide.

In order to confirm the usefulness of hydrophilic water-insoluble particles as a carrier of solid dispersion, we also evaluated porous silica (Sylysia®) prepared by a wet method (Takeuchi et al., 2004a). When the ethanol solution of tolbutamide was spray-dried alone, it became a metastable crystalline form II. In the evaporator method, when the solvent was distilled off, it became a stable crystalline form I, suggesting that the resultant crystal form depends on the drying rate. The spray-dried solid dispersion particles of tolbutamide with porous silica were found to be in metastable form II. The metastable crystals with silica in the solid dispersion particles were maintained even during the storage test period, confirming the importance of the presence of the carrier. In addition, the dissolution of tolbutamide in the solid dispersion particles is significantly faster than that of form II particles prepared by spray-drying without silica. The hydrophilicity of the carrier silica improves the wettability of the solid dispersion particles, resulting in the good dissolution.

In the case of indomethacin (IMC), an amorphous state was obtained by spray drying its ethanolic solution regardless of the presence or absence of a carrier. As for the dissolution characteristics, the solid dispersion particles using the porous silica Sylysia350 as a carrier showed extremely rapid dissolution (**Fig. 4**). When similar indomethacin solid dispersion particles were prepared using porous silica having different pore diameters as a carrier, an amorphous drug was confirmed with any of the silicas. However, when the dissolution rates were compared, it was observed that the drug dissolution was higher in the case of Sylysia®350, which has a larger pore size than Sylysia® 740 (Takeuchi et al., 2003b). When the specific surface areas of the two solid dispersion particles were measured, the value decreased remarkably in the case of Sylysia740, and it was presumed that the pore entrance was closed by the precipitated drug. Therefore, it was concluded that porous silica with a large pore diameter effectively utilizes the pores to amorphize the drug. It is important to pay attention to the prescription ratio of silica and the drug as a carrier and the type of silica, but it has been clarified that porous silica is useful as a carrier of a solid dispersion.

3. Design of orally disintegrating tablets and orally disintegrating films

3.1 Tablet preparation and particle design of excipients

Tablets are usually prepared by compression molding of powder (compaction). Compaction consists of four steps: filling → compression → depressurization → discharge. The powder is discharged from the hopper into the die or into the feeder around the die and then filled in the die. A stirring feeder may be used for discharge from the hopper, but the filling in the die is usually performed by the weight of the powder itself. Powder fluidity is an important factor in these processes. In the next step, i.e., the compression process, the particles are deformed by pressurization to increase the binding force and form a molded product (tablet). Various factors are involved in the binding force between particles. Because the binding force of a substance by van der Waals force is dominant, when the number of bonding points between particles in a tablet is increased, the contact area at the bonding points will be increased, resulting in a stronger molded body. Therefore, particles with large plastic deformability are suitable for compaction. On the other hand, particles with large elastic deformability are not suitable for tablet preparation.

In addition to drug powders, various additive powders (excipients) are used in the preparation of pharmaceutical tablets. One of the most important excipients is filler powder, which has a major influence on compactibility and thus must be designed with care. The commercialization of filler powders for direct tableting began in the 1960s. Lactose is a representative case of a filler that was introduced in the 1960s and has undergone substantial improvement. Lactose is one of the most widely used filler powders for preparing pharmaceutical tablets. The improved compactibility of spray-dried lactose (DCL11) is due to amorphous part of lactose containing 15–20 % in the particle. Anhydrous β-lactose (DCL21), which has better compactibility than a monohydrate (α-lactose) was also commercialized. Over the decades that followed, the development of excipients progressed. As shown in **Table 1**, many co-processed products of lactose and other substances have been developed as products.

Table 1 Co-processed excipients with lactose.

Trade Name	Composition	Manufacturer
Ludipress	Lactose, PVP*[1] (7 %)	BASF
Cellactose	Lactose, Cellulose (25 %)	Meggle
Pharmatose DCL 40	β-Lactose, Lactitol (5 %)	DMV Veghel
MicroceLac	MCC*[2], Lactose	Meggle
StarLac	Lactose, Maize starch	Roquette

*[1] PVP: polyvinyl pyrrolidone
*[2] MCC: micro crystalline cellulose

The amorphous forms affect the compressibility properties of powders as well as the dissolution property of the resultant dosage forms (Pikal et al., 1978; Vromans et al., 1986). However, the amorphous forms of solids can be easily transformed into more stable, crystalline forms by heat and moisture. Regarding amorphous lactose, studies on its compactibility and the stability of amorphous substances have been conducted from various viewpoints (Sebhatu et al., 1994; 1997; Buckton and Darcy, 1996). Stubberud and Forbes (1998) showed the effects of the physical addition of PVP to amorphous lactose on the crystallization of the amorphous lactose by using a gravimetric system for monitoring the moisture sorption. Saleki-Gerhardt and Zografi (1994) studied that crystallization of amorphous sucrose in the presence of other saccharides, such as lactose, trehalose significantly extended the induction time for crystallization of sucrose.

We evaluated the properties of the particles obtained by prescribing NaAlg (sodium alginate) as a water-soluble polymer in the range of up to 50 % for the purpose of stabilizing amorphous lactose (Takeuchi et al., 1999c; 2000b; 2000c). **Fig. 5** shows the results of the thermal stability of amorphous lactose measured by DSC. When no NaAlg or 1 % NaAlg was added, exothermic peaks indicating the crystallization of amorphous lactose were observed. On the other hand, no exothermic peak was detected in the composite particles containing 10 % or more of NaAlg, indicating that the thermal stability was greatly improved. This improvement in thermal stability was found to correlate with an increase in the glass transition temperature (T_g) of lactose detected from the DSC chart. It has been reported that crystallization of amorphous lactose occurs when the T_g value decreases below the storage temperature due to the "plasticizing" effects of water molecules absorbed in lactose (Stubberud et al., 1996). The SD composite particles showed that higher relative humidity values were required for the initiation of crystallization depending on the content of the sodium alginate: 57 % relative humidity

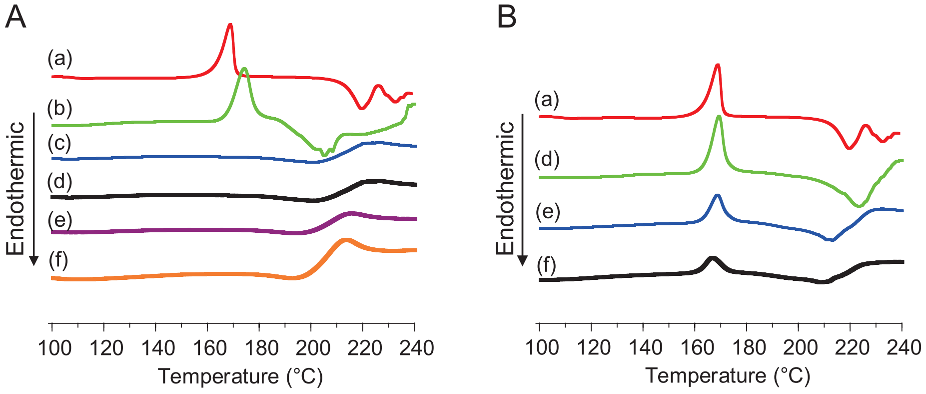

Fig. 5 DSC thermograms of **(A)** SD composite particles and **(B)** physical mixtures of 100 % amorphous lactose and sodium alginate. Sodium alginate content in the mixtures: **(a)** 0 %, **(b)** 1 %, **(c)** 5 %, **(d)** 10 %, **(e)** 30 %, **(f)** 50 %.

for 10 % sodium alginate content and 60 % relative humidity for 30 % sodium alginate content. This increase in the relative humidity required to initiate the crystallization can be attributed to either an increase in the T_g of the composite particles or the absorption of moisture into the sodium alginate.

When the compactibility of the composite particles containing amorphous lactose and NaAlg was evaluated, as shown in **Fig. 6**, excellent compactibility similar to that of amorphous lactose was confirmed up to an amount of 10 % of NaAlg added. However, when the amount of NaAlg was increased to 30 %, a significant decrease in tensile strength was observed, indicating a decrease in compactibility. This change in compression characteristics was well correlated with the change in T_g due to the compositing of NaAlg. The increase in T_g due to NaAlg compositing indicates that the particles become rigid. In fact, when the surface of the tablet is observed with a scanning electron microscope, the fusion of the particles is apparent for the particles with 10 % NaAlg added when compacted under the same conditions, while the shape of the individual particles is almost completely retained in the particles with 30 % addition of NaAlg (**Fig. 7**). The reason that the T_g of lactose in the particles affects the moldability is that when Lac-NaAlg is stored in a humidified state, the T_g decreases and the hardness of the molded product also increases. This result shows that the excellent plasticity of amorphous lactose decreases depending on the type and amount of the polymer added, and as a result, the hardness of the molded product is greatly reduced. It has been shown that the type and content of the substance to be composited are important factors in order to stabilize the amorphous body while maintaining the high moldability characteristics of the amorphous lactose.

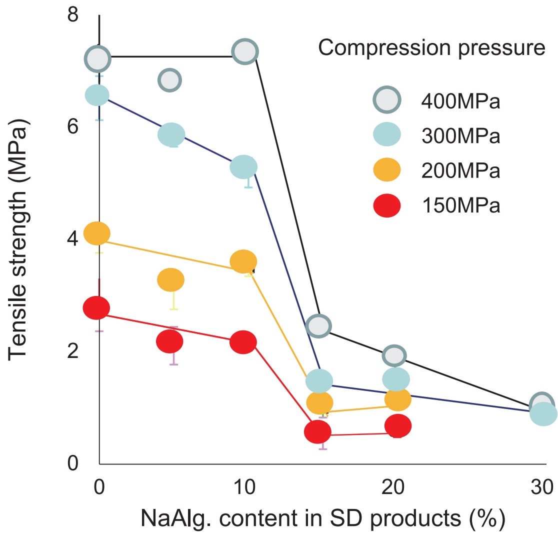

Fig. 6 Tensile strength of tablets prepared with spray-dried composite particles of amorphous lactose containing sodium alginate (0–30 %).

3.2 Particle design for preparation of orally disintegrating tablets

In the design of orally disintegrating tablets (ODTs), various studies have been conducted for the purpose of achieving a tablet that disintegrates extremely rapidly in the oral cavity before swallowing. The first commercialized product, Zydis®, was molded by lyophilizing a solution or suspension of a drug and excipients in a mold (Seager, 1998). Zydis® does not have the strength required for ordinary tablets; rather, the tablet form is maintained by the container. Much research has also been done with the aim of preparing ODTs by using conventional tableting instruments (Sugimoto et al., 2006; Kuno et al., 2008; Okuda et al., 2009). One of the methods is molding a powder layer under wet conditions at a low pressure and then drying it to obtain a tablet hardness close to that of a normal tablet. Another method is to use maltose in the tablet formulation and crystallizing it by humidification and drying treatment after molding to obtain interparticle binding force. A third approach to increase the tablet hardness is to exploit the difference in the melting point of saccharides, and to heat the molded product at an appropriate temperature to promote the crystallization of only one sugar. All three methods have contributed to development of commercial ODTs.

As the demand for ODTs increases, technological development of a method for preparing ODTs using a normal tableting machine is required. Particle design of excipients is important for the preparation of ODTs by conventional tableting processes. Mannitol is most often used as an

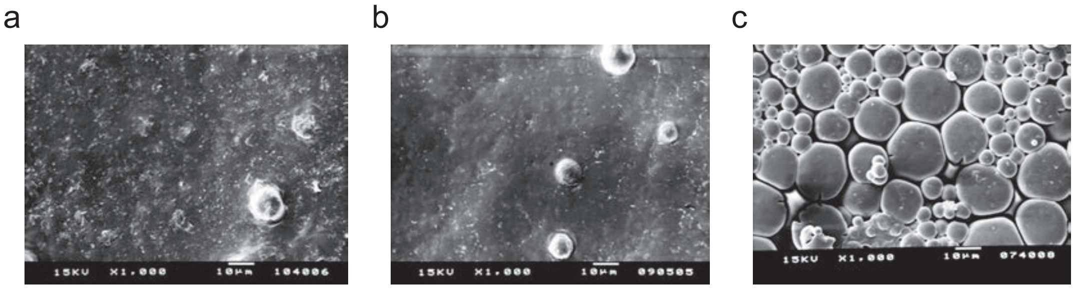

Fig. 7 Scanning electron micrographs of the upper surface of tablets compacted at compression pressure of 400 MPa: **(a)** 100 % amorphous lactose, **(b)** SD composite particles (SDCP) with 10 % sodium alginate, **(c)** SDCP with 30 % sodium alginate.

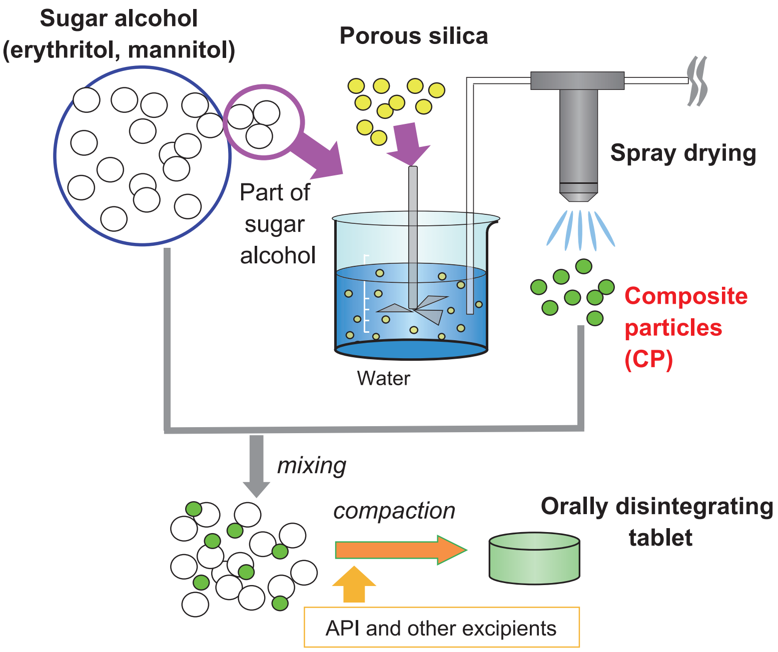

Fig. 8 Schematic presentation of preparation of composite particle of sugar alcohol with porous silica for preparation of orally disintegrating tablets.

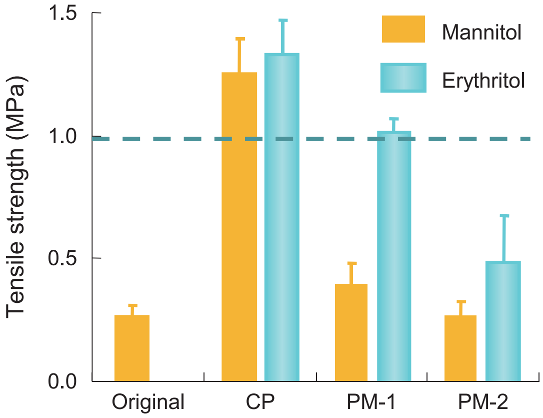

Fig. 9 Tensile strength of tablets of mannitol or erythritol by formulating corresponding composite particles prepared by spray-drying with silica.

Conditions: compaction pressure, 100 MPa; tablet weight, 200 mg.

Formulation of tablets:

Original : Sugar alcohol + 1 % Mg-st
CP : Sugar alcohol + 20 % Sugar alcohol-CP + 1 % Mg-st
PM-1 : Sugar alcohol + 10 % spray-dried Sugar alcohol + 10 % silica + 1 % Mg-st
PM-2 : Sugar alcohol + 10 % silica + 1 % Mg-st

excipient to obtain rapid disintegration properties. Erythritol is also an excellent excipient candidate because of its solubility and refreshing sensation when dissolved. However, both are inferior in compactibility to lactose, which is most commonly used in ordinary tablets. In the case of erythritol, a molded product cannot be obtained even by compression at extremely high pressure.

For nearly a decade now, we have been conducting research for the purpose of improving the moldability of mannitol and erythritol. As shown in **Fig. 8**, we determined that constituents of low formable powder, such as mannitol and erythritol, can be spray-dried together with porous silica to form a composite particle, and then an appropriate amount of this composite particle can be mixed with the original low formable powder to dramatically increase the compactibility (Takeuchi et al., 2012). **Fig. 9** shows the results of tablet hardness achieved using this composite particle method. It is well known that the hardness of tablets is increased by adding an appropriate amount of silica to the tablet formulation, but in the case of mannitol, such an effect is hardly observed. When our new approach was used to blend composite particles, the tablet hardness became as high as that of typical commercial tablets. For erythritol, which cannot be compression-molded by itself at a high pressure, the tablet hardness could be increased to some extent by mixing silica and separately spray-dried erythritol and tableting. By using the composite particle method, the resultant tablet hardness was much improved. We have also used the composite particle method to examine the formulation of specific ODTs. After adding various types and amounts of disintegrants (2, 5, 10 % w/w) to the basic formulation (a mixture of erythritol, erythritol-silica composite particles (10 % w/w) and magnesium stearate (0.2 % w/w)), a tableting test was performed. All the formulations with the various disintegrants achieved good tablet hardness, but the disintegration time of tablets varied greatly depending on the type of disintegrant. When the disintegrant was cross povidone, the resultant tablet showed the best disintegration property at about 15 seconds.

When the crystallinity of erythritol in the composite particles of porous silica-erythritol was evaluated to characterize this composite particle method, the powder X-ray

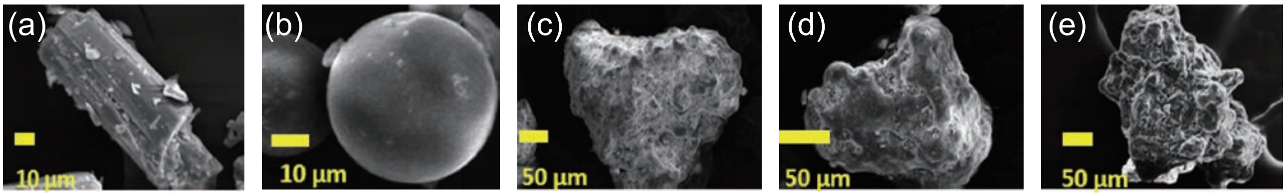

Fig. 10 Scanning electron photographs of typical mannitol crystal and commercial products of mannitol for direct tableting. **(a)** MNP (Mannit P), **(b)** MNQ (Mannit Q), **(c)** PK2 (Parteck M200), **(d)** PL2 (Pearlitol 200 SD), **(e)** GRR (Granutol R).

diffraction evaluation indicated no loss of crystallinity, but the endothermic peak due to melting measured by DSC shifted to the low temperature side (Tanimura et al., 2015). This suggested that the crystal energy was high. Moreover, since the proportion of high-energy crystals and the degree of improvement in compactibility were well correlated, it was concluded that this high-energy erythritol contributed to the improvement in compactibility. In fact, when the silica: erythritol ratio was changed to 1:1, 1:2, or 1:3, the 1:2 composite particles showed the highest tablet hardness.

Like lactose, mannitol has also been studied as an excipient, and product development centered on the granulation method has been conducted. So far, several types of mannitol for direct tableting have been made commercially available from several excipient manufacturers. Scanning electron micrographs of the mannitol particles are shown in **Fig. 10**. In each case, the component is pure mannitol, but the production method alternates between spray-drying and spray-drying granulation. Some particles, such as Mannit Q, have a characteristic particle structure such as a spherical hollow, but the appearance of the other particles in the electron microscopic photographs does not differ substantially (**Fig. 10**). Crystallinity is almost the same. These commercial products are larger than mannitol crystals and have an improved compactibility. As for Mannit Q, it is presumed that the compactibility at compression is improved because the Mannit Q particle is composed of fine mannitol crystals, as can be confirmed by electron micrographs. Excipients for direct tableting require both high fluidity and excellent compactibility. When the fluidity of some mannitol products for direct tableting was evaluated by the Carr's index, it was confirmed that all of them had characteristic values suitable for direct tableting.

Incorporation of a binder into a tablet formulation to improve its compactibility is a common formulation design method. In the formulation design of orally disintegrating tablets, it is necessary to pay sufficient attention to the type and prescription amount of the binder for ODTs in order to obtain the tablet characteristic of an extremely short disintegration time. Increasing the amount of binder increases tablet hardness, but leads to a delay in disintegration time. This is considered to be due to water penetrating the tablet, causing the binder to dissolve and adopt a viscous gel state, which delays the penetration of additional water into the tablet. For example, hydroxypropyl cellulose (HPC), which is a pharmaceutical additive widely used in Japan, has several grades used for granulation as a binder. The grade with low viscosity achieved by decreasing the molecular weight is suitable for rapid disintegration of tablets. When using HPC as a binder for the mixing of other powders, the smaller the particle size of HPC, the better the dispersibility in the prescription powder, and thus the greater the number of bonding points between the powders and the greater the hardness of the tablets. We prepared fine particles of HPC using the spray-drying method and the freeze pulverization method. By controlling the particle size of HPC to an average of about 20 µm or less, tablets having the desired characteristics could be prepared. The hardness of the tablets increased remarkably when the spray-dried spherical HPC fine particles were formulated into a tablet formulation (**Fig. 11**) (Tanimura et al., 2006). In addition, by prescribing the lowest molecular weight and thus lowest viscosity HPC-SSL fine particles as a binder in a model ODT formulation, the desired disintegration of less than 30 seconds and a sufficiently high tablet hardness for practical application could be achieved.

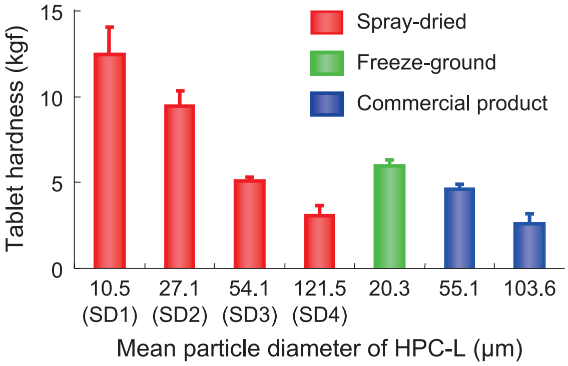

Fig. 11 Hardness of erythritol tablets prepared with a fine binder partilces of HPC-L.
Formulation of tablets: erythritol (88.5 %), HPC-L (10 %) + Mg-st (1 %) + silica (0.5 %).

To realize an easier prescription design of ODTs, particle design research has progressed in diverse directions. Development of commercial products such as premixed filler formulations using other additives or composite particles have been produced by excipient manufacturers to allow direct tableting of ODTs using a tableting machine like those used for ordinary tablets. **Table 2** lists some of the commercial products and their components.

Table 2 Premixed or co-processed excipients with mannitol for direct tableting of ODT.

Trade name	Formulation
F-MELT	Mannitol, xylitol, microcrystalline cellulose, cross povidone, Metasilicate alumic acid magnesium or Anhydrous calcium hydrogen phosphate
SmartEx	Mannitol, L-HPC, PVA
Ludiflash	Mannitol, Collidone CL-SF, Collicoat SR30D
Pearitol FLASH	Mannitol, corn starch
Granfiller D	Mannitol, carmelose, cross-povidone

L-HPC: Low-substituted hydroxy propyl cellulose
PVA: poly vinyl alcohol

3.3 Design of orally disintegrating film

Oral film preparations are preparations having the same characteristics as ODTs. Accordingly, they are sometimes referred to as ODFs (orally disintegrating films). These films are usually stamp-sized and thin as paper. Product development in Europe and the United States has been more active than in Japan, and also the number of products is larger there. In recent years, patient-centric concept has received much attention in dosage form design. Some of pharmaceutical companies are taking account of ODFs as one of the useful dosage forms for sick or pediatric patients who have difficulty in swallowing. In terms of regulation, the ODF is one of the subclasses of dosage forms to be orally administered in the 17th edition of the Japanese Pharmacopeia.

In parallel with the research on ODTs, we have focused on ODFs as a dosage form having the same or more patient-friendly functions. A water-soluble polymer is used as a base corresponding to a filler for tablets; so far, pullulan and hydroxypropyl methylcellulose (HPMC) have been widely used as base polymers for commercial products. In conducting a formulation study of ODFs by using HPMC as a base in the film formulation, we found that the disintegration time could be dramatically shortened by prescribing a small amount of micronized disintegrant low-substituted hydroxypropyl cellulose (L-HPC) as a disintegrant (Takeuchi et al., 2013). It was also shown that the disintegration characteristics could be improved by using insoluble fine particles such as silica and microcrystalline cellulose as well as L-HPC with different particle sizes and shapes in the film. (Takeuchi Y. et al., 2019). The larger particles had a greater impact on disintegration, compared to the smaller particles. However, the addition of larger particles decreased the films' tensile strength.

For the purpose of searching for an optimum formulation of ODFs, we also investigated the effect of the type of base polymer on the characteristics of resultant ODFs by using hydroxypropyl cellulose (HPC) and polyvinyl alcohol (PVA) as well as the more commonly used HPMC. HPC films were found to have suitable characteristics as a base of ODFs from the standpoints of disintegration and mechanical strength. The HPC films showed particularly good mechanical properties. When model drugs were formulated, these characteristics remained (Takeuchi Y. et al., 2018). HPC is also formulated in some commercially available films prepared with HPMC, probably as a plasticizer in the HPMC film formulation. As the mixing ratio of HPC to HPMC is not disclosed, we examined the mixing ratio of HPC and HPMC. While adding a small amount of HPC (< 10 %) yielded films with a good plasticity, the mechanical properties of the films were significantly deteriorated when increasing amounts of HPC were prescribed to HPMC, such as when a 1:1 ratio of HPC:HPMC was used. This may be attributed to poor compatibility between the polymers. PVA was highly flexible when made into a film and had high refraction resistance. Since it is sticky, it is necessary to take measures to mediate the stickiness. However, it was also confirmed that the film base was suitable for drug encapsulation, because its mechanical property values were not easily altered, even if a drug is added in the formulation. (Takeuchi Y. et al., 2020a).

4. Progress on the solid formulation manufacturing process

4.1 Analysis of the powder compaction process

The powder properties required for the formulation of tablets with the desired functions were described above in the sections 3.1 and 3.2. However, the tableting process also has a great influence on the preparation of the compacted product, and thus various studies have been conducted to examine these effects of tableting. There are two main approaches for the preparation of tablets: (1) direct tableting, in which the drug powder and other excipient powder are mixed, and (2) indirect tableting or granule compression, in which part or all of the powder is granulated and compressed in advance. In either case, the compaction process consists of filling the die with powder, compressing, and then discharging the tablet from the die after releasing pressure. A stress-displacement curve (**Fig. 12(A)**) can be drawn by precisely measuring the displacement during compression and the upper punch load over time for obtaining information on the compression characteristics of the powder. Depending on the type of powder, the displacement is reduced (expansion of the compacted product) after the displacement is maximized at the maximum pressure of the upper punch. This is due to elastic recovery of the compacted powder. The net energy required for compaction is calculated by subtracting the energy for elastic recovery

(B) from the total energy required for molding (A + B). The net energy is expressed as a ratio to the total energy and used as an index of compactibility. The compression equation most often used when evaluating compression molding characteristics using a compression model is the Heckel equation (1) (Heckel., 1961a; 1961b).

$$\ln\frac{1}{\varepsilon} = kP + A \tag{1}$$

Here, ε is the porosity of the powder layer, P is the compression pressure, and the pressure from the upper punch is usually used for this measurement.

As shown in **Fig. 12(B)**, when the compression pressure is increased, causing the compression to proceed and the powder layer to begin undergoing plastic deformation, the increase on the left side of the Heckel equation becomes constant and appears as a straight line. This slope is k, and the reciprocal of the slope is used as the yield pressure (P_y) as an index of plastic deformation.

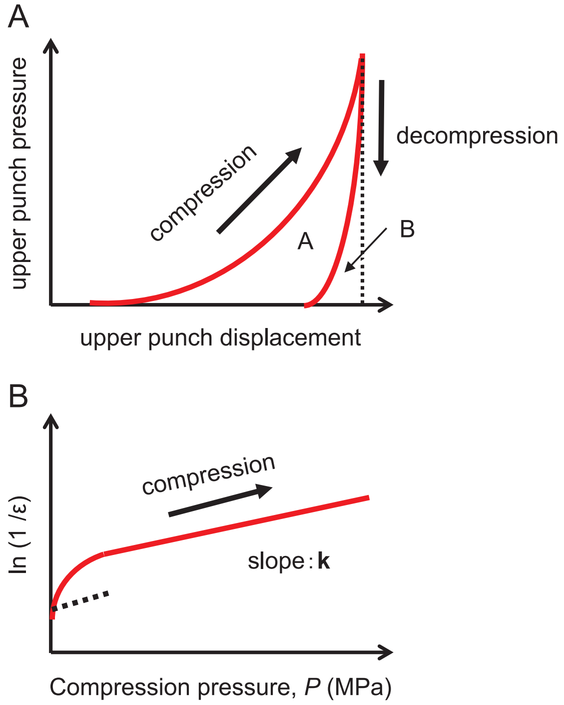

Fig. 12 Analysis methods of compression properties of powders. **(A)** Compression force-displacement curve **(B)** Heckel plot.

$$P_y = 1/k \tag{2}$$

The compaction property of powders has been evaluated with various parameters such as yield pressure measured by Heckel analysis (Humbert-Droz et al., 1983), stress relaxation (van der Voort Maarschalk et al., 1997) and elastic recovery (Picker, 2001). In general, a powder with plastic deformability is preferable for preparing a compacted product as it increases the tablet hardness, while the property of elasticity works in the opposite way.

It is possible to estimate one of the tablet failures in tableting, capping, by using these parameters. Capping, in which the contact surface of the tablet is peeled off with the punch, is thought to be caused by any of several different aspects of the compaction process. Higher elasticity of compacted powder is one of the main factors for capping during compaction. The measurement of die wall pressure may also be a useful method to evaluate the compaction property of powders, because residual die wall pressure reflects the plastic property of the compacted powder in the die (Carless and Leigh, 1974). Some papers have reported that the residual die wall pressure is one of the main factors for capping, with other factors being the elastic recovery during decompression, the stress concentration due to die wall pressure at decompression (Hiestand et al., 1977) and the entrapped air in the tablet during the compaction process (Tanino et al., 1995). Sugimori reported that capping occurs when a tablet is cracked by residual die wall pressure at the final stage of the decompression process (Sugimori et al., 1989a; 1989b).

In the studies mentioned above, the compression parameters were measured by using static compression with a very slow compression speed. We evaluated the compression molding process using a compaction analyzer (Tab All®) that can measure the pressure detected at each site on a single-shot tableting machine for analysis in a dynamic compressed state similar to an actual tableting machine. **Fig. 13** shows an example of the data under

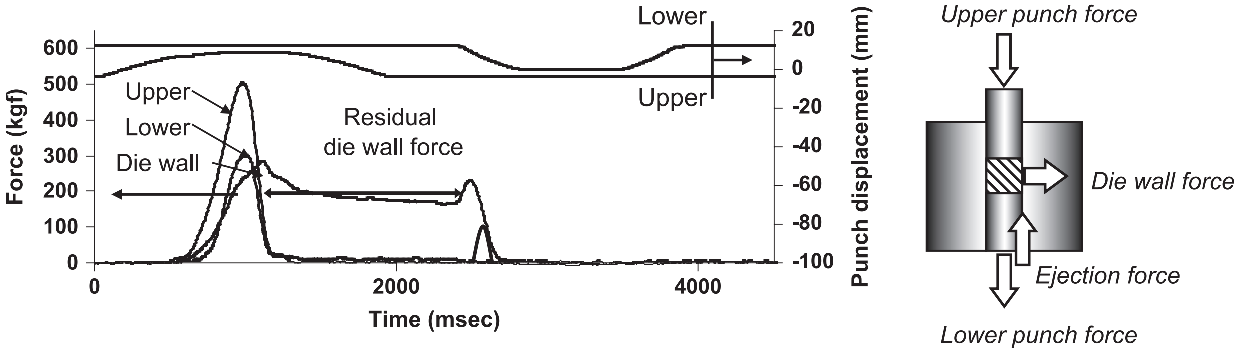

Fig. 13 Upper and lower punch forces and residual die wall force profiles and punch displacement measured by a tableting analysis instrument (TabAll, Okada Seiko Co.).

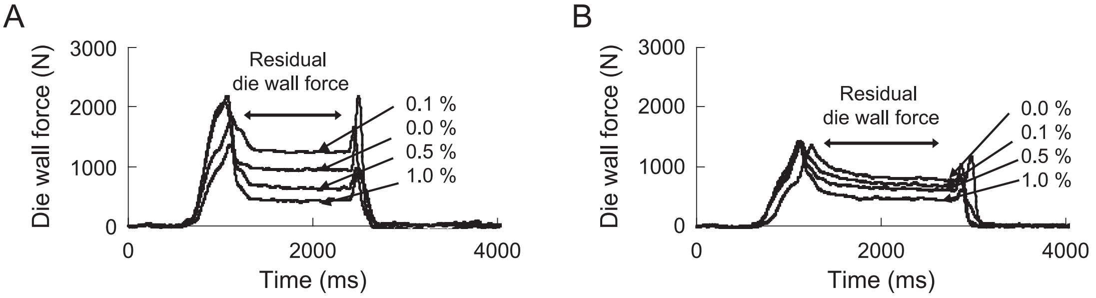

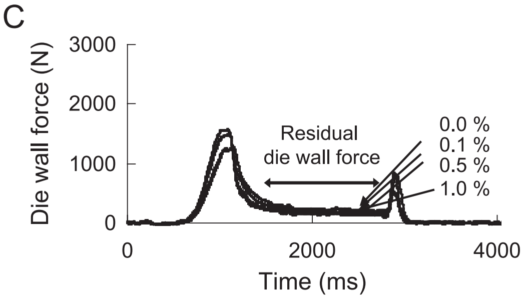

Sample	Mg-st content (%)	RDP (MPa)	MDP (MPa)	RDP / MDP (%)
A) Lactose	0	11.7 ± 1.0	18.7 ± 0.9	62.8 ± 8.2
	0.1	14.0 ± 0.4	23.8 ± 0.2	58.6 ± 1.8
	0.5	7.4 ± 0.3	29.3 ± 0.1	25.2 ± 0.8
	1.0	5.3 ± 0.5	29.7 ± 1.5	18.0 ± 1.9
B) Mannitol	0	9.9 ± 1.0	23.3 ± 2.2	42.4 ± 3.5
	0.1	8.9 ± 0.7	20.9 ± 1.0	42.4 ± 2.0
	0.5	6.9 ± 1.1	22.0 ± 1.2	31.5 ± 5.3
	1.0	5.9 ± 0.6	22.9 ± 0.8	26.0 ± 3.1
C) Sorbitol	0	3.6 ± 0.3	20.2 ± 0.9	17.7 ± 2.1
	0.1	3.1 ± 0.3	19.9 ± 3.3	16.1 ± 3.1
	0.5	2.6 ± 0.1	22.4 ± 1.5	11.6 ± 1.1
	1.0	2.2 ± 0.1	23.6 ± 2.0	9.3 ± 1.2

Fig. 14 Die wall force profile in compacting typical filler powders **(A)** lactose **(B)** mannitol **(C)** sorbitol for pharmaceutical tablets formulating different amount of lubricant, magnesium stearate.

various loads during compaction. The load applied to the wall surface increases with the increase of the upper punch load and shows the maximum die wall pressure (MDP), and then the pressure is reduced and the force detected even after the pressure is completely removed is called the residual die wall surface pressure (RDP). The MDP value increased when the compression pressure was changed with the same powder. In addition, since the MDP value differs greatly depending on the powder even at the same compression pressure, it was proposed to evaluate by the RDP/MDP value standardized by the MDP rather than directly comparing the RDP value. The RDP/MDP value reflected the compacting property of pharmaceutical powders. For example, crystalline lactose and ascorbic acid, which showed a capping tendency, showed relatively larger RDP/MDP values (Takeuchi et al., 2004b). **Fig. 14** shows the results of measuring the residual die wall pressure profile by changing the amount of the lubricant for lactose, mannitol, and sorbitol, which are excipients of three typical pharmaceutical tablets (Takeuchi et al., 2005b). Sorbitol, which has the best compactibility, showed a low residual wall pressure regardless of the prescription amount of the lubricant. Mannitol, as well as lactose, tends to cause tablet failures such as binding and capping depending on the tableting formulation and conditions. For example, if the prescription amount of the lubricant in the tablet formulation increases, the tablet failure tendency is depressed. The decrease in RDP/MDP value with increasing the amount of the lubricant was well correlated to this tendency.

In recent years, for the purpose of more practical analysis of tableting processes, a tableting simulator (Style One®) capable of compression molding in a form closer to that of a rotary tableting machine was developed. Not only does the rotary tableting machine used for production have a faster compression molding speed than the single-punch tableting machine, but also the size of instrument, the installation angle of machine parts such as rotating discs, and often the compression rollers for compression molding (depending on the model of machine) have different characteristics between the rotary and single-punch tableting machine. These differences cause the compression time and the interval of each compression molding process to differ depending on the model of the tableting machine (Narang et al., 2010). In addition, in the process of drug development, it is inevitable that the scale of the tableting machine will change, and it is necessary to set new tableting conditions each time. At that time, process parameters are usually determined based on experience and trial and error, and thus the development of a convenient method for setting the parameters in these cases is strongly required. The tableting simulator developed in recent years can reproduce the tableting process of various rotary tableting machines, and can obtain the compaction parameter values of various rotary tableting machines even though it is a single-punch tableting machine.

Using this tableting simulator, evaluation of the effect of the compression rate on tablet characteristics (Michaut et al., 2010) or evaluation of the pressure applied to the tablet when the tablet is ejected from the die in the tablet ejection process (Sun, 2015) has been reported. Takahashi et al. conducted a series of experiments with the goal of efficiently optimizing the tableting conditions associated with changes in the tableting machine that occur during scale-up and technology transfer. Even if compaction is performed under the same conditions by different types of tableting machines, the tablet characteristics will change. It was found using a tableting simulator that the change in tableting speed was most critical to the change in compactibility and thus tablet properties. As a new prediction model for determining the optimum tableting conditions when changing the tableting machine, it was found that the area under the curve (AUC) in the time-pressure profile considering the compression time is an important parameter (Takahashi et al., 2019). Based on this concept, a model for predicting tableting conditions (locking pressure, rotation speed) was constructed, and its suitability was confirmed by comparing data from different locking machines (Takahashi et al., 2020). Utilizing these parameters, it will be possible to compare parameters in the tableting process to standardize them during scale-up or technology transfer.

4.2 Tableting failures on a production scale

In addition to the capping discussed in section 4.1, several other types of tablet failures occur, such as sticking, binding, and chipping. Among them, sticking, in which a part of the powder adheres to the surface of the punch, may lead to serious problems in the production scale. It is conceivable that the number of tablets will increase, the surface of the punch will deteriorate due to long-term use, and the adhesion of powder will proceed more easily. These sticking obstacles not only affect the product quality, but also lead to damage to the punch due to the application of extremely high pressure to the punch. It seems reasonable to consider that a possible reason for the sticking is that the bonding force between the particles in the powder bed is weaker than that of powder on the surface of the punch. In order to clarify the detailed mechanism responsible for the sticking to avoid this tablet failure, several studies have been conducted. These works have reported various potential causes of the sticking, such as the physical and mechanical properties of active powders (Naito and Nakamichi, 1969; Danjo et al., 1993), water content, hygroscopicity of the formulations, lubricant types and concentrations, (Danjo et al., 1997; Waimer et al., 1999a; Roberts et al., 2004), tableting tools and punch surface shapes, and operating conditions (Newton et al., 2000; Sixsmith and McCluskey, 1981; Waimer et al., 1999b; Kakimi et al., 2010) such as engraving of the punched surface and finishing of the punched surface.

In order to prevent sticking during the production of tablets, it is conceivable that the amount of the binder could be increased or both the amount of the binder and the amount of the lubricant in the tablet formulation could be increased. However, it may be difficult to change the formulation after fixing it for approval. On the production side, attempts will be made to try to control tableting conditions such as the tableting speed or pressure. Recently, tableting machines companies or manufacturers of parts of machines such as punches and dies have proposed alternative methods to avoid these tablet failures. In one case, the surface treatment of the punch was developed for the purpose of suppressing the adhesion between the powder and the surface of the punch and avoiding sticking, and several kinds of punches with different surface treatments are commercially available in Japan. As can be seen from the laser micrograph (**Fig. 15**), the surface of the punch is uneven, unlike the surface of a normal punch. The concept is that the unevenness reduces the contact area with the powder and reduces adhesion of the powder. We evaluated the effect of a punch surface treatment using these punches and the effect of reducing adhesion using two types of pharmaceutical crystals with different plastic deformability (Takeuchi Y. et al., 2020b). Using a single-shot tableting machine, tableting was performed up to several times, and the amount of drug adhering to the surface of the punch was quantified by HPLC. As a result, in the case of a drug such as acetaminophen, which was evaluated to have low plastic deformability as confirmed by the Heckel plot, the unevenness of the punch surface tended to reduce the drug adhesion to the punch surface (**Fig. 16**). On the other hand, in the case of ibuprofen, which has a relatively large plastic deformability, the amount of adhered drug was almost the same regardless of the presence or absence of unevenness on the surface of the punch. Rather, the tendency of increasing adhesion of P3, which has the largest unevenness,

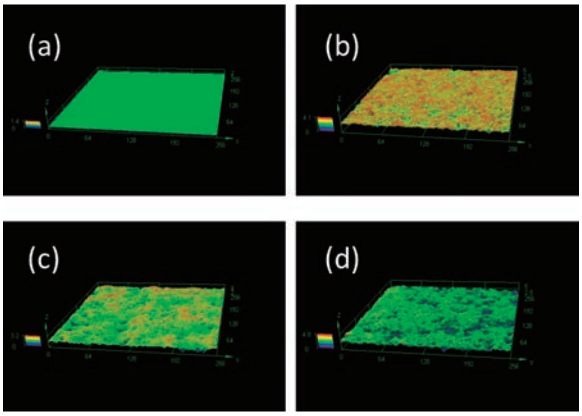

Fig. 15 Three-dimensional surface roughness profiles of tableting punch faces observed by a laser microscope.

Four types of punch, **(a)** P0, **(b)** P1, **(c)** P2 and **(d)** P3, were supplied by TWO NINE JAPAN (Kyoto, Japan). P0 is a usual smooth surface punch and the *Sa* (the arithmetical mean height of the assessed surface) value measured by the laser microscope is 0.014. The surface roughness of the top of punch P1-3 (surface treated punch) is P1 (*Sa*: 0.180 μm) < P2 (*Sa*: 0.222 μm) < P3 (*Sa*: 0.304 μm).

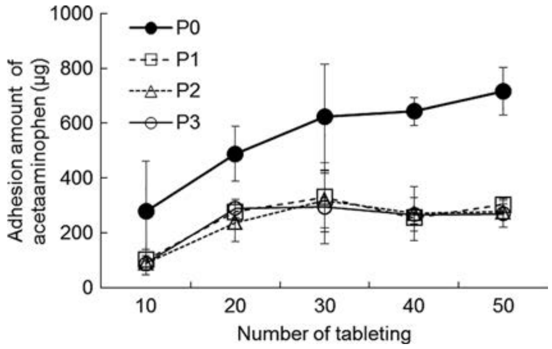

Fig. 16 Relationship between the adhesion amounts of formulated acetaminophen powder on the punch surface and the number of tableting. Compression pressure was 100 MPa. Data are expressed as mean ± SD (*n* = 3). The types of punch were explained in **Fig. 15**.

was observed to be the largest. These results suggested that when the plastic deformability is large, the area of contact of the powder on the uneven punch surface during tableting is large, and thus the adhesion tendency is increased.

As described above, pharmaceutical companies want to avoid problems such as tableting failures during production, and thus predicting such problems at the time of tablet prescription design is an important goal. For this purpose, Pitt et al. (Pitt et al., 2015) conducted a study using the GTP-1® and proposed a criteria for feasibility of tableting with a formulation. The proposed value of the strength of tablet (TFS) as measured by GTP-1 is greater than 2 MPa in tableting at 200 MPa. They also proposed that the discharge pressure (ES) should be smaller than 5 MPa. Osamura et al. (2016) systematically compared the GTP-1 measurement results with the actual tableting results obtained with a rotary tableting machine to determine TFS and ES. They tried to visually express the tableting characteristics of the prescription by classifying them into four areas as an index of compactibility and an index of manufacturability. When the validity of this evaluation system was verified using pharmaceutical excipients with known tableting characteristics, the results reflected the characteristics of individual excipients (**Fig. 17**). Furthermore, it was also shown that even with a practical formulation, a series of formulations that may have an effect on manufacturability, such as a change in the blending amount of a lubricant, can be examined and the effect can be visually confirmed (Osamura et al., 2017). They selected drugs for which a sticking phenomenon was easily observed, changed the blending amount of lubricant and tablet shape, and compared the results obtained using GTP-1 and a rotary tableting machine. A good correlation between the two was obtained even for tablet formulations in which different amount of the lubricant was formulated and/or for tablets prepared by using different punches having various shapes. Using the same method, it was also demonstrated that this estimation for tableting process using the GTP-1® is feasible for indirect tableting with granulated drugs with excipients to avoid sticking (Osamura et al., 2018).

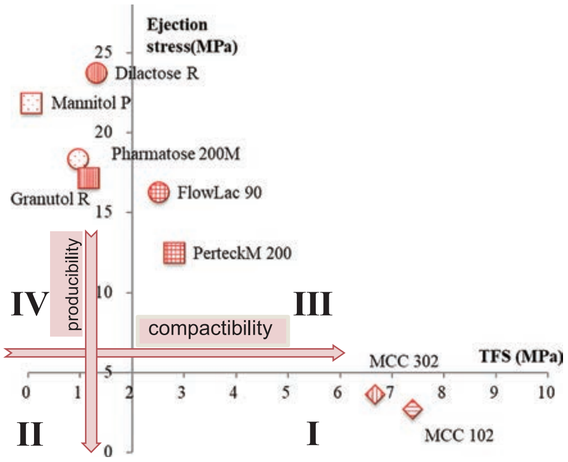

Fig. 17 Plots of compactibility and producibility for pharmaceutical excipients based on the combination of TFS and Ejection stress measured with GTP-1®.

5. Liposomal particle design for drug delivery

5.1 Polymer-coated liposomes for efficient drug delivery

Phospholipids are constituents of cell membranes. The surface of liposomal particles composed of phospholipid bilayers can be easily modified with both positive and negative charges by prescribing a small amount of charged substance together with phospholipids in the preparation. By prescribing an appropriate amount of cholesterol, the fluidity of and the degree of hydrophobicity of liposomal particles can be controlled by controlling the prescribed amount. Furthermore, it has been reported that the surface of liposome particles can be modified with polymers, surfactants, etc. (Sunamoto et al., 1984). Due to these characteristics, liposomes have been studied as drug carriers for targeting drugs in the body after injection. As described in the introduction of this manuscript, liposomal injections of anticancer agents have been developed as commercial products. Liposomes have also been studied as drug carriers to avoid a barrier for entry into the body. Research aimed at gastrointestinal absorption of insulin is a typical example of the latter type of application, and has been studied by multiple research groups since the mid-1970s (Patel and Ryman, 1976; Dapergolas and Gregoriadis, 1976). However, the usefulness of liposomal formulations for the enteral absorption of insulin has not been confirmed (Pateland Ryman, 1981; Shenfield and Hill, 1982).

We have been conducting studies with a goal of imparting various pharmaceutical functions by controlling the surface properties of liposome particles. **Fig. 18** shows

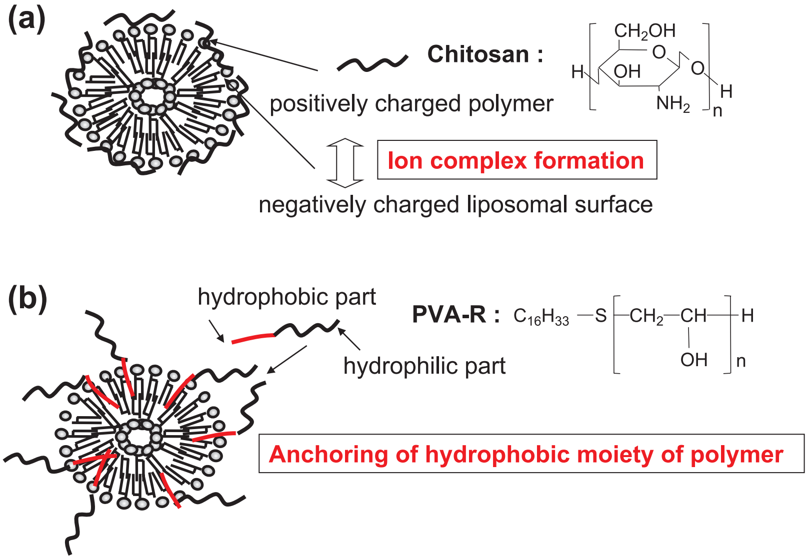

Fig. 18 Schematic presentation of typical polymer-coated liposomes. **(a)** chitosan-coated liposome (CS Lip) **(b)** PVA-R coated liposome.

two typical polymer-coated liposomes designed for this purpose. One is a comb-shaped coating formed by penetrating a hydrophobic moiety chemically bonded to a water-soluble polymer into a liposome lipid bilayer (the anchor ring method), and the other is a coating created by the electrical interaction between a charged liposome surface and a polymer having the opposite charge. Regarding the former, surface modification was demonstrated using a polymer, PVA-R, in which an alkyl group was introduced at the end of polyvinyl alcohol (PVA). The formation of the thick polymer layer was confirmed by measuring the zeta potential of the liposomes treated with several polymers under different polymer concentrations (**Fig. 19**). The zeta potential of the negatively charged liposomes became neutral when the polymer concentration was increased. Compared with the liposomes that physically absorbed PVA, the stabilizing effect of the PVA-R-coated liposomes was excellent due to their three-dimensional coating layer (Takeuchi et al., 1994; 1998).

PEGylated liposomes prepared by formulating polyethylene glycol conjugated phospholipids have been studied extensively as targeting carriers for the anticancer drug doxorubicin and commercial products for clinical use are now available (Senior, 1987; Allen et al., 1989; 1991; Papahadjopoulos et al., 1991). PVA-R-coated liposomes were found to have a similar function to PEGylated liposomes, such as improving blood retention after intravenous injection to deliver a drug effectively to cancer tissues in rats (Takeuchi et al., 1999a; 1999b; 2000a; 2001a,b,c). PEG liposomes form a polymer layer on the surface prepared by formulating PEG conjugated phospholipids as a liposomal component, whereas the polymer layer of PVA-R-coated liposomes is able to be formed after preparation of drug loaded liposomes.

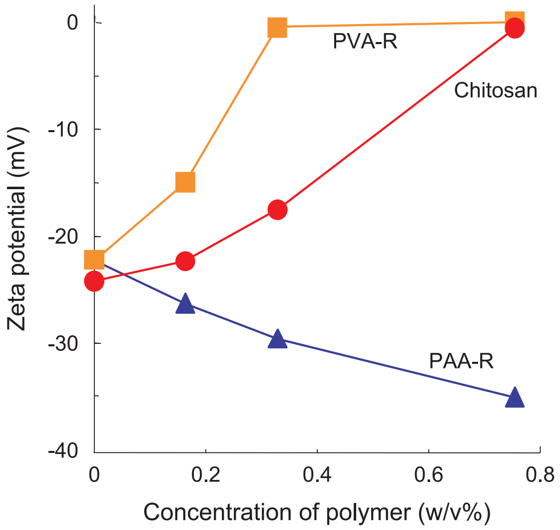

Fig. 19 Zeta potential of liposomes coated with various polymers in phosphate buffer solution (pH 7.4).
Lipid composition of liposomes is DPPC:DCP = 8:2.
PVA-R and PAA-R are the PVA (polyvinyl alcohol) and PAA (poly acrylic acid) modified with hydrophobic moiety (R) in the molecules as shown in **Fig. 18 (b)**.
Chitosan: degree of deacetylation = 85 %, molecular weight = ca.150,000.
PVA: degree of polymerization of PVA = 480. PAA: molecular weight of PAA = 250,000.

5.2 Mucoadhesive liposomes for oral administration of peptide drugs

In order to improve the efficiency of gastrointestinal absorption, it is conceivable to prolong the residence time of the drug or the carrier containing the drug after oral administration. This concept was discussed for potential application to conventional dosage forms such as tablets or granules in the 1980s (Guputa et al., 1990). In order to use liposomes as a carrier for oral insulin administration, we considered improving the retention of liposomal particles in the intestinal tract by allowing their interaction with the mucin layer on the inner surface of the digestive tract.

Polymer-coated liposome particles having a mucoadhesive function were prepared using chitosan (CS), which is prepared by deacetylating chitin and are reported to interact with mucin when used as a topical dosage form (Nagai, 1985). The mucoadhesive property of polymer-coated liposomes was evaluated by using intestinal tubes separated from rats. In this test, the number of liposomal particles withdrawn from the liposomal suspension in the tube was calculated by using a Coulter counter before and after incubation. The extent of adhesion to the mucous layer in the intestinal tube was expressed by the following equation.

$$\text{Adhesive}(\%) = \frac{N_0 - N_{15}}{N_0} \times 100 \tag{3}$$

were, N_0 is the initial number of liposomal particles and N_{15} is the number of liposomal particles 15 min after incubation.

As shown in **Fig. 20**, the highest adhesion property of CS-coated liposome (CS-Lip) was confirmed in this in vitro test (Takeuchi et al., 1994). The affinity of CS-Lip to the mucosa is presumed to be due to the electrostatic interaction between the positive charge of the amino group of CS and the negative charge of mucin, which is a mucosal component. The physical interaction due to the entanglement of both polymers is also responsible for this adhesion. The latter interaction was supported by the fact that negatively charged acrylic acid polymer (PAA)-coated liposomes also showed the mucosal adhesion properties. It is believed that the acid polymer (PAA)-coated liposomes also showed the mucosal adhesion properties. It is believed that the negative charge of PAA extends linearly without shrinking the polymer and works effectively for entanglement with mucin.

CS-Lip encapsulating insulin was orally administered in rats, and the blood glucose levels were measured to evaluate their effectiveness in enteral absorption. A significant decrease in the blood glucose level was observed after administration of CS-Lip, confirming the enteral absorption of insulin. The significant decrease in value was maintained up to 12 hours, suggesting the retention of the liposomal carrier in the intestinal tract due to the mucosal adhesion property (**Fig. 21**) (Takeuchi et al., 1996). The importance of the CS layer for mucosal adhesion and resultant insulin absorption was revealed by the fact that no significant effect was observed under the same conditions when liposomes having a positive charge were used as a carrier. The usefulness of polymer-coated liposomes for the oral administration of peptide drugs was confirmed by using another model peptide drug, calcitonin. A single administration of calcitonin encapsulated in CS-Lip lead to a decrease in the blood calcium concentration in rats for a long period of time (**Fig. 22**) (Takeuchi et al., 2003a). It was also clarified that the particle size is an important factor for drug absorption (pharmacological effect) with mucoadhesive liposomes, because the absorption increased remarkably when the particle size was decreased to submicron size. Since these differences were considered to be related to the behavior of liposomes in the gastrointestinal tract, the intestinal tube was taken out after administration of several types of liposomes containing a lipophilic fluorescent marker in rats and its cross section was observed

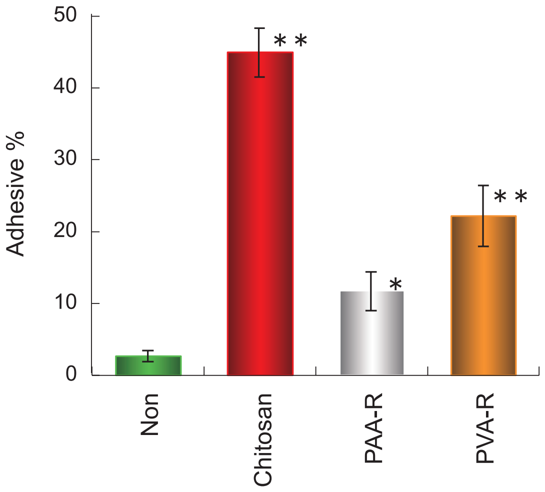

Fig. 20 Adhesive % of polymer-coated liposomes to rat intestine evaluated with the particle counting method.
Lipid composition: DPPC:DCP = 8:2. Polymer concentration: 0.75 %. Dispersion medium: phosphate buffer solution (pH 7.4).
Properties of polymers used for coating liposomes are shown in **Fig. 19**.
The results are expressed as mean ± sd of three experiments.
Significantly different from the value for noncoated liposomes at $p < 0.01$ (**) and $p < 0.05$ (*).

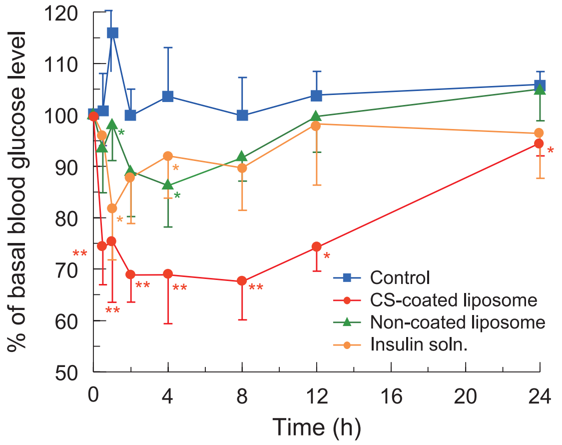

Fig. 21 Change in serum glucose level (%) after oral administration of insulin (24 IU/rat) with the non-coated and polymer-coated liposomes.
Each value represents the mean.SE of four or five rats.;
* : $p < 0.05$, ** : $p < 0.01$. Lipid composition: PPC:DCP = 8:2.
Polymer concentration: 0.75 %

with a confocal laser scanning microscope. It was confirmed that the CS-Lip had a longer residence time in the intestinal tract compared with the uncoated liposomes, and they adhered more to the upper part of the intestinal tract (**Fig. 23(A), (B)**). By reducing the particle size of CS-Lip to the submicron size, the number of liposomes retained in the intestinal tube was considerably increased, and the liposomal particles were observed to be penetrated into the mucosa over time (**Fig. 23(C)**) (Takeuchi et al., 2001d; 2005a). It was also confirmed that CS in the CS-Lip moved in the digestive tract together with liposomal particles (Thongborisute et al., 2006).

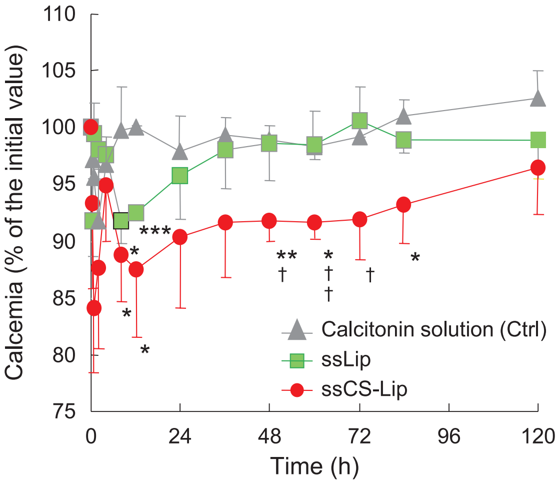

Fig. 22 Profiles of plasma calcium levels after intragastric administration of sub-micron sized liposomes (ssLip) and sub-micron sized chitosan coated liposomes (ssCS-Lip) containing calcitonin.
The measured mean particles sizes of ssLip and ssCS-Lip are 196.4 nm and 473.4 nm, respectively. The formulation of liposomes is DSPC:DCP:Chol. = 8:2:1. The concentration of chitosan for coating is 0.3 %. $*\ p < 0.05$, $**\ p < 0.01$, $***\ p < 0.001$: significantly different from the level for calcitonin solution; $^{\dagger}\ p < 0.05$, $^{\dagger\dagger}\ p < 0.01$: significantly different from the level for ssLip ($n = 3$ in each case).

Following the demonstration of the usefulness of liposomes with mucosal adhesion properties for the oral administration of peptide drugs, studies on the characterization of the mucoadhesive properties of polymers were carried out to understand the mucoadhesive mechanism. Novel methods for evaluating mucoadhesive properties of polymers in vitro were also developed. The methods include a simple mucin particles method and Biacoa method for quantitative evaluation (Takeuchi et al., 2005c). In the latter method, an interaction analyzer, Biacoa, based on surface plasmon resonance is used to try to evaluate the mucoadhesive property. We also tried to improve the mucosal adhesive property of polymers themselves by partly modifying the molecules or conjugation of different types of polymers. One of examples is chitosan-aprotinin (Werle et al., 2009a; 2009b). Carbopol is a commercial product of polyacrylic acid, whose mucoadhesive property has been

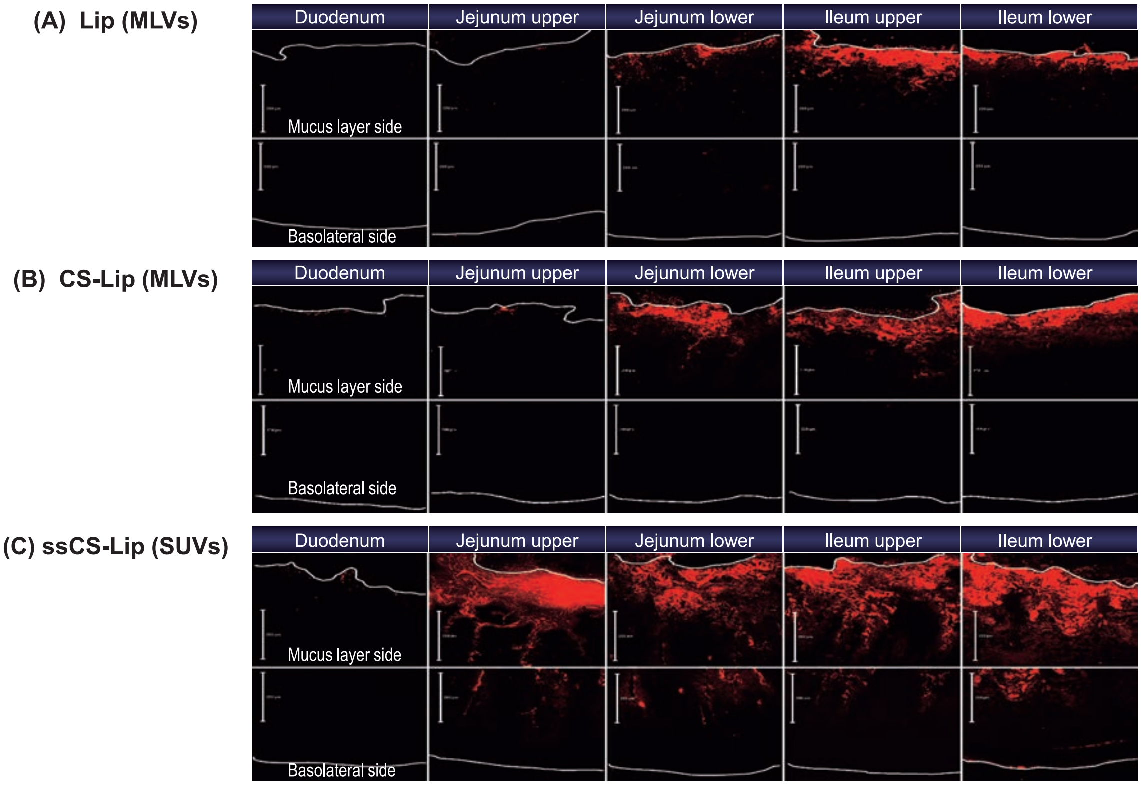

Fig. 23 Confocal laser scanning micrographs of various parts of intestinal tract at 120 min after intragastrical administration of **(A)** Lip (MLVs), **(B)** CS-Lip (MLVs), **(C)** ssCS-Lip in rats and a schematical picture the rat intestinal sample for measuring the CLSM photos.
Lipid formulation of liposomes: DSPC:DCP:Chol. = 8:2:1. Mean particle size of liposomes: **(A)** 7.56 μm, **(B)** 3.58 μm, **(C)** 281.2 nm.
MLVs: multilamellar vehicles. CLSM: Confocal Laser Scanning Microscope.

reported. The mucoadhesive property of Carbopol was found to be improved by conjugating with lectin or WGA (wheat germ agglutinin) (Werle et al., 2010; Makhlof et al., 2011a). It was also confirmed that simultaneous encapsulation of water-soluble absorption enhancers into liposomal carriers greatly improved the absorption of calcitonin (Makhlof et al., 2011b). With respect to the absorption control with these liposomal carriers, the mucoadhesive functions of CS-Lips were demonstrated to render them effective as carriers for a small molecule, indomethacin, by measuring the actual absorption amount (Sugihara et al., 2012). Recently, we also confirmed the delivery of a model hydrophilic macromolecule, dextran labeled with fluorescein isothiocyanate (FITC), with an average molecular weight of ca. 4000 daltons (FD-4) or more, to systemic blood flow by absorption in the digestive tract after oral administration with liposomal formulations. The absorption amount was greatly increased by very small when a FD-4 solution was administered. The amount of absorption was greatly increased by simultaneously encapsulating an absorption enhancer, spermine (**Fig. 24**). The simultaneous administration of spermine dissolved in a FD-4 solution had almost no effect on the absorption, indicating that it is important for the absorption enhancer to be delivered to the absorption site in the gastrointestinal tract together with the absorbed macromolecular drug. These absorption data are well consistent with the pharmacological data shown above in this section.

Comprehensively considering the behavior of liposome particles in the gastrointestinal tract and absorption experiments, the absorption of peptide drugs in the gastrointestinal tract by muco-adhesive micronized liposomes represented by submicron-sized CS-Lip (ssCS-Lip) can be represented schematically as shown in **Fig. 25**. As predicted at the beginning of the study, the mucous membrane (mucosa) presents a large barrier to the absorption of macromolecular drugs in the gastrointestinal tract. CS-Lips interact with and retain the mucous layer on the epithelial cell in the flow of the intestinal tract and penetrate more deeply if the particles are small enough. We speculate that some of the particles are taken up by mucosal epithelial cells as they are. Considering that the absorption enhancer that was administered simultaneously with the particles

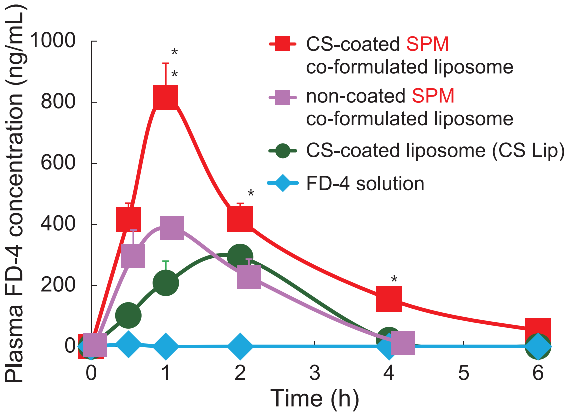

Fig. 24 Plasma FD-4 concentration profiles for 6 hours after oral administration of several liposomal formulations containing FD-4 and FD-4 solution in rats.
FD-4: FITC-dextran, with an average molecular weight of ca. 4000 daltons. SPM: spermine. Dose of FD-4 is 32 mg/kg. $n = 4–5$, ** $p < 0.01$ and *$p < 0.1$ compared with CS Lip.

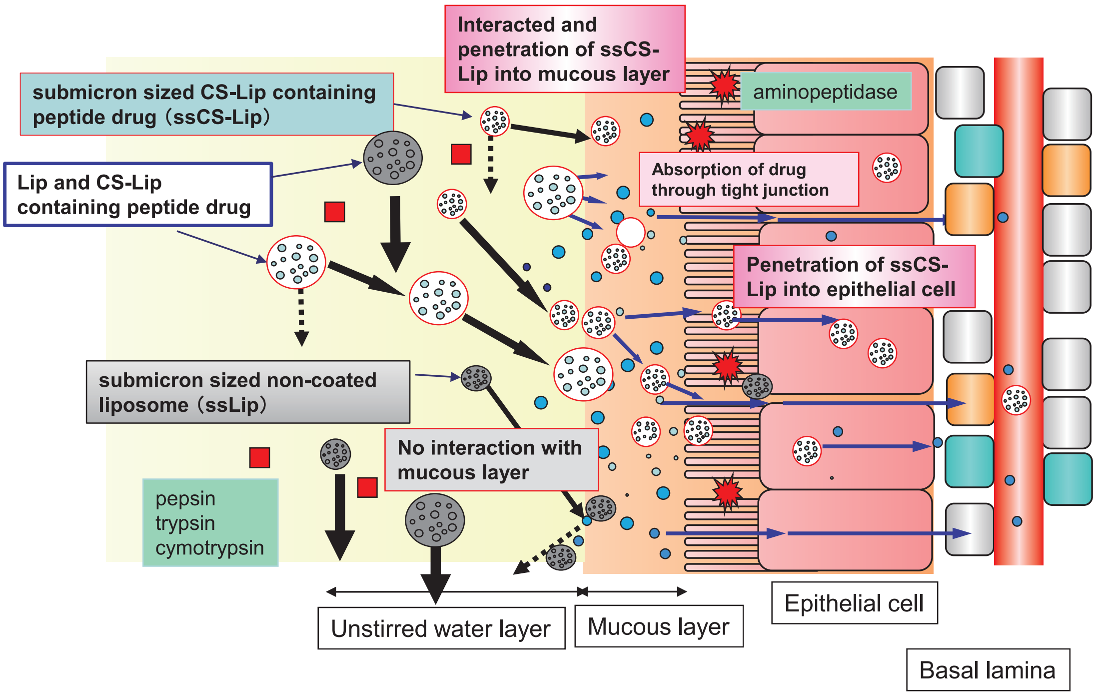

Fig. 25 Possible mechanism of absorption of peptide drug entrapped in CS-Lips in the intestinal tube after oral administration.

worked effectively, it can be inferred that some macromolecular drugs are released in the mucous layer and permeate tight junctions from there.

5.3 Transpulmonary administration of liposomal drugs

Inhalation systems can be a useful drug delivery method for both topical and systemic administration of drugs. Several types of research have been conducted on such administration systems, because particle design including nanoparticle engineering and characterization is important to achieve the most efficient drug delivery (Johnson et al., 2020; Price et al., 2019). Kawashima et al. have also tried to prepare suitable drug crystals and their formulations for dry powder inhalation systems (Kawashima et al., 1998a; 1998b). In terms of peptide drug administration, the lung is highly expected to be a suitable site for systemic administration of drugs. In fact, Exubera® and Afrezza® have been developed and marketed as powdered inhaled insulin preparations. On the other hand, the lungs can be affected by intractable diseases such as lung cancer and chronic obstructive pulmonary disease, and research on new drug treatments such as nucleic acid drugs is progressing. In such cases, it is highly expected that the development of a suitable delivery system such as liposomes will be utilized as a topical dosage form.

In comparing pulmonary administration with oral administration, the lungs are a closed system and there are few degrading enzymes, so it is expected that pulmonary administration of peptide drugs will lead to absorption. When calcitonin solution and various types of polymer-coated liposomes encapsulating calcitonin were administered intrapulmonarily, the effect of the coating polymer on drug absorption was found to be different from that in oral administration, as shown in **Fig. 26** (Murata et al., 2012). There was a difference in the degree, with the highest absorption-enhancing effect being observed for the PVA-R-coated liposomes. We conjectured that the PVA-R-coated liposomes showed the highest absorption because the PVA coating on the liposome avoided phagocytosis by alveolar macrophages and increased the retention time (Nakano et al., 2008). This idea was proved by measuring the retention of these polymer-coated liposomes. In fact, when we evaluated the retention of CS-Lips and PVA-R-coated liposomes in the lungs, we found that a large number of CS-Lips remained in the lung tissue and a large number of PVA-R-coated liposomes remained in the bronchoalveolar lavage fluid (BALF). The finding that the retention of PVA-R-coated liposomes was extended after pulmonary administration was further confirmed by a non-invasive method using an in vivo imaging system and a fluorescence marker, indocyanine green (Murata et al., 2014). In the case of PVA-R, the drug encapsulated in liposomes remained for a longer period of time and then was gradually released into the lungs, which lead to a sustained efficacy. In the case of transpulmonary administration, a trial using the model polymer drug FITC-Dextran confirmed that the absorption actually occurs at the higher level than by oral administration. We have recently confirmed that FITC-Dextran (FD-4), which has an average molecular weight of 4000, was absorbed even when administered as an aqueous solution.

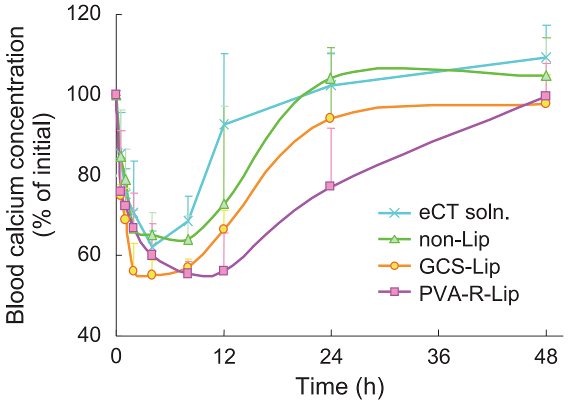

Fig. 26 Blood calcium concentration after intratracheal administration of calcitonin with polymer coated liposomes.

Experimental conditions

Animal	Male Wistar rats (6 weeks), $n = 4$
Route	Intratracheal administration
Dose	125 IU/kg
Analysis	Calcium E-test Wako

5.4 Drug delivery to the posterior segment of the eye with liposomes

As a clearer example of the role of drug delivery systems in the local administration of drugs, we attempted to deliver a drug to the posterior segment of the eye by an instillation centered on the retina. In recent years, with the rapid aging of the population in Japan, the incidence of posterior ocular diseases such as glaucoma, diabetic retinopathy, age-related macular degeneration (AMD), and retinitis pigmentosa has rapidly increased, such that new and more effective drug therapies are needed. VGF, a growth factor, is known to have an important role in cell generation. An anti-VEGF (vascular endothelial growth factor) that suppresses the generation of new, edema-induced blood vessels appearing near the macula of the retina with high probability has been developed. However, its delivery is generally limited to invasive intravitreal injections. However, eye drops containing the anti-VGEF antibody and exerting suitable anti-inflammatory and antioxidant effects are also available, and if these drops could be reliably delivered to the posterior segment of the eye, they could potentially be used to treat the above-named diseases.

For the purpose of evaluating the transfer of liposome particles into the posterior segment of the eye after

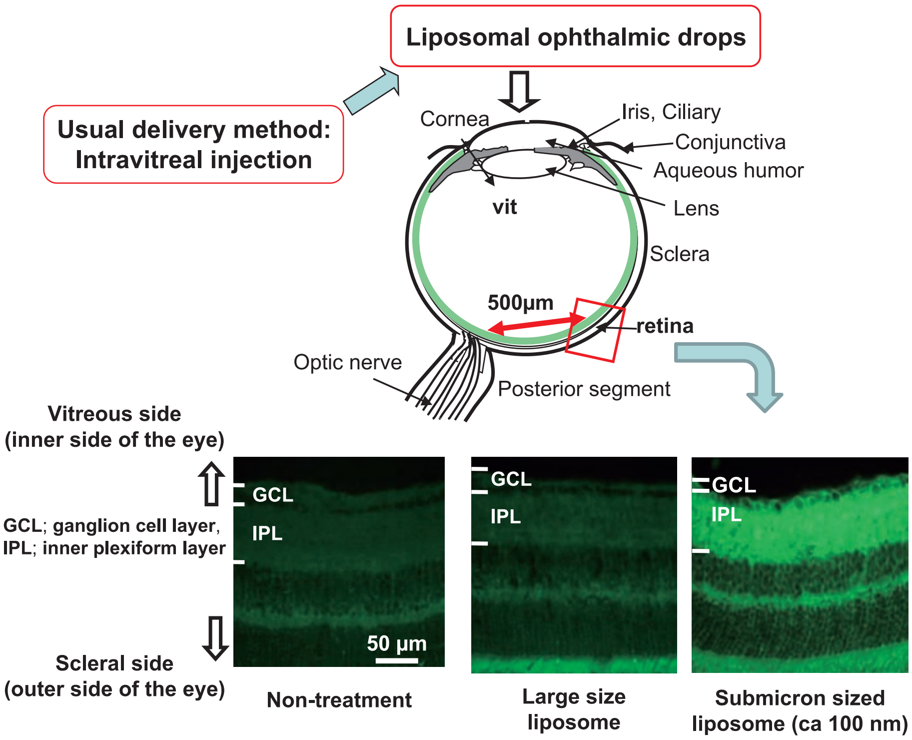

Fig. 27 Delivery of coumarin-6 with liposome to posterior part of eye confirmed by fluorescence microscopy observation.

instillation, a liposome suspension containing coumarin-6 as a fluorescent marker was instilled in mice, and the retina was observed with fluorescent microscopy. In the case of submicron-sized liposomal particles, the observation of the coumarin-6 color was used to confirm that the particles had reached their target (**Fig. 27**) (Hironaka et al., 2009). To confirm that the size of the particles affected their ability to move to the posterior part of the eye, a similar evaluation was performed by using liposomal particles having different particle sizes ranging from the micron order to 100 nm. The results showed that the smaller the particle size, the better the delivery efficiency (Inokuchi et al., 2010). Since not only particle size but also the lipid composition was found to affect the ability to reach the target, the hardness of the liposome particles was also one of the factors.

To confirm the clinical effects of liposomal carriers in eye drop instillation, we tried to conduct animal experiments as a joint research project with a laboratory equipped for ophthalmic evaluation. When liposomes encapsulating edaravone, a free radical scavenger, were instilled into a model mouse before light irradiation to induce retinal photodamage, the liposomal formulation was confirmed to be effective at preventing the subsequent photodamage (Hironaka et al., 2011). It was also clarified that diclofenac, which is one of the NSAIDs (nonsteroidal anti-inflammatory drugs), can suppress choroidal neovascularization due to retinal photodamage in mice when instilled as a drug encapsulated in liposomes (Fujisawa et al., 2012; Shimazawa et al., 2017). In either case, such a pharmaceutical effect in the retinal area was not observed when the solutions dissolving these drugs were instilled under the same conditions for comparison, and it could be judged that the drug could be delivered to the vicinity of the retina by the liposomal eye drop preparation. A newly developed macromolecular API was also applied to this liposomal system and confirmed to achieve a higher pharmacological effect in mice (Taketani et al., 2016).

As with oral and transpulmonary administration, an increase in the amount or duration in drug delivering by polymer-coated liposomes was also investigated. Poly-L-lysine (PLL) and polyarginine (PLA), which have been reported to have affinity for cells, were tested as coating polymers, and the delivery efficiency of these polymer-coated liposomes to the posterior segment of the eye was assessed (Sasaki et al., 2013). The results showed that the larger the molecular weight of the polymer, the greater the effect. However, the efficiency decreased owing to the aggregation of liposomes if the molecular weight of the polymer was too large. Thus, an optimum molecular weight existed, and this weight was determined to be 15,000 daltons in the case of PLL. Active targeting with polymer-coated liposomes has been tested in this ophthalmic liposomal system. One of the targets is folic acid receptors, and an enhancement in delivering efficiency has been observed by modifying the surface of liposomes with folic acid. The delivery of macromolecules to the posterior part of the eye has also been attempted by using FITC-dextran as a drug model, and the feasibility of this approach was confirmed. Based on this finding, it is expected that macromolecular APIs such as siRNA and Bonac nucleic acid can also be delivered to the posterior segment of the eye. Further research is ongoing.

6. Conclusion

Research on formulation design and dosage form design for drug delivery were described in this review. Regarding the design of solid dosage forms, the particle design of drug crystals and several excipients have important roles for the objective functions of the resultant dosage forms. It is important to image the objective functions expected by patients as a final goal of research. Regarding the delivery of macromolecular drugs, colloidal drug carriers have important roles, and the concept of particle design is also important even for these colloidal particles. The suitable design of submicron-sized particles such as polymer-coated liposomes not only improves the efficiency in drug delivery as a drug-targeting tool but also leads to the development of new drug delivery methods such as the oral administration of peptide drugs. As briefly discussed in this paper, it is necessary for pharmaceutical researchers to account for the actual needs of patients as well as the needs of the researchers and medical personnel. It is expected that several types of particle design research for a variety of pharmaceutical materials will contribute to the design of truly patient-friendly dosage forms to solve various issues related to the unmet needs of patients.

References

Allen T.M., Hansen C., Martin F., Redemann C., Yau-Young A., Liposomes containing synthetic lipid derivatives of poly(ethylene glycol) show prolonged circulation half-lives in vivo, Biochimica et Biophysica Acta (BBA)—Biomembranes, 1066 (1991) 29–36. DOI: 10.1016/0005-2736(91)90246-5

Allen T.M., Hansen C., Rutledge J., Liposomes with prolonged circulation times: factors affecting uptake by reticuloendothelial and other tissues, Biochimica et Biophysica Acta (BBA)—Biomembranes, 981 (1989) 27–35. DOI: 10.1016/0005-2736(89)90078-3

Amidon G.L., Lennernäs H., Shah V.P., Crison J.R., A theoretical basis for a biopharmaceutic drug classification: the correlation of in vitro drug product dissolution and in vivo bioavailability, Pharmaceutical Research, 12 (1995) 413–420. DOI: 10.1023/A:1016212804288

Buckton G., Darcy P., Water mobility in amorphous lactose below and close to the glass transition temperature, International Journal of Pharmaceutics, 136 (1996) 141–146. DOI: 10.1016/0378-5173(96)04503-6

Carless J.E., Leigh S., Compression characteristics of powders: radial die wall pressure transmission and density changes, Journal of Pharmacy and Pharmacology, 26 (1974) 289–297. DOI: 10.1111/j.2042-7158.1974.tb09278.x

Chiou W.L., Riegelman S., Preparation and dissolution characteristics of several fast-release solid dispersions of griseofulvin, Journal of Pharmaceutical Sciences, 58 (1969) 1505–1510. DOI: 10.1002/jps.2600581218

Corrigan O.I., Holohan E.M., Sabra K., Amorphous forms of thiazide diuretics prepared by spray-drying, International Journal of Pharmaceutics, 18 (1984) 195–200. DOI: 10.1016/0378-5173(84)90119-4

Corrigan O.I., Sabra K., Holohan E.M., Physicochemical properties of spray dried drugs: phenobarbitone and hydroflumethiazide, Drug Development and Industrial Pharmacy, 9 (1983) 1–20. DOI: 10.3109/03639048309048541

Couvreur P., Kante B., Roland M., Guiot P., Bauduin P., Speiser P., Polycyanoacrylate nanocapsules as potential lysosomotropic carriers: preparation, morphological and sorptive properties, Journal of Pharmacy and Pharmacology, 31 (1979) 331–332. DOI: 10.1111/j.2042-7158.1979.tb13510.x

Danjo K., Kamiya K., Otsuka A., Effect of temperature on the sticking of low melting point materials, Chemical & Pharmaceutical Bulletin, 41 (1993) 1423–1427. DOI: 10.1248/cpb.41.1423

Danjo K., Kojima S., Chen C.Y., Sunada H., Otsuka A., Effect of water content on sticking during compression, Chemical & Pharmaceutical Bulletin, 45 (1997) 706–709. DOI: 10.1248/cpb.45.706

Dapergolas G., Gregoriadis G., Hypoglycæmic effect of liposome-entrapped insulin administered intragastrically into rats, The Lancet, 308 (1976) 824–827. DOI: 10.1016/S0140-6736(76)91209-5

Ford J.L., The current status of solid dispersions, Pharmaceutica Acta Helvetiae, 61 (1986) 69–88. https://pubmed.ncbi.nlm.nih.gov/3520598/

Fujisawa T., Miyai H., Hironaka K., Tsukamoto T., Tahara K., Tozuka Y., Ito M., Takeuchi H., Liposomal diclofenac eye drop formulations targeting the retina: formulation stability improvement using surface modification of liposomes, International Journal of Pharmaceutics, 436 (2012) 564–567. DOI: 10.1016/j.ijpharm.2012.07.024

Gupta P.K., Leung S.-H.S., Robinson J.R., Bioadhesives/mucoadhesives in drug delivery to the gastrointestinal tract, in: Vincent Lenaerts, Gurny Robert (Eds.) Bioadhesive Drug Delivery Systems, CRC Press, Florida, 1990, pp. 65–92, ISBN 9780849353673.

Heckel R.W., Density-pressure relationships in powder compaction, Transactions of the Metallurgical Society of AIME, 221 (1961a) 671–675.

Heckel R.W., An analysis of powder compaction phenomena, Transactions of the Metallurgical Society of AIME, 221 (1961b) 1001–1008.

Hiestand E.N., Wells J.E., Peot C.B., Ochs J.F., Physical processes of tableting, Journal of Pharmaceutical Sciences, 66 (1977) 510–519. DOI: 10.1002/jps.2600660413

Hironaka K., Inokuchi Y., Fujisawa T., Shimazaki H., Akane M., Tozuka Y., Tsuruma K., Shimazawa M., Hara H., Takeuchi H., Edaravone-loaded liposomes for retinal protection against oxidative stress-induced retinal damage, European Journal of Pharmaceutics and Biopharmaceutics, 79 (2011) 119–125. DOI: 10.1016/j.ejpb.2011.01.019

Hironaka K., Inokuchi Y., Tozuka Y., Shimazawa M., Hara H., Takeuchi H., Design and evaluation of a liposomal delivery system targeting the posterior segment of the eye, Journal of Controlled Release, 136 (2009) 247–253. DOI: 10.1016/j.jconrel.2009.02.020

Humbert-Droz P., Gurny R., Mordier D., Doelker E., Densification behaviour of drugs presenting availability problems, International Journal of Pharmaceutical Technology and Product Manufacture, 4 (1983) 29–35.

Inokuchi Y., Hironaka K., Fujisawa T., Tozuka Y., Tsuruma K., Shimazawa M., Takeuchi H., Hara H., Physicochemical properties affecting retinal drug/coumarin-6 delivery from nanocarrier systems via eyedrop administration, Investigative Ophthalmology & Visual Science, 51 (2010) 3162–3170. DOI: 10.1167/iovs.09-4697

Johnson L.M., Mecham J.B., Quinn F., Hickey A.J., Nanoparticle technology for respiratory tract mucosal vaccine delivery, KONA Powder and Particle Journal, 37 (2020) 97–113. DOI: 10.14356/kona.2020013

Kakimi K., Niwa T., Danjo K., Influence of compression pressure and velocity on tablet sticking, Chemical and Pharmaceutical Bulletin, 58 (2010) 1565–1568. DOI: 10.1248/cpb.58.1565

Kakino Y., Hishikawa Y., Onodera R., Tahara K., Takeuchi H., Gelation factors of pectin for development of a powder form of gel, dry jelly, as a novel dosage form, Chemical and Pharmaceutical Bulletin, 65 (2017) 1035–1044. DOI: 10.1248/cpb.c17-00447

Kawashima Y., Serigano T., Hino T., Yamamoto H., Takeuchi H., A new powder design method to improve inhalation efficiency of pranlukast hydrate dry powder aerosols by surface modification with hydroxypropylmethylcellulose phthalate nanospheres, Pharmaceutical Research, 15 (1998a) 1748–1752. DOI: 10.1023/A:1011916930655

Kawashima Y., Serigano T., Hino T., Yamamoto H., Takeuchi H., Design of inhalation dry powder of pranlukast hydrate to improve dispersibility by the surface modification with light anhydrous silicic acid (AEROSIL 200), International Journal of Pharmaceutics, 173 (1998b) 243–251. DOI: 10.1016/S0378-5173(98)00243-9

Keck C.M., Müller R.H., Drug nanocrystals of poorly soluble drugs produced by high pressure homogenisation, European Journal of Pharmaceutics and Biopharmaceutics, 62 (2006) 3–16. DOI: 10.1016/j.ejpb.2005.05.009

Knight C.G. (Ed.), Liposomes: From Physical Structure to Therapeutic Applications, Elsevier, Amsterdam (1981), ISBN: 9780444803207.

Kreuter K. (Ed.), Colloidal Drug Delivery Systems., Marcell Dekker, New York (1994). ISBN: 9780824792145.

Kuno Y., Kojima M., Ando S., Nakagami H., Effect of preparation method on properties of orally disintegrating tablets made by phase transition, International Journal of Pharmaceutics, 355 (2008) 87–92. DOI: 10.1016/j.ijpharm.2007.11.046

Liversidge G.G., Cundy K.C., Particle size reduction for improvement of oral bioavailability of hydrophobic drugs: I. Absolute oral bioavailability of nanocrystalline danazol in beagle dogs, International Journal of Pharmaceutics, 125 (1995) 91–97. DOI: 10.1016/0378-5173(95)00122-Y

Makhlof A., Fujimoto S., Tozuka Y., Takeuchi H., In vitro and in vivo evaluation of WGA–carbopol modified liposomes as carriers for oral peptide delivery, European Journal of Pharmaceutics and Biopharmaceutics, 77 (2011a) 216–224. DOI: 10.1016/j.ejpb.2010.12.008

Makhlof A., Werle M., Tozuka Y., Takeuchi H., A mucoadhesive nanoparticulate system for the simultaneous delivery of macromolecules and permeation enhancers to the intestinal mucosa, Journal of Controlled Release, 149 (2011b) 81–88. DOI: 10.1016/j.jconrel.2010.02.001

McGinity J.W. (Ed.), Aqueous Polymeric Coatings for Pharmaceutical Dosage Forms, 2nd ed., Marcel Dekker, New York (1997), ISBN: 9780824797737.

Merisko-Liversidge E., Liversidge G.G., Cooper E.R., Nanosizing: a formulation approach for poorly-water-soluble compounds, European Journal of Pharmaceutical Sciences, 18 (2003) 113–120. DOI: 10.1016/S0928-0987(02)00251-8

Michaut F., Busignies V., Fouquereau C., Huet de Barochez B., Leclerc B., Tchoreloff P., Evaluation of a rotary tablet press simulator as a tool for the characterization of compaction properties of pharmaceutical products, Journal of Pharmaceutical Sciences, 99 (2010) 2874–2885. DOI: 10.1002/jps.22032

Müller R.H., Peters K., Nanosuspensions for the formulation of poorly soluble drugs: i. preparation by a size-reduction technique, International Journal of Pharmaceutics, 160 (1998) 229–237. DOI: 10.1016/S0378-5173(97)00311-6

Murata M., Nakano K., Tahara K., Tozuka Y., Takeuchi H., Pulmonary delivery of elcatonin using surface-modified liposomes to improve systemic absorption: polyvinyl alcohol with a hydrophobic anchor and chitosan oligosaccharide as effective surface modifiers, European Journal of Pharmaceutics and Biopharmaceutics, 80 (2012) 340–346. DOI: 10.1016/j.ejpb.2011.10.011

Murata M., Tahara K., Takeuchi H., Real-time in vivo imaging of surface-modified liposomes to evaluate their behavior after pulmonary administration, European Journal of Pharmaceutics and Biopharmaceutics, 86 (2014) 115–119. DOI: 10.1016/j.ejpb.2013.09.006

Nagai T., Adhesive topical drug delivery system, Journal of Controlled Release, 2 (1985) 121–134. DOI: 10.1016/0168-3659(85)90038-0

Naito S., Nakamichi K., Studies on techniques of manufacturing pharmacy. i. prediction of tableting troubles such as capping and sticking. (i), Chemical & Pharmaceutical Bulletin, 17 (1969) 2507–2514. DOI: 10.1248/cpb.17.2507

Nakano K., Tozuka Y., Takeuchi H., Effect of surface properties of liposomes coated with a modified polyvinyl alcohol (PVA-R) on the interaction with macrophage cells, International Journal of Pharmaceutics, 354 (2008) 174–179. DOI: 10.1016/j.ijpharm.2007.08.046

Narang A.S., Rao V.M., Guo H., Lu J., Desai D.S., Effect of force feeder on tablet strength during compression, International Journal of Pharmaceutics, 401 (2010) 7–15. DOI: 10.1016/j.ijpharm.2010.08.027

Newton J.M., Haririan I., Podczeck F., The influence of punch curvature on the mechanical properties of compacted powders, Powder Technology, 107 (2000) 79–83. DOI: 10.1016/S0032-5910(99)00173-4

Okuda Y., Irisawa Y., Okimoto K., Osawa T., Yamashita S., A new formulation for orally disintegrating tablets using a suspension spray-coating method, International Journal of Pharmaceutics, 382 (2009) 80–87. DOI: 10.1016/j.ijpharm.2009.08.010

Osamura T., Takeuchi Y., Onodera R., Kitamura M., Takahashi Y., Tahara K., Takeuchi H., Characterization of tableting properties measured with a multi-functional compaction instrument for several pharmaceutical excipients and actual tablet formulations, International Journal of Pharmaceutics, 510 (2016) 195–202. DOI: 10.1016/j.ijpharm.2016.05.024

Osamura T., Takeuchi Y., Onodera R., Kitamura M., Takahashi Y., Tahara K., Takeuchi H., Prediction of effects of punch shapes on tableting failure by using a multi-functional single-punch tablet press, Asian Journal of Pharmaceutical Sciences, 12 (2017) 412–417. DOI: 10.1016/j.ajps.2017.05.001

Osamura T., Takeuchi Y., Onodera R., Kitamura M., Takahashi Y., Tahara K., Takeuchi H., Formulation design of granules prepared by wet granulation method using a multi-functional single-punch tablet press to avoid tableting failures, Asian Journal of Pharmaceutical Sciences, 13 (2018) 113–119. DOI: 10.1016/j.ajps.2017.08.002

Papahadjopoulos D., Allen T.M., Gabizon A., Mayhew E., Matthay K., Huang S.K., Lee K.D., Woodle M.C., Lasic

D.D., Redemann C., Sterically stabilized liposomes: improvements in pharmacokinetics and antitumor therapeutic efficacy, Proceedings of the National Academy of Sciences, 88 (1991) 11460–11464. DOI: 10.1073/pnas.88.24.11460

Patel H.M., Ryman B.E., Oral administration of insulin by encapsulation within liposomes, FEBS Letters, 62 (1976) 60–63. DOI: 10.1016/0014-5793(76)80016-6

Patel H.M., Ryman B. E., Systemic and oral administration of liposomes, In: C.G. Knight (Ed.), Liposomes: From Physical Structure to Therapeutic Applications, Elsevier, Amsterdam, 1981, pp. 409–441. ISBN: 9780444802347.

Picker K.M., Time dependence of elastic recovery for characterization of tableting materials, Pharmaceutical Development and Technology, 6 (2001) 61–70. DOI: 10.1081/PDT-100000014

Pikal M.J., Lukes A.L., Lang J.E., Gaines K., Quantitative crystallinity determinations for β-lactam antibiotics by solution calorimetry: correlations with stability, Journal of Pharmaceutical Sciences, 67 (1978) 767–773. DOI: 10.1002/jps.2600670609

Pitt K.G., Webber R.J., Hill K.A., Dey D., Gamlen M.J., Compression prediction accuracy from small scale compaction studies to production presses, Powder Technology, 270 (2015) 490–493. DOI: 10.1016/j.powtec.2013.10.007

Ponchel G., Montisci M.-J., Dembri A., Durrer C., Duchêne D., Mucoadhesion of colloidal particulate systems in the gastro-intestinal tract, European Journal of Pharmaceutics and Biopharmaceutics, 44 (1997) 25–31. DOI: 10.1016/S0939-6411(97)00098-2

Price D.N., Kunda N.K., Muttil P., Challenges associated with the pulmonary delivery of therapeutic dry powders for preclinical testing, KONA Powder and Particle Journal, 36 (2019) 129–144. DOI: 10.14356/kona.2019008

Roberts M., Ford J.L., Rowe P.H., Dyas A.M., MacLeod G.S., Fell J.T., Smith G.W., Effect of lubricant type and concentration on the punch tip adherence of model ibuprofen formulations, Journal of Pharmacy and Pharmacology, 56 (2004) 299–305. DOI: 10.1211/0022357022827

Saleki-Gerhardt A., Zografi G., Non-isothermal and isothermal crystallization of sucrose from the amorphous state, Pharmaceutical Research, 11 (1994) 1166–1173. DOI: 10.1023/A:1018945117471

Sasaki H., Karasawa K., Hironaka K., Tahara K., Tozuka Y., Takeuchi H., Retinal drug delivery using eyedrop preparations of poly-l-lysine-modified liposomes, European Journal of Pharmaceutics and Biopharmaceutics, 83 (2013) 364–369. DOI: 10.1016/j.ejpb.2012.10.014

Seager H., Drug-delivery products and the Zydis fast-dissolving dosage form, Journal of Pharmacy and Pharmacology, 50 (2011) 375–382. DOI: 10.1111/j.2042-7158.1998.tb06876.x

Sebhatu T., Ahlneck C., Alderborn G., The effect of moisture content on the compression and bond-formation properties of amorphous lactose particles, International Journal of Pharmaceutics, 146 (1997) 101–114. DOI: 10.1016/S0378-5173(96)04777-1

Sebhatu T., Elamin A.A., Ahlneck C., Effect of moisture sorption on tabletting characteristics of spray dried (15 % amorphous) lactose, Pharmaceutical Research, 11 (1994) 1233–1238. DOI: 10.1023/A:1018973923831

Sekiguchi K., Obi N., Studies on absorption of eutectic mixture. i. a comparison of the behavior of eutectic mixture of sulfathiazole and that of ordinary sulfathiazole in man, Chemical & Pharmaceutical Bulletin, 9 (1961) 866–872. DOI: 10.1248/cpb.9.866

Senior J.H., Fate and behavior of liposomes in vivo: a review of controlling factors, Critical Reviews in Therapeutic Drug Carrier Systems, 3 (1987) 123–193. PMID: 3542245.

Shenfield G.M., Hill J.C., Infrequent response by diabetic rats to insulin-liposomes, Clinical and Experimental Pharmacology and Physiology, 9 (1982) 355–361. DOI: 10.1111/j.1440-1681.1982.tb00819.x

Shimazawa M., Inoue Y., Masuda T., Onodera R., Tahara K., Shimizu Y., Mibe Y., Tsuruma K., Takeuchi H., Hara H., Topical diclofenac-loaded liposomes ameliorate laser-induced choroidal neovascularization in mice and non-human primates, Current Neurovascular Research, 14 (2017) 46–52. DOI: 10.2174/1567202614666161104115440

Simonelli A.P., Mehta S.C., Higuchi W.I., Dissolution rates of high energy polyvinylpyrrolidone (PVP)-sulfathiazole coprecipitates, Journal of Pharmaceutical Sciences, 58 (1969) 538–549. DOI: 10.1002/jps.2600580503

Sixsmith D., McCluskey D., The effect of punch tip geometry on powder movement during the tableting process, Journal of Pharmacy and Pharmacology, 33 (1981) 79–81. DOI: 10.1111/j.2042-7158.1981.tb13715.x

Stubberud L., Arwidsson H.G., Hjortsberg V., Graffner C., Water-solid interactions. iii. effect of glass transition temperature, Tg, and processing on tensile strength of compacts of lactose and lactose/polyvinyl pyrrolidone, Pharmaceutical Development and Technology, 1 (1996) 195–204. DOI: 10.3109/10837459609029894

Stubberud L., Forbes R.T., The use of gravimetry for the study of the effect of additives on the moisture-induced recrystallisation of amorphous lactose, International Journal of Pharmaceutics, 163 (1998) 145–156. DOI: 10.1016/S0378-5173(97)00382-7

Sugihara H., Yamamoto H., Kawashima Y., Takeuchi H., Effectiveness of submicronized chitosan-coated liposomes in oral absorption of indomethacin, Journal of Liposome Research, 22 (2012) 72–79. DOI: 10.3109/08982104.2011.621128

Sugimori K., Mori S., Kawashima Y., Characterization of die wall pressure to predict capping of flat- or convex-faced drug tablets of various sizes, Powder Technology, 58 (1989a) 259–264. DOI: 10.1016/0032-5910(89)80052-X

Sugimori K., Mori S., Kawashima Y., Introduction of new index for the prediction of capping tendency of tablets, Chemical & Pharmaceutical Bulletin, 37 (1989b) 458–462. DOI: 10.1248/cpb.37.458

Sugimoto M., Narisawa S., Matsubara K., Yoshino H., Nakano M., Handa T., Development of manufacturing method for rapidly disintegrating oral tablets using the crystalline transition of amorphous sucrose, International Journal of Pharmaceutics, 320 (2006) 71–78. DOI: 10.1016/j.ijpharm.2006.04.004

Sun C.C., Dependence of ejection force on tableting speed—A compaction simulation study, Powder Technology, 279 (2015) 123–126. DOI: 10.1016/j.powtec.2015.04.004

Sunamoto J., Iwamoto K., Takada M., Yuzuriha T., Katayama K., Polymer Coated Liposomes for Drug Delivery to Target Specific Organs, in: Anderson J.M., Kim S.W. (Eds.), Recent Advances in Drug Delivery Systems, Springer US, Boston, MA, 1984, pp. 153–162, ISBN: 978-1-4613-2745-5. DOI: 10.1007/978-1-4613-2745-5_10

Tahara K., Nishikawa M., Matsui K., Hisazumi K., Onodera R., Tozuka Y., Takeuchi H., In vitro and in vivo characterization of drug nanoparticles prepared using PureNano™ continuous crystallizer to improve the bioavailability of poorly water soluble drugs, Pharmaceutical Research, 33 (2016) 2259–2268. DOI: 10.1007/s11095-016-1964-7

Takahashi T., Toyota H., Kuroiwa Y., Yoshino H., Kondou H., Yamashita K., Hakomori T., Takeuchi H., Quantitative evaluation of different rotary tablet presses by compaction velocity based on compaction simulation study, International Journal of Pharmaceutics, 558 (2019) 157–164. DOI: 10.1016/j.ijpharm.2018.12.032

Takahashi T., Toyota H., Kuroiwa Y., Kondo H., Dohi M., Hakomori T., Nakamura M., Takeuchi H., Application of novel compaction indicator for the optimization of compaction conditions based on a compaction simulation study, International Journal of Pharmaceutics, 587 (2020) 119574. DOI: 10.1016/j.ijpharm.2020.119574

Taketani Y., Usui T., Toyono T., Shima N., Yokoo S., Kimakura M., Yamagami S., Ohno S., Onodera R., Tahara K., Takeuchi H., Kuroda M., Topical use of angiopoietin-like protein 2 RNAi-loaded lipid nanoparticles suppresses corneal neovascularization, Molecular Therapy—Nucleic Acids, 5 (2016) e292. DOI: 10.1038/mtna.2016.1

Takeuchi H., Chapter 2.15-Solubility and Dissolution Rate, in: Higashitani K., Makino H., Matsusaka S. (Eds.), Powder Technology Handbook (4th Edition), CRC Press, 2019, pp. 171–178, ISBN: 9781315184258. DOI: 10.1201/b22268

Takeuchi H., Fuji Sylysia Chemical Ltd., Tablet and method for producing the same, Jpn. Patent No. 5026675 (2012).

Takeuchi H., Handa T., Kawashima Y., Enhancement of the dissolution rate of a poorly water-soluble drug (tolbutamide) by a spray-drying solvent deposition method and disintegrants, Journal of Pharmacy and Pharmacology, 39 (1987a) 769–773. DOI: 10.1111/j.2042-7158.1987.tb05117.x

Takeuchi H., Handa T., Kawashima Y., Spherical solid dispersion containing amorphous tolbutamide embedded in enteric coating polymers or colloidal silica prepared by spray-drying technique, Chemical & Pharmaceutical Bulletin, 35 (1987b) 3800–3806. DOI: 10.1248/cpb.35.3800

Takeuchi H., Kojima H., Toyoda T., Yamamoto H., Hino T., Kawashima Y., Prolonged circulation time of doxorubicin-loaded liposomes coated with a modified polyvinyl alcohol after intravenous injection in rats, European Journal of Pharmaceutics and Biopharmaceutics, 48 (1999a) 123–129. DOI: 10.1016/S0939-6411(99)00029-6

Takeuchi H., Kojima H., Yamamoto H., Kawashima Y., Enhanced tumour accumulation of doxorubicin with polymer-coated liposomes in rats, Pharmacy and Pharmacology Communications, 5 (1999b) 445–448. DOI: 10.1211/146080899128735144

Takeuchi H., Kojima H., Yamamoto H., Kawashima Y., Polymer coating of liposomes with a modified polyvinyl alcohol and their systemic circulation and RES uptake in rats, Journal of Controlled Release, 68 (2000a) 195–205. DOI: 10.1016/S0168-3659(00)00260-1

Takeuchi H., Kojima H., Yamamoto H., Kawashima Y., Evaluation of circulation profiles of liposomes coated with hydrophilic polymers having different molecular weights in rats, Journal of Controlled Release: official journal of the Controlled Release Society, 75 (2001a) 83–91. DOI: 10.1016/s0168-3659(01)00368-6

Takeuchi H., Kojima H., Yamamoto H., Kawashima Y., Evaluation of the anti-tumour activity of liposomal doxorubicin coated with hydrophilic polymers in tumour-bearing mice, STP pharma sciences, 11 (2001b) 271–274.

Takeuchi H., Kojima H., Yamamoto H., Kawashima Y., Passive targeting of doxorubicin with polymer coated liposomes in tumor bearing rats, Biological and Pharmaceutical Bulletin, 24 (2001c) 795–799. DOI: 10.1248/bpb.24.795

Takeuchi H., Matsui Y., Sugihara H., Yamamoto H., Kawashima Y., Effectiveness of submicron-sized, chitosan–coated liposomes in oral administration of peptide drugs, International Journal of Pharmaceutics, 303 (2005a) 160–170. DOI: 10.1016/j.ijpharm.2005.06.028

Takeuchi H., Matsui Y., Yamamoto H., Kawashima Y., Mucoadhesive properties of carbopol or chitosan-coated liposomes and their effectiveness in the oral administration of calcitonin to rats, Journal of Controlled Release, 86 (2003a) 235–242. DOI: 10.1016/S0168-3659(02)00411-X

Takeuchi H., Nagira S., Aikawa M., Yamamoto H., Kawashima Y., Effect of lubrication on the compaction properties of pharmaceutical excipients as measured by die wall pressure, Journal of Drug Delivery Science and Technology, 15 (2005b) 177–182. DOI: 10.1016/S1773-2247(05)50023-6

Takeuchi H., Nagira S., Yamamoto H., Kawashima Y., Design of solid dispersion particles of drug with fine porous carriers, Journal of the Society of Powder Technology, Japan, 40 (2003b) 157–162. DOI: 10.4164/sptj.40.157

Takeuchi H., Nagira S., Yamamoto H., Kawashima Y., Solid dispersion particles of tolbutamide prepared with fine silica particles by the spray-drying method, Powder Technology, 141 (2004a) 187–195. DOI: 10.1016/j.powtec.2004.03.007

Takeuchi H., Nagira S., Yamamoto H., Kawashima Y., Die wall pressure measurement for evaluation of compaction property of pharmaceutical materials, International Journal of Pharmaceutics, 274 (2004b) 131–138. DOI: 10.1016/j.ijpharm.2004.01.008

Takeuchi H., Onodera R., Preparation of nano particles from a liquid phase and dosage form design, Funtai-Gijutsu, 7(6) (2015) 537–541.

Takeuchi H., Sasaki H., Niwa T., Hino T., Kawashima Y., Uesugi K., Kayano M., Miyake Y., Preparation of powdered redispersible vitamin e acetate emulsion by spray-drying technique, Chemical & Pharmaceutical Bulletin, 39 (1991) 1528–1531. DOI: 10.1248/cpb.39.1528

Takeuchi H., Thongborisute J., Matsui Y., Sugihara H., Yamamoto H., Kawashima Y., Novel mucoadhesion tests for polymers and polymer-coated particles to design optimal mucoadhesive drug delivery systems, Advanced Drug Delivery Reviews, 57 (2005c) 1583–1594. DOI: 10.1016/j.addr.2005.07.008

Takeuchi H., Yamakawa R., Nishimatsu T., Takeuchi Y., Hayakawa K., Maruyama N., Design of rapidly disintegrating drug delivery films for oral doses with hydroxypropyl methylcellulose, Journal of Drug Delivery Science and Technology, 23 (2013) 471–475. DOI: 10.1016/S1773-2247(13)50068-2

Takeuchi H., Yamamoto H., Kawashima Y., Mucoadhesive nanoparticulate systems for peptide drug delivery, Advanced Drug Delivery Reviews, 47 (2001d) 39–54. DOI: 10.1016/S0169-409X(00)00120-4

Takeuchi H., Yamamoto H., Niwa T., Hino T., Kawashima Y., Mucoadhesion of polymer-coated liposomes to rat intestine in vitro, Chemical & Pharmaceutical Bulletin, 42 (1994) 1954–1956. DOI: 10.1248/cpb.42.1954

Takeuchi H., Yamamoto H., Niwa T., Hino T., Kawashima Y., Enteral absorption of insulin in rats from mucoadhesive chitosan-coated liposomes, Pharmaceutical Research, 13 (1996) 896–901. DOI: 10.1023/A:1016009313548

Takeuchi H., Yamamoto H., Toyoda T., Toyobuku H., Hino T., Kawashima Y., Physical stability of size controlled small unilameller liposomes coated with a modified polyvinyl alcohol, International Journal of Pharmaceutics, 164 (1998) 103–111. DOI: 10.1016/S0378-5173(97)00404-3

Takeuchi H., Yasuji T., Hino T., Yamamoto H., Kawashima Y., Compaction Properties of Composite Particles Consisting of Lactose with Sodium Alginate Prepared by Spray-Drying, Pharmaceutical Research, 16 (1999c) 1193–1198. DOI: 10.1023/A:1018937227794

Takeuchi H., Yasuji T., Yamamoto H., Kawashima Y., Temperature- and moisture-induced crystallization of amorphous lactose in composite particles with sodium alginate prepared by spray-drying, Pharmaceutical Development and Technology, 5 (2000b) 355–363. DOI: 10.1081/PDT-100100551

Takeuchi H., Yasuji T., Yamamoto H., Kawashima Y., Temperature-induced crystallization and compactibility of spray dried composite particles composed of amorphous lactose and various types of water-soluble polymer, Chemical & Pharmaceutical Bulletin, 48 (2000c) 585–588. DOI: 10.1248/cpb.48.585

Takeuchi Y., Ikeda N., Tahara K., Takeuchi H., Mechanical characteristics of orally disintegrating films: comparison of folding endurance and tensile properties, International Journal of Pharmaceutics, 589 (2020a) 119876. DOI: 10.1016/j.ijpharm.2020.119876

Takeuchi Y., Murase Y., Tahara K., Takeuchi H., Impact of surface roughness of pre-treated punches and powder properties on prevention of sticking during pharmaceutical tableting, Journal of Drug Delivery Science and Technology, 60 (2020b) 101999. DOI: 10.1016/j.jddst.2020.101999

Takeuchi Y., Nishimatsu T., Tahara K., Takeuchi H., Novel use of insoluble particles as disintegration enhancers for orally disintegrating films, Journal of Drug Delivery Science and Technology, 54 (2019) 101310. DOI: 10.1016/j.jddst.2019.101310

Takeuchi Y., Umemura K., Tahara K., Takeuchi H., Formulation design of hydroxypropyl cellulose films for use as orally disintegrating dosage forms, Journal of Drug Delivery Science and Technology, 46 (2018) 93–100. DOI: 10.1016/J.JDDST.2018.05.002

Tanimura S., Kawazoe H., Yamamoto H., Takeuchi H., Direct compaction of poorly compactable pharmaceutical powders with spray-dried HPC-L, Journal of the Society of Powder Technology, Japan, 43 (2006) 648–652. DOI: 10.4164/sptj.43.648

Tanimura S., Tahara K., Takeuchi H., Spray-dried composite particles of erythritol and porous silica for orally disintegrating tablets prepared by direct tableting, Powder Technology, 286 (2015) 444–450. DOI: 10.1016/j.powtec.2015.08.011

Tanino T., Aoki Y., Furuya Y., Sato K., Takeda T., Mizuta T., Occurrence of capping due to insufficient air escape during tablet compression and a method to prevent it, Chemical & Pharmaceutical Bulletin, 43 (1995) 1772–1779. DOI: 10.1248/cpb.43.1772

Thongborisute J., Takeuchi H., Yamamoto H., Kawashima Y., Visualization of the penetrative and mucoadhesive properties of chitosan and chitosan-coated liposomes through the rat intestine, Journal of Liposome Research, 16 (2006) 127–141. DOI: 10.1080/08982100600680816

Van der Voort Maarschalk K., Zuurman K., Vromans H., Bolhuis G.K., Lerk C.F., Stress relaxation of compacts produced from viscoelastic materials, International Journal of Pharmaceutics, 151 (1997) 27–34. DOI: 10.1016/S0378-5173(97)04889-8

Vromans H., Bolhuis G.K., Lerk C.F., Kussendrager K.D., Bosch H., Studies on tableting properties of lactose. VI. Consolidation and compaction of spray dried amorphous lactose, Acta Pharmaceutica Suecica, 23 (1986) 231–240. PMID: 3799215.

Waimer F., Krumme M., Danz P., Tenter U., Schmidt P.C., A novel method for the detection of sticking of tablets, Pharmaceutical Development and Technology, 4 (1999a) 359–367. DOI: 10.1081/PDT-100101371

Waimer F., Krumme M., Danz P., Tenter U., Schmidt P.C., The influence of engravings on the sticking of tablets. investigations with an instrumented upper punch, Pharmaceutical Development and Technology, 4 (1999b) 369–375. DOI: 10.1081/PDT-100101372

Werle M., Makhlof A., Takeuchi H., Carbopol-lectin conjugate coated liposomes for oral peptide delivery, Chemical and Pharmaceutical Bulletin, 58 (2010) 432–434. DOI: 10.1248/cpb.58.432

Werle M., Takeuchi H., Chitosan-aprotinin coated liposomes for oral peptide delivery: development, characterisation and in vivo evaluation, International Journal of Pharmaceutics, 370 (2009a) 26–32. DOI: 10.1016/j.ijpharm.2008.11.013

Werle M., Takeuchi H., Bernkop-Schnürch A., Modified chitosans for oral drug delivery, Journal of Pharmaceutical Sciences, 98 (2009b) 1643–1656. DOI: 10.1002/jps.21550

Author's Short Biography

Hirofumi Takeuchi

Dr. Hirofumi Takeuchi is now Professor Emeritus and research Professor of Gifu Pharmaceutical University (2019–). He received his B.S. (1979), M.S. (1981) and Ph.D. (1984) in pharmacy and pharmaceutical sciences from Kyoto University. He joined Gifu Pharmaceutical University (GPU) in 1984, and worked as Lecture, Associate Professor and Professor of pharmaceutical engineering. He also worked as the dean of graduate school of GPU (2010–2011), dean of the faculty of GPU (2012–2013) and vice president of GPU (2014). He became the research Professor of Advanced Pharmaceutical Process Engineering (APPEN) as well as Professor Emeritus of GPU after retirement in 2019.

KONA Powder and Particle Journal No. 39 (2022) 176–192/https://doi.org/10.14356/kona.2022010 Review Paper

The Development of Thin-Film Freezing and Its Application to Improve Delivery of Biologics as Dry Powder Aerosols†

Stephanie Hufnagel, Sawittree Sahakijpijarn, Chaeho Moon,
Zhengrong Cui and Robert O. Williams III*
Division of Molecular Pharmaceutics and Drug Delivery, College of Pharmacy, The University of Texas at Austin, USA

Abstract

While the formulation of pharmaceuticals as liquids is common practice, powders are associated with enhanced stability, avoidance of the cold chain, lower dosing requirements, and more convenient administration. These are particularly critical for proteins, as they are expensive and complicated to manufacture. Powders also have improved aerosol properties for pulmonary delivery. Conventional techniques for formulating powders include spray-drying, shelf freeze-drying, spray freeze-drying, and spray freezing into liquid, but they produce powders with poor aerosol performance and/or activity due to suboptimal powder properties. Thin-film freezing (TFF) is a new cryogenic technique that can engineer highly porous, brittle, powder matrices with excellent aerosol performance properties and stability. Herein, we describe TFF in comparison to other cryogenic techniques. Physical properties of TFF powders such as morphology, moisture sorption, stability, solubility, and dissolution, as well as aerosol properties are discussed. In addition, factors that significantly affect the physical and aerosol properties of dry powders prepared by TFF, such as solids content, drug loading, solvent system, excipient, and dry powder delivery device, are analyzed. Finally, we provide evidence supporting the applicability of using TFF to prepare dry powder formulations of protein-based pharmaceuticals, enabling their cold chain-free storage as well as efficient pulmonary delivery.

Keywords: thin-film freezing, dry powder, cryogenic technique, protein, pulmonary delivery

---

1. Introduction

Therapeutics intended for pulmonary delivery via inhalation are supplied as liquids or powders. While a majority of them are developed as liquids, the preparation of drugs into powders affords several benefits, particularly for proteins and other biologics. Pharmaceutical dry powders are generally associated with enhanced stability, avoidance of the cold chain, improved aerosol properties, lower dosing requirements, and more convenient administration (Johnson, 1997). In particular, expensive biologics can benefit from being prepared as powders, as the dry powder state typically extends the shelf life of biologics and reduces the cost burden of their transportation and storage. Spray-drying (SD) and conventional shelf freeze-drying (shelf FD), as well as spray freeze-drying (SFD) and spray freezing into liquid (SFL) are techniques commonly employed to prepare powders. Unfortunately, in the context of biologics, all techniques cause aggregation, denaturation, and/or loss of activity of the biologics to some degree. In addition, these methods produce powders with low surface area, low yield, and/or a broad particle size distribution (Engstrom et al., 2008), which are not ideal for pulmonary delivery by inhalation, particularly of biologics.

Previously, we reported thin-film freezing (TFF) technology for pharmaceutical applications that can be applied to generate highly porous, brittle, powder matrices with excellent aerosol performance properties (Overhoff et al., 2007a). The resultant dry powder, upon sublimation of the solvent in the frozen thin films, is ideal for pulmonary delivery by inhalation. We have validated that the TFF technology is directly applicable to inhaled delivery of various small and large molecules including proteins, such as cytokines, enzymes (Engstrom et al., 2008), and more recently, antibodies. Currently, many therapeutics, including most biologics, for pulmonary delivery are administered by nebulization of a liquid. Unfortunately, nebulization exposes therapeutics, especially biologics such as proteins, to stressful conditions that can damage them from shear or elevated temperatures applied during delivery. In addition to the aforementioned limitations of liquids, the solution

---

† Received 5 April 2021; Accepted 3 May 2021

* Corresponding author: Robert O. Williams III;
Add: 2409 West University Avenue, PHR 4.214 Austin, TX 78712, USA
E-mail: bill.williams@austin.utexas.edu
TEL: +01-512-471-4681 FAX: +01-512-471-7474

for nebulization may contain excipients that are harmful to the lungs. An alternative to nebulization of a liquid is administration by dry powder inhalation, which addresses many of the limitations of nebulization. While some powders are already approved by the US FDA for inhalation, powders produced by TFF technology can minimize the flow-rate dependence of dry powder inhalers (DPIs), use of carriers (Ung et al., 2014), aggregation, denaturation, and size distribution issues of molecules while improving the surface area and yield. Overall, TFF offers an opportunity to improve powder properties and thus aerosol performance and therapeutic efficacy of therapeutics, which can be applied to biologics.

Biologic drugs continue to exist as a large proportion of FDA-approved products, with 25 % of all new chemical entities that were FDA-approved from 2015–2019 being biologics (de la Torre and Albericio, 2020). Additionally, biologics can be approved as biosimilars. Biologics are particularly challenging to formulate due to their large molecular size and sensitive nature. Unlike small molecules, biologics (e.g., proteins) must maintain primary, secondary, tertiary, and quaternary structures. They are expensive to produce and pulmonary delivery may minimize the required dose, and therefore cost, while still assuring efficacy and minimizing systemic toxicity, especially when they are delivered locally to the lung to treat pulmonary disease. For example, systemic delivery of antibodies, one of the largest and most complex biologics, overall carries a risk of side effects such as cytokine release syndrome (Guilleminault et al., 2014). Alternatively, inhaled antibodies are poorly systemically absorbed from the respiratory tract, providing an opportunity for local delivery to the lungs (Guilleminault et al., 2014). Of the thirty biologics that have undergone clinical trials for pulmonary delivery, only five have been delivered as a powder (Liang et al., 2020). Development of biologic formulations for pulmonary delivery has been reviewed in detail (Fröhlich and Salar-Behzadi, 2021; Liang et al., 2020). Herein we describe the development of the TFF technology, the process of TFF, and the general characteristics of powders prepared using TFF. Then, we discuss our experience in applying this technique to formulate protein dry powders for pulmonary delivery.

2. Thin-film freezing: the technique

2.1 The progression of cryogenic process development

Several techniques have been developed or transitioned from other industries and applied to pharmaceuticals, including SD, SFD, SFL, shelf FD, and TFF, in order to prepare powders. The latter four (i.e., SFD, SFL, shelf FD, and TFF) are considered cryogenic techniques and have the added benefit of avoidance of heat, which can directly and indirectly (e.g., evaporation of water) lead to denaturation or degradation of proteins (Overhoff et al., 2009). In cryogenic techniques, a liquid sample is frozen through the use of a cryogen and then lyophilized to remove the frozen solvent via sublimation.

Lyophilization alone, or shelf FD, is generally not sufficient to produce stable particles with high surface area (Engstrom et al., 2008) and submicron particle sizes, which are both necessary for optimal aerosol performance. Shelf FD involves placing the liquid formulation inside a lyophilizer, allowing the liquid to freeze as the shelf temperature is reduced, typically to around –40 °C to –55 °C. Afterwards, the pressure is reduced, sublimating the solvent until a powder is formed. In this method, the cooling rate is slow, around 0.017 K/s, which allows time for protein particles to grow, and achieving particles with a diameter less than a few microns and surface area greater than 1 m^2/g is difficult (Engstrom et al., 2008). The powder generated can be milled to improve the particle size and surface area, but this can be mechanically stressful for proteins and lead to heterogeneous particle sizes with limited yield. Therefore, the alternative processes SFD, SFL, and TFF have been utilized.

SFD involves spraying a liquid formulation into the gaseous vapor phase of a liquid cryogen. The cooling rate of SFD is high, about 10^6 K/s. Unfortunately, SFD has a large gas-liquid interface and shear stress, which can contribute significantly to protein aggregation (Engstrom et al., 2008). This technique produces porous powders with high surface area; however, the particle size is large (Overhoff et al., 2009). A benefit of SFD is that different atomization nozzles and spray rates can be chosen to optimize the droplet shape and size (Overhoff et al., 2009).

In order to minimize the gas-liquid interfacial area, the liquid formulation can be sprayed directly into the liquid cryogen, known as SFL. While the freezing rate is slower than that of SFD, about 10^3 K/s, SFL still adequately arrests the growth of crystals and has produced protein powders with less adsorption, aggregation, denaturation, and higher enzymatic activity than those prepared using SFD (Engstrom et al., 2008). SFL produces powders with improved activity compared to SFD and shelf FD powders due to the lower air-liquid interfacial area, slower cooling rate, and lower (but still adequately high) surface area. Generally, the slower cooling rate results in a lower surface area, which induces a lower chance of water adsorption, improving stability (Overhoff et al., 2009).

TFF was developed to find a cooling/freeze rate and surface area intermediate to that of shelf FD vs. SFD and SFL. In TFF, the liquid cryogen is filled in a rotating metal drum and a solution or suspension is dropped dropwise from above the drum, where the droplets (e.g., 2–4 mm in diameter) spread upon impact to form thin films

(~10–12 mm in diameter) that freeze at 10^2–10^3 K/s. A metal blade then releases the frozen films from the drum as it rotates, and the films are collected in a cryogen-cooled receptacle situated below the blade/drum. The frozen films are then transferred to a lyophilizer for solvent removal by sublimation. TFF is less complex than SFD and SFL because the liquid cryogen used to cool the metal drum does not need to be sterile and the cooling rate of TFF can be more easily controlled (Engstrom et al., 2008). Furthermore, spray characteristics in SFD or SFL are more complicated to control than drop characteristics during TFF. TFF allows for the processing of more concentrated, viscous protein solutions because they do not need to be atomized. TFF has close to 100 % yield while that of SFD is about 80 % (Engstrom et al., 2008). Powders produced by TFF follow a similar surface area and stability trend as SFL powders due to their similar cooling rates and relatively low air-liquid interface (Engstrom et al., 2008). TFF is a promising technique for the formulation of biologics as powders.

2.2 Modeling the TFF process

The cooling rate of cryogenic techniques is one of the main parameters that contributes to the final powder characteristics. As water freezes, liquid channels are formed between frozen molecules, with thinner channels minimizing collisions between particles (e.g., proteins), therefore preventing particle growth. During freezing, the viscosity of these channels increases, also contributing to slowed particle growth. If sugars are included as carriers, the viscosity will be further increased (Engstrom et al., 2008). Generally speaking, the slower the cooling rate, the fewer the nucleated ice domains, leading to thicker channels and more collisions and protein aggregation. A slower cooling rate also leads to phase separation, which can cause crystallization of the active ingredient (Overhoff et al., 2009). However, there is a point at which loss of protein activity can be attributed to a fast cooling rate (Overhoff et al., 2009). Therefore, an intermediate cooling rate is favorable. The rate of cooling in SFD, SFL, and TFF was measured for comparison, showing that compared to SFD and SFL, TFF had a slower rate of cooling (i.e., 2×10^2 K/s vs 3.8×10^6 and 7.2×10^3 for SFD and SFL, respectively) (Engstrom et al., 2008). These are all considerably faster than that of shelf FD (~1.7×10^{-2} K/s) (Engstrom et al., 2008). The large difference between SFD and TFF cooling rates has been explained by a two-orders-of-magnitude smaller surface area/volume ratio and 20–30 times larger film thickness of TFF compared to SFD. TFF has a slower cooling rate than SFD and SFL but the cooling rate is sufficiently high to prevent or minimize particle growth. TFF and its intermediate freezing rate may be one of the keys to its optimal powder properties. The solute or suspension concentration and processing temperature are additional variables to consider in the context of cooling rate. A high cooling rate coupled with a supersaturated solute leads to a larger number of smaller and more uniform nuclei that are tightly packed, which helps to limit crystal growth. A lower processing temperature in TFF can lead to a higher degree of supercooling, therefore a larger number of nuclei (Engstrom et al., 2007). The higher degree of supercooling and the larger number of nuclei prevent particle growth during the freezing process, generating smaller ice channels. As shown in **Fig. 1**, smaller ice channels were produced when a lysozyme/mannitol (50:50 w/w) powder (TFF MAN/lysozyme (50:50 w/w)) was manufactured at a lower temperature of –100 °C as compared to at –50 °C. Crystalline TFF voriconazole (VCZ) nanoaggregates with smaller nanoparticle size were also generated by processing at a lower temperature than at a higher temperature (Moon et al., 2019a). In contrast, amorphous TFF tacrolimus brittle matrix powder (TFF TAC) showed larger nanoaggregate structures when the processing temperature was lower (–70 °C versus –130 °C), potentially due to the lack of droplet spreading and higher contact angle at the lower temperature (Sahakijpijarn et al., 2020b).

Engstrom et al. compared the specific surface area (SSA) of lysozyme powders prepared by SFD, SFL, and TFF. At the same lysozyme concentration, the SFD powder exhibited the highest SSA, while the TFF powder had the lowest SSA (**Table 1**) (Engstrom et al., 2008). The high SSA of the SFD powder is related to the extremely rapid cooling rate of SFD. The higher cooling rate results in more

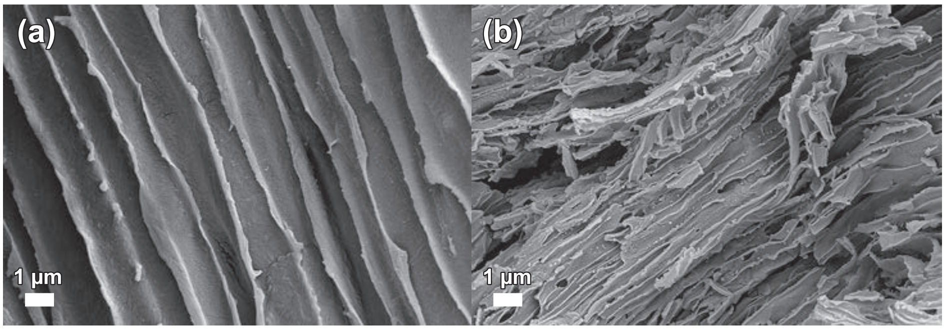

Fig. 1 Representative SEM images of TFF MAN/lysozyme (50:50 w/w) processed at **(a)** –50 °C or **(b)** –100 °C.

Table 1 Specific surface area (SSA) and bulk density of processed and unprocessed drug powders.

Formulation	Process	Specific surface area (m^2/g)	Bulk density (g/mL)	Reference
Tacrolimus unprocessed powder	Unprocessed	0.53	—	(Sinswat et al., 2008)
Tacrolimus	TFF (–70 °C)	42.22 ± 3.02	—	(Sahakijpijarn et al., 2020b)
Tacrolimus/lactose (50:50 w/w)	TFF (–70 °C)	143.13 ± 0.60	—	(Sahakijpijarn et al., 2020b)
Tacrolimus/lactose (95:5 w/w)	TFF (–70 °C)	73.58 ± 5.14	—	(Sahakijpijarn et al., 2020b)
Tacrolimus/mannitol (95:5 w/w)	TFF (–70 °C)	55.79 ± 6.49	—	(Sahakijpijarn et al., 2020b)
Tacrolimus/trehalose (95:5 w/w)	TFF (–70 °C)	57.16 ± 1.96	—	(Sahakijpijarn et al., 2020b)
Itraconazole unprocessed powder	Unprocessed	4.22	—	(Overhoff et al., 2007b)
Itraconazole/hydroxypropyl methylcellulose phthalate (HP55) (1:4 w/w), 2 %w/v	TFF (–60 °C)	19.1	—	(Overhoff et al., 2007b)
Itraconazole/hydroxypropyl methylcellulose phthalate (HP55) (4:1 w/w), 2 % w/v	TFF (–60 °C)	54.2	—	(Overhoff et al., 2007b)
Itraconazole/hydroxypropyl methylcellulose phthalate (HP55) (1:4 w/w), 0.2 % w/v	TFF (–60 °C)	61.8	—	(Overhoff et al., 2007b)
Itraconazole/hydroxypropyl methylcellulose phthalate (HP55) (4: w/w), 0.2 % w/v	TFF (–60 °C)	57.4	—	(Overhoff et al., 2007b)
Voriconazole unprocessed powder	Unprocessed	0.53 ± 0.08	7.86	(Beinborn et al., 2012a)
Micronized voriconazole	Micronization	3.46 ± 0.02	1.20	(Beinborn et al., 2012a)
Voriconazole	TFF (–40 °C)	9.38 ± 3.25	0.45	(Beinborn et al., 2012a)
Voriconazole/mannitol (50:50 w/w)	TFF (–70 °C)	16.3	—	(Moon et al., 2019b)
Voriconazole/PVP K25 (1:3 w/w)	TFF (–40 °C)	43.35 ± 5.67	0.05	(Beinborn et al., 2012a)
Physical mixture of Danazol/povidone K15 (1:2 w/w)	Unprocessed	0.69	—	(Overhoff et al., 2007a)
Danazol/povidone K15 (1:2 w/w)	TFF (–70 °C)	25.93	—	(Overhoff et al., 2007a)
Lysozyme 50 mg/mL	TFF (–100 °C)	31 ± 0.1	—	(Engstrom et al., 2008)
Lysozyme 50 mg/mL	SFL	34 ± 2	—	(Engstrom et al., 2008)
Lysozyme 50 mg/mL	SFD	126 ± 5	—	(Engstrom et al., 2008)
Lysozyme 5 mg/mL	TFF (–100 °C)	73 ± 0.8	—	(Engstrom et al., 2008)
Lysozyme 5 mg/mL	SFL	114 ± 11	—	(Engstrom et al., 2008)
Lysozyme 5 mg/mL	Shelf FD	4.4 ± 0.2	—	(Engstrom et al., 2008)

rapid nucleation and particle growth prevention during freezing. Although TFF produces particles with lower SSA compared to SFD and SFL, the cooling rate of TFF is high enough to prevent particle growth and induce rapid nucleation, thereby still forming particles with relatively high SSA (e.g., 31–73 m^2/g), especially when compared to shelf FD (e.g., 4.4 m^2/g) (**Table 1**, Engstrom et al., 2008). While the cooling rate can affect the SSA to a degree, SFL and SFD have produced lysozyme powders with similar SSAs > 100 m^2/g despite having cooling rates that differ by three orders of magnitude (Engstrom et al., 2007; 2008). The cooling rate had a higher impact on the particle size, as shown by SFL's larger particle size compared to SFD, particularly noticeable in high protein concentration situations (i.e., 50 mg/mL) (Engstrom et al., 2008). Even though TFF had a lower cooling rate, increasing the protein concentration could supersede the cooling rate's impact on the particle size, as TFF powders also had a large particle size at high concentrations. However, at a lower, more relevant protein concentration (i.e., 5 mg/mL), TFF allowed for thinner unfrozen channels with high viscosity, leading to a small particle size.

For TFF, the ability of the droplets to spread upon impact and form films influences the cooling rate, with the droplet spreading time being shorter than the freezing time. Generally, the film thickness is on the scale of 200–400 μm and the diameter is around 10–12 mm (Engstrom et al., 2008). Because the thickness is substantially smaller than the diameter, the radial heat transfer is negligible and the heat transfer is considered to be one-dimensional (Engstrom et al., 2008). Under the assumption of constant thermal diffusivity, the heat transfer can be calculated using the thickness of the film, the temperature of the film, the processing temperature of the drum, and the distance from the top of the spread droplet (Engstrom et al., 2008). Using the heat transfer, the cooling rate can be determined. At 223 K, a 220 μm thick film cooled in 2×10^2 ms with a cooling rate of 3.9×10^2 K/s, for example (Engstrom et al., 2008).

Film diameter was proportional to the droplet diameter and the processing temperature (Engstrom et al., 2008). The processing temperature and parameters that affect the droplet size (e.g., solvent system, drop diameter, drop height) can be tailored for each application. As the processing temperature decreases, the droplet will freeze more quickly, allowing less time for spreading into a film before it becomes solid. While processing lactate dehydrogenase (LDH) protein with TFF, an average film thicknesses of 220 μm was formed at 223 K (–50 °C) and 320 μm was formed at 133 K (–140 °C), respectively. The film thickness was larger when the processing temperature was lower. For comparison, when the small molecule synthetic steroid danazol was prepared using TFF, the resultant film thickness ranged from 100–400 μm (Engstrom et al., 2008).

Infrared imaging was used to study the cooling of thin films prepared from an LDH protein solution. When a film was formed at 223 K, it had a diameter of 12 mm with a smooth edge. The IR camera revealed that the cooling front started at the edge of the film, moving inward. The film came to thermal equilibrium at 1.6 s. When the same film was processed at the lower temperature of 133 K, it had a smaller diameter of 10 mm and a jagged edge, the protrusions of which experiencing the coldest temperatures. In this case, after the cooling front moved inwards, it then reversed direction, causing a longer time of 3 s to reach thermal equilibration. While a low temperature is necessary to cause quick cooling, there is a limitation to how low is favorable. While the edge of the film was thinner and may cool at a different rate than the center of the film, this difference had no impact on the morphology throughout the film (Engstrom et al., 2008).

Thin films prepared by TFF demonstrated that the surface area/volume ratio decreased with an increasing droplet diameter. Once frozen, this ratio was 31–46 cm^{-1}. This is substantially smaller than SFD or SFL (6000 and 600 cm^{-1}, respectively). Loss of protein functionality has been attributed to a high surface area/volume ratio. Alternatively, SFL and TFF have a lower gas-liquid interfacial area than SFD and thus preserve protein functionality better due to their ability to reduce protein adsorption to the interface and thus aggregation (Engstrom et al., 2008).

Several variables describe the droplet spreading, including the density of the liquid (ρ), the impact velocity (V), the droplet diameter (D), and the interfacial tension of the droplet in air (γ). Together, these variables can be used to mathematically describe the droplet spreading, or Weber number (We), by Eqn (1):

$$We = \rho V^2 D/\gamma \quad (1)$$

When We is high (> 30), the droplets spread into a cylindrical film, while when We is low (< 1), the droplets undergo minimal spreading, and the droplets freeze as a spherical dome. These variables can be optimized to a degree: V can be controlled by the drop height, ρ can be controlled through choice of excipients and concentration of all components, and D can be controlled by the gauge of needle through which the droplets are generated. Engstrom et al. compared the typical drop height (H) of 10 cm to a shorter H of 1 cm (Engstrom et al., 2008). When H was 10 cm, the resultant films were cylindrical and the We was found to be 97, while an H of 1 cm yielded spherical domes and the We was 9.8 (Engstrom et al., 2008). A low H also reduced the film diameter (~4 mm) (Engstrom et al., 2008).

Overall, TFF is the optimal cryogenic technique due to its low gas-liquid interfacial area, intermediate cooling rate, sufficient surface area, small particle size, and controllable processing parameters such as temperature.

2.3 Characteristics of TFF powders

2.3.1 Particle morphology

Powder characteristics are generally described by their particle size and the morphology of their nanostructures. The particle size generally refers to the larger micron-ranged structure that is important for adequate aerosolization and lung deposition. The morphology of the nanostructures, however, provides more detailed information about the porosity, surface area, and freezing characteristics of the powder. The particle morphology of powders prepared by cryogenic bottom-up technologies (i.e., starting from drug in solution or suspension) is generally porous. In many cases, small molecule compounds are changed from crystalline to amorphous form after the TFF process, producing a nanostructured brittle matrix (Sahakijpijarn et al., 2020a; 2020b). In the brittle matrix, there are nanoparticles interconnected and agglomerated together as nanostructured aggregates (**Fig. 2(a)**) and are generally irregularly shaped (Sahakijpijarn et al., 2020a). The brittle matrix structure is not only observed in small molecule compounds, but also in the case of biologics, such as lysozyme (Engstrom et al., 2008). **Figs. 2(b)**, **2(c)**, and **2(d)** show the morphology of

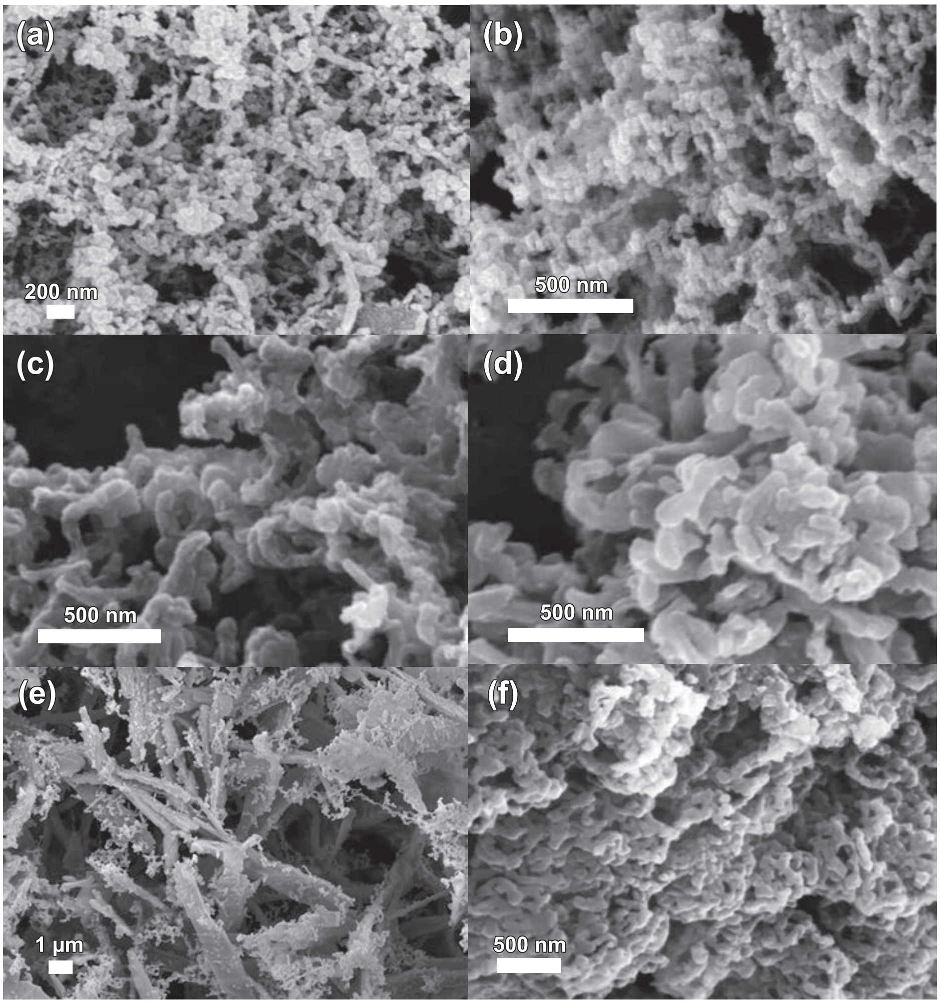

Fig. 2 Particle morphology of particles prepared by cryogenic methods. **(a)** TFF remdesivir with leucine (100 kx) **(b)** TFF lysozyme prepared at –50 °C (60 kx), **(c)** SFL lysozyme (60 kx), **(d)** SFD lysozyme (60 kx), **(e)** TFF VCZ with MAN (20 kx), **(f)** TFF VCZ with PVP K25 (10 kx). Reprinted with permission from **(a)** MDPI: Pharmaceutics (Sahakijpijarn et al., 2020a) **(b)** Springer Nature: Pharm. Res. (Engstrom et al., 2008) **(c–d)** Elsevier: Eur. J. Pharm. Sci. (Yu et al., 2006) **(e)** ACS: Mol. Pharm. (Moon et al., 2019b) and **(f)** Elsevier: Eur. J. Pharm. Sci. (Beinborn et al., 2012a).

lysozyme particles that were prepared by TFF, SFL, and SFD, respectively (Engstrom et al., 2008; Yu et al., 2006).

Among these three techniques, all particles showed similar morphologies. Particle morphology is related to several factors, such as formulation composition, solids content of solutions, solvent, and processing temperature (Moon et al., 2019a; Wang et al., 2014). In addition to the nanostructured brittle matrix, another particle morphology was observed in the case of VCZ. The particle morphology of TFF VCZ combined with mannitol (MAN) was a porous matrix of micron-sized flat irregular-shaped VCZ particles and irregular-shaped mannitol nanoparticles (**Fig. 2(e)**) (Moon et al., 2019b). Atomic force microscopy showed that the VCZ microparticles were packed by VCZ nanoaggregates (150–500 nm) (Moon et al., 2019b). Interestingly, the particle morphology of TFF VCZ combined with povidone K25 (PVP-K25) is a brittle matrix of nanostructured primary particles with a size of approximately 100 nm (**Fig. 1(f)**) (Beinborn et al., 2012a), which is a similar morphology to other brittle matrix powders. The difference in particle morphology of VCZ is related to the crystallinity of VCZ in the formulations. Due to the low glass transition temperature (T_g) of VCZ (1 °C), the inclusion of VCZ with a sufficient amount of a high T_g polymer (e.g., PVP) can inhibit the recrystallization during the drying cycle, resulting in an amorphous structure of VCZ (Beinborn et al., 2012a). In contrast, mannitol, a sugar alcohol, showed no interaction with VCZ, resulting in the crystalline structure of VCZ in TFF VCZ-MAN.

2.3.2 Moisture sorption

Generally, moisture/water sorption depends on the polarity of surface chemical groups and the available surface area (Newman et al., 2008). Although the highly porous nature of particles produced by TFF is beneficial with regard to dispersibility and aerosolization, the high surface area of porous particles can increase the tendency of water sorption compared to unprocessed powder. The hygroscopicity of TFF formulations is also associated with the formulation composition. The formulations that contain a large amount of hydrophilic material can increase the hygroscopicity of the formulations (Sahakijpijarn et al., 2020b). Sahakijpijarn et al. investigated the effect of the amount of lactose (LAC) in the TFF formulations on the moisture sorption, which was determined gravimetrically by dynamic vapor sorption (Sahakijpijarn et al., 2020b). The higher amount of lactose resulted in higher moisture sorption. The moisture sorption of TFF tacrolimus (TAC) formulations containing 0 %, 5 %, and 20 % w/w lactose were 1 %, 2.5 %, and 9 % w/w at 25 °C/80 % relative humidity (RH) (Sahakijpijarn et al., 2020b). According to the hygroscopicity classification of the European Pharmacopoeia, TFF TAC formulations containing lactose are classified as moderately hygroscopic to very hygroscopic, while TFF neat TAC is classified as slightly hygroscopic (Newman et al., 2008). Moreover, mass loss due to surface moisture release during recrystallization was observed in a TAC formulation containing 50 % lactose, but not in other formulations (Sahakijpijarn et al., 2020b).

Another study compared the moisture sorption of different sugar excipients (Watts et al., 2013). The formulations containing lactose and raffinose had more weight gain at > 80 % RH than the formulations containing mannitol without other excipients. Mannitol was crystalline after the TFF process, while lactose and raffinose were amorphous (Watts et al., 2013). Amorphous materials generally tend to absorb moisture more than crystalline materials (Newman et al., 2008). Moreover, the effect of humidity on the aerosolization of low-density microparticles containing different excipients was also investigated. It was reported that water sorption to powder surface can both improve and reduce powder dispersibility. Capillary, electrostatic, and Van der Waals forces are used to describe the cohesive forces in powders, which play a major role in powder dispersibility (Watts et al., 2013). Capillary force is a predominant force at > 60 % RH, while electrostatic adhesion force is a predominant force at low humidity (Watts et al., 2013). In lactose-based formulations, high humidity increased the plasticity of the brittle matrix, thereby reducing the aerosol performance of the formulations. However, in mannitol-based formulations, moisture can improve the powder dispersibility due to a reduction in electrostatic charge (Watts et al., 2013).

2.3.3 Aerodynamic properties

TFF powders have been investigated for pulmonary drug delivery using dry powder inhalers (DPIs). The powder should have an appropriate mass median aerodynamic diameter (MMAD) in the range of 1–5 μm to maximize the delivery of the drug particles to the deep lungs. Powder dispersibility is controlled by the particle cohesive forces, which are related to contact area and separation distance between particles (Weers, 2000). The highly porous, low-density particles with a large geometric particle diameter, characteristics unique to the morphology of TFF powders, demonstrate superior powder dispersibility, as they have higher inter-particle separation distance, less contact area, and lower interparticle cohesive forces compared to the traditional micronized (e.g., milled) powder (Sahakijpijarn et al., 2020b). The highly porous and low-density brittle matrices can be aerosolized and dispersed to small particles of the same structure and density by the inhalation force through a passive DPI (Watts et al., 2013).

The aerodynamic properties of TFF formulations are dependent on the properties of the powder, which are influenced by formulation compositions and processing parameters. Excipients, such as sugars, are typically used to improve the dispersibility of dry powder formulations (Chen et al., 2016). Lactose is widely used as an excipient in FDA-approved inhaled products, while other sugars (e.g., trehalose, sucrose) and amino acids (e.g., leucine, trileucine) have recently gained more interest for pulmonary delivery (Pilcer and Amighi, 2010). Mannitol has been approved in ARIDOL™ for the assessment of bronchial hyperresponsiveness due to its induction of bronchoconstriction (Pharmaxis, 1964; Sahakijpijarn et al., 2020c). In many cases, TFF formulations containing an optimal amount of excipient exhibited high aerosol performance. Beinborn et al. compared the aerosol performance of TFF VCZ with micronized VCZ. The blended powder of inhalation grade, micronized VCZ and lactose (Inhalac® 70, 2 % w/w) exhibited 19.6 % fine particle fraction (FPF) and an MMAD of 2.7 μm when it was emitted from a Handihaler® at 60 L/min. Although TFF neat VCZ exhibited a larger MMAD (4.2 μm), the FPF was about two times higher compared to micronized VCZ and the MMAD was in the acceptable range (Beinborn et al., 2012a).

The effects of the type and amount of excipient and the drug loading on the aerosol performance were investigated in several studies. The drug loading and type of excipients were optimized to maximize the respirable dose for pulmonary delivery (Sahakijpijarn et al., 2020a). It was reported that TFF remdesivir combined with leucine had a larger FPF and smaller MMAD for the whole range of drug loading of remdesivir (20–80 % w/w) (Sahakijpijarn et al., 2020a). The formulations containing 80 % remdesivir with 20 % of different excipients (e.g., Captisol®, mannitol, lactose, leucine) showed good aerosol performance with FPFs ranging from 64.21–82.71 % and MMADs ranging from 2.17–2.53 μm (Sahakijpijarn et al., 2020a). The aerosol performances of formulations containing 95 % TAC with the combination of 5 % w/w lactose, mannitol, or trehalose were compared at 60 L/min using a Plastiape RS01 high resistance inhaler (Sahakijpijarn et al., 2020b). Lactose-based formulations exhibited higher FPFs and smaller MMADs compared to mannitol- and trehalose-based formulations (Sahakijpijarn et al., 2020b). Additionally, it was reported that there was no significant difference in aerosol performance when the drug loading of TFF TAC formulations was increased from 60 % to 95 % w/w (Sahakijpijarn et al., 2020b). This indicates that the drug loading of TAC can be increased up to 95 % while maintaining optimal aerosol performance (69.31 % FPF, 2.61 μm MMAD) (Sahakijpijarn et al., 2020b). Another study from Moon et al. investigated the drug loading and the amount of mannitol in TFF formulations. When the drug loading of VCZ was increased from 50 % to 97 % w/w, the FPF increased from 28.5 % to 40.8 % (Moon et al., 2019b). The small amount of mannitol in TFF VCZ formulations functioned as a surface texture modifier, which can minimize the cohesive and adhesive forces between particles, and subsequently, improve the aerosol performance (Moon et al., 2019b). According to these cases, particles prepared by TFF are aerosolizable with a small amount of excipient needed in the formulation, providing the potential of TFF to prepare high drug loading formulations for pulmonary delivery of drugs requiring a high dose, which can also lower the powder burden for the patient. For large molecules such as nucleic acid-based molecules and proteins, however, increasing the drug loading in the final dry powders to a certain level can lead to a reduction of the aerosol performance properties of the dry powders (unpublished data), likely due to an increase in particle cohesive forces.

2.3.4 Stability, molecular interactions, and miscibility

The stability of TFF powders was investigated in several studies. It is well reported in literature that a crystalline form is more stable than its amorphous counterpart. For example, VCZ/MAN (95:5 w/w) crystalline nanoaggregates prepared by TFF were physically and chemically stable after storage at 25 °C/60 % RH for up to 13 months (Moon et al., 2019b). The MMAD and FPF of TFF VCZ/MAN (95:5 w/w) did not change statistically after the storage (Moon et al., 2019b). In the case of amorphous drugs, TFF TAC/LAC (95:5 w/w) was chemically and physically stable after storage at 25 °C/60 % RH and 40 °C/60 % RH for up to 6 months without the need of a stabilizer (Sahakijpijarn et al., 2020b). The moisture content of powder affected the aerodynamic properties and physical properties of formulations after storage. For example, when TFF TAC/LAC (95:5 w/w) powder was encapsulated in #3 hydroxypropyl methylcellulose (HPMC) capsules and stored in a borosilicate glass vial without desiccant, there was an increase in moisture content during storage, which led to a decrease in SSA and MMAD (Sahakijpijarn et al., 2020b). Since amorphous materials are generally susceptible to water plasticization, moisture on the particle surface resulted in a reduced brittle fracture and increased particle density due to the collapse of the brittle matrix structure (Watts et al., 2013). The changes in particle morphology and powder properties had detrimental effects on the aerodynamic properties, as the powder showed a significant decrease in FPF and emitted fraction (EF) and increase in MMAD (Sahakijpijarn et al., 2020b). However, the stability results suggested that a tightly closed container with desiccant helps to maintain and minimize the changes in the aerodynamic and physical properties of TFF powder (Sahakijpijarn et al., 2020b). When TAC/LAC (95:5 w/w) powder was dried to remove additional moisture absorbed during capsule filling and packing and then stored in a sealed glass container with desiccant, the physical and aerodynamic properties of encapsulated powder did not significantly change over 6 months stored at 25 °C/60 % RH and only slightly changed over 6 months stored at 40 °C/60 % RH (Sahakijpijarn et al., 2020b).

In the case of biologics, Thakkar et al. investigated the stability of a protein subunit vaccine dry powder prepared by TFF (Thakkar et al., 2017). It was reported that the particle size distribution of reconstituted ovalbumin-absorbed aluminum hydroxide dry powder prepared with 2 % w/v trehalose did not significantly change after one month of storage at RT, 30 °C, and 40 °C. After 3 months of storage at 40 °C, particle aggregation was slightly detected, but was not found at other storage temperatures. However, noticeable amounts of particle aggregates were detected after 6 months of storage at RT, 30 °C, and 40 °C, due to the visible buildup of moisture in the vials. The ovalbumin-aluminum hydroxide vaccine powders were reconstituted after storage at various temperatures for 1 or 3 months and were used to immunize mice. Importantly, there was no significant difference in the anti-ovalbumin IgG levels among mice that were immunized with freshly prepared ovalbumin-adsorbed aluminum hydroxide liquid vaccine or with the TFF vaccine powders after 3 months of storage at the different temperatures. The T_g (~120 °C) of the ovalbumin-adsorbed aluminum hydroxide dry powder prepared by TFF was higher than the storage temperatures (i.e., RT, 30 °C, and 40 °C), allowing the vaccine powder to remain chemically, physically, and immunogenically stable at all temperatures up to 3 months (Thakkar et al., 2017). These samples were stored in a desiccator, but not individually packaged in sealed pouches. With optimal storage conditions, they would remain stable for a longer period of time. This study showed the advantage of TFF in producing a biologic powder that is stable when stored for an extended period of time without a requirement for cold chain (Thakkar et al., 2017).

The interaction between a drug and an excipient with a high T_g generally improves the physical stability of amorphous solid dispersions of small molecule drugs, as well as the stability of biologics. The interaction between drug and excipient can increase the T_g of the system, resulting in a less molecularly mobile glassy state. In some cases, however, the interaction is not necessary to stabilize the drug. For example, TAC, a high glass-forming ability drug (GFA class III), showed no interaction with LAC analyzed by ssNMR (Sahakijpijarn et al., 2020b). Although two T_gs were detected by DSC, indicating TAC and LAC were not molecularly dispersed, the analysis of domain size by ssNMR showed that the two compounds had good miscibility at a domain size of ~100 nm (Sahakijpijarn et al., 2020b). Despite phase separation and lack of interactions, TAC was physically stable, remaining amorphous after storage at 40 °C/75 % RH for 6 months in a sealed container and after exposure to 40 °C/75 % RH for 28 days in an open container (Sahakijpijarn et al., 2020b).

2.3.5 Solubility and dissolution

The enhanced dissolution of a drug in a TFF formulation is generally associated with the brittle matrix nature of TFF powders, and the matrix consists of the amorphous forms of the drug and the excipient. A dissolution test showed that TAC combined with lactose (5 % w/w) released a higher amount of drug within 6 hours compared to the physical mixture of unprocessed TAC and lactose (~85 % and ~30 % drug release, respectively) (Sahakijpijarn et al., 2020b). The drug loading and the amount of lactose in the formulation did not affect the rate and extent of drug release, as there was no difference in dissolution profiles between TFF TAC/LAC (50:50 w/w), TFF TAC/LAC (95:5 w/w), and TFF neat TAC (Sahakijpijarn et al., 2020b; Sinswat et al., 2008). The enhanced dissolution of TFF TAC formulations was associated with the enhanced solubility of the amorphous form of TAC. The amorphous form of a drug generally exists in a higher free energy state than its crystalline counterpart, thereby enhancing its solubility and dissolution rate (Trasi et al., 2017). It was reported that the solubility of amorphous TAC was 35-times higher than its crystalline solubility (Trasi et al., 2017). In another study, the dissolution of TFF remdesivir formulations containing different excipients (i.e., Captisol®, mannitol, lactose, and leucine) was compared with the dissolution of TFF neat remdesivir and unprocessed remdesivir (Sahakijpijarn et al., 2020a). All TFF remdesivir formulations exhibited faster and higher dissolution of remdesivir than unprocessed remdesivir (Sahakijpijarn et al., 2020a). Similar to the TAC case, the increased dissolution rate and extent of remdesivir release are also related to the higher solubility of amorphous remdesivir, compared to crystalline remdesivir (Sahakijpijarn et al., 2020a).

In several cases, the presence of a polymer as an excipient in a TFF formulation not only increases the rate and extent of dissolution, but also enhances and prolongs the supersaturated dissolution. The concentration (C) of drug dissolved in the media divided by the equilibrium solubility (C_{eq}) of the crystalline form yields the degree of supersaturation (C/C_{eq}) (Overhoff et al., 2008; Yang et al., 2008). Yang et al. reported that the colloidal dispersion of TFF itraconazole (ITZ)/MAN/lecithin (1:0.5:2 w/w/w) had a C/C_{eq} of 22-times at 5 min and the highest value of 27-times at 15 min in lung simulated fluid (Yang et al., 2008). After 3 h, the supersaturated ITZ concentration of TFF ITZ/MAN/lecithin started to decrease to about 7-times, while the physical mixture only reached 2-times at 15 mins and gradually decreased to a plateau of C_{eq} after 2 hours (Yang et al., 2008). For oral drug delivery, Overhoff et al. investigated the in vitro supersaturation dissolution of a TFF tacrolimus-sodium dodecyl sulfate formulation (TFF TAC-SDS) and the commercial tacrolimus capsule, Prograf®, in the two-stage dissolution test in acidic conditions. It was reported that TFF TAC-SDS exhibited a higher degree of supersaturation than Prograf® after 2 hours (17-times C/C_{eq} versus 14-times C/C_{eq}, respectively). Upon a pH shift from 1.2 to 6.8, the TFF TAC-SDS also exhibited an increase in supersaturation level from 17-times to 22-times at 15 min after the pH shift, while Prograf® did not maintain a high degree of supersaturation and started to precipitate out immediately after the pH shift. Although the degree of supersaturation gradually decreased to 2.5-times C/C_{eq} at 24 h after the pH shift, the area under the dissolution curve (AUC) of the TFF TAC-SDS was higher than that of Prograf® under acidic and pH-shift conditions (Overhoff et al., 2008).

A benefit of formulating proteins as powders as opposed to liquids is that powders are not limited by the solubility of the protein in the dose (Johnson, 1997). The solubility of proteins is directly related to adsorption at the air-liquid interface and aggregation. Techniques that expose proteins to a high liquid interfacial area (e.g., SD, SFD), often require the use of additional excipients, such as cyclodextrins (Ramezani et al., 2017), surfactants (Bhatnagar B. and Tchessalov., 2020), ethanol (Johnson, 1997), or the utilization of acidic conditions (Liu et al., 1991). These excipients may also be necessary to modulate the dissolution of the protein. SFD bovine serum albumin (BSA) protein with or without trehalose was encapsulated in poly(D,L-lactide-*co*-glycolide) (PLG) or PLG/poloxamer microspheres (Carrasquillo et al., 2001). Within 4 h in phosphate-buffered saline (PBS) at 37 °C, SFD BSA/PLG and SFD BSA-trehalose/PLG released > 80 % of the protein, while the inclusion of poloxamer (1:20 and 1:1 PLG/poloxamer) extended the release over 1–2 days (Carrasquillo et al., 2001). Finally, due to their high porosity and high SSA, dry powders of biologics, such as vaccines, prepared by TFF can often rapidly dissolve upon contact with a diluent without any agitation, which is advantageous if there is a need to reconstitute a TFF dry powder. Of course, one can expect that TFF dry powders can readily dissolve in lung fluid once delivered into the lung.

2.4 Formulation and device considerations

2.4.1 Solids content

A few characteristics of TFF powders are affected by solids content, the total amount of solids dissolved or suspended in the liquid (e.g., active ingredient, carriers, other excipients). In terms of aerodynamic properties, a feeding solution with less solids content generally produces more aerosolizable powders. When a comparison of TFF VCZ nanoaggregates was made between 1 % and 3 % (w/v) solids content, 1 % was associated with a higher FPF of 67.5 % compared to 48.5 % at 3 % (Moon et al., 2019a). However, in some cases with an amorphous TFF brittle matrix powder, different solids content does not present significantly different aerodynamic properties (Sahakijpijarn et al., 2020a; 2020b) or a higher solids content actually produces improved aerosol properties (Beinborn et al., 2012b). The solids content can also influence the SSA. High-potency, amorphous TFF TAC powders resulted in about a 50 % larger SSA when the solids content was 0.75 % (w/v), as compared to 2.5 % (w/v) (Sahakijpijarn et al., 2020b). However, crystalline TFF VCZ powders did not show different SSAs when the solids content varied from 0.1 to 10 % (w/v) (Beinborn et al., 2012b).

In addition to aerodynamic properties and SSA, the solids content is also an important parameter for manufacturing with regard to scale up. The formulations developed by TFF are currently beginning Phase II clinical trials. When a large amount of TFF powders, on the scale of multi-kilograms, is necessary, higher solids content will reduce the total manufacture time of the powders.

2.4.2 Solvent system

Solvent systems used for TFF can significantly affect amorphicity, morphology, and aerosol performance. Beinborn et al. showed that TFF VCZ-PVP K12 (1:2 w/w) and TFF VCZ-PVP K30 (1:2 w/w) prepared with 1,4-dioxane as a solvent were amorphous (Beinborn et al., 2012b). However, when binary solvent systems of 1,4-dioxane and water (50:50 or 20:80 v/v) were used for these compositions, both formulations were crystalline (Beinborn et al., 2012b).

When a binary solvent system of water and acetonitrile is used for TFF, cryo-phase separation of the solvent system must be considered. A mixture of water and acetonitrile phase-separates during the freezing if 35–88 % (v/v) acetonitrile is included in the mixture (Zarzycki et al., 2006). When this cryo-phase separation occurs, a different morphology of powder formulations can be observed (Moon et al., 2019a). The mixture of water and acetonitrile not only impacts cryo-phase separation, but also affects the aerosol performance. In the case of TFF VCZ nanoaggregates, the higher portion of water included in the binary solvent system of water and acetonitrile enhanced aerodynamic properties with higher FPFs and smaller MMADs (Moon et al., 2019a).

2.4.3 Excipients

Carrier sugars are the most common excipients in the preparation of powders. Sugars raise the viscosity of the liquid thus slowing particle growth during rapid freezing. Sugars can also enhance the stability. Inclusion of a sugar in the formulation can help water vitrify at a lower cooling rate, meaning the higher cooling rate of SFD and SFL are not necessary.

In general, the characteristic porous particles prepared by TFF have high SSA and low bulk density. As shown in **Table 1**, the bulk density of TFF neat VCZ powder is 17-fold and 2.7-fold lower than that of unprocessed VCZ and micronized VCZ powder, respectively. Similarly, the SSAs of powders processed by TFF with or without an excipient were 4-times higher than unprocessed neat drug powder (**Table 1**). Without excipient, TFF neat VCZ showed lower SSA than TFF neat TAC (Beinborn et al., 2012a; Sinswat et al., 2008), which is related to the crystallinity and the unique morphology of VCZ nanoaggregates. The inclusion of sugars can further improve the SSA of TFF powders and is variable depending on the type and amount of sugar used. At 95 % drug loading, TFF TAC formulations that contained 5 % lactose (w/w) exhibited higher SSA compared to other formulations that contained 5 % w/w mannitol or 5 % trehalose (Sahakijpijarn et al., 2020b). A TFF TAC formulation containing 50 % w/w lactose showed a higher SSA than a TFF TAC formulation containing 5 % w/w lactose (Sahakijpijarn et al., 2020b).

In contrast, the effect of the amount of polymer as an excipient on SSA is not the same as that of sugar excipients (Overhoff et al., 2007b). At 2 % w/w solids content, TFF ITZ formulations containing 80 % w/w hydroxypropyl methylcellulose phthalate (HP55) resulted in lower SSA than the formulation containing 20 % HP55 (Overhoff et al., 2007b). However, at lower solids content (0.2 % w/w), there was no significant difference in SSA between these two formulations (Overhoff et al., 2007b). The higher level of polymer in the solution can prevent the formation of nanoparticles (Overhoff et al., 2007b), which produce a larger and less brittle structure. Overall, SSA is influenced by several parameters, including type of excipient and excipient loading, processing temperature, solids content, and solvent system composition.

2.4.4 Drug loading

The degree of drug loading in TFF powders can influence the particle morphology, but potentially less so if the powder is an amorphous brittle matrix (Sahakijpijarn et al., 2020a; Sahakijpijarn et al., 2020b). However, in the case of crystalline TFF VCZ nanoaggregates, different drug loadings significantly affected particle morphologies

(Moon et al., 2019b). TFF VCZ showed crystalline nanoaggregates when processed with mannitol as a single excipient, which was phase-separated from VCZ (Moon et al., 2019b). While VCZ exhibits as nanoaggregates that are a few micrometers in size, mannitol exhibits as a brittle matrix powder that consists of particles that are smaller than 150 nm (Moon et al., 2019b). As a result of the different morphologies of these two phase-separated crystalline ingredients, a different ratio of VCZ and mannitol resulted in significantly different particle morphologies (Moon et al., 2019b). More interestingly, due to generating small mannitol nanoparticles, when VCZ loading is high (i.e., 90–97 %), the phase-separated mannitol nanoparticles reside on the flat surface of VCZ nanoaggregates and act as a surface modifying agent (Moon et al., 2019b). This reduces cohesive and adhesive energy of VCZ particles and enhances the aerodynamic properties of the powder.

Amorphous, brittle matrix TFF powders do not show different morphologies with different levels of drug loading; however, the aerodynamic properties of these powders still depend on drug loading for certain excipients and drugs. For TFF TAC with lactose, 70–80 % (w/w) TAC loading resulted in the highest FPF at the solids content of 0.75 % (w/v) (Sahakijpijarn et al., 2020b). In the case of TFF-remdesivir with Captisol®, the powders with higher drug loading aerosolized better than those with lower drug loading (Sahakijpijarn et al., 2020a). In contrast, the higher drug loading resulted in less aerosolizable TFF-remdesivir powders with leucine, showing larger MMADs and lower FPFs. However, when TFF-remdesivir was formulated with mannitol or lactose, 50 % and 80 % (w/w) drug loading exhibited similar FPF.

2.4.5 Loading dose and delivery device

The loading dose can also affect the aerosol performance. The aerosol properties of TFF VCZ nanoaggregates were tested and compared with high resistance RS00 and RS01 Plastiape devices (Moon et al., 2019a). When TFF-VCZ nanoaggregates were filled into #3 HPMC capsules with 10, 15, or 20 mg, the high resistance RS00 Plastiape device provided more consistent and enhanced aerosol performance within these filling ranges. While FPF and MMAD were not significantly different between the three doses, the 20 mg dose, with the capsule completely full, presented slightly lower aerosol properties than either the 10 or 15 mg dose.

The type of device used to deliver dry powder formulations is selected for its influence on its aerosol performance. While TFF powder formulations exhibit aerodynamic properties that are independent of flow rate, they are still affected by the type of resistance and device (Moon et al., 2019a; Sahakijpijarn et al., 2020b). The high dose TFF TAC brittle matrix powder demonstrated consistent MMAD and FPF in the range of flow rates between 30 and 60 L/min, which represented 1 and 4 kPa pressure drop, respectively, with a high resistance RS01 Plastiape device. However, when the same TFF TAC was aerosolized using a low resistance RS01 Plastiape device, it was less aerosolizable and relied more on flow rate compared to high resistance RS01 Plastiape device (Sahakijpijarn et al., 2020b). Interestingly, in the case of TFF VCZ nanoaggregates, both low resistance RS00 and RS01 Plastiape devices exhibit excellent aerosol properties (Moon et al., 2019a). Low and high resistance RS00 Plastiape devices perform better than the corresponding low and high resistance RS01 Plastiape devices. The most flow rate independent device for TFF-VCZ nanoaggregates was the high resistance RS00 Plastiape device, which creates smaller holes in the capsule shell wall, likely facilitating deaggregation the TFF nanoaggregates.

3. Applications of TFF: formulation of proteins as powders for pulmonary delivery

3.1 The need for pulmonary delivery of proteins into the lungs

Within the class of proteins, there are various types that have their own unique characteristics. Several proteins have been studied for delivery via the pulmonary route as dry powders: proteins (e.g., insulin, calcitonin, BSA), enzymes (e.g., dornase alpha, LDH, lysozyme), and antibodies (e.g., anti-IgE). The category of antibodies also includes antibody fragments and nanobodies. Antibody fragments typically consist of either the antigen binding fragment (Fab) or crystallization fragment (Fc). One type of antibody fragment is a domain antibody fragment (dAb), which is the smallest functional antigen-binding region of antibodies and are derived from a single variable region of either the light (V_L) or heavy (V_H) chain (Holt et al., 2003; Proudfoot et al., 2018). Antibody fragments can be more susceptible to aggregation after freeze-thawing than full length antibodies (Wang et al., 2007). However, due to their small size, they may have enhanced tissue penetration and are relatively easier to manufacture (Nelson, 2010). Nanobodies are proteins derived from heavy-chain only antibodies (HCAb) found in Camelidae and are about one tenth the size of an antibody. Finally, many vaccines are protein-based. Protein therapeutics continue to become more and more complex (e.g., antibody-drug conjugates) and will require much care when developing them as more stable powders (Bodier-Montagutelli et al., 2018) .

Protein-based therapeutics are often administered by parenteral routes, such as intravenous, subcutaneous, or intramuscular injection. There is a need to deliver some protein-based therapeutics directly to the lungs, largely due to their low distribution to the lungs when administered systemically, which means high doses are required to achieve adequate lung distribution. For example, Guilleminault et al. explored the delivery of cetuximab, an anti-epidermal growth factor receptor (EGFR) antibody, via aerosolization into the lungs for the treatment of lung cancer. In mice with orthotopic lung tumors, aerosolization of cetuximab in solution achieved substantially better delivery of cetuximab to the lung tissues as compared to intravenous administration, which led to a higher dose of cetuximab distributing to the tumors in the lung (i.e., up to 4-fold higher as compared to intravenous injection at 2 h) (Guilleminault et al., 2014). Similar studies and results were produced by Maillet et al. (Maillet et al., 2011). In fact, two proteins have been approved for delivery via the pulmonary route, including insulin for the treatment of diabetes (i.e., for systemic distribution) and dornase alpha, or Pulmozyme, a solution of recombinant human deoxyribonuclease indicated for reducing lung infections and improving lung function in patients with cystic fibrosis (i.e., for local lung distribution). Lungs have a high degree of vasculature, high surface area, thin epithelium, high permeability for large molecules, and fewer enzymes and higher pH compared to the gastrointestinal tract (Liang et al., 2020). The respiratory route is also less invasive (i.e., does not require a needle puncture or a trained health professional), has a faster onset of action, and minimizes systemic toxicity compared to the parenteral routes (Johnson, 1997).

3.2 The need for dry powder formulation of proteins for pulmonary delivery

Many medications are delivered to the lungs via nebulization, which is the aerosolization of liquid preparations and direct inhalation of the mist/aerosols into the lungs. Formulations for nebulization are prepared and stored in a liquid state, which is not ideal for proteins. Proteins are generally less stable in a liquid formulation than in a dry powder, and nebulization exposes proteins to harsh conditions, including shear stress and high temperatures exiting the device (Bodier-Montagutelli et al., 2018) and a high air-liquid interfacial area, causing aggregation (Wang et al., 2007). The percent of functional LDH was measured to be $< 6\ \%$ after nebulization and could only be improved to 62 % with the use of a protectant (e.g., Tween 80, chitosan) (Albasarah et al., 2010). The most common nebulization device is the vibrating-mesh nebulizer because of its ability to deliver relatively high doses while being less destructive than ultrasonic or jet nebulizers (Lightwood et al., 2013; Maillet et al., 2008). Liquid formulations for nebulization can, and typically must, be customized for the specific molecule and often require the use of a surfactant (e.g., polysorbate, polyethylene glycol) or other stabilizer (Bodier-Montagutelli et al., 2018) and organic solvents, which can be toxic to the lungs. Solubility of the formulation excipients also limits how concentrated the dose can be, meaning a large dose may be necessary (Johnson, 1997). Furthermore, nebulizer devices are less convenient for the patient, and they often cannot be as easily transported compared to DPI devices. Administration of a nebulized protein usually requires several minutes of inhaling the aerosol. For example, Pulmozyme, when administered with the eRapid® Nebulizer system, should be inhaled for 1–5 minutes (Genentech, 2018). This is in contrast to a DPI, which can deliver a full dose in a few seconds as a bolus. There are benefits to nebulization, however, such as fewer manufacturing steps (e.g., no drying) (Bodier-Montagutelli et al., 2018), but the overall aerosol performance of nebulizers is worse than DPI devices. For example, tobramycin PulmoSphere dry powder administered via a DPI exhibited an emitted dose of 78.3 %, delivering 34.3 % of the total dose to the lungs, while the nebulized tobramycin product emitted 39.4 % of the dose, delivering only 5.0 % of the dose to the lungs (Newhouse et al., 2003). The nebulized dose had to be administered for 15 min (Newhouse et al., 2003). Preparing proteins as powders for delivery to the lungs can enhance aerosol performance as well as the storage stability of them. Aggregation also occurs in lyophilized powders, however, it can be minimized by inclusion of protectants (Yu et al., 2006).

Only a few protein-based therapeutics developed for pulmonary delivery have been formulated as powders. Human growth hormone (22 kDa protein) SD powder, infliximab (149 kDa antibody) SD powder, and influenza subunit vaccine (225 kDa protein) SD and SFD powders are in preclinical development (Liang et al., 2020). The influenza subunit vaccine SD and SFD powders were found to have FPFs of 37 % and 23 %, respectively (Saluja et al., 2010). A few are in the clinical development stage. For example, Novartis is developing CSJ117, anti-thymic stromal lymphopoietin (46 kDa antibody fragment), as a dry powder for inhalation. They report having completed a phase I trial in 2019, administering CSJ117 with a Concept1 single dose DPI to adult patients with mild, atopic asthma (NCT03138811). CSJ117 was well tolerated and reduced allergen-induced bronchoconstriction compared to placebo (Gauvreau et al., 2020). Recruitment for a phase II trial in adult patients with severe, uncontrolled asthma began in 2020 (NCT04410523). UCB Pharma designed VR942, a dry powder formulation of an anti-IL-13 antibody fragment, also known as CDP7766. A phase I clinical trial was conducted in 2018 with a Multidose F1P DPI showing that it was well tolerated for up to 10 days and achieved inhibition of fractional exhaled nitric oxide (FeNO) as a secondary outcome (Burgess et al., 2018). Patents can be found detailing the Novartis and UCB Pharma products, but it is difficult to determine which formulations were used in clinical trials and their corresponding aerosol properties (Morgan et al., 2019; Rondeau et al., 2017). DAS181, or Fludase® is a 46 kDa sialidase fusion protein in phase 1/II trials for parainfluenza by Ansun BioPharma (Zenilman et al., 2015). It is a dry powder delivered by the Cyclohaler® DPI and its desired site of action is the central/upper respiratory tract and thus is designed to have an FPF of around < 10 % and MMAD 3–8 μm (Malakhov and Li, 2014). Insulin is a small protein (5.7 kDa) that is used to treat diabetes mellitus. Two insulin dry powders for inhalation products, Afrezza® by MannKind and Exubera® by Pfizer, were approved and commercialized. Exubera® was ultimately discontinued due to patient and provider dissatisfaction (Heinemann, 2008).

We have experimental evidence that TFF can be applied to prepare dry powders of proteins or protein-containing products while maintaining the activity of the proteins, and the resultant dry powders have excellent aerosol properties for lung delivery and can be potentially stored without cold chain.

3.3 Protein dry powders engineered using TFF technology

Over the years, we have successfully applied TFF technology to prepare dry powders of proteins and protein-containing products such as vaccines (Engstrom et al., 2008; Li et al., 2015; Moon et al., 2016; Thakkar et al., 2017). We have shown that protein dry powders prepared by TFF maintain their functional activity, have good aerosol performance properties, and have improved thermostability for potential cold chain-free storage.

For example, LDH was formulated into powders with trehalose (1:120, w/w) as a carrier using shelf FD, SFD, SFL, and TFF. For all except SFD, the activity of LDH in the dry powders was 97–100 %, whereas SFD produced an LDH powder with only 74–85 % activity (Engstrom et al., 2008). Around 20–30 % of protein was adsorbed to the gas-liquid interface in SFD, explaining the decrease in the activity of the LDH (Engstrom et al., 2008). Lysozyme at 5 mg/ml or 50 mg/ml was also formulated into powders using SFD, SFL, and TFF. Lysozyme powder prepared by shelf FD at 5 mg/ml showed an SSA of 4.4 ± 0.3 m^2/g (**Table 1**). Lysozyme powder produced via TFF at 5 mg/ml had a high SSA (i.e., 45–73 m^2/g) (**Table 1**, Engstrom et al., 2008). SFD can produce a powder with an even larger SSA (i.e., 126 m^2/g vs. 31–55 m^2/g for TFF at 50 mg/ml) (**Table 1**, Engstrom et al., 2008). As mentioned earlier, **Figs. 2(b)**, **2(c)**, and **2(d)** show the morphology of the lysozyme particles that were prepared by TFF, SFL, and SFD, respectively (Engstrom et al., 2008; Yu et al., 2006). All particles showed similar morphologies. Increasing the protein concentration from 5 to 50 mg/mL deceased the submicron particle fraction from 81–92 % to 62–66 %. The high concentration also produced more micron-sized particles, likely due to a higher degree of collisions contributing to particle growth, but 5 mg/mL is more clinically relevant (Engstrom et al., 2008). TFF and SFL produced similar morphologies when powders were examined by SEM, with the particle size increasing with decreasing freezing temperature. Again, the particle size was increased when the protein concentration was increased. SFD was able to form smaller particles than SFL and TFF.

Lysozyme dry powders were also prepared by TFF with mannitol as the excipient (50:50, w/w), and the resultant dry powders showed excellent aerosol properties, with MMAD values within the range of 1–5 μm and FPF up to 65 % (**Table 2**). As mentioned earlier, increasing the solids content in the lysozyme solution, from 1 % to 10 %, led to a reduction in the FPF.

Finally, dry powders of proteins or protein-containing products prepared by TFF also have excellent thermostability. As mentioned earlier, Li et al. reported that vaccines containing protein as antigens and an insoluble aluminum salt as an adjuvant can be readily transformed from liquid suspension into a dry powder without causing aggregation of the protein-adsorbed aluminum salt microparticles or a decrease in the immunogenicity of the antigen proteins following reconstitution of the dry powders (Li et al., 2015). Due to the presence of the aluminum salt particles in the vaccines, the vaccines may not be subjected to accidental slow freezing during distribution and storage, because slow freezing causes particle aggregation and loss of vaccine activity. Also, the protein antigens in the vaccines are generally unstable at high temperatures (e.g., RT). Therefore, vaccines containing aluminum salts as adjuvants must be kept in cold chain conditions (2–8 °C). The vaccine dry powders prepared by TFF are not sensitive to repeated slow freezing and thawing anymore. More importantly, a model protein antigen-based vaccine adjuvanted with aluminum oxyhydroxide that lost nearly all its immunogenicity after 3 months of storage at even 4 °C as a liquid did not show any significant immunogenicity decrease after it was stored as a TFF powder at 40 °C for 3 months (Thakkar et al., 2017).

TFF is a technology that enables the engineering of dry powder formulations of protein-based therapeutic products and the resultant dry powders have good aerosol

Table 2 Aerosol performance properties of MAN/lysozyme TFF powders (Moon et al., 2016).

Formulation	MMAD (μm)	GSD (μm)	FPF (%)
MAN/lysozyme 50:50 (w/w) TFF 1 % (w/v)	2.820	3.864	65.029
MAN/lysozyme 50:50 (w/w) TFF 5 % (w/v)	3.913	3.552	40.478
MAN/lysozyme 50:50 (w/w) TFF 10 % (w/v)	3.546	2.825	34.150

properties and thermostability. Of course, even within dry powder formulations, challenges that must continue to be addressed are potential immunogenicity and toxicity to lungs due to concentrated doses. As previously described, due to the acceptable aerosol properties of dry powders prepared by TFF, dose and powder burden can be reduced. TFF can also play a role in minimizing the immunogenicity of protein-based products, as the ultra-rapid freezing during TFF helps to minimize protein aggregation.

4. Conclusion

Thin-film freezing is an ultra-rapid cryogenic freezing technique. It can be used to prepare powders with tunable properties. Its intermediate cooling rate allows for the production of powders with high SSA, low aggregation, and submicron size particles. TFF is also a viable processing method for creating protein dry powders for pulmonary delivery. Proteins that are subjected to TFF and then sublimation to remove frozen solvent are able to maintain their structure and functionality. Dry powders of proteins prepared by TFF also have good thermostability as well as aerosol properties for pulmonary delivery.

Conflict of Interest Disclosure

Hufnagel, Moon, Sahakijpijarn, Cui, and Williams are co-inventors on IP related to this review paper. The University of Texas System has licensed this IP to TFF Pharmaceuticals, Inc. Moon, Sahakijpijarn, and Williams acknowledge consulting for TFF Pharmaceuticals, Inc. Williams and Cui own equity in TFF Pharmaceuticals, Inc.

References

Albasarah Y.Y., Somavarapu S., Taylor K.M., Stabilizing protein formulations during air-jet nebulization, International Journal of Pharmaceutics, 402 (2010) 140–145. DOI: 10.1016/j.ijpharm.2010.09.042

Beinborn N.A., Du J., Wiederhold N.P., Smyth H.D., Williams III R.O., Dry powder insufflation of crystalline and amorphous voriconazole formulations produced by thin film freezing to mice, European Journal of Pharmaceutics and Biopharmaceutics, 81 (2012a) 600–608. DOI: 10.1016/j.ejpb.2012.04.019

Beinborn N.A., Lirola H.L., Williams III R.O., Effect of process variables on morphology and aerodynamic properties of voriconazole formulations produced by thin film freezing, International Journal of Pharmaceutics, 429 (2012b) 46–57. DOI: 10.1016/j.ijpharm.2012.03.010

Bhatnagar B., Tchessalov S., Advances in freeze drying of biologics and future challenges and opportunities, in: Ohtake S., Izutsu K.I. and Lechuga-Ballesteros D. (Eds.), Drying Technologies for Biotechnology and Pharmaceutical Applications, (2020) 137–177. 2020, pp.137–177, ISBN: 9783527341122. DOI: 10.1002/9783527802104.ch6

Bodier-Montagutelli E., Mayor A., Vecellio L., Respaud R., Heuzé-Vourc’h N., Designing inhaled protein therapeutics for topical lung delivery: what are the next steps?, Expert Opinion on Drug Delivery, 15 (2018) 729–736. DOI: 10.1080/17425247.2018.1503251

Burgess G., Boyce M., Jones M., Larsson L., Main M.J., Morgan F., Phillips P., Scrimgeour A., Strimenopoulou F., Vajjah P., Zamacona M., Palframan R., Randomized study of the safety and pharmacodynamics of inhaled interleukin-13 monoclonal antibody fragment VR942, EBioMedicine, 35 (2018) 67–75. DOI: 10.1016/j.ebiom.2018.07.035

Carrasquillo K.G., Stanley A.M., Aponte-Carro J.C., De Jésus P., Costantino H.R., Bosques C.J., Griebenow K., Non-aqueous encapsulation of excipient-stabilized spray-freeze dried BSA into poly (lactide-co-glycolide) microspheres results in release of native protein, Journal of Controlled Release, 76 (2001) 199–208. DOI: 10.1016/s0168-3659(01)00430-8

Chen L., Okuda T., Lu X.Y., Chan H.K., Amorphous powders for inhalation drug delivery, Advanced Drug Delivery Reviews, 100 (2016) 102–115. DOI: 10.1016/j.addr.2016.01.002

de la Torre B.G., Albericio F., The Pharmaceutical Industry in 2019. An analysis of FDA drug approvals from the perspective of molecules, Molecules, 25 (2020) 745. DOI: 10.3390/molecules25030745

Engstrom J.D., Lai E.S., Ludher B.S., Chen B., Milner T.E., Williams III R.O., Kitto G.B., Johnston K.P., Formation of stable submicron protein particles by thin film freezing, Pharmaceutical Research, 25 (2008) 1334–1346. DOI: 10.1007/s11095-008-9540-4

Engstrom J.D., Simpson D.T., Lai E.S., Williams III R.O., Johnston K.P., Morphology of protein particles produced by spray freezing of concentrated solutions, European Journal of Pharmaceutics and Biopharmaceutics, 65 (2007) 149–162. DOI: 10.1016/j.ejpb.2006.08.005

Fröhlich E., Salar-Behzadi S., Oral inhalation for delivery of proteins and peptides to the lungs, European Journal of Pharmaceutics and Biopharmaceutics, (2021) DOI: 10.1016/j.ejpb.2021.04.003

Gauvreau G., Hohlfeld J., Grant S., Jain M., Cabanski M., Pertel P., Boulet L.-P., Cockcroft D., Davis B., Fitzgerald J., Efficacy and safety of an inhaled anti-TSLP antibody fragment in adults with mild atopic asthma, Late breaking clinical trials in airway diseases, (2020) A4207-A4207. DOI: 10.1164/ajrccm-conference.2020.201.1_MeetingAbstracts.A4207

Genentech, Inc., Pulmozyme instructions for use, (2018), <gene.com/download/pdf/pulmozyme_IFU.pdf> accessed 19.05.2021.

Guilleminault L., Azzopardi N., Arnoult C., Sobilo J., Herve V., Montharu J., Guillon A., Andres C., Herault O., Le Pape A., Diot P., Lemarie E., Paintaud G., Gouilleux-Gruart V., Heuze-Vourc’h N., Fate of inhaled monoclonal antibodies after the deposition of aerosolized particles in the respiratory system, Journal of Controlled Release, 196 (2014) 344–354. DOI: 10.1016/j.jconrel.2014.10.003

Heinemann L., The failure of Exubera: are we beating a dead horse?, Journal of Diabetes Science and Technology, 2 (2008) 518–529. DOI: 10.1177/193229680800200325

Holt L.J., Herring C., Jespers L.S., Woolven B.P., Tomlinson I.M., Domain antibodies: proteins for therapy, Trends in Biotechnology, 21 (2003) 484–490. DOI: 10.1016/j.tibtech.2003.08.007

Johnson K.A., Preparation of peptide and protein powders for inhalation, Advanced Drug Delivery Reviews, 26 (1997)

3–15. DOI: 10.1016/s0169-409x(97)00506-1

Li X., Thakkar S.G., Ruwona T.B., Williams III R.O., Cui Z., A method of lyophilizing vaccines containing aluminum salts into a dry powder without causing particle aggregation or decreasing the immunogenicity following reconstitution, Journal of Controlled Release, 204 (2015) 38–50. DOI: 10.1016/j.jconrel.2015.02.035

Liang W., Pan H.W., Vllasaliu D., Lam J.K.W., Pulmonary delivery of biological drugs, Pharmaceutics, 12 (2020) 1025. DOI: 10.3390/pharmaceutics12111025

Lightwood D., O'Dowd V., Carrington B., Veverka V., Carr M.D., Tservistas M., Henry A.J., Smith B., Tyson K., Lamour S., The discovery, engineering and characterisation of a highly potent anti-human IL-13 fab fragment designed for administration by inhalation, Journal of Molecular Biology, 425 (2013) 577–593. DOI: 10.1016/j.jmb.2012.11.036

Liu W.R., Langer R., Klibanov A.M., Moisture-induced aggregation of lyophilized proteins in the solid state, Biotechnology and Bioengineering, 37 (1991) 177–184. DOI: 10.1002/bit.260370210

Maillet A., Congy-Jolivet N., Le Guellec S., Vecellio L., Hamard S., Courty Y., Courtois A., Gauthier F., Diot P., Thibault G., Aerodynamical, immunological and pharmacological properties of the anticancer antibody cetuximab following nebulization, Pharmaceutical Research, 25 (2008) 1318–1326. DOI: 10.1007/s11095-007-9481-3

Maillet A., Guilleminault L., Lemarie E., Lerondel S., Azzopardi N., Montharu J., Congy-Jolivet N., Reverdiau P., Legrain B., Parent C., Douvin D.H., Hureaux J., Courty Y., De Monte M., Diot P., et al., The airways, a novel route for delivering monoclonal antibodies to treat lung tumors, Pharmaceutical Research, 28 (2011) 2147–2156. DOI: 10.1007/s11095-011-0442-5

Malakhov M.P., Li T., Microparticle formulations for delivery to the lower and central respiratory tract and methods of manufacture, US Patents (2014) US20140099380A1.

Moon C., Sahakijpijarn S., Koleng J.J., Williams III R.O., Processing design space is critical for voriconazole nanoaggregates for dry powder inhalation produced by thin film freezing, Journal of Drug Delivery Science and Technology, 54 (2019a) 101295.

Moon C., Watts A.B., Lu X., Su Y., Williams III R.O., Enhanced aerosolization of high potency nanoaggregates of voriconazole by dry powder inhalation, Molecular Pharmaceutics, 16 (2019b) 1799–1812. DOI: 10.1021/acs.molpharmaceut.8b00907

Moon C., Watts A.B., Williams III R.O., Thin film freezing for production of an amorphous mannitol/lysozyme formulation for inhalation: a comparison of freezing techniques, Respiratory Drug Delivery, 3 (2016) 611–616.

Morgan F.G., Main M.J., Palframan R., Kirke D., Inhalable powder composition comprising il-13 antibody, US Patent, (2019) US20190247303A1.

Nelson A.L., Antibody fragments: hope and hype, MAbs, 2 (2010) 77–83. DOI: 10.4161/mabs.2.1.10786

Newhouse M.T., Hirst P.H., Duddu S.P., Walter Y.H., Tarara T.E., Clark A.R., Weers J.G., Inhalation of a dry powder tobramycin PulmoSphere formulation in healthy volunteers, Chest, 124 (2003) 360–366. DOI: 10.1378/chest.124.1.360

Newman A.W., Reutzel-Edens S.M., Zografi G., Characterization of the “hygroscopic” properties of active pharmaceutical ingredients, Journal of Pharmaceutical Sciences, 97 (2008) 1047–1059. DOI: 10.1002/jps.21033

Overhoff K.A., Engstrom J.D., Chen B., Scherzer B.D., Milner T.E., Johnston K.P., Williams III R.O., Novel ultra-rapid freezing particle engineering process for enhancement of dissolution rates of poorly water-soluble drugs, European Journal of Pharmaceutics and Biopharmaceutics, 65 (2007a) 57–67. DOI: 10.1016/j.ejpb.2006.07.012

Overhoff K.A., Johnston K.P., Tam J., Engstrom J.D., Williams III R.O., Use of thin film freezing to enable drug delivery: a review, Journal of Drug Delivery Science and Technology, 19 (2009) 89–98. DOI: 10.1016/s1773-2247(09)50016-0

Overhoff K.A., McConville J.T., Yang W., Johnston K.P., Peters J.I., Williams III R.O., Effect of stabilizer on the maximum degree and extent of supersaturation and oral absorption of tacrolimus made by ultra-rapid freezing, Pharmaceutical Research, 25 (2008) 167–175. DOI: 10.1007/s11095-007-9417-y

Overhoff K.A., Moreno A., Miller D.A., Johnston K.P., Williams III R.O., Solid dispersions of itraconazole and enteric polymers made by ultra-rapid freezing, International Journal of Pharmaceutics, 336 (2007b) 122–132. DOI: 10.1016/j.ijpharm.2006.11.043

Pharmaxis, Ltd, ARIDOL package insert, (1964), <accessdata.fda.gov/drugsatfda_docs/label/2010/022368S000lbl.pdf> accessed 13.05.2021.

Pilcer G., Amighi K., Formulation strategy and use of excipients in pulmonary drug delivery, International Journal of Pharmaceutics, 392 (2010) 1–19. DOI: 10.1016/j.ijpharm.2010.03.017

Proudfoot A., Bayliffe A., O'Kane C.M., Wright T., Serone A., Bareille P.J., Brown V., Hamid U.I., Chen Y., Wilson R., Cordy J., Morley P., de Wildt R., Elborn S., Hind M., et al., Novel anti-tumour necrosis factor receptor-1 (TNFR1) domain antibody prevents pulmonary inflammation in experimental acute lung injury, Thorax, 73 (2018) 723–730. DOI: 10.1136/thoraxjnl-2017-210305

Ramezani V., Vatanara A., Seyedabadi M., Nabi Meibodi M., Fanaei H., Application of cyclodextrins in antibody microparticles: potentials for antibody protection in spray drying, Drug Development and Industrial Pharmacy, 43 (2017) 1103–1111. DOI: 10.1080/03639045.2017.1293679

Rondeau J.M.R., Edwards M.J., Miller D., Huang D., Hemmig R., Knopf H.-P., Gupta K., Van Heeke G.A., Haubst N., Andlauer B., Thymic stromal lymphopoietin (tslp)-binding antibodies and methods of using the antibodies, International Patent (2017) WO2017042701A1.

Sahakijpijarn S., Moon C., Koleng J.J., Christensen D.J., Williams III R.O., Development of remdesivir as a dry powder for inhalation by thin film freezing, Pharmaceutics, 12 (2020a) 1002. DOI: 10.3390/pharmaceutics12111002

Sahakijpijarn S., Moon C., Ma X., Su Y., Koleng J.J., Dolocan A., Williams III R.O., Using thin film freezing to minimize excipients in inhalable tacrolimus dry powder formulations, International Journal of Pharmaceutics, 586 (2020b) 119490. DOI: 10.1016/j.ijpharm.2020.119490

Sahakijpijarn S., Smyth H.D.C., Miller D.P., Weers J.G., Post-inhalation cough with therapeutic aerosols: formulation considerations, Advanced Drug Delivery Reviews, 165–166 (2020c) 127–141. DOI: 10.1016/j.addr.2020.05.003

Saluja V., Amorij J., Kapteyn J., De Boer A., Frijlink H., Hinrichs W., A comparison between spray drying and spray freeze drying to produce an influenza subunit vaccine powder for inhalation, Journal of Controlled Release, 144 (2010) 127–133. DOI: 10.1016/j.jconrel.2010.02.025

Sinswat P., Overhoff K.A., McConville J.T., Johnston K.P., Williams III R.O., Nebulization of nanoparticulate amorphous or crystalline tacrolimus–single-dose pharmacokinetics study in mice, European Journal of Pharmaceutics and

Biopharmaceutics, 69 (2008) 1057–1066. DOI: 10.1016/j.ejpb.2008.01.037

Thakkar S.G., Ruwona T.B., Williams III R.O., Cui Z., The immunogenicity of thin-film freeze-dried, aluminum salt-adjuvanted vaccine when exposed to different temperatures, Human Vaccines & Immunotherapeutics, 13 (2017) 936–946. DOI: 10.1080/21645515.2016.1259042

Trasi N.S., Purohit H.S., Wen H., Sun D.D., Taylor L.S., Non-sink dissolution behavior and solubility limit of commercial tacrolimus amorphous formulations, Journal of Pharmaceutical Sciences, 106 (2017) 264–272. DOI: 10.1016/j.xphs.2016.09.016

Ung K.T., Rao N., Weers J.G., Clark A.R., Chan H.K., In vitro assessment of dose delivery performance of dry powders for inhalation, Aerosol Science and Technology, 48 (2014) 1099–1110. DOI: 10.1080/02786826.2014.962685

Wang W., Singh S., Zeng D.L., King K., Nema S., Antibody structure, instability, and formulation, Journal of Pharmaceutical Sciences, 96 (2007) 1–26. DOI: 10.1002/jps.20727

Wang Y.B., Watts A.B., Williams III R.O., Effect of processing parameters on the physicochemical and aerodynamic properties of respirable brittle matrix powders, Journal of Drug Delivery Science and Technology, 24 (2014) 390–396. DOI: 10.1016/s1773-2247(14)50079-2

Watts A.B., Wang Y.B., Johnston K.P., Williams III R.O., Respirable low-density microparticles formed in situ from aerosolized brittle matrices, Pharmaceutical Research, 30 (2013) 813–825. DOI: 10.1007/s11095-012-0922-2

Weers J., Dispersible powders for inhalation applications, Innovations in Pharmaceutical Technology, 1 (2000) 111–116. <http://iptonline.com/articles/public/IPTSEVEN111NP.pdf> accessed 11.06.2021.

Yang W., Tam J., Miller D.A., Zhou J., McConville J.T., Johnston K.P., Williams III R.O., High bioavailability from nebulized itraconazole nanoparticle dispersions with biocompatible stabilizers, International Journal of Pharmaceutics, 361 (2008) 177–188. DOI: 10.1016/j.ijpharm.2008.05.003

Yu Z., Johnston K.P., Williams III R.O., Spray freezing into liquid versus spray-freeze drying: influence of atomization on protein aggregation and biological activity, European Journal of Pharmaceutical Sciences, 27 (2006) 9–18. DOI: 10.1016/j.ejps.2005.08.010

Zarzycki P.K., Wlodarczyk E., Lou D.W., Jinno K., Evaluation of methanol-water and acetonitrile-water binary mixtures as eluents for temperature-dependent inclusion chromatography, Analytical sciences, 22 (2006) 453–456. DOI: 10.2116/analsci.22.453

Zenilman J.M., Fuchs E.J., Hendrix C.W., Radebaugh C., Jurao R., Nayak S.U., Hamilton R.G., Griffiss J.M., Phase 1 clinical trials of DAS181, an inhaled sialidase, in healthy adults, Antiviral Research, 123 (2015) 114–119. DOI: 10.1016/j.antiviral.2015.09.008

Authors' Short Biographies

Stephanie Hufnagel

Stephanie Hufnagel received her Pharm.D. degree in 2016 and her Ph.D. degree in Pharmaceutical Sciences in 2021, both from The University of Texas at Austin, College of Pharmacy. Her primary focus is the formulation of immuno-oncology agents, including both large and small molecules. She currently works on the formulation of antibodies as dry powders.

Sawittree Sahakijpijarn

Sawittree Sahakijpijarn received her B.Sc. degree in Pharmaceutical Sciences from Chulalongkorn University in 2012 and her Ph.D. degree in Pharmaceutical Sciences from The University of Texas at Austin in 2020. She currently works as a postdoctoral research fellow in the Division of Molecular Pharmaceutics and Drug Delivery at The University of Texas at Austin. Her research focuses on pulmonary delivery of small molecule and biological drugs.

Authors’ Short Biographies

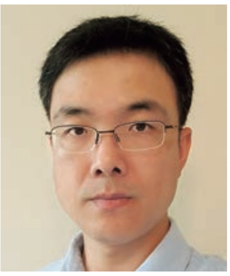

Chaeho Moon

Chaeho Moon was born in South Korea and earned his Ph.D. degree in Molecular Pharmaceutics and Drug Delivery at The University of Texas at Austin. He is currently working as a Postdoc at UT Austin to develop powder formulations for dry powder inhalations, as well as TFF powder formulations of vaccine, mAb, protein, peptide, and mRNA/LNP products.

Zhengrong Cui

Zhengrong Cui is a Professor at The University of Texas at Austin, College of Pharmacy. His research interests lie in pharmaceutical drug and vaccine delivery. He also has extensive experience in thin-film freeze-drying of biologics and their needle-free delivery. Dr. Cui has published extensively in the fields of pharmaceutics, vaccinology, and nanotechnology. He is an inventor on many patents and patent applications. He serves as an editor to International Journal of Pharmaceutics. Dr. Cui holds a Ph.D. degree in Pharmaceutical Sciences from the University of Kentucky, College of Pharmacy. He is a Fellow of the American Association for Pharmaceutical Scientists.

Robert O. (Bill) Williams III

Robert O. (Bill) Williams III is the Johnson & Johnson Centennial Chair, Professor and Division Head of Pharmaceutics at the College of Pharmacy, University of Texas at Austin. Dr. Williams is Fellow of the American Association of Pharmaceutical Scientists, American Institute of Medical and Biological Engineering, and National Academy of Inventors. He was named Inventor of the Year by the University of Texas at Austin. He has founded several pharmaceutical companies. He has published over 220 peer-reviewed papers and co-edited books in pharmaceutical technology and drug delivery. He is an inventor on over 60 patents. He is Editor-in-chief of AAPS PharmSciTech.

KONA Powder and Particle Journal No. 39 (2022) 193–207/https://doi.org/10.14356/kona.2022001 Original Research Paper

Grain-Size Effects on Mechanical Behavior and Failure of Dense Cohesive Granular Materials[†]

Payam Poorsolhjouy[1] **and Anil Misra**[2*]

[1] *Department of the Built Environment, Eindhoven University of Technology, The Netherlands*
[2] *Civil, Environmental and Architectural Engineering Department, University of Kansas, USA*

Abstract

The grain sizes can significantly influence the granular mechano-morphology, and consequently, the macro-scale mechanical response. From a purely geometric viewpoint, changing grain size will affect the volumetric number density of grain-pair interactions as well as the neighborhood geometry. In addition, changing grain size can influence initial stiffness and damage behavior of grain-pair interactions. The granular micromechanics approach (GMA), which provides a paradigm for bridging the grain-scale to continuum models, has the capability of describing the grain size influence in terms of both geometric effects and grain-pair deformation/dissipation effects. Here the GMA based Cauchy-type continuum model is enhanced using simple power laws to simulate the effect of grain size upon the volumetric number density of grain-pair interactions, and the parameters governing grain-pair deformation and dissipation mechanisms. The enhanced model is applied to predict the macroscopic response of cohesive granular solids under conventional triaxial tests. The results show that decreasing grain-sizes can trigger brittle-to-ductile transition in failure. Grain size is found to affect the compression/dilatation behavior as well as the post-peak softening/hardening of granular materials. The macro-scale failure/yield stress is also found to have an inverse relationship with grain-sizes in consonance with what has been reported in the literature.

Keywords: granular micromechanics, grain sizes, brittle to ductile, failure, yield, triaxial compression

1. Introduction

The macro-scale behaviors of dense cohesive granular materials are directly linked to the grain-scale through their granular mechano-morphology, which is represented by their collective arrangements (microstructure) and their interaction mechanisms (micromechnics). The mathematical description of macro-scale response of granular materials must begin from the conception of grain-interactions. From this point of departure, either discrete or continuum descriptions can be elaborated. In discrete models, the macro-scale behavior is inferred by tracking the motion of each grain in response to the external action. Continuum models, in contrast, aim to describe behavior at a spatial scale in which the grains and their motions remain concealed within a material point of a continuous system. While discrete analysis schemes can provide results with detailed description of grain motions, inter-granular deformations, they are limited in their applicability to large-scale problems due to large computational cost, and the challenges of grain-scale verification and validation. On the other hand, classical continuum models, while computationally affordable, suffer from losing characteristic features due to neglecting grain scale phenomena (in terms of both the microstructure and its evolution, as well as the inter-granular mechanisms). In this regards, it is noteworthy that higher-gradient continuum models represent a way to capture the effect of microstructure and its evolution during loading (Placidi L. and Barchiesi E., 2018; Placidi L. et al., 2018a; 2018b), an approach that can be traced to the early development in continuum mechanics (dell'Isola F. et al., 2014; Eugster S.R. and dell'Isola F., 2017).

Granular micromechanics approach (GMA) provides a paradigm that bridges the grain-scale models to appropriate continuum model (Nejadsadeghi N. and Misra A., 2020; Poorsolhjouy P. and Misra A., 2019). In this approach, the constitutive relation for a continuum material point is derived by utilizing the directional average of variously oriented grain-pairs. In this way, GMA incorporates data from the microstructure and micromechanical phenomena at grain scale into the continuum model (Misra A. et al., 2020). It has been shown that by incorporating the grain-pair interactions in different directions, GMA is able to

---

[†] Received 30 April 2020; Accepted 8 July 2020

[*] Corresponding author: Anil Misra;
Add: 1530 W. 15th Street, Learned Hall, Lawrence, KS 66045-7609, USA
E-mail: amisra@ku.edu
TEL: +1-785-864-1750

capture various behavior, that are difficult to attain with classical continuum models, using computational demand which is significantly lower than that associated with discrete models (Poorsolhjouy P. and Misra A., 2017). In a form of GMA that leads to Cauchy-type continuum model with coupled damage and plasticity, Helmholtz free energy density and dissipation potential functions for the continuum model are obtained as the volume averages of corresponding functions defined for the grain-pair. Grain scale constitutive equations are calibrated to ensure that the model replicates the observed behavior. Since the grain-pair behavior is nonlinear, the grain-pair oriented in different directions undergo different unique loading paths as a continuum material point experiences a macro-scale loading sequence. The consequence is that the response of the granular system is highly loading-path dependent. Indeed, when a macro-scale body is subjected to a loading-path, the variously oriented grain-pair can be in different loading stages including loading, unloading, or reloading. The material response, therefore, at any stage of loading is a function of the entire loading history rather than the current loading state.

Since grain-pair interactions are key in GMA-based continuum models, the grain size effect can be incorporated by considering its influence on the grain-pair behavior. Here, we enhance the non-linear damage-plasticity grain-pair interaction previously proposed for cementitious materials by incorporating the effects of grain sizes. We introduce simple scaling relationships, based on power laws, to describe the effect of grain size on grain-pair stiffness, grain-pair damage dissipation, grain-pair branch length, and the volumetric number density of grain-pair interactions in the granular material system. Using these relationships, size-effect relationships for macroscopic response of the material (macroscopic stiffness tensor and the Cauchy stress) are predicted. These results are calculated for parameters that are calibrated using experimental data available in the literature. The predicted results show that grain-sizes can influence brittle to ductile transition and softening-hardening behavior. The results also show that macro-scale failure stress under axisymmetric loading scales with grain-sizes as has been observed from experiments on cohesive granular materials.

2. Granular Micromechanics Approach (GMA)

GMA can be categorized as a meso-scale approach that bridges the gap between continuum models and discrete models as is seen in **Fig. 1**. At the smallest scales, atomic models can be utilized provided the composition and initial structures are known. Indeed, provided a faithful realization of the atomic structure, these models can yield results with high degree of exactness (i.e. fidelity). For examples of their application to atomically complex materials the reader is referred to (Misra A. and Ching W.Y., 2013; Qomi M.J.A. et al., 2014). These models however are computationally costly even with the present computation and memory capacities. Moreover, they are inapplicable to large systems with complex compositions, or disordered and defective structures given the difficulties associated with the characterization and specification of such materials. In larger scales, discrete models are utilized to investigate the material behavior by simulating the interaction of macro-particles that comprise granular system (Gonzalez M. and Cuitino A.M., 2012; Hentz S. et al., 2004; Misra A. et al., 2018; Tavarez F.A. and Plesha M.E., 2007; Turco E. et al., 2019). Discrete models consist of identifying the grains in the material, their interacting neighbors, and the behavior of the interaction. For these models one needs to be able to define grains in a given volume of interest, their shapes and sizes, their contacts with their neighbor grains, their surface properties, etc. Moreover, this identification needs to be done at any loading increment, considering the fact that during loading all properties of grains and their contacts will change due to the displacement, deformation, and rearrangement of grains. If the mechano-morphology of a given granular materials can be faithfully reproduced throughout a loading process, discrete models can be used to extract high-fidelity results as depicted in **Fig. 1** about the micro-level response as well as the micro-macro correlation for the material (Gonzalez M. and Cuitino A.M., 2012; Misra A. and Poorsolhjouy P., 2015b).

GMA incorporates data from the material microstructure and micromechanics into the continuum model in a computationally affordable statistical manner. The antecedents of the granular micromechanics approach may be traced to second quarter of the 20th century in works related to the estimation of wave velocities in granular beds in which the Hertz solution for normal contact between elastic spheres was used to find equivalent elastic moduli of regularly arranged grain packing (see (Duffy J. and Mindlin R.D., 1957; Hara G., 1935) and for a brief review (Misra A. et al., 2019)). This analysis served as the inspiration for the development of stress-strain relations for random packing of grains including certain statistical representation of the packing geometry (Chang C.S. and Misra A., 1990; Digby P.J., 1981; Misra A. and Chang C.S., 1993; Walton K., 1987). In GMA, the exact evolution of grain trajectories within the material point are not investigated. Instead, the macroscopic behavior of the granular system is derived by averaging the behavior of grain-pair interactions in different directions. In our past works, we have presented a derivation of the GMA based model applicable to cementitious granular materials in the framework of thermo-mechanics (Misra A. and Poorsolhjouy P., 2015a; Poorsolhjouy P. and Misra A., 2017). Here, this thermomechanical derivation

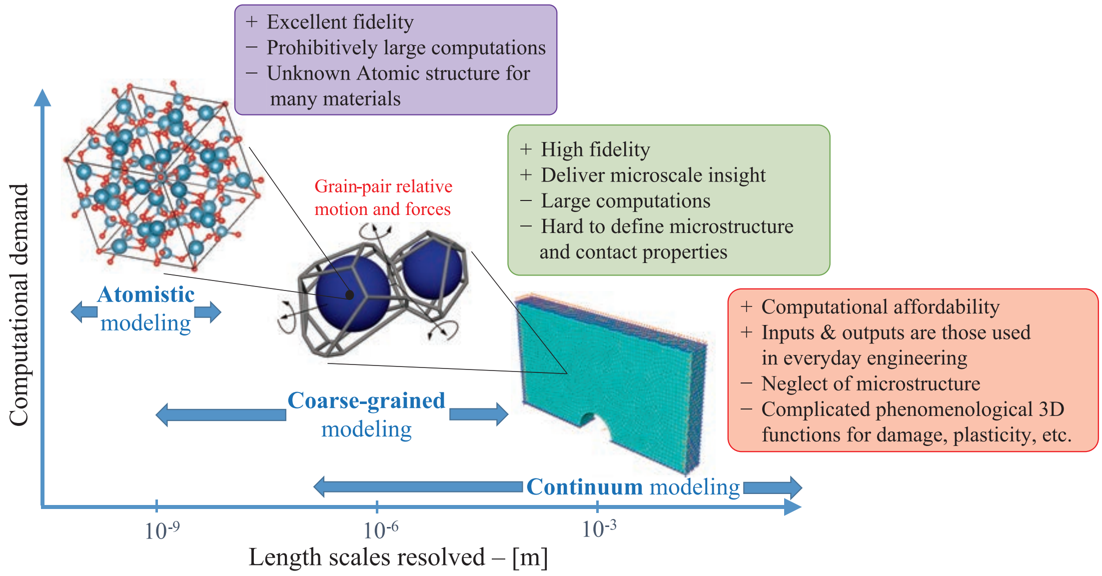

Fig. 1 Modeling Scales: Schematic graph showing the evolution of computational demand needed for modeling material behavior in different scales, expanding from nanometers to centimeters.

of GMA is enhanced to account for the effect of grain-sizes. The paper is structured as follows: In section 2.1, a brief review of the general derivation of GMA within a thermo-mechanical viewpoint is presented for completeness. Section 2.2 focuses on the specifics of coupled damage-plasticity laws at micro-scale for deriving the correct macroscopic behavior of the material (for a more complete description of the micro-scale laws, the reader is referred to (Misra A. and Poorsolhjouy P., 2015a; Poorsolhjouy P. and Misra A., 2017)). In Section 2.3, the relationship between grain sizes on one hand and model variables (including branch vector, density of grain-pair contacts, as well as stiffness and damage variables) on the other, have been discussed and size-effect laws are implemented within the model. Section 3 is devoted to results of simulations for samples of various grains sizes and under different confinements. Particularly, effects of changing grain sizes on failure and its type (brittle or ductile) has been discussed. Finally, a summary and conclusion, along with an outline of continued research is presented in Section 4.

2.1 Thermo-mechanical derivation

The GMA hypothesizes that the deformation energy of a volume of granular materials can be effectively expressed in terms of the deformation energies of all its grain-pair interactions. As a consequence, the macro-scale Helmholtz free energy density, W, and dissipation potential, ψ, can be obtained as volume averages of their grain-pair counterparts, which are expressed in terms of grain-scale variables as (Misra A. and Poorsolhjouy P., 2015a; Poorsolhjouy P. and Misra A., 2017)

$$W = \frac{1}{V}\sum_{\alpha=1}^{N_\mathrm{c}} W^{\alpha}\left(\delta_j^{\alpha}, \delta_j^{p}, D_j^{\alpha}\right) \tag{1a}$$

$$\psi = \frac{1}{V}\sum_{\alpha=1}^{N_\mathrm{c}} \psi^{\alpha}\left(\delta_j^{\alpha}, D_j^{\alpha}, \dot{D}_j^{\alpha}, \delta_j^{p\alpha}, \dot{\delta}_j^{p\alpha}\right) \tag{1b}$$

where the summations go over all grain-pair interactions, superscript α refers to the α^{th} grain-pair, total number of grain-pair interactions is N_c, and the superimposed dots imply time derivative. The grain scale kinematic variables consist of the relative displacement and the plastic relative displacement between neighbor grains, δ_j^{α} and $\delta_j^{p\alpha}$. Here, we note that in this model, the relative displacements between grains represents the relative displacement between the centroids of each two neighboring grains. This relative displacement can have various sources including deformation of individual grains, or relative movement between grains centroids, or deformation concentrated at the contacts, e.g. in Hertzian contact. These phenomena are not addressed separately in this model and their collective effect is lumped into the relative displacement between grain centroids. The same is true for plastic relative displacement between grain centroids. In addition, the unitless grain-scale damage parameter, $\boldsymbol{D}_j^{\alpha}$, is a vector variable which represents the loss of grain-pair stiffness coefficients. In the entire document, the summation convention over repeated indices is implied, unless explicitly noted otherwise.

In this analysis, we only account for the so-called macro-displacements and do not introduce any additional kinematic descriptors or higher-gradient terms and grain-spins/rotations that are necessary for complete description of the complex granular systems (Misra A. and Poorsolhjouy P., 2016a; 2016b; Nejadsadeghi N. and Misra A., 2020; Poorsolhjouy P. and Misra A., 2019). In this case, the grain-pair relative displacement, δ_j^α, is related only to the first gradient of macro-displacement field. With this in mind, the macro-scale Helmholtz free energy density, W, and dissipation potential, ψ, can also be defined as functions of macroscopic variables as follows

$$W = W\left(\varepsilon_{ij}, \varepsilon_{ij}^p, D_{ij}\right) \tag{2a}$$

$$\psi = \psi\left(\varepsilon_{ij}, D_{ij}, \dot{D}_{ij}, \varepsilon_{ij}^p, \dot{\varepsilon}_{ij}^p\right) \tag{2b}$$

where the superscript p denote plastic, ε_{ij} is the independent kinematic variable (strain tensor), and D_{ij} is the damage tensor which for a given direction, $\boldsymbol{n}_j$, yields the damage vector, D_i, i.e. $D_i = D_{ij}n_j$. As standard in classical continuum mechanics, the power density of internal forces is expressed as $p^i = \sigma_{ij}\dot{u}_{(i,j)} = \sigma_{ij}\dot{\varepsilon}_{ij}$, where σ_{ij} is the Cauchy stress tensor. Using the Clausius-Duhem inequality and the above definitions, the following is obtained (Poorsolhjouy P. and Misra A., 2017)

$$\left(\sigma_{ij} - \frac{\partial W}{\partial \varepsilon_{ij}}\right)\dot{\varepsilon}_{ij} - \left(\frac{\partial W}{\partial D_{ij}} + \frac{\partial \psi}{\partial \dot{D}_{ij}}\right)\dot{D}_{ij} - \left(\frac{\partial W}{\partial \varepsilon_{ij}^p} + \frac{\partial \psi}{\partial \dot{\varepsilon}_{ij}^p}\right)\dot{\varepsilon}_{ij}^p = 0 \tag{3}$$

Since the equality in Eq. 3 should be satisfied for any arbitrary set of kinematic variables, all three terms must simultaneously vanish. For the second and third terms, since the coefficients are functions of the same kinematic variables, the weaker orthogonality condition can be sufficient (Ziegler H., 1983). As a result, the following equations are obtained

$$\sigma_{ij} - \frac{\partial W}{\partial \varepsilon_{ij}} = 0 \tag{4a}$$

$$\left(\frac{\partial W}{\partial D_{ij}} + \frac{\partial \psi}{\partial \dot{D}_{ij}}\right)\dot{D}_{ij} = 0 \tag{4b}$$

$$\left(\frac{\partial W}{\partial \varepsilon_{ij}^p} + \frac{\partial \psi}{\partial \dot{\varepsilon}_{ij}^p}\right)\dot{\varepsilon}_{ij}^p = 0 \tag{4c}$$

Further substituting Eq. 1a into Eq. 4a and applying chain rule the following expression for the Cauchy stress can be obtained

$$\sigma_{ij} = \frac{\partial W}{\partial \varepsilon_{ij}} = \frac{1}{V}\sum_{\alpha=1}^{N_c}\frac{\partial W^\alpha}{\partial \delta_k^\alpha}\frac{\partial \delta_k^\alpha}{\partial \varepsilon_{ij}} \tag{5}$$

In Eq. 5 the derivative of grain-pair interaction energy with respect to the displacement is defined as the conjugate force measure in the grain-scale

$$f_k^\alpha = \frac{\partial W^\alpha}{\partial \delta_k^\alpha} \tag{6}$$

Assuming that the macroscopic variables including strain, ε_{ij}, plastic strain, ε_{ij}^p, and damage tensor, D_{ij}, are distributed linearly in the material point, the corresponding local variables defining the relative kinematics of two neighbor grains, i.e. the relative displacement, δ_i, plastic relative displacement, δ_i^p, and the damage vector specifying the loss of stiffness between the two grains, D_i, can be derived (Misra A. and Poorsolhjouy P., 2015a; Poorsolhjouy P. and Misra A., 2017). Approximating the displacement and plastic displacement of a grain using the Taylor series expansion of the displacement and plastic displacement of its neighbor grain, allows us to define the relative displacement and relative plastic displacement between two neighbor grains (δ_i and δ_i^p) as the product of their macroscopic counterparts (ε_{ij} and ε_{ij}^p) with the branch vector. In other words, the displacements are written as the projections of their macroscopic counterparts, in the direction of the grain-pair interaction, and then scaled by the magnitude of the branch vector. In addition, based on the definition of the macroscopic damage tensor, D_{ij}, the grain-scale damage vector, D_i, is given, by definition, as the product of the damage tensor and the direction of grain-pair interaction (i.e. as the projection of tensor, D_{ij}, in the direction of the grain-pair).

$$\delta_i^\alpha = \varepsilon_{ij}l_j;\ \delta_i^{p\alpha} = \varepsilon_{ij}^p l_j;\ D_i^\alpha = D_{ij}n_j \tag{7}$$

where l_j is the branch vector joining the centroids of two neighbor grains which is given as the product of the length of the branch vector, l, and the unit vector in the direction of the contact, n_j as $l_j = ln_j$. Substituting Eq. 6 and 7 into Eq. 5 the expression for Cauchy stress can be rewritten as

$$\sigma_{ij} = \frac{1}{V}\sum_{\alpha=1}^{N_c} f_k^\alpha \delta_{ki}\delta_{lj}l_l = \frac{1}{V}\sum_{\alpha=1}^{N_c} f_i^\alpha l_j \tag{8}$$

It is remarked here that the widely used Eq. 8 is valid under specific assumptions as outlined in Eq. 7. Further, we observe that based on the definition of the damage vector and damage tensor (see Eq. 7) the partial derivative of the damage vector with respect to the damage tensor is given as $\partial D_k/\partial D_{ij} = n_l\partial D_{kl}/\partial D_{ij} = \delta_{ik}n_j$. In the same way, the partial derivative of the rate of the damage vector with respect to the rate of the damage tensor can be derived as $\partial \dot{D}_k/\partial \dot{D}_{ij} = n_l\partial \dot{D}_{kl}/\partial \dot{D}_{ij} = \delta_{ik}n_j$. The same relationships can be formulated for the partial derivative of plastic displacement with respect to plastic strain as, $\partial \delta_k^p / \partial \varepsilon_{ij}^p = l_l \partial \varepsilon_{kl}^p / \partial \varepsilon_{ij}^p = \delta_{ik} l_j$, and for their time rates, $\partial \dot{\delta}_k^p / \partial \dot{\varepsilon}_{ij}^p = l_l \partial \dot{\varepsilon}_{kl}^p / \partial \dot{\varepsilon}_{ij}^p = \delta_{ik} l_j$. It is therefore derived that $\partial D_k^\alpha / \partial D_{ij} = \partial \dot{D}_k^\alpha / \partial \dot{D}_{ij}$ and $\partial \dot{\delta}_k^{p\alpha} / \partial \dot{\varepsilon}_{ij}^p = \partial \delta_k^{p\alpha} / \partial \varepsilon_{ij}^p$. Substituting this assumption, as well as Eqs. 1a and 1b into Eqs. 4b and 4c, results in

$$\sum_{\alpha=1}^{N_c}\left(\left(\frac{\partial W^\alpha}{\partial D_i^\alpha} + \frac{\partial \psi^\alpha}{\partial \dot{D}_i^\alpha}\right)\dot{D}_i^\alpha\right) = 0 \tag{9a}$$

$$\sum_{\alpha=1}^{N_c}\left(\left(\frac{\partial W^{\alpha}}{\partial \delta_i^{p\alpha}}+\frac{\partial \psi^{\alpha}}{\partial \dot{\delta}_i^{p\alpha}}\right)\dot{\delta}_i^{p\alpha}\right)=0 \tag{9b}$$

Now it should be noted that the summations in Eq. 9 should hold for any number of grain-pair interactions and thus, the equality should be satisfied in a term-by-term manner.

$$\left(\frac{\partial W^{\alpha}}{\partial D_i^{\alpha}}+\frac{\partial \psi^{\alpha}}{\partial \dot{D}_i^{\alpha}}\right)\dot{D}_i^{\alpha}=0 \tag{10a}$$

$$\left(\frac{\partial W^{\alpha}}{\partial \delta_i^{\alpha}}+\frac{\partial \psi^{\alpha}}{\partial \dot{\delta}_i^{p\alpha}}\right)\dot{\delta}_i^{p\alpha}=0 \tag{10b}$$

Combining Eq. 6 and 10 results in

$$\begin{aligned}&\left(f_j^{\alpha}-\frac{\partial W^{\alpha}}{\partial \delta_j^{\alpha}}\right)\dot{\delta}_j^{\alpha}-\left(\frac{\partial W^{\alpha}}{\partial D_j^{\alpha}}+\frac{\partial \psi^{\alpha}}{\partial \dot{D}_j^{\alpha}}\right)\dot{D}_j^{\alpha}\\&\quad-\left(\frac{\partial W^{\alpha}}{\partial \delta_j^{\alpha}}+\frac{\partial \psi^{\alpha}}{\partial \dot{\delta}_j^{p\alpha}}\right)\dot{\delta}_j^{p\alpha}=0\end{aligned} \tag{11}$$

which leads to the following micro-scale Clausius-Duhem type inequality for the α^{th} inter-granular interaction:

$$f_j^{\alpha}\dot{\delta}_j^{\alpha}-\dot{W}^{\alpha}=d^{\alpha}\geq 0 \tag{12}$$

where the grain-scale dissipation, d^{α}, is defined as

$$d^{\alpha}=\frac{\partial \psi^{\alpha}}{\partial \dot{D}_j^{\alpha}}\dot{D}_j^{\alpha}+\frac{\partial \psi^{\alpha}}{\partial \dot{\delta}_j^{p\alpha}}\dot{\delta}_j^{p\alpha}\geq 0 \tag{13}$$

and the time derivative of micro-scale free energy, W^{α}, is

$$\dot{W}^{\alpha}=\frac{\partial W^{\alpha}}{\partial \delta_j^{\alpha}}\dot{\delta}_j^{\alpha}+\frac{\partial W^{\alpha}}{\partial D_j^{\alpha}}\dot{D}_j^{\alpha}+\frac{\partial W^{\alpha}}{\partial \delta_j^{p\alpha}}\dot{\delta}_j^{p\alpha} \tag{14}$$

Thus, employing appropriate formulation for the Helmholtz energy, W^{α}, and dissipation potential, ψ^{α}, we can completely describe the grain-pair force-displacement relationships (using Eq. 12) and in turn, the classical stress-strain behavior of a granular system (using Eq. 8).

2.2 Grain-scale coupled damage-plasticity relationships

At this juncture, it is useful to formulate the grain-pair energy and dissipation functions in terms of grain-pair displacement decomposed into two components, one along the vector connecting the two grain-centroids (branch vector), termed as normal component, and the other in the orthogonal direction, termed as the tangential component (as depicted in the inset in **Fig. 2**). Accordingly, a local Cartesian coordinate system, ***nst***, is defined composed of three unit vectors: unit normal vector n_i in the direction of branch vector, l_i, and two orthogonal vectors lying in the tangential plane denoted as s_i and t_i. The direction cosines of these local coordinate axes are given as

$$\begin{aligned}n_i&=\langle\cos\theta,\sin\theta\cos\phi,\sin\theta\sin\phi\rangle\\s_i&=\langle-\sin\theta,\cos\theta\cos\phi,\cos\theta\sin\phi\rangle\\t_i&=\langle 0,-\sin\phi,\cos\phi\rangle\end{aligned} \tag{15}$$

using spherical coordinates (See **Fig. 2**). The normal and tangential components of a grain-pair are then given as

$$\left.\begin{aligned}\delta_{\mathrm{n}}&=\delta_i n_i\\\delta_{\mathrm{w}}&=\sqrt{(\delta_i s_i)^2+(\delta_i t_i)^2}\end{aligned}\right\};\ \text{where}\ \ \delta_i=\varepsilon_{ij}l_j \tag{16}$$

It should be noted that the subscripts *n* and *w*, refer to normal and tangential components and they do not represent vector quantities. Summation convention, therefore, does not apply to them. The grain free energy and dissipation potential are written as the summations of their normal and tangential components, $W^{\alpha}=W_{\mathrm{n}}^{\alpha}+W_{\mathrm{w}}^{\alpha}$ and $\psi^{\alpha}=\psi_{\mathrm{n}}^{\alpha}+\psi_{\mathrm{w}}^{\alpha}$. To account for damage and plasticity, the normal and tangential components of inter-granular free energy take the following form (Misra A. and Poorsolhjouy P., 2015a; Poorsolhjouy P. and Misra A., 2017)

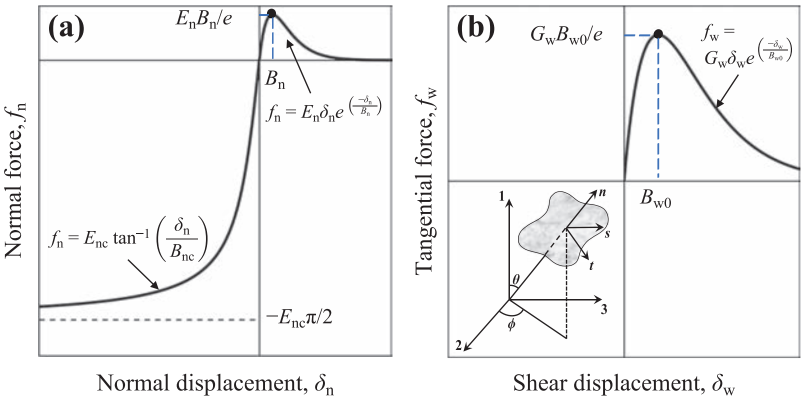

Fig. 2 Intergranular Force-Laws: **(a)** Grain-pair force-displacement curve in normal direction showing the tension-compression asymmetry typical of cohesive grain interactions. **(b)** Grain-pair force-displacement curve in the tangential direction and inset schematic of an interface between two grains and the global and local coordinate axes. Damage and stiffness parameters defining the grain-pair interactions are displayed on the graphs.

$$
\begin{aligned}
W_{\mathrm{n}}^{\alpha} &= \frac{1}{2} E_{\mathrm{n}}^{\alpha}\left(1-D_{\mathrm{n}}^{\alpha}\right)\left(\delta_{\mathrm{n}}^{\alpha}\right)^{2} - h_{\mathrm{n}}^{\alpha}\delta_{\mathrm{n}}^{p\alpha} \\
W_{\mathrm{w}}^{\alpha} &= \frac{1}{2} G_{\mathrm{w}}^{\alpha}\left(1-D_{\mathrm{w}}^{\alpha}\right)\left(\delta_{\mathrm{w}}^{\alpha}\right)^{2} - h_{\mathrm{w}}^{\alpha}\delta_{\mathrm{w}}^{p\alpha}
\end{aligned}
\tag{17}
$$

Where E_{n}^{α} and G_{w}^{α} are the grain-pair elastic stiffness, h_{n}^{α} and h_{w}^{α} are the grain-pair generalized forces, and $\delta_{\mathrm{n}}^{p\alpha}$ and $\delta_{\mathrm{w}}^{p\alpha}$ are the grain-pair plastic displacements in normal and tangential directions, respectively. Normal and tangential components of inter-granular dissipation potential are represented by the sum of the dissipations due to damage and plasticity

$$
\begin{aligned}
\psi_{\mathrm{n}}^{\alpha} &= Y_{\mathrm{n}}^{\alpha}\left|\dot{D}_{\mathrm{n}}^{\alpha}\right| + Z_{\mathrm{n}}^{\alpha}\left|\dot{\delta}_{\mathrm{n}}^{p\alpha}\right| \geq 0 \\
\psi_{\mathrm{w}}^{\alpha} &= Y_{\mathrm{w}}^{\alpha}\left|\dot{D}_{\mathrm{w}}^{\alpha}\right| + Z_{\mathrm{w}}^{\alpha}\left|\dot{\delta}_{\mathrm{w}}^{p\alpha}\right| \geq 0
\end{aligned}
\tag{18}
$$

where dissipation coefficients Y and Z denote generalized forces that are conjugates of the inter-granular damage and plastic dissipation, respectively. The forms assumed in Eqs. 17 and 18 result in rate-independent form of damage and plasticity as opposed to rate-dependent form that are also relevant to certain granular systems (Giorgio I. and Scerrato D., 2017; Misra A. and Singh V., 2014a; 2014b). Substituting Eqs. 17 and 18 into Eqs. 10a and 10b rewritten for normal and tangential directions one can find the dissipation coefficients, Y and Z, duals of inter-granular damage and plastic displacements respectively.

$$
Y_{\mathrm{n}}^{\alpha} = \frac{1}{2} E_{\mathrm{n}}^{\alpha}\left(\delta_{\mathrm{n}}^{\alpha}\right)^{2}\operatorname{sign}\left(\dot{D}_{\mathrm{n}}^{\alpha}\right); \quad Y_{\mathrm{w}}^{\alpha} = \frac{1}{2} G_{\mathrm{w}}^{\alpha}\left(\delta_{\mathrm{w}}^{\alpha}\right)^{2}\operatorname{sign}\left(\dot{D}_{\mathrm{w}}^{\alpha}\right) \tag{19a}
$$

$$
Z_{\mathrm{n}}^{\alpha} = h_{\mathrm{n}}^{\alpha}\operatorname{sign}\left(\dot{\delta}_{\mathrm{n}}^{p\alpha}\right); \quad Z_{\mathrm{w}}^{\alpha} = h_{\mathrm{w}}^{\alpha}\operatorname{sign}\left(\dot{\delta}_{\mathrm{w}}^{p\alpha}\right) \tag{19b}
$$

Further, normal and tangential components of grain-pair force vector can be found by substituting Eq. 17 into Eq. 7

$$
\begin{aligned}
f_{\mathrm{n}}^{\alpha} &= \frac{\partial W^{\alpha}}{\partial \delta_{\mathrm{n}}^{\alpha}} = k_{\mathrm{n}}^{\alpha}\delta_{\mathrm{n}}^{\alpha} = E_{\mathrm{n}}^{\alpha}\left(1-D_{\mathrm{n}}^{\alpha}\right)\delta_{\mathrm{n}}^{\alpha} \\
f_{\mathrm{w}}^{\alpha} &= \frac{\partial W^{\alpha}}{\partial \delta_{\mathrm{w}}^{\alpha}} = k_{\mathrm{w}}^{\alpha}\delta_{\mathrm{w}}^{\alpha} = G_{\mathrm{w}}^{\alpha}\left(1-D_{\mathrm{w}}^{\alpha}\right)\delta_{\mathrm{w}}^{\alpha}
\end{aligned}
\tag{20}
$$

The details of particular forms of the damage functions D_{n} and D_{w} and related parameters that are applicable to cohesive granular materials have been described in details in our previous work and is therefore not repeated here (Poorsolhjouy P. and Misra A., 2017). **Fig. 2** contains the force-displacement relationships, as well as schematic curves of the functional forms of the force-laws. Moreover, a selection of the major parameters used in the relationships and their role in the force-displacement curves are depicted in the **Fig. 2**. The tension-compression asymmetry of grain-pair behavior and the post peak softening due to damage under grain-pair tension and shear is clearly illustrated. The grain-pair tension-compression asymmetry is significant in induced anisotropy evolution in granular systems (Jia H. et al., 2017). **Table 1** lists all the model parameters and their numerical values used in this study. For more details and implementation of loading-unloading-reloading criteria, ratio between failure force in normal compression to that in normal tension (captured in parameter R), effect of grain-scale relative normal displacement on the grain-scale damage parameter in shear direction (captured in parameters α_1, α_2, and α_3), the effect of confinement on the compressive behavior of grain-pair interactions (captured in the parameter α_4), as well as the incorporation of permanent deformation in grain-pair interactions (captured in parameters β_{n} and β_{w}), the reader is referred to (Misra A. and Poorsolhjouy P., 2015a; Poorsolhjouy P. and Misra A., 2017).

Substituting Eqs. 7 and 20 into the equation for Cauchy stress (Eq. 8) and taking the strain tensor out of the summation, the equation for the fourth rank stiffness tensor can be derived as

$$
C_{ijkl} = \frac{1}{V}\sum_{\alpha=1}^{N_{\mathrm{c}}} k_{ik} l_j l_l \tag{21}
$$

where N_{c} is the total number of grain-pair interactions within the material point. Total number of grain-pair interactions can be calculated as half of the product of the total number of grains, N, and the mean coordination number, z. Using two new parameters, namely the volumetric number density of grain-pair interactions $\rho^{\mathrm{c}} = N_{\mathrm{c}}/V$ and the directional density distribution of grain-pair contacts, $\xi(\theta,\phi)$, this summation over all contacts can be transformed into an integration over all different orientations as

$$
C_{ijkl} = l^2 \rho^{\mathrm{c}} \int_{\theta=0}^{\pi}\int_{\phi=0}^{2\pi} \left(k_{ik} n_j n_l\right)\xi(\theta,\phi)\sin\theta \,\mathrm{d}\theta\,\mathrm{d}\phi \tag{22}
$$

Table 1 Model parameters used in this study.

Model Parameters	Value
E_{no}^{T}	3.5 kN/m
R	17.5
G_{w}	1 kN/m
B_{n}	7E-10 m
B_{nc}	3E-9 m
B_{wo}	1.5E-9 m
α_1	10.5
α_2	7
α_3	0.01
α_4	0.05 MPa^{-1}
β_{n}	0.0
β_{w}	0.6
l_0	10E-6 m
ρ^{c}	1E18 mm^{-3}

where l is the average value of grain-pair branch length in the whole RVE. Using the same approach, the Cauchy stress will also be derived in the integral form as

$$\sigma_{ij} = l\rho^{\mathrm{c}} \int_{\theta=0}^{\pi} \int_{\phi=0}^{2\pi} \left(f_i n_j\right) \xi \sin\theta \mathrm{d}\theta \mathrm{d}\phi \tag{23}$$

For more detailed description of the procedure used to transform the summations into integration see (Misra A. and Poorsolhjouy P., 2016c).

2.3 Scaling laws for grain-size effect

Let us consider two different granular materials whose average grain sizes are d_1 and d_2, where without loss on generality say $d_1 < d_2$, and the subscripts refer to the material type 1 and type 2. A set of size scaling relationships are hypothesized, inspired by the principles of renormalization, to compare the two materials based upon physical arguments. For example, it is reasonable to expect that the average grain-pair branch length of material 2 is related to that of the material 1, through the following simple scaling (in the subsequent equations (Eqs. 24–28) the subscripts 1 and 2 will refer to the two granular materials and are not tensor quantities)

$$l_2 = l_1 \left(\frac{d_2}{d_1}\right) \tag{24}$$

Similarly, the volumetric number density of grain-pair interactions, ρ^c, of the two types of granular materials can be related to each other through the following scaling relationship

$$\rho^{\mathrm{c}}{}_2 = \rho^{\mathrm{c}}{}_1 \left(\frac{d_2}{d_1}\right)^{\alpha} \tag{25}$$

Where the exponent, α, can vary widely depending not only upon the average grain sizes but also the grain size distributions as well as the packing density. The exponent, α, will also depend upon the problem dimension (that is whether the granular material is a packing of 2D grains or 3D grains) and the grain geometry. For the ideal case of 3D packings of monodisperse spherical particles in a regular closed-pack assembly, the exponent, α, will reach the lower bound of –3 (negative 3). It is evident that the value of the exponent α should be negative since the volumetric number density of grain-pair interactions is inversely related to grain size. Calibrating the value will be complicated for random packings of cohesive particles with irregular geometries and complex particle size distributions. However, the exponent will be bound within the bound $-3 < \alpha < 0$.

Further, the deformation behavior of grain-pair depends not only upon the grain-shape, its surface characteristics as well as the cohesive mechanisms, but also on the size of the grain. While the grain size dependence of grain-pair stiffness is complex, the following size scaling is expected even for grains of similar composition and shapes

$$(E_{\mathrm{n}})_2 = (E_{\mathrm{n}})_1 \left(\frac{d_2}{d_1}\right)^{\beta} \text{ and } (G_{\mathrm{w}})_2 = (G_{\mathrm{w}})_1 \left(\frac{d_2}{d_1}\right)^{\beta} \tag{26}$$

where parameter β determines the relative scaling of grain-pair initial (unloaded) stiffness coefficients depending on grain-size. Considering size-effect laws discussed in the literature (Cordero N.M. et al., 2010; 2012; Fredrich J.T. et al., 1990), the numerical value of parameter β is expected to be negative, that is the larger grains result in less stiff grain-pair in comparison to smaller grains.

In addition, the complete force-displacement behavior of a grain pair, particularly its failure behavior, will also be scaled with the change of grain size. The following scaling relationships are introduced for those model parameters that describe the relative displacement where the grain-pair forces reach their peak

$$\begin{aligned} &(B_{\mathrm{n}})_2 = (B_{\mathrm{n}})_1 \left(\frac{d_2}{d_1}\right)^{\gamma};\ (B_{\mathrm{nc}})_2 = (B_{\mathrm{nc}})_1 \left(\frac{d_2}{d_1}\right)^{\gamma}; \\ &(B_{\mathrm{wo}})_2 = (B_{\mathrm{wo}})_1 \left(\frac{d_2}{d_1}\right)^{\gamma}; \end{aligned} \tag{27}$$

Based on experimental results in the literature, it is evident that coarser grains show a more ductile behavior, which means they can store more energy. As a result, the damage parameter used in our model (in normal tension B_{n}, in normal compression, B_{nc}, and in tangential direction, B_{wo}) should be proportional to the grain size. That is, aggregates of larger sizes will fail at a larger displacement. This implies that the size-effect parameter should have a positive value, $\gamma > 0$.

Fig. 3 presents an illustrative parametric study to demonstrate how the size-effect parameters influence the grain-pair behavior. The schematic curves in **Fig. 3** present force-displacement relationships for normal interaction of grain-pairs, under tension, for varying grain-sizes and for varying size-effect parameters. The effect of the size-effect laws on tangential interaction as well as the normal compressive interactions is similar and not presented here for brevity. It is seen in **Fig. 3a** that negative β values lead to stiffer behavior for smaller grains. It is also seen that by keeping β constant and increasing γ, smaller grains show smaller energy storage capacities and smaller failure stress. Inversely, keeping β constant and increasing γ results in larger grains showing a more ductile behavior.

It is also observed (from both **Figs. 3a** and **3b**) that for positive values of γ, if $\gamma = -\beta$, smaller grains show larger stiffness, however, they fail at the same force value and smaller displacement values compared to larger grains. Accordingly, larger grains have a more ductile behavior and a larger work of failure (more energy storage capacity) which is in agreement with typical empirical observations reported in the literature.

It is noted that here that the choice of parameter set

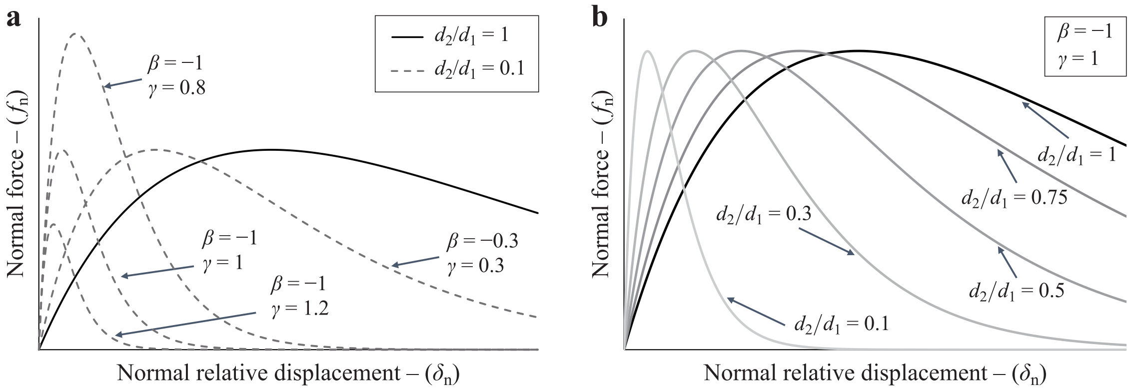

Fig. 3 Parametric Studies: Investigating the effects of size-effect parameters on the behavior of contacts in normal tension. Force-displacement curves for constant grain size and varying model parameters **(a)** and force-displacement curves for varying grain sizes with constant model parameters, **(a)**. Model parameters used in **(b)**, $\beta = -1$ and $\gamma = 1$, are those used in the analysis. Normal interactions in tension are chosen as examples to show the effects of size effect parameters on stiffness and damage.

for simulating the behavior of the specific material investigated in this paper, was done by considering the macroscopic behavior of the material. At the macroscopic level, combining (i) Eq. 20, which describes the mathematical form of the grain-pair stiffness coefficients as function of the stiffness and damage parameters, (ii) Eq. 24, which describes the effect of grain sizes on the magnitude of the branch vector, and (iii) Eq. 26, which describes the effect of grain sizes on the volumetric number density of grain-pair interactions and substituting them into Eq. 22 which derives the macroscopic stiffness tensor, we can derive the ratio between initial macroscopic stiffness tensor of a material with grain size of d_2 to that of a material with grain size of d_1 as follows

$$\frac{(C_{ijkl})_2}{(C_{ijkl})_1} = \frac{(l_2)^2\,\rho_2^c\left(\int\limits_{\theta=0}^{\pi}\int\limits_{\phi=0}^{2\pi}(k_{ik}n_jn_l)\,\xi(\theta,\phi)\sin\theta\,\mathrm{d}\theta\,\mathrm{d}\phi\right)_2}{(l_1)^2\,\rho_1^c\left(\int\limits_{\theta=0}^{\pi}\int\limits_{\phi=0}^{2\pi}(k_{ik}n_jn_l)\,\xi(\theta,\phi)\sin\theta\,\mathrm{d}\theta\,\mathrm{d}\phi\right)_1} = \left(\frac{d_2}{d_1}\right)^2\left(\frac{d_2}{d_1}\right)^{\alpha}\left(\frac{d_2}{d_1}\right)^{\beta} \tag{28}$$

since the magnitude of the branch vector, l, is scaled linearly with size, volumetric number density of grain-pair interactions, ρ^c, scales with grain size through exponent α, and the initial stiffness coefficient of interacting grains at the unloaded state is scaled by β. Accordingly, the initial macroscopic stiffness tensor of a material with grain size d_2 can be derived as a function of the stiffness tensor of the material with grain size of d_1 as follows

$$(C_{ijkl})_2 = (C_{ijkl})_1\left(\frac{d_2}{d_1}\right)^{2+\alpha+\beta} \tag{29}$$

It should be noted that this simple close-form solution is only available for the components of stiffness tensor at the initial (virgin) state. Once the material is subjected to loading, every grain-pair will experience a unique history of relative displacements according to its direction and therefore its force-displacement relationship will be scaled in a nonlinear manner dictated by Eq. 27. As a result, the macroscopic behavior, represented by the evolution of macroscopic tangent stiffness tensor, will be scaled by grain size in a nonlinear fashion which depends on the loading path. In what follows, numerical results of the effects of changing grain size on the stress-strain behavior of a specific granular material is presented to demonstrate the effectiveness of the model and the scaling laws presented.

3. Results

Inspired by the experimental results presented in (Fredrich J.T. et al., 1990), the enhanced GMA based model described in section 2 was applied to simulate the conventional triaxial behavior of cohesive granular materials for a range of grain sizes. The nominal grain sizes of for these simulations ranged from 0.02 m to 0.00001 m. Furthermore, the confining pressure for these conventional triaxial simulations ranged from 0.0 MPa to 400.0 MPa. In these simulations, the parameter values used in our previous work on cohesive granular materials (Misra A. and Poorsolhjouy P., 2015a; Poorsolhjouy P. and Misra A., 2017) are used (See **Table 1**).

Calibration of size-effect parameters was done by investigating their combined effect on the grain-scale behavior as well as the macroscopic continuum level behavior. By considering the physical meaning of each of the exponents, as it was already discussed in Section 2.3, it is clear that $\alpha < 0$, $\beta < 0$, and $\gamma > 0$. However, the choice of the exact value of the parameters is done based upon their combined effect in the overall behavior of the material and by mimicking experimental results. In this paper, we calibrate model parameters based on the experimental results presented in (Fredrich J.T. et al., 1990). We first observe that, for the material under consideration, the initial stiffness coefficients are inversely related to grain-sizes. Considering this and using Eq. 29, it is clear that for this material we need to confine the size-effect parameters such that $2 + \alpha + \beta < 0$. However, it is also seen in (Fredrich J.T. et al., 1990) that this inverse relationship is not very strong and therefore, $|2 + \alpha + \beta|$ should be a small number.

Once these the limits stated above are set, the calibration of the exact values of the parameters, is done by comparing the model results to the stress-strain curves for conventional triaxial test under different confining pressures for materials with different grain sizes. Just like in the grain-scale (as shown in the parametric studies in **Fig. 3**), the effect of size-effect parameters on the macroscopic behavior of the material is also complicated. Accordingly, the choice of the parameters used in this study and for the material under consideration (presented in **Table 2**) is done for deriving an overall fit between the results. A detailed investigation of the influence of the various parameters remains a topic for further research and investigation.

The simulated conventional triaxial compressive experiments are typically performed in two, sequential phases. In the first phase, termed as the confinement phase, the material specimen is subjected to an incrementally increasing hydrostatic confinement to the desired confining pressure, such that ($\sigma_{11} = \sigma_{22} = \sigma_{33} = \sigma_{\text{conf}}$). In the second phase, the material specimen is subjected to deviatoric loading by incrementally increasing the stress in the vertical direction. In this deviatoric phase, the vertical strain, ε_{11}, is increased while the two horizontal stresses (σ_{22} and σ_{33}) are kept constant.

It is well known for cohesive granular materials that increasing confinement results in increasing the material tangential stiffness as well as the failure stress under triaxial loading. The simulations described in this paper, show that reducing grain-size can also result in increasing stiffness and failure stress. For a clear visualization, the results of the triaxial compression simulations are categorized into two cases: Case 1 for small confinements (0.0, 5.0, and 20 MPa), and Case 2 for large confinements (50, 100, 200, and 400 MPa). This distinction has been made to highlight the significant change in the nature of stress-strain relationship as the confinement becomes larger than a value lying between 20 and 50 MPa. The different natures of the stress-strain relationship are clear from the plots given in **Figs. 4** and **5** for the two cases. In **Fig. 4**, we give the evolution of the deviatoric stress, $q = \sigma_{11} - \sigma_{\text{conf}}$, as the applied vertical strain, ε_{11}, is increased for granular materials of different grain sizes for the case of small confinements (< 20 MPa). Further, in **Fig. 5**, we show the same set of results for granular materials of different grain sizes for the case of large confinement (> 50 MPa). It is clear from **Figs. 4** and **5**, that both the stiffness and strength increase as the grain-sizes decrease. Moreover, this stiffening and strengthening effects are greater at the higher levels of confinements as seen from **Fig. 5**.

Table 2 Size effect parameters.

Size effect Parameters	Value (unitless)
α	–1.2
β	–1.0
γ	1.0

More importantly, the results in **Figs. 4** and **5** illustrate the transition in the nature of stress-strain behavior from “brittle failure” to “ductile failure”. The observation that failure behavior transforms from brittle to ductile with increasing confinement is well-known from experiments (Bažant Z.P. et al., 1996; Mahboubi A. and Ajorloo A., 2005; Sfer D. et al., 2002) as well as from simulations using GMA that support the experimental results (Misra A. and Poorsolhjouy P., 2015a). A clear peak in the stress-strain relationship, defined by the point at which the stiffness (slope of the stress-strain curve) reaches zero, characterizes brittle failure. On the other hand, the lack of a peak but a clear change in slope of the stress-strain curve characterizes a ductile failure. Granular materials showing ductile response have a yield point (defined here as the stress and strain point at which there is a significant reduction in stiffness), followed by ideal plastic behavior or a hardening-type behavior.

As expected for a given grain size and changing confinement, the simulation results presented in **Figs. 4** and **5** confirm the above observations. It is noteworthy, however, that the transition from brittle to ductile failure can also be affected by decreasing the grain size for a given confinement as explicated in both **Figs. 4** and **5**. Indeed, if we examine the behavior for different grain sizes at 20 MPa confinement given in **Fig. 4**, we can observe that for grain sizes $d > 0.0001$ mm, there is a clear peak in the stress-strain curves which implies a brittle failure. We note that in this context, the term “brittle failure” signifies a loss of ability of the material to support additional stress. The described “brittle failure” is distinct from the term “brittle behavior”, which, as opposed to “ductile behavior”, implies a low capacity to store energy (i.e. a low work of failure). In contrast, for the same confinement (20 MPa), a “ductile failure” can be observed in **Fig. 5** characterized by a yield point followed by strain-hardening for the material. The transition between brittle and ductile failure happens for material with smaller grain sizes of $d \le 0.0001$ at a confining pressures between 5 MPa and 20 MPa (see **Fig. 4** for $d = 0.0001$, 0.00002 mm and 0.00001 mm). For larger grains, this transition is observed at confinement between 20 MPa and 50 MPa as seen from comparison of results in

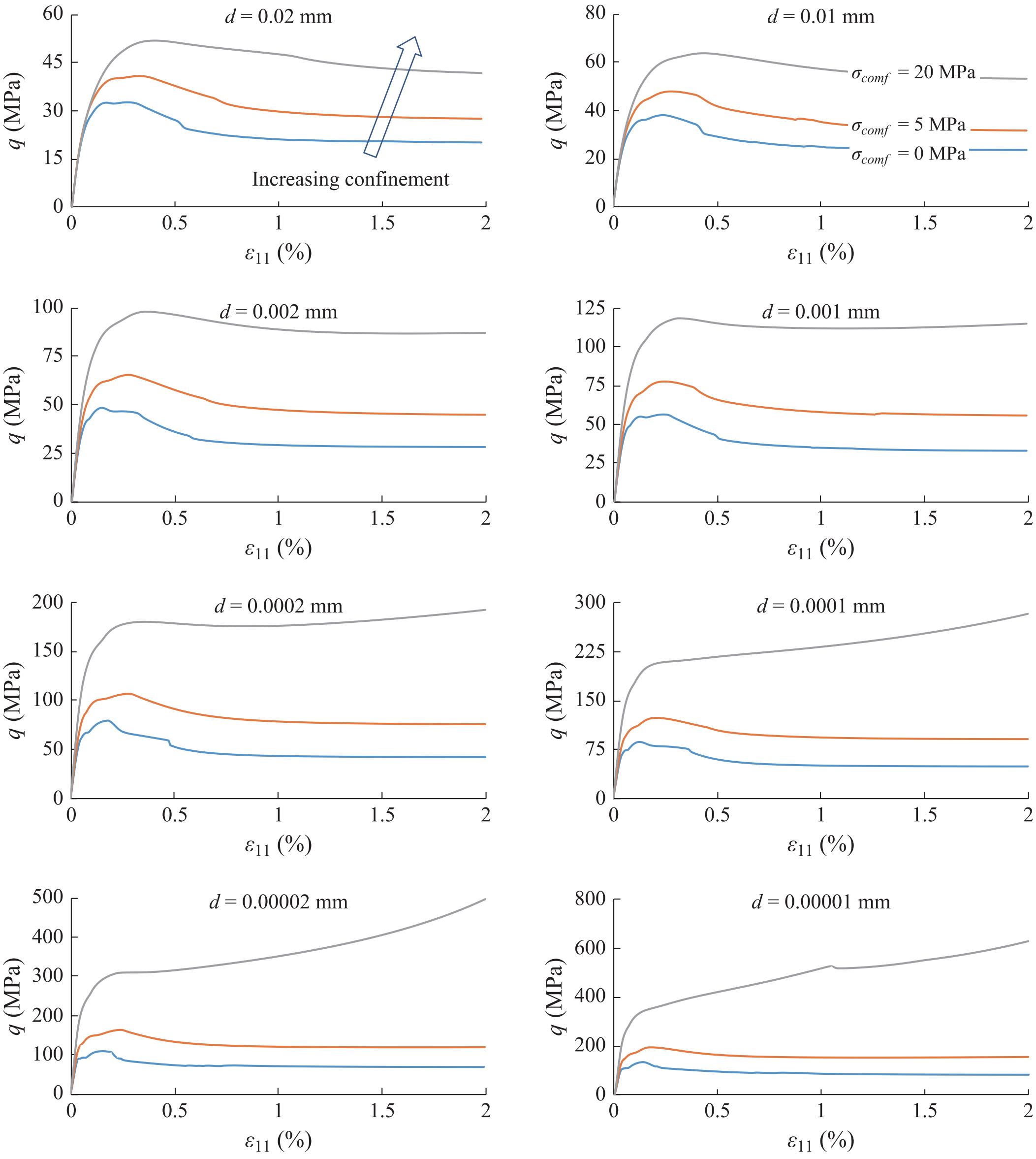

Fig. 4 Stress-Strain in Small Confinement: Evolution of the deviatoric stress, $q = \sigma_{11} - \sigma_{22}$, during triaxial loading (application of ε_{11}) for initial confining pressures of 0.0, 5.0, and 20.0 MPa for all different grain sizes.

Figs. 4 and **5**. This transition from brittle to “ductile failure” is also observed experimentally as seen in (Fredrich J.T. et al., 1990).

The above observation can be further elucidated by investigating the evolution of failure stresses and yield stresses with the grain-sizes. For the case of small confinements, we can identify a failure point as the peak of the stress-strain curve. **Fig. 6a** gives a plot of the *failure* deviatoric stress versus grain sizes for small confinements. On the other hand, for large confinements, it is possible to identify a *yield* deviatoric stress as the point of rapid slope change of the stress-strain curve. In **Fig. 6b**, the *yield* deviatoric stress is plotted against grain sizes for large confinements.

For both the failure and yield stress we see a clear trend of inverse relationship with grain sizes from **Figs. 6a** and **6b**. Interestingly, both failure stress and yield stress increase proportionally with increasing $1/\sqrt{d}$ as a good approximation (note the values of R-squared in the graphs). It is remarkable that the same linear patterns describing the dependency of the failure and yield values on $1/\sqrt{d}$ has been observed experimentally for granular geomaterials (Fredrich J.T. et al., 1990). The inverse relationship of yield stress with grain-size have been shown through finite element modeling using generalized continuum models (Cordero N.M. et al., 2012) as well as experiments (Jia D. et al., 2003).

Finally, it is interesting to investigate the effect of grain-sizes on the evolution of lateral deformations during triaxial tests. In **Fig. 7**, the evolution of volumetric strain ($\varepsilon_v = \varepsilon_{ii} = \varepsilon_{11} + \varepsilon_{22} + \varepsilon_{33}$) is plotted against the applied vertical strain, ε_{11}, during the deviatoric phase. In these plots,

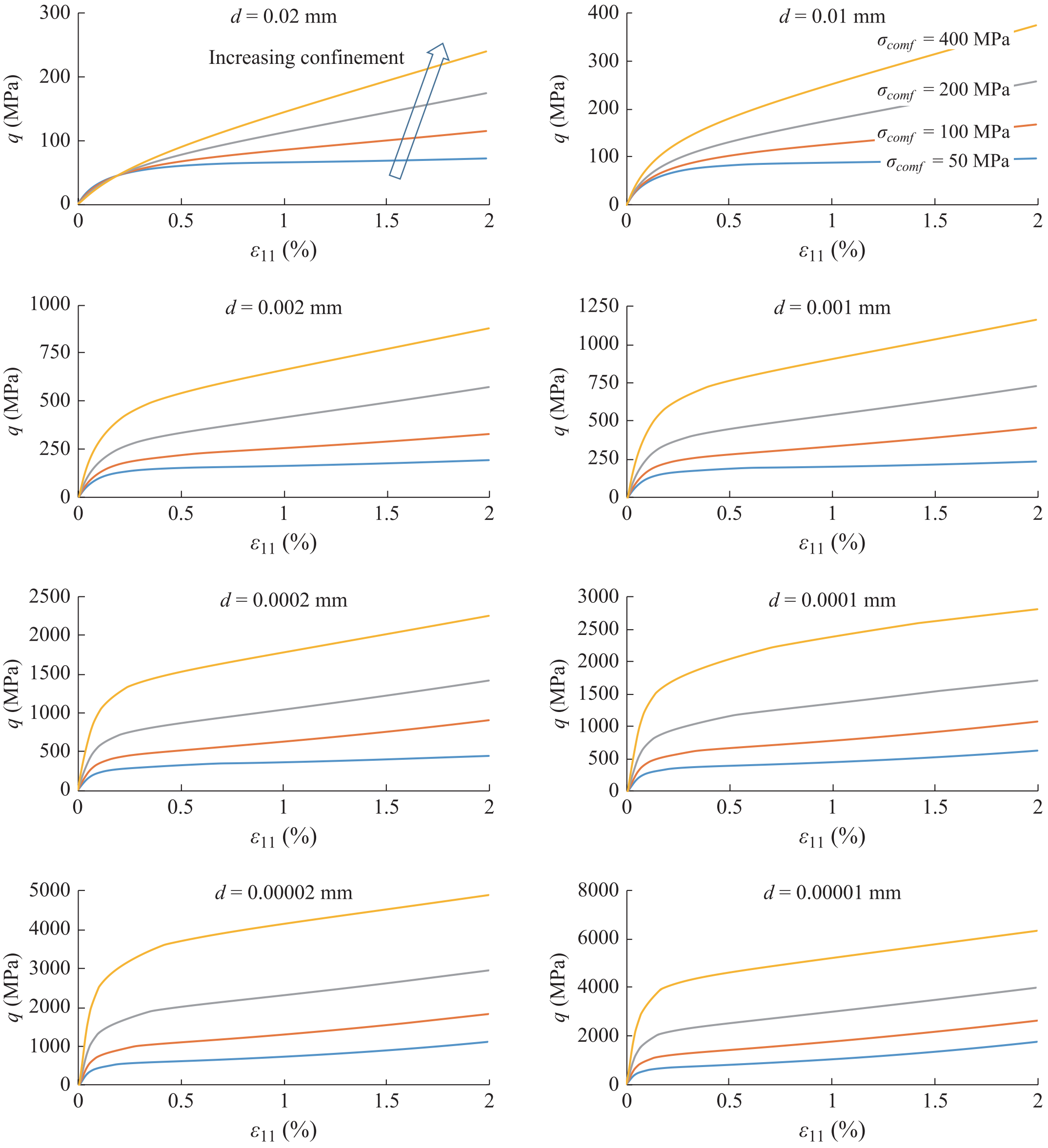

Fig. 5 Stress-Strain in Large Confinement: Evolution of the deviatoric stress, $q = \sigma_{11} - \sigma_{22}$, during triaxial loading (application of ε_{11}) for initial confining pressures of 50, 100, 200, and 400 MPa for all different grain sizes.

the compressive volumetric stress is shown as positive as is standard in granular mechanics. These results show that increasing grain size (as well as increasing confinement) result in a transition from dilation to compaction during triaxial testing. Triaxial tests with low confinement experience compaction (compressive volume strain) over a small interval of axial strain before transitioning to dilation (tensile volume strain). For larger confinement, however, the volumetric strain evolution tends towards compressive region. In fact, for very large confinement, no dilation is observed and the volume monotonically decreases as the loading progresses.

More importantly, these results show the clear effect of grain sizes on the volumetric strain evolution. As grain sizes decrease, the volumetric strain evolves increasingly to the tensile region. Indeed for the smallest grain size ($d = 0.00001$ mm) used in the simulations, the volumetric strain if found to be tensile for all the simulated confinement levels. These results predict that granular materials composed of small grains tend to be more dilative than those composed of large grains. Moreover, the dilative behavior of small-grained materials appears to have limited effect of confinement (particularly for the granular system simulated in this work). We note that in the present study, the focus upon dense cohesive granular materials such as rocks, concrete, and other cementitious materials, in which the effect of initial density variation on the volumetric strain is typically limited. It is noteworthy though that in the present model the effect of initial porosity is incorporated within the parameters of grain-pair interactions. Here, we have evaluated the effect of confining stress on volumetric strain for different grain sizes as shown in

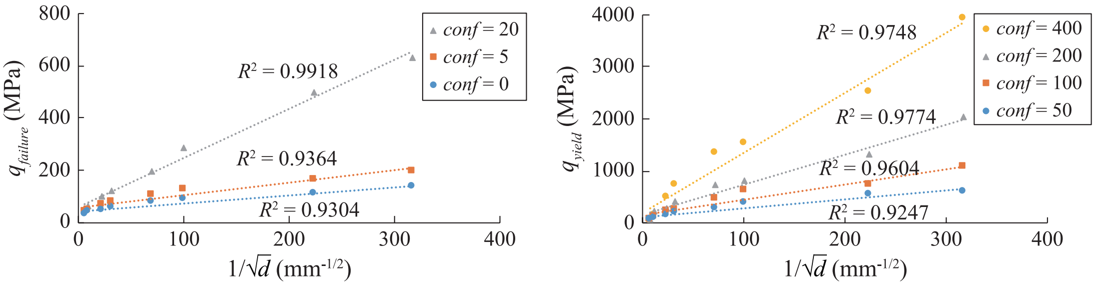

Fig. 6 Failure/Yield Stress vs. Size: Change of failure stress for lowly confined cases, $\sigma_{\mathrm{conf}} \leq 20$ MPa, and yield stress for highly confined cases, $\sigma_{conf} > 20$ MPa by change of grain size.

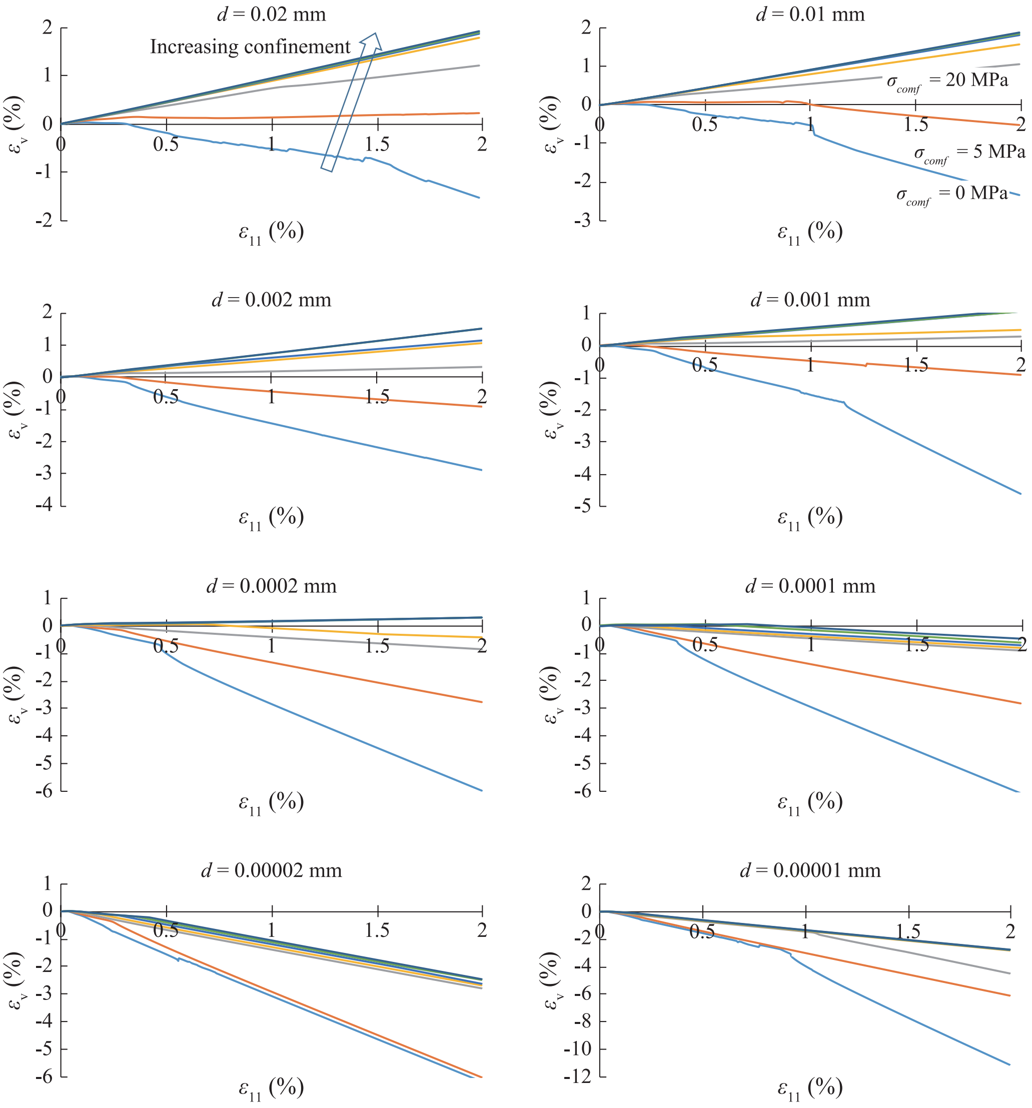

Fig. 7 Volumetric Strain Behavior: Evolution of volumetric strain during deviatoric loading for all different sizes and different initial confinements (0, 5, 20, 50, 100, 200, and 400 MPa). Curves for higher confinements (50 MPa to 400 MPa are too close to distinguish). Note that in these plots compression is taken as positive.

Fig. 7. The effect of initial porosity can also be evaluated for similar materials with varying initial porosities.

4. Summary and conclusions

The described work represents an effort to systematically investigate the influences that grain-sizes have upon the macro-scale or collective response of granular systems with very large number (> 10^6) of grains. It was shown that the GMA based model for damage and plasticity of cohesive granular materials, which was previously derived and validated by the authors, can be enhanced to incorporate the effects of grain size. To this end, a micromechanical viewpoint is utilized to implement the grain-size effect. The set of scaling laws was incorporated into the GMA based model. These include scaling laws for: volume density of grain-pair interactions, grain-pair branch lengths, grain-pair elastic stiffness in normal and tangential directions, and the grain-pair damage parameters in normal and tangential directions. In the presented modeling approach, these microscopic (grain-scale) scaling laws are found to profoundly influence the macro-scale stress-strain response of a granular system.

The derived model is applied to simulate triaxial compressive tests for cohesive granular materials for a range of grain sizes and confinements. The simulation results demonstrate that reduction in grain size results in a stiffer stress-strain behavior, a transition from *brittle* to *ductile* type of failure characterized by peak or yield points in the stress-strain curves, and an increase in the failure and yield stresses. These effects, in some ways, mirror the behavior of granular materials for a given grain-size with change in confinement. It is remarkable, therefore, that change of grain-sizes show similar variation in the material macro-scale behavior. Furthermore, the volumetric behavior of the samples are also seen to depend, in addition to the amount of initial confinement, on the grain sizes. Samples of smaller grain sizes demonstrate more tendency towards dilation (tensile volume strain) compared to samples of larger grain sizes. At very small grain sizes, no amount of compaction is sufficient to keep the volumetric strain in compressive domain. Future work will consider further details of the effect of grain-size on deformation and failure mechanism of granular system, including the formation of shear, compression-tension or mixed-model localization bands and their orientation with respect to the loading directions.

Acknowledgements

This research is supported in part by the United States National Science Foundation grant CMMI-1068528 and CMMI-1727433

Nomenclature

B_n, B_w	damage parameters in the normal and tangential directions
$\boldsymbol{C}_{ijkl}$	fourth rank stiffness tensor
d_1, d_2	grain-sizes
$\boldsymbol{D}_i$, D_n, D_w	grain-pair damage vector and normal and tangential components
$\boldsymbol{D}_{ij}$	continuum damage tensor
E_n	normal stiffness parameter
$\boldsymbol{f}_\mathrm{i}$, f_n, f_w	grain-pair force vector and normal and tangential components
G_w	tangential stiffness parameter
$\boldsymbol{k}_{ij}$, k_n, k_w	grain-pair stiffness tensor and normal and tangential components
$\boldsymbol{l}_i$, l	grain-pair branch vector and branch length
$\boldsymbol{n}_i$	unit vector in the direction of grain-pair branch vector
N	total number of grain
N_c	total number of grain-pair interactions
R	compression-tension ratio
$\boldsymbol{s}_i$	unit vector on the plane orthogonal to grain-pair branch vector forming
$\boldsymbol{t}_i$	unit vector on the plane orthogonal to grain-pair branch vector forming
W, W_n, W_w	macro-scale, normal and tangential grain-pair Helmholtz free energy density
Y	generalized force conjugate to grain-pair damage
Z	generalized force conjugate to grain-pair plastic displacements
α	size scaling parameter for grain-pair volumetric number density
α_1, α_2, α_3, α_4	model parameters controlling damage
β	size scaling parameter for grain-pair initial stiffness
γ	size scaling parameter for grain-pair damage parameters
$\boldsymbol{\delta}_\mathrm{i}$, δ_n, δ_w	grain-pair displacement vector and normal and tangential components
$\boldsymbol{\varepsilon}_{ij}$	infinitesimal strain tensor
ϕ	spherical coordinate
$\boldsymbol{\sigma}_{ij}$	Cauchy stress tensor
θ	spherical coordinate
ψ, ψ_n, ψ_w	macro-scale, normal and tangential grain-pair dissipation potential

References

Bažant Z.P., Xiang Y., Adley M.D., Prat P.C., Akers S.A., Microplane model for concrete: II: data delocalization and verification, Journal of Engineering Mechanics, 122 (1996) 255–262. DOI: 10.1061/(ASCE)0733-9399(1996)122:3(255)

Chang C.S., Misra A., Packing structure and mechanical-properties of granulates, Journal of Engineering Mechanics, 116 (1990) 1077–1093. DOI: 10.1061/(Asce)0733-9399(1990)

116:5(1077)

Cordero N.M., Forest S., Busso E.P., Generalised continuum modelling of grain size effects in polycrystals, Comptes Rendus Mécanique, 340 (2012) 261–274. DOI: 10.1016/j.crme.2012.02.009

Cordero N.M., Gaubert A., Forest S., Busso E.P., Gallerneau F., Kruch S., Size effects in generalised continuum crystal plasticity for two-phase laminates, Journal of the Mechanics and Physics of Solids, 58 (2010) 1963–1994. DOI: 10.1016/j.jmps.2010.06.012

dell'Isola F., Maier G., Perego U., Andreaus U., Esposito R., Forest S., The complete works of Gabrio Piola: Volume I: Commented English Translation-English and Italian Edition, Springer International Publishing, 2014, ISBN: 978-3-319-00262-0

Digby P.J., The effective elastic-moduli of porous granular rocks, Journal of Applied Mechanics-Transactions of the ASME, 48 (1981) 803–808. DOI: 10.1115/1.3157738

Duffy J., Mindlin R.D., Stress-strain relations and vibrations of a granular medium, Journal of Applied Mechanics, 24 (1957) 585–593.

Eugster S.R., dell'Isola F., Exegesis of the introduction and Sect. I from “Fundamentals of the Mechanics of Continua” by E. Hellinger, ZAMM—Journal of Applied Mathematics and Mechanics, 97 (2017) 477–506. DOI: 10.1002/zamm.201600108

Fredrich J.T., Evans B., Wong T.F., Effect of grain-size on brittle and semibrittle strength—implications for micromechanical modeling of failure in compression, Journal of Geophysical Research-Solid Earth and Planets, 95 (1990) 10907–10920. DOI: 10.1029/JB095iB07p10907

Giorgio I., Scerrato D., Multi-scale concrete model with rate-dependent internal friction, European Journal of Environmental and Civil Engineering, 21 (2017) 821–839. DOI: 10.1080/19648189.2016.1144539

Gonzalez M., Cuitino A.M., A nonlocal contact formulation for confined granular systems, Journal of the Mechanics and Physics of Solids, 60 (2012) 333–350. DOI: 10.1016/j.jmps.2011.10.004

Hara G., Theorie der akustischen Schwingungsausbreitung in gekornten Substanzen und experimentelle Untersuchungen an Kohlepulver, Elektrische Nachrichten Technik, 12 (1935) 191–200.

Hentz S., Daudeville L., Donze F.V., Identification and validation of a discrete element model for concrete, Journal of Engineering Mechanics-Asce, 130 (2004) 709–719. DOI: 10.1061/(Asce)0733-9399(2004)130:6(709)

Jia D., Ramesh K.T., Ma E., Effects of nanocrystalline and ultrafine grain sizes on constitutive behavior and shear bands in iron, Acta Materialia, 51 (2003) 3495–3509. DOI: 10.1016/S1359-6454(03)00169-1

Jia H., Misra A., Poorsolhjouy P., Liu C., Optimal structural topology of materials with micro-scale tension-compression asymmetry simulated using granular micromechanics, Materials & Design, 115 (2017) 422–432. DOI: 10.1016/j.matdes.2016.11.059

Mahboubi A., Ajorloo A., Experimental study of the mechanical behavior of plastic concrete in triaxial compression, Cement and Concrete Research, 35 (2005) 412–419. DOI: 10.1016/j.cemconres.2004.09.011

Misra A., Chang C.S., Effective elastic-moduli of heterogeneous granular solids, International Journal of Solids and Structures, 30 (1993) 2547–2566. DOI: 10.1016/0020-7683(93)90165-4

Misra A., Ching W.Y., Theoretical nonlinear response of complex single crystal under multi-axial tensile loading, Scientific Reports, 3 (2013) 1488. DOI: 10.1038/srep01488

Misra A., Nejadsadeghi N., De Angelo M., Placidi L., Chiral metamaterial predicted by granular micromechanics: verified with 1D example synthesized using additive manufacturing, Continuum Mechanics and Thermodynamics, (2020) DOI: 10.1007/s00161-020-00862-8

Misra A., Placidi L., Turco E., Variational methods for discrete models of granular materials, in: Altenbach H., Öchsner A. (Eds.), Encyclopedia of Continuum Mechanics, Springer Berlin Heidelberg, Berlin, Heidelberg, 2018, pp. 1–14, ISBN: 978-3-662-53605-6. DOI: 10.1007/978-3-662-53605-6_172-1

Misra A., Placidi L., Turco E., Variational methods for continuum models of granular materials, in: Altenbach H., Öchsner A. (Eds.), Encyclopedia of Continuum Mechanics, Springer Berlin Heidelberg, Berlin, Heidelberg, 2019, pp. 1–11, ISBN: 978-3-662-53605-6. DOI: 10.1007/978-3-662-53605-6_343-1

Misra A., Poorsolhjouy P., Granular micromechanics model for damage and plasticity of cementitious materials based upon thermomechanics, Mathematics and Mechanics of Solids, (2015a) 1081286515576821. DOI: 10.1177/1081286515576821

Misra A., Poorsolhjouy P., Identification of higher-order elastic constants for grain assemblies based upon granular micromechanics, Mathematics and Mechanics of Complex Systems, 3 (2015b) 285–308. DOI: 10.2140/memocs.2015.3.285

Misra A., Poorsolhjouy P., Elastic behavior of 2D grain packing modeled as micromorphic media based on granular micromechanics, Journal of Engineering Mechanics, 143 (2016a) C4016005. DOI: 10.1061/(ASCE)EM.1943-7889.0001060

Misra A., Poorsolhjouy P., Granular micromechanics based micromorphic model predicts frequency band gaps, Continuum Mechanics and Thermodynamics, 28 (2016b) 215–234. DOI: 10.1007/s00161-015-0420-y

Misra A., Poorsolhjouy P., Granular micromechanics model of anisotropic elasticity derived from Gibbs potential, Acta Mechanica, 227 (2016c) 1393–1413. DOI: 10.1007/s00707-016-1560-2

Misra A., Singh V., Nonlinear granular micromechanics model for multi-axial rate-dependent behavior, International Journal of Solids and Structures, 51 (2014a) 2272–2282. DOI: 10.1016/j.ijsolstr.2014.02.034

Misra A., Singh V., Thermomechanics-based nonlinear rate-dependent coupled damage-plasticity granular micromechanics model, Continuum Mechanics and Thermodynamics, 27 (2014b) 787–817. DOI: 10.1007/s00161-014-0360-y

Nejadsadeghi N., Misra A., Extended granular micromechanics approach: a micromorphic theory of degree n, Mathematics and Mechanics of Solids, 25 (2020) 407–429. DOI: 10.1177/1081286519879479

Placidi L., Barchiesi E., Energy approach to brittle fracture in strain-gradient modelling, Proceedings of the Royal Society A: Mathematical, Physical and Engineering Sciences, 474 (2018) 20170878. DOI: 10.1098/rspa.2017.0878

Placidi L., Barchiesi E., Misra A., A strain gradient variational approach to damage: a comparison with damage gradient models and numerical results, Mathematics and Mechanics of Complex Systems, 6 (2018a) 77–100. DOI: 10.2140/memocs.2018.6.77

Placidi L., Misra A., Barchiesi E., Two-dimensional strain gradient damage modeling: a variational approach, Zeitschrift für angewandte Mathematik und Physik, 69 (2018b) 56. DOI: 10.1007/s00033-018-0947-4

Poorsolhjouy P., Misra A., Effect of intermediate principal stress and loading-path on failure of cementitious materials using granular micromechanics, International Journal of Solids and Structures, 108 (2017) 139–152. DOI: 10.1016/j.ijsolstr.2016.12.005

Poorsolhjouy P., Misra A., Granular micromechanics based continuum model for grain rotations and grain rotation waves, Journal of the Mechanics and Physics of Solids, 129 (2019) 244–260. DOI: 10.1016/j.jmps.2019.05.012

Qomi M.J.A., Krakowiak K.J., Bauchy M., Stewart K.L., Shahsavari R., Jagannathan D., Brommer D.B., Baronnet A., Buehler M.J., Yip S., Ulm F.J., Van Vliet K.J., Pellenq R.J.M., Combinatorial molecular optimization of cement hydrates, Nature Communications, 5 (2014) 4960. DOI: 10.1038/ncomms5960

Sfer D., Carol I., Gettu R., Etse G., Study of the behavior of concrete under triaxial compression, Journal of Engineering Mechanics-Asce, 128 (2002) 156–163. DOI: 10.1061/(Asce)0733-9399(2002)128:2(156)

Tavarez F.A., Plesha M.E., Discrete element method for modelling solid and particulate materials, International Journal for Numerical Methods in Engineering, 70 (2007) 379–404. DOI: 10.1002/nme.1881

Turco E., dell’Isola F., Misra A., A nonlinear Lagrangian particle model for grains assemblies including grain relative rotations, International Journal for Numerical and Analytical Methods in Geomechanics, 43 (2019) 1051–1079. DOI: 10.1002/nag.2915

Walton K., The effective elastic-moduli of a random packing of spheres, Journal of the Mechanics and Physics of Solids, 35 (1987) 213–226. DOI: 10.1016/0022-5096(87)90036-6

Ziegler H., An Introduction to Thermomechanics, 2nd edition, North-Holland, Amsterdam, 1983, ISBN: 9780444598936.

Authors’ Short Biographies

Payam Poorsolhjouy

Payam Poorsolhjouy is an Assistant Professor in the Chair of Applied Mechanics at Eindhoven University of Technology. His research interest is multiscale modeling and design of materials with complicated microstructure. He received his PhD in Civil Engineering with honors and as the Outstanding PhD graduate of the School of Engineering, from University of Kansas in 2016. He then joined Purdue University as a PostDoc working on multiscale material modeling. Prior to joining TU/e he was a University Assistant at Graz University of Technology. He has co-authored multiple journal papers and presented his research in various national and international conferences.

Anil Misra

Anil Misra is Professor of Civil Engineering and Associate Director of the Bioengineering Research Center at the University of Kansas, Lawrence. He has more than 30 years of experience in the area of multi-scale modeling, constitutive behavior of interfaces, granular soils and cement/asphalt concrete, and multi-modal material characterization using high-resolution techniques. He has pioneered the method of granular micromechanics. He has co-edited four books, guest edited five journal special issue, and authored more than 300 papers in journals, edited books and conference proceedings. He serves as a reviewer for multiple journals, extramural funding agencies and provides consulting services to industry.

KONA Powder and Particle Journal No. 39 (2022) 208–218/https://doi.org/10.14356/kona.2022013 Original Research Paper

Verification of Polyhedral DEM with Laboratory Grinding Mill Experiments†

Alberto M. Puga [1], Nicolin Govender [2,3] and Raj K. Rajamani [1]*

[1] *Department of Material Science and Engineering, University of Utah, USA*
[2] *Department of Mechanical Engineering, University of Johannesburg, South Africa*
[3] *Research Center Pharmaceutical Engineering GmbH, Austria*

Abstract

The simulation of grinding mills with the discrete element method (DEM) has been advancing. First, it emerged as a method for studying charge motion with spherical balls and predicting the power draw of the mill. Subsequently, studies on liner wear, charge motion with ellipsoidal and polyhedral shaped particles simulated with three dimensional DEM followed. Further, the impact energy spectra computed in the DEM algorithm is leading to the development of models for the breakage of brittle particles in mills. The core elements in such simulations are the shape of particles in the mill charge and the power draw of the mill due to operating variables. To advance the field, we present a set of experimental data and the corresponding DEM validation results for a 90 × 13 cm mill. The DEM algorithm uses the volume-overlap method which is more realistic for multifaceted irregular particle collisions. Further, we use the scanned shape of the rock media and multifaceted spherical shape for the grinding media to represent as close as possible the actual charge in the mill. First, we present DEM validation for spherical grinding media-only experiments, rock-only experiments, and a mixture of spherical grinding media and rocks, as well as aluminum cubes only to represent the theme of particle shape. Finally, a discussion of the contact mechanics parameters in the four modes of experiments is given. Since the feed ore to plant scale mills can vary in shape, mill simulations with scanned shape of typical particles are the future for more accurate results.

Keywords: DEM, discrete element method, polyhedral, simulation

1. Introduction

In hard rock mining and metal production, the grinding unit operation follows stages of crushing mined ore. Naturally, occurring ores contain metal-bearing minerals. The purpose of grinding is to liberate metal-bearing mineral grains from the host particles. Next, the valuable mineral particles are recovered in subsequent processes. Since the grade of metal values in ores is in the range of one percent or less, thousands of tons of ore are milled every hour. As a result, the grinding mills are massive in size requiring a few megawatts of power to operate. Being such an energy consuming operation, grinding mills have been studied by researchers around the world to improve energy efficiency. Since the mills are massive in size, the tumbling environment inside the mill is very harsh, defying any attempt at quantifying the charge dynamics with sensors. However, laboratory-scale experiments have been done tactfully to provide information on power draw and charge profiles of material inside the mill. One of the critical needs in milling is to understand charge flow inside the cylindrical mill shell. Since the internal forces produced inside the charge mass are the cause for particle size reduction, this study has fallen under the realm of the numerical methods known as the Discrete Element Method (DEM) (Tavares et al., 2020). It provides a direct numerical simulation of the motion of thousands of particles tumbling inside the cylindrical mill shell, and besides, the forces acting on the particles can be used to model particle breakage. Djodjeric et al. (2006) studied the competency of large pieces of rocks in an AG mill with DEM. They presented charge pressure due to normal forces acting on the bed of rock to account for the breakage or non-breakage of rocks.

1.1 Grinding mills

Almost every mining plant operation employs either a Semi-autogenous (SAG) or Autogenous (AG) mill, followed by ball mills. Since SAG and AG mills are capable of performing the size reduction of one or two-stage

---

† Received 10 March 2021; Accepted 16 June 2021
J-STAGE Advance published online 7 August 2021

* Corresponding author: Raj K. Rajamani;
Add: William Browning Bldg, Salt Lake City, UT 84112, USA
E-mail: albertopuga15@gmail.com
TEL: +1-801-581-3107

crushing size reduction circuits, they are found extensively in many mineral ore processing operations. The product of SAG or AG mills is represented by size, called “transfer size”, which is in the range of few millimeters. Material contained in these sizes is suitable for further size reduction in ball mills to a size of 100–200 µm. Typical SAG mills are 9–12 m in diameter. The top size of feed ore to SAG/AG mills is around 10–35 cm. These mills usually operate with a screen deck at the discharge end to recycle the coarse portion of the material back into the mill.

AG mills take advantage of the weaker competence of the ore to break them. The ore particles impact directly against the mill shell and break readily. This mode of breakage is called self-breakage, and only a few ore deposits around the world are amenable for breakage in AG mills. In SAG mills, in addition to self-breakage, the grinding balls due to their greater density add to ball-to-rock impact breakage. Besides these two major modes of impacts, the grinding action includes attrition grinding or chipping of sharp edges. The entire system of grinding modes is influenced by design factors such as liners, lifters, grate opening, operating conditions (mill filling and speed), and ore hardness.

1.2 DEM simulation of grinding mills

It is apparent from the foregoing that real-world particles are irregular in shape. However, early numerical DEM studies began with spherical shapes, partly because they are the easiest to model collisions numerically (Mishra and Rajamani, 1990; 1992; Cleary, 2001; Cleary et al., 2003; Morrison and Cleary, 2004). Although, researchers in the DEM field recognized the importance of particle shape, yet the cost of computational time-restricted them to basic spherical shape and its close variants. The earliest of these were shapes generated with superquadrics algebra. During milling, particles with high angularity lose their sharp edge readily mainly due to chipping and abrasion, not to mention these sharp edges are the weakest in the modes of breakage. Hence, superquadrics in a preliminary sense were well adapted to simulate such rounded particles. Rothenburg and Bathurst (1991) presented a DEM algorithm for contact detection and collision of elliptical particles in the simulation of micromechanics of granular assemblies. Hopkins et al. (1991) used polygonal shape particles to create a two-dimensional of rocks and sea ice blocks to simulate the formation of multilayers floes. Potapov and Campbell (1996) created a three-dimensional technique to simulate the brittle solid fracture by “gluing” together convex polyhedral particles. Realizing the need for non-spherical shapes in DEM, Latham et al. (2008) published a library of three-dimensional shapes. Cleary (1998) was the first author to introduce superquadrics for the DEM simulation of grinding mills. This author (Cleary, 1998) described the simulation of a 5-m diameter ball mill in detail including particle segregation, collisional force distributions, and liner wear. Delaney et al. (2010) went a step further using superquadrics in the simulation of particle breakage in comminution processes: a set of smaller particles were packed inside a superellipsoid, and the superellipsoid was made to break upon experiencing a certain energy limit releasing the smaller particles representing the breakage of the larger ellipsoid. Besides the spherical grinding media in ball mills, a shape termed “cylpebs” was developed to produce improved media packing in the tumbling mill charge. Kiangi et al. (2013) used DEM simulation spherical and multi-faceted polyhedron shapes to predict the load and power draw in a pilot-scale mill filled with spheres and cylpebs. Xu et al. (2019) using the superellipsoid particle model studied the effect of spherical and cuboidal particles on the wear of a mill. Realistic DEM simulations of plant size grinding mills require particle filling in the millions. Govender et al. (2015) showed how graphic processing unit (GPU) computation can speed up 3D DEM simulation of mill charge. The framework for such high-performance computing is described in Govender et al. (2016). This was followed by the introduction of irregular shaped particles such as scaled hexagonal prisms, truncated tetrahedra, cubes, and other shapes in GPU-based DEM computing. Govender et al. (2018a) presented the grinding mill simulation of regular polyhedral particles such as cube, tetrahedra, hexagonal prism, Biluna, and mixed polyhedral particles. This study investigated the role of particle angularity and aspect ratio on power draw. In particular, the normal and shear energy dissipation components on the power draw were shown to differ depending on the shape of the particle. Particle shape and angularity contribute to interlocking and shear slippage between particles (Govender et al., 2018b) for the study of particle mixing. The next logical choice for irregular particles was a cluster of spheres or clumped spheres. Like superquadrics, this object too was amenable to easier collision detection (Latham et al., 2008), since at the time of contact only a pair of spheres in the outermost periphery of colliding objects are involved. Hence, the problem reverts to spherical particle collision. This cluster of spheres particles model is adopted in the commercial software EDEM (2011).

There have been numerous studies of DEM applied to the simulation of grinding mills. Some have even applied smoothed particle hydrodynamics (Cleary et al., 2006; 2008) to describe the motion of ore particle slurry along with the motion of larger DEM particles. The single most advance in DEM modeling of grinding mills is the use of collision energy spectra (number of collisions of an energy class versus collision energy) to predict the breakage rate of brittle ore particles (Tavares and Carvalho, 2009). Tavares and Carvalho (2009) described the breakage rate of coarse particles taking into account direct impact breakage of particles by grinding media as well as the weakening of particles by repeated collisions. In a review paper on this subject, Tavares (2017) describes the evolution of microscopic particle breakage rate models from the 1980s to recent advances such as the detailed models of breakage probabilities as a function of impact energy, body and surface breakage, mass of powder caught in each collision, weakening or damage of particles due to repeated collisions, and the incorporation of these models in DEM. In this manuscript, we present a DEM simulation of non-spherical or polyhedral shaped particles tumbling in a laboratory-scale mill. In particular, the scanned polyhedral shapes of rock particles are used in DEM simulation. This study demonstrates that mill power draw can be modeled directly with a mixture of spherical and polyhedral particles. Laboratory-scale measurements of power and captured images of charge motion are compared with DEM simulation done with Blaze-DEM GPU framework software. The method of modeling irregular particles is presented followed by experimental and simulated results. The novelty of this study lies in the fact that the introduction of real rock shapes mixed in with spheres allows improved charge motion representation in DEM simulation of grinding mills. We show the actual scanned polyhedra shapes can lead to accurate prediction of the power draw and charge motion in the tumbling mill. This work paves the way forward for the simulation of plant scale SAG/AG mills using actual large rock shapes passing through these mills.

2. DEM Computing

The simulation of few thousands of particles in DEM is relatively less cumbersome and can be done readily in single-core central processing units (CPU). For hundreds of thousands of particles, parallel computing on multi-core CPUs can be done in a reasonable time frame. However, when millions of particles are simulated, it takes several days of computing for a mere 1 second of real-time on CPUs. Hence, the next step in the development of the DEM framework is the use of graphic processor unit (GPU) computing that has become readily available in the last ten years and which is going to increase in popularity due to many software advances. Today’s GPU offers 24–48 GB of memory and hence handling millions of particles is not a problem. However, DEM requires more severe memory transactions compared to mere numerical computations. These transactions become an order of magnitude higher when computing with polyhedral particles with the number of faces as large as thirty-two. Hence, DEM algorithms must be extremely efficient even with GPU computing.

2.1 Blaze-DEM framework

Blaze-DEM is a GPU-based computational framework for the discrete element methodology (Govender et al., 2016). The evolution of this code has been described in previous publications and we present a few details about the simulation results here. The first feature is that the simulation object geometry can be represented using typical CAD geometry (STL format). This feature is especially useful in importing, for simulation, mill geometry with liners, lifters, grate plates, and pulp lifters in STL format. The code implements “world” objects, to indicate the process vessel under simulation, in this case, a primitive cylinder. Besides, the world object accommodates STL files depicted in triangulated geometry. Next, volume objects in the code can accommodate liners, lifters, grate plates, and pulp lifters. Finally, the material object includes steel spheres and rock particles of different shapes and solid densities. These objects are represented as convex polyhedral shapes joined by planes.

Contact detection is a key feature of DEM. The usual approach is to compute the distance between the center of mass of two colliding objects comparing it to the distance between the two foremost colliding surfaces. Blaze-DEM uses a unique approach named “ray-tracing” in which independent rays (computational threads) are projected from each vertex of polyhedron or center of mass of spheres to check if there is contact with the other surfaces. The ray-tracing algorithm is common in computer graphics. This approach is very convenient to detect contact between two polyhedra since polyhedron is just a collection of surfaces. More details of contact detection involving broad phase, narrow phase, and detailed phase of contact detection are found in Govender et al. (2018).

2.2 Contact mechanics

The mechanics used in the collision between two polyhedra is much different from that commonly used in a pair of colliding spheres. With spheres, the virtual penetration distance is the primary quantity from which forces are estimated in various ways. Herewith polyhedra, the forces are calculated from overlapping volumes (Govender et al., 2018). The advantage of contact volume is that both the direction and magnitude of forces can be resolved with an energy-conserving contact scheme (Govender et al., 2019). The contact scheme is illustrated with a cube and a polyhedral particle colliding with a larger cube, shown in **Fig. 1**. The intersecting volume is a convex hull formed by the vertices at the intersections between the cube’s edges and polyhedron surfaces.

Computing the volume of a convex hull, with a computationally efficient algorithm is not a trivial task. The details of volume computing are given in Govender et al. (2018a;

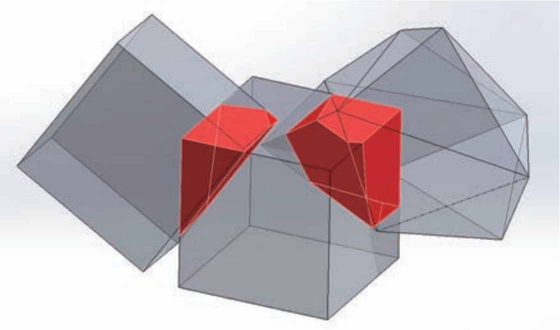

Fig. 1 Intersecting vertices of overlap and volume overlap between cubes and polyhedron.

2018b; 2018c). First, the bounding surfaces and their respective normal are determined. Using Green's theorem, the triple integral of the volume is computed with double integration as a summation over the computed areas.

The simulation shown here involves a few hundreds of polyhedral rock particles and multifaceted steel spheres. As detailed above, even for a few hundred particles, contact detection, and computing intersecting volume becomes an intensive computational task. Besides, the simulations were carried out for eight complete revolutions of the mill cylinder. These computations took a few hours of computing time with an Intel Core i7-6850K 3.6 GHz with an NVIDIA GeForce RTX 2060 GPU.

Normal Contact: The well-known linear viscoelastic spring dashpot model is found to reproduce grinding mill results (Rajamani et al., 2000). The spring force that stores energy and the dissipative force that dissipates energy are given by Eqn. (1) and Eqn. (2), respectively.

$$\boldsymbol{F}_{\mathrm{n}}^{\text{spring}} = (K_{\mathrm{n}} \Delta v^{\frac{1}{3}}) \hat{\boldsymbol{n}} \tag{1}$$

$$\boldsymbol{F}_{\mathrm{n}}^{\text{dash}} = C_{\mathrm{n}} (V_{\mathrm{R}} \hat{\boldsymbol{n}})\ \hat{\boldsymbol{n}} \tag{2}$$

where K_{n} is the spring stiffness ($\frac{\mathrm{m}}{\mathrm{s}}$), $\hat{\boldsymbol{n}}$ is the normal direction along which the force acts, C_{n} is the damping coefficient ($\frac{\mathrm{Ns}}{\mathrm{m}}$), v is the intersecting volume and V_{R} is the relative velocity between contacting polyhedra. In the simulation results presented here following refinement of spring constant K_{n} and dashpot constant C_{n} were used.

$$K_{\mathrm{n}} = \frac{m_{\mathrm{eff}}}{t_{\mathrm{contact}}^{2}} \ln(\epsilon)^{2} + \pi^{2} \tag{3}$$

$$C_{\mathrm{n}} = \frac{2\ln(\epsilon)\sqrt{K_{\mathrm{n}} m_{\mathrm{eff}}}}{\sqrt{\ln(\epsilon)^{2} + \pi^{2}}} \tag{4}$$

where ϵ is the coefficient of restitution, and m_{eff} is the effective mass of colliding bodies, which is given by Eqn. (5).

$$m_{\mathrm{eff}} = \left(\frac{1}{m_1} + \frac{1}{m_2}\right)^{-1} \tag{5}$$

The common practice in contact force calculations is to 'break contact' or terminate contact calculations when the normal force changes direction and is turned inward toward the contact. However, by limiting the contact time, conservation of energy is maintained. Contact time is usually chosen as multiples of computational time steps depending on the properties of the pair of materials in contact.

Tangential contact: Although there are many variations of the spring-dashpot model for tangential contact, the best one that produces consistent mill simulation results in the history-dependent tangential contact proposed by Cundall and Strack (1979). The current time step tangential force is calculated by Eqn. (6) and Eqn. (7).

$$\boldsymbol{F}_{\mathrm{t}}^{\text{spring}} = -K_{\mathrm{t}} (V_{\mathrm{t}} \Delta t) + \boldsymbol{F}_{\mathrm{t}}{}' \tag{6}$$

$$\boldsymbol{F}_{\mathrm{t}}^{\text{dashpot}} = \min\left(C_{\mathrm{t}} V_{\mathrm{t}}, \mu \boldsymbol{F}_{\mathrm{n}}^{\text{spring+dashpot}}\right) + \boldsymbol{F}_{\mathrm{t}}{}' \tag{7}$$

where $\boldsymbol{F}_{\mathrm{t}}{}'$ is the tangential force existing in the contact at the previous time step, but projected onto the current tangential plane and V_{t} is the relative tangential velocity. It should be mentioned implementing history dependence in GPU architecture is a formidable task since contact detection among millions of particles is done with a hashing algorithm. It is nearly impossible to synchronize a particular previous instant contact with the current one in hashing algorithms.

Power Calculation: The verification of DEM prediction for grinding mills relies on mill power prediction. In addition, a comparison of the experimental charge profiles with simulated profiles offers additional proof. Unfortunately, measurement of stresses on mill shells or lifters is only possible under very particular conditions in the laboratory and pilot-scale mills. The total energy consumed in a collision is simply the energy dissipated in the numerous collision events. Therefore, the power is calculated by summing all the dissipated energy over one full revolution of the mill, given by Eqn. (8).

$$E = \sum_{i}^{k} (\boldsymbol{F}^{\text{dashpot}} \Delta x) \tag{8}$$

The F^{dashpot} force defined in Eqn. (2) and Eqn. (7), respectively, and Δx refers to the distance over which the dissipative force acts in each collision. In this intersecting volume approaching Δx in the value $\Delta v^{\frac{1}{3}}$. Finally, the estimated power is given by Eqn. (9).

$$P = \frac{E}{t_{\mathrm{rev}}} \tag{9}$$

where t_{rev} is the time for one revolution. It is customary to run the simulation to about eight revolutions and take the average power over the last few revolutions.

3. Experiment work and Blaze-DEM validation

In this paper, we validate the volume-based polyhedral contact model with a history-dependent tangential model via experiments in a tumbling mill. First, we show the validation for the mill running with spherical steel balls, next with rocks, and finally with a mixture of steel balls and rocks. In addition, an experiment with aluminum cubes is also included for model validations.

3.1 Experimental setup

We used a laboratory-scale slice of a mill fitted with a clear plexiglass front plate for capturing the motion of the charge with a camera. The mill is 90 cm in diameter and 13 cm in internal length (15 cm including front and back plates). The mill is fitted with eight square lifters with a cross-section of 4 × 4 cm. The grinding media were 5.08 cm steel balls of density 7859 $\frac{\text{kg}}{\text{m}^3}$. The irregular ore particles had a length dimension in the range of 3 and 5 cm and a height dimension in the range of 3 and 4 cm. The mill is fitted with a torque sensor on the drive shaft attached to the cylinder to measure the power drawn by the charge. Thus, the energy losses in the electric motor, are avoided.

Ore particles: Rocks from a local quarry were used in these experiments. These rocks were chosen for their high hardness because they did not break during experiments retaining the integrity of their shape. To characterize the shape of the rocks, four rocks were chosen randomly, shown in **Fig. 2**. Although it is possible to map the three-dimensional shape with laser scanners, we needed to have fewer faces in the polyhedral representation. Otherwise, the simulation would take unusually long compute times. The rocks were placed in a three-dimensional graduated cardboard axis frame. First, the rocks were triangulated with a pen as well as possible. Next, the *x*, *y*, and *z* co-ordinates were measured with a ruler and the axis frame. Finally, the polyhedral particle was reconstructed in CAD software. We only expect to get an approximate polyhedron representation of the rock's shape. **Fig. 2** shows the reconstructed polyhedral shapes. It is our view that a much higher shape resolution is not necessary for tumbling mill predictions. These shapes are referred to as PolyA, PolyB, PolyC, PolyD, PolyE, and PolyF in the simulations. The measured density of the rock was 2636 $\frac{\text{kg}}{\text{m}^3}$. Grinding balls: The diameter of the balls was 2 in and only one single size was used in all the experiments.

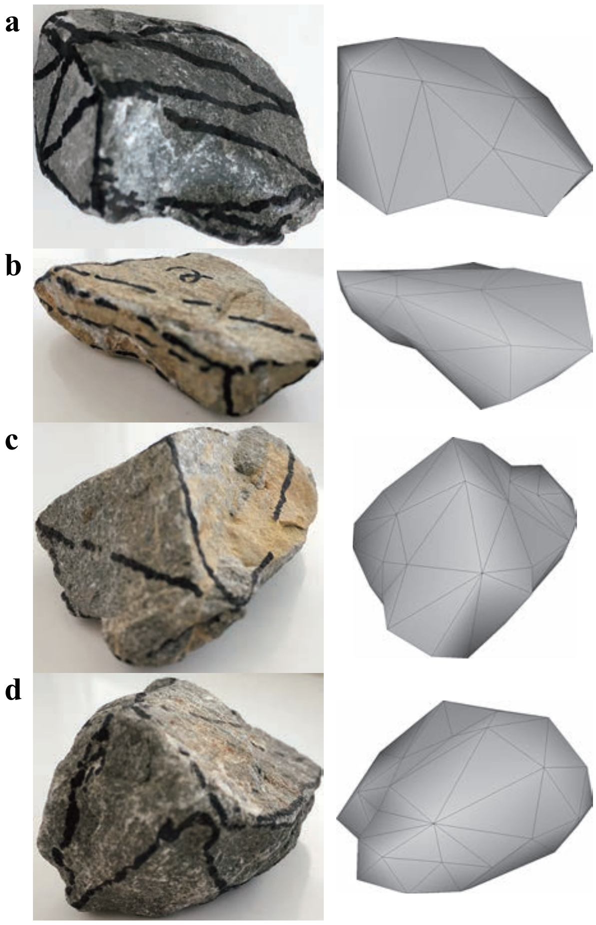

Fig. 2 Four random rock particles **a**, **b**, **c**, and **d** on the left, and their polyhedral representation on the right.

4. Experimental results and DEM validation

As a prelude to experimental results in milling, it is useful to understand the general picture of the charge shape inside the mill. Due to the presence of lifters, the charge in contact with the mill shell moves at the same velocity as the mill shell except for slippage of charge in between the lifters. The particles leaving from the shell at the shoulder of the mill executed a parabolic trajectory. These trajectories meet the mill shell on the other side of the mill. To describe different locations on the mill shell, we use the ubiquitous mathematical notation depicted (on **Fig. 3**) of angle increasing counterclockwise from the *x*-axis, reaching 90° at the positive *y*-axis, and gradually increasing to 180° at the negative side of the *x*-axis followed by 270° at the negative *y*-axis, where the mill's center is the origin for the *x*-axis and *y*-axis frames. At a higher percentage of critical speeds, the particles leaving the shoulder may strike in the vicinity of 180° or even higher at 150°.

The fully cascading charge shape has a bi-linear shape for the free surface above the charge. The free surface starts in between 210° and 240° marks, termed "toe", rising at a shallow angle, to the inflection point near the center of the mill, and then the charge rises steeply to the shoulder position, which is around 30° to 60° mark. This profile is entirely directed by the mill filling volume. Between the mill shell and charge surface, there is a layer traveling

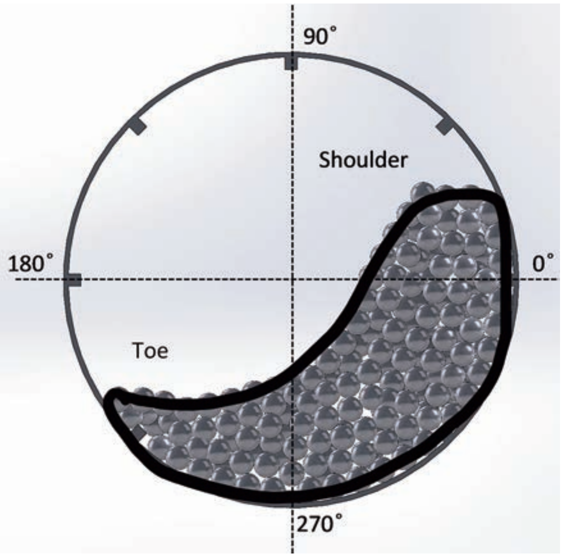

Fig. 3 Description of the definition of shoulder and toe in the charge profile.

Table 1 Simulation parameter for Case 8, P2P indicates particle-particle and P2W indicates particle-wall settings.

Parameter	Symbol	Value	Unit
Normal Particle Stiffness	K_n	4×10^6	N/m
Tangent Particle Stiffness	K_t	3×10^6	N/m
Damping Coefficient	C	0.01	
Coefficient of Restitution (P2P)	ε	0.85	
Static Friction (P2P)	μ_s	0.7	
Kinetic Friction (P2P)	μ_k	0.7	
Coefficient of Restitution (P2W)		0.7	
Static Friction (P2W)		0.6	
Kinetic Friction (P2W)		0.6	
Time Step	Δt	1×10^{-4}	s

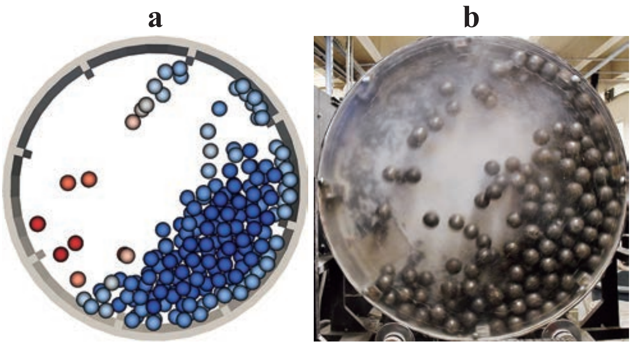

Fig. 4 **(a)** Simulation velocity profile and **(b)** experimental results for Case 8 (25 % balls, 31.8 rev/min).

upward followed by layers cascading downward. Between these two layers, there are a few layers of particles that are nearly stationary.

Next, we show a set of experimental results and DEM simulation comparisons for mill charge flow and power draw. The experiments were run with balls only, rocks only, and then a mixture of balls and rocks. Finally, an experimental run with aluminum cubes is shown. The DEM simulation requires 10 sets of parameters for the respective contact mechanics between balls, rocks, and the mill shell. In each of the experiments shown here a table of the contact parameter is also included. A discussion of this parameter set is given at the end of this section.

Case 8: This case contains 190 steel spherical balls which contribute to 25 % volume filling of the mill for a total mass of 97.4 kg. The density of the steel sphere was set to 7800 $\frac{\mathrm{kg}}{\mathrm{m}^3}$. The mill speed was set at 31.6 $\frac{\mathrm{rev}}{\mathrm{min}}$. **Table 1** gives the DEM parameters used in the simulation. **Fig. 4(a)** shows the image of the charge velocity profile for the DEM simulation, and **Fig. 4(b)** shows the image of the charge in the mill. With the mill filling being all steel spheres, the two charge profiles match very well at the toe, shoulder, and belly positions. There were a few balls cataracting in the actual experiment. The balls are hitting above the toe region and between 180° to 270°. This characteristic of the profile is also seen in the DEM simulation, which is a clear indication of the simulation accuracy. The experimental power is 1762 ± 30 W, whereas the DEM simulation predicts 1609 ± 40 W.

We now present the simulation results for the polyhedral (rock) particles alone or in a mixture with spherical steel balls, comparing the power draw and charge profiles. The experimental mill reaches a steady-state in two full revolutions of the mill and hence all the results presented here are at a steady-state.

Case 11: This case is a mixture with 354 rock particles (12 %) and 99 5 cm steel balls (13 %) for a total mass of 66.3 kg. The mill speed was set at 25.1$\frac{\mathrm{rev}}{\mathrm{min}}$. **Table 2** gives the DEM parameters used in the simulation. **Fig. 5(a)** shows the image of the charge and **Fig. 5(b)** depicts the DEM profile colored by particle type. In this case, the spherical particle too was modeled as a 32-equisided polyhedron. Due to repeated impacts, the steel spheres become non-round over time. Hence, we capture the shape of the sphere that looks like a soccer ball with the 32-sided polyhedron. Such representations of the shapes, adds to the accuracy of the particle trajectories. The two profiles agree well regarding the toe position, shoulder position, and the belly of the charge. Also, few particles cataracting is well matched between experiment and DEM simulation. Due to a very high degree of angularity in the rock particles, the charge seems to lock up with each other and hence we see a steeper shoulder position than normal. The DEM simulation captures this behavior. The DEM power draw of 1,010 W ± 5 compares well with the experimental value of 1105 W.

Case 1: In these experiments, a low-level filling of rocks

(15 %) made up of 434 pieces was used. The mill speed was set at 27.4 $\frac{\text{rev}}{\text{min}}$. **Fig. 6(a)** shows the image of the experimental mill charge and **Fig. 6(b)** is the corresponding DEM simulation snapshot. Once again, the two charge profiles agreed quite well. In both the experimental and simulation, the charge is confined between 240° mark (toe) and 30° marks (shoulder). Further, **Fig. 6(a)** shows five to eight rock particles that are carried up by the square lifter, above the shoulder of the cascading charge. These rock particles then follow the parabolic trajectory downward. We see exactly similar transport by the lifter in the simulation too. Although not perfect, the nearly close charge profile structure between the experiment and DEM simulation, in this case, shows that the friction part of the contact model is bearing out the trends. This case stands in contrast to mill operating with only spherical steel spheres, wherein DEM simulation has produced picture-perfect results coinciding with experimental work (Venugopal (2001), Govender et al. (2015)). Finally, the DEM power 482 W ± 30 compares well with the experimental value of 424 W.

Table 2 Simulation parameter for Case 11, P2P indicates particle-particle and P2W indicates particle-wall settings. * Rock/Spheres values.

Parameter	Symbol	Value	Unit
Normal Particle Stiffness	K_n	*2/4(× 10^6)	N/m
Tangent Particle Stiffness	K_t	*1/3(× 10^6)	N/m
Damping Coefficient	C	0.001/0.1	
Coefficient of Restitution (P2P)	ε	0.4/0.85	
Static Friction (P2P)	μ_s	0.2	
Kinetic Friction (P2P)	μ_k	0.2	
Coefficient of Restitution (P2W)		0.7	
Static Friction (P2W)		0.6	
Kinetic Friction (P2W)		0.6	
Time Step	Δt	1×10^{-5}	s

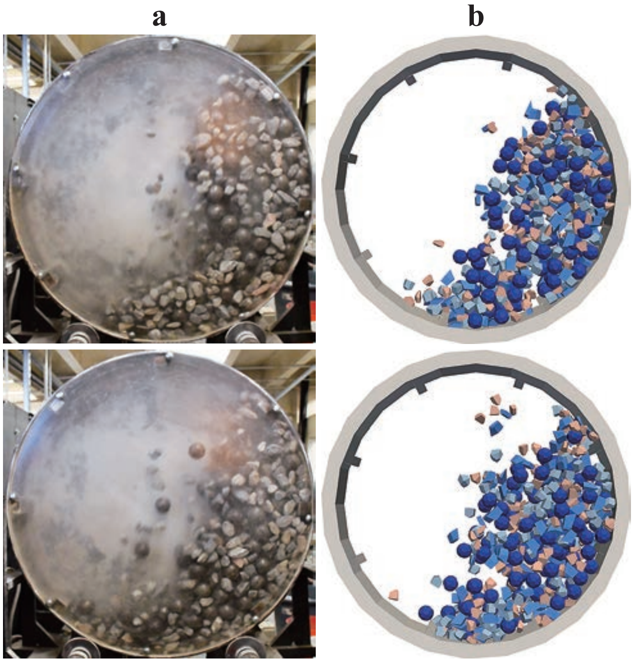

Fig. 5 **(a)** Experimental profile and **(b)** DEM results for Case 11 (12 % rocks, 13 % balls, 25.1 rev/min).

Case 20: In this experiment, a very high filling made up of 1031 rock particles (35 % filling) was run to test the ability of DEM simulation to predict higher power draw, which in turn involves numerous polyhedra collisions. The primary purpose of these experiments work is to verify the volume of contact mechanics used in the Blaze-DEM code. **Table 3** gives the DEM parameters used in the simulation. **Fig. 7(a)** shows the experimental mill snapshot and **Fig. 7(b)** shows the snapshot from DEM simulation. Due to the high load, the shoulder of the charge is almost at the 80° mark. The speed of the mill too was very high set at 33.6 $\frac{\text{rev}}{\text{min}}$ or 75 % of mill critical speed. The simulation tracks the overall structure of the central body of the charge including the toe and shoulder. However, the simulated charge is slightly expanded compared with the experimen-

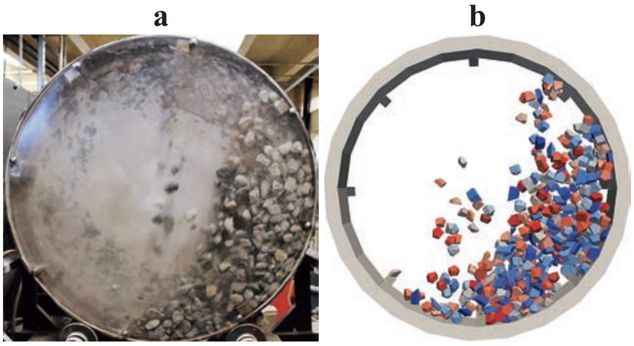

Fig. 6 **(a)** Experimental and **(b)** DEM result for Case 1 (15 % rocks, 27.4 $\frac{\text{rev}}{\text{min}}$).

Table 3 Simulation parameters for Case 1, P2P indicates particle-particle and P2W indicates particle-wall settings.

Parameter	Symbol	Value	Unit
Normal Particle Stiffness	K_n	2×10^6	N/m
Tangent Particle Stiffness	K_t	1×10^6	N/m
Damping Coefficient	C	0.01	
Coefficient of Restitution (P2P)	ε	0.4	
Static Friction (P2P)	μ_s	0.5	
Kinetic Friction (P2P)	μ_k	0.2	
Coefficient of Restitution (P2W)		0.7	
Static Friction (P2W)		0.6	
Kinetic Friction (P2W)		0.6	
Time Step	Δt	5×10^{-5}	s

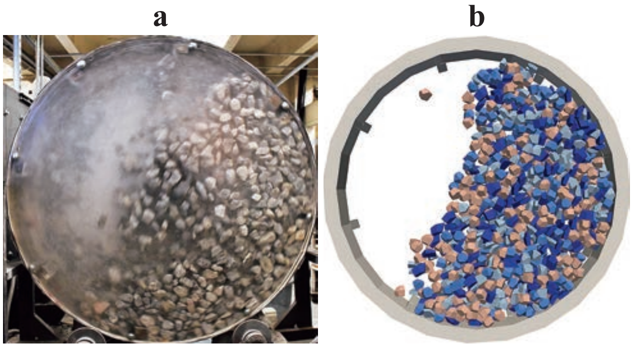

Fig. 7 **(a)** Experimental and **(b)** DEM charge profile for Case 20: 35 % rocks, 33.6 rev/min.

Table 4 Simulation parameters for Cases 4c and 6c, P2P indicates the particle-particle and P2W indicates particle-wall settings.

Parameter	Symbol	Value	Unit
Normal Particle Stiffness	K_n	6×10^6	N/m
Tangent Particle Stiffness	K_t	3×10^6	N/m
Damping Coefficient	C	0.01	
Coefficient of Restitution (P2P)	ε	0.8	
Static Friction (P2P)	μ_s	0.6	
Kinetic Friction (P2P)	μ_k	0.6	
Coefficient of Restitution (P2W)		0.7	
Static Friction (P2W)		0.6	
Kinetic Friction (P2W)		0.6	
Time Step	Δt	5×10^{-5}	s

tal frame. This is attributed to the representation of the rock particles with only four polyhedral shapes depicted in **Fig. 2**. A more comprehensive sample from the 1031 particles, could have provided more accurate modeling of the charge. Yet, in milling, we are interested mainly in the cascading and cataracting charge motion and mill power. Hence, the results presented here verify the ability of the polyhedral contact algorithms at best. The computed power draw of 796 ± 10 W compares well with the experimental power draw of 856 W.

Case 4C: A mill charge of cubes is an obvious choice for DEM verification since the entire mass is made up of cubes. In previous experiments, although we used irregular rock particles, we had to model only a few rock shapes as polyhedrons for the sake of expediency. Hence, there is a difference between experimental results and simulation results due to the variations in the rock shape. In this experiment, the entire charge was made up of 25.4 mm aluminum cubes, with a density of 1800 $\frac{\text{kg}}{\text{m}^3}$. These cubes were identical in shape since they were cut from a rod of square cross-section (25.4 × 25.4 mm). **Table 4** gives the DEM parameters used in the simulation. **Fig. 8(a)** shows the mill operating with 884 aluminum cubes at a mill speed of 29.2 $\frac{\text{rev}}{\text{min}}$. There is a much closer resemblance between the experimental charge profile and the simulated profile (**Fig. 8(b)**), simply because all the particles are identical in shape. The shoulder and toe position agree very well. The cataracting stream from the shoulder also shows good agreement. Similarly, the cubes striking the toe region too is well predicted. The experimental power is 711 ± 11 W, whereas the DEM simulation predicts 752 ± 72 W.

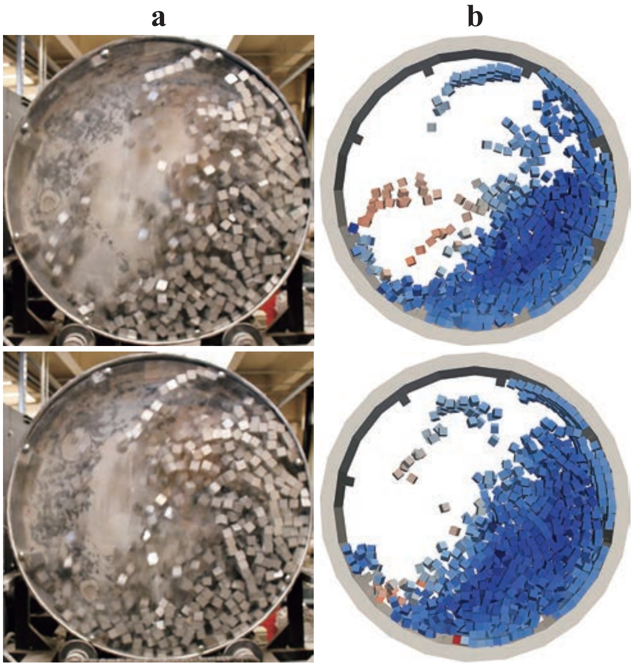

Fig. 8 **(a)** Experimental and **(b)** DEM charge profiles for Case 4c: 25 % filling with 25 mm aluminum cubes at 29.2 $\frac{\text{rev}}{\text{min}}$.

Case 6C: in this experiment, the number of cubes was increased to 1061, making up a mill volume filling of 30 %. Here too, we see excellent agreement between DEM polyhedral model and experimental profiles, as shown in **Fig. 9**. The computed power draw of 752 ± 37 W agrees with experimental values of 740 ± 11 W.

4.1 Contact mechanics parameters

The parameters used in the simulation deserve an explanation here in the milling study. The four main parameters are the two spring constants and the two dashpot constants, normal and tangential, respectively. The spring constants mainly control the time of contact, i.e number of time steps the particle pair interpenetrate before disengaging. The dashpot constant controls the energy dissipated (computed as contact force reduction) during the entire duration of contact between a pair of particles. A reasonable choice of these four parameters produces acceptable simulation results with DEM. A point to note here is that, in a majority of cases published in the literature, DEM simulation target has been bulk charge motion simulation as inflow discharge from a silo, motion over a conveyor chute, mixing vessels, rock-scooping buckets, and many others. In all these simulations principally the metric in bulk particle velocity, for the simulation to resemble measured experiments. In fact, in most such cases, approximate agreement of bulk flow is shown between simulation and DEM results.

Milling, on the other hand, requires correct prediction of charge motion as well as mill power draw, so the four parameters mentioned earlier, have to reach a compromise between accurately predicting charge motion and power. In this compromise, the dashpot constants play a critical role. In addition, the spring constants determine the energy dissipated in each collision since they determine the duration of the collision event. Suffice it to say, there is no unique set of contact parameters that will universally describe a system. In any particular system, a set of parameters is arrived at through trial and error carried over numerous experiments and simulations.

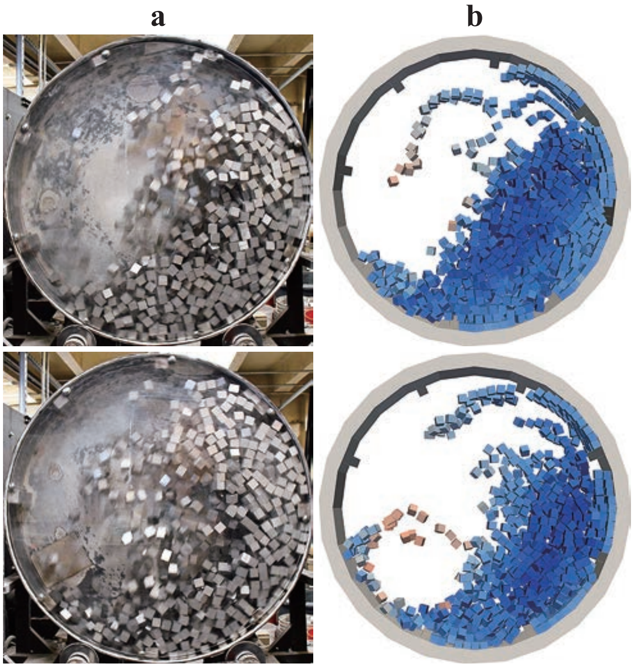

Fig. 9 **(a)** Experimental and **(b)** DEM charge profiles for Case 6C: 30 % filling with 25-mm aluminum cubes at 29.2 $\frac{\text{rev}}{\text{min}}$.

Table 5 shows the contact parameters used in the simulation shown in this manuscript. They range from balls only, rocks only to a combination of rock and balls followed by aluminum cubes. In this particular set of experiments, the spring constant (normal/tangential) for balls only (4×10^6, 3×10^6) and rocks only (2×10^6, 1×10^6) seems to predict well for the mixture of balls and rocks ($4 \times 10^6/2 \times 10^6$, $3 \times 10^6/1 \times 10^6$). The same trend is noticed with the coefficient of restitution values. The static and kinetic friction values trigger minor changes in the energy of collisions. This level of perfect agreement between rock, ball, and rock+ball parameters is fortuitous and may not hold good for all kinds of variations in mill operations. Nevertheless, the magnitude of the constants shown in **Table 5** describes laboratory milling operation both in two-dimensional and three-dimensional simulations. This order of magnitude in parameters when carried on to large mill simulations (9 m diameter × 3.5 m length) also produces reasonable power results. In summary, the parameter set in DEM is still an ongoing open question.

5. Conclusion

It is shown that volume-of-contact contact mechanics is able to successfully predict the motion of charge in a laboratory-scale mill. The polyhedral particle model helps in modeling rock and ball assembly that is commonly encountered in mineral ore grinding plant operations. The actual rock shapes, especially in the size range of 0.2–0.4 m can be scanned and modeled as irregular polyhedra. In addition, GPU-based codes such as Blaze-DEM enables one to study mill discharge through grate slots and pulp lifters, simply because such codes can handle millions of particles.

References

Cleary P.W., Recent advances in DEM modelling of tumbling

Table 5 Summary of simulation parameters used during the simulation, where (b) ball only, (r) rock only, (b&r) mixed ball and rock, and (a) aluminum cubes.

Case #	6, (b)	1, (r)	20, (r)	11, (b&r)	4C, (a)	6C, (a)
ε	0.85	0.4	0.4	0.85/0.4	0.8	0.8
μ_s	0.7	0.7	0.7	0.2	0.8	0.6
μ_k	0.7	0.7	0.7	0.2	0.8	0.6
$K_n(10^6)$	4	2	2	4/2	6	6
$K_t(10^6)$	3	1	1	3/1	3	3
% mill filling	15	15	35	25	25	30
Speed $\frac{\text{rev}}{\text{min}}$	31.6	27.4	33.7	25.1	29.2	29

mills, Minerals Engineering, 14 (2001) 1295–1319. DOI: 10.1016/s0892-6875(01)00145-5

Cleary P.W., Morrisson R., Morrell S., Comparison of DEM and experiment for a scale model SAG mill, International Journal of Mineral Processing, 68 (2003) 129–165. DOI: 10.1016/s0301-7516(02)00065-0

Cleary P.W., Predicting charge motion, power draw, segregation and wear in ball mills using discrete element methods, Minerals Engineering, 11 (1998) 1061–1080. DOI: 10.1016/s0892-6875(98)00093-4

Cleary P.W., Sinnott M., Morrison R., Prediction of slurry transport in SAG mills using SPH fluid flow in a dynamic DEM based porous media, Minerals Engineering, 19 (2006) 1517–1527. DOI: 10.1016/j.mineng.2006.08.018

Cleary P.W., Sinnott M.D., Morrison R.D., DEM prediction of particle flows in grinding processes, International Journal for Numerical Methods in Fluids, 58 (2008) 319–353. DOI: 10.1002/fld.1728

Cundall, P.A., Strack, O.D.L., A discrete numerical model for granular assemblies, Geotechnique, (1979) 47–65. DOI: 10.1680/geot.1979.29.1.47

Delaney G.W., Cleary P.W., Sinnott M.D., Morrison R.D., Novel application of DEM to modelling comminution processes, IOP Conference Series: Materials Science and Engineering, 10 (2010) 012099. DOI: 10.1088/1757-899x/10/1/012099

Djordjevic N., Morrison R., Loveday B., Cleary P., Modelling comminution patterns within a pilot scale AG/SAG mill, Minerals Engineering, 19 (2006) 1505–1516. DOI: 10.1016/j.mineng.2006.07.003

EDEM, User Guide, DEM solution Ltd., Edinburgh, Scotland, UK Copyright © (2011). <http://tm.spbstu.ru/images/2/28/EDEM2.4_user_guide.pdf> accessed 30.07.2021.

Govender N., Rajamani R.K., Kok S., Wilke D.N., Discrete element simulation of mill charge in 3D using the BLAZE-DEM GPU framework, Minerals Engineering, 79 (2015) 152–168. DOI: 10.1016/j.mineng.2015.05.010

Govender N., Wilke D.N., Kok S., Blaze-DEMGPU: Modular high performance DEM framework for the GPU architecture, SoftwareX, 5 (2016) 62–66. DOI: 10.1016/j.softx.2016.04.004

Govender N., Rajamani R., Wilke D.N., Wu C.-Y., Khinast J., Glasser B.J., Effect of particle shape in grinding mills using a GPU based DEM code, Minerals Engineering, 129 (2018a) 71–84. DOI: 10.1016/j.mineng.2018.09.019

Govender N., Wilke D.N., Pizette P., Abriak N.-E., A study of shape non-uniformity and poly-dispersity in hopper discharge of spherical and polyhedral particle systems using the Blaze-DEM GPU code, Applied Mathematics and Computation, 319 (2018b) 318–336. DOI: 10.1016/j.amc.2017.03.037

Govender N., Wilke D.N., Wu C.-Y., Tuzun U., Kureck H., A numerical investigation into the effect of angular particle shape on blast furnace burden topography and percolation using a GPU solved discrete element model, Chemical Engineering Science, 204 (2019) 9–26. DOI: 10.1016/j.ces.2019.03.077

Govender N., Wilke D.N., Wu C.-Y., Rajamani R., Khinast J., Glasser B.J., Large-scale GPU based DEM modeling of mixing using irregularly shaped particles, Advanced Powder Technology, 29 (2018c) 2476–2490. DOI: 10.1016/j.apt.2018.06.028

Hopkins M.A., Hibler III W.D., Flato G.M., On the numerical simulation of the sea ice ridging process, Journal of Geophysical Research: Oceans, 96 (1991) 4809–4820. DOI: 10.1029/90jc02375

Kiangi K., Potapov A., Moys M., DEM validation of media shape effects on the load behaviour and power in a dry pilot mill, Minerals Engineering, 46–47 (2013) 52–59. DOI: 10.1016/j.mineng.2013.03.025

Latham J.-P., Munjiza A., Garcia X., Xiang J., Guises R., Three-dimensional particle shape acquisition and use of shape library for DEM and FEM/DEM simulation, Minerals Engineering, 21 (2008) 797–805. DOI: 10.1016/j.mineng.2008.05.015

Mishra B.K., Rajamani R.K., Motion analysis in tumbling mills by the discrete element method, KONA Powder and Particle Journal, 8 (1990) 92–98. DOI: 10.14356/kona.1990016

Mishra B.K., Rajamani R.K., The discrete element method for the simulation of ball mills, Applied Mathematical Modelling, 16 (1992) 598–604. DOI: 10.1016/0307-904x(92)90035-2

Morrison R.D., Cleary P.W., Using DEM to model ore breakage within a pilot scale SAG mill, Minerals Engineering, 17 (2004) 1117–1124. DOI: 10.1016/j.mineng.2004.06.016

Potapov A.V., Campbell C.S., A three-dimensional simulation of brittle solid fracture, International Journal of Modern Physics C, 07 (1996) 717–729. DOI: 10.1142/s0129183196000594

Rajamani R.K., Mishra B.K., Venugopal R., Datta A., Discrete element analysis of tumbling mills, Powder Technology, 109 (2000) 105–112. DOI: 10.1016/s0032-5910(99)00230-2

Rothenburg L., Bathurst R.J., Numerical simulation of idealized granular assemblies with plane elliptical particles, Computers and Geotechnics, 11 (1991) 315–329. DOI: 10.1016/0266-352x(91)90015-8

Tavares L.M., André F.P., Potapov A., Maliska C., Adapting a breakage model to discrete elements using polyhedral particles, Powder Technology, 362 (2020) 208–220. DOI: 10.1016/j.powtec.2019.12.007

Tavares L.M., A review of advanced ball mill modelling, KONA Powder and Particle Journal, 34 (2017) 106–124. DOI: 10.14356/kona.2017015

Tavares L.M., de Carvalho R.M., Modeling breakage rates of coarse particles in ball mills, Minerals Engineering, 22 (2009) 650–659. DOI: 10.1016/j.mineng.2009.03.015

Venugopal R., Rajamani R.K., 3D simulation of charge motion in tumbling mills by the discrete element method, Powder Technology, 115 (2001) 157–166. DOI: 10.1016/s0032-5910(00)00333-8

Xu L., Luo K., Zhao Y., Fan J., Cen K., Influence of particle shape on liner wear in tumbling mills: a DEM study, Powder Technology, 350 (2019) 26–35. DOI: 10.1016/j.powtec.2019.03.033

Authors’ Short Biographies

Alberto Puga

Alberto Puga completed his Bachelor’s degree in Mechanical Engineering from the University of Utah in Salt Lake City, in 2015. In 2016, he joined the Department of Metallurgical Engineering at the University of Utah in Salt Lake City as MS student. Later, he transferred to pursue a PhD in Metallurgical Engineering with an emphasis in mineral processing. As a student, he was a research assistant in comminution projects involving breakage mechanics in ball mills. He worked as a teaching assistant for the mineral processing and statistics courses. Because of his interaction with the students, he was awarded the “Teaching Assistant of the Year” in the department.

Nicolin Govender

Dr. Nicolin Govender is a principal scientist at Mondelez International in the position of global lead for granular material physics and GPU/HPC computing for the creating of digital twins. Prior to this, he held the prestigious EU Marie Curie Research Fellowship in the Department of Chemical and Process Engineering at the University of Surrey. Dr. Govender is the primary investigator (PI) of the NVIDIA GPU Research Centre for Discrete Element Particle Modeling, which he established in 2013 with the support for NVIDIA, specializing in GPU computing of particle systems. He has been working on GPU clusters since the advent of general-purpose GPU computing in 2008 and is an esteemed international expert in the field. He has solely developed the open source GPU-based DEM code “Blaze-DEM”, that is hosted by Elsevier, which is used by a growing number of institutes, nationally and internationally.

Raj K. Rajamani

He has been on the research and teaching faculty position at the University of Utah since 1979. Currently he is Professor of Material Science and Engineering. Dr. Rajamani’s research interests include: Breakage rate of mineral particle in ball mills and scale-up to plant scale mills, computational Fluid Dynamic study of hydrocyclones, Discrete Element Simulation of mineral ore grinding mills and electrodynamic sorting of auto-shredder scrap stream to recover aluminum and copper. Dr. Rajamani received the Antoine M. Gaudin Award, presented by the Society of Mining, Metallurgy and Exploration Engineers Inc. in the year 2009. The award plaque reads, “For his seminal work in the application of discrete element methods in the modeling of charge motion in semi-autogenous and ball mill grinding, and for his contribution to the basic science of comminution and classification.”

KONA Powder and Particle Journal No. 39 (2022) 219–229/https://doi.org/10.14356/kona.2022004 Original Research Paper

Smart Mechanical Powder Processing for Producing Carbon Nanotube Reinforced Aluminum Matrix Composites[†]

Behzad Sadeghi[1], Genlian Fan[1]*, Zhanqiu Tan[1], Zhiqiang Li[1], Akira Kondo[2] and Makio Naito[2]

[1] *State Key Laboratory of Metal Matrix Composites, Shanghai Jiao Tong University, China*
[2] *Joining and Welding Research Institute (JWRI), Osaka University, Japan*

Abstract

The central concern in the fabrication of carbon nanotube (CNT) reinforced metal composites is the well balance between uniform dispersion and structural integrity of CNTs. Rapid and uniform self-assembly of CNTs and spherical Aluminum (Al) particles into a core-shell structure is realized by a smart mechanical powder processing. The factors influencing the dispersion uniformity and structural integrity of CNTs during the processing are studied, including the size of Al particles, mixing speed and mixing time. It is revealed that a size of 35 μm is preferred for the Al particles to tear apart the CNT clusters and obtain a uniform dispersion of CNTs on Al surface. Different composite states, CNTs are singly dispersed, thickly wrapped, or embedded in the Al particles, can be obtained by changing the mixing speed. Well coordination between the CNT dispersion homogeneity and structural integrity could be achieved under suitable processing condition. Therefore, it can be adopted as an efficient and intelligent technology to achieve the desired performance in CNT/Al composites.

Keywords: dispersion, structural integrity, high-shear pre-dispersion, CNTs reinforced metal matrix composite, smart powder processing

1. Introduction

During the past two decades, significant progress has been achieved in the fabrication of carbon nanotubes reinforced metal matrix composites (MMCs). Regardless of the material type and fabrication technique, the balance between the uniform dispersion of CNTs in the Al matrix and its structural integrity is vital prerequisite that needs to be considered (Fan G.L. et al., 2014; Wei H. et al., 2014). How to realize the rapid, efficient, and uniform dispersion of CNTs in the Al matrix is one of the key factors restricting the industrial application of CNT/Al and alloy composite materials. It is well known that fine powders are not able to flow freely due to the strong inter-particle cohesion, mainly ascribed to the Van der Waals forces for dry, neutral, and inert particles (Deng X. and Davé R.N., 2017b; Eggersdorfer M.L. et al., 2010), dominating the particle weight. The situation can be more serious when the reinforcement is one-dimensional, namely tubular and flexible such as CNTs (Han Y. et al., 2015; Narh K.A. et al., 2008; Zhang K. and Choi H.J., 2014). The unique geometry, along with large specific surface area and significant Van der Waals force, strongly affects the dispersion status of CNTs.

In addition, the structural integrity of CNTs is considered to be another key factor affecting the strengthening effect by interfacial reaction and the formation of harmful products. Therefore, the MMCs community, especially those CNTs reinforced Aluminum composites, have significant concerns in overcoming the dilemmas associated with dispersion and structural integrity. From this point of view, these factors should be taken into account when designing appropriate preparation processes.

Presently, many CNT/Al composite preparation methods can meet the requirements of CNTs reinforced Al Matrix Composite, but each has its shortcomings. Melt casting and thermal spraying can realize the rapid preparation of large block materials with a high content of CNTs. Still, it is difficult to solve the dispersion of CNTs and the control of interface reaction (Baig Z. et al., 2018). Great efforts have also been made in the field of both large plastic deformation technologies such as accumulative roll bonding (ARB) (Salimi S. et al., 2010), high-pressure torsion (HPT) (Asgharzadeh H. et al., 2014; Tokunaga T. et al., 2008), friction stir processing (FSP) (Johannes L.B. et al., 2006; Sadeghi B. et al., 2018b; Sadeghi B. et al., 2018d) and solid-phase powder metallurgy (PM) techniques (Sadeghi B. et al., 2018a). One could be found that PM based techniques are effective and low cost, so that bring into a clear

---

[†] Received 14 October 2020; Accepted 17 December 2020

[*] Corresponding author: Genlian Fan;
Add: 800 Dongchuan Road, Shanghai, Shanghai 200240, China
E-mail: fangenlian@sjtu.edu.cn
TEL: +86-21-5474 5872 FAX: +86-21-3420 2749

insight to solve the dilemma mentioned above. The PM based methods include high-energy ball milling (Esawi A.M.K. et al., 2009; Sadeghi B. et al., 2020; Sadeghi B. et al., 2019), flake powder metallurgy (Flake PM) (Fan G.L. et al., 2014; Jiang L. et al., 2012), liquid phase ball milling (Chen B. et al., 2015; Jiang L. et al., 2012), nanoscale dispersion method (Kwon H. et al., 2009; Noguchi T. et al., 2004), molecular level mixing (Cha S.I. et al., 2005; Nam D.H. et al., 2012), in-situ growth of CNTs combined with low-energy ball milling (He C., 2007; Cao L.L. et al., 2012; Yang X. et al., 2013) and so on (Baig Z. et al., 2018). However, whether wet ball milling or in-situ growth is used as the initial dispersion method of CNTs, it is a time-consuming and high energy consumption method, which is challenging to match with industrial production. Therefore, it is of great significance to study an effective pre-dispersion way for the preparation of CNT/Al composite with high performance. Precisely, despite recent advances in powder-based processing techniques such as Flake PM (Fan G.L. et al., 2014; Jiang L. et al., 2011; Jiang Y. et al., 2019; Tan Z. et al., 2011), there is still a challenging effort to achieve the extraordinary balance between dispersion and structural integrity of CNTs through Al matrix. In sum, it seems that PM is still the best macro quantitative preparation method for controllability and operability, but there is still much room for improvement.

Recently, various dry particle coating technologies have been developed for advanced material production through covering the surface of larger core (host) particles with fine shell (guest) particles by mechanical forces, which were induced through four different mechanical devices (Foppoli A.A. et al., 2017; Sharma R. and Setia G., 2019). All of those are well designed to prompt de-agglomeration of cohesive nanopowders (NP) to facilitate the NP dispersion (Bhaumik S., 2015; Naito M. et al., 2009; Wei D. et al., 2002). Among these technologies, Mechano Fusion® (MF) system as a smart powder process (Naito M. et al., 2009) has attained a considerable amount of attention to produce the composite powders with desired tailor-made properties for advanced MMCs (Chen M. et al., 2018; Ghoroi C. et al., 2013; Naito M. et al., 2009). Comparing to the wet-based (Jiang L. et al., 2012; Sadeghi B. et al., 2012a; Sadeghi B. et al., 2012b; Zhou S.-M. et al., 2007) and gas-based (He C. et al., 2007; Yang X. et al., 2016) coating techniques, the smart powder process can produce advanced composite materials with minimum energy consumption and environmental impact in a dry environment. In principle, the MF system is expected to achieve the dry and uniform composite of nano-sized CNTs and micron-sized metal powders. Still, CNTs are different from ordinary nanoparticles because of their complex structure and could be easily intertwined and clustering. In such circumstances, opening the clusters and wrapping on the surface of metal powder by mechanofusion is a challenging issue. Very recently, Chen et al. (Chen M. et al., 2018) demonstrated that dry particle coating (also termed as high-shear pre-dispersion) combined Flake PM route not only improves the dispersion efficiency of CNTs in the ball milling process but also well-preserves the structural integrity of CNTs comparing to other PM routes (Chen M. et al., 2018; Chen M. et al., 2019). Nevertheless, the effect of host particle size and the operation conditions on the dispersion and structural integrity of CNTs were not demonstrated. Considering the low cost, simplicity, and low energy consumption of the processing, there is a great potential to transit it from laboratory to large-scale commercial applications. Therefore, there is a pressing need to develop a better understanding of the factors that affect the coating effectiveness of the high-shear pre-dispersion process.

Many factors may affect the composite effects of particles, and subsequently, dry coating effectiveness, including host particle size, mixing speed and time. Very recently, Zheng et al. (Zheng K. et al., 2020) studied the effects of particle properties such as their sizes, stiffness and surface energies on the coating effectiveness and demonstrated that the host particle size has no significant effect on the coating quality when it is orders of magnitude larger than that of guest particles. They also reported that increasing processing intensity led to guest particles bouncing off of host particles, indicating poor coating performance. It was reported that the discharge efficiency of $LiNi_{0.5}Mn_{1.5}O_4$ cathode could enhance by the CNT coat provided by the mechanofusion method (Hwang T. et al., 2016). Narh et al. (Narh K.A. et al., 2008) studied dry coating of polymer powder particles with de-agglomerated CNTs and reported an acceptable extent of the CNT dispersity. Chen et al. (Chen M. et al., 2019) could effectively tailor the pre-dispersion state of CNT/6061Al composite powders by controlling the high-shear process speed. No comprehensive research has mentioned that host particle size and operating conditions (mixing time and speed of high-shear pre-dispersion process) simultaneously affect the dispersion and structural integrity degree in CNT/Al composite powders. To this end, the current study is trying to uncover the various aspects of the pre-dispersion and structural integrity degree of CNTs in the Al matrix composite. It should be interesting to note that the dispersion and binding mechanisms involved in the high-shear pre-dispersion process depend on the initial size of host particles and guest particles (Ötles S. et al., 2009; Wei D. et al., 2002; Zheng K. et al., 2020). However, it is well known that the contact surface between powder materials is subjected to extremely high local temperature and pressure, resulting in unique phenomena between host and guest or among fine particles or even generating mechanical stress (Naito M. et al., 2009).

In this study, an environmentally friendly and smart powder processing technology, the namely high-shear pre-dispersion process is successfully adopted to fabricate

1.5 wt.% CNT/Al composite powders. Specifically, the effects of host particle size, mixing time, and rotational speed of powder mixing process on the balance of dispersity and structural integrity of CNTs in final composite powders and consequently composite effects are discussed.

2. Experimental

2.1 Raw materials

Atomized near-spherical Al powders with a various average diameter of 2, 5, 10, 15, 35, 70 μm, and industrial multi-walled CNTs with a diameter of about 10–20 nm, length of about 0.5–2 μm and purity of more than 95 % are chosen to explore the size dependence in the high-shear pre-dispersion process. **Fig. 1a** shows the original shape of 35 μm-Al powder have a round surface. A small number of tiny Al particles are attached on the surface, and size distribution is relatively narrow. **Fig. 1b–c** show the initial CNTs, which are in the form of particles with a size of tens of microns. Long and entangled CNTs can be seen at higher magnifications. **Fig. 1d** shows the Raman spectrum of raw CNTs. It is well-known that there are two characteristic peaks at 1346 cm^{-1} and 1570 cm^{-1}, which are called D peak and G peak, respectively (Cavaliere P. et al., 2019; Kwon H. and Leparoux M., 2012; Sadeghi B. et al., 2018c; Zhao Q. and Wagner H.D., 2004). Former is attributed to defects in the hexagonal graphite layer structure, resulting in the in-plane vibration. The latter is related to a single-photon emission generated by the tangential tensile mode of the graphite layer plane (Loa I., 2003; Zhao Q. and Wagner H.D., 2004). The ratio of two peaks (I_D/I_G) is usually used to characterize the graphitization degree of CNTs. The lower the ratio, the fewer the defects of CNTs and the higher graphitization degree is. So it is useful to track the changing trend of the structural integrity of CNTs (Chen M. et al., 2019). The I_D/I_G value of raw CNTs is about 0.95.

2.2 Preparation of CNT/Al composite powder

1.5 wt.% of CNTs were processed with Al powder of different diameters in a prototype of MF system (MECHANO FUSION®) from Hosokawa Micron Corporation, Japan (Naito M. et al., 1993). As illustrated in **Fig. 2a**, it has a container diameter of 80 mm and the clearance/gap between the rotor and container is of 2 mm. The powder mixture was first processed at the speed of 300 rpm for 2 min to homogenize and then processed at the designated speed (1000–4000 rpm) for different times (5–15 min) to obtain composite powders.

2.3 Characterization

The morphology of the powder is observed by Sirion 200 field emission scanning electron microscope (FESEM) at the working voltage of 20 kV. The influence of the process condition on the structural integrity of CNTs is characterized by Raman spectroscopy (SENTERRA R200-L), by using the 532 nm line of an Ar+ laser as the excitation source.

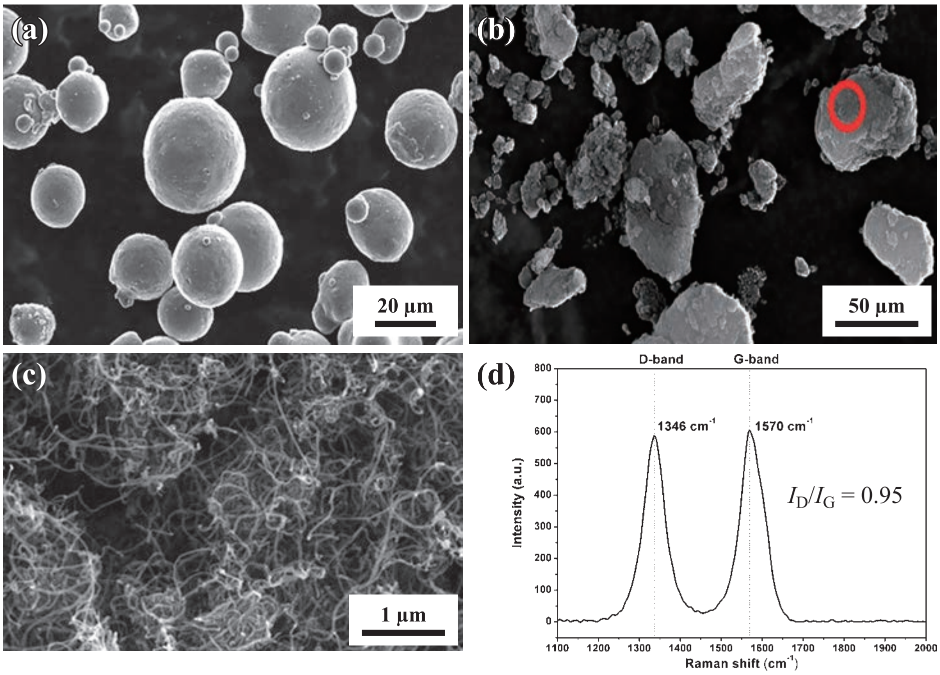

Fig. 1 FESEM of **(a)** spherical 35 μm-Al powders, **(b)** raw CNTs, **(c)** magnification of CNTs in **(b)**, **(d)** Raman spectrum of raw CNTs.

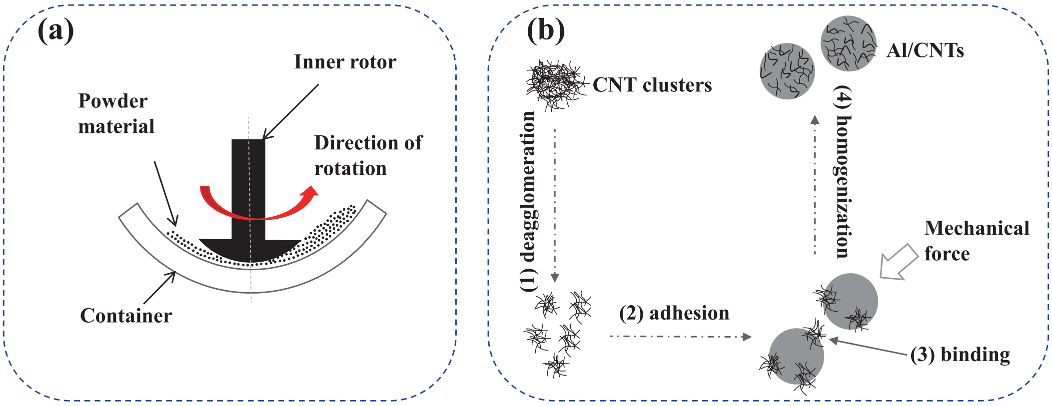

Fig. 2 Illustrations of **(a)** prototype of Mechano Fusion® system (Naito M. et al., 1993), **(b)** the working principle of CNTs dispersion on Al powder in MF system.

3. Result and discussion

The main working principle of the MF system is to use the centrifugal force generated by the high-speed rotation of the rotor and the gravity effect of the material itself to make the material pass through the clearance between the rotor and the container at high speed. The mutual shear force and impact force between the materials make the smaller particles adhered onto the more considerable materials, to realize the core-shell structured composite particles (Naito M. et al., 2009; Qu L. et al., 2015). In the case of CNTs and Al particles, as illustrated in **Fig. 2b**, the CNTs as the guest particles should be first torn apart by the shear forces of Al particles (host particles) into smaller particles or even individual CNTs, and then adhered onto the surface of Al particles. The repeating collision between Al particles made CNTs uniformly dispersed on the surface of Al particles, forming a Al/CNTs core-shell structured composite powder. Therefore, the dispersion status is mostly affected by the particle size or mass ratio between host/guest particles, the processing speed and time.

3.1 Effect of Al particle size

The average particle size of the initial Al powders not only determines the surface area of the powders but also determines the mass ratio between the particles and CNTs. On the one hand, the smaller the average particle size of Al powder is, the larger the corresponding surface area is, which is more conducive to the uniform distribution of CNTs; on the other hand, the smaller the mass of a single Al particle is, the weaker its impact energy on CNTs clusters will be. Precisely, smaller Al particles provide lower collision energy but higher surface area, which in turn controls the type of contacts and interparticle adhesion force (Deng X. and Davé R.N., 2017a) and subsequent dispersion of CNTs.

Fig. 3 shows FESEM of CNT/Al composite powder obtained by mixing 1.5 wt.% CNTs with Al powder of different particle sizes at 2500 rpm for 10 min. As one can see, the shape of Al particle is not significantly changed during the high-shear pre-mixing process as reported (Chen M. et al., 2018). The main reason for this was due to the fact that the processing condition applied was still below the limit of Al particle deformation. For the smaller Al particle size, namely 2, 5 µm, the de-agglomeration and dispersion of CNTs hardly occurred. Most CNTs remained in clusters (indicates by yellow arrows in **Fig. 3a–b)**; only very few individual CNTs were attached on the surface of Al particles (**Fig. 3d–e**). When the particle size increased to 10, 15 µm, more individual CNTs were attached on the surface of Al particles, while a small number of clusters still existed. Further increasing the particle size to 35, 70 µm, only tiny flattened CNT clusters can be occasionally found, indicating almost all the CNTs were torn apart and attached on the surface of Al particles. That is, the larger the particle size of the Al particle is, the more CNTs are attached to the surface. The larger the mass or volume of Al particles is, the easier it is to wrap CNTs on the surface. The initial size of the CNTs clusters is of tens of microns, and so the collision force exerted from those small Al particles (smaller than 10 µm) are not high enough to tear the CNT clusters apart. Still, on the contrary, these collisions made the CNT clusters more solid than initial CNTs. Therefore, there is a size limit that the pre-dispersion of CNTs on the Al surface can be applied.

Further observation of the micromorphology of the Al particle surface shows that the degree of the surface smoothness is changed in larger sizes of Al particle. The surface of the Al particle is no longer smooth, and a certain number of pits appear, which should be related to the significant improvement of the impact force between the larger Al particles. The small Al particles that initially attached on the surface of big particles were flattened and stuck on the Al surface, making a rougher surface (**Fig. 3i**) with CNTs embedded in the surface pits. By and large,

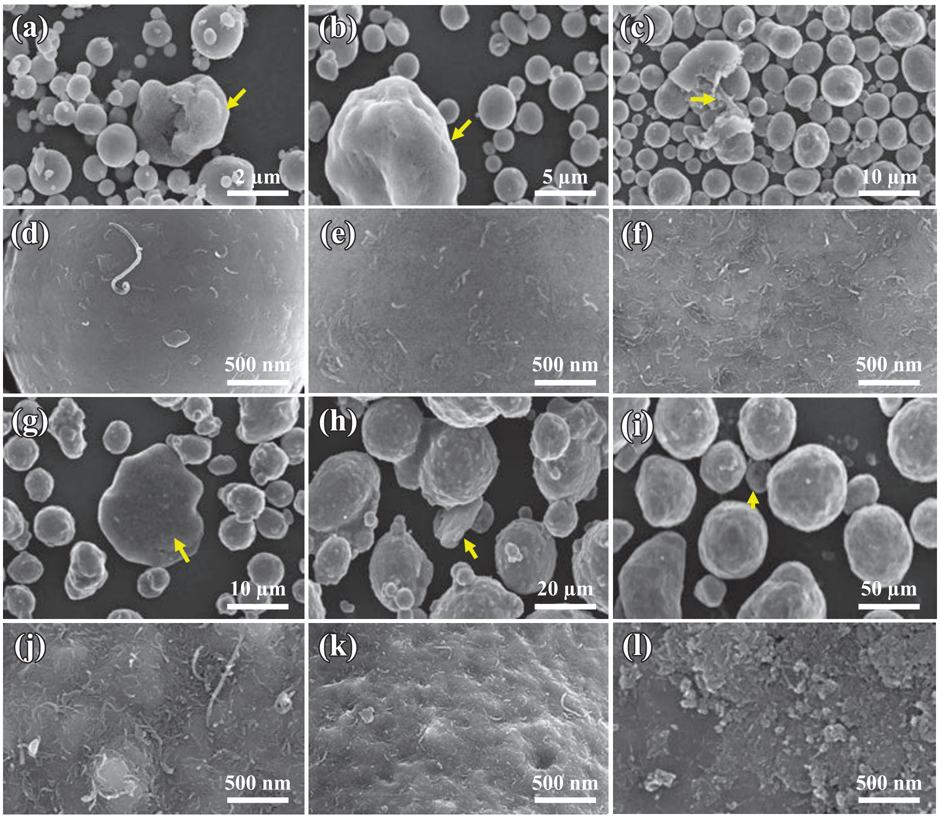

Fig. 3 FESEM of pre-mixed CNT/6061Al composite powders with different particle sizes processed at 2500 rpm for 10 min, **(a, d)** 2 μm, **(b, e)** 5 μm, **(c, f)** 10 μm, **(g, j)** 15 μm, **(h, k)** 35 μm, **(i, l)** 70 μm. Arrows indicate the presence of the CNT clusters.

under the current mixing conditions, Al particles with the average size above 35 μm can provide the appropriate level of pre-dispersion of CNTs and complete the pre-dispersion process well. Considering that the essential purpose of the pre-dispersion process is to reduce the pressure of subsequent powder milling, to shorten the time required for CNT dispersion, as well as keeping the structural integrity of CNTs, the Al powders with 35 μm particle size is preferred.

3.2 Effect of pre-dispersion speed (rotational speed) on CNT dispersion

It is well known that the force acting on the powder blend generally increases with rotational speed (Naito M. et al., 1993). The higher the speed, the more robust and useful the interaction force can be produced between the materials and subsequently affect the flowability of the processed powder. As described in the previous section, the 35 μm Al powder succeeds in completing the task of opening the CNT clusters completely at 2500 rpm. Therefore, it is considered to alter the pre-dispersion speed further and observe its effect on the dispersion status.

Fig. 4 shows the FESEM of CNT/Al composite powder after mixing 35 μm Al powder with CNTs for 10 min at different rotational speeds. Big and flattened CNT clusters can be easily observed at low rotational speed (1000 rpm, **Fig. 4a**), but the amount and size of CNT clusters progressively decreased with the increasing rotational speed up to 2000 rpm. A thick layer of dispersed CNTs can be observed on Al particle surface at 2000 rpm, as shown in **Fig. 4f**. With the increase of mixing speed to 2500, 3000, 4000 rpm, small Al chips were attached on the surface of Al particles, and only a small number of CNT ends can be observed on the surface of Al particles, as shown in **Fig. 4j–l**. It can be deduced that with the increase of speed, CNTs show a gradual “in-depth” change process from the surface to the interior of the Al particle, which is completed by the embedding of CNTs into Al chips and the mutual grinding of Al powders.

The above results depict the trend that de-agglomeration and dispersion of CNTs increase as a function of increasing rotational speed. This is because as the rotational speed increases, the intensity of collisions between Al particles and CNT clusters violently increases when passing through the clearance between the rotor and container. Because of severe shear, friction, and compression forces, big CNT clusters are quickly torn apart and broken into the smaller ones. And then the small CNT clusters adhered on the surfaces of Al particles were further de-agglomerated and uniformly dispersed throughout the surface of Al particles by the repeating collision between Al particles throughout the processing time.

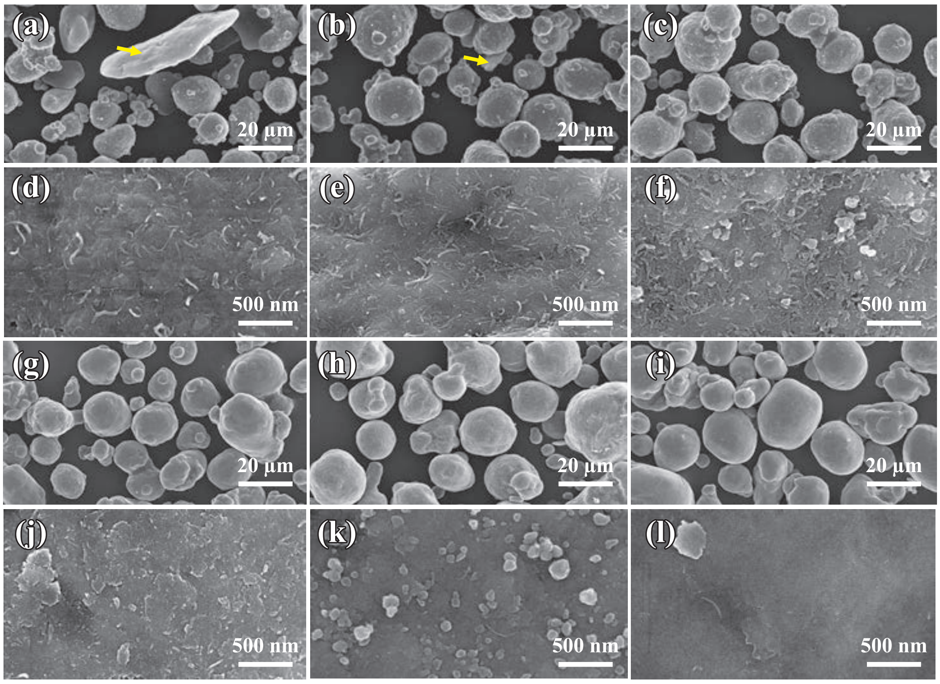

Fig. 4 FESEM images of Al at CNT composite powders processed by high-shear pre-dispersion process with various rotational speed, **(a, d)** 1000 rpm; **(b, e)** 1500 rpm; **(c, f)** 2000 rpm; **(g, j)** 2500 rpm, **(h, k)** 3000 rpm, **(i, l)** 4000 rpm. The yellow arrows indicate the CNT clusters.

The tentative conclusion to be drawn is that by changing the mixing speed (rotational speed), the type of contacts between CNTs (as guest) and Al particles (as host) can be changed to strongly affect the dispersity status. On the one hand, at too slow rotational speeds, guest-guest (CNT clusters) and host-host (Al-Al) contacts remain due to insufficient mechanical forces. And on the other hand, at high rotational speeds, CNTs both in the form of cluster and individual are embedded in Al particles (host-guest contact). The former results in the remaining of CNT cluster, and the latter causes heterogeneity dispersion of CNTs in Al particles. Therefore, it can be inferred that the best condition for uniform dispersion of CNTs is that CNTs are singly dispersed throughout the surface of Al particles at a moderate rotational speed.

Additionally, it is shown that when rotational speed increases from 2500 rpm to 4000 rpm, small Al particles attached on the surface of bigger ones were gradually stuck and probably embedded in Al particles, generating Al particles with a bigger size and smoother surface (**Fig. 4h–i**), compared to lower rotational speeds (**Fig. 4a–b**).

3.3 Effect of pre-dispersion time on CNTs dispersion

The mixing process of CNTs and Al powder is the process of gradually opening and coating CNTs clusters on the surface of Al powder. The efficiency of the dry particle coating process is determined by the total mass, mass ratio, mixing speed and mixing time. Among these affecting parameters, mixing time not only has a significant influence on dispersity status and structural integrity of CNTs but also leads to alteration of the appearance of Al powder.

To study the effect of mixing time on the dispersion status of CNTs during the high-shear pre-dispersion process, the Al powder and CNTs with a medium particle size of 35 µm are selected as the primary materials. According to the tailored objectives, two different rotational speeds of 1500 rpm and 2500 rpm are chosen to do the mixing process at different mixing times of 5, 10 and 15 min. **Fig. 5a–c** show that the CNTs on the surface of Al particles can be observed under 1500 rpm for different mixing times. After a short mixing time (5–10 min, **Fig. 5a–b**), CNTs coated onto the Al surfaces are discrete, and by increasing the mixing time, a continuous film-like CNT coating is gradually formed (15 min, **Fig. 5c**). Also, the length of CNTs decreased from 0.5–2 µm to 0.2–0.5 µm, indicating that CNTs clusters were cut short during the opening process due to shear and compression stresses. For the mixing time of 15 min, no CNT clusters can be observed, which indicates that CNTs have been completely attached on the surface of Al particles. **Fig. 5d–f** show the CNT dispersion status at 2500 rpm for various mixing times. After 5 min processing, we can see that more CNTs are attached on the surface than mixed at the speed of 1500 rpm for the same time. With the increase of processing time, most CNTs are embedded underneath the Al chips, which should be attributed to the presence of the enormous impact, compression, and shear forces between the Al particles when they passed through the clearance between the rotor

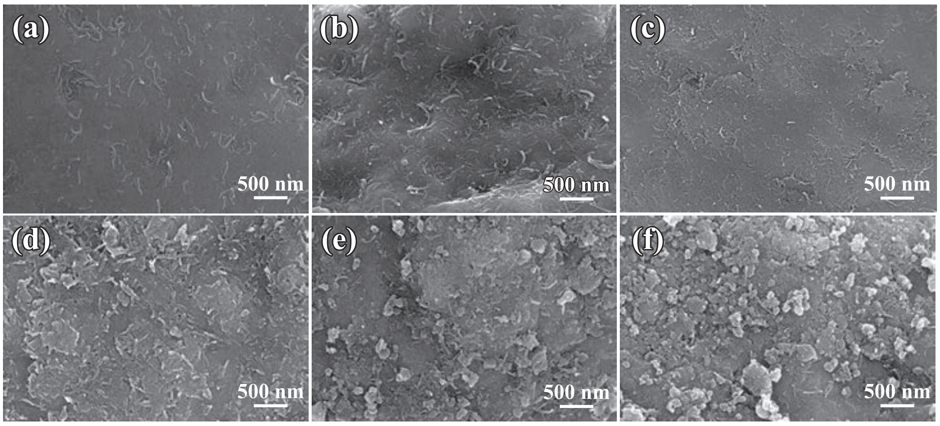

Fig. 5 FESEM images of CNT/Al composite powders premixed at **(a–c)** 1500 rpm and **(d–f)** 2500 rpm for different time: **(a, d)** 5 min, **(b, e)** 10 min, **(c, f)** 15 min.

and container. Due to such severe shear and compression stress, a long-time mixing may result in the embedding of some CNT clusters underneath Al chips before they were fully de-agglomerated and spread over the surfaces. It could increase the responsibility of subsequent ball milling dispersion at the expense of more structure damage of CNTs under high energy ball milling dispersion. It can, therefore, be used to suggest an optimum mixing time to achieve uniform distribution of individual CNTs onto the surface of Al particles without embedding them and thus, the improvement of pre-dispersion efficiency.

3.4 Pre-mixing speed dependence of structural integrity

The good maintenance of structural integrity of CNTs is considered to be one of the main factors that should be considered during the processing, although some results showed that in the absence of a significant interface reaction, the failure of the tubular structure on the surface of CNTs can enhance the interface bonding between CNTs and Al matrix, its bearing capacity and strengthening effect (Chen B. et al., 2014; Ci L.J. et al., 2006; Kwon H. et al., 2013).

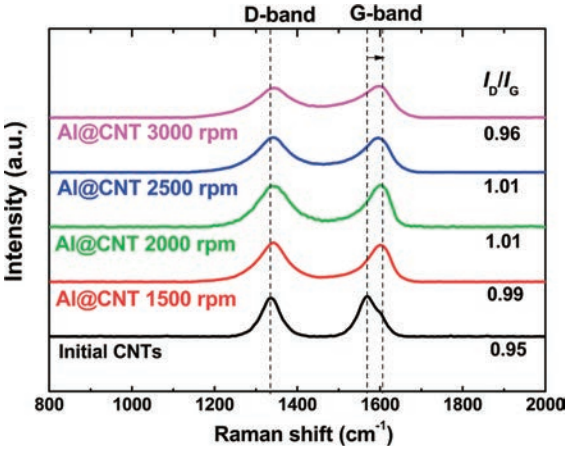

Fig. 6 Raman spectrum of pre-dispersed CNT/Al composite powder at different rotational speeds.

As shown in **Fig. 6**, compared with the I_D/I_G value (0.95) of the initial CNTs powder, it is found that the mechanofusion pre-dispersion process had little damage to the structural integrity of CNTs. With the increase of rotational speed, the I_D/I_G value first increased to about 1.01 and then decreased to about 0.96 at 2800 rpm. The decrement of the I_D/I_G value indicates less damage. This is very likely that, the pre-dispersed CNTs are rapidly embedded underneath the surface of the Al chips at high speed, resulting in a better protection of CNTs (Chen M. et al., 2019). Therefore, it can be concluded that CNTs are just cut short efficiently without much structural integrity damage during the pre-dispersion process. The structural integrity is much better preserved than those traditional ball milling dispersion process.

To sum up, for the raw CNT clusters with dozens of microns, the size of Al particles should over 15 µm, as to provide sufficient impact energy to tear apart the clusters via mechanical forces under the MF system. Changing the rotational speed can obtain different composite states. With the increase of speed, CNTs show a gradual “in-depth” change from the surface to the interior of the Al particles, which is completed by the embedding of CNTs into Al chips and the mutual grinding of Al powders. However, the effect of their combination with the subsequent powder milling process needs to be considered to select the best pre-dispersion process parameters. Chen’s work (Chen M. et al., 2019) shows that only by pre-dispersion at moderate speed, in which CNTs are well de-agglomerated and partially embedded in Al matrix, can provide a controllable balance between the CNT dispersity and structural integrity protection compared with the other processing conditions.

4. Conclusion

The smart powder processing based on the Mechano Fusion® system can realize the rapid composite of CNTs and Al powders. The particle size of Al powders, the mixing speed and time have a significant influence on the dispersion status. For the raw CNTs with dozens of microns, there is a size and speed limit to provide sufficient impact to tear apart the clusters and coat them onto the surface of Al particles. Considering the dispersion uniformity and surface area of Al powders to bear CNTs, the size of 35 μm Al powder and the speed around 2000–2500 rpm are preferred. The efficiency of processing is very high and under suitable speed, 15 min is sufficient to obtain a uniform dispersion of CNTs all over the surfaces of Al particles. The CNTs were cut short, but structural integrity was not severely damaged. Therefore, a high-shear pre-dispersion process as a smart mechanical powder processing is a relatively simple and environmentally friendly approach to produce CNT/Al composite powder with the desired balance between dispersion and structural integrity of CNTs in metallic matrix.

Acknowledgements

This work was supported by the National Natural Science Foundation of China (Nos. 51671130, 51871149, 51971206), Shanghai Science and Technology Committee (No. 19ZR1474900) and JWRI International Research Collaboration.

References

Asgharzadeh H., Joo S.-H., Kim H.S., Consolidation of carbon nanotube reinforced aluminium matrix composites by high-pressure torsion, Metallurgical and Materials Transactions A, 45 (2014) 4129–4137. DOI: 10.1007/s11661-014-2354-6

Baig Z., Mamat O., Mustapha M., Recent progress on the dispersion and the strengthening effect of carbon nanotubes and graphene-reinforced metal nanocomposites: a review, Critical Reviews in Solid State and Materials Sciences, 43 (2018) 1–46. DOI: 10.1080/10408436.2016.1243089

Bhaumik S., Principles and applications of mechanical dry coating—review and state-of-the-art, 5, Master of Science, New Jersey Institute of Technology, 2015. https://digitalcommons.njit.edu/theses/223/

Cao L.L., Li Z.Q., Fan G.L., Jiang L., Zhang D., Moon W.J., Kim Y.S., The growth of carbon nanotubes in aluminum powders by the catalytic pyrolysis of polyethylene glycol, Carbon, 50 (2012) 1057–1062. DOI: 10.1016/j.carbon.2011.10.011

Cavaliere P., Sadeghi B., Shamanian M., Ashrafizadeh F., Al-based nanocomposites produced via spark plasma sintering: effect of processing route and reinforcing phases, in: Cavaliere P. (Ed.) Spark Plasma Sintering of Materials: Advances in Processing and Applications, Springer International Publishing, Cham, Switzerland, 2019, pp. 161–190. ISBN: 978-3-030-05327-7. DOI: 10.1007/978-3-030-05327-7

Cha S.I., Kim K.T., Arshad S.N., Mo C.B., Hong S.H., Extraordinary strengthening effect of carbon nanotubes in metal-matrix nanocomposites processed by molecular-level mixing, Advanced Materials, 17 (2005) 1377–1381.

Chen B., Jia L., Li S., Imai H., Takahashi M., Kondoh K., In situ synthesized Al_4C_3 nanorods with excellent strengthening effect in aluminum matrix composites, Advanced Engineering Materials, 16 (2014) 972–975. DOI: 10.1002/adem.201400232

Chen B., Li S., Imai H., Jia L., Umeda J., Takahashi M., Kondoh K., An approach for homogeneous carbon nanotube dispersion in Al matrix composites, Materials & Design, 72 (2015) 1–8. DOI: 10.1016/j.matdes.2015.02.003

Chen M., Fan G., Tan Z., Xiong D., Guo Q., Su Y., Zhang J., Li Z., Naito M., Zhang D., Design of an efficient flake powder metallurgy route to fabricate CNT/6061Al composites, Materials & Design, 142 (2018) 288–296. DOI: 10.1016/j.matdes.2018.01.044

Chen M., Fan G., Tan Z., Yuan C., Xiong D., Guo Q., Su Y., Naito M., Li Z., Tailoring and characterization of carbon nanotube dispersity in CNT/6061Al composites, Materials Science and Engineering: A, 757 (2019) 172–181. DOI: 10.1016/j.msea.2019.04.093

Ci L.J., Ryu Z.Y., Jin-Phillipp N.Y., Ruhle M., Investigation of the interfacial reaction between multi-walled carbon nanotubes and aluminum, Acta Materialia, 54 (2006) 5367–5375. DOI: 10.1016/j.actamat.2006.06.031

Deng X., Davé R.N., Adhesion and friction of dry-coated nano-rough particles, Powder Technology, 314 (2017a) 20–27. DOI: 10.1016/j.powtec.2016.07.035

Deng X., Davé R.N., Breakage of fractal agglomerates, Chemical Engineering Science, 161 (2017b) 117–126. DOI: 10.1016/j.ces.2016.12.018

Eggersdorfer M.L., Kadau D., Herrmann H.J., Pratsinis S.E., Fragmentation and restructuring of soft-agglomerates under shear, Journal of Colloid and Interface Science, 342 (2010) 261–268. DOI: 10.1016/j.jcis.2009.10.062

Esawi A.M.K., Morsi K., Sayed A., Gawad A.A., Borah P., Fabrication and properties of dispersed carbon nanotube–aluminum composites, Materials Science and Engineering: A, 508 (2009) 167–173. DOI: 10.1016/j.msea.2009.01.002

Fan G., Jiang Y., Tan Z., Guo Q., Xiong D.-B., Su Y., Lin R., Hu L., Li Z., Zhang D., Enhanced interfacial bonding and mechanical properties in CNT/Al composites fabricated by flake powder metallurgy, Carbon, 130 (2018) 333–339. DOI: 10.1016/j.carbon.2018.01.037

Fan G.L., Xu R., Tan Z.Q., Zhang D., Li Z.Q., Development of flake powder metallurgy in fabricating metal matrix composites: A review, Acta Metallurgica Sinica-English Letters, 27 (2014) 806–815. DOI: 10.1007/s40195-014-0148-x

Foppoli A.A., Maroni A., Cerea M., Zema L., Gazzaniga A., Dry coating of solid dosage forms: an overview of processes and applications, Drug Development and Industrial Pharmacy, 43 (2017) 1919–1931. DOI: 10.1080/03639045.2017.1355923

Ghoroi C., Han X., To D., Jallo L., Gurumurthy L., Davé R.N., Dispersion of fine and ultrafine powders through surface modification and rapid expansion, Chemical Engineering Science, 85 (2013) 11–24. DOI: 10.1016/j.ces.2012.02.038

Han Y., Zhang X., Yu X., Zhao J., Li S., Liu F., Gao P., Zhang Y., Zhao T., Li Q., Bio-inspired aggregation control of carbon nanotubes for ultra-strong composites, Scientific Reports, 5 (2015) 11533. DOI: 10.1038/srep11533

He C., Zhao N., Shi C., Du X., Li J., Li H., Cui Q., An approach to obtaining homogeneously dispersed carbon nanotubes in Al powders for preparing reinforced Al-matrix composites, Advanced Materials, 19 (2007) 1128–1132. DOI: 10.1002/adma.200601381

Hwang T., Lee J.K., Mun J., Choi W., Surface-modified carbon nanotube coating on high-voltage $LiNi_{0.5}Mn_{1.5}O_4$ cathodes for lithium ion batteries, Journal of Power Sources, 322 (2016) 40–48. DOI: 10.1016/j.jpowsour.2016.04.118

Jiang L., Li Z., Fan G., Cao L., Zhang D., The use of flake powder metallurgy to produce carbon nanotube (CNT)/aluminum composites with a homogenous CNT distribution, Carbon, 50 (2012) 1993–1998. DOI: 10.1016/j.carbon.2011.12.057

Jiang L., Li Z.Q., Fan G.L., Zhang D., A flake powder metallurgy approach to Al_2O_3/Al biomimetic nanolaminated composites with enhanced ductility, Scripta Materialia, 65 (2011) 412–415. DOI: 10.1016/j.scriptamat.2011.05.022

Jiang Y., Wang D., Liang S., Cao F., Zou J., Xiao P., Effect of local alloying on interfacial bonding in laminated copper matrix composites reinforced by carbon nanotubes, Materials Science and Engineering: A, 748 (2019) 173–179. DOI: 10.1016/j.msea.2019.01.013

Johannes L.B., Yowell L.L., Sosa E., Arepalli S., Mishra R.S., Survivability of single-walled carbon nanotubes during friction stir processing, Nanotechnology, 17 (2006) 3081–3084. DOI: 10.1088/0957-4484/17/12/044

Kwon H., Estili M., Takagi K., Miyazaki T., Kawasaki A., Combination of hot extrusion and spark plasma sintering for producing carbon nanotube reinforced aluminum matrix composites, Carbon, 47 (2009) 570–577. DOI: 10.1016/j.carbon.2008.10.041

Kwon H., Leparoux M., Hot extruded carbon nanotube reinforced aluminum matrix composite materials, Nanotechnology, 23 (2012) 415701. DOI: 10.1088/0957-4484/23/41/415701

Kwon H., Takamichi M., Kawasaki A., Leparoux M., Investigation of the interfacial phases formed between carbon nanotubes and aluminum in a bulk material, Materials Chemistry and Physics, 138 (2013) 787–793. DOI: 10.1016/j.matchemphys.2012.12.062

Loa I., Raman spectroscopy on carbon nanotubes at high pressure, Journal of Raman Spectroscopy, 34 (2003) 611–627. DOI: 10.1002/jrs.1035

Naito M., Abe H., Kondo A., Yokoyama T., Huang C.C., Smart powder processing for advanced materials, KONA Powder and Particle Journal, 27 (2009) 130–143. DOI: 10.14356/kona.2009013

Naito M., Kondo A., Yokoyama T., Applications of Comminution Techniques for the Surface Modification of Powder Materials, ISIJ International, 33 (1993) 915–924. DOI: 10.2355/isijinternational.33.915

Nam D.H., Cha S.I., Lim B.K., Park H.M., Han D.S., Hong S.H., Synergistic strengthening by load transfer mechanism and grain refinement of CNT/Al–Cu composites, Carbon, 50 (2012) 2417–2423. DOI: 10.1016/j.carbon.2012.01.058

Narh K.A., Agwedicham A.-T., Jallo L., Dry coating polymer powder particles with deagglomerated carbon nanotubes to improve their dispersion in nanocomposites, Powder Technology, 186 (2008) 206–212. DOI: 10.1016/j.powtec.2007.12.004

Noguchi T., Magario A., Fukazawa S., Shimizu S., Beppu J., Seki M., Carbon nanotube/aluminium composites with uniform dispersion, Materials Transactions, 45 (2004) 602–604. DOI: 10.2320/matertrans.45.602

Ötles S., Lecoq O., Dodds J.A., Dry particle high-impact coating of biopowders: coating strength, Particulate Science and Technology, 27 (2009) 352–361. DOI: 10.1080/02726350902993987

Qu L., Morton D.A., Zhou Q.T., Particle engineering via mechanical dry coating in the design of pharmaceutical solid dosage forms, Current Pharmaceutical Design, 21 (2015) 5802–5814. DOI: 10.2174/1381612821666151008151001

Sadeghi B., Cavaliere P., Nosko M., Trembošová V., Nagy Š., Hot deformation behaviour of bimodal sized Al_2O_3/Al nanocomposites fabricated by spark plasma sintering, Journal of Microscopy, (2020). DOI: 10.1111/jmi.12947

Sadeghi B., Cavaliere P., Roeen G.A., Nosko M., Shamanian M., Trembošová V., Nagy Š., Ebrahimzadeh N., Hot rolling of MWCNTs reinforced Al matrix composites produced via spark plasma sintering, Advanced Composites and Hybrid Materials, 2 (2019) 549–570. DOI: 10.1007/s42114-019-00095-7

Sadeghi B., Sarraf-Mamoory R., Shahverdi H.R., Surface modification of $LiMn_2O_4$ for lithium batteries by nanostructured $LiFePO_4$ phosphate, Journal of Nanomaterials, 2012 (2012a) 743236. DOI: 10.1155/2012/743236

Sadeghi B., Sarraf-Mamoory R., Shahverdi H.R., The effect of $LiFePO_4$ coating on electrochemical performance of $LiMn_2O_4$ cathode material, Iranian Journal of Chemistry and Chemical Engineering (IJCCE), 31 (2012b) 29–34. https://www.sid.ir/en/journal/ViewPaper.aspx?id=276841

Sadeghi B., Shabani A., Cavaliere P., Hot rolling of spark-plasma-sintered pure aluminium, Powder Metallurgy, 61 (2018a) 285–292. DOI: 10.1080/00325899.2018.1478779

Sadeghi B., Shamanian M., Ashrafizadeh F., Cavaliere P., Rizzo A., Friction stir processing of spark plasma sintered aluminum matrix composites with bimodal micro- and nano-sized reinforcing Al_2O_3 particles, Journal of Manufacturing Processes, 32 (2018b) 412–424. DOI: 10.1016/j.jmapro.2018.03.013

Sadeghi B., Shamanian M., Cavaliere P., Ashrafizadeh F., Effect of processing parameters on the microstructural and mechanical properties of aluminum–carbon nanotube composites produced by spark plasma sintering, International Journal of Materials Research, 109 (2018c) 900–909. DOI: 10.3139/146.111686

Sadeghi B., Shamanian M., Cavaliere P., Ashrafizadeh F., Sanayei M., Szpunar J.A., Microstructural and mechanical behavior of bimodal reinforced Al-based composites produced by spark plasma sintering and FSP, International Journal of Advanced Manufacturing Technology, 94 (2018d) 3903–3916. DOI: 10.1007/s00170-017-1144-x

Salimi S., Izadi H., Gerlich A.P., Fabrication of an aluminum–carbon nanotube metal matrix composite by accumulative roll-bonding, Journal of Materials Science, 46 (2010) 409–415. DOI: 10.1007/s10853-010-4855-z

Sharma R., Setia G., Mechanical dry particle coating on cohesive pharmaceutical powders for improving flowability—a review, Powder Technology, 356 (2019) 458–479. DOI: 10.1016/j.powtec.2019.08.009

Tan Z., Li Z., Fan G., Li W., Liu Q., Zhang W., Zhang D., Two-dimensional distribution of carbon nanotubes in copper flake powders, Nanotechnology, 22 (2011) 225603. DOI: 10.1088/0957-4484/22/22/225603

Tokunaga T., Kaneko K., Horita Z., Production of aluminum-matrix carbon nanotube composite using high pressure torsion, Materials Science and Engineering: A, 490 (2008) 300–304. DOI: 10.1016/j.msea.2008.02.022

Wei D., Dave R., Pfeffer R., Mixing and characterization of nanosized powders: an assessment of different techniques, Journal of Nanoparticle Research, 4 (2002) 21–41. DOI:

10.1023/A:1020184524538

Wei H., Li Z.Q., Xiong D.B., Tan Z.Q., Fan G.L., Qin Z., Zhang D., Towards strong and stiff carbon nanotube-reinforced high-strength aluminum alloy composites through a microlaminated architecture design, Scripta Materialia, 75 (2014) 30–33. DOI: 10.1016/j.scriptamat.2013.11.014

Yang X., Liu E., Shi C., He C., Li J., Zhao N., Kondoh K., Fabrication of carbon nanotube reinforced Al composites with well-balanced strength and ductility, Journal of Alloys and Compounds, 563 (2013) 216–220. DOI: 10.1016/j.jallcom.2013.02.066

Yang X., Zou T., Shi C., Liu E., He C., Zhao N., Effect of carbon nanotube (CNT) content on the properties of in-situ synthesis CNT reinforced Al composites, Materials Science and Engineering: A, 660 (2016) 11–18. DOI: 10.1016/j.msea.2016.02.062

Zhang K., Choi H.J., Smart polymer/carbon nanotube nanocomposites and their electrorheological response, Materials, 7 (2014) 3399–3414. DOI: 10.3390/ma7053399

Zhao Q., Wagner H.D., Raman spectroscopy of carbon-nanotube-based composites, Philosophical Transactions of the Royal Society of London Series A: Mathematical, Physical and Engineering Sciences, 362 (2004) 2407–2424. DOI: 10.1098/rsta.2004.1447

Zheng K., Kunnath K., Ling Z., Chen L., Davé R.N., Influence of guest and host particle sizes on dry coating effectiveness: when not to use high mixing intensity, Powder Technology, 366 (2020) 150–163. DOI: 10.1016/j.powtec.2020.02.059

Zhou S.-M., Zhang X.-B., Ding Z.-P., Min C.-Y., Xu G.-L., Zhu W.-M., Fabrication and tribological properties of carbon nanotubes reinforced Al composites prepared by pressureless infiltration technique, Composites Part A: Applied Science and Manufacturing, 38 (2007) 301–306. DOI: 10.1016/j.compositesa.2006.04.004

Authors' Short Biographies

Behzad Sadeghi

Dr. Behzad Sadeghi is currently a Postdoctoral Researcher at Shanghai Jiao Tong University, China. He received his PhD in 2018 from Isfahan University of Technology, Iran. He also worked at Salento university, Italy from 2016 to 2017. His research mainly focuses on microstructure-property relationships and understanding the underlying deformation mechanisms in advanced engineering materials especially aluminum matrix composites.

Genlian Fan

Dr. Genlian Fan is an Associate Professor at Shanghai Jiao Tong University. She received her BS degree and PhD degree from Xi'an Jiaotong University in 2003 and 2009, respectively, followed by postdoctoral research at Shanghai Jiao Tong University. She has authored and coauthored over 80 papers. Her research interests include nanocarbon reinforced metal matrix composites, smart powder processing of the advanced composites.

Zhanqiu Tan

Dr. Zhanqiu Tan is an Assistant Researcher in Shanghai Jiao Tong University. He received his Ph.D. degree in Materials Science and Engineering from Shanghai Jiao Tong University in 2014, and completed the postdoctoral research here in 2014–2016. He has authored and coauthored over 60 papers. His current research focuses on the high-performance nanocarbon reinforced aluminum matrix composites for light-weight structural applications.

Authors’ Short Biographies

Zhiqiang Li

Prof. Zhiqiang Li is a Professor at Shanghai Jiao Tong University. He received his BS (1996), MS (1998) and PhD (2001) degrees from Harbin Institute of Technology. He worked in State Key Lab of Metal Matrix Composites in Shanghai Jiao Tong University since 2002. His research interests focus on the bioinspired fabrication techniques, architecture design, and carbon-based metal matrix nanocomposites. He has authored and coauthored more than 100 journal publications and held over 20 patents.

Akira Kondo

Dr. Akira Kondo received BS and MS degrees in chemical engineering from Nagoya University, Japan in 1989 and 1991, respectively. He received PhD degree in material science from Osaka University in 1999. He was with Hosokawa Micron Corp. from 1991 to 2005, where he engaged in the R&D of powder processing technology. He became a specially designated researcher at the Joining and Welding Research Institute (JWRI), Osaka University in 2005, and is engaged in the R&D of powder processing for advanced materials.

Makio Naito

Prof. Makio Naito is a Professor at the Joining and Welding Research Institute (JWRI), Osaka University in Japan. He served as the President of The Society of Powder Technology, Japan from 2015 to 2019. His publications cover a wide range of studies in the fields of advanced materials and novel powder processing and characterization. He has received several prestigious awards including the Richard M. Fulrath Award from the American Ceramic Society (ACerS) in 2002 and the KONA Award in 2019. He has been a Fellow of the ACerS since 2010, and serves on the ACerS Board of Directors from 2020.

KONA Powder and Particle Journal No. 39 (2022) 230–239/https://doi.org/10.14356/kona.2022016 Original Research Paper

Correlating Granule Surface Structure Morphology and Process Conditions in Fluidized Bed Layering Spray Granulation[†]

Maike Orth[*]**, Paul Kieckhefen, Swantje Pietsch and Stefan Heinrich**

Institue of Solids Process Engineering and Particle Technology, Hamburg University of Technology, Germany

---

Abstract

A workflow for developing a multidimensional, linear correlation between the process conditions during fluidized bed spray granulation and the surface morphology of the resulting granules is presented. Spray coating experiments with Cellets®500 particles and sodium benzoate solution were performed in a lab-scale fluidized bed varying liquid spray rate, fluidization air flow rate, fluidization air temperature, spray air temperature and spray atomization pressure. To characterize the surface structure, the surface roughness of the coated particles was quantified using confocal laser-scanning microscopy. The roughness was correlated to the process conditions, and the resulting correlation was rigorously analyzed for the importance and co-linearities of the individual process parameters using a principal component analysis. The surface roughness is strongly dependent on the spray rate of the coating solution, the fluidization air temperature and the atomization pressure at the nozzle. In general, wet process conditions and large droplets with a low initial velocity favor the formation of particles with a rough surface structure, while dry conditions and fine droplets with a high velocity result in granules with a smooth and compact coating layer.

Keywords: fluidized bed spray granulation, coating, surface roughness, laser-scanning microscopy, product property correlation

---

1. Introduction

1.1 Motivation

Fluidized bed spray granulation is a key process used in various industries for the production of high-quality granular solids. The processing of particles in a fluidized bed with liquid injection allows the production of a wide variety of particles for different applications. Products from spray granulation include pharmaceuticals, food powders, fertilizers and detergents, among others. The variation of process conditions is used to obtain defined product properties like certain sizes, shapes or structures, which then define the application properties like flowability, stability or taste and odor masking (Dewettinck and Huyghebaert, 1999). A coating can also be applied to protect the core from environmental influences and prevent oxidation or moisture absorption (Werner et al., 2007). Controlled release of active substances is another application in which the structure of the coating is essential (Turton, 2008; Tzika et al., 2003). A detergent, for example, requires a short release time, whereas fertilizers should usually be released at a defined rate over a longer time period.

To induce particle growth, a solid-containing liquid is sprayed onto the fluidized particles. The size increase occurs via either agglomeration or layering granulation or coating. In the case of agglomeration, the liquid acts as a binder between the primary particles. When two wet particles collide, a liquid bridge forms and solidifies after the liquid evaporates due to the hot fluidization gas. Thus, agglomerates are formed by connecting several primary particles via solid bridges (Fries, 2012). In layering granulation or coating, the droplets come into contact with the particle surface, where they spread and form a liquid film around the particle. Due to evaporation of the liquid, this film becomes a solid shell. By repeating these steps, several coating layers can be added to the particle (Uhlemann and Mörl, 2000). Usually, the application of thin layers onto the particle surface is defined as coating, whereas granulation refers to a layering growth resulting in an onion-like structure (Rieck et al., 2015). In this work the particle growth due to layering is defined as granulation.

[†] Received 14 May 2021; Accepted 6 August 2021

[*] Corresponding author: Maike Orth;
Add: Denickestraße 15, 21073 Hamburg, Germany
E-mail: maike.orth@tuhh.de
TEL: +49-40-42878-4279 FAX: +49-40-42731-3621

The formation of a coating layer during the fluidized bed spray granulation depends on several micro-processes that are affected by the process conditions. The deposition and spreading of droplets on the particles depend on properties of the particle surface—such as roughness and chemical composition—as well as the droplet characteristics. The latter includes not only the size and velocity of the droplets, but also coating solution properties like viscosity and surface tension. Another important micro-process is the evaporation of the liquid due to the heated fluidization gas, which is strongly influenced by the drying conditions (Fries, 2012; Uhlemann and Mörl, 2000). Depending on the chosen material system, additional phenomena like crystallization or penetration of the solution into the pores of porous particles can occur and influence the granule properties (Hoffmann et al., 2015; Uhlemann and Mörl, 2000). The knowledge of the effect of different process parameters on the micro processes in the fluidized bed and the resulting granule structures is invaluable for the production of tailor-made particles.

1.2 Previous works

The influence of process parameters on different particle properties has been investigated in several previous works. In most of these studies, either a small set of parameters was chosen or a one-factor-at-a-time approach was used, meaning that interaction between the parameters is not considered. Rieck et al. (2015) and Hoffmann et al. (2015) investigated the influence of the drying conditions on the layer porosity for the coating of glass and γ-Al_2O_3 particles with sodium benzoate. Their experiments were carried out in top-spray configuration at different fluidization air inlet temperatures and spray rates of the coating solution. The overall drying conditions were described by a drying potential, which was correlated to the shell porosity measured by X-ray micro-tomography. For both glass and γ-Al_2O_3, a linear decrease of the porosity was observed with increasing drying potential, characterized by a higher air temperature and lower spray rate.

The drying conditions were also examined by Hampel (2015). Cellulose particles (Cellets®200) were coated with sodium benzoate in a Wurster fluidized bed process and qualitatively analyzed afterwards regarding their surface morphology via scanning electron microscopy. The varied parameters were the gas inlet temperature, the spray rate of the coating solution and the fluidization air mass flow rate. The increase of the gas temperature led to the formation of a more compact coating, whereas the increase of the gas mass flow resulted in a higher shell porosity. No unambiguous change in surface morphology was observed when varying the mass flow of the coating liquid.

Tzika et al. (2003) observed non-uniform coatings and serious surface defects for fertilizer particles that were coated with a polymer latex at very low or very high fluidization air velocities. This poor coating quality was attributed to the low frequency at which the particles entered the coating zone for the low air velocity and to the reduced time in the coating zone per pass in addition to frequent collisions of the particles with each other and the wall for the high velocity. The best coating quality was achieved by choosing an intermediate air fluidization flow rate.

The continuous granulation of sodium benzoate in a horizontal fluidized bed with sieve-milling circuit was investigated by Diez et al. (2018). Similar to Rieck et al. (2015) and Hoffmann et al. (2015), Diez et al. (2018) produced particles with a compact and smooth surface at high air temperatures and low liquid spray rates, whereas low temperatures and high spray rates resulted in a higher surface roughness.

Schmidt et al. (2017) performed coating experiments with γ-Al_2O_3 particles and a suspension of limestone, hydroxy propyl methyl cellulose and water at different atomization pressures of the top-spray nozzle used for the injection of the suspension. The shell porosity was found to decrease with increasing pressure.

The surface morphology and layer thickness of particles coated in a fluidized bed were also studied by Depypere et al. (2009) and Perfetti et al. (2010). Depypere et al. (2009) coated glass particles with sodium caseinate and gelatine hydrolysate in bottom-spray configuration and in top-spray configuration at three different nozzle heights. The coatings were analyzed via confocal laser-scanning microscopy. For sodium caseinate coatings, the coating thickness and uniformity decreased with increasing distance between the nozzle tip and the fluidized bed, meaning that the particles from the bottom-spray set-up had the most homogeneous coating while the highest top-spray nozzle position resulted in a wider layer thickness distribution. With gelatine hydrolysate as coating material, however, the highest coating quality was achieved at the lowest nozzle position in top-spray configuration.

Perfetti et al. (2010) used X-ray micro-tomography to characterize polymer-coated sodium benzoate and cellulose particles that were coated with polyvinyl alcohol and hydroxy propyl methyl cellulose in a top-spray fluidized bed. The coating layer thickness was determined with different methods based on the two-dimensional and three-dimensional particle structures obtained from the tomography data. Most results were in good agreement with the theoretical thickness as well as with each other. Furthermore, the micro-CT allowed the measurement of several structural parameters of the coating shell, including surface density, porosity and pore volume.

In these previous works, the coating quality was either evaluated qualitatively or a one-dimensional approach was used to correlate individual parameters or the drying potential with the surface morphology. However, a multidimensional correlation between process conditions and granule surface morphology is yet to be developed. Such a correlation is crucial as individual parameters are not able to reflect all the parameters involved during fluidized bed spray granulation. For example, it was already shown that the shell porosity is influenced by the atomization pressure, but this value is not included into the drying potential. Thus, a correlation is needed that indicates the influencing parameters qualitatively and quantitatively.

1.3 Structure

To develop a multidimensional, linear correlation that connects the process parameters and the granule surface roughness, coating experiments were carried out in a lab-scale fluidized bed. As a result of the literature study and previous investigations, the liquid spray rate, the fluidization gas flow rate and inlet temperature, the spray air temperature and the spray atomization pressure were chosen as varying parameters. To investigate the influence of these five process parameters within a reasonable amount of runs while still obtaining a significant result, the experiments were statistically planned. The resulting granules were analyzed regarding their surface roughness via laser-scanning microscopy. Therefore, a 3D-profile of the particle surface was created which was then evaluated in a defined measurement area. The roughness was correlated to the process parameters and the resulting linear correlation was rigorously analyzed for the importance and co-linearities of the parameters using a principal component analysis.

2. Materials and methods

2.1 Materials

For all experiments, Cellets®500 (Harke Pharma GmbH, Germany) with a diameter between 500 and 710 µm were used as primary particles. Cellets® consist of microcrystalline cellulose and are often utilized as pharmaceutical excipient. Because of their non-porous surface, no droplet imbibition occurs during the coating process. The material provides a smooth surface and high sphericity. In addition, the Cellets® are chemically inert and insoluble in water, which makes them suitable for coating experiments with a salt solution. **Table 1** lists the main properties of the particles. As coating material, an aqueous solution with 30 wt% sodium benzoate was used. Sodium benzoate is a white, crystalline powder with a good solubility in water that is used as a preservative in the food industry.

Table 1 Properties of Cellets®500.

Sauter diameter	639	µm
Sphericity	0.96	–
Surface roughness	1.5	µm
Solid density	1445	kg/m^3

2.2 Coating experiments

The coating experiments were carried out in the ProCell® 5 LabSystem with the fluidized bed process chamber GF3 (Glatt, Germany), which is shown in **Fig. 1**. The diameter at the gas inlet of the chamber is 180 mm. For the injection of the coating solution, a two-fluid nozzle of type 970-S4 (Schlick, Germany) with an orifice size of 1.2 mm was installed in bottom-spray configuration in the center of the sieve plate distributor (mesh size 105 µm). The solution is conveyed to the nozzle with a peristaltic pump (Medorex TB, Germany) and compressed air is used to atomize the liquid into fine droplets. The experiments were performed batch-wise with an initial bed mass of 2 kg of Cellets®500 per batch. For each run, 1 kg of the 30 wt% sodium benzoate solution was injected into the process chamber.

As previously mentioned, five parameters were varied: the spray rate of the coating solution $\dot{m}_l$, the fluidization air volume flow $\dot{V}_{air}$, the fluidization air inlet temperature T_{in}, the spray air temperature T_{at} and the spray atomization pressure p_{at}. The different values that were set for each parameter are shown in **Table 2**. The limits were chosen in such a way that a broad range was covered while the stability of the process was still maintained. An overview of the experiments, including the process parameters, average bed temperature, theoretically expected outlet air temperature after evaporation of the water and surface roughness

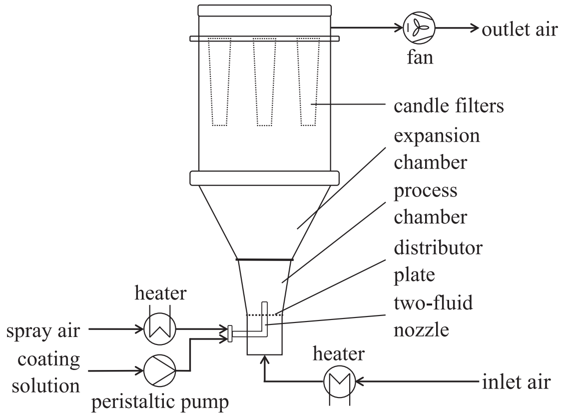

Fig. 1 Scheme of the experimental fluidized bed set-up.

Table 2 Process parameters and values used in coating experiments.

$\dot{m}_l$ [g/min]	$\dot{V}_{air}$ [m^3/h]	T_{in} [°C]	T_{at} [°C]	p_{at} [bar]
10	80	50	20	0.5
15	105	85	70	1.75
20	130	120	120	3.0

data, is provided on J-STAGE Data website.

2.3 Design of experiments

A design of experiments approach is used to investigate the effects of multiple input variables on a response at the same time. In this case, the effect of the process parameters on the surface roughness was investigated. By planning the experiments statistically, interactions between the parameters can be considered while the number of runs is reduced compared to the full factorial experimental plan. For the granulation experiments in this work, a three-level experimental plan including the five parameters listed in **Table 2** was created using the statistics software Minitab 18 (Minitab, USA). For each parameter an upper and lower limit was defined. In addition, the mean value of these limits was chosen as the third level. Since the three-level full factorial approach consisted of 243 experiments, the response surface methodology with central composite design was used instead. Choosing the half fraction of the thereby obtained design resulted in a total of 29 experiments.

2.4 Surface roughness measurement

2.4.1 Confocal laser-scanning microscopy

In a conventional optical microscope, the entire sample is illuminated by a light source, so the photodetector, where the light reflected from the sample forms an image, detects not only the sample itself but also unfocused planes in the background. In contrast, only a small part of the sample is illuminated at each time in confocal laser-scanning microscopy. The surface of a sample can be scanned by moving the position of the focal point on the sample surface. By scanning the image area within the field of view, a two-dimensional image at a given height is captured. This scan is repeated several times with the objective lens at different Z-axis positions in order to reconstruct the three-dimensional structure of the sample and gather height information. The confocal laser technology allows for the acquisition of images with a large depth of field that are in focus across the entire screen (Keyence, 2015).

2.4.2 Roughness quantification

The surface roughness was measured using the 3D Laser Scanning Confocal Microscope VK-X160K (Keyence, Japan). The microscope uses a two-way light source with laser light and white light. The light emitted from the laser light source is focused on the sample surface by the objective lens with a magnification of 10×, 20×, 50× or 100×. Based on the detected height information and laser intensity, a 3D-profile of the particle surface is constructed. The relatively short measurement time compared to other surface morphology characterization methods, like X-ray micro-tomography, as well as the possibility to quantify the surface structure make the laser-scanning microscopy the ideal analysis method for this work.

To quantify the surface morphology of the coated particles, the surface roughness was evaluated. Roughness consists of a sequence of peaks and valleys forming a complex shape due to their difference in height, depth and intervals (Keyence, 2015). A wide variety of parameters, based either on lines or areas on the surface, can be used to describe the roughness. These parameters are defined in DIN EN ISO 4287:2010-07 (2010) and DIN EN ISO 25178-2:2012 (2012). In this work, the arithmetical mean height S_a, one of the most commonly used roughness quantifiers, was used to characterize the roughness. The arithmetical mean height is a surface-based parameter which describes the average height difference of each point on the surface from the mean height of the particle surface within a defined measurement area A:

$$S_\mathrm{a} = \frac{1}{A} \iint_A \left| h(x,y) - \bar{h} \right| \, \mathrm{d}x \, \mathrm{d}y \tag{1}$$

The measured 3D-profiles of the coated particles were smoothed using a Gauss filter to reduce measurement noise. Additionally, the surface shape was corrected with image processing to avoid an influence of the particle shape on the measured roughness. The surface-based arithmetical mean height was evaluated at 50× magnification over the whole surface area that was covered by the microscope. For each sample three particles were analyzed at three different positions on the surface of each particle.

To validate the observations regarding the surface morphology, particles from two experiments with extremely different process conditions—due to the parameters being set to either their minimum or maximum values in these runs—were analyzed with a scanning electron microscope (type: Supra VP55, Zeiss, Germany).

3. Results and discussion

3.1 Regressing process parameters and granule roughness

A linear regression model is fitted to the roughness data using the ordinary least squares method. This allows for the pre-factors for a linear equation connecting the five varied process parameters to the surface roughness to be determined. With a principal component analysis, principal components that reduce the variance in a data set can be identified.

To perform the principal component analysis, a matrix **A** is created in which each column contains the data for one experiment, including process parameters during the coating experiment as well as the granule surface roughness. Afterwards, the eigenvalues and eigenvectors of the corresponding covariance matrix Cov(**A**) = $\mathbf{AA}^T$ are determined. The distribution of the residual decreases with the number of included components. **Fig. 2** shows how the residual distribution changes when a certain number of principal components is included in the model. It can be seen that the distribution of the residual can be reduced to a reasonable range by including four components in the model. To avoid over-fitting of the model, the components that correspond to the lowest eigenvalues are dropped and only statistically significant parameters are considered.

3.2 Linear correlation for the surface roughness

During the fluidized bed spray granulation, the particle surface structure formation is dependent on several micro-processes occurring within the droplets and at the solid-liquid interface. The droplet characteristics and the interaction of solid and liquid on the other hand are influenced by the process variables that determine the overall state of the fluidization air as well as the conditions in the spray zone and the drying zone of the fluidized bed. Using the previously described approach to create a linear model connecting the chosen process parameters to the granule surface roughness, the following correlation for the arithmetical mean height is obtained:

$$S_\mathrm{a} = 8.718 + 0.085\dot{m}_\mathrm{l} - 0.038T_\mathrm{in} - 0.843p_\mathrm{at} \qquad (2)$$

According to the correlation, the surface roughness S_a depends on three of the five investigated parameters: the fluidization air temperature T_in in °C, the atomization pressure p_at in bar and the liquid spray rate $\dot{m}_\mathrm{l}$ in g/min. The spray air temperature and the fluidization air volume flow, however, did not show a significant effect on the surface structure and were therefore removed from the model. As the signs in Eqn. (2) suggest, a high surface roughness is achieved at low fluidization air temperatures, low atomization pressures and high spray rates of the coating solution. Conversely, at high air temperatures, high spray pressures and low liquid spray rates, particles with smooth and compact surfaces are produced. These observations are confirmed by the SEM images of the granules in **Fig. 3**. As predicted by the model, the particle coated at $\dot{m}_\mathrm{l}$ = 20 g/min, T_in = 50 °C and p_at = 0.5 bar has a significantly rougher and more uneven surface than the particle coated at $\dot{m}_\mathrm{l}$ = 10 g/min, T_in = 120 °C and p_at = 3.0 bar.

As depicted in **Fig. 4**, the roughness values predicted by the linear model show an overall good agreement with the measured data. Only the two highest roughness values are overestimated by the correlation and lie significantly below the 45°-line. With increasing roughness the particle structure becomes more irregular, which makes

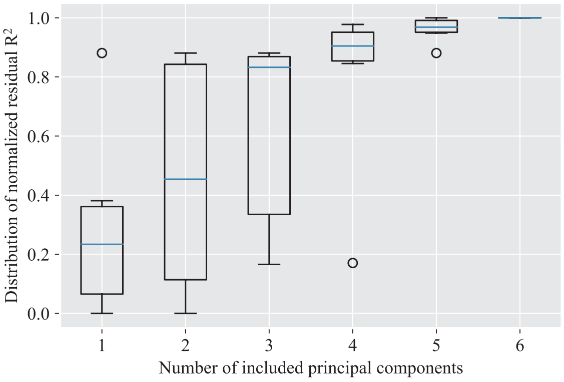

Fig. 2 Normalized residual distribution in dependence of number of included principal components (eigenvectors).

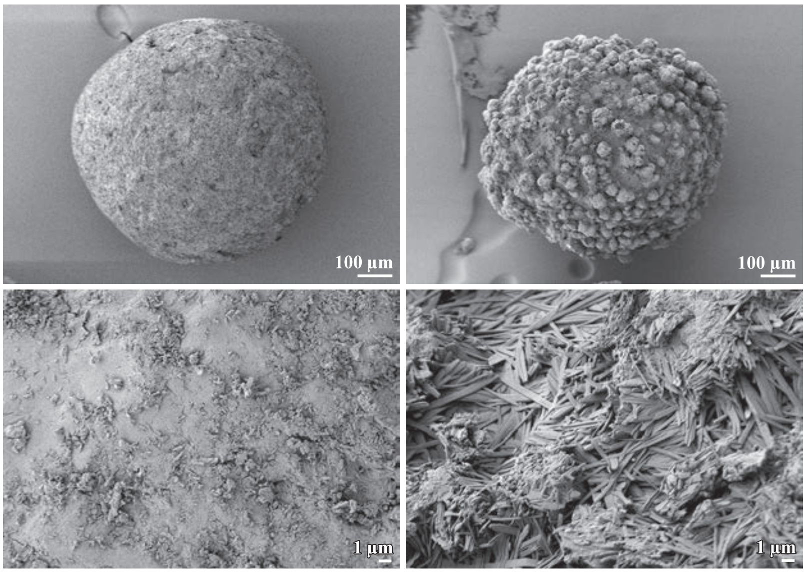

Fig. 3 SEM images of Cellets®500 particles coated with sodium benzoate at different process conditions. Left: $\dot{m}_\mathrm{l}$ = 10 g/min, $\dot{V}_\mathrm{air}$ = 130 m³/h, T_in = 120 °C, T_at = 20 °C, p_at = 3.0 bar; right: $\dot{m}_\mathrm{l}$ = 20 g/min, $\dot{V}_\mathrm{air}$ = 80 m³/h, T_in = 50 °C, T_at = 20 °C, p_at = 0.5 bar.

the characterization of the overall surface morphology challenging. Furthermore, there are few data points at high roughness values, which makes the fitting of the model difficult in this roughness range. For values below 9 µm, where most of the data points lie, the model shows a good fit. Moreover, it has to be considered that, while the surface structure analysis via laser-scanning microscopy is an improved characterization method in terms of measurement time compared to the X-ray tomography and scanning electron microscopy approaches used in previous studies, the amount of analyzed granules is still very low compared to the whole particle bed for each experiment.

An advantage of the linear model is the easy interpretation since the influence of each variable on the response can be directly seen in the correlation. This allows for the analysis of the individual process parameters and their impact on the formation of the coating and the resulting surface morphology. In the following sections, the influence of the three primary influencing factors on the surface structure is discussed in detail.

3.2.1 Influence of the liquid spray rate

In **Fig. 5**, the partial dependence of the surface roughness on the spray rate of the sodium benzoate solution is shown. The higher roughness at an increased spray rate predicted by the linear model is confirmed by the laser-scanning microscope images in **Fig. 6**. At the maximum spray rate of 20 g/min, a rough and irregular surface was formed, whereas the particles from the experiment with the lowest spray rate of 10 g/min and otherwise similar parameters have a smooth surface without any noticeable peaks. This dependence of the roughness on the spray rate

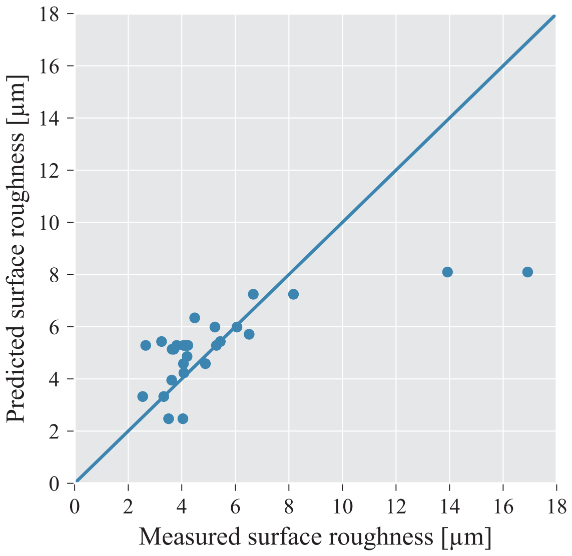

Fig. 4 Surface roughness predicted by the linear model in Eqn. (2) compared to the surface roughness measured via confocal laser-scanning microscopy.

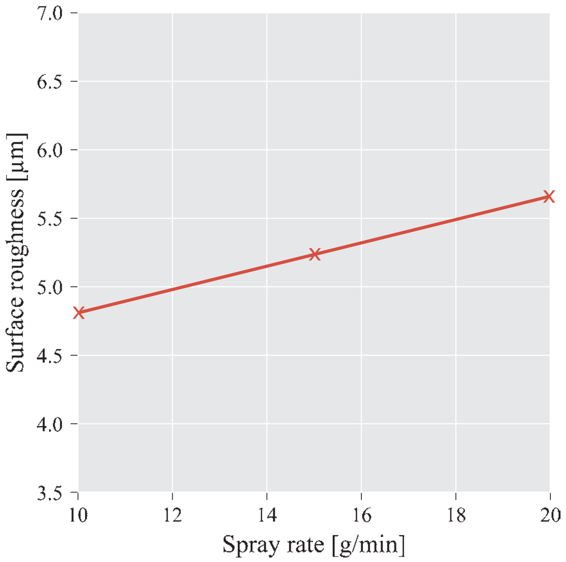

Fig. 5 Partial dependence of the surface roughness on the liquid spray rate. The crosses mark the experimentally investigated spray rates.

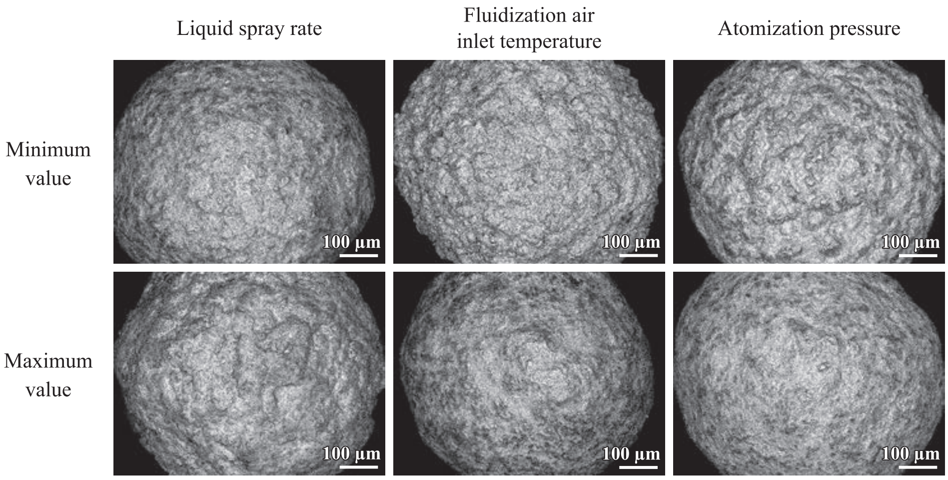

Fig. 6 Laser-scanning microscope images of Cellets®500 particles coated with sodium benzoate at different process conditions. Within each column all remaining process parameters were the same for both experiments.

can be explained by the crystallization of sodium benzoate in the evaporating solution droplets on the particle surface. At low spray rates, the drying conditions in the fluidized bed are intense due to the low amount of liquid in the process chamber. In this case, the liquid evaporates quickly, causing a high over-saturation of sodium benzoate in the shrinking droplet. Due to the short drying time, nuclei formed in the droplets do not have enough time to grow into larger crystals. These precipitated nuclei form a dense coating with a smooth surface. High spray rates, however, cause a large temperature drop over the fluidized bed due to the high amount of liquid that evaporates. This effect can be observed in the theoretical outlet air temperature given on J-STAGE Data website, that corresponds to the decreased fluidization air temperature after passing the particle bed due to the evaporation of the water in the process chamber. Consequently, at high spray rates and therefore moderate drying conditions, the slow evaporation of water and long drying time of the droplets allow the growth of larger sodium benzoate crystals on the particle surface, resulting in a rough and irregularly shaped coating. This crystalline surface structure formed under wet process conditions is especially apparent in the SEM images in **Fig. 3**. The dependence of the crystallization of sodium benzoate on the drying conditions during fluidized bed coating was also observed by Rieck et al. (2015) and Hoffmann et al. (2015).

3.2.2 Influence of the fluidization air inlet temperature

As shown in the partial dependence plot in **Fig. 7**, an increase in the fluidization air inlet temperature results in a lower roughness and therefore smoother particle surface. Just like the liquid spray rate, the temperature of the fluidization air has a major impact on the drying conditions during the granulation process. Due to the reduced relative humidity, the heated air can absorb a higher amount of water, which results in a high drying rate. Under these conditions, small crystal seeds are precipitated from the droplets due to the fast evaporation and short drying time rather than growing into larger crystals. The smooth surface that is formed under intense drying conditions at the highest investigated temperature of 120 °C is depicted in **Fig. 5**. Conversely, the particles coated at 50 °C and otherwise similar parameters show a rough surface with many visible peaks and valleys. At these moderate drying conditions, due to the lower air temperature, crystal growth is enhanced as previously explained, and the larger crystals form a rougher and irregular surface. This observation is confirmed by the SEM images in **Fig. 3**, in which the surface morphology of the right particle is clearly defined by sodium benzoate crystals, whereas no such crystal structures are visible on the left particle's surface.

3.2.3 Influence of the atomization pressure

The partial dependence of the surface roughness on the atomization pressure in **Fig. 8** shows a decreasing arithmetical mean height with increasing pressure. This trend is also apparent in the microscope images in **Fig. 5**, in which the surface formed at the minimum pressure of 0.5 bar is significantly rougher than the surface of the particle coated at the maximum atomization pressure of 3.0 bar. The droplet characteristics during granulation are strongly influenced by the nozzle parameters. The pressure of the spray air determines the droplet size as well as the initial droplet velocity. At higher pressures the shear stress acting on the injected liquid is also higher, which causes

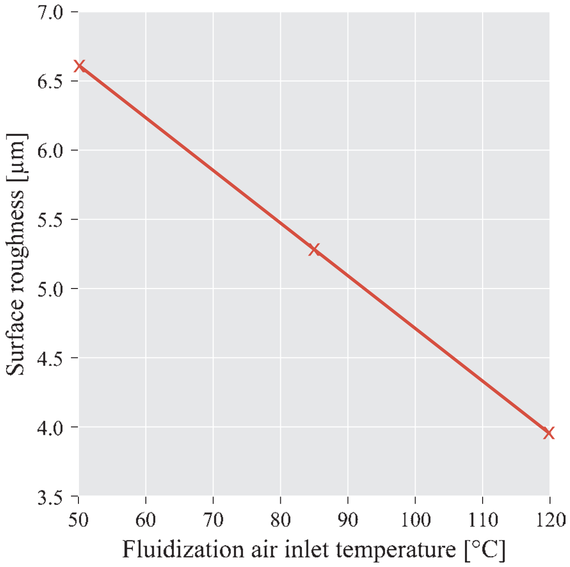

Fig. 7 Partial dependence of the surface roughness on the fluidization air inlet temperature. The crosses mark the experimentally investigated temperatures.

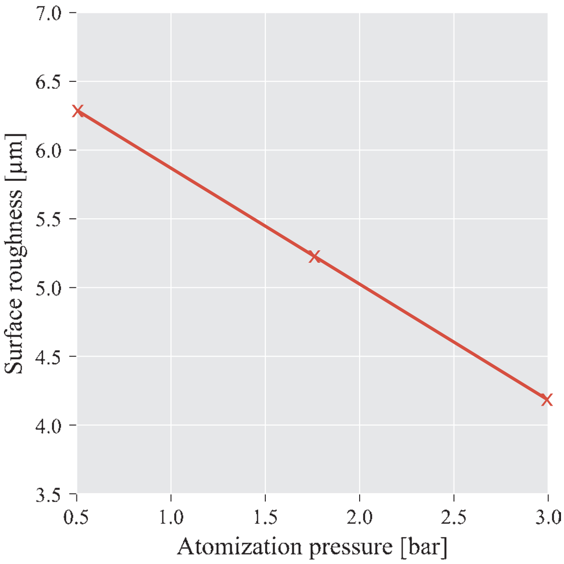

Fig. 8 Partial dependence of the surface roughness on the spray atomization pressure. The crosses mark the experimentally investigated pressures.

the formation of finer droplets with high velocity. Once a droplet collides with a particle, this high velocity leads to a homogeneous spreading of the droplet on the particle surface. The fast and even spreading of the droplets before the water completely evaporates leads to the formation of a smooth and uniform coating. Furthermore, existing surface defects can be filled by the small liquid droplets, which further increases the smoothness of the surface. In contrast, the larger droplets produced at low nozzle pressures have a lower velocity upon impact with the particles, thus spreading in a less homogeneous way and creating a more uneven coating.

Besides the spray air pressure, the droplet characteristics are dependent on the properties of the spray solution, like viscosity and surface tension. The surface tension, along with the solid-vapor and solid-liquid interfacial energy, determine the contact angle of a droplet on the particle surface, which characterizes the wetting behavior and indicates, how well a liquid spreads on a solid surface. The viscosity influences the flow behavior of the coating solution and therefore the spreading velocity of the droplets on the particle surface. Due to the evaporation of the liquid in the fluidized bed, the viscosity of a droplet is not constant and increasing with the decreasing water content and therefore increasing solid concentration within the droplet. In combination with the droplet size and velocity these factors strongly influence the deposition of the droplets on the particle surface and therefore the resulting granule morphology.

4. Conclusions

To investigate the influence of process conditions on surface morphology, fluidized bed spray granulation experiments were performed with different process parameter combinations according to a statistical experimental plan. To characterize the surface structure, the roughness was measured via confocal laser-scanning microscopy. Compared to the surface characterization methods used in most previous works, this roughness analysis is advantageous in terms of measurement time and the possibility of quantifying the morphology. To connect the surface structure to the process parameters, a linear model was fitted to the roughness data. A principal component analysis was used to identify the principal components with significant impact on the roughness.

It can be concluded that the surface roughness is primarily influenced by the drying conditions in the fluidized bed and the properties of the injected liquid droplets. The former depends on the spray rate of the coating solution, which determines the amount of liquid introduced into the process chamber per time step, and the inlet temperature of the fluidization air, which impacts the amount of water that the air can absorb. It was shown that moderate drying conditions lead to the formation of a coating with a rough surface, whereas particles with a smooth surface were produced at high drying rates. This dependence of the roughness on the drying parameters is explained by the crystallization of sodium benzoate. Apart from the properties of the coating solution, the droplet characteristics are affected by the spray atomization pressure at the two-fluid nozzle in such a way that finer droplets with a higher initial velocity are formed at higher pressures. Consequently, a smooth surface was observed for particles coated at high atomization pressures, while a decrease in atomization pressure led to higher roughness values.

The correlation obtained in this work allows the prediction of the surface roughness for any combination of the five investigated process parameters. To improve the prediction of product properties in fluidized bed spray granulation and gain a further understanding of the process, the work flow presented in this study can be applied to other material systems, in which different micro-processes and parameters might be important for the surface structure formation, as well as different apparatus geometries and configurations.

Future studies will be concerned with the application of different granulator geometries, like spouted beds that are used for coating (Pietsch et al., 2018), and scale-up to pilot-scale granulators with different mixing times (Diez et al., 2019), as well as utilization of the CFD-DEM method (Kieckhefen et al., 2020) to correlate mixing times and particle-scale drying conditions with the resulting surface structures.

Acknowledgements

Maike Orth acknowledges funding from the German Research Foundation within the DFG Graduate School GRK 2462 “Processes in natural and technical Particle-Fluid-Systems (PintPFS)” (Project No. 390794421). Paul Kieckhefen acknowledges funding from BASF SE.

Nomenclature

A	measurement area for surface roughness (μm^2)
h	height at one point of the particle surface (μm)
$\bar{h}$	mean height of the particle surface (μm)
$\dot{m}_1$	liquid spray rate (g/min)
p_{at}	spray atomization pressure (bar)
T_{at}	spray air temperature (°C)
T_{in}	fluidization air inlet temperature (°C)
$\dot{V}_{\mathrm{air}}$	fluidization air flow rate (m^3/h)

Data Availability Statement

The experimental data from spray granulation experiments and surface roughness measurements is available publicly in J-STAGE Data (https://doi.org/10.50931/data.kona.16656814).

References

Depypere F., Van Oostveldt P., Pieters J.G., Dewettinck K., Quantification of microparticle coating quality by confocal laser scanning microscopy (CLSM), European Journal of Pharmaceutics and Biopharmaceutics, 73 (2009) 179–186. DOI: 10.1016/j.ejpb.2009.04.007

DIN EN ISO 4287:2010-07, Geometrical Product Specifications (GPS)—Surface Texture: Profile Method—Terms, Definitions and Surface Texture Parameters, DIN (Deutsches Institut für Normung e.V.), Berlin, 2010.

DIN EN ISO 25178-2:2012 Geometrical Product Specifications (GPS)—Surface Texture: Areal—Part 2: Terms, Definitions and Surface Texture Parameters, DIN (Deutsches Institut für Normung e.V.), Berlin, 2012.

Dewettinck K., Huyghebaert A., Fluidized bed coating in food technology, Trends in Food Science & Technology, 10 (1999) 163–168. DOI: 10.1016/S0924-2244(99)00041-2

Diez E., Kieckhefen P., Meyer K., Bück A., Tsotsas E., Heinrich S., Particle dynamics in a multi-staged fluidized bed: particle transport behavior on micro-scale by discrete particle modelling, Advanced Powder Technology, 10 (2019) 2014–2031. DOI: 10.1016/j.apt.2019.05.025

Diez E., Meyer K., Bück A., Tsotsas E., Heinrich S., Influence of process conditions on the product properties in a continuous fluidized bed spray granulation process, Chemical Engineering Research and Design, 139 (2018) 104–115. DOI: 10.1016/j.cherd.2018.09.032

Fries L., Discrete particle modeling of a fluidized bed granulator (Dissertation), Cuvillier Verlag, 2012. ISBN: 9783954042456.

Hampel N.A., Diskontinuierliches und kontinuierliches Pelletcoating im Wurster-Wirbelschichtprozess (Dissertation), Otto-von-Guericke-Universität Magdeburg, 2015. http://dx.doi.org/10.25673/4340

Hoffmann T., Rieck C., Bück A., Peglow M., Tsotsas E., Influence of granule porosity during fluidized bed spray granulation, Procedia Engineering, 102 (2015) 458–467. DOI: 10.1016/j.proeng.2015.01.189

Keyence, 3D Laser Scanning Confocal Microscope VK-X250K/X260K, VK-X150K/X160K, VK-X120K/X130K: User’s Manual, 2015.

Kieckhefen P., Pietsch S., Dosta M., Heinrich S., Possibilities and limits of computational fluid dynamics-discrete element method simulations in process engineering: a review of recent advancements and future trends, Annual review of chemical and biomolecular engineering, 11 (2020) 397–422. DOI: 10.1146/annurev-chembioeng-110519-075414

Perfetti G., Van de Casteele E., Rieger B., Wildeboer W.J., Meesters G.M.H., X-ray micro tomography and image analysis as complementary methods for morphological characterization and coating thickness measurement of coated particles, Advanced Powder Technology, 21 (2010) 663–675. DOI: 10.1016/j.apt.2010.08.002

Pietsch S., Kieckhefen P., Heinrich S., Müller M., Schönherr M., Kleine Jäger F., CFD-DEM modelling of circulation frequencies and residence times in a prismatic spouted bed, Chemical Engineering Research and Design, 132 (2018) 1105–1116. DOI: 10.1016/j.cherd.2018.01.013

Rieck C., Hoffmann T., Bück A., Peglow M., Tsotsas E., Influence of drying conditions on layer porosity in fluidized bed spray granulation, Powder Technology, 272 (2015) 120–131. DOI: 10.1016/j.powtec.2014.11.019

Schmidt M., Bück A., Tsotsas E., Shell porosity in spray fluidized bed coating with suspensions, Advanced Powder Technology, 28 (2017) 2921–2928. DOI: 10.1016/j.apt.2017.08.020

Turton R., Challenges in the modeling and prediction of coating of pharmaceutical dosage forms, Powder Technology, 181 (2008) 186–194. DOI: 10.1016/j.powtec.2006.12.006

Tzika M., Alexandridou S., Kiparissides C., Evaluation of the morphological and release characteristics of coated fertilizer granules produced in a Wurster fluidized bed, Powder Technology, 132 (2003) 16–24. DOI: 10.1016/S0032-5910(02)00345-5

Uhlemann H., Mörl L., Wirbelschicht-Sprühgranulation, Springer Berlin Heidelberg, Berlin, Heidelberg, 2000, ISBN: 9783642631252. DOI: 10.1007/978-3-642-57004-9

Werner S.R.L., Jones J.R., Paterson A.H.J., Archer R.H., Pearce D.L., Air-suspension particle coating in the food industry: Part I—state of the art, Powder Technology, 171 (2007) 25–33. DOI: 10.1016/j.powtec.2006.08.014

Authors’ Short Biographies

Maike Orth

Maike Orth is a doctoral student at the Institute of Solids Process Engineering and Particle Technology at the Hamburg University of Technology. There, she obtained her M.Sc. in Process Engineering with distinction in 2019. During her Master’s studies, she spent one semester at the University of Waterloo, Canada. Her research interests include particle formulation in fluidized beds, particle characterization and CFD-DEM simulations of fluidized bed spray processes.

Paul Kieckhefen

Paul Kieckhefen is a is a doctoral student at the Institute of Solids Process Engineering and Particle Technology of the Hamburg University of Technology. There, he obtained a M.Sc. in Process Engineering with distinction in 2018. He interned at BASF in the departments of Chemical and Process Engineering in 2016 and Digitalization in Research & Development in 2017. He performed research stays in the group of Prof. Pirker at the Johannes-Kepler University in Linz, Austria. His research interests comprise efficient simulation methods that describe multiphase flows, time-scale extrapolation methods and product-property prediction approaches using multi-scale simulations.

Swantje Pietsch

Dr.-Ing. Swantje Pietsch is a senior engineer in the Institute of Solids Process Engineering and Particle Technology at Hamburg University of Technology. She obtained her PhD in 2018 on the experimental and numerical investigations of fluidization behavior and liquid injection in three-dimensional prismatic spouted beds. Her research is focused on particle formulation in fluidized beds and CFD-DEM simulations of these processes.

Stefan Heinrich

Stefan Heinrich obtained his diploma in Process Engineering and a doctoral degree at the University Magdeburg. After positions as Assistant and Junior Professor and a Habilitation, he became Full Professor at the TUHH and director of the Institute of Solids Process Engineering and Particle Technology in 2008. He is editor of Advanced Powder Technology and Particuology, chairman of the Working Party on Agglomeration and Bulk Solids Technology of VDI-ProcessNet and of the EFCE Working Party on Agglomeration. His main research interests are fluidized bed technology, mainly for drying and particle formulation, particle simulation methods as well as contact, deformation and breakage mechanics of particles. He received the DECHEMA-Prize 2015.

KONA Powder and Particle Journal No. 39 (2022) 240–250/https://doi.org/10.14356/kona.2022007 Original Research Paper

Carbonation Kinetics of Fine CaO Particles in a Sound-Assisted Fluidized Bed for Thermochemical Energy Storage[†]

Federica Raganati and Paola Ammendola *

Istituto di Scienze e Tecnologie per l'Energia e la Mobilità Sostenibili (STEMS) - CNR, Italy

Abstract

The calcium-looping process, relying on the reversible calcination/carbonation of $CaCO_3$, is one of the most promising solution to perform thermochemical energy storage (TCES) for concentrating solar power (CSP) plants. Indeed, CaO precursors such as limestone can rely on the high energy density, low cost, large availability and nontoxicity. In this work, the study of the sound-assisted carbonation of fine CaO particles (< 50 μm) for TCES-CSP has been furthered. In particular, a kinetic study has been performed to analyze the effect of the particular carbonation conditions to be used in TCES-CSP applications, i.e. involving carbonation under high CO_2 partial pressure and at high temperature. All the experimental tests have been performed in a lab-scale sound-assisted fluidized bed reactor applying high intensity acoustic field with proper frequency (150 dB–120 Hz). The carbonation kinetics has been analyzed by applying a simple kinetic model, able to properly describe the fast (under kinetic control) and slow (under diffusion control) stage of the reaction. In particular, the reaction rate, the intrinsic carbonation kinetic constant and the characteristic product layer thickness have been evaluated, also highlighting their dependence on the temperature between 800 and 845 °C; a value of 49 kJ mol^{-1} has been obtained for the activation energy. Finally, a good agreement between the conversion-time profiles, evaluated from the applied kinetic models, and the experimental data has been obtained.

Keywords: calcium looping, fine particles, Concentrating Solar Power (CSP), Thermochemical Energy Storage (TCES), sound-assisted fluidization, kinetics

1. Introduction

One of the main challenge for a short-term wider utilization of solar energy, which is characterized by an intrinsic intermittency, is represented by energy storage (Ammendola et al., 2020). In this framework, the calcium-looping (CaL), performed in fluidized bed reactors, is attracting growing research interest for thermochemical energy storage (TCES) in concentrating solar power (CSP) plants, in light of the high energy density, small costs, non-toxicity, and large availability of natural CaO precursors (Chacartegui et al., 2016; Ortiz et al., 2018). It is based on the cyclic calcination/carbonation of $CaCO_3$:

$$CaCO_3 \rightleftharpoons CaO + CO_2 \quad \Delta H^0_{\mathrm{rxn}} = 178\ \mathrm{kJmol^{-1}} \tag{1}$$

The thermodynamics of the system is strongly dependent on the CO_2 partial pressure (P_{CO_2}) (Ortiz et al., 2019), which can be evaluated as a function of the temperature (T) according to (Stanmore and Gilot, 2005):

$$P_{\mathrm{eq}} = Py_{\mathrm{eq}} = 4.137\times10^{7}\exp\left(-\frac{20474}{T}\right) \tag{2}$$

The equilibrium P_{CO_2} ($P^{\mathrm{eq}}_{CO_2}$) of the carbonation-calcination reaction, calculated according to Eq. (2), is plotted in **Fig. 1** between 650 and 1000 °C, at different inlet CO_2 molar ratio (y_{CO_2}).

It is clear from **Fig. 1** that increasing values of $P^{\mathrm{eq}}_{CO_2}$ at a constant temperature or decreasing values of the temperature at a constant $P^{\mathrm{eq}}_{CO_2}$ favors the carbonation reaction thermodynamically, i.e. thus yielding larger values of CaO carbonation conversion.

It is important to highlight that the optimal operating conditions of the CaL process and, therefore, also the CaO multicycle performance, deeply depend on the particular application (Ortiz et al., 2018). In particular, high CO_2 partial pressure and temperature (≥ 800 °C) can be used to perform carbonation in order to obtain high global efficiency for energy storage and electricity production in CSP plants (Ortiz et al., 2018). In contrast, relatively low temperature (~750 °C) and CO_2 partial pressure can be adopted to perform the calcination; this can be achieved

---

† Received 2 March 2021; Accepted 26 April 2021
J-STAGE Advance published online 26 June 2021

* Corresponding author: Paola Ammendola;
Add: Piazzale Tecchio 80, 80125 Naples, Italy
E-mail: paola.ammendola@stems.cnr.it
TEL: +39-081-7682-237 FAX: +39-081-5936-936

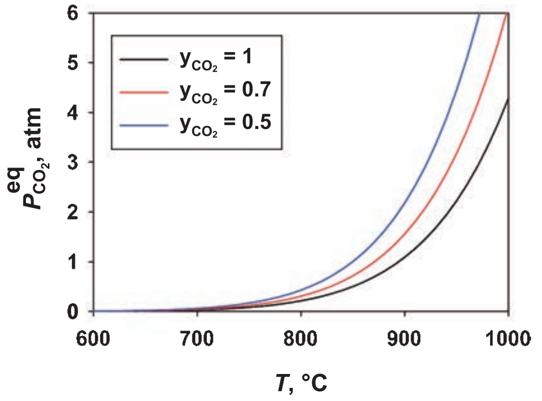

Fig. 1 Equilibrium pressure of CO_2 as function of the temperature for the CaO-$CaCO_3$ system at different inlet CO_2 molar ratio (y_{CO_2}).

using either steam or helium, namely a gas that can be easily separated from CO_2 (Karasavvas et al., 2018). As discussed by (Chacartegui et al., 2016), this reduction of the calcination temperature would allow, on the one hand, to limit the sorbent deactivation over repeated cycle (i.e. increased residual effective conversions with respect to conventional CaL for CCS), and, on the the other, to use less expensive solar receivers. Lower calcination temperatures decrease the radiative losses, thus enhancing the efficiency of the process. Clearly, if He is used for calcination the He/CO_2 gas mixture exiting from the calciner must be subjected to a separation step, which can be performed quite easily using selective membranes thanks to the different molecular size of He and CO_2. Another crucial point to take into account is the necessity to have a process with free CO_2 emissions. In this framework, a viable solution, proposed by (Chacartegui et al., 2016), is to realize the looping process according to a closed cycle scheme: the carbonator will be fed with a pure CO_2 stream with a rate remarkably larger than the stoichiometric rate needed for the carbonation reaction. Then, the CO_2 in excess exiting the carbonator will be used as heat carrier fluid in a closed Brayton cycle and finally sent to a compression stage before being stored for the subsequent cycles. Clearly, being a closed cycle entails that there is no need for a continuous feed of any fresh gas stream, which is especially important in the case of the expensive He (Chacartegui et al., 2016).

The strong reduction of the CaO carbonation conversion with cycling operations, caused by sintering and pore-plugging, is still one of the main drawbacks and open challenges in CaL (Benitez-Guerrero et al., 2018; Ortiz et al., 2019; Sarrión et al., 2018). In this context, it has been showed that the carbonation conversion can be enhanced by using fine CaO particles, thus also increasing the obtainable energy density, thanks to the maximization of the available sorbent surface (i.e. the surface which is actually in direct contact to the gaseous phase) and to the hindrance of the intrinsic loss of CaO multicyclic activity (Durán-Martín et al., 2020). However, the fluidization of fine particles is difficult; it is characterized by agglomeration, channeling and plugging (Raganati et al., 2018; Raganati and Ammendola, 2021) caused by the strong interparticle forces (Raganati et al., 2017; Seville et al., 2000). In this framework, the acoustic vibrations have been proved to promote and improve the fluidization of fine particles due to the dynamic break-up of the large particle clusters, thus also increasing the gas/solids contact efficiency (Raganati et al., 2020a, 2015). Besides this, sound waves can also promote other phenomena at the interface between the gaseous and the solid phase, such as acoustic streaming (Valverde, 2013), which also contributes to improve the mass and heat transfer rates (Raganati et al., 2020a). In fact, we demonstrated in a previous work that the carbonation performances of fine limestone particles under TCES-CSP operating conditions can be remarkably improved by the application of high intensity acoustic fields (Raganati et al., 2020a). Besides the multicycle carbonation conversion, also the carbonation kinetics is crucial for the reactor design, especially for the scale-up of thermal processes.

This work represents a further development of the above-mentioned research activity on the carbonation reaction of fine CaO particles (< 10 µm) for TCES-CSP. In particular, considering that the carbonation reaction (i.e. multicyclic CaO conversion and reaction kinetics) is remarkably affected by the operating conditions (carbonation thermodynamics and kinetics are strongly dependent on temperature and pressure), a kinetic study has been performed to point out the effect of the particular operating conditions to be applied for TCES-CSP, namely involving high CO_2 partial pressure and high temperature carbonation. A lab-scale sound-assisted fluidized bed reactor has been used to perform all the experimental tests, applying acoustic fields of proper intensity (150 dB) and frequency (120 Hz). The carbonation kinetics has been studied using a simple kinetic model, able to properly describe the fast and slow stage of the of the reaction, thus obtaining valuable data for designing and operating the carbonation reactor. In particular, the evaluation of the reaction rate, activation energy and the characteristic product layer thickness has been performed.

2. Experimental

2.1 Materials and their fluidization behavior

A limestone provided by OMYA with a Sauter diameter of 3.61 µm and density of 2.71 g cm^{-3}, namely belonging to Group C of Geldart's classification, has been used as sorbent. Further details regarding both the chemico-physical characterization and the fluid-dynamic behavior can be found elsewhere (Raganati et al., 2020a). Briefly, the limestone particles are characterized by a natural tendency to form large agglomerates (tens of microns) and by a relatively low BET specific surface area (S_0) of 1.6 $m^2 g^{-1}$, according to the typical values of natural limestones (Raganati et al., 2020a).

With reference to the fluid-dynamic behavior, as discussed by (Raganati et al., 2020a), the powder cannot be properly fluidized under ordinary conditions due to agglomeration and channeling; i.e. the pressure drops are always lower than the material weight per unit area, thus meaning that the bed is not completely fluidized, as typical of cohesive powders. More specifically, the predominance of the interparticle forces over weight and drag forces causes the individual particles to stick to each other and form agglomerates (agglomeration), which causes, in turn, a remarkable worsening of the permeability of the bed by the fluidizing gas (channeling and plugging). In contrast to this, the application of the acoustic perturbation makes it possible to remarkably enhance the fluidization quality; indeed, a regular pressure drop curve has been obtained. This improvement of the fluidization behavior is due to the fact that the propagation of the sound wave inside the bed causes a continuous break-up of the large particle agglomerates into smaller fluidizable structures. More specifically, the internal cohesive forces are counteracted by the external drag and inertial forces generated by the acoustic perturbation. In particular, according to the cluster/sub-cluster oscillators model discussed by (Raganati et al., 2017), the clusters break-up into smaller sub-clusters at the contact points between them, namely where the collision energy generated by the sound wave overcome the cohesive interparticle force. In line with these theoretical considerations, it has been obtained that under sound assisted conditions the fine limestone particles can be properly fluidized as agglomerates which are interested by a dynamic break-up and re-aggregation mechanism. In particular, the fluidizing agglomerate size (30–80 μm), i.e. the real size of the fluidizing structures, is always bigger than the nominal size of the powder (3.61 μm, the Sauter diameter obtained from the granulometric analysis), regardless of the applied acoustic parameters.

With reference to the effect of the sound parameters, it has been found that increasing the SPL (sound pressure level) value from 120 to 150 dB has a beneficial effect on the fluidization quality, thus meaning that acoustic field with higher intensity should be employed to maximize the fluidization quality. Indeed, both the fluidizing aggregate size and the minimum fluidization velocity are always decreased by passing from 120 to 150 dB. This is due to the enhancement of the energy introduced inside the bed when the SPL is increased, which implies that the break-up mechanism becomes more and more efficient. Indeed, when the SPL is increased from 120 to 150 dB, the size of the fluidizing agglomerates is reduced, thus resulting in the decrease of the minimum fluidization velocity. Sound frequency, on the contrary, has been found to have a non-monotonic effect on the fluidization quality. Indeed, both the fluidizing aggregate size and the minimum fluidization velocity are characterized by a nonlinear relationship with the sound frequency, i.e. an optimum value of frequency equal to 120 Hz can be observed. This behavior has been explained considering that the frequency directly affects the relative motion between clusters and sub-clusters, which, in turn, promotes the break-up and re-aggregation mechanism. In particular, for too high values of frequency, the propagation of the acoustic wave through the bed of particles is poor due to the increased sound absorption coefficient, which is proportional to the square of sound frequency. Hence, for a sound source positioned at the top of the fluidization column, the upper part of the bed absorbs most of the acoustic energy and only a very attenuated sound wave manages to reach the bottom part of the bed. Consequently, the disruption of the large agglomerates present at the bottom of the bed is very weak, thus causing a reduction of the fluidization quality, i.e. an increase of the minimum fluidization velocity. Contrarily, for too small sound frequencies, there is no relative motion between larger agglomerates and smaller sub-agglomerates, which also leads to a weak break-up mechanism and poor fluidization quality.

Finally, also the effect of the temperature on the fluidization behavior has been analyzed by (Raganati et al., 2020a) performing test at different temperatures (25–850 °C), pointing out that increased fluidization difficulty is encountered as the temperature is increased. This result has been explained referring to the fact that interparticle forces are intensified at higher temperatures. Then, as more and more particles tend to adhere to one another, larger fluidizing agglomerates (passing from 30 to 80 μm when temperature is increased from 25 to 850 °C) result from the intensification of the interparticle forces. Consequently, the minimum fluidization velocity is also increased when temperature is increased from 25 to 850 °C, as a result of the increased fluidizing agglomerates size.

2.2 Experimental apparatus and procedure

In this work, sound-assisted (150 dB–120 Hz) fluidization tests have been performed to experimentally study the kinetics of the carbonation reaction of fine natural CaO particles at operating conditions relevant in the CaL-CSP integration for TCES. Optimal parameters of the acoustic field, i.e. those providing the best fluidization quality, have been chosen according to the results obtained from the fluid-dynamic characterization of the limestone (Raganati et al., 2020a), briefly summarized in the **Section 2.1**.

All the experimental tests have been performed in a lab-scale sound-assisted fluidized bed (40 mm ID) at atmospheric pressure. Further details regarding the sound-generation system have been reported in previous works

(Raganati et al., 2020a). The gas feed has been prepared using N_2 and CO_2 cylinders (99.995 % vol.); two mass flow controllers (Brooks 8550S) have been used to set/control the inlet flowrates. A heating jacket (Tyco Thermal Controls GmbH) has been used to heat the column up to the desired temperature. The temperature of the reactor is monitored and controlled by means of a type K thermocouple linked to a PID controller. The outlet CO_2 concentration is continuously monitored by means of an analyzer provided with an infrared detector (ABB AO2020, URAS 14) (Raganati et al., 2020b). Before the carbonation tests, a pre-treatment of the limestone particles was performed; in order to obtain pure CaO, the $CaCO_3$ sample (100 g) is calcined ($T = 900$ °C) under sound-assisted fluidization conditions (150 dB–120 Hz) for 2 h and using N_2 as fluidizing gas (115 NL/h, corresponding to a superficial gas velocity of 2.5 cm/s, i.e. about five times the minimum fluidization velocity of the sorbent material (Raganati et al., 2020a)). On the basis of the fluid-dynamic characterization, optimal parameters (intensity and frequency) of the acoustic perturbation have been selected (Raganati et al., 2020a). Then, the sample is carbonated under sound-assisted fluidization conditions (150 dB–120 Hz) using CO_2 (70 vol% CO_2 in N_2) as inlet gas flowrate (115 NL/h) and at different temperatures (800 °C, 815 °C, 830 °C, 845 °C and 860 °C) until the sorbent is completely saturated. The CaO conversion (X) has been calculated from the amount of CO_2 reacted with CaO, which, in turn, has been evaluated from the measured outlet CO_2 concentration profiles (Raganati et al., 2020a).

3. Carbonation kinetics

The carbonation involves the reaction of a solid reactant (CaO) with a gaseous reactant (CO_2) to produce another solid ($CaCO_3$) (Khawam and Flanagan, 2006).

In particular, the carbonation reaction takes place in two stages with two different kinetic regimes (Raganati et al., 2020a). At the beginning, the carbonation occurs fast under the control of by the kinetics of the chemical reaction between the CO_2 molecules and the CaO (Stage A) (Raganati et al., 2020a). After this initial kinetically-controlled period, the free sorbent particle surface is covered by a thin layer of carbonate; therefore, the diffusion of CO_2 molecules through this solid layer starts to control the reaction (stage B) (Raganati et al., 2020a). In this context, the product layer thickness is a very important factor to analyze the shift from the fast to the slow reaction stages (Alvarez and Abanades, 2005).

The reaction rate is evaluated as the time evolution of the conversion degree, *X(t)*, which can assume characteristic shapes (Li Z. et al., 2012). Then, the kinetic analysis aims to examine these shapes and explain them by means of physical fundamental mechanisms (Khawam and Flanagan, 2006).

The reaction rate ($\mathrm{d}X/\mathrm{d}t$) can be written as:

$$\frac{\mathrm{d}X}{\mathrm{d}t} = r(T)\,f(X) \tag{3}$$

where $r(T)$ (min^{-1}) is the temperature-dependent reaction rate and $f(X)$ is the reaction model describing the reaction mechanism. By integrating Eq. (3), the integral form of the kinetic model $g(X)$ can be obtained:

$$g(X) = \int_0^t \frac{\mathrm{d}X(t)}{f(X)} \tag{4}$$

After the time evolution of the carbonation degree has been evaluated experimentally, the reaction kinetics can be analyzed by selecting the most appropriate apparent kinetic model to fit the experimental data (Ashraf and Olek, 2018; Khawam and Flanagan, 2006).

The most important feature of these models is that they lump together all the mass transfer resistances, such as external diffusion, diffusion in the pores, and surface reaction (Khawam and Flanagan, 2006; Sun J. et al., 2008). Then, the selected kinetic model is used to experimental data in order to calculate an apparent global kinetic rate (Ammendola et al., 2021; Khawam and Flanagan, 2006; Sun J. et al., 2008). By definition, an apparent kinetic rate is different from the intrinsic reaction rate, which will be dependent on a number of experimental variables and/or sorbent morphological features (Goodbrake et al., 1979; Khawam and Flanagan, 2006; Sun J. et al., 2008). Clearly, the use of apparent kinetic models holds the advantage to be more simple, i.e. all the reaction steps can be accounted in one expression (Salaudeen et al., 2018). However, these models are scale-dependent due to the influence of transport phenomena (Khawam and Flanagan, 2006; Sun J. et al., 2008).

So far, several apparent models have been developed for the carbonation reaction, based on different mechanistic assumptions (Fedunik-Hofman et al., 2019a). In this framework, Lee (Lee, 2004) proposed a model equation for the apparent kinetics of the CaO carbonation in differential and integral form:

$$\frac{\mathrm{d}X}{\mathrm{d}t} = r\left(1 - \frac{X}{X_\mathrm{u}}\right)^2 \tag{5}$$

$$X(t) = \frac{X_\mathrm{u} t}{(X_\mathrm{u}/r) + t} \tag{6}$$

where r (min^{-1}) is the apparent reaction rate and X_u is the ultimate CaO carbonation conversion; with the time evolution of the carbonation reaction, the reaction becomes slower since the carbonate product layer starts to form, thus hampering the access of CO_2 molecules to the residual CaO and leading to values of ultimate conversions

< 100 %. Then, the reaction rates of the two carbonation stages (stage A and B), r_A and r_B, can be determined by data fitting, using the linear form of Eq. (6):

$$\frac{1}{X} = \frac{1}{r}\left(\frac{1}{t}\right) + \frac{1}{X_u} \tag{7}$$

In particular, a bi-linear plot will be obtained, i.e. two lines with different slopes depending on whether the reaction is either under kinetic control (stag A) or under diffusion control (stage B). Then, r_A and r_B are evaluated from the slope of the plot, whereas, the ultimate conversion at the end of stage A and B, X_{uA} and X_{uB}, can be calculated from the intercept of the plot (Lee, 2004). Since the carbonation reaction may be incomplete, the extent of conversion, α, is also used; it is evaluated as X/X_u.

The coefficient of correlation, R^2, assuming values between 0 to 1, and the sum of squares errors function (SSE) (Foo and Hameed, 2010), where the lower the SEE value the better the fitting quality is, have been calculated to assess the fitting quality of the kinetic model to the experimental data. In particular, SSE can be calculated according to:

$$\text{SSE} = \sum_{i=1}^{i=n}\left(X_{\text{mod}_i} - X_{\text{exp}_i}\right)^2 \tag{8}$$

where X_{exp} and X_{mod} are the experimental and modeled carbonation conversion degree, respectively, and n is the number of experimental points.

According to several works available in the literature (Alvarez and Abanades, 2005; Biasin et al., 2015; Criado et al., 2018; Li Z. et al., 2012a,b), the conversion, X_{uA}, at which the reaction shifts from stage A (i.e. kinetic control) to stage B (diffusion control) is also linked to the thickness of product layer. Hence, the effect of the temperature on X_{uA} has been linked to the variation of the product layer thickness with the carbonation temperature. In fact, X_{uA} represents the value of the CaO conversion degree specifically corresponding to the critical product layer thickness (Alvarez and Abanades, 2005). As discussed in (Alvarez and Abanades, 2005), knowing the value of X_{uA}, the product layer thickness at the end of stage A, h, can be evaluated as:

$$h = \frac{X_{uA}}{S_0}\frac{V^{M}_{CaCO_3}}{M_{CaO}} \tag{9}$$

where M_{CaO} is the molecular weight of CaO, $V^{M}_{CaCO_3}$ is the molar volume of $CaCO_3$ and S_0 is the CaO specific surface area.

As proposed by in (Sun P. et al., 2008), the grain model has been used to calculate the intrinsic reaction rate constant (k_s), which is an intrinsic feature of the material, of the carbonation reaction in the stage A (i.e. the kinetically-controlled period). The main assumptions of this model are: i) the diffusion resistance can be neglected at the beginning of the reaction (stage A) whereas the reaction is large; therefore, reaction is under kinetic control (Sun P. et al., 2008); ii) the reaction rate, r_A, evaluated from the slope of the linear plot, as discussed above, is extended to represent the true rate at the zero conversion point (i.e. $r_A = r_0$) (Sun P. et al., 2008).

The reaction rate at the beginning can be written in power law as (Sun P. et al., 2008):

$$\left.\frac{dX}{dt}\right|_{t=0} = 3r_A = M_{CaO}k_s\left(P_{CO_2} - P^{eq}_{CO_2}\right)^n S_0 \tag{10}$$

where $\left(P_{CO_2} - P^{eq}_{CO_2}\right)$ is the reaction thermodynamic driving force, n is the reaction order and k_s is the intrinsic chemical reaction rate constant. k_s can be calculated using the Arrhenius equation:

$$k_s = k_0 \exp\left(-E/RT\right) \tag{11}$$

being E the activation energy and k_0 the pre-exponential factor.

According to Sun P. et al. (2008), the reaction is zero-order ($n = 0$) for $\left(P_{CO_2} - P^{eq}_{CO_2}\right) > 10$ kPa. Considering that P_{CO_2} of 0.7 atm has been used for all the tests performed in this work, the assumption that the reaction order is zero is always valid. Then, considering Eq. (11), Eq. (10) can be re-written in logarithmic form as:

$$\ln(r_1) = \ln(M_{CaO}k_0S_0/3) - E/RT \tag{12}$$

Hence, fitting Eq. (12) with the values of r_A, obtained at the different investigated temperatures, E and k_0 can be calculated.

4. Results and discussions

The results obtained in terms of time evolution of CaO carbonation conversion at different temperatures are reported in **Fig. 2**.

Clearly, the CaO carbonation rate varies with the evolution of the conversion degree, i.e. the reaction is kinetically-controlled at very small conversion values (stage A), whereas it is diffusion-controlled at larger conversion values (stage B). In particular, the reaction proceeds relatively fast at low levels of conversion degree, with the temperature strongly affecting the initial rates. After this initial stage, with the carbonation reaction going on and the conversion increasing and becoming closer to the ultimate conversion value, X_u, at which no more significant conversion is obtained at each temperature, the carbonation rate gets close to zero. More specifically, the dense product layer forming on the pore wall hinders the diffusion of the CO_2 molecules through it and, therefore, the reaction continues to take place under diffusion control.

The tight link between the carbonation rate and the temperature has been more evidently highlighted plotting the extent of carbonation (α) (**Fig. 1(b)**), i.e. removing the effect of X_u which is itself temperature dependent.

Fig. 3 shows the plots of the experimental values of $1/X$ vs $1/t$ for the different temperatures. Then, the apparent reaction rates (r_A and r_B) and the ultimate conversion (X_{uA} and X_{uB}) have been evaluated (**Fig. 3**) from the slope and intercept of the two linear segments of the plot. In particular, X_{uA} and X_{uB} have been calculated as the values of carbonation conversion corresponding to the change of the slope and for $1/t$ tending to 0, respectively. It is clear that the experimental data reported in **Fig. 3** follow a bi-linear pattern. The two different linear segments of the plots confirm the existence of stage A and stage B of the carbonation reaction, occurring under two different rate-controls (i.e. kinetic and diffusive controls).

As regards the fast kinetically controlled stage (stage A), it is evident, from the analysis of **Fig. 4(a)**, that that the reaction rate does not monotonically increase with increasing temperatures. Indeed, increasing the temperature from 800 to 850 °C, r_A, i.e. the rate of the fast carbonation stage, is increased according to the reaction kinetics being typically favored by increasing values of temperature. However, for temperature larger than 850 °C the carbonation rate

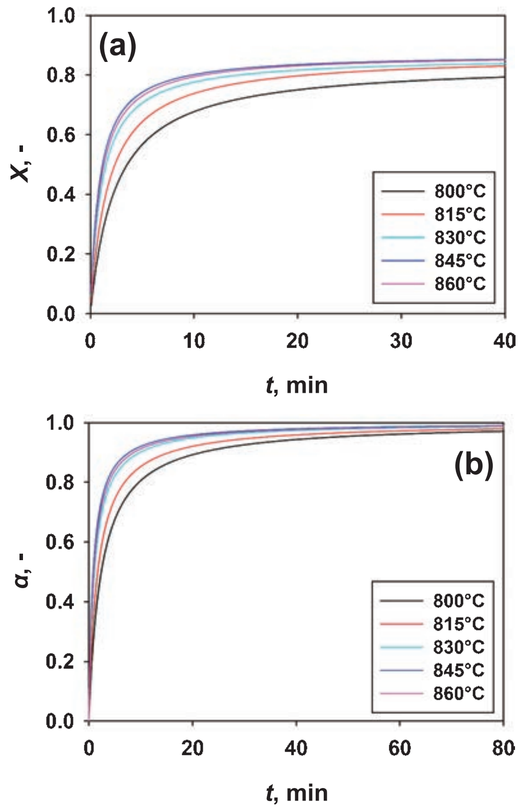

Fig. 2 Time evolution of the conversion degree (X) **(a)** and carbonation extent (α) **(b)** experimentally measured at different temperatures.

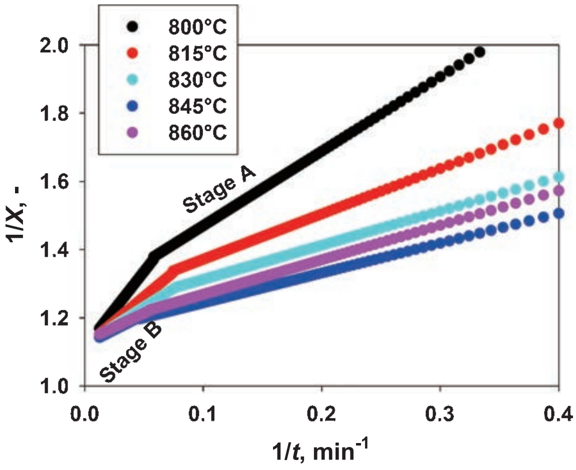

Fig. 3 Plot of $1/X$ versus $1/t$ for the experimental carbonation conversion data.

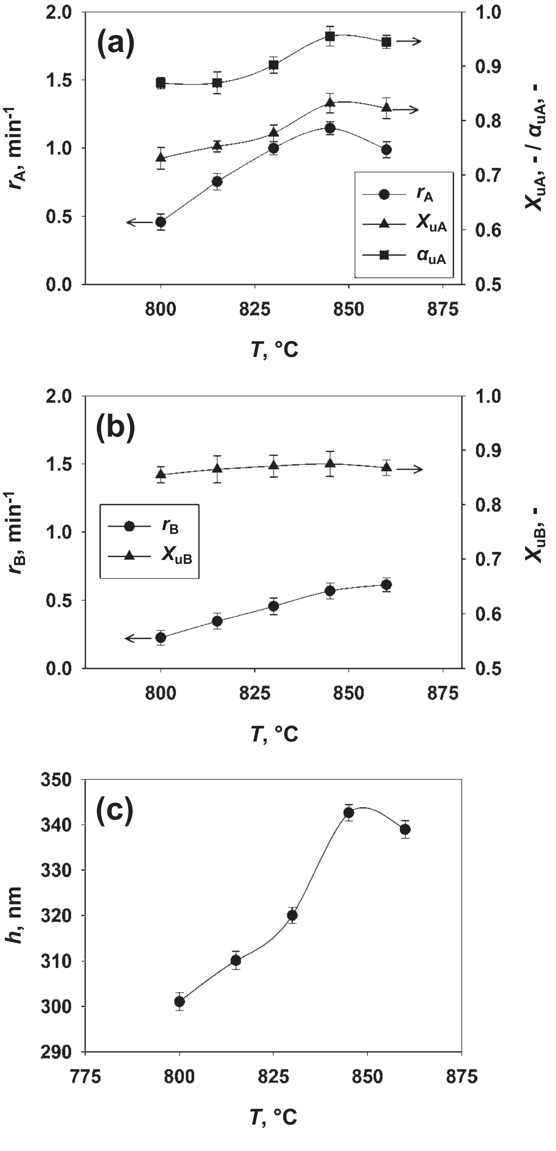

Fig. 4 Apparent kinetic rates (r), ultimate carbonation conversion degree (X_u) and carbonation extent (α_u) of the stage A **(a)** and stage B **(b)** of the carbonation reaction and thickness (h) of the $CaCO_3$ product layer (h) **(c)** as functions of the temperature.

decreases.

Therefore, r_A reaches a maximum value at a certain temperature (845 °C); above this temperature, i.e. approaching the equilibrium temperature (870 °C), it gradually decreases. In accordance to thermodynamic principles and as clearly shown **Fig. 1**, the carbonation reaction occurs, at a certain temperature, for values of P_{CO_2} larger than $P_{CO_2}^{eq}$. In particular, at a fixed CO_2 partial pressure, $P_{CO_2}^{eq}$ increases when the temperature is increased (Eq. (2)), thus leading to a decrease of $\left(P_{CO_2} - P_{CO_2}^{eq}\right)$, i.e. the thermodynamic pressure driving force; therefore, as typical of exothermic reactions, the carbonation reaction has the tendency to become thermodynamically unfavored with increasing temperatures (Fedunik-Hofman et al., 2019b; Sedghkerdar et al., 2015; Sun P. et al., 2008; Yin et al., 2014). In other words, increasing the temperature at fixed P_{CO_2}, the reverse reaction (calcination) tends to be favored thermodynamically as the equilibrium temperature is approached (870 °C) (Fedunik-Hofman et al., 2019b; Sedghkerdar et al., 2015; Sun P. et al., 2008; Yin et al., 2014).

This experimental evidence agrees with the data reported in (Ortiz et al., 2018) and (Kyaw et al., 1998) for the $CaO/CaCO_3$ system when operated at the high temperatures useful for TCES, i.e. near equilibrium conditions. Clearly, the evidence that, at TCES-CSP operating conditions, the fast carbonation rate does not show a monotonic increasing trend when the temperature is increased is very important.

In particular, the temperature (845 °C) at which the reaction rate can be maximized is a key point for real applications. Indeed, it must be considered that the selection of the plant operating temperatures needs to be the result of a compromise between the kinetic and thermodynamic requirements. On the one hand, working at higher carbonation temperatures will enhance the power generation efficiency, in line with the second law of thermodynamics (Ortiz et al., 2018). But, on the other hand, working at temperatures approaching the thermodynamic equilibrium will eventually hinder the carbonation kinetics.

Also regarding stage A, of the carbonation reaction (namely the kinetics-controlled stage), it can be inferred from the corresponding linear segment of the plot (**Fig. 3**) that the ranges of data characterized by a linear correlation become narrower and narrower as the temperature is decreased from 845 °C (i.e. before the trend inversion caused by the thermodynamic equilibrium approach) to 800 °C. On the contrary, at lower values of temperature, the rate of the fast carbonation stage depends more on the diffusion limitation, thus moving away from the kinetic control even at lower values of carbonation conversion (**Fig. 3**). In fact, the carbonation reaction occurs mostly under kinetic control, i.e. almost up to the ultimate conversion (X_{uB}), as the temperature is increased up to 845 °C, with less effect of the diffusion-controlled stage. This is also clearly inferable from **Fig. 4(a)**, showing that the carbonation conversion achievable at the end of the kinetic-controlled stage (X_{uA}), namely when the CaO conversion levels start to move away from the kinetic control, increases when the temperature is increased up to 845 °C. In contrast, X_{uA} decreases with a further increase of the temperature. This agrees with the increase of the reaction rate when the temperature is increased up to 845 °C and with its decrease for larger values of the temperature. This same trend is also obtained for the extent of carbonation, α, which means that increasing the temperature up to 845 °C leads to an increase of the fraction of lime reacted in the fast kinetic-controlled stage, i.e. the fast carbonation stage provides a larger contribution to the global carbonation conversion.

The obtained non-linear dependence of r_a on the temperature has been also linked to the critical product layer thickness, i.e. the values of product layer thickness at the end of stage A (Alvarez and Abanades, 2005), being maximum at 1000 °C (**Fig. 4(c)**). Evidently, the product layer thickness increases (from 301 to 342 nm) when the carbonation temperature is increased from 800 to 850 °C, namely for temperatures sufficiently away from the equilibrium temperature (i.e. before the inversion of the reaction rate caused by the thermodynamic limitations (Sun P. et al., 2008)). This result agrees with previous works available for the $CaO/CaCO_3$ system even under different operation conditions (Abanades and Alvarez, 2003; Alvarez and Abanades, 2005; Biasin et al., 2015; Criado et al., 2018; Li Z. et al., 2012a,b; Mess et al., 1999). The explanation of this result can be found in a mechanistic kinetic study recently performed by Alvarez and Abanades (2005). The effect of the reaction temperature on the carbonation reaction has been studied through images of the CaO and $CaCO_3$ surfaces reacting with CO_2, obtained using atomic force microscopy. It was pointed out that larger product islands formed at higher carbonation temperatures, as a result of the diffusion of product molecules or ions becoming faster at higher temperatures (Alvarez and Abanades, 2005). Therefore, a bigger product layer tends to form at higher temperatures, thus enhancing the CO_2 carrying capacity of CaO (Alvarez and Abanades, 2005).

As regards the slow carbonation stage, a monotonic increase with increasing temperatures has been observed (**Fig. 4(b)**), in agreement with the diffusion of CO_2 molecules within the carbonate layer becoming more efficient at higher temperatures. It can also be inferred, from the analysis of **Fig. 4(b),** that, as the temperature is increased up to 845 °C, the carbonation reaction achieves greater conversion levels, even though, according to the thermodynamic principles, the carbonation reaction should be favored, thus resulting in greater conversion levels at lower temperatures. In fact, according to thermodynamics, higher final conversion should be achieved at lower temperatures. This is due to the exothermicity of the carbonation reaction and is in agreement with the fact that the thermodynamic driving force of the carbonation reaction $\left(P_{\mathrm{CO_2}} - P_{\mathrm{CO_2}}^{\mathrm{eq}}\right)$ is reduced as the temperature gets close to the equilibrium temperature. However, even though in contrast to thermodynamic predictions, this result, which agrees with results previously reported on CaO carbonation (Bhatia and Perlmutter, 1983), is due to the enhancement of CO_2 diffusion through the carbonate product layer at higher temperatures (Rouchon et al., 2013). On the contrary, at lower temperatures the diffusion becomes slower, thus hindering the achievement of larger ultimate conversions within reasonable time frames (Rouchon et al., 2013). Clearly, an excessive increase of temperature eventually ends up in decreasing the final conversion degree as the thermodynamic limitations outbalance the enhanced CO_2 diffusional mobility.

Then, values of the rates obtained in the chemical reaction control regime (r_A) have been used to evaluate the intrinsic rate constant (k_s) and its temperature dependence between 800 and 850 °C, namely before the reaction rate is inverted due to thermodynamic limitations (Sun P. et al., 2008). In particular, the activation energy of the reaction, E, and the pre-exponential factor, k_0, have been calculated (**Fig. 5**), thus obtaining the dependence of the intrinsic rate constant, k_s, on the temperature in the temperature range of 800–850 °C:

$$k_{\mathrm{s}} = 3.56 \times 10^{-2} \exp\left(-49.19 / RT\right) \tag{13}$$

The obtained activation energy ($E = 49.19\ \mathrm{kJ\ mol^{-1}}$) for the carbonation reaction of the fine CaO is in line with data reported in the literature (Lee, 2004; Salaudeen et al., 2018).

Using the kinetic parameters obtained in the two carbonation reaction stages, the time evolution of the carbonation conversion has been evaluated, thus validating the results obtained from the kinetic analysis. In particular, the plots obtained applying the model equation, using the kinetic constants obtained in the stage A and B of the reaction, are shown in **Fig. 6** in comparison with the experimental curves. Clearly, using the kinetic parameters obtained in the chemical reaction controlled regime makes it possible to fairly predict the initial stage of conversion, whereas, using the kinetic parameters obtained in the diffusion controlled regime makes it possible to predict well the last stage of conversion.

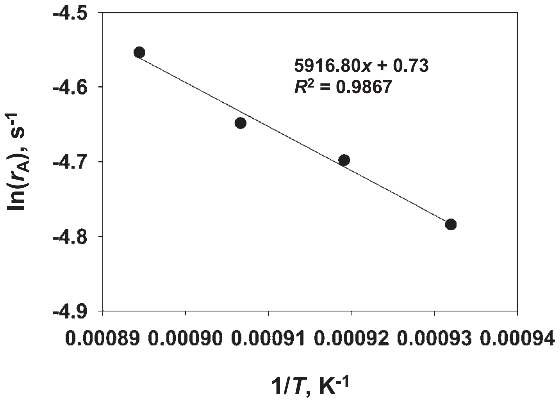

Fig. 5 ln (r_A) *vs* $1/T$ (Eq. (12)) for the carbonation reaction.

Therefore, there is not a unique kinetic constant able to properly describe the entire carbonation reaction, i.e. over the entire time frame. Indeed, there is always a period of time in which the carbonation reaction is influenced by both the chemical reaction between the CO_2 molecules and the CaO surface and by the diffusion of CO_2 through the solid layer. Considering that the proposed model can separately describe the two stages of the carbonation reaction with a rather good accuracy (i.e. the experimental data of the stage A and stage B agree well with the predicted values), the combination of the two different predictions, i.e. using the parameters separately obtained in the two control regimes, makes it possible to fairly describe the carbonation reaction in the entire time frame.

5. Conclusions

The carbonation kinetics of fine CaO particles (< 10 μm) has been investigated for TCES-CSP at realistic operating conditions, namely at high CO_2 partial pressure and temperature (800–845 °C). Tests have been performed in a lab-scale sound-assisted fluidized bed and the carbonation kinetics has been analyzed using a simple apparent kinetic model. Then, the reaction rate, activation energy and the characteristic product layer thickness have been evaluated.

The main conclusions and observations derived from the kinetic study are:

- At operating conditions functional for TCES-CSP applications, the rate of the fast carbonation reaction does not monotonically increase with the temperature. Indeed, the reaction rate reaches a maximum at 845 °C; above this temperature, i.e. approaching the equilibrium temperature, it gradually decreases.
- X_{uA}, i.e. the carbonation conversion at the end of the stage A, also increases when the temperature is increased up to 845 °C; on the contrary, it decreases when the temperature is increased further, in line with the trend observed for the reaction rate. This has been also related to the critical carbonate product layer, h, at the end of stage A, which also increases (from 301 to 342 nm) when the temperature is increased up to 845 °C.
- The rate of the slow carbonation reaction monotonically increases with increasing temperatures, due to the enhancement of the diffusion of CO_2 molecules within the carbonate layer at higher temperatures.
- As the temperature is increased from 800 up to 845 °C, the carbonation reaction achieves higher ultimate

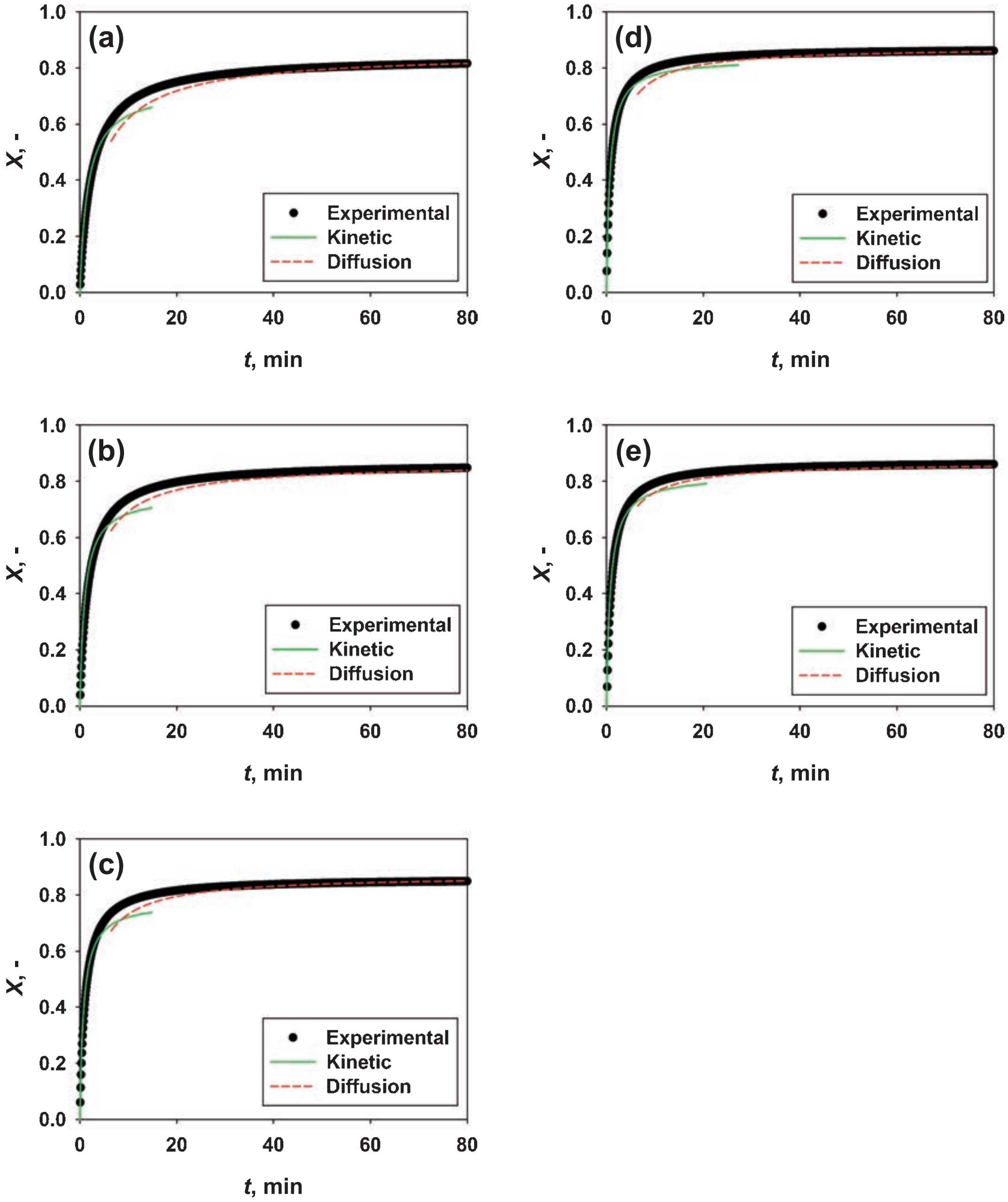

Fig. 6 Comparison between the experimental and theoretical values of *X* predicted using the kinetic parameters obtained in the kinetic (stage A) and diffusion (stage B) rate control regimes. Carbonation temperature: **(a)** 800, **(b)** 815, **(c)** 830, **(d)** 845, **(e)** 860 °C.

conversion levels, in contrast to thermodynamics predicting greater conversion levels at lower temperatures. On the contrary, the final conversion degree is decreased for temperatures larger than 845 °C due to the fact that the thermodynamic limitations outbalance the enhanced CO_2 diffusional mobility.

- The intrinsic carbonation kinetic constant and its temperature dependence have been also evaluated between 800 and 845 °C; a value of 49 kJ mol^{-1} has been obtained for the activation energy.

The proposed model can separately describe the two stages of the carbonation reaction; therefore, the carbonation reaction can be fairly described in the entire time frame combining the two different predictions, i.e. using the parameters separately obtained in the two controlling regimes.

Acknowledgements

This work has been done in the framework of the project SOCRATCES, which has received funding from European Union's Horizon 2020 research and innovation programme under the Grant Agreement no.727348.

Nomenclature

E	activation energy of the intrinsic kinetic rate of the fast carbonation reaction
$f(X)$	reaction kinetic model
$g(X)$	integral form of the reaction kinetic model
h	thickness of the $CaCO_3$ product layer at the transition between the fast and slow reaction periods
k_0	pre-exponential factor of the intrinsic kinetic rate of the fast carbonation reaction
M_{CaO}	molecular weight of CaO
P_{CO_2}	CO_2 partial pressure
$P_{CO_2}^{eq}$	equilibrium CO_2 partial pressure
S_0	CaO specific surface per unit mass
t	time
r_A	apparent reaction rate of stage A (min^{-1})
r_B	apparent reaction rate of stage B (min^{-1})
X	carbonation conversion degree (–)
X_{uA}	ultimate carbonation conversion degree at the end of stage A (–)
X_{uA}	ultimate carbonation conversion degree at the end of stage B (–)
$V_{CaCO_3}^{M}$	$CaCO_3$ molar volume

Greek letters

α	extent of carbonation conversion (–)

References

Abanades J.C., Alvarez D., Conversion limits in the reaction of CO_2 with lime, Energy & Fuels, 17 (2003) 308–315. DOI: 10.1021/ef020152a

Alvarez D., Abanades J.C., Determination of the critical product layer thickness in the reaction of CaO with CO_2, Industrial & Engineering Chemistry Research, 44 (2005) 5608–5615.

Ammendola P., Raganati F., Landi E., Natali Murri A., Miccio F., Kinetics of the carbonation reaction of an SrO-Al_2O_3 composite for thermochemical energy storage, Chemical Engineering Journal, 420 (2021) 129618. DOI: 10.1016/j.cej.2021.129618

Ammendola P., Raganati F., Miccio F., Murri A.N., Landi E., Insights into utilization of strontium carbonate for thermochemical energy storage, Renewable Energy, 157 (2020) 769–781. DOI: 10.1016/j.renene.2020.05.048

Ashraf W., Olek J., Carbonation activated binders from pure calcium silicates: reaction kinetics and performance controlling factors, Cement and Concrete Composites, 93 (2018) 85–98. DOI: 10.1016/j.cemconcomp.2018.07.004

Benitez-Guerrero M., Valverde J.M., Sanchez-Jimenez P.E., Perejon A., Perez-Maqueda L.A., Calcium-looping performance of mechanically modified Al_2O_3-CaO composites for energy storage and CO_2 capture, Chemical Engineering Journal, 334 (2018) 2343–2355. DOI: 10.1016/j.cej.2017.11.183

Bhatia S.K., Perlmutter D.D., Effect of the product layer on the kinetics of the CO_2-lime reaction, AIChE Journal, 29 (1983) 79–86. DOI: 10.1002/aic.690290111

Biasin A., Segre C.U., Strumendo M., $CaCO_3$ crystallite evolution during CaO carbonation: critical crystallite size and rate constant measurement by in-situ synchrotron radiation X-ray powder diffraction, Crystal Growth and Design, 15 (2015) 5188–5201. DOI: 10.1021/acs.cgd.5b00563

Chacartegui R., Alovisio A., Ortiz C., Valverde J.M., Verda V., Becerra J.A., Thermochemical energy storage of concentrated solar power by integration of the calcium looping process and a CO_2 power cycle, Applied Energy, 173 (2016) 589–605. DOI: 10.1016/j.apenergy.2016.04.053

Criado Y.A., Arias B., Abanades J.C., Effect of the carbonation temperature on the CO_2 carrying capacity of CaO, Industrial and Engineering Chemistry Research, 57 (2018) 12595–12599. DOI: 10.1021/acs.iecr.8b02111

Durán-Martín J.D., Sánchez Jimenez P.E., Valverde J.M., Perejón A., Arcenegui-Troya J., García Triñanes P., Pérez Maqueda L.A., Role of particle size on the multicycle calcium looping activity of limestone for thermochemical energy storage, Journal of Advanced Research, 22 (2020) 67–76. DOI: 10.1016/j.jare.2019.10.008

Fedunik-Hofman L., Bayon A., Donne S.W., Kinetics of solid-gas reactions and their application to carbonate looping systems, Energies, 12 (2019a) 2981. DOI: 10.3390/en12152981

Fedunik-Hofman L., Bayon A., Donne S.W., Comparative kinetic analysis of $CaCO_3$/CaO reaction system for energy storage and carbon capture, Applied Sciences (Switzerland), 9 (2019b) 5–9. DOI: 10.3390/app9214601

Foo K.Y., Hameed B.H., Insights into the modeling of adsorption isotherm systems, Chemical Engineering Journal, 156 (2010) 2–10. DOI: 10.1016/j.cej.2009.09.013

Goodbrake C.J., Young J.F., Berger R.L., Reaction of beta-dicalcium silicate and tricalcium silicate with carbon dioxide and water vapor, Journal of the American Ceramic Society, 62 (1979) 168–171. DOI: 10.1111/j.1151-2916.1979.tb19046.x

Karasavvas E., Panopoulos K.D., Papadopoulou S., Voutetakis S., Design of an integrated CSP-calcium looping for uninterrupted power production through energy storage, Chemical Engineering Transactions, 70 (2018) 2131–2136. DOI: 10.3303/CET1870356

Khawam A., Flanagan D.R., Solid-state kinetic models: basics and mathematical fundamentals, Journal of Physical Chemistry B, 110 (2006) 17315–17328. DOI: 10.1021/jp062746a

Kyaw K., Kubota M., Watanabe F., Matsuda H., Hasatani M., Study of carbonation of CaO for high temperature thermal energy storage, Journal of Chemical Engineering of Japan, 31 (1998) 281–284. DOI: 10.1252/jcej.31.281

Lee D., An apparent kinetic model for the carbonation of calcium oxide by carbon dioxide, Chemical Engineering Journal, 100 (2004) 71–77. DOI: 10.1016/j.cej.2003.12.003

Li Z., Fang F., Tang X., Cai N., Effect of temperature on the carbonation reaction of CaO with CO_2, Energy & Fuels, 26 (2012a) 2473–2482. DOI: 10.1021/ef201543n

Li Z., Sun H., Cai N., Rate equation theory for the carbonation reaction of CaO with CO_2, Energy and Fuels, 26 (2012b) 4607–4616. DOI: 10.1021/ef300607z

Mess D., Sarofim A.F., Longwell J.P., Product layer diffusion during the reaction of calcium oxide with carbon dioxide, Energy and Fuels, 13 (1999) 999–1005. DOI: 10.1021/ef980266f

Ortiz C., Valverde J.M., Chacartegui R., Perez-Maqueda L.A., Carbonation of limestone derived CaO for thermochemical energy storage: from kinetics to process integration in concentrating solar plants, ACS Sustainable Chemistry & Engineering, 6 (2018) 6404–6417. DOI: 10.1021/acssuschemeng.8b00199

Ortiz C., Valverde J.M., Chacartegui R., Perez-Maqueda L.A., Giménez P., The calcium-looping ($CaCO_3$/CaO) process for thermochemical energy storage in concentrating solar power plants, Renewable and Sustainable Energy Reviews, 113 (2019) 109252. DOI: 10.1016/j.rser.2019.109252

Raganati F., Ammendola P., Sound-assisted fluidization for temperature swing adsorption and calcium looping: a review, Materials, 14 (2021) 672. DOI: 10.3390/ma14030672

Raganati F., Ammendola P., Chirone R., Role of acoustic fields in promoting the gas-solid contact in a fluidized bed of fine particles, KONA Powder and Particle Journal, 32 (2015) 23–40. DOI: 10.14356/kona.2015006

Raganati F., Chirone R., Ammendola P., Effect of temperature on fluidization of Geldart's group A and C powders: role of interparticle forces, Industrial & Engineering Chemistry Research, 56 (2017) 12811–12821. DOI: 10.1021/acs.iecr.7b03270

Raganati F., Chirone R., Ammendola P., Gas–solid fluidization of cohesive powders, Chemical Engineering Research and Design, 133 (2018) 347–387. DOI: 10.1016/j.cherd.2018.03.034

Raganati F., Chirone R., Ammendola P., Calcium-looping for thermochemical energy storage in concentrating solar power applications: evaluation of the effect of acoustic perturbation on the fluidized bed carbonation, Chemical Engineering Journal, 392 (2020a) 123658. DOI: 10.1016/j.cej.2019.123658

Raganati F., Chirone R., Ammendola P., CO_2 capture by temperature swing adsorption: working capacity as affected by temperature and CO_2 partial pressure, Industrial & Engineering Chemistry Research, 59 (2020b) 3593–3605. DOI: 10.1021/acs.iecr.9b04901

Rouchon L., Favergeon L., Pijolat M., Analysis of the kinetic slowing down during carbonation of CaO by CO_2, Journal of Thermal Analysis and Calorimetry, 113 (2013) 1145–1155. DOI: 10.1007/s10973-013-2950-5

Salaudeen S.A., Acharya B., Dutta A., CaO-based CO_2 sorbents: a review on screening, enhancement, cyclic stability, regeneration and kinetics modelling, Journal of CO_2 Utilization, 23 (2018) 179–199. DOI: 10.1016/j.jcou.2017.11.012

Sarrión B., Perejón A., Sánchez-Jiménez P.E., Pérez-Maqueda L.A., Valverde J.M., Role of calcium looping conditions on the performance of natural and synthetic Ca-based materials for energy storage, Journal of CO_2 Utilization, 28 (2018) 374–384. DOI: 10.1016/j.jcou.2018.10.018

Sedghkerdar M.H., Mostafavi E., Mahinpey N., Investigation of the kinetics of carbonation reaction with CaO-based sorbents using experiments and aspen plus simulation, Chemical Engineering Communications, 202 (2015) 746–755. DOI: 10.1080/00986445.2013.871709

Seville J.P.K., Willett C.D., Knight P.C., Interparticle forces in fluidisation: a review, Powder Technology, 113 (2000) 261–268. DOI: 10.1016/S0032-5910(00)00309-0

Stanmore B., Gilot P., Review—calcination and carbonation of limestone during thermal cycling for CO_2 sequestration, Fuel Processing Technology, 86 (2005) 1707–1743. DOI: 10.1016/j.fuproc.2005.01.023

Sun J., Bertos M.F., Simons S.J.R., Kinetic study of accelerated carbonation of municipal solid waste incinerator air pollution control residues for sequestration of flue gas CO_2, Energy and Environmental Science, 1 (2008) 370–377. DOI: 10.1039/b804165m

Sun P., Grace J.R., Lim C.J., Anthony E.J., Determination of intrinsic rate constants of the CaO–CO_2 reaction, Chemical Engineering Science, 63 (2008) 47–56. DOI: 10.1016/j.ces.2007.08.055

Valverde J.M., Acoustic streaming in gas-fluidized beds of small particles, Soft Matter, 9 (2013) 8792. DOI: 10.1039/c3sm50780g

Yin J., Qin C., Feng B., Ge L., Luo C., Liu W., An H., Calcium looping for CO_2 capture at a constant high temperature, Energy & Fuels, 28 (2014) 307–318. DOI: 10.1021/ef401399c

Authors' Short Biographies

Federica Raganati

Federica Raganati received her degree in Chemical Engineering from the University Federico II of Naples (Italy) in 2010 and her PhD in Chemical Engineering from the same university in 2014. She has a permanent position as researcher at the Istituto di Scienze e Tecnologie per l'Energia e la Mobilità Sostenibili (STEMS) of the Consiglio Nazionale delle Ricerche (CNR). Her main research topics are the set-up of innovative fluidized bed reactor configurations, the reduction of CO_2 emissions through post-combustion capture processes and the energy storage through thermochemical processes. She is the author of 3 patents and about 80 papers published in peer-reviewed international journals or proceedings of national/international conferences.

Paola Ammendola

Paola Ammendola received her degree in Chemical Engineering from the University Federico II of Naples (Italy) in 2003 and her PhD in Chemical Engineering from the same university in 2006. She has a permanent position as researcher at the Istituto di Scienze e Tecnologie per l'Energia e la Mobilità Sostenibili (STEMS) of the Consiglio Nazionale delle Ricerche (CNR). Her main research topics are the sound-assisted fluidization of cohesive powders, the set-up of innovative catalytic systems and the use of fluidized bed reactors for clean energy production and the study of renewable energy sources (solar energy and biomass). She is the author of 5 patents and about 150 papers published in peer-reviewed international journals or proceedings of national/international conferences.

KONA Powder and Particle Journal No. 39 (2022) 251–261/https://doi.org/10.14356/kona.2022018 Original Research Paper

Biodegradable PLGA Microsphere Formation Mechanisms in Electrosprayed Liquid Droplets†

Moe Tanaka[1], Ayaka Ochi[1], Aiko Sasai[1], Hiroyuki Tsujimoto[1], Hitomi Kobara[2], Hiromitsu Yamamoto[3] and Akihiro Wakisaka[2]*

[1] *Pharmaceutical/Beauty Science Research Center of the Hosokawa Micron Corporation, Japan*
[2] *National Institute of Advanced Industrial Science and Technology (AIST), Japan*
[3] *School of Pharmacy, Aichi Gakuin University, Japan*

Abstract

Microspheres composed of poly (lactic-co-glycolic acid) (PLGA) were formed in liquid droplets using the electrospray technique. The structure of the microspheres was controlled by changing the electric voltage of the electrospray. PLGA microspheres with porous structures and micro-sized nanocomposite particles comprising PLGA nanosphere aggregates were formed at 5.0–7.0 kV and 2.5–3.5 kV, respectively. The structural change was related to the extent of evaporation of the solvent from the droplets during their flight. When the evaporation was completed in the relatively small droplets, the microspheres with porous structures were formed in the droplets. To study the mechanism, we observed the effects of the electric voltage of the electrospray, PLGA concentration, flight distance of the droplets, and molecular weight of PLGA on the structure of the PLGA particles. The novelty of this study is the analysis of the size and structure of the PLGA microparticles, which were controlled by the electrospray technique. Therefore, this research has important implications for the structural design and preparation of nanocomposite particles.

Keywords: electrospray, emulsion solvent diffusion method, poly (lactic-co-glycolic acid), porous microparticle, nanosphere

1. Introduction

The emulsion solvent diffusion (ESD) method in water devised by Kawashima et al. (Kawashima et al., 1982; 1998) is an established method for producing drug-loaded poly (lactic-co-glycolic acid) (PLGA) nanospheres. PLGA and the drug are dissolved in a mixture of acetone and ethanol and dropped into a stirred polyvinyl alcohol (PVA) aqueous solution. Nano-sized emulsion droplets are formed by spontaneous emulsification associated with the rapid diffusion of acetone into the external aqueous phase after dropping. Then, mutual diffusion of the solvents causes PLGA and the drug to precipitate as the solubility decreases. At this time, the external PVA phase is adsorbed onto the surface of the emulsion droplets and prevents the coalescence of emulsion droplets. This principle makes this method suitable for the production of ~200-nm-sized drug-loaded PLGA nanospheres, with a uniform particle size distribution, and it has been researched extensively as a new drug delivery system (DDS) technology (Kimura et al., 2008; Nakano et al., 2009; Hara et al., 2008; Tsujimoto et al., 2007a; 2007b).

In this study, the ESD method was scaled (crystallizer size, 100 L) at the Pharmaceutical/Beauty Science Research Center of the Hosokawa Micron Corporation. The following steps were completed: (1) mass production of PLGA nanospheres loaded with useful ingredients for cosmetics and quasi-drugs (Charlesworth et al., 1960), and manufacturing and sale of unique skincare products and hair growth formulas containing these PLGA nanospheres; (2) development of a Good Manufacturing Practice (GMP) production method (Tsujimoto et al., 2004; 2007b) for ~80-nm-sized PLGA nanospheres that can undergo sterile pressure filtration (Tsukada et al., 2009), for use in injectable pharmaceutical formulations. The study developed a production method for the practical use of PLGA nanospheres. However, there were issues in applying the ESD method regarding (1) the formation of PLGA microspheres and (2) the formation of PLGA nanocomposites. For example, in the manufacture of the PLGA microspheres, it is difficult to apply methods other than a W/O/W emulsion solvent evaporation method (in-liquid drying method) (Toguchi et

---

† Received 21 June 2021; Accepted 17 August 2021

* Corresponding author: Akihiro Wakisaka;
Add: 1-1-1 Umezono, Tsukuba, Ibaraki 305-8560, Japan
E-mail: akihiro-wakisaka@aist.go.jp
TEL: +81-29-861-8088 FAX: +81-29-861-8252

Table 1 Chemical properties of PLGA used in experiments.

	Sample A	Sample B	Sample C
Average molecular weight	5,000	20,000	50,000
Ratio of lactic acid and glycolic acid	75:25	75:25	75:25
Manufacturer	FUJIFILM Wako Pure Chemical Corporation	FUJIFILM Wako Pure Chemical Corporation	MITSUI Chemicals, Inc.

al., 1991; Okada et al., 1997) using a strong solvent (chloroform, dichloromethane); however, the method carries a high environmental load. Regarding PLGA nanocomposites, an example of typical use is dry powder inhaler (DPI) formulations. Microcomposite particles comprised of drug-loaded PLGA nanospheres possess both the flowability (capsule fillability and alveolar delivery) and redispersibility into nanospheres (absorption into alveolar tissue) required of DPI formulations (Tsujimoto et al., 2005; Yamamoto et al., 2004; 2007). However, the manufacturing process requires the formation of PLGA nanospheres using the conventional ESD method and a subsequent mechanical compounding process (Yamamoto et al., 2004; 2007) which can be time consuming and labor intensive. Therefore, a new manufacturing process is desirable.

The electrospray fine particle preparation method is attracting attention because particle size can be controlled by varying the electrostatic potential between the counter electrode and liquid (Kobara et al., 2019). In this study, as a novel method, we used an electrospray of the PLGA solution onto the surface of the PVA aqueous solution phase. From the results obtained, it can be inferred that, unlike in the conventional ESD method, it is possible to control the particle size from submicron to several micrometers with the same solvent composition without using a chlorinated solvent. In particular, it was found that the characteristic PLGA microspheres, such as PLGA microspheres with a porous structure and micro-sized nanocomposite particles, comprising PLGA nanosphere aggregates, can be produced by changing the preparation conditions. This result is important for the structural design and preparation of nanocomposite particles when applying PLGA microspheres as various platforms for DDS.

We would like to report herein this paper the mechanism for the PLGA microspheres formed in the electrosprayed liquid droplets, and the structure-controlling factors such as electric voltage, concentration of PLGA, flight distance of the electrosprayed droplets and molecular weight of PLGA.

2. Experimental

2.1 Apparatus and method

In this experiment, three types of PLGA (Sample A, B: Fujifilm Wako Pure Chemicals, Sample C: Mitsui Chemicals) were used without further purification. **Table 1** lists the basic chemical properties of the materials. Sample B (molecular weight (MW): 20,000 Da) was used for the experiments except for the experiment concerning the effect of the molecular weight.

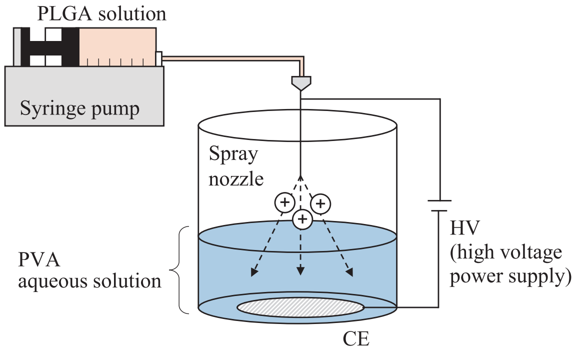

Fig. 1 Schematic picture of experimental setup for the PLGA particle formation with electrospray.

Fig. 1 shows a schematic of the experimental setup for the PLGA particle formation. A glass beaker (cylindrical shape, outer diameter of 53 mm, height of 70 mm) was filled with 50 ml of 0.25 wt% PVA aqueous solution, and placed on a temperature-controlled stirrer. A stainless-steel nozzle (outer diameter of 0.26 mm, inner diameter of 0.13 mm) was situated above the PVA aqueous solution surface. The distance between the nozzle tip and PVA aqueous solution surface was set to 20 mm as the standard condition. A high voltage for the electrospray was supplied between this nozzle and the counter electrode through a high-voltage DC power supply unit (HJPQ-10P3, HJPQ-10N3 (Matsusada Precision Inc.)). Because the counter electrode was in the aqueous solution, the surface of the aqueous solution acted as the counter electrode for the electrospray, as shown in **Fig. 1**.

For the preparation of PLGA particles, PLGA (33 mg/ml) was dissolved in an acetone/ethanol mixture with a 2:1 volume ratio. The PLGA solution was pumped with a constant flow rate of 0.03 ml/min using a microsyringe pump (YSP-101, YMC Co., Ltd.) to the electrospray nozzle, which was supplied with a high voltage. The concentration of the PLGA solution (33 mg/ml) was the same as that used in the conventional ESD method.

At the nozzle tip, the PLGA solution was fragmented into charged droplets according to the electrospray principle. The charged droplets were continuously sprayed onto the surface of the PVA aqueous solution, which was gently stirred using a magnetic stirrer (stirrer size: 8 × 25 mm, cylinder type, and 800 rpm).

For each experiment, the PLGA solution was electrosprayed at 0.03 ml/min for 60 min, i.e., 1.8 ml of PLGA solution was sprayed onto the surface of the PVA aqueous solution. This experiment was conducted at room temperature (288–293 K). After spraying, the PLGA particles suspended in the PVA solution were analyzed using the following procedures: (i) centrifugation of the PVA solution containing PLGA particles (48,000 × g, 4 °C, 30 min); (ii) removal of supernatant; (iii) redispersion with purified water and observation with a scanning electron microscope. **Fig. 2** shows a typical SEM image of the PLGA particles produced using Run 4 (**Table 2**). The Feret diameters of the particles were measured from the SEM images (magnification: 500–2000×). The average particle size was calculated by measuring the Feret diameters of 20–30 particles.

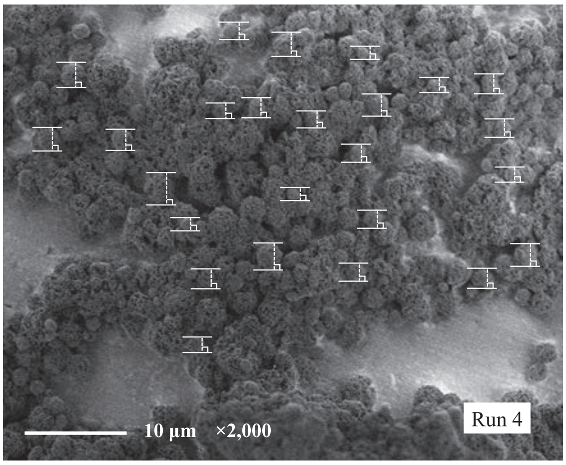

Fig. 2 An example of Feret diameter measurement using a SEM image of Run 4.

2.2 Liquid droplets generated by electrospray

The PLGA solution was electrosprayed in a strong electric field between the nozzle tip and counter electrode. The electrospray was started at 2.5 kV, and the electric voltage was increased slowly, while the PLGA solution was fed into the strong electric field at 0.03 ml/min through the nozzle, as shown in **Fig. 3**. At 2.5 kV, a Taylor cone and relatively large liquid droplets, which fragmented from the Taylor cone, were observed (**Fig. 3(a)**). The formation of the Taylor cone, which is a characteristic of the electrospray, indicates that the electrospraying was accurately performed. The liquid droplets were generated by the electrostatic repulsion between the electric charges formed on the Taylor cone, which is called "coulombic explosion." Coulombic explosion can occur several times when the charge density is increased, owing to solvent evaporation from the droplets. With the increase in electric voltage, from 2.5 kV to 7.0 kV, the size of the liquid droplets decreased, owing to more coulombic explosion events. When the electric voltage was higher than 3.5 kV, multiple Taylor cones were formed (**Figs. 3(b)**, **(c)**, **(d)**). The droplet size was too small to be observed through a high-speed camera

Table 2 Experimental conditions.

Run	Voltage (kV)	Distance of nozzle-interface (mm)	Spray rate (ml/min)	Type of PLGA	PLGA concentration (mg/ml)	Ratio of PLGA concentration to standard concentration of 33 mg/ml	Ratio of acetone and ethanol	Particle size (µm)
1	+2.0	20	0.03	B	33	× 1	2:1	–
2	+2.5	20	0.03	B	33	× 1	2:1	6.19 ± 0.40
3	+3.5	20	0.03	B	33	× 1	2:1	3.13 ± 0.83
4	+5.0	20	0.03	B	33	× 1	2:1	2.04 ± 0.40
5	+7.0	20	0.03	B	33	× 1	2:1	1.86 ± 0.54
6	+5.0	20	0.03	B	3	× 1/10	2:1	–
7	+5.0	20	0.03	B	7	× 1/5	2:1	–
8	+5.0	20	0.03	B	17	× 1/2	2:1	1.83 ± 0.70
9	+5.0	20	0.03	B	67	× 2	2:1	3.44 ± 0.39
10	+5.0	20	0.03	B	133	× 4	2:1	4.83 ± 0.43
11	+5.0	10	0.03	B	33	× 1	2:1	1.52 ± 0.14
12	+5.0	40	0.03	B	33	× 1	2:1	3.65 ± 0.44
13	+5.0	20	0.03	A	33	× 1	2:1	1.30 ± 0.70
14	+5.0	20	0.03	C	33	× 1	2:1	4.08 ± 0.40

Run 4: Criteria condition of this experiment.

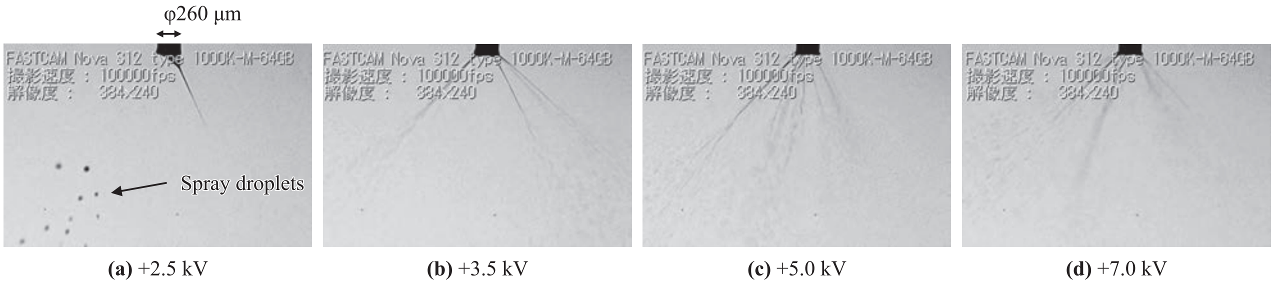

Fig. 3 Photographs taken with high speed camera of electrospray pattern according to the supplied voltage. The video is available publicly at https://doi.org/10.50931/data.kona.17030060

(Photron, 100,000 fps). When the voltage was increased above a certain level, the size of the liquid droplet was assumed to be ≤ 10 µm based on the high-speed camera resolution. The video demonstrating the electrospray patterns, is provided on J-STAGE Data website.

2.3 Particleization of PLGA using electrospray

When the droplets of the PLGA solution were generated via the electrospray, the solvent in the droplets was vaporized. This increased the PLGA concentration during the flight of the droplets from the nozzle tip to the surface of the PVA aqueous solution. The solidification to form the PLGA particles was related to this condensation process. To investigate the effect of condensation on the electrosprayed liquid droplets and particleization, the following experimental conditions were observed, as listed in **Table 2**: (i) electrospray electric voltage (Run 1, 2, 3, 4, 5); (ii) PLGA concentration (Run 4, 6, 7, 8, 9, 10); (iii) distance between the nozzle tip and surface of the PVA aqueous solution (Run 4, 11, 12); (iv) molecular weight of PLGA (Run 4, 13, 14). In each experiment, Run 4 was considered the standard condition, because the PLGA particles formed in Run 4 reflected the original characteristics of the electrospray. Other experimental conditions, such as the flow rate of the PLGA solution, aqueous PVA solution (concentration and volume), and stirring conditions, were fixed.

3. Experimental results and discussion

3.1 Effect of electric voltage of the electrospray on the formation of PLGA particles

In the conventional ESD method, the PLGA solution with the acetone/ethanol mixed solvent (volume ratio of 2:1) is mixed with water, containing PVA as a stabilizer. The ESD method uses the difference in solubility of PLGA in the acetone/ethanol mixture and water. PLGA is highly soluble in the acetone/ethanol mixture. In contrast, PLGA is hardly soluble in water. Therefore, precipitation of PLGA occurs when the two solutions are mixed, which results in the formation of nanospheres. In this study, electrospray was used to mix these two solutions; however, evaporation of the solvent from the electrosprayed droplets was found to play an important role in particleization, as discussed below.

As shown in **Fig. 1**, the PLGA solution with the acetone/ethanol mixed solvent was electrosprayed, and the resulting liquid droplets traveled to the surface of the PVA aqueous solution through the electric field. PLGA particles were formed in the aqueous PVA solution owing to the mixing of the two solutions. The microscopic structures of the resulting particles were observed through SEM. As shown in **Fig. 4**, the PLGA particle formation process was classified into three groups, depending on the electric voltage of the electrospray.

Group I at low electric voltages, 0 to +2.0 kV: PLGA nanospheres similar to the nanospheres formed in the conventional ESD method were observed (**Figs. 4(a)**, **(b)**).

Group II at intermediate electric voltages, +2.5 kV to +3.5 kV: Microparticles composed of PLGA nanospheres were observed (**Figs. 4(c)**, **(d)**).

Group III at high electric voltages, +5.0 kV to +7.0 kV: Microspheres with porous structures were observed (**Figs. 4(e)**, **(f)**).

The effect of the supplied electric voltage on the structure of the PLGA particles is schematically depicted in **Fig. 5**.

In Group I, electrospraying was performed at low electric voltages. Relatively large droplets of the PLGA solution were fed into the PVA aqueous solution. The droplets were diffused into the PVA aqueous solution, which resulted in the formation of the PLGA nanospheres owing to the decrease in solubility of PLGA through interaction with water. This mechanism is the same as that of the conventional ESD method, reported previously (Kawashima et al., 1998).

In Group II, electrospraying was performed at electric voltages of +2.5 kV to +3.5 kV, and electrospray-generated fine droplets were formed. The solvent molecules of acetone and ethanol were evaporated out of the liquid droplets of the PLGA solution during the flight of the droplets from the nozzle to the surface of the PVA aqueous solution.

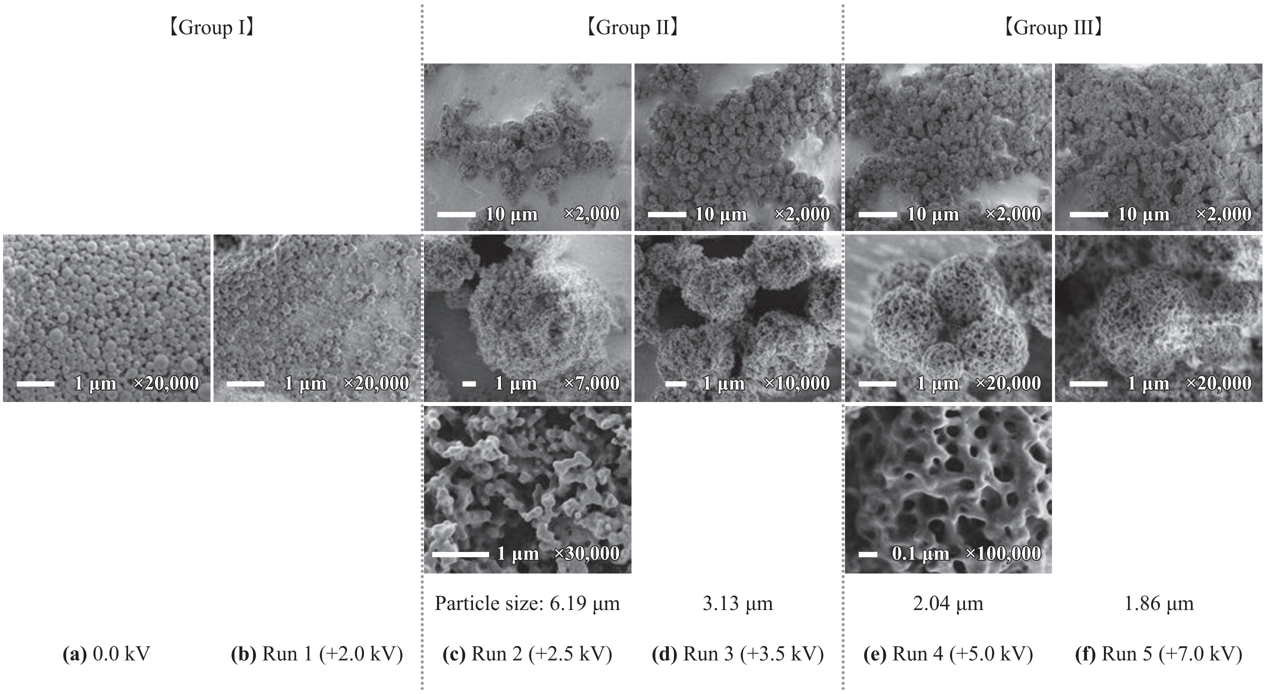

Fig. 4 Scanning electron micrographs of the PLGA particles (granules) prepared by changing the electric voltage for the electrospray.

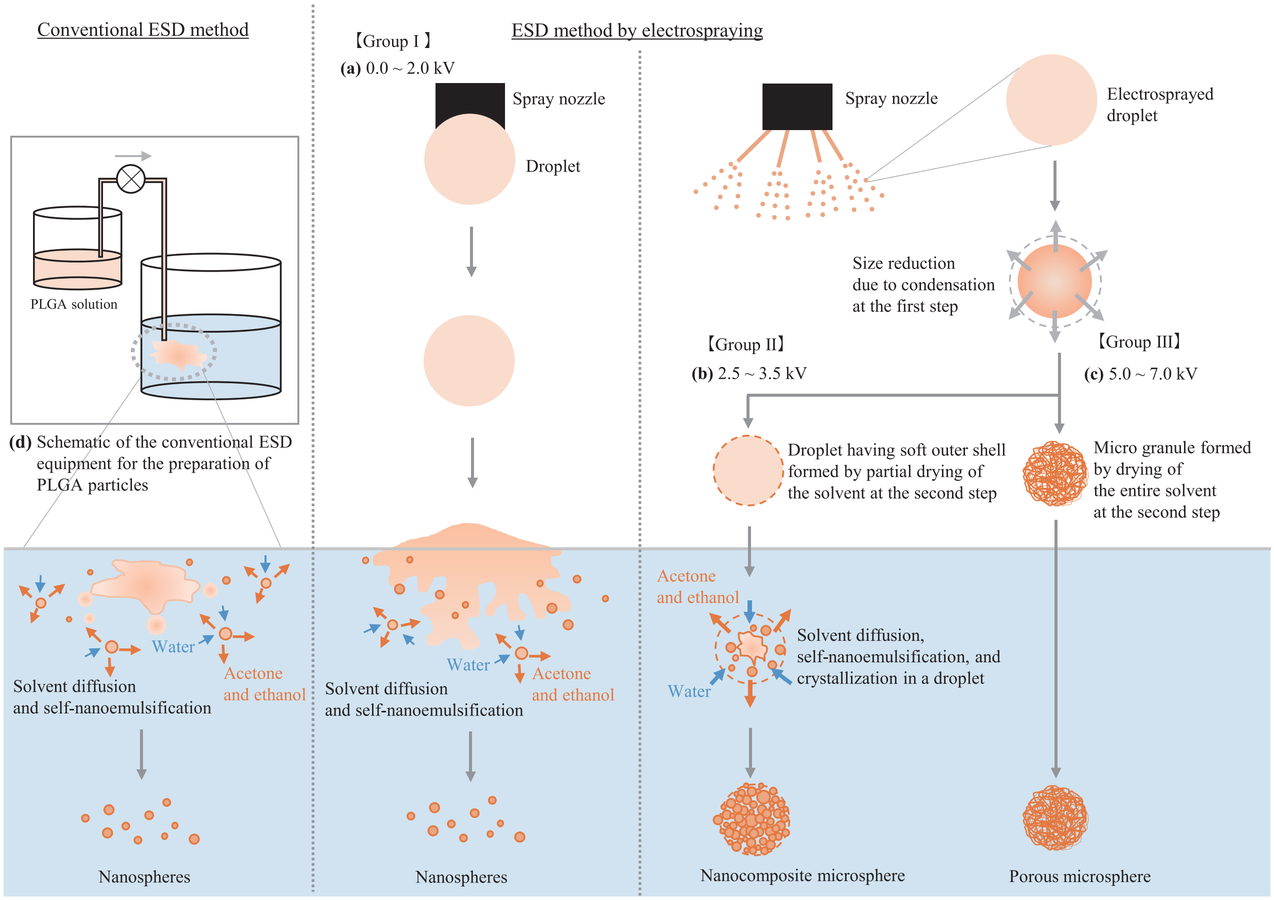

Fig. 5 Schematic illustration of the formation process of PLGA particle by the conventional ESD method and the electrospray method.

Owing to the evaporation of the solvent molecules, the PLGA concentration increased, which solidified the PLGA partially in the droplets and especially on the surface of the liquid droplets. The diffusion of PLGA into the aqueous solution became difficult owing to the solidification on the surface of the liquid droplets; microparticles composed of nanospheres were formed. When the droplets landed on the surface of the aqueous solution, the interaction of PLGA with water was limited to the partially solidified liquid droplets. This led to the formation of microspheres through the aggregation of PLGA nanospheres. In **Fig. 4(c)**, the SEM image, which was magnified 30,000 times, shows a microsphere formed through the aggregation of PLGA nanospheres. The specific surface area of the microspheres was measured using the gas adsorption method, and found to be larger than that of the microspheres in Group III, as listed in **Table 3**. The microspheres in Group II had nanocomposite structures. The size of the microparticles formed in Group II was in the range of 2–10 µm. This size of the microparticles was in good agreement with that of the electrosprayed liquid droplets, suggesting that one microparticle was formed per liquid droplet.

In Group III, owing to high electric voltages (+5.0 kV to +7.0 kV), much smaller liquid droplets were generated. During the flight of the droplets, the solvent molecules of acetone and ethanol evaporated, leading to the precipitation of PLGA, and microspheres with a porous structure were formed. In **Fig. 4(e)**, the SEM image, which was magnified 100,000 times, shows such a microsphere with a porous structure. The size of the microspheres in Group III was smaller than that in Group II. This was in agreement with the decrease in the size of the liquid droplets at higher electric voltages. This also supports the hypothesis that one microsphere of PLGA was formed per liquid droplet.

In the conventional ESD method, the number of microspheres formed was negligible. In contrast, by using electrospray, microspheres were formed when the solvent molecules were evaporated out of the electrosprayed liquid droplets.

Table 3 Specific surface area of PLGA particles.

Run	2	4	8
Voltage (kV)	+2.5	+5.0	+5.0
PLGA concentration (mg/ml)	33	33	17
Specific surface area (m^2/g)	107	80	162

3.2 Effect of PLGA concentration on the formation of PLGA particles

As shown in **Figs. 4** and **5**, the formation of PLGA microspheres was promoted by the solidification of the electrosprayed liquid droplets through the evaporation of the solvent molecules. To verify the mechanism in **Fig. 5**, the effect of the PLGA concentration on the formation of PLGA particles was examined. The concentrations of PLGA in the acetone/ethanol mixture (volume ratio: 2:1) were 3, 7, 17, 33, 67, and 133 mg/ml. The concentration used in the experiments on the effect of the electric voltage (**Fig. 4**) was 33 mg/ml. The SEM images of the resulting PLGA particles are shown in **Fig. 6**.

It was observed that the particle structures were dependent on the PLGA concentration; they were classified into three categories. At lower concentrations (3 and 7 mg/ml), microspheres were not formed. Instead, film-like structures were formed. At suitable concentrations of 17, 33, and 67 mg/ml, porous microspheres were generated. At higher concentrations, such as 133 mg/ml, microspheres were formed, but they did not have porous structures. They were dense and partially dimpled.

The observed effect of concentration is schematically illustrated in **Fig. 7**. At lower concentrations (**Fig. 7(a)**), during the flight of the electrosprayed liquid droplets, the solvent molecules were evaporated out of the liquid droplets; however, the concentration of PLGA, required for solidification, was insufficient to form the outer shell structure. Owing to the hydrophobicity of the PLGA solution, the electrosprayed fine droplets were eager to stay on the surface of the aqueous PVA solution (**Fig. 1**). Thus, the nanospheres resulting from the interaction of PLGA in

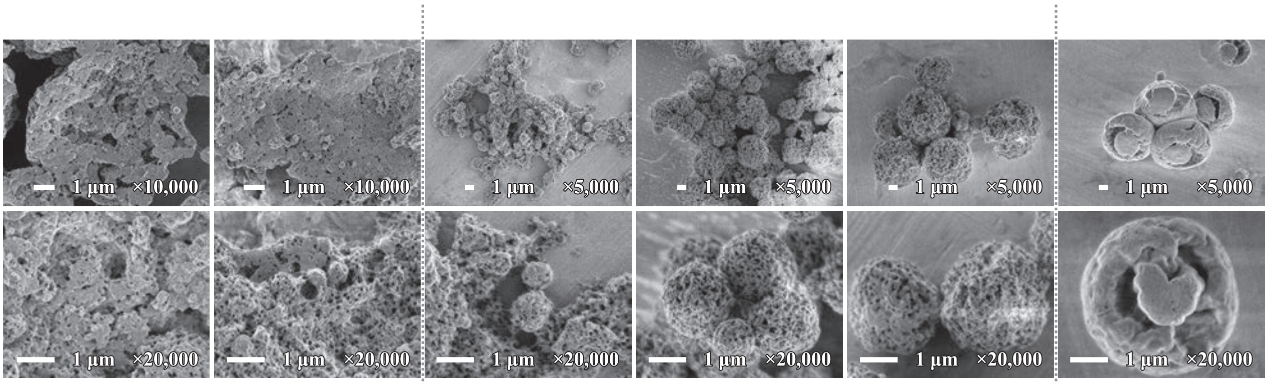

Particle size: 1.75 µm 2.04 µm 3.44 µm 4.88 µm

(a) Run 6 (×1/10) **(b)** Run 7 (×1/5) **(c)** Run 8 (×1/2) **(d)** Run 4 (×1) **(e)** Run 9 (×2) **(f)** Run 10 (×4)

Fig. 6 Scanning electron micrographs of the PLGA particles (granules) prepared at various PLGA concentration.

the droplets with water on the surface of the PVA aqueous solution were present on the surface of the PVA aqueous solution. The resulting nanospheres aggregated on the surface of the PVA aqueous solution to form a thin film structure. Note that the acetone/ethanol solvent was also present around the surface of the aqueous PVA solution. This acetone/ethanol mixture may have contributed to the formation of the PLGA thin-film structure. It was assumed that the aggregating PLGA nanospheres were transformed into thin-film structures through the partial dissolution of the acetone/ethanol mixture.

At suitable concentrations, porous microspheres were formed; moreover, the porosity and size of the microspheres decreased and increased, respectively, with increasing PLGA concentration (**Figs. 6(c)**, **(d)**, **(e)**). This was in agreement with the measurements of the specific surface area, which is listed in **Table 3**. When the PLGA concentration in the solution was increased from 17 to 33 mg/ml, the specific surface area decreased from 162 to 80 m^2/g. This indicates a decrease in porosity with an increase in the PLGA concentration. Furthermore, the size of the microspheres increased with increasing PLGA concentration in this concentration range. This is related to the increase in size of the liquid droplets with the increase in the concentration. Because the viscosity of the PLGA solution increased with increasing PLGA concentration (**Table 4**), the size of the electrosprayed liquid droplets also increased.

At higher concentrations, such as 133 mg/ml, porous structures were difficult to generate. Moreover, numerous PLGA molecules in the droplets formed denser structures.

We observed that porous structures were generated for a specific range of PLGA concentrations. This also supports the hypothesis that one microsphere was formed per liquid droplet. Various studies on particle formation in emulsion droplets in a liquid have been conducted (Mersmann, 1998; Kawashima et al., 2002; Yoshizawa, 2004). However, the particle formation mechanism in the proposed electrospray method is better equipped to create various particle structures than the particle formation mechanisms reported

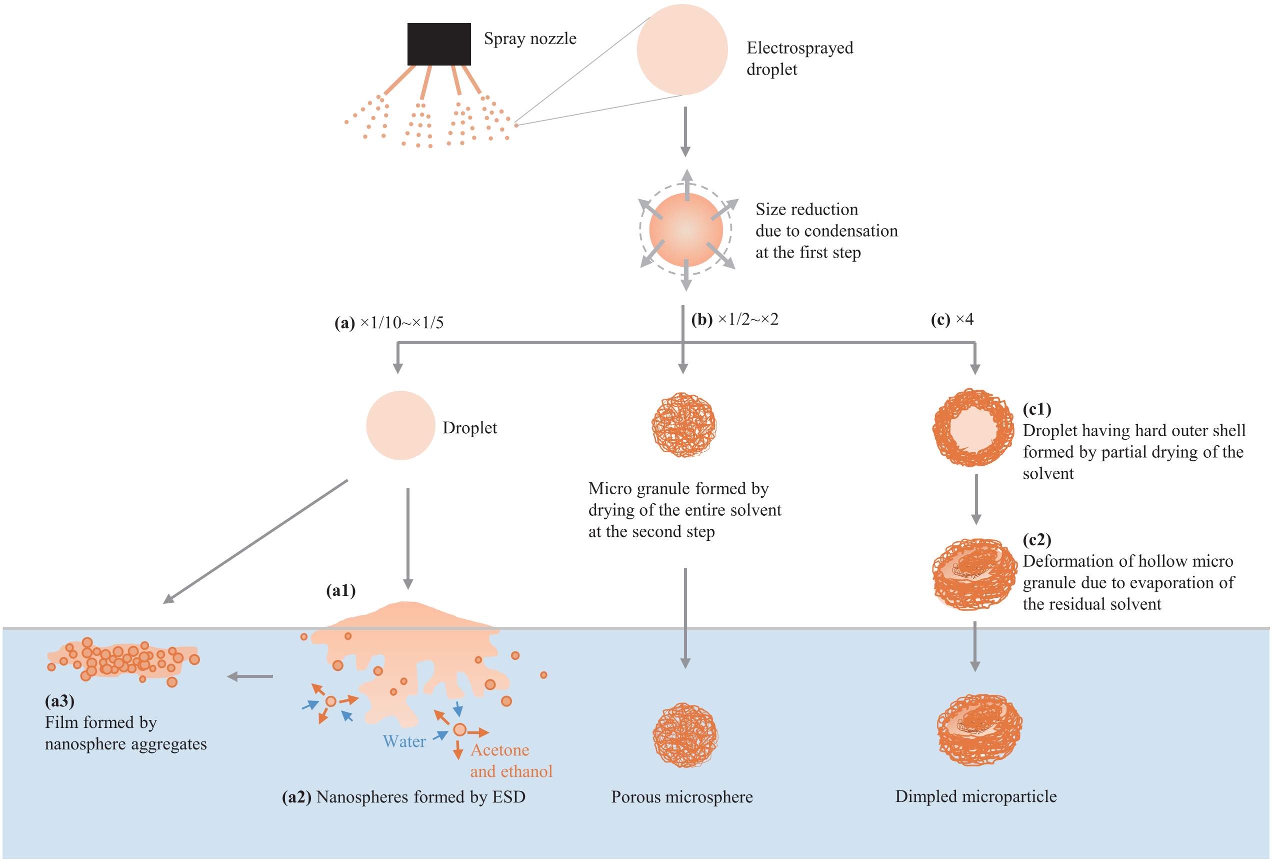

Fig. 7 Schematic illustration of the formation process of PLGA particle by changing PLGA concentration.

Table 4 Relation of the PLGA concentration to the viscosity of PLGA solution.

PLGA concentration (mg/ml)	0	3	7	17	33	67	133
PLGA concentration ratio to standard concentration of 33 mg/ml	–	× 1/10	× 1/5	× 1/2	× 1	× 2	× 4
Viscosity of PLGA solution (cP)	0.44	0.46	0.46	0.51	0.65	1.05	2.61

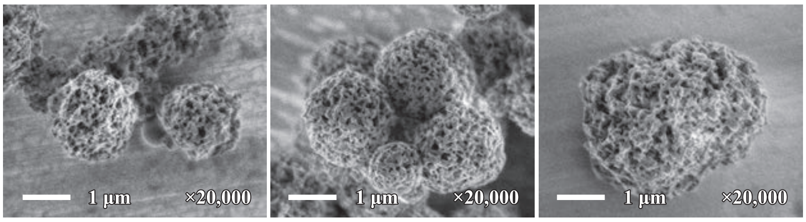

Particle size: 1.51 μm | 2.04 μm | 3.62 μm

(a) Run 11 (10 mm) | **(b)** Run 4 (20 mm) | **(c)** Run 12 (40 mm)

Fig. 8 Scanning electron micrographs of the PLGA particles (granules) prepared by changing the spray distance between nozzle tip and water surface.

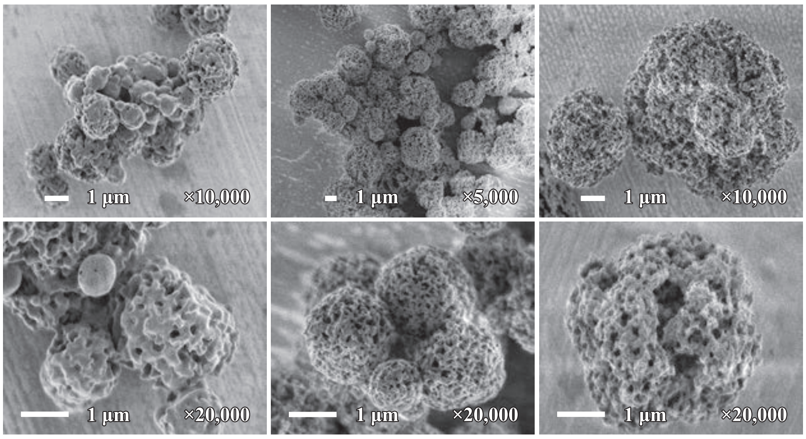

Particle size: 1.37 μm | 2.04 μm | 4.09 μm

(a) Run 13 (5,000) | **(b)** Run 4 (20,000) | **(c)** Run 14 (50,000)

Fig. 9 Scanning electron micrographs of the PLGA particles (granules) prepared by various polymers with different molecular weight.

previously. This is because the solvent diffuses from the emulsion droplets in the liquid and evaporates from the surface of the droplet in the air.

3.3 Effect of flight distance of the electrosprayed droplets on the formation of PLGA particles

Fig. 8 shows the results of particle formation by changing the distance between the nozzle tip and surface of the PVA aqueous solution. When the distance was increased, the droplet size also increased owing to the decrease in the electric field. The SEM images (**Fig. 8**) show that larger particles with porous structures were produced as the distance increased. Although the size of the droplet increased, solidification in the air occurred during long-distance flights.

3.4 Effect of PLGA molecular weight on the formation of PLGA particles

PLGA with a molecular weight of 20,000 Da was used. The size of the PLGA particles, resulting from the electrospray method, depended on the molecular weight of PLGA. **Fig. 9** shows the observed SEM images of the PLGA particles, generated from the PLGAs with molecular weights of 5,000, 20,000, and 50,000. Porous structures were observed for these three molecular weights, and the average diameter increased with an increase in the molecular weight. Because the viscosity and solubility also change with the molecular weight, the effect of the molecular weight was studied more systematically.

Table 5 Relation of the PLGA average molecular weight to the viscosity of PLGA solution.

Type of PLGA	A	B	C
Average molecular weight (Da)	5,000	20,000	50,000
Viscosity (cP)	0.55	0.65	0.71

4. Conclusions and future prospects

(1) We found that PLGA microparticles were formed in the liquid droplets using the proposed electrospray technique. Porous PLGA microparticles and microparticles composing PLGA nanospheres, which cannot be produced by the conventional ESD method, were generated. The formation mechanism of these PLGA particles was classified into three categories depending on the extent of solvent

evaporation from the droplets. (i) The evaporation of the droplets was completed in the air, leading to the formation of microspheres with a porous structure. (ii) Owing to the evaporation of the solvent from relatively large droplets, solidification began on the surface of the droplets, leading to the formation of microparticles composed of nanospheres. (iii) The evaporation was insufficient for solidification in large droplets, leading to the formation of nanospheres similar to those in the conventional ESD method.

(2) If these microparticles can be loaded with drugs, they can be used for solid pharmaceutical preparations. The possibility of application in DPI and subcutaneous injection formulations will be the subject of future studies.

(3) Currently, we are also investigating the following subjects: (i) the mass production procedure of PLGA microparticles using electrospray; (ii) the size-distribution control of PLGA nanospheres using electrospray in a liquid medium instead of air. We will report these results in the future.

Acknowledgements

We would like to thank T. Iwakami of AIST for his technical assistance with the experiments. We would also like to thank Hitachi High-Tech Corporation for the FE-SEM images magnified 30,000 times in **Fig. 4(c)** and 100,000 times in **Fig. 4(e)**.

Nomenclature

AIST	National Institute of Advanced Industrial Science and Technology
CE	Counter Electrode
DC	Direct Current
DDS	Drug Delivery System
DPI	Dry Powder Inhaler
ESD	Emulsion Solvent Diffusion.
FE-SEM	Field Emission Scanning electron Microscopy
HV	High Voltage power supply
MW	Molecular Weight
PLGA	poly (Lactic-co-Glycolic acid)
PVA	Poly Vinyl Alcohol
SEM	Scanning Electron Microscopy

Data Availability Statement

The video data from electrospray experiments is available publicly in J-STAGE Data (https://doi.org/10.50931/data.kona.17030060).

References

Charlesworth D.H., Marshall Jr. W.R., Evaporation from drops containing dissolved solids, AIChE Journal, 6 (1960) 9–23. DOI: 10.1002/aic.690060104

Hara K., Tsujimoto H., Tsukada Y., Huang C.C., Kawashima Y., Tsutsumi M., Histological examination of PLGA nanospheres for intratracheal drug administration, International Journal of Pharmaceutics, 356 (2008) 267–273. DOI: 10.1016/j.ijpharm.2007.12.041

Kawashima Y., Imai M., Takeuchi H., Yamamoto H., Kamiya K., Development of agglomerated crystals of ascorbic acid by the spherical crystallization technique for direct tableting, and evaluation of their compactibilities [Translated], KONA Powder and Particle Journal, 20 (2002) 251–262. DOI: 10.14356/kona.2002028

Kawashima Y., Okumura M., Takenaka H., Spherical crystallization: direct spherical agglomeration of salicylic acid crystals during crystallization, Science, 216 (1982) 1127–1128. DOI: 10.1126/science.216.4550.1127

Kawashima Y., Yamamoto H., Takeuchi H., Hino T., Niwa T., Properties of a peptide containing dl-lactide/glycolide copolymer nanospheres prepared by novel emulsion solvent diffusion methods, European Journal of Pharmaceutics and Biopharmaceutics, 45 (1998) 41–48. DOI: 10.1016/s0939-6411(97)00121-5

Kimura S., Egashira K., Nakano K., Iwata E., Miyagawa M., Tsujimoto H., Hara K., Kawashima Y., Tominaga R., Sunagawa K., Local delivery of imatinib mesylate (STI571)-incorporated nanoparticle ex vivo suppresses vein graft neointima formation, Circulation, 118 (2008) S65–S70. DOI: 10.1161/circulationaha.107.740613

Kobara H., Nakatsuka K., Wakisaka A., Size-selected synthesis of metal nanoparticles by using electrospray in a liquid medium, Colloids and Surfaces A: Physicochemical and Engineering Aspects, 581 (2019) 123836. DOI: 10.1016/j.colsurfa.2019.123836

Mersmann A., Crystallization and precipitation, KONA Powder and Particle Journal, 16 (1998) 60–67. DOI: 10.14356/kona.1998009

Nakano K., Egashira K., Masuda S., Funakoshi K., Zhao G., Kimura S., Matoba T., Sueishi K., Endo Y., Kawashima Y., Hara K., Tsujimoto H., Tominaga R., Sunagawa K., Formulation of nanoparticle-eluting stents by a cationic electrodeposition coating technology: efficient nano-drug delivery via bioabsorbable polymeric nanoparticle-eluting stents in porcine coronary arteries, JACC: Cardiovascular Interventions, 2 (2009) 277–283. DOI: 10.1016/j.jcin.2008.08.023

Okada H., One- and three-month release injectable microspheres of the LH-RH superagonist leuprorelin acetate, Advanced Drug Delivery Reviews, 28 (1997) 43–70. DOI: 10.1016/s0169-409x(97)00050-1

Toguchi H., Ogawa Y., Okada H., Yamamoto M., Once-a-month injectable microcapsules of leuprorelin acetate, Yakugaku Zasshi, 111 (1991) 397–409. DOI: 10.1248/yakushi1947.111.8_397

Tsujimoto H., Hara K., Huang C.C., Yokoyama T., Kawashima Y., The applications of biodegradable poly lactide-co-glycolide (PLGA) nano-spheres for pulmonary and transdermal drug deliveries, Foods & Food Ingredients Journal of Japan, 5 (2005) 437–448.

Tsujimoto H., Hara K., Tsukada Y., Huang C.C., Kawashima Y., Arakaki M., Okayasu H., Mimura H., Miwa N., Evaluation of the permeability of hair growing ingredient encapsulated

PLGA nanospheres to hair follicles and their hair growing effects, Bioorganic & Medicinal Chemistry Letters, 17 (2007a) 4771–4777. DOI: 10.1016/j.bmcl.2007.06.057

Tsujimoto H., Hara K., Yokoyama T., Yamamoto H., Takeuchi H., Kawashima Y., Akagi K., Miwa N., Huang C.C., Percutaneous absorption study of biodegradable PLGA nano-spheres via human skin biopsies, Journal of the Society of Powder Technology, Japan, 41 (2004) 867–875. DOI: 10.4164/sptj.41.867

Tsujimoto H., Tsukada Y., Hara K., Kawashima Y., New particle design and its preparation of NFkB decoy oligodeoxynucleotide (NDON) loaded PLGA nanospheres for gene delivery, Journal of the Society of Powder Technology, Japan, 44 (2007b) 453–458. DOI: 10.4164/sptj.44.453

Tsukada Y., Hara K., Bando Y., Huang C.C., Kousaka Y., Kawashima Y., Morishita R., Tsujimoto H., Particle size control of poly(DL-lactide-co-glycolide) nanospheres for sterile applications, International Journal of Pharmaceutics, 370 (2009) 196–201. DOI: 10.1016/j.ijpharm.2008.11.019

Yamamoto H., Hoshina W., Kurashima H., Takeuchi H., Kawashima Y., Yokoyama T., Tsujimoto H., Engineering of poly(DL-lactic-co-glycolic acid) nanocomposite particles for dry powder inhalation dosage forms of insulin with the spray-fluidized bed granulating system, Advanced Powder Technology, 18 (2007) 215–228. DOI: 10.1163/156855207780208592

Yamamoto H., Kurashima H., Katagiri D., Yang M., Takeuchi H., Kawashima Y., Yokoyama T., Tsujimoto H., Poly (lactic-co-glycolic acid) nanosphere composite prepared with Mechanofusion® dry powder composition system for improving pulmonary insulin delivery with dry powder inhalation, Journal of Pharmaceutical Science and Technology, Japan, 64 (2004) 245–253. DOI: 10.14843/jpstj.64.245

Yoshizawa H., Trends in microencapsulation research, KONA Powder and Particle Journal, 22 (2004) 23–31. DOI: 10.14356/kona.2004009

Authors' Short Biographies

Moe Tanaka

Moe Tanaka received her bachelor's degree in pharmacy in 2019 from Osaka University of Pharmaceutical Sciences. As a pharmacist and researcher, she has joined the Pharmaceutical /Beauty Science Research Center in Material Business Division of Hosokawa Micron Corporation in 2019 and engaged in the research and development of skincare and haircare products containing PLGA particles. Her current research interests are in formulation design using PLGA and its application to functional cosmetics.

Ayaka Ochi

Ayaka Ochi received her bachelor's degree in 2018 and master's degree in fermentation chemistry in 2020 from Ehime University, Japan. As a researcher, she has joined the Pharmaceutical /Beauty Science Research Center in Material Business Division of Hosokawa Micron Corporation in 2020. Her current research interests are in skincare and aging care utilizing PLGA nanosphere technology and the development of functional cosmetics as an application of those technologies.

Aiko Sasai

Aiko Sasai is the vice director of the Pharmaceutical /Beauty Science Research Center in Material Business Division of Hosokawa Micron Corporation. She earned her Ph.D. degree in material engineering from Iwate University, Japan in 2009. Since joining Hosokawa Micron Corp. in 2009, she has been engaged in research on PLGA nanoparticles, and has been developing many cosmetics applying PLGA nanoparticle technology.

Authors' Short Biographies

Hiroyuki Tsujimoto

Hiroyuki Tsujimoto is an operating officer of Hosokawa Micron Corp. He received Ph.D. degree in industrial chemistry from Chuo University in 2001. He introduced innovative PLGA nanosphere technologies developed by Prof. Yoshiaki Kawashima of Gifu Pharmaceutical University in 2001. After that, he developed the PLGA nanosphere's applications by participating in 11 government projects. He has authored or coauthored more than 250 technical articles, including 48 refereed journal articles and 22 book chapters. In addition, he has received 11 awards from academia and industry segments on the practical realization of PLGA nanospheres for cosmetics and DDS.

Hitomi Kobara

Hitomi Kobara is a senior researcher of National Institute of Advanced Industrial Science and Technology (AIST). She has studied generation/transformation processes of gas-phase particles and received Ph.D. degree in engineering from Kanazawa University, Japan in 2004. She also has studied electrospray to supply liquid fine particles acting as ultra-small reaction fields, named Femtoreactor®. She has been engaged material synthesis and evaluation using the Femtoreactor® system.

Hiromitsu Yamamoto

Hiromitsu Yamamoto is a Professor in the Laboratory of Pharmaceutical Engineering at Aichi Gakuin University. He received Ph.D. of Pharmacy from Gifu Pharmaceutical University (supervised by Prof. Yoshiaki Kawashima) in 1999. He started research on peptide drug delivery systems using particle carriers as an Assistant Professor at Gifu Pharmaceutical University in 1995. In 2006, he moved to the faculty of school of Pharmacy at Aichi Gakuin University, where he is engaged in research on pharmaceutical engineering based on powder technology and particulate design. He has (co-) authored more than 130 peer-referred papers, 14 review papers and 13 patents.

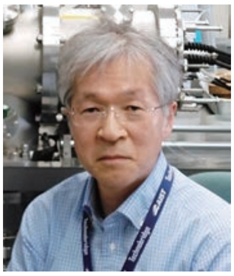

Akihiro Wakisaka

Akihiro Wakisaka is a guest researcher of National Institute of Advanced Industrial Science and Technology (AIST). He received Doctor of Science, Ph.D. from University of Tsukuba in 1988. He started studying the electrospray as an interface of the mass spectrometer to measure the cluster-level structures of solutions in 1995, and then investigated the application of the electrospray to the chemical reaction control. He has organized 6 publicly funded projects (JST and NEDO) concerning about the practical application of the electrospray from 2013 to the present.

KONA Powder and Particle Journal No. 39 (2022) 262–269/https://doi.org/10.14356/kona.2022011 Original Research Paper

Continuous Synthesis of Precision Gold Nanoparticles Using a Flow Reactor[†]

Jiaqi Dong[1], Jonathan Lau[2], Spyros A. Svoronos[3] and Brij M. Moudgil[1*]

[1] *Center of Particulate and Surfactant Systems, Department of Materials Science and Engineering, University of Florida, USA*
[2] *Department of Mechanical Engineering, University of Florida, USA*
[3] *Department of Chemical Engineering, University of Florida, USA*

Abstract

Nanoparticle synthesis using flow chemistry has the potential to enhance the large-scale accessibility of precision-engineered nanomaterials at lower prices. This goal has been difficult to achieve primarily due to reactor fouling and the lack of efficient reagent mixing encountered, especially in those scaled-up systems. The present study aimed to overcome the two challenges by integrating a liquid-liquid biphasic segmented flow system with static mixing. This strategy was applied to the synthesis of gold nanoparticles (AuNPs) using citrate reduction chemistry. It was demonstrated that reactor fouling was eliminated by implementing the biphasic flow strategy. As a result, the overall mean particle size of the as-synthesized AuNPs was measured to be 15.5 nm with a polydispersity index (PDI) of 0.07, and with the reproducibility of ± 6.4 %. The biphasic flow system achieved a reaction yield of 88.7 ± 1.1 % reliably with a throughput of 60 mL/hour up to 8 hours.

Keywords: gold nanoparticles, continuous nanoparticle synthesis, flow chemistry, liquid-liquid biphasic flow, segmented flow

1. Introduction

Nanoparticle synthesis using flow chemistry has attracted significant attention in the last decade because of its potential for automated, low-cost production of high-precision nanomaterials with minimal downtime (Nightingale et al., 2014; Stitt, 2002). The majority of the research in flow synthesis involved the study of single-phase flow in microfluidic systems, in which miscible fluids are continuously introduced into chip-based microfluidic cells under specific flow conditions (Wagner et al., 2008). However, reactor fouling (Schoenitz et al., 2015; Wagner et al., 2004), inefficient mixing (Song et al., 2003b), relatively broad residence time distribution (Trachsel et al., 2005), and relatively low throughput are some of the major challenges encountered in bench-top single-phase microfluidic reactors. They present a great barrier to the precision control over the properties of the synthesized nanoparticles, especially when the system is scaled up. These challenges must be overcome before technology transfer to the industry can occur.

For these reasons, the present work aims to develop a chemical flow reactor that allows the continuous synthesis of high-precision metal nanoparticles with higher throughput. Ultimately, the goal is to generate a knowledge base that would be valuable to flow synthesis of precision nanoparticles on a broader scale.

2. Methods

2.1 Chemistry of gold nanoparticle synthesis

The chemical reaction known as the Turkevich method (Turkevich et al., 1951) was used to synthesize AuNPs. For the conventional batch reaction, a specific volume of 1.0 wt% (34.0 mM) trisodium citrate dihydrate ($Na_3C_6H_5O_7 \cdot 2H_2O$, or NaCt, Sigma-Aldrich) solution was injected into the solution of 0.25 mM gold chloride ($HAuCl_4$, Sigma-Aldrich) at 100 °C under ambient pressure and with vigorous agitation. The molar ratio of NaCt to $HAuCl_4$ is the primary factor that determines the final size and size distribution of the AuNPs (Dong et al., 2020; Frens, 1973). The effects of other parameters were studied with more details in the literature (Polte et al., 2010; Wuithschick et al., 2015).

[†] Received 7 April 2021; Accepted 18 May 2021
J-STAGE Advance published online 22 July 2021

[*] Corresponding author: Brij M. Moudgil;
Add: Gainesville, FL 32611, USA
E-mail: bmoudgil@perc.ufl.edu
TEL: +1-352-846-1194 Fax: +1-352-846-1196

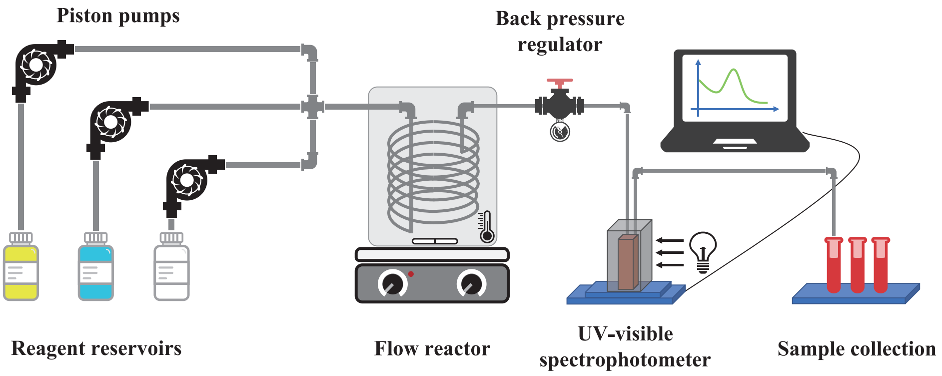

Fig. 1 The layout of the flow reactor system. Note: the diagram is not drawn to scale. The cross junction does not represent the actual fluid junctions used.

2.2 Flow reactor design and setup

The layout of the flow system is illustrated in **Fig. 1**. The reagents were freshly prepared and stored in individual media bottles (Fisherbrand^{TM} Sterile PETG). The continuous synthesis was initiated by introducing the reagents into the tubular reactor using independent piston pumps (Syrris, FRX) with a precisely controlled volumetric flow rate (± 0.01 mL/min). The reagents were joined, mixed, and heated as they flow through the reactor in which the particle synthesis occurred. The reactor temperature was controlled using an oil bath on a hotplate (Syrris, FRX). The pressure inside the reactor was controlled using a needle valve (IDEX, PEEK P-447) as a back-pressure regulator at the outlet of the reactor. The absorption spectrum of the as-synthesized particles was recorded inline when the sample passes through a quartz flow cell (FireflySci, Inc.) in the light chamber of a UV-visible spectrophotometer (Ocean Optics, USB2000+ UV-VIS). Finally, the nanoparticles were collected in centrifuge tubes for further analysis.

The flow reactor integrated an aluminum framework and polymer tubing in a temperature-controlled oil bath, as illustrated in **Fig. 2**. The framework was made of 6061 aluminum (McMaster-Carr, sheet aluminum 6.35 mm thick 30 cm × 13 cm; threaded rod 6.35 mm diameter, 20 cm length; matching hex nuts and washer 6.35 mm screw size). Aluminum was selected because of its temperature tolerance (≤ 150 °C) for long-time service, high corrosion resistance, nonmagnetic nature, and good machinability. Perfluoroalkoxy tubing (PFA, Cole-Parmer, 3.18 mm OD, 1.59 mm ID) was selected due to its chemical compatibility, temperature tolerance (≤ 260 °C), pressure rating (≤ 40.8 bar), and better optical transparency as compared to Teflon^{TM}, polytetrafluoroethylene (PTFE).

2.3 Single-phase continuous flow system

In a typical single-phase flow AuNP synthesis experiment, NaCt (1.7 mM) and $HAuCl_4$ (0.54 mM) solutions were continuously introduced into the flow reactor in parallel. The solutions were merged using a Y-junction (IDEX, PEEK P-514), as shown in **Fig. 3**. The mixture was heated to 100 °C as it flowed through the reactor. The volumetric flow rate of each solution (1 mL/min) was kept constant so that the residence time (8.7 min) ensured that particle synthesis was complete before the sample exited the reactor. The pressure inside the reactor was maintained at 3 bar to minimize bubble formation that would impact the concentration and disrupt the steady-state flow condition. The AuNP suspension was sampled with a 30-min time interval for particle size characterization. Each experiment was continued for 4 hours, and each experiment was repeated three times on different dates.

Fig. 2 Schematic of the flow reactor (framework and tubing).

2.4 Biphasic segmented flow system

The liquid-liquid biphasic segmented flow system, as shown in **Fig. 4**, involved the parallel introduction of two immiscible liquids. The liquid that preferentially wets the surface of the channel is the continuous phase; the other

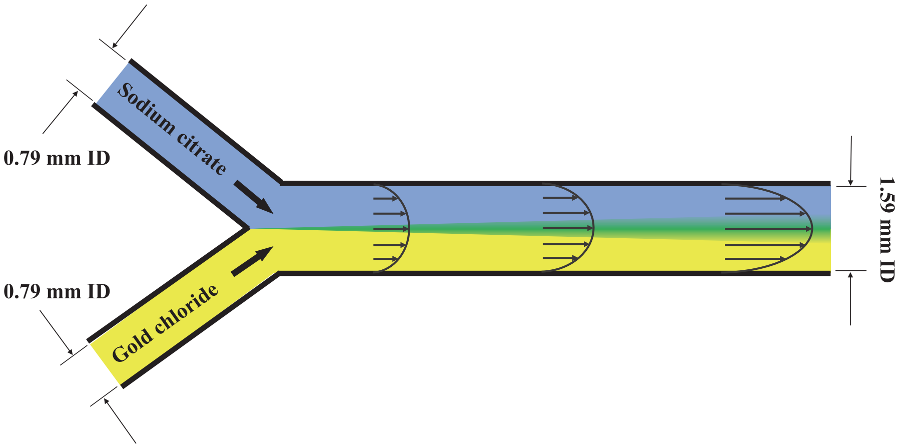

Fig. 3 Schematic of the Y-junction and flow field in single-phasic flow experiment. System: volumetric flow rate ratio of NaCt to $HAuCl_4$ = 1:1; total flow rate = 2.00 ± 0.02 mL/min, reaction temperature = 100 ± 1 °C, pressure = 3 ± 1 bar, molar ratio of NaCt to $HAuCl_4$ = 3.2, Reynolds number ≈ 90.

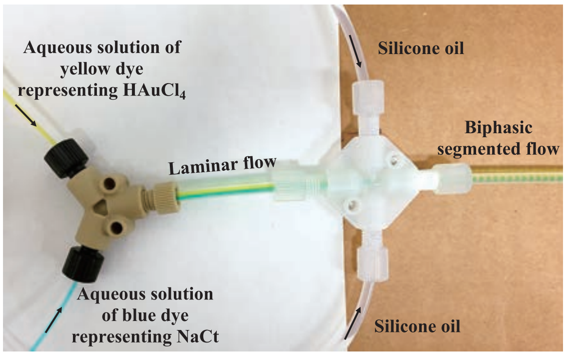

Fig. 4 Experimental setup showing the generation of biphasic segmented flow. The yellow and blue dye represent $HAuCl_4$ and NaCt solutions, respectively. System: volumetric flow rate ratio of NaCt to $HAuCl_4$ to silicone oil = 1:1:2; total flow rate = 2.00 ± 0.04 mL/min, reaction temperature = 100 ± 1 °C, pressure = 3 ± 1 bar, molar ratio of NaCt to $HAuCl_4$ = 3.2, Capillary number ≈ 0.021, Reynolds number ≈ 45 in the laminar flow region.

liquid carried by the continuous phase is the dispersed phase. Segmented flow, also referred to as slug flow in the literature (Baroud et al., 2010; Nightingale and Demello, 2013), is different from droplet flow in which the dispersed droplets exhibit an average size smaller than the channel's inner diameter.

In the biphasic flow experiments, silicone oil (Fisher Chemical^{TM}, viscosity = 45–55 mm^2/s) was selected because of its low surface tension (21.3 ± 0.3 mN/m at ambient temperature (Svitova et al., 2002)), temperature stability (decomposition temperature > 250 °C), and it is chemically inert. As illustrated in **Fig. 4**, silicone oil was introduced from both sides of the cross-junction (IDEX, ETFE P-723). Droplets of aqueous reactants were generated when the aqueous solution was merged with silicone oil. Each aqueous droplet became an individual mini-reactor that was carried by silicone oil. Despite the relatively slow diffusion-limited mixing in the laminar flow region ($Re \approx 45$), ninety percent of reagent mixing could be completed in the mini-reactor in approximately 5 seconds due to the presence of recirculating flow field (Baroud et al., 2010; Bringer et al., 2004; Tice et al., 2003). The detail of the mixing time calculation is provided in the Supplementary Material Section 1. The collected mixture of oil and aqueous AuNP suspension was centrifuged (Eppendorf 5810R, 2000 RCF for 20 min) to expedite the phase separation between oil and water.

2.5 Particle characterization

The mean particle size and size distribution of the collected AuNP samples were characterized using dynamic light scattering (DLS, Malvern Zetasizer Ultra). All measurements were taken at room temperature (22 °C).

3. Results and discussion

3.1 Single-phase flow AuNP synthesis

In general, the AuNP samples synthesized in the single-phase flow experiments did not agree with the reference values of particle size and size distribution (18.1 ± 3.5 nm by intensity distribution (Dong et al., 2020)) based on the DLS measurements as given in **Fig. 5** (UV-vis spectrum analysis and DLS data of individual trials are provided in Supplementary Material Section 2.). The AuNP samples generally exhibited a larger mean particle size (26.9 nm) than the reference value as a consequence of fouling. Besides, the AuNP size increased and became more polydispersed after 90 min. The detection of sub-10 nm nanoparticles suggested the presence of secondary nucleation in the bulk phase. It is possibly caused by a local decrease in the molar ratio of NaCt to $HAuCl_4$ in the bulk phase (Dong et al., 2020), which is due to the imbalanced consumption and competition of reactants from fouling.

3.1.1 Reactor fouling

The increase in the mean particle size and broadening of the size distribution could be attributed to reactor fouling which is an uncontrolled material deposition or growth process on the reactor surface, as shown in **Fig. 6**. Reactor fouling was identified by the change in color and the decrease in optical transparency of the PFA tubing as the experiment progressed. A clean PFA tubing has a translucent and greyish appearance, as illustrated in **Fig. 6(a)**. A black haze could be observed on the tubing 30 min after the experiment began. The transparency of the surface decreased over time. Eventually, the interior surface became covered in purple, red, or gold materials, as highlighted in **Fig. 6(b)**. The observation agreed with Huang et al. (2018), who investigated the deposited materials using X-ray photoelectron spectroscopy and infrared spectroscopy. Their results suggested that the deposited material consisted of metallic gold, unreacted gold, and citrate-gold complex.

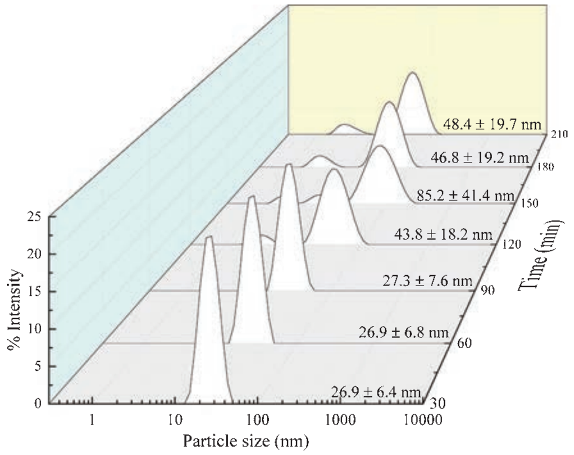

Fig. 5 The DLS measurements of the AuNP samples showed varying particle size and size distribution as a function of time in the single-phase flow experiments. Note: each sample was a pool of collection over 30 min intervals, e.g., Sample 210 was collected from 210 min to 240 min. The measured values represented the particle size and size distribution of the major peak of each sample.

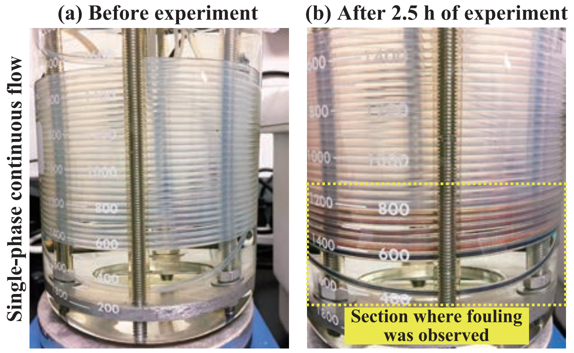
(a) Before experiment **(b) After 2.5 h of experiment**

Fig. 6 **(a)** The clean reactor before the experiment. **(b)** Reactor fouling was observed at the bottom section of the reactor in the single-phase flow experiments. Note: the fouling can be cleaned by flushing aqua regia, followed by deionized water through the reactor after it is cooled to room temperature.

The fouling was observed only at the bottom section of the reactor. It was noticed that the residence time of the fouling section matched with the extent of the chemical reaction (approx. 2.5 min at 100 °C). Based on this observation, it was hypothesized that fouling was caused by heterogeneous nucleation on the reactor surface during the synthesis reaction of AuNPs.

The following experiments were conducted to investigate the proposed hypothesis. First, the flow rate was doubled while keeping other parameters constant. The result showed that the length of the section that exhibited fouling was doubled. In the second experiment, the flow direction in the reactor was changed by switching the inlet and the outlet of the reactor. As expected, the section that exhibited fouling was relocated near the new inlet (upper section) with the same length. In the third experiment, 500 mL of colloidal AuNPs (15 nm in diameter) were synthesized in a batch reactor. The AuNP suspension was then circulated in the flow reactor at the same temperature (100 °C), pressure (3 bar), and flow rate (2 mL/min) for 12 hours. The absorption spectrum of the suspension was continuously monitored; it showed minimal change during the experiment, and no fouling was observed. The colloidal concentration of AuNPs was estimated using the Beer-Lambert law in **Fig. 7**, which suggested less than 2 % loss of nanoparticles due to adsorption on the reactor surface. The results indicated that once the AuNP synthesis reaction was complete, the citrate stabilized AuNPs would not cause fouling.

3.1.2 Strategies to mitigate fouling

Various strategies were reported in the literature to mitigate reactor fouling (Schoenitz et al., 2015), for instance, increasing the flow rate, i.e., shear force at the solid-liquid interface (Wagner and Köhler, 2005; Yang et al., 2007); increasing the electrostatic repulsion between the surface and the depositing materials by tuning pH (Wagner and Köhler, 2005); modifying the wettability of the reactor surface (Wagner and Köhler, 2005); and implementing coaxial fluid injection (Baber et al., 2015). A few of these

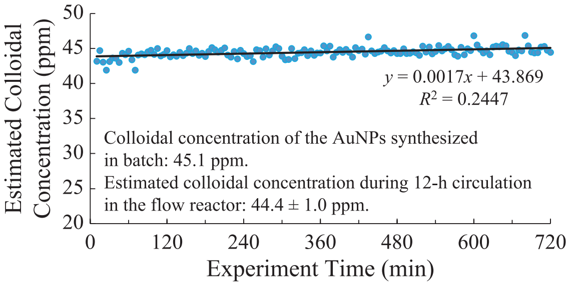

Fig. 7 The colloidal concentration of the fully synthesized and stabilized AuNPs exhibited minimal change while circulating in the flow reactor for 12 hours. System: temperature (100 ˚C), flow rate (2 mL/min), pressure (3 bar), initial concentration (45.1 ppm).

strategies were investigated, including the test of different reactor materials (glass vs. Teflon^{TM}), different surface roughness, and increasing the flow rate up to 5 mL/min. However, these methods were found to be ineffective in the present study. An alternative strategy (Shestopalov et al., 2004) involving the biphasic flow system was investigated to overcome fouling.

3.2 Biphasic flow AuNP synthesis

When silicone oil was introduced in the flow system, it was noticed that fouling was no longer visible during the AuNP synthesis, as shown in **Fig. 8**. The reason was suspected to be the elimination of direct physical contact between the aqueous phase and the reactor surface due to the presence of the oil phase (Shestopalov et al., 2004).

3.2.1 Particle size and size distribution

The AuNP synthesis in the biphasic segmented flow system resulted in much better reproducibility than the single-phase flow system, as demonstrated in **Fig. 9**. The overall mean particle size from the biphasic experiments was 15.5 ± 4.1 nm (from the intensity distribution of DLS measurements), which agreed with the reference value (18.1 ± 3.5 nm (Dong et al., 2020), *p* ≈ 0.26). The particle size distribution, represented by the error bar in **Fig. 9**, also showed a significant improvement in the precision of the nanoparticles (tabular data is provided in the Supplementary Material Section 2 and on J-STAGE Data website).

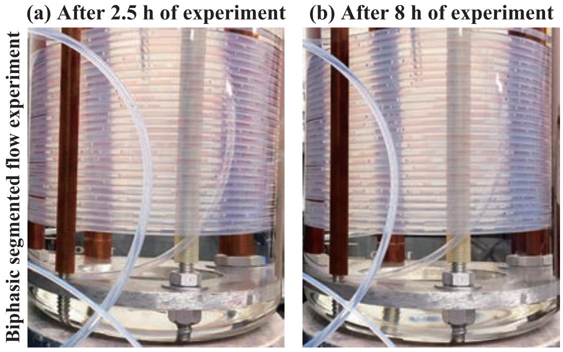

Fig. 8 Reactor fouling was not observed within **(a)** 2.5 hours or **(b)** 8 hours in the biphasic flow experiments (aqueous reactants dispersed in silicone oil).

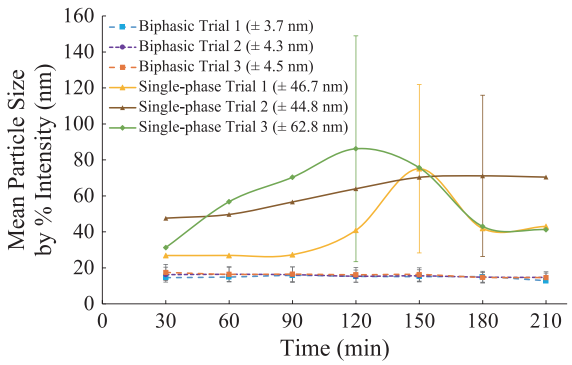

Fig. 9 The DLS measurements of the mean particle size of the AuNPs synthesized in biphasic flow experiments was reproducible and consistent with the reference value (18.1 ± 3.5 nm). The particle size distribution is presented for each trial by showing the highest standard deviation of the data points of that trial. The raw DLS data is available publicly at https://doi.org/10.50931/data.kona.15022002

3.2.2 Reaction yield

The reaction yield was calculated from the experimental and the theoretical colloidal concentration. The experimental concentration of the AuNP samples was estimated based on the Beer-Lambert law and the calibration curve using UV-vis absorption spectrum and ICP-MS data (Dong et al., 2020). The theoretical concentration was calculated with the assumption of 100 % conversion from the reactant to the product in the AuNP synthesis reaction.

In the biphasic flow experiments, the colloidal concentration of AuNPs resulted in a constant value of 46.5 ± 0.5 ppm, which was approximately 88 % of the theoretical value compared to a maximum of 83 % in the single-phase experiments, as shown in **Fig. 10**. The decrease in the yield in the single-phase reaction systems can be attributed to reactor fouling that alters the physical and chemical nature of the surface (PFA) so that heterogeneously nucleation on the reactor surface becomes more favorable.

3.2.3 Reliability of the biphasic flow system

A biphasic flow experiment was continuously run for over 8 hours without reactor fouling, as shown in **Fig. 8(b)**. The DLS data plotted in **Fig. 11** shows that the mean particle size of the AuNP samples was maintained at 16.9 ± 3.7 nm, which was consistent with the reference value (18.1 ± 3.5 nm (Dong et al., 2020), *p* ≈ 0.59) and the previous biphasic experiment results (15.5 ± 4.1 nm). The

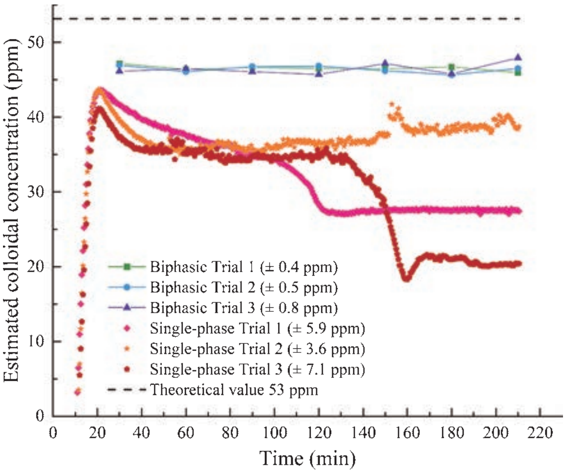

Fig. 10 The colloidal concentration of the AuNP samples from the biphasic flow experiments was maintained constantly and reproducibly at 46.5 ± 0.5 ppm, which was approx. 88 % of the theoretical value.

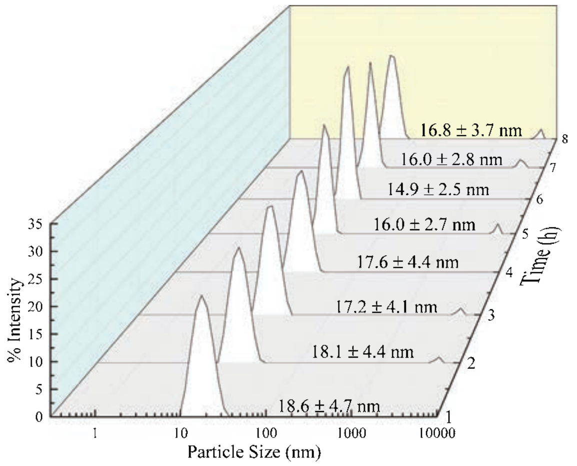

Fig. 11 The DLS measurements of particle size and size distribution of the AuNP samples collected in an uninterrupted biphasic flow experiment. System: molar ratio of citrate to gold (3.2), temperature (100 ˚C), pressure (3 bar), flow rate (2 mL/min), volumetric flow rate ratio of oil to water (1:1), residence time (8.7 min).

colloidal concentration was also maintained at the same value, 46.4 ± 0.7 ppm, equivalent to a percentage yield of 87.5 ± 1.3 %.

3.2.4 Precision (size distribution) of AuNP

The precision of nanoparticles, i.e., size distribution, was quantified using the polydispersity index (PDI) (ISO13321, 1996; Malvern, 2011). PDI can be calculated using Eq. (1) (NanoComposix, 2015). The average PDI of the samples synthesized in biphasic flow experiments (0.12 ± 0.02) was lower by nearly one order of magnitude than the single-phase flow experiments (1.02 ± 0.43).

$$PDI = \left(\frac{Standard\ deviation}{Mean\ particle\ size}\right)^2 \tag{1}$$

The improvement of particle size precision in the biphasic flow system can be attributed to the enhanced reagents mixing efficiency due to the recirculating flow field inside each aqueous segment (Song et al., 2003a). The time required to complete the reagent mixing in each droplet depends on the channel size, the droplet size, and the traveled distance. The average mixing time was estimated to be approximately 5 seconds. Detailed calculation is provided in the Supplementary Material Section 1.

The mixing by diffusion generally becomes less efficient as the reactor channel size increases (Stitt, 2002). To overcome this challenge, an inline static mixer was implemented. Based on the concept of packed bed column reactors, a packed bed static mixer (PBSM) was fabricated by filling yttria-stabilized zirconia beads (80 μm in diameter) in the PFA tubing. The PBSM was installed ahead of the fluid junction that introduced silicone oil, as illustrated in the graphic abstract. Statistical analysis indicated that the PDI of the AuNP samples was reduced by an additional 40 % with the implementation of the PBSM ($p \approx$ 2E-9), as shown in **Table 1**.

Table 1 Comparison of polydispersity index (PDI) of the AuNP samples synthesized using the biphasic flow system under specific conditions.

	PDI	SD
Reference value, batch method	0.065	0.009
Without static mixing, Fresh oil	0.119	0.021
With static mixing, Fresh oil	0.068	0.008
With static mixing, Recycled oil	0.079	0.018

For the purposes of developing a greener and more sustainable process, preliminary experiments using recycled silicone oil were conducted. The used silicone oil was separated from the aqueous phase using a separation funnel, then cleaned by centrifugation and vacuum filtration, and reused in the subsequent experiments. Using the recycled silicone oil resulted in a 16 % increase in PDI ($p \approx$ 4E-3) while the mean particle size remained unaffected ($p \approx 0.37$). It was noticed that the samples generated from the experiments using the recycled oil had a higher degree of oil contamination possibly due to thermal degradation of the silicone oil.

4. Conclusions

In the present study, gold nanoparticles (AuNPs) were continuously synthesized in a flow reactor using citrate reduction chemistry. Reactor fouling was a major problem in the single-phase experiments, which affected the consistency, reproducibility, and precision control of the AuNP size, size distribution, and reaction yield. The main reason for fouling was ascribed to the occurrence of the heterogeneous nucleation reaction in the vicinity of the reactor surface, leading to growth and accumulation of materials there. The fouling problem was solved by introducing a water-immiscible silicone oil to the system that preferentially wetted the reactor surface. Compared with the single-phase flow system, the AuNPs produced in the biphasic flow experiments exhibited significantly narrower size distribution (PDI: 0.07 ± 0.01), higher and more consistent yield (approx. 88 %), and reproducibility of ± 6.4 % to the mean particle size.

Future research is suggested for inline particle functionalization using secondary reactors and further scale-up of the present reactor system. It could be achieved by increasing the overall flow rate, increasing the chemical concentration, and utilizing parallel channels. One of the major challenges encountered in the scaled-up flow system was inefficient reagent mixing. For precision AuNP synthesis, it was critical to ensure that the mixing was completed before the reaction began. Other challenges could be maintaining the flow stability at a higher flow velocity, maintaining the stability of AuNPs, and homogenizing the heat and mass transfer and pressure across parallel channels. Overall, the knowledge base developed in the present study should enable designing scalable systems for commercially viable larger-scale production of precisely engineered nanomaterials.

Acknowledgment

This work was primarily supported by the National Science Foundation (NSF Award No. 1602032) and our industrial partner OndaVia, Inc. Any opinions, findings, and conclusions or recommendations expressed in this material were those of the author(s) and did not necessarily reflect the views of the NSF or OndaVia, Inc. The authors want to acknowledge and express gratitude to Paul Carpinone (formerly University of Florida, UF), Gary Scheiffele (UF), and Bahar Basim (formerly UF) for their advice and assistance.

Data Availability Statement

The raw DLS data is available publicly in J-STAGE Data (https://doi.org/10.50931/data.kona.15022002).

References

Baber R., Mazzei L., Thanh N.T.K., Gavriilidis A., Synthesis of silver nanoparticles in a microfluidic coaxial flow reactor, RSC Advances, 5 (2015) 95585–95591. DOI: 10.1039/c5ra17466j

Baroud C.N., Gallaire F., Dangla R., Dynamics of microfluidic droplets, Lab on a Chip, 10 (2010) 2032–2045. DOI: 10.1039/c001191f

Bringer M.R., Gerdts C.J., Song H., Tice J.D., Ismagilov R.F., Microfluidic systems for chemical kinetics that rely on chaotic mixing in droplets, Philosophical Transactions of the Royal Society A: Mathematical, Physical and Engineering Sciences, 362 (2004) 1087–1104. DOI: 10.1098/rsta.2003.1364

Dong J., Carpinone P.L., Pyrgiotakis G., Demokritou P., Moudgil B.M., Synthesis of precision gold nanoparticles using Turkevich method, KONA Powder and Particle Journal, 37 (2020) 224–232. DOI: 10.14356/kona.2020011

Frens G., Controlled nucleation for the regulation of the particle size in monodisperse gold suspensions, Nature Physical Science, 241 (1973) 20–22. DOI: 10.1038/physci241020a0

Huang H., Toit du H., Besenhard M.O., Ben-Jaber S., Dobson P., Parkin I., Gavriilidis A., Continuous flow synthesis of ultrasmall gold nanoparticles in a microreactor using trisodium citrate and their SERS performance, Chemical Engineering Science, 189 (2018) 422–430. DOI: 10.1016/j.ces.2018.06.050

ISO13321 I.S., Methods for determination of particle size distribution part 8: photon correlation spectroscopy, International Organisation for Standardisation (ISO), 1996.

Malvern, Dynamic light scattering—common terms defined, Malvern Guides, 2011 (2011) 1–5.

NanoComposix, NanoComposix's guide to dynamic light scattering measurement and analysis, NanoComposix, 1.4 (2015) 1–8.

Nightingale A.M., Demello J.C., Segmented flow reactors for nanocrystal synthesis, Advanced Materials, 25 (2013) 1813–1821. DOI: 10.1002/adma.201203252

Nightingale A.M., Phillips T.W., Bannock J.H., De Mello J.C., Controlled multistep synthesis in a three-phase droplet reactor, Nature Communications, 5 (2014) 3777. DOI: 10.1038/ncomms4777

Polte J., Ahner T.T., Delissen F., Sokolov S., Emmerling F., Thünemann A.F., Kraehnert R., Mechanism of gold nanoparticle formation in the classical citrate synthesis method derived from coupled in situ XANES and SAXS evaluation, Journal of the American Chemical Society, 132 (2010) 1296–1301. DOI: 10.1021/ja906506j

Schoenitz M., Grundemann L., Augustin W., Scholl S., Fouling in microstructured devices: a review, Chemical Communications, 51 (2015) 8213–8228. DOI: 10.1039/c4cc07849g

Shestopalov I., Tice J.D., Ismagilov R.F., Multi-step synthesis of nanoparticles performed on millisecond time scale in a microfluidic droplet-based system, Lab on a Chip, 4 (2004) 316–321. DOI: 10.1039/b403378g

Song H., Bringer M.R., Tice J.D., Gerdts C.J., Ismagilov R.F., Experimental test of scaling of mixing by chaotic advection in droplets moving through microfluidic channels, Applied Physics Letters, 83 (2003a) 4664–4666. DOI: 10.1063/1.1630378

Song H., Tice J.D., Ismagilov R.F., A microfluidic system for controlling reaction networks in time, Angewandte Chemie—International Edition, 42 (2003b) 768–772. DOI: 10.1002/anie.200390203

Stitt E.H., Alternative multiphase reactors for fine chemicals: a world beyond stirred tanks?, Chemical Engineering Journal, 90 (2002) 47–60. DOI: 10.1016/S1385-8947(02)00067-0

Svitova T., Theodoly O., Christiano S., Hill R.M., Radke C.J., Wetting behavior of silicone oils on solid substrates immersed in aqueous electrolyte solutions, Langmuir, 18 (2002) 6821–6829. DOI: 10.1021/la020006x

Tice J.D., Song H., Lyon A.D., Ismagilov R.F., Formation of droplets and mixing in multiphase microfluidics at low values of the Reynolds and the capillary numbers, Langmuir, 19 (2003) 9127–9133. DOI: 10.1021/la030090w

Trachsel F., Günther A., Khan S., Jensen K.F., Measurement of residence time distribution in microfluidic systems, Chemical Engineering Science, 60 (2005) 5729–5737. DOI: 10.1016/j.ces.2005.04.039

Turkevich J., Stevenson P.C., Hillier J., A study of the nucleation and growth processes in the synthesis of colloidal gold, Discussions of the Faraday Society, 11 (1951) 55–75. DOI: 10.1039/DF9511100055

Wagner J., Kirner T., Mayer G., Albert J., Köhler J.M., Generation of metal nanoparticles in a microchannel reactor, Chemical Engineering Journal, 101 (2004) 251–260. DOI: 10.1016/j.cej.2003.11.021

Wagner J., Köhler J.M., Continuous synthesis of gold nanoparticles in a microreactor, Nano Letters, 5 (2005) 685–691. DOI: 10.1021/nl050097t

Wagner J., Tshikhudo T.R., Köhler J.M., Microfluidic generation of metal nanoparticles by borohydride reduction, Chemical Engineering Journal, 135 (2008) S104–S109. DOI: 10.1016/j.cej.2007.07.046

Wuithschick M., Birnbaum A., Witte S., Sztucki M., Vainio U., Pinna N., Rademann K., Emmerling F., Kraehnert R., Polte J., Turkevich in new robes: key questions answered for the most common gold nanoparticle synthesis, ACS Nano, 9 (2015) 7052–7071. DOI: 10.1021/acsnano.5b01579

Yang S., Zhang T., Zhang L., Wang S., Yang Z., Ding B., Continuous synthesis of gold nanoparticles and nanoplates with controlled size and shape under UV irradiation, Colloids and Surfaces A: Physicochemical and Engineering Aspects, 296 (2007) 37–44. DOI: 10.1016/j.colsurfa.2006.09.017

Authors' Short Biographies

Jiaqi Dong

Jiaqi Dong received his B.S. in Materials Science and Engineering from the Illinois Institute of Technology in 2013. He then attended the University of Florida as a graduate student and received his M.S. in Materials Science and Engineering in 2016. Currently, he is a Ph.D. candidate under the supervision of Dr. Brij Moudgil and Dr. Bahar Basim at the Center for Particulate and Surfactant Systems (CPaSS). His current research focus is metallic nanoparticle synthesis and functionalization using flow chemistry.

Jonathan Lau

Jonathan Lau is currently a student at the University of Florida. He is expecting to complete a B.S. in Mechanical Engineering in 2022. He has conducted undergraduate research under the supervision of Ph.D. candidate Jiaqi Dong and Dr. Brij Moudgil at the Center for Particulate and Surfactant Systems (CPaSS). His current research interests are fluid flow and computational fluid dynamics. He has previous industry experience with GE Aviation in 2019, Cummins in 2021, and Texas Instruments in 2021.

Spyros A. Svoronos

Dr. Spyros A. Svoronos is the Harry & Bertha Bernstein Professor of Chemical Engineering at the University of Florida. He received his B. A in Chemistry from Oberlin College and his M.S. and Ph.D. degrees in Chemical Engineering from the University of Minnesota. His current research interests are in modeling and optimization of a variety of processes, including bioreactors and nanoparticle synthesis. In addition, he is developing low-cost Arduino-controlled experimental equipment for teaching laboratories. He has published more than 70 technical papers and has been awarded four patents.

Brij M. Moudgil

Dr. Brij M. Moudgil is a Distinguished Professor of Materials Science and Engineering at the University of Florida. He received his B.E from the Indian Institute of Science, Bangalore, India, and his M.S. and Eng.Sc.D degrees from Columbia University, New York. His current research interests are in surfactant and polymer adsorption, dispersion and aggregation of fine particles, adhesion, and removal of microbes from surfaces, synthesis of functionalized nanoparticles, anti-scaling and surfactant mediated corrosion inhibitors, photocatalytic degradation of hazardous microbes, and nanotoxicity. He has published more than 400 technical papers and has been awarded over 25 patents. He is a member of the U.S National Academy of Engineering.

KONA Powder and Particle Journal No. 39 (2022) 270/https://doi.org/10.14356/kona.2022006 Addition/Correction

Author Correction: Analysis of Industry-Related Flows by Optical Coherence Tomography—A Review[†]

Antti I. Koponen[1*] **and Sanna Haavisto**[2]

[1] *VTT Technical Research Centre of Finland Ltd., Finland*
[2] *Spinnova Ltd., Finland*

Correction to: KONA Powder and Particle Journal No. 37 (2020) 42–63, https://doi.org/10.14356/kona.2020003, published on 10 January 2020.

On page 45 the sentence after Eq. (2) should be: The maximum measurable velocity can be increased by increasing the measurement angle α between the DOCT beam and the velocity vector.

On page 45 **Fig. 3c** should be:

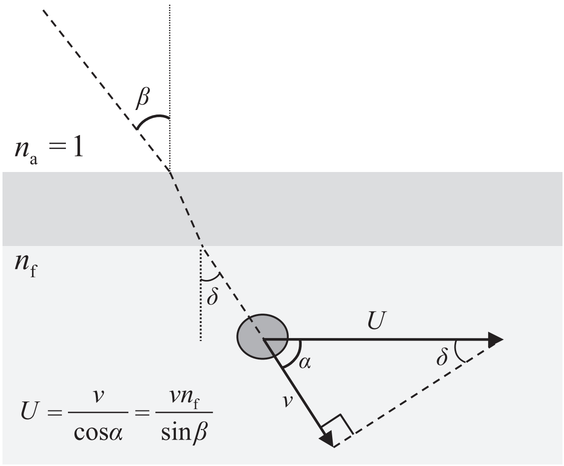

Fig. 3 **c)** A closer look at the measurement optics. Here U is the real velocity, v is the component of velocity in the direction of the measurement beam, and n_f is the refractive index of the medium. Angle α is obtained by calculating first angle δ by applying the Snell's law of refraction to the two interfaces.

On page 46 the paragraph related to Eq. (3) should be: **Fig. 3b** shows as an example a measurement setup of pipe flow. From **Fig. 3c**, we get the real axial velocity in the pipe to be

$$U = \frac{vn_f}{\sin\beta} \tag{3}$$

where β is the DOCT measurement angle (the angle between the camera axis and pipe surface normal), v is the velocity given by the DOCT device, and n_f is the refractive index of the monitored medium. Similar reasoning also works, e.g., for plate-plate and bob and cup rheometer geometries.

The mistakes were found by the authors after the paper was published online. The authors apologize for the inconvenience to readers and editors by this oversight. The results and conclusions of this paper were not affected by the errors.

[†] Received 18 February 2021; Accepted 24 February 2021
J-STAGE Advance published online 20 March 2021

[1] P.O. Box 1603, FIN-40401 Jyväskylä, Finland
[2] Palokärjentie 2-4, FIN-40320 Jyväskylä, Finland
[*] Corresponding author: Antti I. Koponen;
E-mail: antti.koponen@vtt.fi
TEL: +358-20-722-2717 FAX: +358-20-722-2720

WETSUS, 2020, 256 p.
ISBN: 978-1-71663-242-6,
DOI: 10.20850/9781716632426

Book Review

“Synthetic Nano- and Microfibers”, edited by R. Martijn Wagterveld, Jan C.M. Marijnissen, Leon Gradon and Arkadiusz Moskal

Global production of fibrous material is significantly growing with expectation of reaching 145 million metric tons in 2030. Production includes mostly synthetic polymers fibers, cotton fibers and man-made cellulosic (viscose) fibers. A smaller contribution comes from animal-made fibers (wool, silk). The main uses of fibrous material are in clothing, household and furnishing, industrial construction, automotive and other.

Increasing consumption of fabric material causes the accumulation of single fibers into the natural environment. Significant numbers of fibers are discharged into wastewater from washing clothes, deposition from atmosphere or by other ways of transport. Fibers are now the most prevalent type of anthropogenic particles found by microplastic pollution surveys around the world. Substantial concentration of fibers has been detected in surface water, deep-sea and fresh water ecosystems. As a consequence, fibers are present in food, drinking water, human lungs and digestive tracts of aquatic animals. Currently, there is great concern for the release of plastic nano-and micro fibers and micro-particles (microplastics) to the natural environment for which nobody knows, so far, the ultimate consequences for health and ecological homeostasis.

The potential risk introduced by the presence of fibers in the environment induces significant interests of researchers in this problem as becomes clear from an increasing number of publications related to microplastics. The aforementioned challenges were the source of inspiration for organization a workshop.

During November 4 and 5, 2019, a group of scientists from different parts in the world met at Wetsus, the European Centre of Excellence for Sustainable Water Technology in Leeuwarden the Netherlands, to discuss all known aspects of synthetic nano- and microfibers. This includes the morphology, physicochemical properties, production and origin of nano/micro fibers entering the atmosphere, water and food chain; the potential consequences of inhalation and ingestion for human health, and exposure and ingress via life cycle for aquatic biota; analytical and measurement methods; techniques to clean air and water, and protection means against inhalation or other ways to enter the human body. The group of top-experts from different disciplines, but all involved with small fibers, gathered to share their view from scientific, technical and health perspective, presented their subject of expertise, contributed to the discussion and made their contribution into a chapter for the book: “Synthetic Nano- and Microfibers”.

The chapters in this book have been placed in a logic sequence, starting with the statement of the problem, properties of small fibers, fibrous particle identification, via environmental and health issues, and ending with possible cleaning methods. It is very evident that still much is not known and that in each discipline more must be investigated. For almost each sub-research program reliable on-line measuring techniques are indispensable. We assume that this book presents the state of the art and will give directions on how to proceed to answer the many remaining questions. It is indisputable that it is essential to work together with all involved subdisciplines.

Table 1 Contents

Day One

Day Two

Author’s Short Biography

Jan Marijnissen

Jan C.M. Marijnissen is a former Associate Professor and Head of the Aerosol Laboratory at Delft University of Technology, the Netherlands, and a PERC visiting Professor at the University of Florida, USA. He is a visiting Professor at the University of Nairobi, Kenya. He has been an advisor for Wetsus, European Centre of Excellence for sustainable water technology in Leeuwarden, the Netherlands and is an advisor for the University of Applied Science in Leeuwarden, the Netherlands. Jan Marijnissen received a Master degree from Delft University of Technology and a Ph.D. degree in environmental engineering from the University of Minnesota, U.S.A.. He has more than 45 years of experience in the field of mine-ventilation and aerosol science and technology and is especially involved in the development of advanced aerosol measuring instrumentation, air cleaning methods and the production of particles via aerosol routes. He has (co)authored many articles, is co-editor of eight books on aerosols, and holds several patents. He is a member of several associations and a former president of the European Aerosol Assembly.

The 8th APT (Asian Particle Technology Symposium) 2021 Held in Osaka

The 8th APT (Asian Particle Technology Symposium) 2021 was held at Grand Front Osaka from Monday, October 11th to Thursday, October 14th, 2021. This APT was launched mainly by the Japanese Society of Powder Technology, Japan in order to promote the development of the powder technology in Asia and the exchange of researchers in this field. The first meeting was held in December 2000 in Bangkok, the capital of Thailand. It has been held about once every three years, but this is the first time it is held in Japan. The Hosokawa Powder Technology Foundation supported this symposium as part of its grant projects of the fiscal year 2021.

In the opening remarks on the first day, Professor Satoru Watano, Osaka Prefecture University, the chairperson of the symposium, reported that the venue of this symposium had to be changed just before holing it due to the sudden official decision to use the reserved facility for the vaccination to control the COVID pandemic. He explained about the situation which required to take the style of hybrid conference using both face-to-face and online communication. He announced that despite such strict conditions, there were more than 300 presentations and more than 400 applications for participation from home and abroad. The symposium began with the plenary lecture by Professor Makio Naito of Osaka University. At the symposium, the lectures and research presentations were given for four days using five hall/rooms, until after 6 o’clock in the evening on the longest day, and there was also a live question-and-answer session with active discussions.

At this symposium, the “Young KONA Award” was set for young researchers under the age of 40 as part of the 30th anniversary specific projects of the Hosokawa Powder Technology Foundation. About 40 presentations applied for this award, which were reviewed on the second day. From these applicants, six researchers were selected as the awardees. The whole process concerning this award was managed by the Organizing Committee of this symposium, from application reception to screening and awarding, under the auspices of the Hosokawa Powder Technology Foundation. Then, before the closing on the 14th, the final day, there was an award ceremony in the main hall of the venue. President Yoshio Hosokawa handed each award winner a letter of presentation and a supplementary prize.

In the closing remarks, the Chairperson Professor Watano reported that most of the research presentations were made as scheduled and it was a great success. Although it was difficult for researchers overseas to attend face-to-face meeting, they could join the symposium virtually. It was then announced that the next symposium would be held in Brisbane, Australia in three years, and the next chairpersons sent online invitation messages.

The venue for the symposium, Grand Front Osaka. The conference room was on the second basement floor.

Lecture scene, opening remarks being given by Chairperson Prof. Watano.

Young KONA Award presentation ceremony. President of Hosokawa Powder Technology Foundation, Mr. Hosokawa (center left in the photo), Symposium Chairperson, Prof. Watano (center right in the photo) and six winners.

KONA Powder and Particle Journal No. 39 (2022) 276/https://doi.org/10.14356/kona.2022024 Information Article

The KONA Award 2020

The KONA Award 2020 was presented to Dr. Brij M. Moudgil, Distinguished Professor of Materials Science and Engineering at the University of Florida, USA. Overall goal of his research program has been to develop science and technology platforms for the design and synthesis of nanostructured material with targeted performance and safety specifications. Specifically, controlling nano and atomic scale forces between particles, and synthesis of functionalized particles has formed the foundation for targeted advances in minerals, advanced materials, biomedical, microelectronics, health & hygiene, energy, agriculture, sensor, nanotoxicity and antimicrobial coating technologies.

He has served as Director of the Particle Engineering Research Center (PERC - formerly the National Science Foundation Engineering Research Center for Particle Science & Technology) since its inception in 1994. He has also served as Associate Vice President for Interdisciplinary Research Programs at UF from 2004 to 2012, with the primary responsibilities of promoting new interdisciplinary research teams, evaluating over 160 university centers and institutes, and serving as a liaison with several U.S. funding agencies. He has been invited as an evaluator of individual and team funded research proposals and interdisciplinary research centers, by funding agencies across the continents.

Dr. Moudgil has strongly supported and enthusiastically promoted particle technology related research and education opportunities, and challenges. He has invited world class research scholars to PERC from all over the globe and has mentored several visiting young scientists and post-doctoral students including several of them from Japan. He feels truly privileged to have had the opportunity to work with a talented group of students, research scientists & staff, visiting research scholars, faculty colleagues, domestic and international collaborators, and industry researchers. He is proud of his team members achievements – a number of whom continue to make pioneering research and leadership contributions in the private sector and in the academic institutions alike. Over the years, he has forged strategic alliances for research and education between UF-Particle Engineering Research Center and the other institutions that have common vision and complimentary expertise in particulate systems including University of Leeds, UK; Kyoto University, Japan; University of Melbourne, Australia; Delft University of Technology, The Netherlands; Indian Institute of Technology-Bombay, India, and CMRDI, Cairo, Egypt.

He has been invited as a plenary and keynote speaker at conferences and seminars in Japan, Europe, India, South Korea, Egypt, South America and Australia. He has authored/co-authored 13 books and has been awarded 31 patents. He has served as 2006 President of the Society for Mining, Metallurgy and Exploration, Inc. (SME). His contributions have been recognized with several honors and awards including the NSF Presidential Young Investigator Award (NSF-PYI), APT Distinguished Paper Award, Fellow of the National Academy of Inventors (NAI), Fellow of the American Association for the Advancement of Science (AAAS), Fellow of the Indian National Academy of Engineering (INAE), Distinguished Alumnus Award of the Indian Institute of Science, Bangalore (IISc), and Member of the National Academy of Engineering (NAE), USA. Overall, Dr. Brij M. Moudgil has made pioneering contributions to particle and powder technology research and education and is most deserving of the prestigious KONA award.

Selected research achievements for the KONA Award 2020: Interfacial engineering of particulate system for enhanced performance.

KONA Powder and Particle Journal No. 39 (2022) 277/https://doi.org/10.14356/kona.2022025 Information Article

General Information

History of the Journal

The KONA journal (currently called "KONA Powder and Particle Journal") was first published in 1983 by the Council of Powder Technology, Japan (CPT), which had been established in 1969 by Hosokawa Micron Corporation as a nonprofit organization to promote powder technology, in order to introduce excellent Japanese papers to the world. From the issue of No.8, the CPT changed its editorial policy to internationalize the KONA journal and to incorporate papers by authors throughout the world. In response to this change, three editorial blocks have been organized in the world: Asian-Oceanian, American and European. The issues from No.1 (1983) to No.12 (1994) of the KONA were published by the CPT and the issues from No.13 (1995) by the Hosokawa Powder Technology Foundation. The policy and system have not changed even after the Hosokawa Foundation has taken over the publication from the CPT. From the issue of No.27 (2009), publication of translated papers has been terminated and only original papers have been published.

Aims and Scope

KONA publishes review and original research papers in a broad field of powder & particle science and technology, ranging from fundamental principles to practical applications. The papers on critical reviews of existing knowledge in special areas are very welcome.

The submitted papers are published only when they are judged by the Editor to contribute to the progress of powder science and technology, and approved by any of the three Editorial Committees.

The paper submitted to the Editorial Secretariat should not have been previously published.

Category of Papers

- Invited articles
  Review papers and feature articles invited by the KONA Editorial Committees.
- Contributed papers
  Original review papers and some limited number of original research papers of high quality submitted to the KONA Editorial Committees, and refereed by the reviewers and editors.

Submission of Papers

It is now possible to submit your paper online via **Editorial Manager® for KONA Online Paper Submission and Peer Review System**. For all further information, please go to the journal's homepage on http://www.kona.or.jp/jp/journal/info.html.

Publication in KONA is free of charge.

Publication Schedule

KONA is published annually. The publication date is around January 10th.

Subscription

KONA is distributed free of charge to senior researchers at universities and laboratories as well as to institutions and libraries in the field throughout the world. The publisher is always glad to consider the addition of names of those, who want to obtain this journal regularly, to the mailing list.

Instructions to Authors

(1) Language

All submissions should be written in good English. Authors may choose either British or American English, provided that the chosen style is used consistently. Authors from non-English-speaking countries are encouraged to use a professional English editing service to proofread their manuscript.

(2) Data Repository Information

In order to promote open data discoverability and use of research outputs, this journal encourages authors to submit the data files supporting your manuscript work, which can be deposited in the journal's J-STAGE Data site <https://jstagedata.jst.go.jp/kona> after acceptance of the paper through the peer-review process.

These data may describe observations, experiments, modeling or analyses and may take the form of databases, simulations, movies, large figures or as otherwise appropriate.

If you have any questions or would like more information, please contact the KONA Editorial Office (contact_zainq@hmc.hosokawa.com).

(3) Manuscript format

- Electric files should be submitted to the Editorial Secretariat by online. Authors' short biography with less than 100 words per person and color photographs of all the authors should be attached to the final version.
- The structure of manuscripts should follow the following order; title, authors, affiliations, abstract, graphical abstract, keywords, main text, (acknowledgement), (appendix), (nomenclature), references. The items with parentheses are not mandatory.
- Full postal addresses must be given for all the authors. Indicate the corresponding author by the asterisk mark"*" after the name. Telephone and fax numbers and e-mail address should be provided for the corresponding author.
- Abstract should not exceed 200 words.
- Graphical abstract should be a concise, visual summary of the article which will be displayed in the contents list both online and print.
- The appropriate number of keywords is 5 or 6.
- The maximum pages printed in KONA are supposed to be:
  15 for an original paper and 25 for a review paper.
- Symbols and units should be listed in alphabetical order with their definition and dimensions in SI units.
- The color figures will appear in color both on the KONA Website (http://www.kona.or.jp) and also in the paper version.
- Concerning references, the alphabetical system should be adopted. Please use reference management software such as Endnote to manage references as far as possible.

  List: References should be arranged first alphabetically and then further sorted chronologically if necessary. More than one reference from the same author(s) in the same year must be identified by the letters "a", "b", "c", etc., placed after the year of publication.

  Examples:

  - Reference to a book:
    Strunk Jr. W., White E.B., The Elements of Style, fourth ed., Longman, New York, 2000.
  - Reference to a chapter in an edited book:
    Mettam G.R., Adams L.B., How to prepare an electronic version of your article, in: Jones B.S., Smith R.Z. (Eds.), Introduction to the Electronic Age, E-Publishing Inc., New York, 2009, pp.281–304.
  - Reference to a journal publication:
    Tsuji Y., Tanaka T., Ishida T., Lagrangian numerical simulation of plug flow of cohesionless particles in a horizontal pipe, Powder Technology, 71 (1992) 239–250. DOI: 10.1016/0032-5910(92)88030-L

  Text: All citations in the text should refer to:

  1. Single author: the author's name (without initials, unless there is ambiguity) and the year of publication;
  2. Two authors: both authors' names and the year of publication;
  3. Three or more authors: first author's name followed by "et al." and the year of publication.

  Citations may be made directly (or parenthetically). Groups of references should be listed first alphabetically, then chronologically.

  Examples:

  > "as demonstrated (Hidaka J. et al., 1995; Tsuji Y., 1992a, 1992b, 1993). Mori Y. and Fukumoto Y. (2002) have recently shown ...."

(4) Copyright and permission

- The original paper to be submitted to KONA has not been published before in any language or in any journals or media; it is not submitted and not under consideration for publication in whole or in part elsewhere.
- Authors are responsible for obtaining permission from the copyright holders to reproduce any figures, tables and photos for which copyright exists.
- The KONA Journal applies the Creative Commons Attribution License to all works published by the Journal. Copyright stays with the agreed copyright owner, and the Hosokawa Powder Technology Foundation is granted the exclusive right to publish and distribute the work, and to provide the work in all forms and media.
- Users of the journal will be able to reuse the contents in any way they like, provided they are accurately attributed. No permission is required from either the authors or the publisher.

Free electronic publication of KONA is available at http://www.kona.or.jp


picoline
HOSOKAWA ALPINE


MAJSx2
MIKRO AIR JET SIEVE
HOSOKAWA MICRON

HOSOKAWA MICRON GROUP

The Hosokawa Micron Group will always be the leading global company covering the mountain range of Powder Technologies. The Group has been a pioneer in the filed of powder and particle processing and blown film processing. We provide R&D, engineering, manufacturing and services in various fields of the world's major industrial markets.

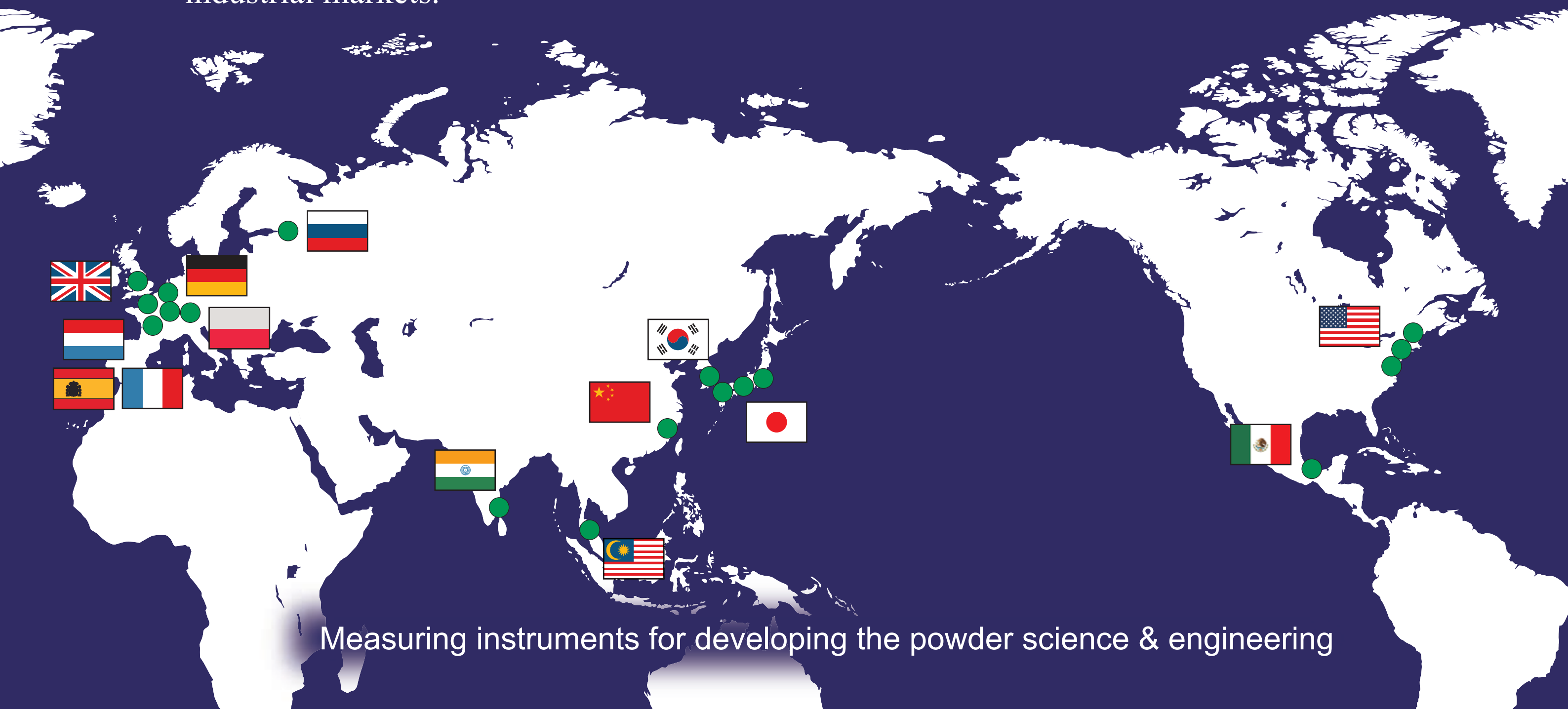

Measuring instruments for developing the powder science & engineering

Dynamic Particle Image Analyzer
Parshe Analyzer

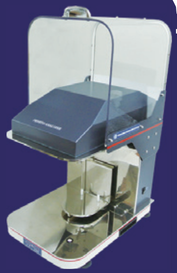

Penetration speed
Peneto Analyzer, PNT-N

Carr's indicies
Powder characteristics tester, PT-X

Wet sieving
Viblette, VBL-F

Process Technologies for Tomorrow

HOSOKAWA MICRON CORPORATION

Headquaters Location :
HOSOKAWA MICRON CORPORATION
https://www.hosokawamicron.com/